

Université de Montréal

**Plaques de glace permanentes : étude de leurs caractéristiques intrinsèques et
de leurs effets sur la dynamique hydrologique et biogéomorphologique des
versants du désert polaire arctique**

Par

Gautier DAVESNE

Département de Géographie

Faculté des Arts et Sciences

Thèse présentée à la Faculté des études supérieures

en vue de l'obtention du grade de

Philosophiæ Doctor (Ph.D.) en Géographie

Septembre 2021

© Gautier Davesne, 2021

Université de Montréal

Département de Géographie, Faculté des Arts et Sciences

Cette thèse intitulée

**Plaques de glace permanentes : étude de leurs caractéristiques intrinsèques et
de leurs effets sur la dynamique hydrologique et biogéomorphologique des
versants du désert polaire arctique**

Présentée par

Gautier DAVESNE

A été évaluée par un jury composé des personnes suivantes

Julie Talbot
Présidente-rapporteur

Daniel Fortier
Directeur de recherche

Christophe Kinnard
Membre du jury

Derek Mueller
Examinateur externe

Étienne Léveillé-Bourret
Représentant du doyen

Résumé

Les plaques de glace forment de petites masses de glace et de neige permanentes qui sont considérées comme un stade intermédiaire dans le continuum neige-glacier. Elles sont omniprésentes dans les régions polaires, ce qui leur confère une fonction centrale dans l'hydrologie et la géomorphologie des versants. Pourtant, très peu d'études s'y sont intéressées jusqu'à présent. Acquérir des connaissances sur ces plaques apparaît donc essentiel, non seulement pour comprendre leurs caractéristiques intrinsèques, mais aussi parce que cela ouvre des perspectives importantes pour comprendre la dynamique du géosystème polaire. Afin de répondre à ce besoin, cette thèse cherche à établir l'origine et le fonctionnement des plaques de glace à l'île Ward Hunt (Haut-Arctique canadien) et d'en comprendre les effets sur la dynamique de versant du désert polaire. Cette recherche sur les plaques de glace a été guidée par une approche multidisciplinaire, conduisant à des études glaciologiques, nivologiques, hydrologiques et biogéomorphologiques.

Nos résultats ont montré que les plaques de glace se développent par l'aggradation de glace surimposée qui se forme suite au regel de l'eau de fonte à la base de l'accumulation de neige saisonnière. La texture et les propriétés physiques de cette glace varient en fonction de son âge et de l'intensité des processus de recristallisation. La variabilité spatio-temporelle des plaques de glace est principalement contrôlée par la topographie locale et les conditions micrométéorologiques. En hiver, les apports en neige dans les niches topographiques où se forment les plaques de glace sont assurés par le vent. En été, l'intensité de l'ablation est fortement influencée par le vent et le brouillard, qui modulent les échanges d'énergie à la surface des plaques. L'évolution des plaques de glace se caractérise par une stabilité à long terme due à un mécanisme d'autorégulation du bilan de masse assuré par le contexte topoclimatique. Cependant, en raison de leur petite taille, les plaques de glace peuvent disparaître rapidement lorsque l'ablation estivale dépasse un seuil à partir duquel les conditions topoclimatiques ne peuvent plus assurer leur préservation. À Ward Hunt, la présence des plaques de glace depuis au moins plusieurs siècles fait qu'elles ont fortement contribué au développement des versants. Les apports durables en eau et sédiments qui en découlent en été ont enclenché une suite de processus abiotiques et biotiques azonaux dans les marges pronivales. Il en a résulté la formation de systèmes biogéomorphologiques qui consistent en des lobes de solifluxion et des milieux humides colonisés par de la végétation et

un couvert de croute biologique. Les modifications morphologiques et physiques du sol en aval des plaques de glace influencent le régime thermique de surface et les profondeurs de dégel. En outre, le développement des zones humides entraîne une modification locale des propriétés physiques de la neige en exacerbant le métamorphisme cinétique qui aboutit à la croissance d'une couche de givre de profondeur à la base du manteau neigeux.

En apportant une compréhension holistique des plaques de glace polaires, cette thèse permet des avancées empiriques et conceptuelles importantes qui contribuent à mieux comprendre la dynamique du géosystème de désert polaire à un moment charnière où ces environnements subissent en transition rapide en réponse au changement climatique.

Mots-clés : Plaque de glace, Neige, Cryosphère, Nivation, Désert polaire, Solifluxion, Hydrologie, Évolution des versants, Île Ward Hunt

Abstract

Ice patches are small perennial masses of ice and snow that are considered as part of the continuum between seasonal snow and glacier. They are ubiquitous in the Polar Regions, which gives them an important function in slope hydrology and geomorphology. Ice patches have, however, received very little scientific attention so far. Gaining new knowledge on these cryospheric elements thus appears essential, not only to understand their intrinsic characteristics, but also because it holds important perspectives for understanding the dynamics of the polar geosystem. To address this need, this thesis aims to investigate the origin and functioning of the ice patches at Ward Hunt Island (Canadian High Arctic) and to understand their effects on polar desert slope dynamics. This research on ice patches was guided by a multidisciplinary approach, involving glaciological, snow, hydrological and biogeomorphological studies.

Our results demonstrated that ice patches develop through the aggradation of superimposed ice that forms by the refreezing of meltwater at the base of the seasonal snowpack. The texture and physical properties of this ice vary according to its age and the intensity of recrystallization processes. The spatio-temporal variability of ice patches is mainly controlled by local topography and micrometeorological conditions. In winter, the snow supply to the topographic niches where ice patches form is provided by the wind. In summer, the intensity of ablation is strongly influenced by wind and fog, which modulate energy exchange at the surface of the patches. The evolution of ice patches is characterized by long-term stability due to a self-regulating mass balance mechanism provided by the topoclimatic context. However, because of their small size, ice patches can disappear very quickly when summer ablation exceeds a threshold at which topoclimatic conditions can no longer ensure their preservation. At Ward Hunt Island, the presence of the ice patches for at least several centuries makes them important drivers of slope development. Sustained meltwater and sediment supplies delivered by ice patches to their proximal margin have triggered a sequence of abiotic and biotic azonal processes. This led to the formation of a biogeomorphic system, consisting of solifluction lobes and humid zones colonized by vegetation and an organic crust cover. Morphological and physical changes in the soil downslope of the ice patches influenced the surface thermal regime and thaw depths. Furthermore, our results show that the humid zone development leads to a local modification of the physical properties of snow by enhancing kinetic metamorphism responsible for the growth of a depth hoar layer at the base of the snowpack.

Through a comprehensive understanding of polar ice patches and their effects, this thesis provides important empirical and conceptual advances that contribute to a better understanding of polar desert geosystem dynamics at a pivotal time when these environments are undergoing a rapid transition in response to climate change.

Keywords : Ice patch, Snow, Cryosphere, Nivation, Polar desert, Solifluction, Hydrology, Slope evolution, Ward Hunt Island

Table des matières

Résumé	iv
Abstract.....	vi
Table des matières	viii
Liste des tableaux	xv
Liste des figures	xvii
Liste des sigles et abréviations.....	xxxi
Remerciements	xxxviii
Avant-propos	xli
Chapitre 1 – Introduction générale	1
1.1. Mise en contexte	1
1.2. Structure de la thèse.....	4
1.3. État des connaissances	6
1.3.1. Historique de la recherche sur les plaques de glace.....	6
1.3.2. Définition floue et multiplicité des termes	7
1.3.3. De la neige saisonnière à la glace permanente	12
1.3.4. Bilan de masse d'un système de plaque de glace	15
1.3.5. Les plaques de glace et le contexte climatique régional	27
1.3.6. Conclusion sur l'état des connaissances	30
1.4. Approche, hypothèse et questions de recherche	31
1.5. Objectifs et axes de recherche	33
1.6. Pertinence du projet de recherche.....	34
1.6.1. Force et originalité de la thèse	34
1.6.2. Contributions et retombées scientifiques de la recherche.....	35

1.7. Présentation générale du site d'étude	37
1.7.1. Le désert polaire.....	37
1.7.2. L'île Ward Hunt et ses environs	40
Chapitre 2 – Properties and stratigraphy of polar ice patches in the Canadian High Arctic reveal their current resilience to warm summers	44
2.1. Avant-propos	44
2.2. Résumé	44
2.3. Abstract.....	45
2.4. Introduction	46
2.5. Study site	49
2.6. Materials and methods.....	50
2.6.1. Seasonal snowpack characterization	51
2.6.2. Ice sampling procedure.....	52
2.6.3. The crystalline structure of the ice	53
2.6.4. Gas and sediments inclusions in the ice	54
2.6.5. Environmental monitoring.....	56
2.7. Results	56
2.7.1. Seasonal snow accumulation over the ice patches	56
2.7.2. Perennial ice properties	59
2.8. Discussion.....	66
2.8.1. Snow stratigraphy and metamorphism over the ice patches.....	66
2.8.2. Structural characteristics and origin of the ice patches.....	68
2.8.3. Mechanisms of the ice formation.....	74
2.8.4. A long-term preservation of ice patches at WHI?	78
2.9. Conclusions	81

2.10. Acknowledgments.....	82
2.11. Appendices A1	84
Appendix A1-1: Snow pits	84
Appendix A1-2: Drilling procedure	84
Appendix A1-3: Thin section procedure	84
Appendix A1-4: CT-scan technology and image analysis	85
Appendix A1-5: Calculation of ice crystal kinetic growth.....	86
2.12. Supplementary material S1	88
Chapitre 3 – Mass balance and ablation processes of a perennial ice patch on the northern coast of Ellesmere	97
3.1. Avant-propos	97
3.2. Résumé	97
3.3. Abstract.....	98
3.4. Introduction	100
3.5. Study site	102
3.6. Instrumentation and data acquisition.....	105
3.6.1. Snow regime	105
3.6.2. Mass balance variables	105
3.6.3. Environmental monitoring during the melt season	108
3.6.4. Surface Energy balance	109
3.6.5. Spatio-temporal distribution of late summer ice-snow surfaces	110
3.7. Results	112
3.7.1. Snow and wind regimes.....	112
3.7.2. Mass balance variables at the ice patch IP1.....	114
3.7.3. Surface energy balance	118

3.7.4. Spatio-temporal evolution of the ice patch and late summer snow patches at the scale of Ward Hunt Island	123
3.8. Discussion.....	127
3.8.1. Main mass gain to the ice patch system	127
3.8.2. Factors controlling the summer ablation	129
3.8.3. Spatial distribution of the ice patches at the landscape scale	133
3.8.4. Sensitivity of the ice patches to climate change	134
3.9. Conclusion.....	138
3.10. Acknowledgements	139
3.11. Appendices A2	141
Appendix A2-1: Ground Penetrating radar (GPR).....	141
Appendix A2-2: Terrestrial Laser Scanning (TLS).....	141
Appendix A2-3: Time-lapse photograph.....	142
Appendix A2-4: Wind speed estimation	142
Appendix A2-5: Surface Energy Balance	143
Appendix A2-6: Topographical variables derived from a DEM	145
Appendix A2-7: Longterm air temperature reconstruction	146
Appendix A2-8: Map of turbulent sensible heat flux	146
3.12. Supplementary material S2.....	148
Chapitre 4 – Ice patches and their biogeomorphic system in the High Arctic polar desert	162
4.1. Avant-propos	162
4.2. Résumé	162
4.3. Abstract.....	163
4.4. Introduction	165
4.5. Study site	167

4.6. Methods	169
4.6.1. UAV-based mapping of the pronival margin of the ice patch.....	169
4.6.2. Instrumentation and field measurements.....	169
4.7. Results	173
4.7.1. Geomorphic assemblage of the pronival margin	173
4.7.2. Hydrology and meltwater quality of the pronival zone of IP1	176
4.7.3. The ground thermal regime of pronival margin.....	180
4.7.4. Soil and ecological studies.....	182
4.8. Discussion.....	188
4.8.1. Water and mass transfers related to the ice patch system.....	188
4.8.2. Functioning of the biogeomorphic system of ice patch.....	191
4.8.3. Various stages of development of slope below an ice patch	194
4.8.4. Long-term evolution of the studied pronival slope.....	198
4.9. Conclusion	199
4.10. Acknowledgments.....	200
4.11. Appendices A3	202
Appendix A3-1: UAV surveys and image processing	202
Appendix A3-2: Water discharge and quality	203
Appendix A3-3: Canonical Correspondence Analysis.....	203
Appendix A3-4: Sediment analysis in the laboratory.....	204
4.12. Supplementary material S3	205
Chapitre 5 – Effects of meteorology and soil moisture on the spatio-temporal evolution of the depth hoar layer in the polar desert snowpack	215
5.1. Avant-propos	215
5.2. Résumé	215

5.3. Abstract.....	216
5.4. Introduction	217
5.5. Study site	219
5.6. Methods	221
5.6.1. Snow studies	221
5.6.2. Environmental Monitoring	224
5.7. Results	226
5.7.1. Small-scale variability of the snow height.....	226
5.7.2. Snow physics	228
5.7.3. Monitoring data.....	231
5.8. Discussion.....	235
5.8.1. Mechanism of DH formation.....	235
5.8.2. Characteristics of the snow season 2018/19	237
5.8.3. Small-scale variability of DH	238
5.8.4. Factors controlling DH spatial variability in 2018/19	239
5.8.5. The inter-annual variability in the DH development.....	242
5.9. Conclusion.....	244
5.10. Acknowledgments.....	246
5.11. Supplementary material S4	247
Chapitre 6 – Conclusion générale et perspectives	255
6.1. Synthèse des résultats et avancées scientifiques.....	255
6.1.1. L'origine et les mécanismes de formation des plaques de glace (Obj. 1) ...	256
6.1.2. Les facteurs de contrôle spatio-temporels du bilan de masse des plaques de glace (Obj. 2)	257
6.1.3. Évolution sur le long terme des plaques de glace : entre résilience et vulnérabilité aux changements climatiques (Obj. 2)	258

6.1.4. Le rôle central des plaques de glace dans le géosystème de désert polaire (Obj. 3 et 4) 259	
6.2. Plaques de glace et géosystème polaire en transition	262
6.2.1. Vers une disparition des plaques de glace permanentes?	262
6.2.2. Changement de régime et réactions en chaîne.....	262
6.3. Recommandations pour de futurs travaux :.....	265
Références bibliographiques	269

Liste des tableaux

Table 1. Mean (\pm SD) of major axis, crystal surface area, roundness (inverse of the aspect ratio) and density of the upper and lower section of IP1 and IP2. In addition, the same data were obtained for the ice samples collected at the bottom of the seasonal snowpack on IP1 (IS#1), on the freshly exposed ice near the frontal margin on IP1 (IS#2) and IP2 (IS#3), and on the side of a supra-ice channel on IP1 (IS#4). Values in parentheses are the number of samples for which the hydrostatic density was measured. See Figure S8 for examples of photographs of thin sections of ice samples. X means the horizontal plan while Z means the vertical plan of ice cores.....	58
Table 2. Summary of physical properties of the ice found in perennial and semi-permanent ice patches (modern and buried) in various environments. For the crystal shape: Eq =Equidimensionnal; Poly = polygonal; Ir=irregular and El = elongated. For the bubble shape: Sb= Spherical bubble; SSb= Sub-spherical bubble; Ecb= Elongated cylindrical bubble; Irb = Irregular bubble. For sediment: Si= Silt; Sa= sand and Gr= gravel. References: [1] Østrem (1963); [2] Wakahama and Narita (1975); [3] Lewkowicz and Harry (1991); [4] Meulendyk et al. (2012); [5] Lacelle et al. (2009); [6] Hirvas et al. (2000); [7] Yamamoto and Yoshida (1987); [8] This study. “n.d.” means “no data”.	69
Table 3. Climate of the Ellesmere Island’s northern coast (Ward Hunt Island and Alert) relative to other polar desert localities of the Canadian High Arctic, Greenland and Antarctica for the period 1980-2019, unless for Ward Hunt (2006-2019). Mean annual air temperature (MAAT), Mean summer and winter air temperature (MAT _s and MAT _w , mean annual precipitation and mean annual and summer relative humidity (RH _{annual} and RH _S). Summer averages are calculated for Jun-Jul-Aug for Northern Hemisphere sites and Dec-Jan-Feb for Southern Hemisphere sites, and conversely for winter averages (Source: CEN, 2021; Environment Canada, 2021; www.ncdc.noaa.gov/cdo-web/ ; Doran and Fountain, 2019).104	
Table 4. Summary of remote sensing data used. Sources: National Air Photo Library, of the U.S. Geological Survey, Pax Arctica and Planet Action Initiative © NSPO 2008 - National Space Organization, TaiwanDistribution Spot Image S.A., France All rights reserved.	111
Table 5. Cover of vascular plants (by species), non-vascular taxa, organic crust (black and white) and inorganic soil surface (gravel/barren soil and freshly deposited sediments) in each of the	

four habitat types that characterized the downslope margin of the ice patch IP1, namely the central tread and external treads of the lobes which are humid zones, and lateral risers as well as the parent slope. Sign “ < ” means a cover <0.1 %. Values in brackets indicate the proportion of the total vascular plant cover for each habitat. Species names were retrieved from the Integrated Taxonomic Information System (ITIS) (<http://www.itis.gov>).....185

Liste des figures

Figure 1. Photographie aérienne illustrant l'omniprésence des plaques de neige et de glace dans le désert polaire de l'île Devon au Nunavut (Canada) prise le 23 juillet 2019.....3

Figure 2. Exemples de petites masses de glace permanentes entrant dans la catégorie de « plaque de glace ». a) et b) Plaques de glace de Juvfonne et Langfonne situées dans le sud de la Norvège (Ødegård et al., 2017 ; Pilø et al., 2021) ; c) Plaque de glace située dans le nord de la Finlande, désignée comme « permanent snowfield » par les auteurs (Hirvas et al., 2000) ; d) Plaque de glace de Hamaguri - yuki dans les Alpes Japonaises, désignée comme « snow patch » par les auteurs (Fujita et al., 2010); e) et f) Plaques de glace dans les Alpes Juliennes dans le massif du Pirins en Europe centrale (Gachev et al, 2016 ; Colucci et al., 2021). Pour a,b,c,d, les plaques de glace appartiennent au système morphodynamique nival tandis que pour e et f, les plaques de glace appartiennent au système morphodynamique glaciaire (Serrano et al., 2011).....10

Figure 3. Les deux systèmes morphodynamiques de plaque de glace : le système glaciaire et le système nival (modifié de Serrano et al., 2011).11

Figure 4. Subdivision de la zone d'accumulation d'un glacier selon les conditions de surface (neige, névé, glace exposée) à la fin de la saison de fonte. Zone A : zone de neige sèche où il n'y a pas de fonte estivale. Zone B : zone de percolation, les eaux de fonte de surface s'infiltrent dans le manteau neigeux et régèlent. Zone C : zone de saturation (ou zone de neige humide) où la température de l'ensemble du manteau neigeux a atteint le point de fusion à un moment donné de la saison de fonte et où l'eau de fonte atteint l'interface neige-glace et y régule pour former de la glace surimposée. La limite inférieure de la zone de saturation est appelée la ligne de névé. Zone D : zone où l'ensemble de la neige saisonnière fond avant la fin de la saison de fonte et où la glace surimposée est exposée à la fonte. La ligne d'équilibre est située à la limite inférieure de cette zone et relie tous les points où le bilan annuel net est nul. L'altitude de cette ligne est appelée altitude de la ligne d'équilibre (Equilibrium-line altitude : ELA). La zone de glace de glacier correspond à la zone d'ablation où la fonte estivale élimine la totalité de l'accumulation annuelle de neige et glace de surimposée. L'encadré rouge indique la section d'un glacier où les processus d'accumulation et de fonte sont similaires à ceux impliqués dans le bilan de masse d'une plaque de glace (inspiré de Paterson, 1994)..13

Figure 5. Schématisation du concept de bilan de masse net (Paterson, 1994)	15
Figure 6. Diagrammes représentant les contextes topographiques favorables à développement d'accumulations préférentielles de neige.....	17
Figure 7. Redistribution de la neige saisonnière par des processus éoliens amenant à la formation d'accumulations préférentielles de neige (inspiré de Pomeroy et al., 1997).	18
Figure 8. Conceptualisation du bilan d'énergie d'un couvert nival saisonnier sur une plaque de neige (inspiré de Garen et Marks, 2005 ; Ohmura, 1984)	22
Figure 9. Conceptualisation des différents mécanismes d'autorégulation du bilan de masse des plaques de glace. a) Rétroaction entre les accumulations de neige en hiver et l'espace disponible dans la niche topographique à la fin de l'été précédent ; b) Rétroaction entre l'ablation et l'exposition aux rayonnements solaires ; c) Rétroaction entre l'ablation et l'exposition au vent (inspiré de Glazirin et al, 2004).	26
Figure 10. Différence entre la ligne d'équilibre régionale des glaciers (ELA-R), déterminée par les conditions climatiques (c.-à-d. la température estivale et les précipitations hivernales) et la ligne d'équilibre locale des glaces et neiges permanentes (ELA-L), principalement contrôlée par la topographie et le vent (modifié de Dahl et al., 2003).	27
Figure 11. Représentation du gésystème de désert polaire dans lequel les plaques de glace jouent un rôle central.	32
Figure 12. Représentation schématique des 4 axes de recherche autour desquels la thèse s'articule (modifié de Davesne te al., 2019).	34
Figure 13. Carte circumpolaire délimitant la zone de désert polaire arctique selon l'isotherme 5°C en juillet et l'isohyète de précipitation annuelle inférieure à 250 mm. Le site d'étude de cette recherche, l'île Ward Hunt, représente la base de recherche la plus septentrionale en Arctique.	38
Figure 14. Carte de localisation de l'île Ward Hunt à l'échelle circumpolaire (a) et à l'échelle de l'île d'Ellesmere (b). c) Localisation de l'île Ward Hunt au large du fjord de Disraeli, le long de la côte nord de l'île d'Ellesmere. Autour de l'île, la cryosphère est omniprésente avec notamment les restes de la plateforme glaciaire de Ward Hunt (Ward Hunt Ice Shelf, WHIS) et un dôme de glace (Ward Hunt Ice Rise, WHIR) ; b) Image World-View 3 de l'île Ward Hunt capturée le 19 août 2019. Le centre de l'île est occupé par le lac Ward Hunt et sa couverture de glace désormais pluriannuelle (Paquette et al., 2015). Les multiples plaques de	

glace permanentes et les plaques de neige représentent les seuls éléments de la cryosphère terrestre visibles depuis la surface.	41
Figure 15. Location of Ward Hunt Island (WHI) at the northern tip of Ellesmere Island (a, b); WHIS: Ward Hunt Ice Shelf; WHIR: Ward Hunt Ice Rise (delimitation of the end of summer 2012). GeoEye satellite image (c) taken on 26 August 2011. The red squares indicate the investigated ice patch 1 (IP1) and ice patch 2 (IP2). The GeoEYE image shows the ice patches at their minimal extent at the end of the warm summer 2011 which was marked by the complete disappearance of the perennial ice cover on Ward Hunt Lake (WHL) for the first time since observations began in the 1950s (Paquette et al., 2015).....	50
Figure 16. Oblique photograph taken from helicopter showing the ice patches selected for this study: IP1 (transverse ice patch) and 2 (circular ice patch). The snow analysis and ice coring were undertaken in summers 2016 and 2017. The extent of the ice patches at the end of the particularly warm summer 2011 was inferred from the GEOEYE image shown in Figure 15 . Details of snowpits, ice cores and ice samples are presented in Table S1 in the supplementary material.	51
Figure 17. Investigation of the ice properties through a) ice crystal analysis using thin sections and b) gas and sediment inclusion analysis using microtomodensitometry (CT-scan).....	54
Figure 18. Graphical representation of the stratigraphy and physical properties of the seasonal snowpack measured over perennial ice patches. Snowpits Sp1_17a and Sp2_17 (a and b) were dug on IP1 and IP2, respectively, in early June 2017, the snowpit Sp1_16 (c) was dug one year earlier (7 June 2016) at the same site than Sp1_17a and the snowpit Sp1_17a (d) was dug on 2 July 2017 close to the site of Sp1_17a. Snow-type symbols are those used by Fierz et al. (2009) and Domine et al. (2018a). The horizontal grey lines represent the stratigraphic discontinuities that delimit the different layers observed in the snowpack.	57
Figure 19. Evolution of the daily air and ice surface temperature, of the daily snow depth (inferred from the SILA station) and of the temperature gradient in the snowpack on IP1 through the cold season 2016/17 calculated from Equation 2.1. Vertical dash lines delimit the three periods in the temperature gradient evolution. “Sp” during period 3 shows when snow pits were dug.....	59
Figure 20. Physical description of the ice cores retrieved at the IP1 (a) and IP2 (b) sites. A is the crystal surface area, D1 and D9 are 10th percentile and the 90th percentile, respectively; Lx	

- and L_z are the maximum length of the ice crystals for the horizontal plane (X-plane) and vertical plane (Z-plane), respectively; ρ_i is the ice density, V and C are the bubble volume and bubble concentration, respectively.....61
- Figure 21.** Summary of the ice porosity, and the bubble size distribution, bubble volume and bubble concentration in the upper and lower sections of IP1 and IP2. V is the bubble volume. The red line in the box plot is the median, the black cross is the mean and the circles represent the outliers.....63
- Figure 22.** Examples of the various forms of sediment inclusions found in the ice; a) A band of suspended sediments at 45 cm depth in the upper section of IP1; b) A thin layer of fine-grained sediments at 145 cm (lower section) depth in IP2; c) A 2 cm thick band of compact fine-grained sediments at 135 cm depth (lower section) in IP2; d) A 15 cm thick band of ice-bonded gravel and sand at 190 cm depth in IP1; e) Brown coloration of ice sample IS #2 collected in the seasonal fringe of IP1 due to suspended very fine sediments; f) Mix of gravels and fine-grained sediments frozen in the side of a supra-ice channel on IP1.....64
- Figure 23.** Thermal regime of the perennial ice patch IP1; a) Mean monthly and annual ice temperature profile averaged over the two years of record (July 2017-June 2019) from the 320 cm deep borehole drilled in IP1 (Fortier and Davesne, 2021b); b) Daily evolution of ice temperature at various thermistor depths and b) Daily evolution of the air temperature and snow depth provided by SILA station between July 2017 and June 2019 (CEN, 2021). The snow depth dataset was corrected by a multiplication coefficient (x1.5) to be representative of the maximal snow depth measured on IP1.....65
- Figure 24.** Automatic time-lapse photographs of the ice patch IP1. Photo (a) was taken in the late summer 2017 (2017-08-06), during which most of the ice patch surface consisted of exposed ice after particularly warm conditions. Photo (b) was taken at the end of the cool summer 2018 (2018-08-08) during which a thick seasonal snowpack remained over the ice surface to form a firn layer. The red line delineates the seasonal snow extent from the exposed ice surface.....66
- Figure 25.** Vertical variation of the estimated age of the ice derived from the normal grain growth law in solid-phase for Unit 2 of the ice patch IP1 (a) and IP2 (b). The black curve represents the age profile at current ice temperature (see **Figure 23**) and the blue curve represents the

age profile with ice temperature 2°C colder than today. The grey bands indicate core sections with clear-ice facies where ice crystal size is partly the result of water freezing processes. 73

Figure 26. Conceptual model of ice aggradation on a polar ice patch system: a) Seasonal snow accumulation at the end of the cold season; b) Early stage of warming phase; c) Advanced stage of warming phase; d) Ripening phase; e) End of the melt season after a strong ablation resulting in the complete disappearance of the seasonal snow (case 1); f) End of the season after weak ablation resulting in the persistence of part of the seasonal snow layer that forms firn layer with the fall freeze-back (case 2). 75

Figure 27. Observations of sediment deposits on ice patches IP1 and IP2. a) Niveo-aeolian deposits emerging on the seasonal snow surface over IP2 in mid-June 2017; b) Fine-grained sediment retained in the snow porosity (filtering effect) and incorporated in the superimposed ice in the downslope edge of IP1 at the end of June 2019; c) Zoom in on the newly formed superimposed ice (black square in b) where entrapped fine-grained sediment are visible; d) Silty-sand deposits (up to 5 cm thick) in the inlet of a rill flow in the upper edge of IP1 due to snow filtering (early July 2019); e) Slush flow transporting silty to coarse sandy material over the ice surface of IP1 (mid-July 2019); f) Streamflow carved in perennial ice revealing large pebbles incorporated in blue ice (site where the sample IS#4 was collected). 77

Figure 28. a) Map showing the ~2.7 million km² of the ice-free land surface characterized as polar desert in the circumpolar Arctic (annual precipitation <250 mm and July temperature <5 °C). The black line delineates Ellesmere Island, which is the northernmost large island of the Canadian Arctic Archipelago, and the black circles locate weather stations of the arctic desert detailed in **Table 3**. 1: Ward Hunt Island (Ca); 2: Alert (Ca); 3: Eureka (Ca); 4: Resolute Bay (Ca); 5: Mould Bay (Ca); 6: Station Nord (Dk); b) Localization of Ward Hunt Island (WHI) 6 km north of the nearest shore of Ellesmere Island and about 760 km from the North Pole; c) Topographic map of WHI (10 meter contours) showing the Ward Hunt Lake (WHL), the Ward Hunt Ice Rise (WHIR), the field station and the SILA weather station managed by the CEN. The red square indicates the location of the studied ice patch at the foot of the north face of Walker Hill. 103

Figure 29. 3D view of the studied ice patch (IP1). Red lines indicate the snow-depth measurement transects and blue dotted lines indicate the GPR profile. The black cross locates the AWS installed during field season 2019, the red triangle shows the site where the air temperature

was recorded in 2017 and the blue polygons indicate the location of the cut-throat flumes in the downslope margin of IP1. The background image is an orthomosaic captured with an unmanned aerial vehicle (UAV) on 17 July 2019.106

Figure 30. Snow and wind regimes recorded at SILA station from 2006 to 2019; a) Time-series of the daily snow height (incomplete data in 2010/11, 2011/12, 2014/15) and wind index (WI) of the cold season (Sept-May) (red crosses; incomplete wind data in 2006/07, 2007/08, 2010/11 and 2011/12). The wind index represents the cumulative maximum hourly wind speed $> 6 \text{ m s}^{-1}$, for the cold season (Sep-May). The green line represents the mean maximum snow height from 2006 to 2019; b) Wind rose of the cold season (Sept-May) constructed from hourly wind data for the 2006-2019 period; c) Close up on cold seasons 2015/16, 2016/17, 2017/18 and 2018/19 showing the hourly snow height and daily WI.113

Figure 31. Average evolution of the snow regime throughout the cold season in the snow patch at the SILA station for the period 2006-2019. a) Mean monthly snow gains and losses (including erosion and compaction) and the resulting net mass balance and b) mean monthly snow height expressed as a proportion of the total end-of-winter snow height (SH_{\max}) and the number of snowdrift events ($\Delta\text{SH} > 5\text{cm}$) as a proportion of the total number of potential blowing snow events ($V_{\max} > 6 \text{ ms}^{-1}$). Vertical bars indicate the standard deviation.114

Figure 32. Time-lapse photographs of the ice patch system and its surrounding terrain and maps of the end-of-winter snow height (SH_{\max}) on 5 June 2016, 6 June 2017 and 10 June 2019. The black line delimits the contour of the ice body as it was at the end of summer 2016. The average density of the snow column obtained by excavating the snow pit (ρ_s , kg m^{-3}), the average and maximum snow height (SH , cm) and the total volume of snow (V_{snow} , m^3 w.e.) for each of the three dates are shown at the bottom of the figure.115

Figure 33. a) 2D visualization of a profile made in the central part of the ice patch in 2019 using 200 MHz antennas (the track is represented by the black line in b); b) Interpolated map of the ice thickness based on the series of GPR tracks made in July 2019 (see **Figure 29** for all GPR tracks location). The black line in b delimits the contour of the ice body as it was at the end of summer 2016.116

Figure 34. Maps of the total surface ablation ($\Delta\text{SH}_{\text{TLS}}$, in cm) during the study periods 2017 and 2019 based on daily terrestrial laser scan (TLS) surveys of snow/ice surface position. The black boxes represent the averaging area used to highlight the spatial variability of the

ablation. Mean (\pm Std Dev) values for the whole ice patch and each zone are presented below each panel. See Figure S7 for the daily evolution of ΔSH_{TLS} of each zone.116

Figure 35. Monitoring of the snowmelt from 10 June 2017 to 12 July 2017 (left side) and from 10 June to 20 July 2019 (right side): a and a') The daily evolution of the areal extent of the ice patch system IP1 (A, m^2) within Zone B (Fig. S2-1) and of the seasonal snow cover fraction (SCF, %) within Zone A (Fig. S2-1) derived from a time-lapse camera; b and b') daily evolution of the total ice patch system volume (snow and ice together) (V_{total}, m^3) along with the daily volume change in water equivalent ($\Delta V, m^3 d^{-1}$ w.e.) measured by terrestrial laser scan (TLS). The red bars (negative ΔV) give an estimation of the melt rate ($M, m^3 d^{-1}$ w.e.); c and c') Daily meltwater outflow discharge (Qf_{total}) measured at flumes; d and d') Picture of IP1 illustrating the condition the system at the end of each study period.117

Figure 36. Summary of hourly measured meteorological variables during the study periods. (a) 2017 air temperature (T_a) and mean wind speed (WS). (b) 2019 T_a and relative humidity (RH); (c) 2019 WS and daily precipitation; d) 2019 Incoming solar radiation ($SW \downarrow$) and net radiation (Qr); and e) 2019 snow temperature (T_{snow}). The upper two thermistors (190 and 150 cm above the ice surface) emerged from the snow due to melting on June 21 and June 29, respectively. Subsequent temperatures are not shown in the graph. The cable was removed on July 5. The background colors indicate the sky conditions; white for fog, grey for overcast and blue for clear sky.....119

Figure 37. a) Daily mean values of energy balance terms with net radiation (Qr), sensible heat flux (Qh), latent heat flux (Qe), heat flux by conduction to the underlying ice (Qc) and the melt flux (Qm). The background colors indicate the sky condition; white for fog, grey for overcast and blue for clear-sky; b) Comparison between daily melt rate calculated from the surface energy balance ($\Delta SWE_{SEB}, mm d^{-1}$ w.e.) and measured by TLS ($\Delta SH_{TLS}, mm d^{-1}$ w.e.). The red line is the linear regression line and the grey lines are the 95% confidence intervals. RMSE means Root Mean Square Error.....121

Figure 38. Diurnal cycle of the meteorological variables, including the 15-min average air temperature ($T_a, ^\circ C$) at 2 m and 0.5 m above the snow surface, wind speed ($WS, m s^{-1}$) and incoming solar radiation ($SW \downarrow, W m^{-2}$), and the hourly evolution of surface energy balance terms, i.e. net radiations ($Qr, W m^{-2}$), sensible heat fluxes ($Qh, W m^{-2}$), latent heat fluxes ($Qe, W m^{-2}$), the melt fluxes (Qm) and time-lapse photos for the three different cases that

reflected the dominant conditions encountered along the north coast of Ellesmere Island: (a) Case 1 (28 June 2019) was characterized by sunny and calm conditions; (b) Case 2 (5 July 2019) was a foggy day and (c) Case 3 (9 July 2019) was marked by the influence of a low-pressure system with high winds and warm air advection. Red cross on the picture locates the automatic weather station on the ice patch. Note that the daily solar radiation peak early in the morning due to the northeast orientation of the ice patch.....123

Figure 39. Map of the seasonal, semi-permanent and perennial ice patches on Ward Hunt (WHL=Ward Hunt Lake). Graphs show the distribution of the perennial ice patches with respect to topo-climatic parameters. Maps of topographic position index (TPI), slope aspect, wind exposure index and potential incoming solar radiation (PISR) index are presented in Figure S2-2.124

Figure 40. a) Reconstructed (NCEP/NCAR re-analysis, 1948-2002) and measured mean annual air temperatures (2003-2019) (MAAT) and corresponding positive degree-days (PDD_{air}) for the warm season from 1948 to 2019 at WHI. The colour solid lines represent the 5-year running mean for MAAT (blue) and PDD_{air} (red) and the green line marked the 1980-2010 average of PDD_{air} with black dashed lines representing the two-standard deviation line (- 2σ and + 2σ). Summers with PDD_{air} above the + 2σ line are considered abnormally warm; b) Long-term evolution of extents of the late summer snow/ice surfaces at the scale of WHI (A_{WHI}) and the ice patch IP1 (A_{IP1}); c) Relationship between A_{IP1} and PDD_{air} for the period from 2001-2019 with the colour scale of points according to the previous summer PDD_{air} (s_{-1}), and d) Relationship between A_{IP1} and the average between PDD_{air} of a given summer (s_0) and PDD_{air} of the previous summer (s_{-1}). For c and d, the black line is the linear regression line and grey lines are the 95% confidence interval.126

Figure 41. Scatter plots showing the relationship between the frequency of wind events and the maximum snow height (SH_{max}) observed at the SILA site (left Y-axis) and the maximum snow volume (V_{snow}) measured on IP1 (right Y-axis). a) for wind events in the range of 4-10 $m s^{-1}$; b) for wind events with speed > 15 $m s^{-1}$. The dashed black lines are linear regressions for the SILA station only.129

Figure 42. Time-lapse photographs of the ice patch during the melt season 2017 and 2018 showing a contrasting situation in terms of surface albedo. In 2017, the pronounced ablation led to

progressive exposure of the dirty ice surface giving a dark colouration to the ice patch while in 2018 the seasonal snowpack persisted throughout the summer. 132

Figure 43. Spatial variation of (a) the total potential incoming solar radiation (PISR, W m^{-2}) from June to September and (b) of the mean hourly turbulent sensible heat flux during a hypothetical high wind event (5 m s^{-1} from the west at IP1) with an air temperature of 6°C . The black cross shows the location of the ice patch IP1. 134

Figure 44. Projection of summer temperature at Ward Hunt Island to 2050 based on the Coupled Model Intercomparison Project phase 5 (CMIP5) for the scenario RCP4.5 ensemble average (Data from Climate Change Institute, 2021). Modelled summer (JJA) air temperature anomalies at 2 m over the period 1980-2050 are presented along with the 2 years running mean of the PDD_{air} at Ward Hunt Island reconstructed from NCEP-NCAR reanalysis for the period 1980-2005 and measured at SILA for the period 2005-2019. 137

Figure 45. Study site: a) Location of Ward Hunt Island (WHI) at the northern tip of Ellesmere Island (Canadian High-Arctic Archipelago) and World-View 3 image of the whole island taken on 19 August 2019 showing the study site in the red box. North is up in (a) map unlike in (b) and (c). b) 3D visualization of the studied ice patch (IP1) and its biogeomorphic system (red box) based on UAV orthomosaic (flight carried out on 22 July 2019) and ESRI ArcScene 10.6 software. The location of the water quality sampling sites and the flumes are shown in this image; c) close-up of the studied biogeomorphic system (red box in b) showing the solifluction lobes A and B, where most of the fieldworks was undertaken, and small lobe C. 167

Figure 46. Geomorphological map of the pronival margin of the perennial ice patch IP1 illustrating the complex biogeomorphic system. The map details the soil composition, geomorphology and hydrology of the studied slope section. For the soil composition: Gr=gravel, Sa=sand; Si=silt. Black boxes show the paired lobes A and B and the lobe C in an early stage of development. 174

Figure 47. Geomorphic features encountered in the pronival margin of the ice patch IP1: a) Beach deposits characterized by coarse rounded and sub-angular gravel of diverse lithology; b) Erratic rock observed in the parent slope between lobe A and B; c) Series of terracettes with turf front that trap a significant amount of fine-grained sediments on the lobe treads; d) Parallel rills in the upper section of lobe B that drained the meltwater on the tread of lobes;

e) Ephemeral small pond in the front of lobe B during peak flows; f) Sorted stripe between the lateral riser and the central tread of lobe A; g) Lobe C is delineated by the red dotted line. The arrow points downslope; h) Small alluvial fan that overrode the beach gravels in front of IP1; i) Field of hummocks downslope of lobe B.....175

Figure 48. The hydrological regime and water quality at flumes A and B in the pronival margin of the ice patch IP1. a) Daily evolution of the discharge of the surface runoff along with the daily melt rate of the ice patch system ($\Delta\text{SWE}_{\text{SEB}}$, mm w.e. d^{-1}) calculated from the surface energy balance (SEB) in Chap. 2 for the period from 11 June to 20 July 2019; b) Hourly and mean daily water temperature at flumes A and B along with the mean daily air temperature; c) Hourly and mean daily total dissolved sediment (TDS, mg L^{-1}) calculated from continuous specific conductivity measurements; d) Mean daily value of pH obtained from bi-daily measurements; e) Reconstructed hourly evolution of the turbidity (NTU) based on the close relationship between bi-daily turbidity measurements and discharge (see Fig. S3-2a). The green line indicates the detection threshold (2.5 NTU) below which the TSS is considered negligible. The grey bars show the daily fluxes of TSS at flume A calculated from the linear correlation between NTU and TSS obtained by filtration (see Fig. S3-2b).177

Figure 49. Daily evolution of the water temperature (T_w), total dissolved sediment concentration (TDS) and total suspended sediment concentration (TSS) at the three sample sites along lobes A and B in the margin of the ice patch IP1 (i.e. T1; Flume and T3) and at the sites above the ice patch (sites IP_up).....179

Figure 50. a) Map of the mean summer ground surface temperature (GST_{JULY}) for summer 2016, 2017, 2018 measured over the pronival margin of the ice patch IP1. The seasonal margin on the map is bounded by the snow line on 26 June 2019 (green line) and on 19 August 2019 (red line). b) Scatterplots representing the regression between GST_{JULY} and the volumetric water content of soil (VWC) which is the variable that explained most of the GST spatial variability over the pronival margin IP1 (excluding the seasonal margin) as identified in the correlation matrix in Table S3-4. The colour of the dots indicates the dominant surface composition of each site (Table S3-1). The background image in (a) is a high-resolution orthomosaic acquired by UAV on 8 July 2019.....180

Figure 51. Thaw depth measurements carried out on 18 July 2019. a) Map showing thaw depth at each probing point along transect T1, T2 and T3 that cut lobes A and B; b) Box plots

comparing the thaw depth between the dominant soil surface found along the transects (Gr=gravel, Sa=sand, OM=organic matter, Veg=vegetation cover); c) Evolution of thaw depths as a function of surface morphology and position on the slope: T1=upper section of lobes; T2=middle section; T3 =frontal section. The background image in (a) is the same as in **Figure 50** 182

Figure 52. Displacement rates derived from VX station measurements in 2016 and 2019 along transects T1, T2 and T3 on lobe B. On the left, general view of the lobe B; on the right, close-up on each transect. Points represent surface marker and arrows represent the direction of the movement. The size of the arrows is proportional to the magnitude of the displacement rate. The background image is the same as in **Figure 50** 183

Figure 53. Mosaic of photographs and sketch illustrating the soil pit excavated in Lobe A (see **Figure 45**) that showed the transition between the central tread of the lobe and the adjacent dry soil that composes the lateral riser and parent slope. The black boxes in the sketch indicate where samples P1, P2, P3 and P4 were collected. 184

Figure 54. Canonical correspondence analysis (CCA) ordination plots for species and soil surface composition of various habitats and four environmental variables on the 27 sites sampled over the downslope margin of the ice patch IP1 at WHI. Filled coloured circles indicate the sampling sites (blue = central section of lobes; green =internal side of lateral risers; orange =external side of lateral risers and red= parent slope) and coloured squares represent vegetation and soil surface compositions (black=Vascular taxa; grey=Non-vascular taxa and organic crust; brown=Non-organic soils). Arrows represent environmental explanatory variables (red=statistically significant; blue=non statistically significant) with arrowheads indicating their direction of increase. The 95% confidence ellipses highlight the clustering of sampling sites according to the CCA analysis and the overlap between the different ellipses illustrates the contact and transitions between habitats. 187

Figure 55. a) Photograph of the upper section of Lobe B (near T1) showing the dense distribution of *Phippsia algida* associated with moss patches in the central tread of the lobe. On each side, the external tread is covered by black organic matter b) Terminal section of the lobe B dominated by a cover of black organic matter and scattered patches of *Saxifraga*. 188

Figure 56. A three-stage conceptual model of the development of an ice patch biogeomorphic system on a low-gradient polar desert slope. a) Stage 1: Initiation stage characterized by the

formation of an alluvial fan-like deposit in front of the ice patch; b) Stage 2: Growth stage marked by the colonization of pioneer species and by the activation of sorting and solifluction processes; c) Mature stage during which the solifluction lobe gets fully developed and exhibits zonation of processes and feedback mechanisms as a function of distance from the ice patch front.....	195
Figure 57. a) Location of the study sites within the Canadian Arctic Archipelago; b and c) Map showing the location of snowpits and the trench as well as the instrumented sites at Resolute Bay and Ward Hunt Island; d) Close-up of Site 1 of WHI located in the downslope margin of a perennial ice patch. The red lines delimit the humid soils which are mostly associated with solifluction lobes. Background image for (b): Worldview-2 taken on 26 July 2019 (source: Esri, DigitalGlobe, GeoEye, i-cubed, USDA FSA, USGS, AEX, Getmapping, Aerogrid, IGN, IGP, swisstopo, and the GIS User Community); for (c) Worldview-3 taken on 14 August 2019 and for (d): High-resolution orthomosaic derived from unmanned aerial vehicle (UAV) images taken on 18 July 2019.....	220
Figure 58. Example of snowpit excavations made at WHI in early June 2019 on a humid site (a: snowpit #2) and a dry site (b: snowpit #4).....	222
Figure 59. a) view of the SILA weather station on 11 July 2016 at WHI. Note the remaining snowdrift at the forefront where the Sonic ranger SR50A is installed; b) view of the site 5 on 6 July 2017, looking towards Ward Hunt Lake. The surface runoff in water tracks is clearly visible.....	225
Figure 60. a) Map of small-scale distribution of the snowpack on 12 June 2019 over Site 1 at Ward Hunt Island obtained by UAV surveys, b) Map of the microtopographic features based on the Topographic Position Index (TPI) computation. The black dots represent the 21 manual snow height measurement points. The black line delimits the humid soils. Snow height (cm) and TPI along the profile 1 (c) and 2 (d) identified by red lines in b, and e) shows the relationship between the snow height and the TPI for both profiles 1 and 2 with the best-fitting regression curve.....	227
Figure 61. a) Boxplots of the depth hoar fraction ($DH_{fraction}$) measured in snowpits made in Ward Hunt Island snowpits (WH-SP) and Resolute Bay snowpits (RB-SP) in humid and dry sites, and measured along the trench dug at Ward Hunt Island in Site 1 (WH-T). The red line is the median, the black cross is the mean, the blue box delineates the interquartile range, and	

- whiskers extend to the highest and lowest values; b) Histograms showing the relative contribution (%) of the snow grain types in both humid and dry sites. 228
- Figure 62.** a) Schematic representation of the depth hoar layer and soil surface observed along the trench WH-T that crossed a solifluction lobe in Site 1 at Ward Hunt Island in early June 2019; b) High-resolution UAV orthomosaic showing the soil surface at the trench location on 16 July 2019; c) Spatial evolution of the DH_{fraction} along the trench. 229
- Figure 63.** Vertical profiles of density (ρ_s), SSA and thermal conductivity (k_{eff}) for snowpits dug in dry and humid zones at Ward Hunt Island and Resolute Bay (only density) in early June 2019. The high Thermal conductivity values of WH_2#1 ($0.55 \text{ W m}^{-1} \text{ K}^{-1}$) and WH_3#1 ($0.38 \text{ W m}^{-1} \text{ K}^{-1}$) are due to the presence of a dense melt-freeze layer. The site RB_3 at Resolute Bay, does not appear because only one density measurement was done. 230
- Figure 64.** a) Boxplot of basal DH density (ρ_s) values in humid and dry zones at Ward Hunt Island (WHI) and Resolute Bay (RB) and b) the same as (a) but for the thermal conductivity (k_{eff}) and only for WHI. 231
- Figure 65.** Environmental monitoring at the SILA station at Ward Hunt Island during the snow season 2018/19. a) Snow height measurements by the snow gauge and normalized with the readings of the snow stakes visible on the time-lapse photos; b) Hourly maximum wind speed according to their direction (North/East/South/West) and averaged daily maximum wind speed; c) Hourly temperature records at the soil surface (0 cm) and of the air; d) Hourly temperature gradient in the snowpack calculated from equation 5-1. Photographs on the right side were taken by the automatic time-lapse camera of the SILA tower, showing the snow surface evolution in the early cold season. Their dates are represented by red crosses in graph a; e) 22 August; f) 1 September; g) 21 September; h) 22 October. A close-up of the 5 weeks after snow onset is presented in Fig. S4-3. 232
- Figure 66.** Spatial variability of the moisture and temperature conditions at Ward Hunt Island during the 2018/19 snow season. a and b) Time-series of near-surface (-5 cm) volumetric water content (VWC, m^3/m^3) and temperature at the SILA site and Site 5 in intertrack (IT), water track (WT) and upper thermistor of the borehole; c) Time-series of average near-surface temperature (-5 cm) recorded by Trix-8 sensors in humid zones and dry zones in Site 1. The shaded bands delimit the maximum and minimum values. d) Average calculated temperature gradient (daily and monthly averages) based on equation 5-1 between sensors in

humid and dry monitoring sites (Site 1; Site 5 and SILA site) during the snow season 2018/19.

.....234

Figure 67. Comparison between thermal and wind conditions at the SILA station between falls 2015, 2016- and 2018, a) Wind speed distribution of hourly maximum above 6 m s^{-1} for 60 days after the snow onset; b) Wind index for wind speed over 6 m s^{-1} for the 60 days following the snow onset; c) Soil surface temperature for the August to December period, the crosses marked the snow onset date for each date; d) Diffusive water vapour fluxes through the snowpack calculated from equation (5.2) for the 60 days following the snow onset.....242

Liste des sigles et abréviations

Symboles

A	Superficie / surface area
AP	Pression atmosphérique / atmospheric pressure
c	Capacité calorifique / heat capacity
C	Chaleur spécifique / specific heat
CC	Contenu en froid / cold content
Cf	Coefficient d'écoulement libre / free flow coefficient
D	Coefficient de transfert global / bulk exchange coefficients
D_{eff}	Coefficient de diffusion effectif / effective diffusion coefficient
D_m	Momentum / momentum
e	Pression de vapeur / vapor pressure
E	Taille des grains de neige / snow grain size
e_{ss}	Pression de vapeur saturante / saturated pressure vapor
F	Flux de vapeur diffus / diffusive vapor flux
g	Constante gravitationnelle / gravitational constant
h	Hauteur (épaisseur) / height (thickness)
h_u	Niveau d'eau / Level of water
HU	Échelle de Hounsfield / Hounsfield units
k	Taux de croissance / growth rate
k_0	Facteur pre-exponentiel / pre-exponential factor
k_{eff}	Conductivité thermique / thermal conductivity

K_f	Facteur de correction en écoulement libre / free flow correction factor
K_p	Perméabilité / permeability
L	Longueur maximale / maximum length
L_f	Chaleur latente de fusion / latent heat of fusion
L_v	Chaleur latente d'évaporation / latent heat of vaporization
$LW\uparrow$	Rayonnement thermique émis / outgoing longwave radiation
$LW\downarrow$	Rayonnement thermique incident / incoming longwave radiation
M	Taux de fonte journalier / daily melt rate
n_f	Exposant d'écoulement libre / free flow exponent
P	Concentration de vapeur / vapor concentration
p	Probabilité d'accepter l'hypothèse nulle d'un test statistique / probability of accepting the null hypothesis in a statistical test
Q	Énergie d'activation / activation energy
Q^*	Flux d'énergie net / net energy flux
Q_c	Flux de chaleur par conduction / conductive heat flux
Q_e	Flux turbulent de chaleur latente / turbulent latent heat flux
Q_f	Débit / discharge
Q_h	Flux turbulent de chaleur sensible / turbulent sensible heat flux
Q_m	Flux chaleur utilisé pour la fonte / melt flux
Q_p	Flux de chaleur apporté par les précipitations ou le ruissellement / rainfall heat
Q_r	Flux de chaleur net du rayonnement solaire absorbé par la surface / net solar radiation heat absorbed at the surface
r	Coefficient de corrélation de Pearson / Pearson correlation coefficient

R	Constante universelle des gaz parfaits / gas constant
R^2	Coefficient de détermination / coefficient of determination
r_{es}	Équivalent du rayon de la sphère / equivalent sphere radius
R_i	Nombre global de Richardson / bulk Richardson number
R_T	Résistance thermique / thermal insulance
$SW\uparrow$	Rayonnement solaire réfléchi / outgoing solar radiation
$SW\downarrow$	Rayonnement solaire incident / incoming solar radiation
T	Température absolue / absolute temperature
T_a	Température de l'air / air temperature
T_{is}	Température à l'interface neige-glace / temperature at the snow-ice interface
T_m	Température de fonte / temperature of melting
T_{snow}	Température de la neige / Snow temperature
T_{soil}	Température de surface du sol / soil surface temperature
T_{ss}	Température de surface de la neige / snow surface temperature
T_w	Température de l'eau / water temperature
V	Volume / volume
WS	Vitesse du vent / wind speed
z_0	Rugosité de surface / roughness lenght
ΔSH	Changement de la haute de neige / height change of the snow surface
ΔSWE	Fonte de surface potentielle de la neige-glace / potential melt of snow-ice
ΔT	Gradient de température / temperature gradient
ΔV	Changement de volume / volume change
ρ_i	Densité de la glace / ice density

ρ_s	Densité de la neige / snow density
ρ_w	Densité de l'eau / water density
κ	Constante de Karman / karman's constant
$\partial Q/\partial t$	Stockage d'énergie / heat storage

Abbréviations

ASTM	American Section of the international association for Testing Materials
AWS	Station météorologique automatique / automatic weather station
a.s.l.	Au-dessus du niveau marin / above sea level
BP	Avant aujourd'hui / before present
CCA	Analyse canonique des corrélations / canonical-correlation analysis
CMIP	Projet d'intercomparaison des modèles couplés / coupled Model Intercomparison Project
CMP	Point commun milieu / common midpoint
DH	Givre de profondeur / depth hoar
DIR	Direction / direction
DSM	Modèle numérique de surface / digital surface model
DTM	Modèle numérique de terrain / digital terrain model
ECb	Bulle cylindrique allongée / elongated cylindrical bubble
El	Bulle allongée / Elongated bubble
ELA	Ligne d'équilibre des glaciers / Equilibrium-Line Altitude of glacier
GCP	Point de contrôle au sol / Ground Control Point

GDD _{surf}	Degrés jour de croissance à la surface du sol / degree-day of growing at the ground surface
GIS	Système d'information géographique / Geographic Information System
GPR	Géoradar / Ground Penetrating Radar
GPS	Système de positionnement global / Global Positioning System
Gr	Gravier / Gravel
GST	Température de surface du sol / Ground Surface Temperature
IP1	Plaque de glace 1 / Ice Patch 1
IP2	Plaque de glace 2 / Ice Patch 2
Irb	Bulle irrégulière / Irregular bubble
IT	Intertrack / Intertrack
ITIS	Système intégré d'information de taxonomique / Integrated Taxonomic Information System
MAAT	Température moyenne annuelle de l'air / Mean Annual Air Temperature
MMAT	Température moyenne mensuelle de l'air / Mean Monthly Air Temperature
NTU	Unité de turbidité néphélométrique / Nephelometric Turbidity Units
OM	Matière organique / Organic matter
PDD _{air}	Degrés-jour de dégel de l'air / degree-day of melting of the air
PDD _{surf}	Degrés-jour de dégel à la surface du sol / degree-day of melting at the ground surface
PISR	Rayonnement incident potentiel / Potential Incoming Solar Radiation
RB	Resolute Bay / Resolute Bay
RGB	Rouge-vert-bleu / Red-Green-Blue
RH	Humidité relative / Relative Humidity

RMSE	Racine de l'erreur quadratique moyenne / Root Mean Square Deviation
Sa	Sable / Sand
Sb	Bulle sphérique / Spherical bubble
SCF	Fraction de couverture neigeux / Snow Cover Fraction
SEB	Bilan d'énergie de surface / Surface Energy Balance
SfM	Structure acquise à partir d'un mouvement / Structure from Motion
SH	Hauteur de neige / Snow Height
SpC	Conductivité spécifique / Specific Conductivity
SSA	Surface spécifique de la neige / Snow Surface Area
SSb	Bulle sphérique / Sub-spherical bubble
Std dev.	Écart-type / standard deviation
TDS	Somme des solides dissous / Total Dissolved Solids
TLS	Scanner laser terrestre / Terrestrial Laser Scanning
TPI	Indice de position topographique / Topographic Position Index
TSS	Somme des sédiments en suspension / Total Suspended Sediments
UAV	Drone / Unmanned aerial vehicle
Veg	Végétation / Vegetation
VWC	Contenu en eau volumétrique / Volumetric Water Content
w.e.	Équivalent en eau / water equivalent
WHI	Ile Ward Hunt / Ward Hunt Island
WHIR	Dôme de glace de Ward Hunt / Ward Hunt Ice Rise
WHIS	Plateforme de glace de Ward Hunt / Ward Hunt Ice Shelf
WHL	Lac Ward Hunt / Ward Hunt Lake

WI Indice de vent / Wind Index

WT Water track / Water Track

ZC Zero curtain

Remerciements

Le parachèvement de cette thèse marque la fin d'une aventure. Et quelle aventure ! Des mois de terrain dans le Grand Nord canadien, des journées dans un congélateur pour analyser la glace, des conférences et surtout des milliers d'heures derrière mon ordinateur. Ce doctorat est l'aboutissement d'années de travail, d'abnégation et d'enrichissement autant personnel que professionnel. Il n'aurait pas vu le jour sans l'influence d'acteurs clés que je tiens à remercier ici.

Mes premiers remerciements vont à Daniel Fortier, mon directeur de recherche, pour m'avoir fait confiance et m'avoir accueilli dans son laboratoire. Daniel m'a accepté au Géocryolab voilà près d'une décennie dans le cadre d'un échange CREPUQ avec la France qui m'a permis de travailler sur le pergélisol du Mont Jacques-Cartier en Gaspésie. J'étais loin de me douter que mon parcours universitaire s'étirerait jusqu'au doctorat et m'amènerait à travailler sur l'un des territoires les plus septentrionaux et les plus isolés du monde. Je dois bien avouer que le site d'étude et ma fascination pour le monde polaire m'ont grandement décidé à faire ce doctorat – bien plus que le diplôme en lui-même. Merci Daniel de m'avoir offert cette opportunité unique qui marquera ma vie et de m'avoir partagé ta passion pour le Nord. Avec Daniel, j'ai aussi eu la chance de tomber sur un superviseur qui m'a laissé une totale liberté dans le choix de mon projet de thèse et dans la façon de le mener. Daniel a su m'inculquer le sens de l'autonomie, des responsabilités et de l'organisation. J'ai ainsi pu découvrir et affronter les étapes à franchir pour les demandes de financement et les permis de recherche, ainsi que la planification minutieuse du matériel et des ressources nécessaires pour mener des expéditions de manière sécuritaire et efficace.

Je témoigne aussi ma gratitude à Florent Dominé. Merci Florent pour le temps que tu m'as accordé et tes précieux conseils sur les aspects « neige » et « glace ». Travailler à ses côtés a été très enrichissant et particulièrement plaisant, que ce soit sur le terrain ou sur Zoom. Je tiens à adresser une mention spéciale au gastronome en lui qui a eu l'audace d'apporter un Reblochon bien coulant jusqu'au pôle, nous permettant de concocter la *northermost* tartiflette jamais réalisée. Je garde un souvenir ému de ce festin savoureux.

Je remercie l'ensemble de la grande famille du Géocryolab et plus largement du Département de Géographie, collègues et ami(e)s avec qui ce fût toujours un réel plaisir de passer du temps au labo, sur le terrain et aux 5@7 historiques du Strathcona. L'implication personnelle de chacun lorsque j'ai eu besoin de conseils ou d'aide a permis de rendre plus effectives et efficaces mes recherches. Un merci spécial à Slei pour son aide bienvenue au laboratoire et à Lin pour ses conseils sur les calculs du bilan d'énergie. J'ai aussi une pensée toute particulière pour mes partenaires de terrain ; Paquette, Audrey et Karine. Merci infiniment à vous trois pour votre aide à Ward Hunt, vous avez contribué à rendre possible cette thèse.

Merci aux organismes subventionnaires : le Fonds de Recherche du Québec Nature et Technologies (FRQNT), les Études supérieures et postdoctorales (ESP) de l'Université de Montréal qui m'ont permis de mener à bien mes recherches. Merci au Centre d'Études Nordiques (CEN), à Parc Canada et au Programme du Plateau Continental Polaire (PPCP) canadien pour les appuis financiers et logistiques cruciaux qui ont rendu les travaux de terrain à Ward Hunt possibles. Merci également au Département de Géographie pour les aides financières et pour m'avoir offert l'opportunité de donner plusieurs charges de cours durant mon doctorat. Ces expériences m'ont permis de développer un goût certain pour la pédagogie et l'enseignement de la géographie. Merci également au personnel du département de Géographie, Isabelle Pelletier, Fanny Duval, Sabine Démosthènes. Un merci particulier à Marie-Andrée Desgagnés pour sa patience et son aide avec nos factures de terrain.

Un immense merci à mes parents, ma sœur et mon frère, qui m'ont transmis le goût du voyage et des régions nordiques. Leur soutien inconditionnel pour tous mes projets et leur encouragement ont été indispensables pour garder le cap dans ce long périple doctoral.

Et finalement, un remerciement tout spécial à ma conjointe. Merci Fatéma de m'avoir soutenu et supporté durant ces années doctorales que tu as rendues belles. Merci pour ta patience durant mes longs mois passés sur le terrain. Merci pour tes encouragements qui m'ont donné la force d'aller jusqu'au bout de cette thèse et qui m'ont donné envie de me dépasser. Merci de m'avoir poussé à faire des pauses de travail pour laisser respirer mon cerveau ramolli. Pour tout cela, et bien plus encore, je suis très chanceux de partager ta vie !

Avant-propos

La neige et la glace saisonnières et permanentes font partie intégrante du paysage des régions polaires. Ensemble, elles forment la cryosphère qui inclut les masses de glace terrestres (glaciers, calotte et inlandsis), les glaces flottantes de lacs, de rivières et de mer (banquise, plateforme de glace), le pergélisol (sol gelé en permanence) ainsi que le couvert de neige saisonnier et permanent (Benn et Evans, 2010). Ces glaces proviennent de précipitations solides, principalement sous forme de neige, ou du gel de l'eau liquide de surface ou souterraine. La cryosphère consiste en un système ouvert, dynamique et complexe, qui exerce une influence directe sur les flux d'eau, de gaz et d'énergie à la surface terrestre. Elle constitue un élément central du système Terre puisqu'elle entretient des liens et des rétroactions importantes sur l'hydrosphère, l'atmosphère, la biosphère et la lithosphère, et affecte à cet égard profondément les communautés humaines. Les principaux effets de la cryosphère sont liés à (i) l'albédo élevé des surfaces de neige et de glace, (ii) l'effet isolant de la couverture neigeuse sur le sol, (iii) la chaleur latente impliquée dans les changements de phase de la glace (fonte/gel), (iv) la modification physique induite par le passage de l'eau solide à liquide et (v) son rôle de régulateur des ressources hydriques en stockant plus ou moins longtemps l'eau sous forme solide et la libérant par la fonte.

En réponse au réchauffement climatique récent, un déclin généralisé de l'ensemble des composantes de la cryosphère est observé. Cela se manifeste par la dégradation du pergélisol (Biskaborn et al., 2019 ; Liljedahl et al., 2016), la réduction de l'étendue de la banquise estivale (Lindsay et Schweiger, 2015), une durée d'enneigement plus courte (Callaghan et al., 2011a,b) et une régression de la superficie et du volume des masses de glaces continentales (AMAP, 2019) et une perte du couvert de glace permanent des lacs polaires (Mueller et al., 2009; Paquette et al., 2015;). Quelle que soit sa forme, la fonte des glaces est un point de basculement qui peut générer des périodes de changement significatif, rapide et/ou irréversible dans le géosystème polaire. La conséquence directe du déclin de la cryosphère est l'enclenchement d'une série de rétroactions positives sur le forçage radiatif aboutissant à une amplification polaire du réchauffement (Bengtsson et al., 2013 ; Goosse et al., 2018). Parallèlement, la régression des masses de glace sur les continents entraîne une altération du régime hydrologique des bassins versants à l'échelle locale et régionale et contribue de manière significative à l'élévation du niveau marin global (Gardner et al., 2012). Le recul des marges glaciaires a aussi des conséquences directes sur la dynamique du

paysage en exposant des surfaces terrestres qui vont subir une série de réajustements géomorphologiques sous l'action des conditions périglaciaires et de certains processus azonaux (gravitaires, fluviaux) durant la phase dite « paraglaciale » (Ballantyne, 2002). La fonte plus précoce du manteau neigeux au printemps est quant à elle critique pour le bilan d'énergie des surfaces continentales puisqu'elle diminue drastiquement l'albédo de surface au début de la saison chaude (Callaghan et al., 2011a,b). Par effet d'enchainement, les changements dans le régime nival, la distribution des ressources en eau douce et dans les conditions de glace ont des conséquences majeures sur la faune et la flore (Fauchald et al., 2017 ; Jia et al. 2009 ; Vincent et Mueller, 2020) et sur les sociétés humaines des régions polaires (Olsen et al., 2011 ; Vincent, 2020).

L'ensemble des changements qui affecte la cryosphère bouleverse donc aujourd'hui profondément l'équilibre du géosystème polaire, aboutissant à une modification dans sa structure et de sa dynamique spatiale et temporelle (Gooseff et al., 2017 ; Vincent et al., 2011a). Face à aux enjeux environnementaux et humains d'un monde polaire en transition rapide, la cryosphère est plus que jamais au centre des préoccupations scientifiques, mais aussi médiatiques, ce qui crée une demande sans précédent de données et d'informations. L'étude de ses changements et ses impacts à l'échelle globale comme locale nécessite une attention croissante au sein des géosciences afin de comprendre et d'anticiper l'évolution future des régions polaires. Cette thèse a pour but de contribuer à cet effort de recherche en se penchant sur une composante peu connue de la cryosphère terrestre mais importante pour les environnements polaires : les plaques de glace permanentes.

Chapitre 1 – Introduction générale

1.1. Mise en contexte

Les masses de neige et de glace permanentes recouvrent près de 10% des surfaces continentales de la planète (Benn et Evans, 2010). Celles-ci englobent une grande diversité de tailles et de formes selon le contrôle climatique et les contraintes topographiques du milieu. Malgré un long historique de recherche dans le domaine de la glaciologie, l'état des connaissances est très inégal entre les différentes composantes de la cryosphère terrestre en raison de l'intérêt variable qu'elles suscitent. Les grands systèmes glaciaires qui regroupent les glaciers et les calottes glaciaires (Benn et Evans, 2010) ont traditionnellement concentré la majorité des recherches. Des pionniers comme R.M. Koerner ou W. S. B. Paterson ont mené des études sur les principales calottes glaciaires dès les années 1970 dans l'Arctique canadien (ex. Koerner, 1968 ; Koerner, 1970 ; Koerner et al., 1973; Koerner et Paterson, 1974; Paterson, 1969). Au cours des dernières décennies, le retrait des grands systèmes glaciaires est devenu emblématique du réchauffement climatique, renforçant ainsi l'intérêt qu'ils suscitent. Ceci s'est traduit par une multiplication des études sur la dynamique spatiale et temporelle des glaciers, basées notamment sur des modélisations numériques et des mesures par satellite du bilan de masse (ex. Mortimer et al., 2018 ; Noël et al., 2018)

À l'autre extrémité se trouvent les petites masses de glaces terrestres. Elles englobent les petits glaciers ($< 1 \text{ km}^2$; Bahr et Radić, 2012), ainsi que toutes les petites masses de neige et de glace permanentes qui ne relèvent pas des systèmes glaciaires et qui sont généralement regroupées sous le terme générique de « plaques de glace » (Ødegård et al., 2017 ; Serrano et al., 2011). Malgré qu'elles soient les éléments de la cryosphère dominants à la surface terrestre en nombre absolu, les petites masses de glace ont été largement négligées jusqu'à présent, principalement parce qu'elles répondent moins aux problématiques actuelles de la glaciologie, davantage animée par les enjeux globaux tels que la hausse du niveau marin et les rétroactions sur le bilan énergétique terrestre (Fischer et al., 2016). Pourtant, les petites masses de glace sont susceptibles de jouer un rôle important dans la disponibilité et la distribution des ressources en eau douce et dans la dynamique des environnements naturels des milieux froids. D'un point de vue technique, la rareté des études sur ces petites composantes de la cryosphère est également attribuable à une limite des techniques

de télédétection par imagerie satellitaire, dont la résolution grossière a longtemps contraint les travaux d'inventaire à exclure des analyses les éléments d'une superficie inférieure à 0,05 km² (Leigh et al., 2019).

Cette thèse s'intéresse spécifiquement aux plaques de glace polaires. Les plaques de glace constituent de petits systèmes composés d'un corps de glace pluriannuel et surmonté d'un épais couvert de neige saisonnière et de névé, c'est-à-dire une neige ayant survécu à au moins une saison chaude (Cogley et al., 2011). Malgré leur taille et leur épaisseur réduites, certaines plaques de glace peuvent persister de façon continue pendant des siècles, voire des millénaires (Ødegård et al., 2017 ; Serrano et al., 2011). Du fait de leur caractère permanent, elles sont considérées comme un état intermédiaire dans le continuum entre les plaques de neige saisonnière et les petits glaciers (Glazirin et al., 2004), ce qui rend leur définition et caractérisation difficile. L'existence et la préservation des plaques de glace sont le résultat de processus locaux produits par un contexte topoclimatique qui favorisent les accumulations préférentielles de neige en hiver (ex. dépôts avalancheux, congères), et, dans certains cas, réduit l'ablation estivale (ex. effet d'ombrage ; inversion thermique) (Serrano et al., 2011). Dans les régions polaires, malgré leur omniprésence, les plaques de glace ont rarement fait l'objet d'études individuelles de terrain, ce qui en fait l'une des composantes les moins documentées de la cryosphère terrestre. Des lacunes importantes existent dans les connaissances relatives à leur structure, à leur formation et à leur évolution spatio-temporelle.

Les plaques de glace constituent de petits réservoirs d'eau et ont de ce fait un rôle central sur le cycle hydrologique en générant des écoulements de fonte qui participent à l'alimentation des bassins versants tout au long de la saison chaude (Carey et Woo, 2001). En raison de l'humidification prolongée du sol et des ruissellements de surface et de subsurface qui en résultent, les plaques de glace ont également une importante action géomorphologique en activant une série de processus azonaux qui contribuent grandement au développement d'un paysage dit « nival » (Kunitsky et al., 2000 ; Paquette et al., 2020). Ces processus, historiquement étudiés dans les régions de montagne sous le concept de « nivation », englobent la météorisation chimique et mécanique, l'érosion et le transport de sédiments (ex. processus fluviaux et de solifluction) (Ballantyne, 1978 ; Ballantyne et al., 1989; Berriford, 1991; Hall, 1980; Rapp et Nyberg, 1988; Thorn, 1978). Le développement des formes de nivation, telles que des lobes de solifluxions, des

cônes alluviaux et des escarpements (Christiansen, 1998 ; Stromquist, 1985), peut fortement modifier le profil de pente allant parfois jusqu'au façonnement de terrasses de cryoplanation (Mitchell et al., 2021 ; Nyland et Nelson, 2020). En tant que source durable d'humidité, les plaques de glace jouent également un rôle majeur sur la répartition de la végétation et l'alimentation en eau des milieux humides (Walker et al., 2001 ; Woo et Young, 2003).

Dans le désert polaire arctique (ex. dans le Haut-Arctique canadien) auquel s'est intéressée cette thèse, le rôle des plaques de glace sur le milieu physique est d'autant plus important qu'elles représentent la principale source d'eau en été (**Figure 1**). De ce fait, la distribution des plaques de glace contrôle fortement l'organisation des différentes unités du paysage et des écosystèmes en favorisant la formation de microenvironnements humides, souvent assimilés à des oasis polaires, qui contrastent avec les environnements secs et stériles dominants (Abnizova et Young, 2010 ; Christiansen, 1998 ; Woo et Young, 2003). Pour l'heure, les plaques de glace dans les régions de désert polaire ont été surtout étudiées à travers leur contribution au bilan hydrologique des bassins versants (Ballantyne, 1978 ; Lewkowicz et French, 1982a ; Lewkowicz et Young, 1990; Woo et Steer, 1982) et dans la recharge de milieux humides (Abnizova et Young, 2008, 2010; Assini et Young, 2012). En revanche, les études de terrain axées sur les processus géomorphologiques, les flux de sédiment et le régime thermique du sol des versants en aval des plaques de glace sont très peu nombreuses et restent qualitatives (ex. Christiansen, 1998 ; Kňažková et al., 2021 ; St-Onge et Gullentops, 2005).



Figure 1. Photographie aérienne illustrant l'omniprésence des plaques de neige et de glace dans le désert polaire de l'île Devon au Nunavut (Canada) prise le 23 juillet 2019.

Le manque de recherche sur les plaques de glace permanente en tant que partie intégrante de la cryosphère terrestre et sur leurs effets sur l'environnement physique fait que leur implication est largement sous-estimée dans les modèles d'évolution du paysage et des écosystèmes polaires (Christiansen, 1998). Cela représente une limitation majeure dans la compréhension de la dynamique actuelle des régions polaires et de leur réponse au réchauffement climatique. Une étude publiée par Woo et Young (2014) a montré qu'à Resolute (Haut-Arctique canadien), les plaques de glace ont considérablement régressé au cours de la dernière décennie et que la plupart ont perdu leur statut permanent. Les effets sur le milieu physique des versants en aval ont été immédiats, avec l'assèchement de certaines zones humides et une diminution de la densité et de la diversité des espèces végétales. Dans cette étude, les auteurs ont insisté sur la menace que la disparition des plaques de glace représente pour les environnements de désert polaire, en particulier pour la pérennité des milieux humides, et ont appelé à porter une attention particulière sur cet élément peu connu de la cryosphère.

Force est de constater que depuis 2014, aucune recherche n'a été menée sur le sujet alors que le réchauffement se fait de plus en plus sentir aux plus hautes latitudes et amène vraisemblablement la plupart des plaques de glace dans un état critique. La présente recherche doctorale a donc été développée pour répondre à la nécessité d'apporter de nouvelles connaissances sur les plaques de glace polaires en tant qu'élément à part entière de la cryosphère terrestre, mais aussi parce leur étude ouvre des perspectives importantes, non seulement pour le domaine de la glaciologie, mais aussi pour la géomorphologie, hydrologie, biologie et climatologie des milieux polaires.

1.2. Structure de la thèse

En préambule, le **chapitre 1** (ce chapitre) apporte une mise en contexte générale de la thèse et présente une brève revue de littérature afin de préciser et discuter des bases sémantiques associées à la notion de « plaques de glace » et de faire un point sur l'état des connaissances quant à leur formation et leur évolution spatio-temporelle. Cette section met en évidence les lacunes importantes dans les connaissances sur les plaques de glace polaires qui ont guidé l'élaboration de la recherche. Une section détaille également la pertinence et les retombées de la recherche présentée dans cette thèse. Finalement, le chapitre se termine par une mise en contexte géographique du site d'étude.

Les chapitres 2 à 5 présentent les quatre manuscrits de cette thèse. La volonté de partager et valoriser les connaissances établies dans cette thèse justifie l'adoption d'un format « thèse-articles ». Les travaux présentés sont publiés dans des revues internationales indexées avec comité d'évaluation par les pairs ou destinés à être publiés à la suite du dépôt initial de la thèse. Un bref avant-propos ainsi qu'un résumé en français ont été ajoutés en préalable des manuscrits afin de faciliter leur lecture. L'ensemble de ces articles sont originaux et ont été rédigés de manière indépendante par le candidat de cette thèse. Celui-ci a également été responsable de l'élaboration du cadre méthodologique, de la collecte des données sur le terrain ainsi que de leurs traitements et analyses. Daniel Fortier, en tant que superviseur, a contribué aux quatre manuscrits en aidant l'auteur à définir les objectifs de recherche et en fournissant des commentaires et des suggestions sur les manuscrits. Florent Dominé en raison de sa contribution au travail de terrain pour les aspects reliés à la neige et pour ses commentaires sur les manuscrits, figure également comme co-auteur sur trois des articles. Les titres sont listés ci-dessous :

Chapitre 2 : « *Properties and stratigraphy of polar ice patches in the Canadian High Arctic reveal their current resilience to warm summers* » (**Davesne, G., Fortier, D. et Dominé, F., accepté pour publication, septembre 2021, Arctic Science**)

Chapitre 3 : « *Mass balance and ablation processes of a perennial ice patch on the northern coast of Ellesmere* » (**Davesne, G., Fortier, D. et Dominé, F., en préparation**)

Chapitre 4 : « *Ice patches and their biogeomorphic system in the High Arctic polar desert* » (**Davesne, G. et Fortier, D.; en préparation**)

Chapitre 5 : « *Effects of meteorology and soil moisture on the spatio-temporal evolution of the depth hoar layer in the polar desert snowpack* » (**Davesne, G., Dominé, F. et Fortier, D., accepté pour publication, août 2021, Journal of Glaciology**)

La thèse est clôturée par le [chapitre 6](#) qui dresse une synthèse des principaux résultats obtenus dans les différents articles et répond aux questions et objectifs de recherche qui ont guidé cette thèse. À partir de l'ensemble des connaissances établies, une discussion est proposée sur l'évolution future des plaques de glace en réponse au réchauffement climatique et les conséquences potentielles sur les versants de désert polaire. Finalement, ce chapitre présente des recommandations pour les travaux futurs qui pourraient découler de cette thèse.

1.3. État des connaissances

1.3.1. Historique de la recherche sur les plaques de glace

La compréhension des caractéristiques physiques des systèmes de plaques de glace et de leurs variations spatio-temporelles est une étape indispensable à leur définition. L'étude de ces petits éléments de la cryosphère est considérée comme de la « microglaciologie », un domaine scientifique qui fait le lien entre la glaciologie classique et la géomorphologie périglaciale (Gachev, 2017). Jusqu'à maintenant, les études microglaciologiques sont peu nombreuses et, paradoxalement, sont principalement réalisées par des géographes ou des géomorphologues (ex. Gachev et al., 2016 ; Lewkowicz et Harry, 1991 ; Serrano et al., 2011) tandis que les plaques de glace ont reçu que peu d'attention de la part des glaciologues ou des nivologues. Ceci est en fait révélateur des échelles d'analyse propres à chaque discipline. Les glaciologues se préoccupent principalement des grandes composantes de la cryosphère terrestre, tandis que les nivologues se concentrent sur les propriétés à microéchelle du couvert de neige saisonnier (c.-à-d. grain de neige, strates) et l'hydrologie nivale. Du côté des géomorphologues et biologistes, les plaques de neige et glace ont suscité un intérêt en raison des effets qu'elles génèrent sur le milieu abiotique et biotique. Pour les géomorphologues, elles ont été principalement abordées à travers le prisme de la nivation (Ballantyne, 1985 ; Nyberg, 1986 ; Thorn, 1988). Pour les biologistes, elles ont été étudiées pour leur rôle dans la distribution de la végétation (Billings et Bliss, 1959 ; Bliss et al., 1984). Aucune de ces disciplines ne s'est attardée sur les plaques de glace en tant qu'objet d'étude à part entière. Étonnamment, un engouement important pour les plaques de glace a récemment émergé dans le domaine de l'archéologie (ex. Yukon Ice Patches Project, Hare et al., 2012). La fonte progressive des plaques en réponse au réchauffement libère un grand nombre d'artefacts préservés dans, ou sous, ces masses de glace quasi stationnaires durant plusieurs millénaires (Farnell et al., 2004 ; Pilø et al., 2021). Les travaux récents menés dans le cadre de l'archéologie glaciaire ont permis des avancées dans la compréhension de l'évolution des plaques de glace sur le long terme (Meulendyk et al., 2012 ; Ødegård et al., 2017). Certains travaux en paléogéographie ont également porté sur les propriétés des plaques de glace enfouies préservées dans le pergélisol continu, car elles représentent une base intéressante pour la reconstruction du climat et de l'environnement au quaternaire (ex. French et Pollard, 1986 ; Lacelle et al., 2009 ; Spektor et al., 2011). Le processus

d'enfouissement des plaques de glace par des mouvements de masse a été jusqu'à maintenant complètement ignoré par la communauté des géocryologues.

L'analyse de la répartition géographique des recherches sur le sujet montre que la grande majorité des études a été menée dans des régions montagneuses des moyennes latitudes ne présentant pas ou peu de glaciers. Les plaques de neige et de glace y représentent alors l'élément dominant de la cryosphère terrestre comme au Japon (Fujita et al., 2010 ; Higuchi, 1980; Kawashima et al., 1993 ; Sakai et al., 2006 ; Wakahama et Narita, 1975 ; Watanabe, 1988), dans massifs d'Europe centrale et méridionale (ex. les monts Pirin : Gachev et al., 2016; les monts Tatras : Gądek, 2008; les monts Cantabriques : Serrano et al., 2011), ainsi que dans les montagnes subarctiques du Canada (Farnell et al., 2004 ; Meulendyk et al., 2012) et en Scandinavie (Ødegård et al., 2017 ; Pilø et al., 2021). Dans les régions polaires arctiques, les seules publications disponibles sur les propriétés et le fonctionnement des plaques de glace se limitent à une étude de Østrem, (1963) menée dans le nord de la Norvège et à une série d'études menées dans les années 1990 par Lewkowicz et Harry (1991) ; Lewkowicz et Young (1990) ; Young et Lewkowicz (1990) dans le Haut-Arctique canadien.

1.3.2. Définition floue et multiplicité des termes

Bien que certains travaux aient été réalisés spécifiquement sur les plaques de glace, une confusion sémantique perdure autour de cet objet d'étude. Le travail de simplification et de classification nécessaire pour poser les bases d'une définition claire se heurte au caractère protéiforme des plaques de glace qui sont considérées comme un état intermédiaire dans le continuum entre les plaques de neige et les glaciers. De ce fait, la frontière sémantique est très floue entre les plaques de glace et les plaques de neige d'une part, et les plaques de glace et les petits glaciers d'autre part. La difficulté de définir les plaques de glace est aussi amplifiée par un manque de consensus et d'uniformité dans les terminologies adoptées, reflétant les opinions, approches et pratiques des glaciologues, des géomorphologues et des nivologues. Ainsi, dans la littérature anglo-saxonne, des termes comme « *snow field* » (Hirvas et al., 2000 ; Mott et al., 2019), « *perennial snowbank* » (Lewkowicz et Young, 1990), « *perennial snow patch* » (Watanabe, 1988), « *glacieret* » (Gachev et al., 2009), « *micro-glacier* » (Gachev et al., 2016) ou « *firn-ice patch* » (Gądek, 2008) ont été utilisés de manière plus ou moins interchangeable pour désigner de petites masses de glace pérennes sans que l'on puisse distinguer clairement la signification de chaque terme

et ce qui les distingue. Ce manque de clarté est également véhiculé par les glossaires de référence en glaciologie comme le « *Glossary of glacier mass balance and related terms* » de Cogley et al. (2011) selon lequel :

“*Snowfields are more extensive than snowpatches, but the distinction is not made precisely in common usage. A snowfield that is perennial may be difficult to distinguish from a glacier.*”

“*Snowpatches are less extensive than snowfields, but the distinction is not made precisely in common usage. A snowpatch that is perennial may be difficult to distinguish from a glacieret.*”

“*A very small glacier, typically less than 0.25 km² in extent, with no marked flow pattern visible at the surface. To qualify as a glacieret, an ice body must persist for at least two consecutive years.*”

La faiblesse de ces définitions est qu'elles sont basées uniquement sur des critères de taille et de durée de persistance établis selon des seuils purement arbitraires qui ne permettent pas de discriminer les différents systèmes.

Afin de remédier à cette confusion sémantique entourant les différentes petites masses de glace terrestres, Serrano et al. (2011) ont proposé de distinguer les petits glaciers, les plaques de neige et les plaques de glace en fonction de leur mouvement ou absence de mouvement, de leur structure (glace, névé, neige, déformation) et leur genèse (glaciaire ou nival).

Tous les glaciers, y compris les plus petits, sont définis comme des masses de glace sédimentaire qui se sont constituées par la compaction progressive de la neige et qui se déforment et s'écoulent sous l'influence de la gravité (Benn et Evans, 2010). Les petits glaciers sont fortement contrôlés par les contraintes topographiques et se déclinent en une grande variété de formes, de tailles et de régimes différents. Il y a, par exemple, les petites calottes et les crêtes de glace sommitales (*Miniature ice cap, Ice crest* ; Haeberli et al., 2004 ; Holmlund et Holmlund, 2019 ; Serreze et al., 2017), les glacierets (Colucci et al., 2015 ; Gachev et al., 2016 ; Kuhn, 1995) ou encore les tabliers de glace suspendus (*Ice apron*) qui sont spécifiques aux parois de haute montagne (Guillet et Ravanel, 2020). Bien que de dimension limitée ($>0.5 \text{ km}^2$; Huss et Fischer, 2016), ces petits systèmes glaciaires présentent des signes de déformation par des mouvements

internes (ex. failles, fractures, crevasses) même si ceux-ci sont généralement lents (Leigh et al., 2019).

Une plaque de neige (*snow patch* ou *snowbank*) définit une accumulation de neige qui persiste longtemps pendant la saison chaude mais qui disparaît complètement avant la fin de l'été, hormis dans de rares cas où elle peut survivre à un été plus frais que la normale (Nesje et al., 2012). Une plaque de neige est typiquement formée de neige à grain grossier, ayant subi un métamorphisme avancé de fonte, et éventuellement d'une couche de glace basale issue de la percolation et du regel de l'eau de fonte à la base de l'accumulation de neige (Woo et al., 1982).

Une plaque de glace (*ice patch*) représente une petite masse de glace dont la forme et la taille peuvent être très variables (**Figure 2**). Elle se distingue principalement d'un petit glacier par le fait que la glace ne présente pas de structures de déformation en surface et qu'elle n'a pas de zones d'accumulation et d'ablation distinctes. La masse de glace peut avoir plus de 15 mètres d'épaisseur (Kawashima et al., 1993 ; Ødegård et al., 2017) et se trouve le plus souvent recouverte d'une couche de névé (Cogley et al. 2011). Par exclusion, le terme de « plaque de glace » regroupe toutes les masses de glace présentes à la surface terrestre et qui ne sont pas des systèmes glaciaires actifs. Les plaques de glace peuvent être préservées sur de longues périodes pouvant aller jusqu'à plusieurs siècles, voire plusieurs millénaires. Elles sont alors qualifiées de permanentes. Des datations réalisées sur des plaques de glace au Yukon et en Norvège ont par exemple prouvé leur présence continue depuis la fin de l'Optimum climatique Holocène (~ 6000 ans BP) (Farnell et al., 2004 ; Ødegård et al., 2017). Lorsque les plaques de glace persistent pendant plusieurs années consécutives, mais qu'elles disparaissent occasionnellement lors d'été particulièrement chauds, elles sont dites pluriannuelles ou semi-permanentes (Woo et Young, 2014).

Serrano et al. (2011) a proposé de distinguer deux types de plaques de glace permanentes en fonction de leur origine et de leur structure interne (**Figure 3**). Le premier, appelé « système morphodynamique nival » (**Figure 2a,b,c,d; Figure 3**), se réfère aux plaques de glace qui sont le résultat de fortes accumulations locales de neige pendant la saison froide par la redistribution éolienne et/ou par des processus gravitaires d'avalanches (Fujita et al., 2010 ; Glazirin et al., 2004 ; Mott et al., 2019). Typiquement, ce type de plaques de glace se trouve dans les dépressions topographiques, au pied d'une paroi rocheuse ou sur des versants sous le vent et ombragés. Lorsque ces accumulations de neige sont suffisamment importantes, elles ne sont pas complètement

détruites par l'ablation estivale et vont être préservées jusqu'à la saison froide suivante. La neige saisonnière persistante se densifie et se transforme rapidement en glace par le regel de l'eau de fonte à la surface de la glace de l'année précédente formant de la glace surimposée (*superimposed ice*) (Kawashima et al., 1993).

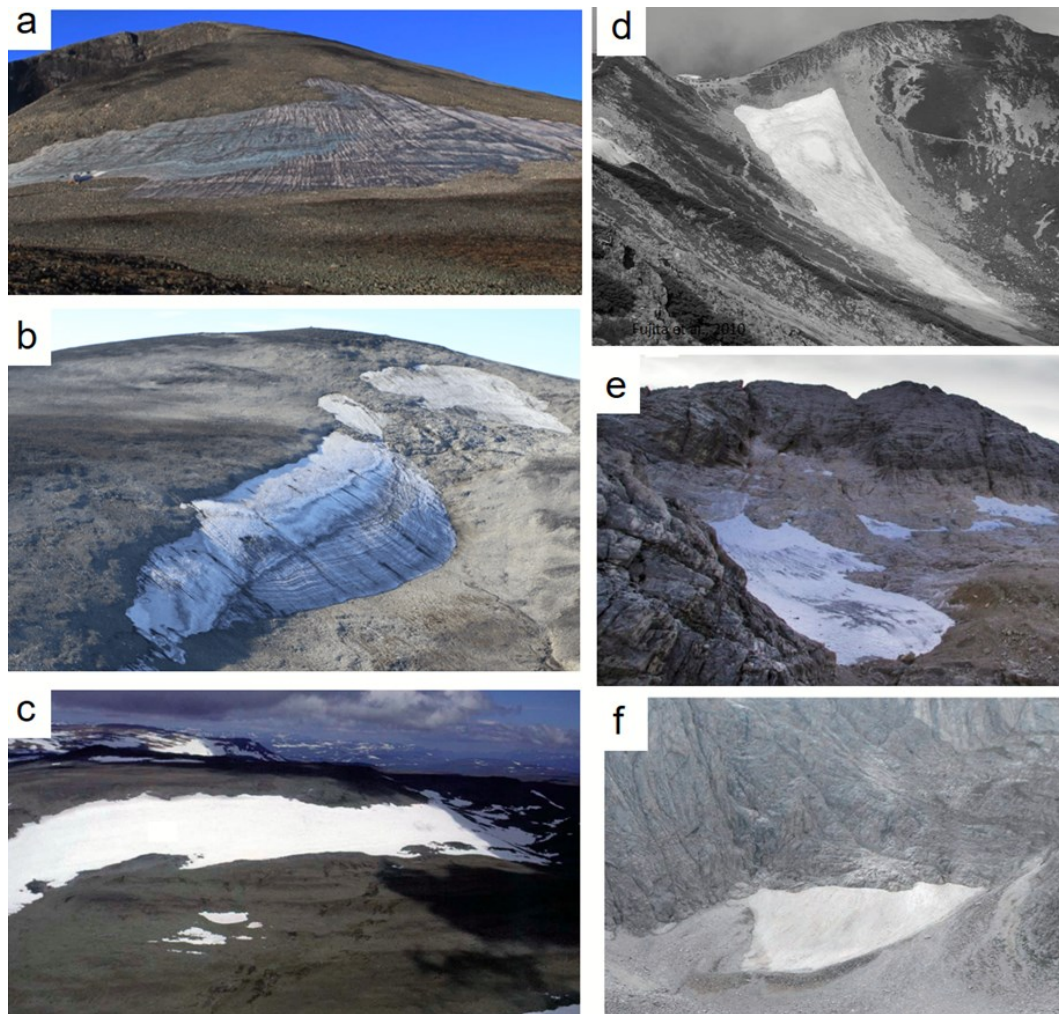


Figure 2. Exemples de petites masses de glace permanentes entrant dans la catégorie de « plaque de glace ». a) et b) Plaques de glace de Juvfonne et Langfonne situées dans le sud de la Norvège (Ødegård et al., 2017 ; Pilø et al., 2021) ; c) Plaque de glace située dans le nord de la Finlande, désignée comme « permanent snowfield » par les auteurs (Hirvas et al., 2000) ; d) Plaque de glace de Hamaguri- yuki dans les Alpes Japonaises, désignée comme « snow patch » par les auteurs (Fujita et al., 2010); e) et f) Plaques de glace dans les Alpes Juliennes dans le massif du Pirins en Europe centrale (Gachev et al, 2016 ; Colucci et al., 2021). Pour a,b,c,d, les plaques de glace appartiennent au système morphodynamique nival tandis que pour e et f, les plaques de glace appartiennent au système morphodynamique glaciaire (Serrano et al., 2011).

Le second type, appelé « système morphodynamique glaciaire » (**Figure 2e,f; Figure 3**), décrit les plaques de glace formées par les restants d'un ancien glacier devenu inactif pendant une période de déglaciation (c.-à-d. un environnement paraglaciaire). La désintégration d'un glacier laisse alors une masse de glace "morte" qui présente un faciès typique de la glace de glacier avec des fractures et des failles liées à son ancien mouvement. Ces plaques de glace d'origine glaciaire se trouvent généralement au fond des cirques glaciaires (Kawashima et al., 1993 ; Kuhn, 1995) ou sur des plateaux (ex. reliques de petites calottes glaciaires; White et Copland, 2018). Dans un contexte topographique favorable, les masses de glace peuvent être durablement préservées par un apport actif de neige par avalanche ou par transport éolien aboutissant à leur enfouissement sous une couche de névé et de « nouvelle » glace surimposée. Dans ce cas, un système hybride se développe avec différents faciès de glace (Yamamoto et Yoshida, 1987).

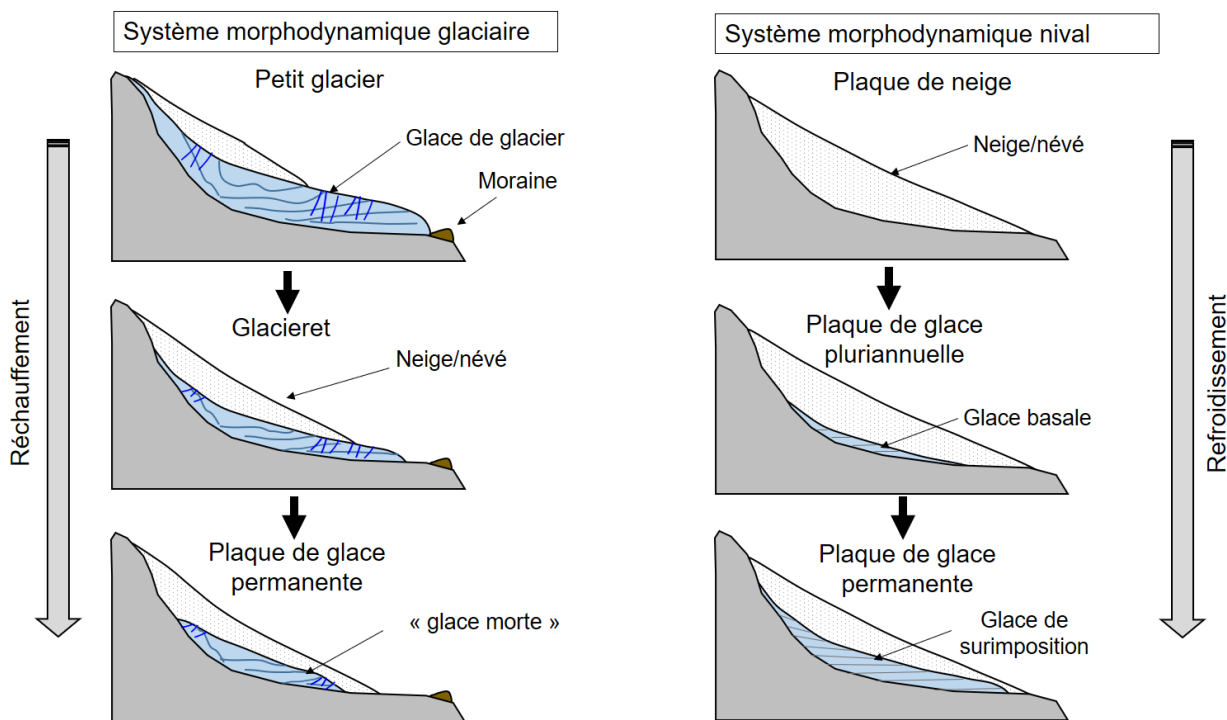


Figure 3. Les deux systèmes morphodynamiques de plaque de glace : le système glaciaire et le système nival (modifié de Serrano et al., 2011).

Cette classification des différentes petites masses de glace terrestre apportée par Serrano et al. (2011) a posé les bases d'une définition plus claire du concept de « plaque de glace ». Elle a également permis de souligner la nécessité d'une connaissance approfondie de la structure interne

et des propriétés physiques de la glace pour identifier au mieux l'origine d'un système de plaque de glace et en comprendre le fonctionnement.

1.3.3. De la neige saisonnière à la glace permanente

Le peu de littérature sur les processus de formation des plaques de glace d'origine nivale nécessite de se tourner vers les études glaciologiques menées sur les systèmes glaciaires qui offrent une base théorique importante sur les mécanismes de transformation de la neige saisonnière en glace. Il existe deux mécanismes principaux : la compaction et le regel de l'eau de fonte (Cuffey et Paterson, 2010).

La compaction est un processus lent qui consiste en différentes phases de densification transitoires amenant à la transformation de la neige saisonnière en neige de névé (*Firnification*) et finalement du névé en glace. La neige de névé se caractérise par des pores encore partiellement interconnectés (Cogley et al., 2011) et possède une densité très variable selon son âge et son environnement physique, allant de 400 à 830 kg m⁻³ (Cuffey et Paterson, 2010 ; Fierz et al., 2009). Dans la zone des glaciers dite de « neige sèche » où aucune fonte ne se produit pendant l'été (**Figure 4**), le névé évolue essentiellement sous l'influence du gradient de température en surface puis par métamorphisme mécanique de compression plus en profondeur. Dans la zone de « percolation » (**Figure 4**), le métamorphisme de fonte est dominant qui mène à un grossissement des grains. Par ailleurs, la présence d'eau liquide accélère le tassemement de la colonne de névé (Cuffey et Paterson, 2010). À mesure qu'une couche de névé se fait enfouir, la pression grandissante sous le poids des couches de neige supérieures entraîne une expulsion de l'air, ce qui aboutit à une diminution progressive de la porosité et une densification du névé. La hausse de la pression amorce parallèlement un grossissement de la taille des grains de glace par recristallisation dynamique (Montagnat et al., 2009). Dès lors que les pores entre les grains se ferment, généralement lorsque la densité dépasse 800 à 850 kg m⁻³, le névé devient de la glace. Cette dernière demeure riche en bulles d'air (environ 10% d'air) dans un premier temps, puis la teneur en air décroît à mesure que la pression augmente (Marsh, 2005 ; Paterson, 1994). Le temps nécessaire pour une couche de neige saisonnière de devenir de la glace varie selon les environnements, allant de quelques années pour les glaciers tempérés à plusieurs centaines d'années en Antarctique.

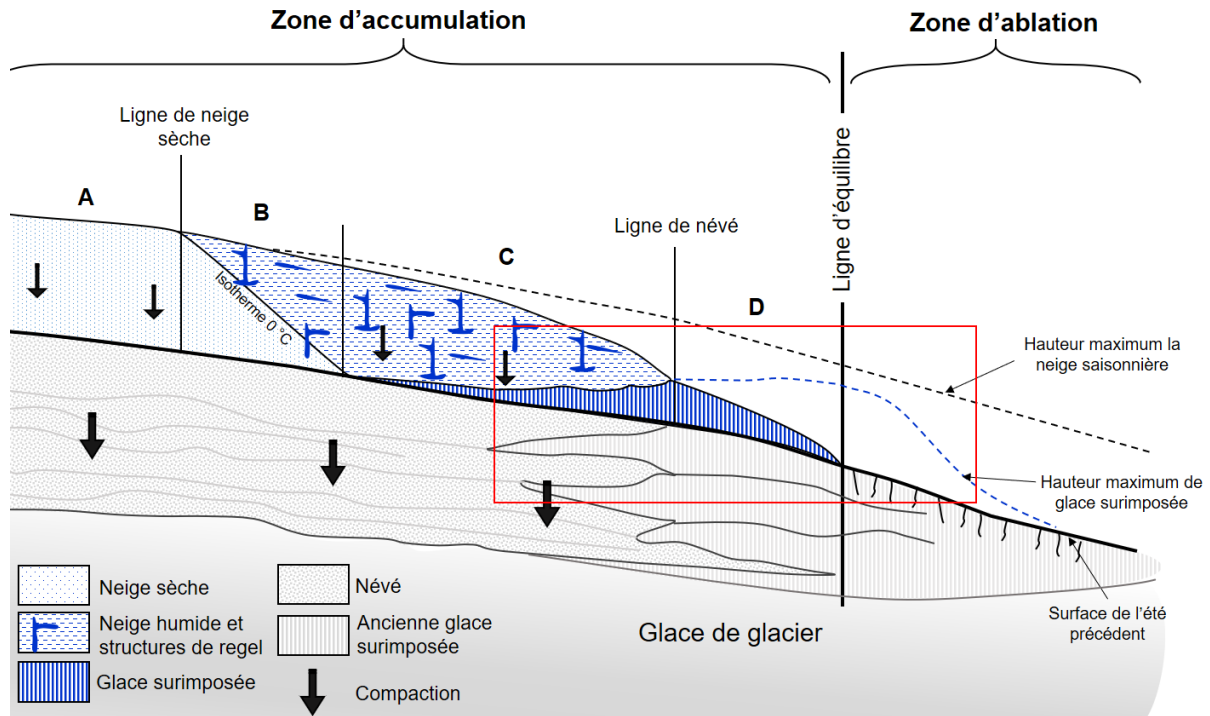


Figure 4. Subdivision de la zone d'accumulation d'un glacier selon les conditions de surface (neige, névé, glace exposée) à la fin de la saison de fonte. Zone A : zone de neige sèche où il n'y a pas de fonte estivale. Zone B : zone de percolation, les eaux de fonte de surface s'infiltrent dans le manteau neigeux et régèlent. Zone C : zone de saturation (ou zone de neige humide) où la température de l'ensemble du manteau neigeux a atteint le point de fusion à un moment donné de la saison de fonte et où l'eau de fonte atteint l'interface neige-glace et y régèle pour former de la glace surimposée. La limite inférieure de la zone de saturation est appelée la ligne de névé. Zone D : zone où l'ensemble de la neige saisonnière fond avant la fin de la saison de fonte et où la glace surimposée est exposée à la fonte. La ligne d'équilibre est située à la limite inférieure de cette zone et relie tous les points où le bilan annuel net est nul. L'altitude de cette ligne est appelée altitude de la ligne d'équilibre (Equilibrium-line altitude : ELA). La zone de glace de glacier correspond à la zone d'ablation où la fonte estivale élimine la totalité de l'accumulation annuelle de neige et glace de surimposée. L'encadré rouge indique la section d'un glacier où les processus d'accumulation et de fonte sont similaires à ceux impliqués dans le bilan de masse d'une plaque de glace (inspiré de Paterson, 1994).

Le processus de fonte/regel entraîne quant à lui une transformation rapide (quelques jours à quelques semaines) de la neige saisonnière en glace, généralement sans passer par le stade de névé. Ce processus se produit au niveau de la « zone de percolation » et surtout dans la « zone de saturation » (**Figure 4**). Au début de la saison chaude, l'eau de fonte des couches de neige de surface percole profondément dans le couvert nival, remplissant la porosité. Lorsque la température de la neige est inférieure au point de fusion, cette eau de fonte régèle et forme des structures de glace verticales et horizontales (ex. colonnes, lentilles et strates de glace). Dans la section inférieure

de la zone de saturation, l'apport en eau de fonte est important de sorte qu'elle s'accumule à l'interface entre la neige et la glace imperméable où elle règle en une couche de glace dite surimposée (*superimposed ice* en anglais) (**Figure 4**). La quantité de glace formée et la rapidité du processus dépendent de l'apport en eau liquide et surtout du contenu en froid (*cold content*) du couvert de neige et de la glace sous-jacente à la fin de la saison froide (Obleitner et Lehning, 2004). La formation de glace superposée est courante dans les systèmes glaciaires polaires où elle constitue une composante importante du bilan de masse des glaciers et calottes de glace (Koerner, 1968 ; Koerner, 1970 ; Wadham et Nuttall, 2002). Le même processus se produit sur la banquise (Kawamura et al., 2004), les plateformes de glace (*Ice shelf* ; Jeffries et al., 1991) et en milieu terrestre où le regel de l'eau de fonte à l'interface neige-sol forme de la « glace basale » (Woo et al., 1982). Les processus de regel se produisent également à la fin de l'été au-dessus de la ligne de névé lorsqu'une couche de neige saturée en eau regèle avec le refroidissement atmosphérique et produit une glace désignée sous le terme de « *iced-firn* » (Cuffey et Paterson, 2010 ; Koerner, 1968).

Dans les systèmes de plaques de glace permanentes, les conditions de surface ressemblent à celles que l'on trouve près de la ligne d'équilibre des glaciers (*Equilibrium-line altitude* : ELA; voir encadré rouge, **Figure 4**), ce qui suppose une grande contribution des processus de fonte/regel. Dans son étude de 1963, Østrem a apporté les premières observations glaciologiques d'une plaque de glace permanente en Norvège et a identifié à partir d'une analyse de lames mince le rôle important des processus de fonte/regel aboutissant à la formation de couches de glace surimposée. Des interprétations similaires ont été rapportées par Kawashima et al. en 1993 lors de l'étude d'une plaque de glace dans les Alpes japonaises. Les auteurs ont suggéré que l'aggradation du corps de glace se fait par la combinaison de trois processus, à savoir la formation de glace surimposée, la densification d'une couche de névé saturée en eau et le regel du névé au début de l'hiver. Dans le Haut-Arctique, Lewkowicz et Harry (1991) ont également suggéré que la formation de la glace surimposée était le principal processus d'aggradation du corps de glace d'une plaque de glace étudiée sur l'île Melville (Arctique canadien). Cette étude reste la seule à ce jour à s'être intéressée aux propriétés physiques d'une plaque de glace polaire.

Ces trois études pionnières ont posé les bases de la compréhension des caractéristiques physiques des plaques de glace, cependant seule l'étude d'Østrem (1963) a été étayée par une

analyse cristallographique rigoureuse basée sur une collection de lames minces de glace. Ce manque d'études glaciologiques se traduit par des lacunes importantes dans l'identification des différents faciès de glace (ex. glace riche en bulles d'air, glace pure, glace riche en sédiments) qui peuvent exister dans les plaques de glace et dans la compréhension des mécanismes thermodynamiques qui conduisent à leur formation, et en particulier la nature des interactions complexes entre la neige saisonnière, l'eau de fonte et la masse de glace permanente.

1.3.4. Bilan de masse d'un système de plaque de glace

Les plaques de glace permanentes se forment dès lors que les accumulations de neige/glace ne sont pas complètement détruites par l'ablation estivale. Dans un système glaciaire, le volume et la dimension des masses de glace évoluent dans le temps selon le bilan de masse net qui est la différence entre les gains de masse lors de la saison froide et les pertes de masse lors de la saison chaude sur une année hydrologique (**Figure 5**). Si le bilan de masse net est positif (accumulation > ablation), le volume de glace augmente et s'il est négatif (accumulation < ablation), il diminue, et s'il est nul, il est stable (Cuffey et Paterson, 2010). Dans le cas des plaques de glace, le bilan de masse est toujours proche de 0 sur le moyen et long terme, même si de légères fluctuations à court terme peuvent se produire. Pour les systèmes morphodynamiques nivaux (**Figure 5**), cet équilibre entre les apports et les pertes résulte du contrôle dominant des contraintes topographiques (c.-à-d. taille de la niche topographique) qui empêchent la masse de glace et de neige de croître au-delà d'un certain seuil (Glazirin et al., 2004).

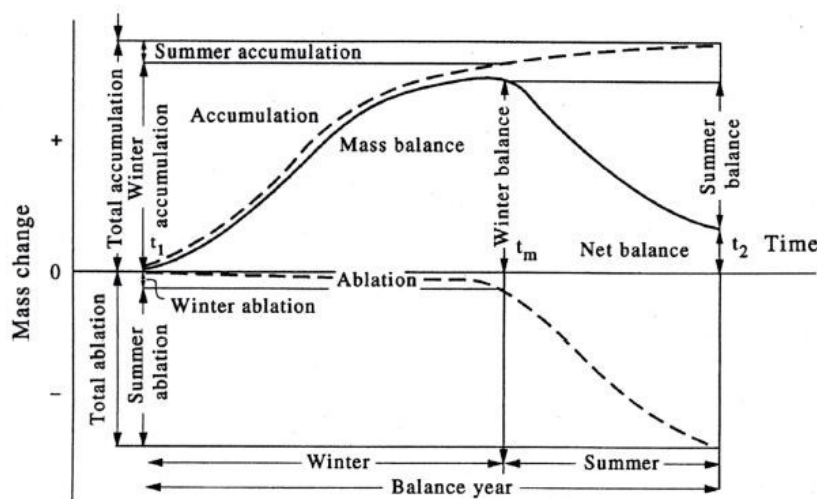


Figure 5. Schématisation du concept de bilan de masse net (Paterson, 1994).

Pour les plaques de glace d'origine glaciaire, en revanche, le bilan de masse peut devenir durablement positif (ex. hausse des apports ; diminution des pertes) car le volume de glace n'est pas restreint par la topographie. Cependant, dès lors qu'une plaque de glace grossit, elle commence à se déformer et à fluer ce qu'il l'amène dans une transition vers un système glaciaire (**Figure 5**; (Serrano et al., 2011).

Contrairement aux glaciers, les plaques de glace n'ont pas de zones distinctes d'accumulation et d'ablation, ce qui explique l'absence de transfert de masse au sein du système. L'accumulation et l'ablation se produisent donc théoriquement partout et le bilan de masse reste proche de 0 en tout point, malgré le fait que l'accumulation et l'ablation nettes peuvent être très variables à fines échelles. Par effet de compensation, les zones qui reçoivent le plus de matière sont également celles qui en perdent le plus (Fujita et al., 2010). En raison de leur petite taille et de l'absence d'un transfert de masse par mouvement, la mesure du bilan de masse est relativement simple par rapport à celui des glaciers. Les méthodes la plus couramment utilisées visent à mesurer l'épaisseur de neige et de glace à la fin de la saison de fonte et à la fin de la saison froide par des techniques de sondage (ex. forage, géoradar) et/ou des mesures spatiales (ex. Laser Scan Terrestre) (ex. Meulendyk et al., 2012 ; Rebecca Mott et al., 2019 ; Ødegård et al., 2017).

1.3.4.1. Processus d'accumulation

L'existence de plaques de glace et de neige est avant tout liée à des accumulations préférentielles de neige durant la saison froide. Ces dernières sont contrôlées par des facteurs topoclimatiques qui induisent des mécanismes de redistribution de la neige par processus éoliens, gravitaires, ou à une combinaison des deux (**Figure 6**) (Fujita et al., 2010 ; Watanabe, 1988).

- *Processus éolien*

Le vent contrôle fortement la distribution de la neige pendant et après les précipitations et agit à différentes échelles spatiales. Les processus éoliens sont désormais bien documentés et modélisés. Une revue complète de l'état des connaissances sur le sujet a été récemment proposée par Mott et al., (2018). Dans cette section, nous n'aborderons que les processus qui se produisent après les précipitations, car ils sont le facteur de contrôle premier dans la distribution du couvert nival à l'échelle locale et donc dans la formation des accumulations préférentielles.

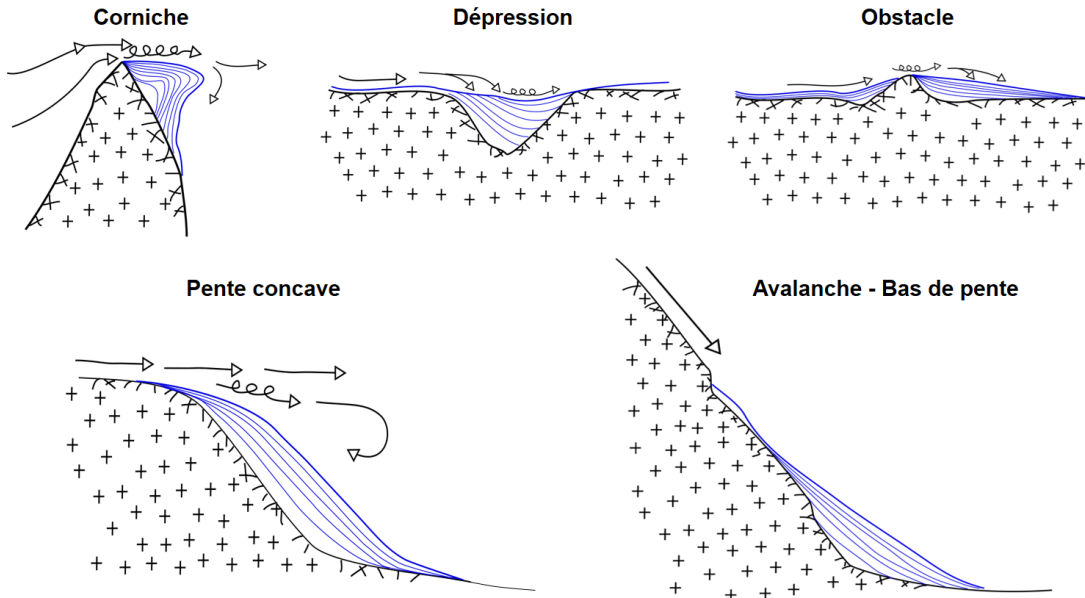


Figure 6. Diagrammes représentant les contextes topographiques favorables à développement d'accumulations préférentielles de neige.

L'action du vent sur le couvert nival à l'échelle locale englobe trois processus, à savoir l'érosion, le transport et la déposition. L'ensemble de ces processus dépend de la vitesse du vent dans la couche limite de l'atmosphère et de son interaction avec la rugosité de surface produite par la microtopographie, la végétation ou la surface de la couche de neige au sol. L'érosion de la neige se produit dès lors que la contrainte de cisaillement du vent (force motrice) excède la force résistante de la neige. La mise en mouvement des grains de neige est donc très dépendante de la texture et de la cohésion de la neige, qui dépendent elles-mêmes des processus de métamorphisme et de la température. Le seuil de vitesse de vent pour éroder une surface de neige est donc très variable selon les conditions de neige et donc difficile à établir (Vionnet et al., 2013). À partir de mesures de terrain dans les prairies canadiennes, Li et Pomeroy (1997) ont établi une relation entre le seuil de vitesse du vent pour la mobilisation de la neige et la température de l'air. Leurs résultats suggèrent que le seuil de vitesse de vent à 10 m au-dessus du sol pour l'érosion de la neige sèche était en moyenne de 4–11 m s⁻¹ (moyenne = 7.7 m s⁻¹) tandis qu'elle était de 7–14 m s⁻¹ (moyenne = 9.9 m s⁻¹) pour la neige humide. Généralement, les seuils de vitesse de vent couramment utilisés dans la littérature pour les travaux de modélisation sont de 6 m s⁻¹ pour la neige sèche peu compactée, 10 m s⁻¹ pour la neige sèche légèrement consolidée et plus de 15 m s⁻¹

pour la neige sèche très compactée par de forts vents (Essery et Pomeroy, 2004 ; Gray et Male, 1981 ; Royer et al., 2021 ; Sturm et al., 2001).

Une fois mis en mouvement, les grains de neige vont être transportés sur une distance plus au moins longue selon le mode de transport. La reptation et la saltation des particules se produisent généralement sur de courtes distances, tandis que le transport en suspension turbulente a le potentiel de transporter la neige sur plusieurs centaines de mètres voire plusieurs kilomètres (Mott et al., 2011 ; Pomeroy et al., 1997). Le transport par reptation (**Figure 7**) est dominant lorsque la vitesse du vent est faible ($< 8 \text{ m s}^{-1}$) et que la plupart des grains de neige mobilisés roulent sur la surface du couvert nival dans la direction du vent. Les quantités de neige transportées par la reptation restent généralement limitées comparées aux autres processus de transport (Filhol et Sturm, 2015 ; Mott et al., 2018).

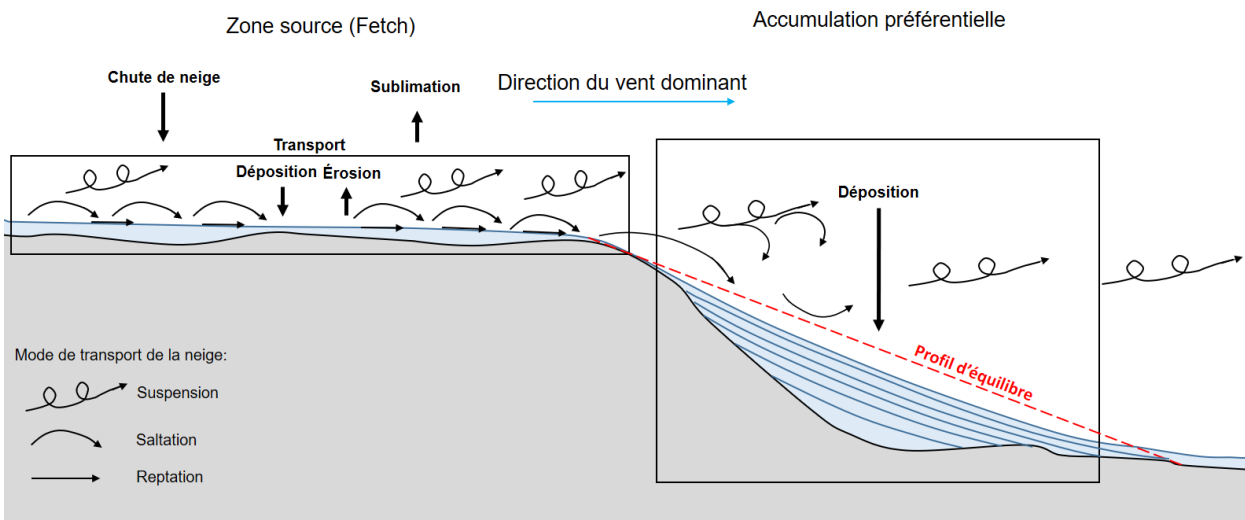


Figure 7. Redistribution de la neige saisonnière par des processus éoliens amenant à la formation d'accumulations préférentielles de neige (inspiré de Pomeroy et al., 1997).

Lorsque la vitesse du vent se situe entre 8 et 15 m s^{-1} , le transport se fait essentiellement par saltation (**Figure 7**). Les grains de neige sont alors soulevés verticalement dans l'air en raison du gradient vertical de vitesse et ils suivent des trajectoires contrôlées par les forces du vent et de la gravité. La hauteur de cette couche de saltation est limitée aux premiers décimètres au-dessus de la surface et la longueur de ces sauts de saltation dépasse rarement un mètre (Liston et Sturm, 1998). L'impact des grains de neige qui percutent la surface du couvert nival libère d'autres grains. Cette réaction en chaîne (*Splash entrainment*) induit un entraînement exponentiel des grains de

neige pour une même vitesse de vent (Mott et al., 2018). Dans les milieux ouverts, la saltation est le mode de transport dominant, représentant souvent de 50 à 75% du transport éolien total de la neige (Gray et Male, 1981 ; Pomeroy et Gray, 1990). Finalement, pour les vents les plus forts ($> 15 \text{ m s}^{-1}$), des flux turbulents se développent dans la couche limite et produisent un transport des grains de neige en suspension (**Figure 7**). Lorsque la contrainte de cisaillement des flux d'air est égale au poids des grains de neige, ceux-ci sont en effet transportés horizontalement par le vent. Généralement, le transport en suspension se concentre dans les premiers mètres au-dessus de la surface du sol (Mott et al., 2018 ; Pomeroy, 1989).

Pendant le transport par saltation et surtout par suspension turbulente, les particules de neige perdent rapidement de leur masse dans l'atmosphère par sublimation (**Figure 7**). Dans les régions polaires, où l'air est souvent très sec en hiver, le taux de sublimation peut être important. Pomeroy et al (1997) ont rapporté des pertes par sublimation d'environ 28% des chutes de neige annuelles en moyenne à Inuvik (Territoires du Nord-Ouest, Canada). Par conséquent, en raison de l'effet conjugué de l'érosion éolienne et de la sublimation, l'épaisseur de neige en équivalent en eau à la fin d'hiver est largement inférieure au total des précipitations.

Lorsque les flux d'air ralentissent, le vent perd de sa compétence au transport et laisse la neige se redéposer. Spatialement, le vent entraîne une distribution très hétérogène du couvert nival entre les zones les plus exposées à la déflation (ex. les sommets, les crêtes, les corniches, les hauts plateaux), où l'érosion et le transport de la neige dominent, et les zones abritées où se forment les accumulations préférentielles (**Figure 7**; Glazirin et al., 2004 ; Liston et al., 2002 ; Sturm et al., 2001). Ces accumulations nivéoéoliennes, appelées congères (*snowdrift*), se développent par séparation des flux d'air, typiquement en aval d'obstacles (ex. irrégularité du terrain, végétation), d'une rupture de pente (ex. crête) ou au niveau d'une dépression (ex. combe à neige, profil de pente concave) (**Figure 7**). Le volume total de neige qui parvient à s'accumuler est d'abord contrôlé par la disponibilité en neige, qui dépend des précipitations et de la superficie du terrain exposé à la déflation, appelée le fetch (**Figure 7**) (Benson et Sturm, 1993 ; Pomeroy et al., 1997). L'accumulation de neige est également régie par le contexte topographique où elle se forme. Deux cas de figure ont été identifiés : les niches topographiques à remplissage limité (*filling snowdrift*) et celles à remplissage virtuellement illimité (*unfilling snowdrift*) (Benson et Sturm, 1993). Pour le premier cas, Tabler (1975) a introduit le concept de « profil d'équilibre » des dépôts préférentiels

de neige édifié sur les lois de l'aérodynamique, selon lequel le remplissage d'une niche topographique élimine la séparation des flux d'air. Ainsi, une fois qu'un dépôt de neige atteint son profil d'équilibre, le volume total de la neige se stabilise, quelle que soit l'ampleur des apports éoliens en neige subséquents (Benson et Sturm, 1993 ; Mases et al., 1998 ; Sturm et al., 2001). Le moment où ce profil d'équilibre est atteint dépend des apports en neige et de la taille de la niche topographique. Logiquement, plus une niche est petite, plus elle se remplit rapidement au début de la saison froide. Ainsi dans le cas des *filling snowdrifts*, la variabilité interannuelle dans les accumulations de neige est très réduite car le contexte topographique est le facteur de contrôle dominant. En ce qui concerne les *unfilling snowdrifts*, les niches topographiques sont de plus grands volumes ce qui implique que le remplissage est beaucoup plus long et que le profil d'équilibre n'est généralement pas atteint avant la fin de la saison froide. Dans ce cas, la variabilité interannuelle des accumulations de neige est beaucoup plus grande car elle dépend avant tout des apports en neige (Benson et Sturm, 1993 ; Parr et al., 2020).

Dans les régions polaires, les processus de remobilisation de la neige sont fréquents et extrêmes produisant un couvert de neige particulièrement hétérogène selon la topographie (Eveland et al., 2013a,b ; Parr et al., 2020). Les processus éoliens sont donc centraux dans la dynamique des plaques de glace permanentes. Cependant, pour l'heure, le manque d'études quantitatives sur le régime des vents et les processus de redistribution de la neige limite la compréhension des interactions entre le vent, la topographie et les propriétés physiques de la neige qui exercent un contrôle direct sur les mécanismes de remplissage des systèmes de plaques de glace polaires. Ces lacunes empêchent une compréhension complète du bilan de masse des plaques de glace.

- *Processus gravitaires*

Dans les environnements de montagne, de nombreuses plaques de neige et de glace doivent leur existence à des apports gravitaires importants en neige par avalanches. Dans les couloirs et à la base des pentes raides, les dépôts avalancheux peuvent atteindre plusieurs dizaines de mètres d'épaisseur, prenant souvent la forme de talus ou cône de neige (**Figure 6**; Gachev et al., 2016). Le volume total qui peut s'accumuler n'est généralement pas limité par la topographie et dépend donc essentiellement de la fréquence des avalanches, laquelle est contrôlée par les précipitations et les propriétés physiques de la neige. Il en résulte une forte variabilité interannuelle. Les dépôts de neige gravitaires représentent la source principale d'alimentation de petits glaciers et des plaques

de glace à la base de parois rocheuses et dans le fonds des cirques glaciaires (ex. Gachev et al., 2016; Glazirin et al., 2004; Ishikawa et Sawagaki, 2001; Mott et al., 2019; Watanabe, 1988) (**Figure 2f**).

- *Apports par le ruissellement*

Une source secondaire de masse peut être apportée à un système de plaque de glace par le ruissellement de l'eau de fonte en provenance de la section amont de la pente (Ballantyne, 1978 ; Lewkowicz et Young, 1990). Au début de l'été, l'eau de fonte de la neige s'écoule à la surface du sol gelé imperméable et atteint les plaques de glace. Cette eau va d'abord regeler à l'interface neige-glace, où les températures sont inférieures au point de fusion, contribuant ainsi à l'aggradation de la glace surimposée. Ce processus se produit essentiellement dans un contexte polaire où le contenu en froid des accumulations de neige et des masses de glace apporte une capacité de regel potentielle de l'eau liquide importante.

1.3.4.2. Processus d'ablation

La principale perte de masse d'un système de plaque de glace se produit par la fonte estivale des accumulations préférentielles de neige et du corps de glace sous-jacent lorsque celui-ci est exposé. Comme pour les glaciers, cette fonte est déterminée par le bilan d'énergie de surface qui est lui-même contrôlé par les conditions topoclimatiques (Fujita et al., 2010 ; Mott et al., 2011 ; Sato et al., 1984 ; Young et Lewkowicz, 1990). Les plaques de glace se forment essentiellement dans les zones où l'ablation est atténuée par une réduction locale de l'apport de chaleur, typiquement dans les zones ombragées et abritées du vent (Fujita et al., 2010 ; Mott et al., 2019). À l'échelle locale, les processus d'ablation sont aussi fortement influencés par les propriétés de la neige saisonnière et de la glace qui déterminent la capacité du système à absorber, perdre ou stocker de l'énergie. En hiver, des pertes non négligeables se produisent également par sublimation, notamment dans un contexte de désert polaire (Leppäranta et al., 2013), mais celles-ci sont rapidement compensées par les apports éoliens en neige. Jusqu'à présent, peu d'études ont porté spécifiquement sur les processus d'ablation des systèmes de plaques de glace, mais la littérature sur la dynamique de la neige saisonnière fournit une base théorique importante pour aborder cette question.

- *Le bilan d'énergie de surface de la neige*

Le bilan d'énergie complet d'une couche de neige est complexe car il intègre les processus de changement de phase par la fonte, de condensation, de sublimation, d'évaporation et de regel. Il est également influencé par l'évolution du bilan de masse du manteau neigeux selon les apports et les pertes en neige. Traditionnellement, la fonte d'une masse de neige ou de glace est estimée à partir d'un modèle physique simplifié consistant au calcul du bilan d'énergie de surface (abrégé en SEB pour *Surface energy balance*) (Garen et Marks, 2005 ; Ohmura, 1984; **Figure 8**). Lorsque la température de la couche de surface atteint 0 °C, tout surplus d'énergie est utilisé pour la fonte. L'énergie disponible pour la fonte d'une couche de neige/glace de surface (noté Q_m , W m⁻²) est exprimée par les équations (1) et (2) (Dewalle et Rango, 2008 ; Boike et al., 2003a) :

$$-Q_m = Q_r + Q_h + Q_e + Q_p + Q_c - \left(\frac{\partial Q}{\partial t} \right) \quad (1)$$

$$Q_r = (SW \downarrow - SW \uparrow) + (LW \downarrow - LW \uparrow) \quad (2)$$

Q_r représente le bilan du rayonnement net à la surface de la neige. $SW \downarrow$ et $SW \uparrow$ sont respectivement le rayonnement solaire reçu et réfléchi par la surface de neige/glace dont le rapport est déterminé par l'albédo de surface. $LW \downarrow$ et $LW \uparrow$ sont respectivement le rayonnement thermique (infrarouge, 4-100 μm) émis par l'atmosphère et par la surface de la neige/glace.

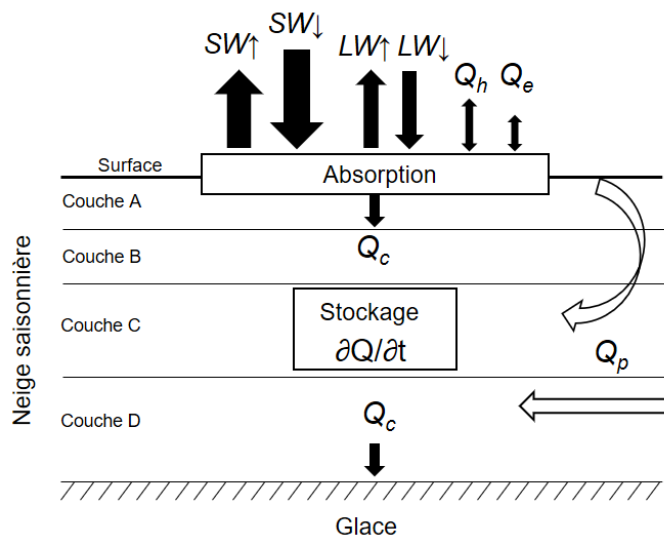


Figure 8. Conceptualisation du bilan d'énergie d'un couvert nival saisonnier sur une plaque de neige (inspiré de Garen et Marks, 2005 ; Ohmura, 1984)

Dans l'Arctique, Qr est dominé par le rayonnement infrarouge pendant l'hiver tandis qu'il est dominé par le rayonnement solaire pendant l'été. Qh et Qe sont les flux turbulents de chaleur sensible et latente, respectivement. Ces flux de chaleur sont contrôlés par l'intensité et le signe du gradient vertical thermique et d'humidité entre la surface de la neige et l'atmosphère. Ils sont également fortement modulés par le vent dans la couche limite de l'atmosphère ainsi que la rugosité de surface (Gray et Male, 1981). Qp représente les flux de chaleur sensible apportés par les précipitations et le ruissellement d'eau liquide et Qc représente les flux de chaleur par conduction des couches de surfaces vers les couches inférieures jusqu'à la glace ou le sol sous-jacent. Finalement $\partial Q / \partial t$ est le stockage d'énergie dans une couche de neige (**Figure 8**) (Fujita et al., 2010 ; Mott et al., 2011 ; Sato et al., 1984 ; Young et Lewkowicz, 1990).

Aux plus hautes latitudes, la période d'ablation ne s'étend que sur 2 à 3 mois. Dans le Haut-Arctique, la seule étude réalisée sur le SEB d'une plaque de glace permanente a été menée par Young et Lewkowicz (1990) sur l'île Melville (Arctique canadien). Les résultats ont montré que l'ablation de la neige/glace est principalement due au rayonnement solaire. Les flux de chaleur sensible (Qe) sont secondaires tandis que les flux de chaleur latente (Qh) sont faibles à négligeables. Ces observations concordent avec des études réalisées sur la fonte du couvert de neige saisonnier (Boike et al., 2003a,b ; Westermann et al., 2009). En Antarctique, Leppäranta et al., (2013) ont également constaté que les apports de chaleur à une plaque de neige sur le Basen Nunatak sont principalement fournis par le rayonnement solaire. En revanche, les flux de chaleur sensible y sont négligeables tandis que les flux de chaleur latente représentent une perte d'énergie significative par sublimation en raison de l'air très sec et des vents catabatiques.

- *Les facteurs de la variabilité spatio-temporelle de l'ablation*

Spatialement, la variabilité dans l'intensité de l'ablation de la neige saisonnière et des plaques de glace dépend de l'exposition aux rayonnements solaires et aux vents. Ainsi, les sites sur les versants ombragés et abrités du vent sont globalement ceux où les apports d'énergie sont les plus faibles en été et donc où l'ablation est la plus faible (Mott et al., 2019).

Plus localement, l'advection de chaleur en provenance des surfaces environnantes a également un effet important. Pendant la saison d'ablation, la contribution des flux turbulents devient généralement de plus en plus importante dans la fonte des neiges résiduelles, pouvant aller jusqu'à environ 50% de la fonte totale lorsque le couvert de neige devient très parcellaire (Pohl et

al., 2006). La transition d'une couverture de neige continue à des plaques de neige résiduelle conduit au développement de conditions thermiques de surface hétérogènes entre les zones encore enneigées (fort albédo) et les zones où le sol est exposé (faible albédo). Il en résulte un gradient horizontal de température qui se traduit par des transferts de chaleur par conduction via le sol, mais aussi et surtout par advection (c.-à-d. par transport latéral de chaleur) lorsqu'une masse d'air se réchauffe en circulant au-dessus du sol et restitue cette chaleur aux plaques de neige et de glace persistantes. L'advection de chaleur affecte ainsi principalement les bordures des plaques exposées au vent ce qui contribue à produire une hétérogénéité dans les taux d'ablation à l'échelle locale (DeBeer et Pomeroy, 2017 ; Mott et al., 2011, 2013, 2015; Neumann et Marsh, 1998; Schlögl et al., 2018). Par ailleurs, les écoulements d'eau amont qui pénètrent dans le système de plaque de glace participent à apporter de la chaleur au système et génèrent des phénomènes de thermo-érosion (Woo et al., 1982).

Finalement, la variabilité spatio-temporelle de l'albédo de la neige/glace au cours de la saison chaude est également un facteur critique pour le SEB. L'albédo est fortement influencé par les propriétés physiques de la neige et en particulier par la taille et la forme des cristaux qui sont généralement évaluées par la mesure de la surface spécifique (SSA ; Gallet et al., 2009). Le grossissement et l'arrondissement des cristaux, par le métamorphisme de fonte et la recristallisation suite à des épisodes de gel/dégel, entraînent une diminution rapide de la surface spécifique de la neige et de son albédo (Domine et al., 2007). L'albédo peut également être très altéré par la concentration d'impuretés à la surface de la neige-glace. Ces impuretés incluent des dépôts nivéo-éoliens (c.-à-d. un mélange de neige avec des sédiments fins et des fragments de matière organique apportés par le vent) et des dépôts atmosphériques de carbone noir (*black carbon*) (Lewkowicz, 1998 ; Lewkowicz et Young, 1991 ; Woo et Dubreuil, 1985). La croissance de micro-organismes vivants (algues et cyanobactéries) à la surface de la neige-glace est également connue pour contribuer à réduire l'albédo (Kohshima et al., 1994). Pour un système de plaque de glace, la durée de persistance de l'accumulation de neige saisonnière est aussi particulièrement critique pour le SEB. En effet, lorsque la neige disparaît complètement, l'exposition de la glace surimposée, souvent riche en sédiments, diminue drastiquement l'albédo de surface (Young et Lewkowicz, 1990). Fujita et al., (2010) ont montré dans une étude sur l'ablation de plaques de glace permanentes dans les Alpes japonaises que l'albédo de surface pouvait être divisé par 2 lors cette transition entre la neige saisonnière et la glace exposée.

Les observations préliminaires du SEB et l'ablation des plaques de glace et du manteau neigeux saisonnier dans les régions polaires soulignent l'importance des processus à fine échelle produits par l'interaction entre les variables météorologiques et les facteurs topographiques locaux. Ainsi, les facteurs et processus dominants sont spécifiques à chaque site, de sorte que la quantification de l'évolution de l'ablation au cours d'une saison n'est possible que si elle est étayée par des données de terrain complètes. Dans les régions polaires, ce travail constitue un défi majeur.

1.3.4.3. Mécanismes d'autorégulation d'un système de plaque de glace

Le rôle important de processus locaux relié au contexte topographique sur les processus d'accumulation et d'ablation complexifie la compréhension de la variabilité spatio-temporelle du bilan de masse des systèmes de plaques de glace. Dans des études menées sur des plaques de glace permanentes dans les Alpes japonaises, Fujita et al., (2010) et Glazirin et al., (2004) ont démontré que le contrôle de la topographie apporte une série de processus de rétroactions produites par l'interaction entre les conditions topoclimatiques et la taille des plaques de glace (**Figure 9**). Ces rétroactions agissent comme des mécanismes d'autorégulation du bilan de masse, expliquant l'équilibre entre les apports et les pertes de masse des systèmes de plaque de glace sur le moyen et long terme.

Les mesures de terrain ont d'abord montré que dans le cas des niches topographiques à remplissage limité (voir section [1.3.4.1.](#)) les accumulations de neige pendant la saison froide sont fortement corrélées au volume atteint par la plaque de glace à la fin de la saison d'ablation précédente (**Figure 9a** ; Glazirin et al., 2004). Ainsi, plus une plaque de glace fond en été, plus la recharge en neige du système sera importante l'hiver suivant, et inversement. Concernant l'ablation, une rétraction négative a été identifiée entre la taille d'une plaque de glace et son taux de fonte par effet d'ombrage dans certains contextes topographiques (**Figure 9b**). Par conséquent, plus la taille d'une plaque de glace est réduite en été, moins la surface de celle-ci est exposée aux radiations solaires (Glazirin et al., 2004 ; Mott et al., 2019). De même, lorsque les plaques de glace sont présentes dans une dépression concave, l'évolution du volume de neige/glace affecte la dynamique locale des vents et par ce biais agit sur les transferts de chaleur turbulents et donc sur l'ablation (**Figure 9c** ; Fujita et al., 2010 ; Mott et al., 2019). Grâce à cette position d'abri, une couche stable d'air froid va alors se former au-dessus de la plaque de glace par inversion thermique

(*cold-air pooling*) entraînant une déconnexion avec les conditions atmosphériques. La fonte est par conséquent considérablement réduite.

Ces mécanismes de rétroaction établis par Glazirin et al. (2004) et Fujita et al. (2010) pour les plaques de glace de montagne sont susceptibles d'être fonctionnels dans la plupart des systèmes de plaques de glace appartenant au système morphodynamique nival. Cependant, à notre connaissance, aucune étude n'a tenté de documenter et quantifier ces phénomènes dans les régions polaires, ce qui représente une lacune supplémentaire dans la compréhension du bilan de masse et du fonctionnement des plaques de glace.

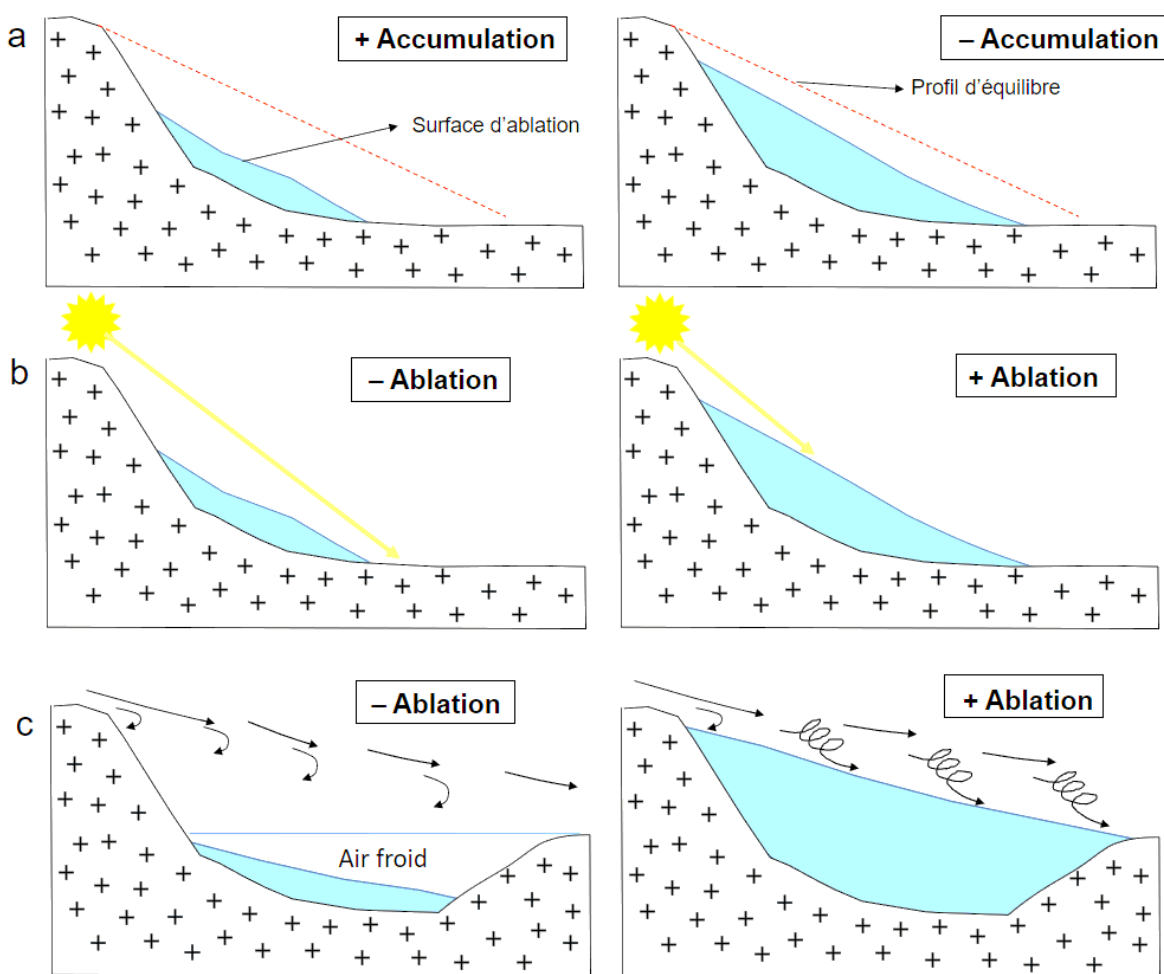


Figure 9. Conceptualisation des différents mécanismes d'autorégulation du bilan de masse des plaques de glace. a) Rétroaction entre les accumulations de neige en hiver et l'espace disponible dans la niche topographique à la fin de l'été précédent ; b) Rétroaction entre l'ablation et l'exposition aux rayonnements solaires ; c) Rétroaction entre l'ablation et l'exposition au vent (inspiré de Glazirin et al, 2004).

1.3.5. Les plaques de glace et le contexte climatique régional

1.3.5.1. Ligne d'équilibre des glaciers

Du fait du rôle clé de la topographie sur leur bilan de masse, les systèmes de plaque de glace ne sont que partiellement influencés par les conditions climatiques régionales. Pour cette raison, il est courant de trouver des plaques de glace très en dessous de l'altitude moyenne régionale de la ligne d'équilibre des glaciers (abrégée en ELA pour *Equilibrium line Altitude* ; **Figure 10**) qui définit la ligne théorique moyenne à la surface d'un glacier où l'accumulation et ablation s'équilibrivent. Cette ligne est souvent associée à la limite des neiges permanentes. La ELA régionale est dictée par la température et les précipitations (Dahl et al., 2003). Lorsque des plaques de glace sont présentes en dessous de la ELA régionale (**Figure 10**), elles ne sont donc pas en équilibre avec les conditions climatiques. Ces plaques ne doivent alors leur existence qu'à des phénomènes topoclimatiques locaux ayant pour effet d'abaisser la ELA par l'amplification des apports en neige ([section 1.3.4.1.](#)), et/ou une réduction locale de l'ablation ([section 1.3.4.2.](#); **Figure 9**; DeBeer et Sharp, 2009 ; Fujita et al., 2010 ; Glazirin et al., 2004).

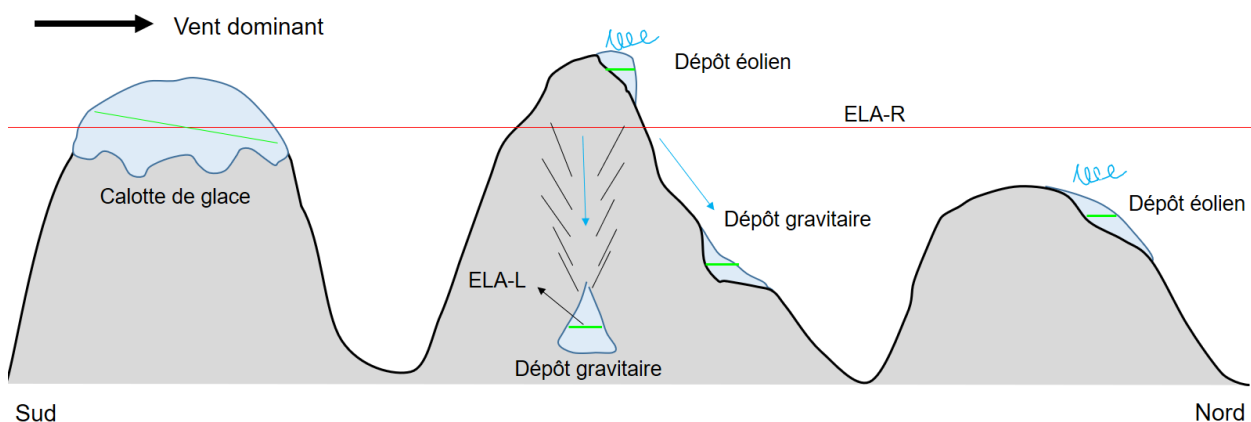


Figure 10. Différence entre la ligne d'équilibre régionale des glaciers (ELA-R), déterminée par les conditions climatiques (c.-à-d. la température estivale et les précipitations hivernales) et la ligne d'équilibre locale des glaces et neiges permanentes (ELA-L), principalement contrôlée par la topographie et le vent (modifié de Dahl et al., 2003).

Inversement, le contrôle dominant de la topographie peut aussi entraîner une remontée locale de la ELA, permettant la présence de plaques de glace au-dessus de la ELA régionale sans qu'elles se transforment en glacier. Cela se produit typiquement lorsque la topographie et le vent limitent les accumulations de neige (ex. parois rocheuses de haute altitude ; Guillet et Ravanel, 2020).

1.3.5.2. La sensibilité des plaques de glace aux changements climatiques

La déconnexion partielle du bilan de masse des plaques de glace par rapport au climat leur confère une réponse particulière aux fluctuations climatiques dont la nature est encore peu comprise en raison du manque de données de terrain et de l'absence de suivi régulier sur le long terme comme il en existe pour les glaciers. Cette complexité dans l'évaluation de la sensibilité et la vulnérabilité de ces petits éléments de la cryosphère est notamment illustrée par les conclusions contradictoires qui ressortent des rares études qui ont été menées sur le sujet. D'un côté, certains travaux ont montré que les plaques de glace et petits glaciers sont restés d'une grande stabilité au cours des dernières décennies en raison des mécanismes d'autorégulation (voir section [1.3.4.3.](#)) qui réduisent, voire annulent, les effets du réchauffement. Dans ce cas, les masses de glace sont jugées peu sensibles aux fluctuations climatiques (ex. DeBeer et Sharp, 2009 ; Gachev et al., 2016 ; Gądek, 2008 ; Huss et Fischer, 2016). D'un autre côté, des travaux ont fait état d'un déclin et une disparition rapide de plaques de glace en réponse à la hausse récente des températures de l'air. Woo et Young, (2014) ont par exemple montré qu'un nombre important de plaques de glace permanentes près de Resolute Bay au Nunavut (Haut-Arctique canadien) avaient perdu leur statut permanent lors des étés exceptionnellement chauds de 2011 et 2012. Ces observations sont cohérentes avec d'autres travaux menés dans des environnements montagneux des latitudes moyennes, où une diminution de volume, inédite depuis le Petit Âge Glaciaire, a également été constatée (ex. Farnell et al., 2004 ; Fischer et al., 2014 ; Moreno et al., 2021 ; Mott et al., 2019). De ce point de vue, les plaques de glace sont sensibles à la hausse des températures et réagissent rapidement au signal climatique.

Les réponses non linéaires des plaques de glace et petits glaciers aux fluctuations climatiques sont en fait le reflet de la complexité des mécanismes de contrôle de leur bilan de masse et leur caractère protéiforme. Comme décrit dans la section [1.3.4.](#), les plaques de glace sont contrôlées par le contexte topographique mais celui-ci peut s'exercer à un degré plus ou moins fort. Ainsi, il semble que les systèmes les moins exposés aux réchauffements climatiques sont ceux où l'effet d'ombrage et les inversions thermiques (*cold-air pooling*) sont les plus forts ce qui permet une déconnexion quasi-totale du bilan d'énergie de surface par rapport aux conditions atmosphériques (Debeer et Sharp, 2009). Des modifications d'autres facteurs climatiques comme le vent sont susceptibles de briser cet effet local mais aucune étude n'a étudié cet aspect pour le moment. Pour les systèmes dominés par une alimentation par avalanches, une hausse des

événements extrêmes de neige et des redoux en hiver pourrait augmenter les apports en neige. Ce phénomène a été observé localement dans les Alpes européennes où la hausse des apports avalancheux a permis à de petits glaciers et plaques de glace de se maintenir au cours des dernières années alors même que les grands systèmes glaciaires locaux ont connu un déclin rapide (Colucci et al., 2021 ; Huss et Fischer, 2016). Pour le cas des plaques de glace d'origine glaciaire (**Figure 3**; Serrano et al., 2011), leur réponse aux fluctuations climatiques est particulièrement complexe car celle-ci change lors de la transition d'un petit glacier à une plaque de glace. Au cours de leur déclin lors d'une phase de réchauffement, le contrôle des facteurs climatiques sur le corps de glace diminue au profit d'un contrôle de plus en plus dominant des facteurs topoclimatiques locaux (ex. effet d'ombrage, inversion thermique, moindre exposition au vent). Ces masses de glace passent donc d'une situation où elles évoluaient linéairement avec le climat à une situation où elles en sont partiellement, voire totalement, déconnectées, ce qui permet leur préservation durable (Kuhn, 1995 ; Moreno et al., 2021).

La compréhension du lien entre les plaques de glace et le climat représente donc un défi en raison de la grande variabilité des réponses possibles selon les spécificités des sites (ex. Topographie ; climat), les processus à petites échelles qui s'y développent (ex. effet d'ombrage, inversion thermique, avalanche), le type de système (ex. nival vs. glaciaire) et la forme que prennent les changements climatiques (ex. hausse des précipitations hivernales, augmentation du vent). Dans les régions polaires, le manque de données de terrain ne permet pas pour le moment de savoir si les observations de Woo et Young (2014) à Resolute Bay sont représentatives de la tendance régionale dans le Haut-Arctique.

1.3.6. Conclusion sur l'état des connaissances

Les plaques de glace sont des éléments de la cryosphère incontournables des régions froides. Pourtant, elles sont encore largement méconnues ce qui se traduit notamment par des désignations et définitions nébuleuses dans la littérature scientifique. Cette revue de littérature permet de préciser les termes et de présenter les diverses formes de plaque de glace. Elle montre aussi la complexité du fonctionnement des systèmes de plaques de glace et de leur évolution en raison du contrôle important de processus et phénomènes locaux. Dans les régions polaires, les bases scientifiques sur ces plaques se limitent à quelques études, souvent anciennes, qui n'ont pas permis d'imposer les plaques de glace comme un élément à part entière de la cryosphère terrestre. La rareté des recherches dédiées aux plaques de glace est notamment imputable à leurs caractéristiques intrinsèques (ex. la taille, les facteurs de contrôle) qui ne peuvent être étudiées qu'à l'échelle locale sur la base de travaux de terrain. Ce manque d'études dans les régions polaires rend notamment incertaine la représentativité des connaissances acquises dans les milieux de montagnes.

Nous résumons ici plusieurs lacunes identifiées dans la revue de la littérature que nous considérons comme essentielles à combler afin de mieux comprendre le fonctionnement des plaques de glace :

- Il existe très peu de données relatives à la structure et aux propriétés physiques des plaques de glace polaires.
- Les processus thermodynamiques de formation de la glace pluriannuelle dans des conditions polaires restent peu connus et les interactions dynamiques entre la glace, le couvert de neige saisonnier et les conditions topoclimatiques n'ont jamais été documentées.
- Les mécanismes de rétroaction sur le bilan de masse des plaques de glace liés aux facteurs topoclimatiques n'ont jamais été examinés en milieu polaire.
- Le contrôle des conditions micrométéorologiques et des environnements proximaux sur le bilan d'énergie de surface des plaques de glace et leur ablation estivale reste peu documenté.
- L'évolution sur le long terme des plaques de glace et leur réponse aux changements climatiques restent ambiguës.

1.4. Approche, hypothèse et questions de recherche

L'étude de l'évolution de la cryosphère terrestre et de ses conséquences sur les environnements naturels est un domaine de recherche tout juste émergeant dans les régions polaires en transition (Vincent et al. 2017). Dans le contexte récent des changements climatiques et de transition au niveau des biogéosystèmes, il est de plus en plus reconnu que la recherche polaire ne peut pas se réduire à une juxtaposition d'études cloisonnées par discipline et doit davantage se tourner vers une vision intégrée et multidisciplinaire pour mieux comprendre les diverses connexions et interactions (actions et rétroactions) à différentes échelles entre la cryosphère, le paysage, les écosystèmes, l'hydroosphère et le climat (Rocha et al., 2018 ; Wrona et al., 2016).

Dans cette perspective, une approche géosystémique a été adoptée dans cette thèse pour obtenir une compréhension holistique de la dynamique spatio-temporelle des plaques de glace et de leur environnement. Cela sous-entend une réflexion autour des notions d'organisation des systèmes, de forçage, de rétroactions, d'échanges et de flux, d'équilibre, de seuils, état transitoire, réaction en chaîne et de résilience. L'approche géosystémique permet de mettre l'accent sur les interactions (c.-à-d. les flux d'eau, de matières et d'énergie) et couplages entre les diverses composantes d'un géosystème pour en comprendre le fonctionnement (Stephani et al., 2014). Elle permet aussi d'évaluer adéquatement la réponse et la vulnérabilité des systèmes face aux changements climatiques et environnementaux. Selon le principe des réactions en chaîne, la modification d'une seule composante du système peut affecter la dynamique de toutes les autres.

Dans cette thèse, nous nous sommes essentiellement concentrés sur l'échelle du versant qui représente un sous-système au géosystème de désert polaire (**Figure 11**). Le système de versant intègre une combinaison de composantes « internes », incluant les formes de relief, les éléments de la cryosphère (neige saisonnière, pergélisol et plaques de glace), les réseaux de drainage, le sol et le couvert végétal, ainsi que des forçages « externe », notamment climat (Stephani et al., 2014 ; Woo et Young, 2003).

En adéquation avec l'approche géosystémique et sur la base des connaissances actuelles sur les plaques de glace, nous émettons l'hypothèse suivante :

En raison de leurs propriétés intrinsèques et du contrôle important du contexte topoclimatique sur leur bilan de masse, les plaques de glace sont des éléments de la

cryosphère avec une résilience importante aux changements climatiques, garantissant leur préservation sur de longues périodes. La présence durable des plaques de glace sur les versants du désert polaire leur confère un rôle central dans le fonctionnement du géosystème en enclenchant une série de processus hydrologiques, géomorphologiques et biologiques, qui à leur tour ont des effets sur les propriétés du pergélisol et du couvert nival saisonnier (Figure 11).

La validation de cette hypothèse amène les deux questions de recherche suivantes :

Question 1 : **Comment les facteurs topoclimatiques impliqués dans la formation des plaques de glace contrôlent-ils leur évolution sur le court et long terme ?**

Question 2 : **Quels sont les effets de la présence sur le long terme des plaques de glace sur la variabilité et la dynamique des versants qui se trouvent en aval ?**

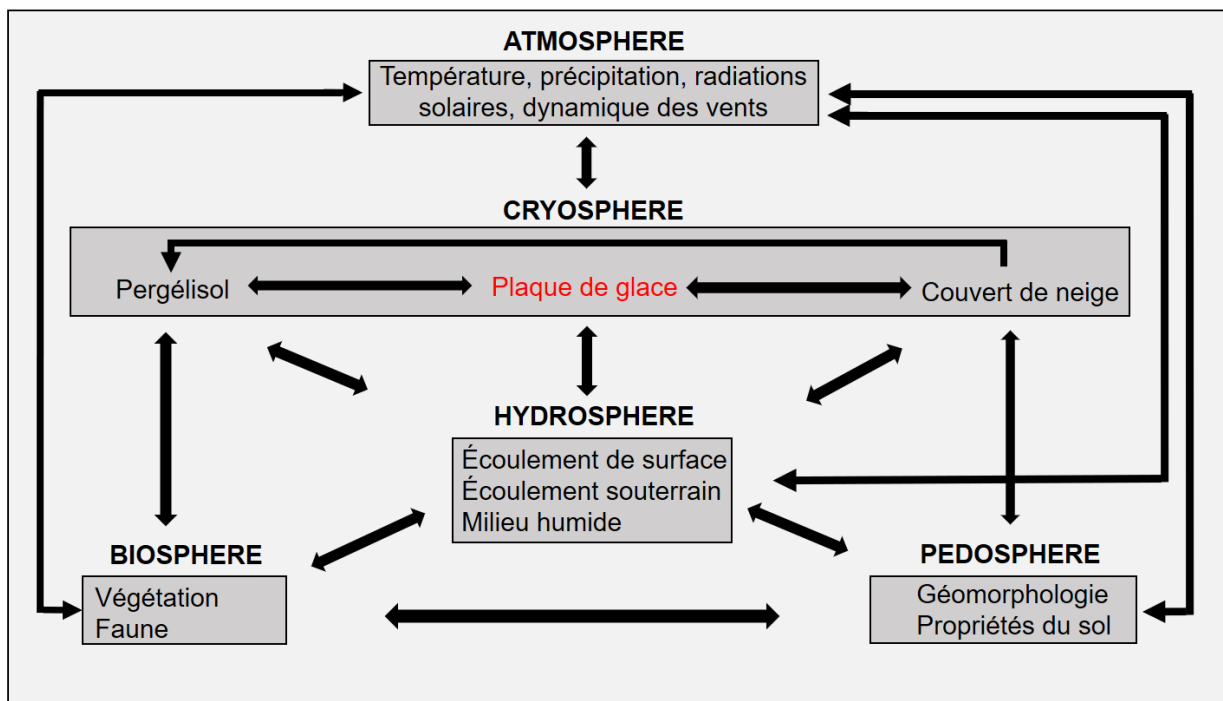


Figure 11. Représentation du géosystème de désert polaire dans lequel les plaques de glace jouent un rôle central.

1.5. Objectifs et axes de recherche

Afin de combler les lacunes dans les connaissances sur les plaques de glace polaires et de répondre aux questions de recherche énoncées ci-dessus, l'objectif principal de cette thèse est de développer une base de connaissances qualitative et quantitative sur l'origine et le fonctionnement des plaques de glace et leurs effets sur les versants de désert polaire.

Plus spécifiquement, le projet comprend 4 sous-objectifs qui ont guidé cette thèse :

- 1) Caractériser un système de plaque de glace en analysant les propriétés physiques de la neige et de la glace qui le composent afin de déterminer les processus de métamorphisme et de regel qui sont à l'origine de l'aggradation de glace.**
- 2) Identifier les processus locaux qui contrôlent la variabilité spatio-temporelle de l'accumulation et de l'ablation de la neige/glace dans un système de plaque de glace et évaluer leur sensibilité aux changements climatiques.**
- 3) Identifier et quantifier les conséquences de la présence d'une plaque de glace sur la dynamique hydrologique, biologique et géomorphologique d'un versant.**
- 4) Caractériser le couvert nival saisonnier de désert polaire et évaluer l'influence des conditions de sol azonales produites par les plaques de glace sur les propriétés physiques de la neige et les processus de métamorphisme.**

Pour atteindre ces objectifs, une recherche fondamentale a été développée en se basant sur quatre campagnes de terrain (été 2015 ; été 2016 ; été 2017 ; été 2019) menées sur l'île Ward Hunt située au nord de l'île d'Ellesmere dans le Haut-Arctique canadien (Vincent et al., 2011b). Ces travaux se sont articulés autour de 4 axes de recherche multidisciplinaires et complémentaires permettant de collecter un jeu de données diversifié s'appuyant sur différentes méthodes et techniques. Ces 4 axes sont résumés dans la **Figure 12**.

Système de plaque de glace permanente

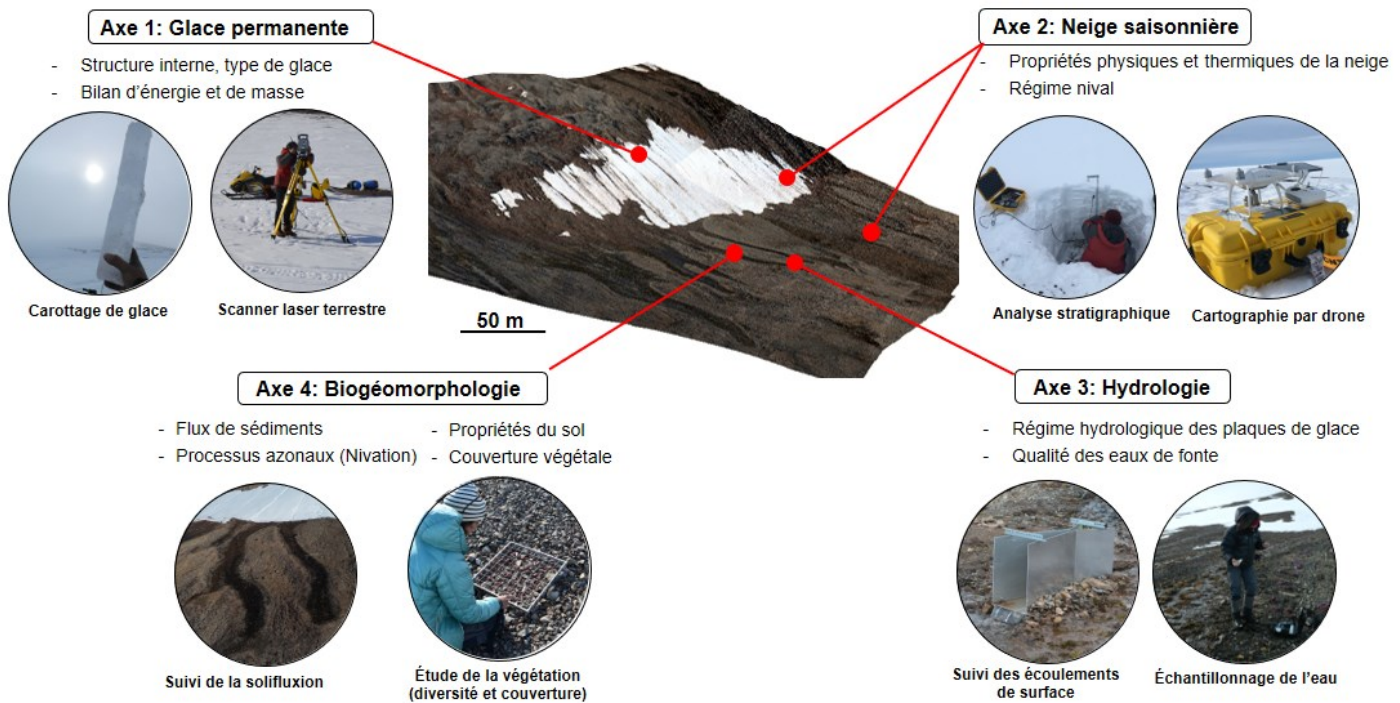


Figure 12. Représentation schématique des 4 axes de recherche autour desquels la thèse s'articule (modifié de Davesne et al., 2019).

1.6. Pertinence du projet de recherche

1.6.1. Force et originalité de la thèse

En se penchant sur un élément très peu documenté de la cryosphère, un trait majeur de l'originalité de cette thèse est le fait même de son sujet. Les données et résultats qui émanent de cette recherche permettront de constituer une base de connaissances unique sur les systèmes de plaque de glace du désert polaire Arctique. Au-delà de son sujet propre, la force de cette thèse est d'avoir adopté une approche intégrée, multitechnique et multidisciplinaire, combinant la glaciologie, la nivologie, la géomorphologie et la biologie végétale (**Figure 12**). Cette vision va de pair avec une conception géosystémique des milieux naturels qui représente le seul moyen de saisir et comprendre leur complexité et leur fonctionnement.

L'importance et l'originalité de cette recherche doctorale reposent également sur le site d'étude où elle a été réalisée. Les régions de désert polaire sont parmi les environnements les moins étudiés et connus de la planète en raison de l'éloignement et contraintes environnementales (ex. climat extrême; faune, etc.). Comme démontré par Metcalfe et al., (2018), la recherche scientifique reste encore très parcellaire dans le Haut-Arctique, ce qui génère des lacunes et des biais importants dans les connaissances scientifiques de ces régions, toutes disciplines confondues. Ce manque de données d'observation fiables sur des variables clés comme la neige, l'humidité du sol, la végétation et le pergélisol constitue un obstacle majeur à l'amélioration des modèles climatiques régionaux. En adoptant une approche essentiellement axée sur le travail de terrain, cette thèse a permis l'acquisition d'un large éventail de données empiriques, ce qui est unique pour un site à cette latitude.

1.6.2. Contributions et retombées scientifiques de la recherche

En raison de la place centrale des plaques de glace dans le fonctionnement du géosystème de désert polaire, les nouvelles données et connaissances apportées par cette thèse pourront avoir des retombées pour plusieurs domaines des géosciences. Les principales contributions et avancées scientifiques sont détaillées ci-dessous en 5 grands thèmes

- Glaciologie

Les connaissances empiriques et conceptuelles apportées par cette thèse contribuent à documenter les plaques de glace et à les faire reconnaître comme une composante à part entière de la cryosphère terrestre. Plus spécifiquement, les analyses détaillées des propriétés physiques de la glace ouvriront la voie à la constitution d'une base de données glaciologiques permettant de documenter les caractéristiques physiques de la glace des plaques (ex. cristallographie, densité, inclusions de sédiments) et d'identifier des faciès de glace typiques. Au-delà de l'aspect fondamental, ces informations pourront fournir une base de comparaison très utile pour l'identification de l'origine des masses de glace enfouies dans le pergélisol (French et Pollard, 1986 ; Gilbert et al., 2016 ; Lacelle et al., 2009).

- Nivologie

L'analyse détaillée de la neige saisonnière et des variables clés qui contrôlent ses propriétés physiques (ex. le vent, l'humidité et la température du sol) offre des données uniques sur la

variabilité spatio-temporelle des propriétés et des processus de métamorphisme de la neige en fonction du contexte topoclimatique. Cette thèse contribue donc à combler les importantes lacunes dans les connaissances fondamentales sur la neige de désert polaire et à identifier les spécificités de cette neige par rapport aux autres régions froides. Une partie de la base de données sur la neige saisonnière collectées dans le cadre de cette thèse a déjà été utilisée par Royer et al. (2021) pour développer une nouvelle classification du manteau neigeux arctique dans laquelle une nouvelle classe spécifique à la neige de désert polaire a été créée. Les résultats de notre recherche permettront également d'améliorer le paramétrage des modèles physiques de neige tels que Crocus (Vionnet et al., 2012) et SNOWPACK (Lehning et al., 2002). Ces modèles ne sont actuellement pas assez performants pour modéliser correctement le manteau neigeux polaire, notamment la couche basale de givre de profondeur (Barrere et al., 2017 ; Domine et al., 2019) entraînant de grandes incertitudes dans les simulations des conditions de neige actuelles et futures et de leurs effets sur le régime thermique du pergélisol.

- **Hydrologie des pentes**

Une meilleure connaissance du fonctionnement et de l'évolution saisonnière et interannuelle des plaques de glace permet d'approfondir la compréhension du régime hydrologique des versants de désert polaire. Ces informations viennent compléter la série d'études récentes de Paquette et al., (2017, 2018, 2020a) réalisées à Ward Hunt. Ces auteurs ont mis en évidence que la fonte des plaques de neige saisonnières est la principale source d'eau qui alimente les d'écoulements préférentiels (*water tracks*) qui s'organisent sur les versants et qui contribuent fortement à leur dénudation. L'étude du bilan de masse et du régime hydrologique des plaques de glace pourrait amener à une meilleure compréhension de la variabilité spatio-temporelle des flux d'eau, d'énergie, de sédiments et de nutriments le long des versants de désert polaire. À Ward Hunt, les connaissances sur le rôle hydrologique des plaques de glace pourraient aussi avoir des retombées importantes pour l'étude des écosystèmes viraux et microbiens (Comte et al., 2018) et les études limnologiques du lac Ward Hunt qui est principalement alimenté par les eaux de fonte de la neige saisonnière et des plaques de glace présentes dans le bassin versant (Bégin et al., 2020 ; Paquette et al., 2015).

- Géomorphologie-Paysage

Les connaissances sur les processus et formes géomorphologiques reliées à la présence des plaques de glace contribuent à mettre en évidence l’implication et l’efficacité des processus azonaux dans le façonnement des versants de désert polaire (Paquette et al., 2020a). Les nouvelles données apportées par cette thèse permettent de mieux comprendre les interactions entre les processus périglaciaires et azonaux et la façon dont ces processus sont modulés par le régime des plaques de glace. La compréhension de l’action géomorphologique des plaques de glace amènera également des perspectives importantes pour l’étude du pergélisol. Paquette et al. (2020b) et Verpaelst et al. (2017) ont en effet montré que les marges en aval des plaques de neige et de glace étaient propices à la formation d’un pergélisol syngénétique riche en glace en raison du développement de milieux humides et de processus de solifluxion. Finalement, les recherches locales, à l’échelle du versant, menées dans cette thèse constitueront un socle important pour une compréhension plus large de la dynamique et de l’organisation du paysage de désert polaire.

- Changements climatiques

La réponse de la cryosphère au réchauffement climatique est une préoccupation majeure aujourd’hui dans plusieurs domaines des géosciences. La compréhension de l’évolution sur le long terme des plaques de glace et de la relation complexe qu’elles entretiennent avec le climat permettra de mieux anticiper leur évolution future. Ces informations seront cruciales pour comprendre l’évolution et la vulnérabilité du géosystème de désert polaire à un moment charnière où les environnements polaires sont en transition rapide en réponse au changement climatique.

1.7. Présentation générale du site d’étude

1.7.1. Le désert polaire

Les travaux de recherche présentés dans cette thèse ont été menés sur l’île Ward Hunt qui présente un environnement typique de désert polaire. Le désert polaire définit les zones continentales non glacées des hautes latitudes arctiques et antarctiques, marquées par des températures très froides, des vents violents, une courte saison de dégel, une saisonnalité très marquée (nuit polaire en hiver et jour polaire en été) et surtout une disponibilité en eau liquide très limitée (Barry et Hall-McKim, 2018).

Selon les critères climatiques, le désert polaire est défini spatialement par la combinaison de deux facteurs, à savoir des précipitations annuelles inférieures à 250 mm et une température moyenne mensuelle du mois le plus chaud, typiquement juillet, inférieure à 5°C (**Figure 13** ; Barry et Hall-McKim, 2018). Les faibles précipitations dans les déserts polaires sont principalement liées à la capacité hygrométrique réduite de l'air froid. À cela s'ajoutent des phénomènes azonaux comme la continentalité, dont l'effet est renforcé en hiver lorsque les surfaces océaniques et lacustres environnantes sont englacées (Oliver, 2008). Malgré des précipitations annuelles tout aussi faibles que dans les régions de désert chaud, l'évapotranspiration est beaucoup plus faible dans les déserts polaires en raison des basses températures. Ainsi, les déserts polaires ne répondent pas toujours à la définition climatique de l'aridité qui implique une évapotranspiration potentielle (ETP) supérieure aux précipitations (P) conduisant à un déficit hydrique (Thomas, 2011).

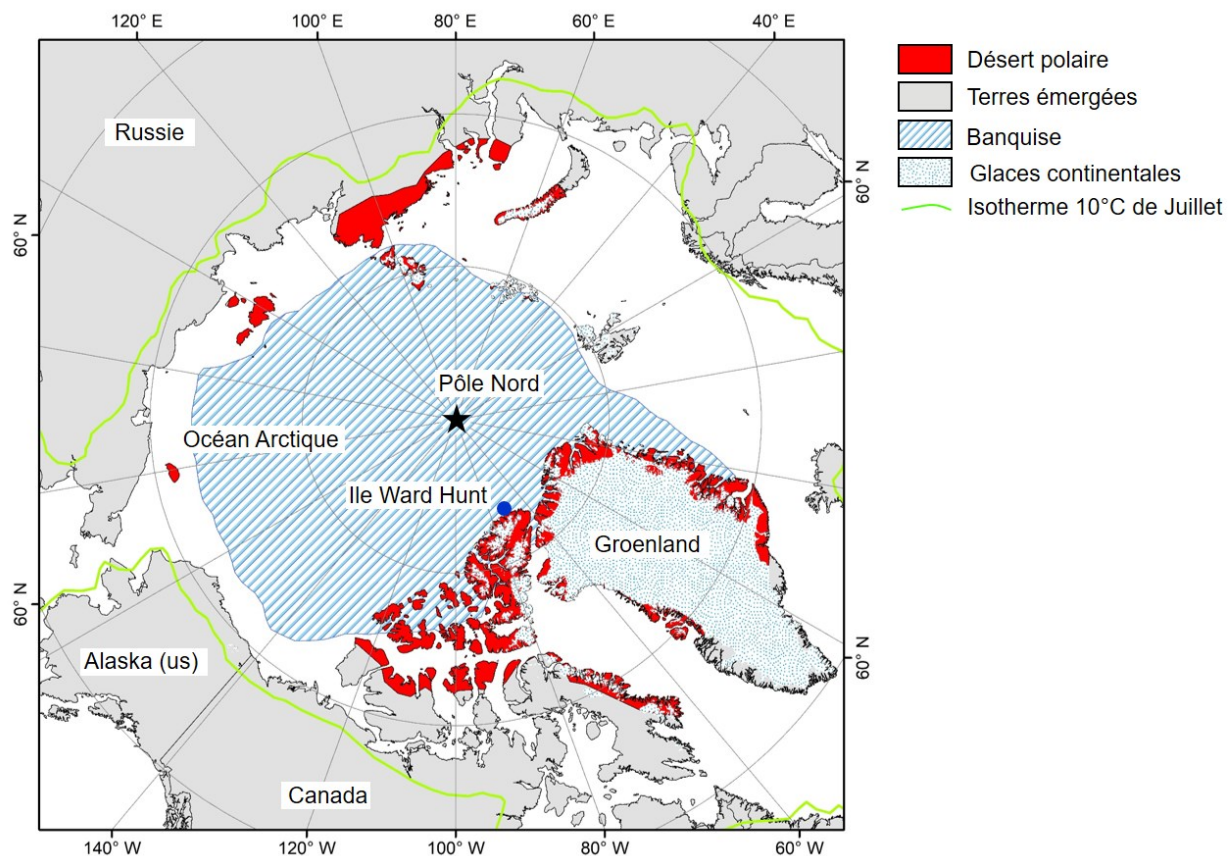


Figure 13. Carte circumpolaire délimitant la zone de désert polaire arctique selon l'isotherme 5°C en juillet et l'isohyète de précipitation annuelle inférieure à 250 mm. Le site d'étude de cette recherche, l'île Ward Hunt, représente la base de recherche la plus septentrionale en Arctique.

Le désert polaire couvre environ 2.7×10^6 km² de territoire de l'hémisphère nord, dont 85% sont présents dans l'extrême Haut-Arctique tandis que les 25 % restant englobent, le nord de la Sibérie et les zones non glacées du nord du Groenland (**Figure 13**). La température moyenne annuelle de l'air (TMAA) de ces régions varie généralement de -15 à -18 °C. La moyenne des mois d'hiver est de l'ordre de -30 à -35 °C tandis que celle des mois d'été est de 1 à 5 °C. La période de dégel ne dure que de 2 à 3 mois (Serreze et Barry, 2014 ; Vincent et al., 2011b). Certaines régions abritées de l'Arctique canadien (ex. Eureka, Nu) et du Groenland reçoivent moins de 150 mm par année, dont près des trois quarts sous forme de neige (Woo, 1983).

Dans l'Arctique, les environnements de désert polaire se démarquent des environnements de toundra par une domination absolue des surfaces minérales et une quasi-absence de végétation. La pédogenèse y est très limitée et le sol consiste typiquement en des dépôts sédimentaires grossiers ou un régolite provenant de la gélification de la roche en place (French, 2017). La couverture végétale totale est généralement inférieure à 2 %, ne dépassant que localement 5 %. La combinaison d'une saison de croissance végétale très courte, de l'humidité limitée du sol et des températures estivales froides résulte en une diversité et une croissance réduites des espèces vasculaires et une totale absence des espèces ligneuses. Les bryophytes, les lichens, ainsi que les algues sont en revanche communs (Bliss et Gold, 1999).

Les conditions climatiques et environnementales (végétation, humidité du sol) de désert polaire ont une grande influence sur les propriétés du couvert de neige saisonnier qui couvre le sol entre 8 à 10 mois par année. Récemment, la compilation de données stratigraphiques du couvert de neige provenant de plusieurs études réalisées dans le Haut-Arctique canadien – incluant les données collectées à l'île Ward Hunt dans le cadre de cette thèse – a permis à Royer et al. (2021) de développer une nouvelle classification de la neige polaire en incluant une classe spécifique pour la neige de désert polaire. Cette classification constitue une amélioration importante de celle de Sturm et al. (1995) qui regroupait la neige polaire dans une classe imprécise de "neige de toundra". Dans le désert polaire, le couvert de neige saisonnier est très peu épais (>30 cm) et se démarque de celui de toundra par une couche basale de givre de profondeur peu épaisse et peu développée en raison du sol froid et majoritairement sec qui réduit le gradient thermique et de vapeur dans le couvert de neige au début de la saison froide (Domine et al., 2018a). Au-dessus, les couches de neige consistent en une succession de *windslabs*, une neige très compactée par le vent, dont la densité

peut dépasser 500 kg m^{-3} (Domine et al., 2002). Cette description des propriétés du couvert de neige de désert polaire reste pour l'heure très sommaire car elle repose sur seulement deux études réalisées dans le Haut-Arctique canadien, l'un à Alert (NU) (Dominé et al., 2002) et l'autre à l'île Ward Hunt (Domine et al., 2018a).

D'un point de vue du paysage et de la morphodynamique, les déserts polaires appartiennent au domaine périglaciaire. Bien que dépourvus de glaciers, les éléments de la cryosphère sont omniprésents et jouent un rôle majeur dans l'évolution du paysage et des écosystèmes avec en premier lieu les plaques de neige et de glace en surface (Christiansen, 1998 ; Kňažková et al., 2021 ; Paquette et al., 2020) et le pergélisol continu et froid en profondeur (French, 2017 ; Ball et al., 2011). La couche active excède rarement 60-80 cm dans le Haut-Arctique (Vincent et al., 2011b). Des formes de contraction thermique (ex. fentes de gel, des coins de glace) et de cryoturbation (ex. forme de triage du sol) et de fluages (ex. solifluxion) sont très répandues et sont intimement liées à la distribution de l'humidité (Levy et al., 2011 ; Paquette et al., 2020a ; Verpaelst et al., 2017). En raison du peu de précipitation, les systèmes fluviaux y sont peu développés. Dans la plupart des bassins versants non glacés du Haut-Arctique canadien, le régime hydrologique est alimenté à 80% par la fonte des neiges. Les 20% restant sont partagés entre les précipitations estivales et l'eau issue de la fonte de la glace présente dans la couche active (Lewkowicz et Kokelj, 2002 ; Paquette et al., 2018 ; Woo et Steer, 1982). Étant donné l'imperméabilité du pergélisol continu sous-jacent, le transit de l'eau sur les versants se limite à des mouvements latéraux par écoulements de surface et hypodermiques dans la couche active qui s'organisent souvent selon le patron des formes périglaciaires (Paquette et al., 2017 ; Woo et Steer, 1982).

1.7.2. L'île Ward Hunt et ses environs

1.7.2.1. Géographie/physiographie de l'île Ward Hunt

L'île Ward Hunt ($83^{\circ}05'09''\text{N}$, $74^{\circ}06'19''\text{W}$) se situe au large de l'embouchure du fjord Disraeli à environ 5.6 km au nord de côte la plus proche de l'île d'Ellesmere qui appartient à l'ensemble des îles de la Reine Élisabeth et plus largement à l'Archipel Arctique canadien (**Figure 13**; **Figure 14 a,b,c**). L'île Ward Hunt est baignée par les eaux de l'Océan Arctique. L'île mesure 6 km de long (d'est en ouest) et 3 km de large pour environ 14 km^2 et abrite le lac Ward Hunt (**Figure 14d** ; Vincent et al., 2011b). L'île est située dans le parc national de Quttinirpaaq

(«Дюснр») et abrite le camp de recherche permanent le plus au nord de la planète, lequel comporte notamment un laboratoire construit et géré par le Centre d'Études Nordiques (Université Laval) en 2010. L'île est devenue un site de recherche de référence pour plusieurs disciplines qui œuvre à comprendre le système complexe d'interactions entre la cryosphère, les mouvements de masse, l'hydrologie des pentes et la limnologie des lacs dans les régions polaires extrêmes. L'île Ward Hunt offre un cadre idéal pour mener notre recherche car elle présente un environnement typique de désert polaire et les plaques de glace permanentes y sont nombreuses.

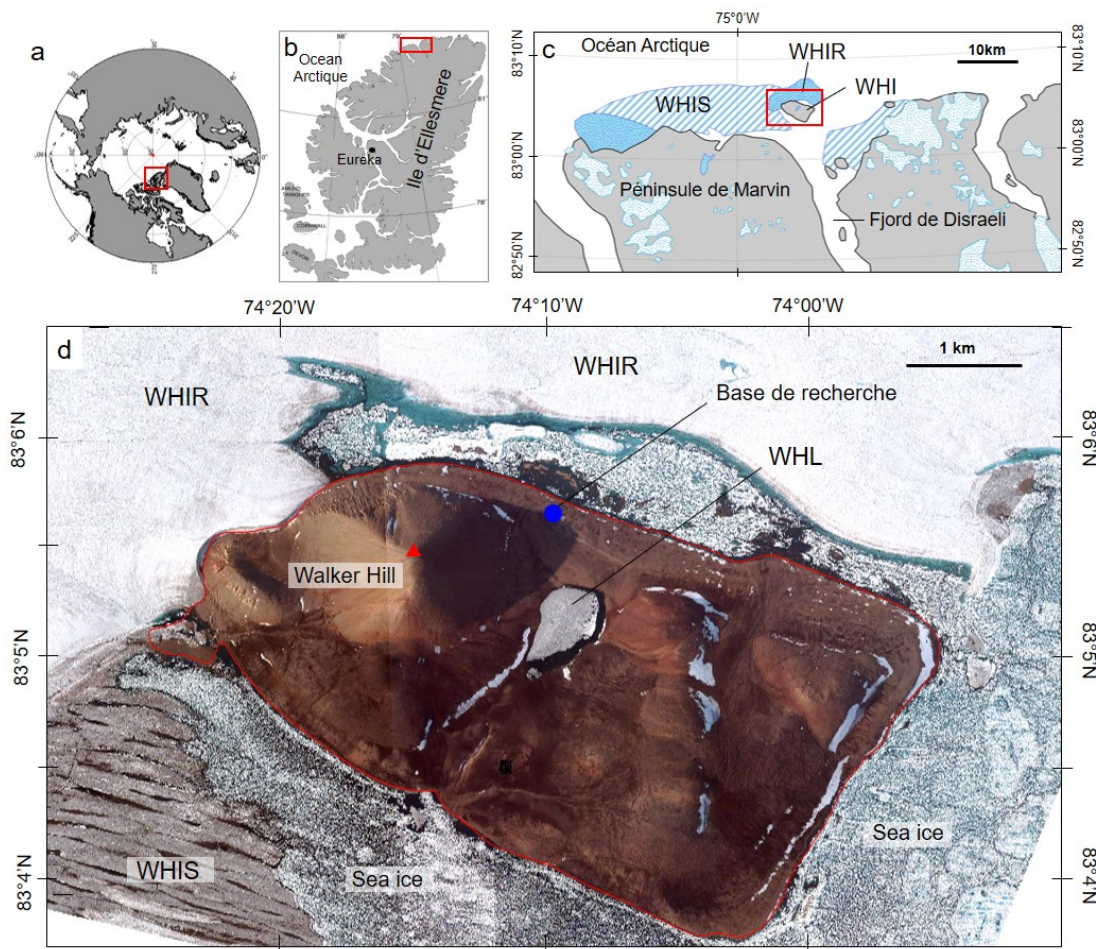


Figure 14. Carte de localisation de l'île Ward Hunt à l'échelle circumpolaire (a) et à l'échelle de l'île d'Ellesmere (b). c) Localisation de l'île Ward Hunt au large du fjord de Disraeli, le long de la côte nord de l'île d'Ellesmere. Autour de l'île, la cryosphère est omniprésente avec notamment les restes de la plateforme glaciaire de Ward Hunt (Ward Hunt Ice Shelf, WHIS) et un dôme de glace (Ward Hunt Ice Rise, WHIR) ; b) Image World-View 3 de l'île Ward Hunt capturée le 19 août 2019. Le centre de l'île est occupé par le lac Ward Hunt et sa couverture de glace désormais pluriannuelle (Paquette et al., 2015). Les multiples plaques de glace permanentes et les plaques de neige représentent les seuls éléments de la cryosphère terrestre visibles depuis la surface.

L'île Ward Hunt appartient à la province géologique du terrane de Pearya caractérisée par quatre successions paléozoïques principales qui s'échelonnent de la fin du Protérozoïque à la fin du Silurien, incluant des formations variées de roches sédimentaires, métamorphiques et volcaniques (Trettin 1991 ; Schiffer et Stephenson, 2018). Au sud de l'île, la côte nord d'Ellesmere est marquée par l'imposante chaîne de montagnes de GrantLand dont les plus hauts sommets culminent à près de 2500 m. Sur l'île, le relief est caractérisé par une colline calcaire, Walker Hill, de 436 m d'altitude et deux collines secondaires (165 m et 240 m d'altitude) de roche intrusive et volcanique (**Figure 14d**).

Les détails sur le climat, la végétation et la géomorphologie de l'île Ward Hunt seront donnés dans les quatre articles qui composent cette thèse.

1.7.2.2. La cryosphère actuelle

La cryosphère est omniprésente et très diversifiée le long de la côte nord d'Ellesmere. Sur l'île Ward Hunt, aucun glacier n'est présent actuellement, mais plusieurs plaques de glace permanentes sont observables auxquelles s'ajoutent d'innombrables plaques de neige saisonnières qui perdurent durablement durant la saison chaude (**Figure 14d** ; Davesne et Fortier, 2018). Au centre de l'île, le lac Ward Hunt était recouvert d'un épais couvert de glace permanent jusqu'à récemment (**Figure 14d**). En 2011, le lac est devenu complètement libre de glace pour la première fois depuis au moins 50 ans. Cette fonte complète s'est répétée en 2012 et 2016 (Bégin et al., 2020 ; Paquette et al., 2015), suggérant une transition vers un régime de couverture de glace semi-permanente. Le sous-sol est constitué d'un pergélisol froid dont la température à 3 m de profondeur a été de – 14 °C en moyenne à la station météorologique SILA entre 2015 et 2019 (CEN, 2021). La profondeur du pergélisol est inconnue à l'île Ward Hunt mais elle est probablement similaire aux estimations de 600 m établies près d'Alert à 170 km à l'est de l'île Ward Hunt (Smith et al., 2012).

L'île est bordée au sud par la banquise pluriannuelle et les restants de la plate-forme de glace de la côte nord d'Ellesmere qui s'étendait au début du XXe siècle au-delà de Cape Aldrich à l'est et qui englobait le fjord M'Clintock à l'ouest (Antoniades et al., 2011). Les plates-formes de glace flottantes (*Ice shelf*) sont formées d'une couche de glace de mer pluriannuelle sur laquelle s'est formée une épaisse couche de glace météoritique provenant de l'accumulation de glace de surimposée et du regel d'accumulation d'eau (Barrette et Sinha, 1996 ; Crary, 1960 ; Jeffries et al.,

1991 ; Ragle et al., 1964). Le déclin progressif de la plate-forme de glace a entraîné son morcellement. Jusqu'à la fin des années 2000, la plate-forme autour de Ward Hunt (*Ward Hunt Ice Shelf*; noté WHIS) occupait encore le bras de mer qui sépare l'île de la côte nord d'Ellesmere et s'étendait sur l'ensemble de l'embouche du fjord de Disraeli (**Figure 14c;d**). Elle a commencé à se fracturer et s'amincir au début des années 2000, amorçant une phase de désintégration rapide avec des détachements massifs à partir de 2008 (Copland et al., 2007 ; Mueller et al., 2008 ; 2017 ; Vincent et Mueller, 2020). Selon les estimations de Mueller et al. (2008), l'épaisseur de la plate-forme de glace a été divisée par deux, passant de ~50 m à ~25 m, entre les années 1980 et les années 2010. Au nord et à l'ouest de l'île se trouve le dôme de glace de Ward Hunt (*Ward Hunt Ice Rise*, noté WHIR; **Figure 14c;d**) qui forme une petite calotte glaciaire qui s'est formée par l'ancrage de la plate-forme de glace sur le fond marin il y a environ 1500 ans (Braun et al., 2004). Le dôme de glace a aujourd'hui une épaisseur de 100 m en son point le plus épais. À l'instar du WHIS, le WHIR a connu un bilan de masse négatif depuis 1959, et particulièrement depuis le début des années 2000, menant à une perte de ~1.68 m de glace en équivalent en eau entre 1959 et 2004 (Braun, 2017). Finalement, la côte nord d'Ellesmere au sud de Ward Hunt est parsemée de petits glaciers de cirque, de plaques de glace et de champs de glace qui s'écoulent par des glaciers de vallée vers les fjords (Lemmen et England, 1992 ; White et Copland, 2018).

Chapitre 2 – Properties and stratigraphy of polar ice patches in the Canadian High Arctic reveal their current resilience to warm summers

Auteurs : Gautier Davesne, Daniel Fortier, Florent Domine

2.1. Avant-propos

Le chapitre 2 représente l'intégralité d'un article soumis à la revue *Arctic Science* qui a été accepté pour publication. Il est une contribution à l'édition spéciale du programme T-MOSAIC qui est un projet de recherche et de synthèse, visant à fournir une évaluation intégrée et transdisciplinaire de la façon dont les régions arctiques évoluent face aux changements climatiques. L'article présente de nouvelles données et connaissances quant aux propriétés physiques de la neige et de la glace qui forment le système de plaque de glace dans le désert polaire de l'île Ward Hunt, répondant ainsi à l'[objectif 1](#) de la thèse. Deux plaques de glace ont été caractérisées en détail en étudiant les propriétés physiques et stratigraphiques du couvert de neige et de carottes de glace. Ces dernières ont été analysées à partir de lames minces et de l'imagerie par tomodensitométrie (CT-scan). La description des propriétés physiques de la neige et de la glace incluant l'analyse des cristaux, des bulles et des sédiments a permis de déterminer les processus thermodynamiques à l'origine de la formation des plaques de glace et de déduire un modèle conceptuel de formation des plaques de glace. Par ailleurs, les propriétés de la glace en profondeur ont permis de spéculer quant à l'âge et l'évolution sur le long terme des plaques de glace.

Citation complète: **Davesne, G., Fortier, D. & Domine, F. (2021) Properties and stratigraphy of polar ice patches in the Canadian High Arctic reveal their current resilience to warm summers. *Arctic Science*, accepté pour publication.**

2.2. Résumé

Les plaques de glace sont omniprésentes dans les régions polaires et constituent un élément clé de l'évolution du paysage. Dans cette étude, nous présentons de nouvelles connaissances sur la formation des plaques de glace dans les déserts polaires, basées sur les propriétés de la neige et de la glace, à l'île Ward Hunt (Haut-Arctique canadien, 83°N). Nos résultats démontrent que les plaques de glace étudiées sont composées de deux unités distinctes. L'unité supérieure est

caractérisée par une glace très fine, riche en bulles d'air et présentant une stratification oblique. En revanche, l'unité inférieure est étonnamment différente avec des cristaux grossiers, une porosité plus faible et une fréquence élevée de fractures. Pour les deux unités, la formation de glace surimposée à la base du manteau neigeux saisonnier apparaît comme le principal processus d'aggradation de la glace. Les propriétés distinctes de l'unité inférieure résultent probablement d'une longue période de croissance cinétique des cristaux de glace indiquant un âge minimum de plusieurs centaines d'années. Une date radiocarbone de $3\ 487 \pm 20$ cal BP suggère que les plaques de glace pourraient potentiellement remonter à l'Holocène tardif. Cette vieille glace a récemment été tronquée pendant les étés plus chauds entre 2008 et 2012, mais la plaque de glace a rapidement récupéré son volume pendant les étés plus frais. Le vieil âge des plaques de glace et leur capacité de régénération rapide après les événements de fonte importants suggèrent leur résilience aux étés plus chauds actuels.

2.3. Abstract

Ice patches are ubiquitous in Polar Regions and are a key element for landscape evolution. We present new insights into polar desert ice patch formation based on snow and ice properties at Ward Hunt Island (Canadian High Arctic, 83°N). Our results demonstrate that investigated ice patches are composed of two distinct units. The upper unit is characterized by very fine granular and bubbly ice with a clear oblique layering. In contrast, the lower unit is strikingly different with coarse crystals, lower porosity and a high frequency of fractures. For both units, superimposed ice formation at the base of the deep snowpack stands out as the primary ice aggradation process. The distinct properties of the lower unit likely result from a long period of kinetic ice crystal growth indicating a minimum age of several hundred years. A radiocarbon date of $3\ 487 \pm 20$ cal BP suggests that ice patches could potentially date back to the Late Holocene. This old ice was recently truncated during warmer summers between 2008 and 2012, but the ice patch quickly recovered its volume during cooler summers. The old age of the ice patches and their rapid regeneration after melt events suggest their resilience to current warmer summers.

2.4. Introduction

The cryosphere includes the terrestrial, freshwater and oceanic systems of the Polar Regions and plays a key role in the climate system through its influence on freshwater resources, gas fluxes and regulation of energy at various scales (Meredith et al., 2019). In the Arctic, the long-term temperature trend shows a rapid rate of warming from 1990 to present, leading to major changes throughout the north polar cryosphere (Post et al., 2019). This results in a wide range of environmental and climatic effects, which have attracted increased attention on cryospheric features. Most studies dealing with the terrestrial cryosphere have mainly considered medium-size and large features such as ice sheets, ice caps and glaciers. In contrast, smaller ice masses received little scientific attention because until recently their detection by remote sensing was limited by the availability of aerial photographs or by the resolution of satellite imagery products, and field investigations were limited. Their exclusion from terrestrial cryosphere inventories and studies leads to a significant source of error, on the order of 10% in the total terrestrial ice volume (Bahr and Radić, 2012; Colucci et al., 2021; Leigh et al., 2019) and to a knowledge gap regarding their dynamics, their environmental effects, and their responses to short and long-term climate fluctuations.

The term “small ice masses” collectively describes all perennial ice bodies at the Earth's surface whose size is below the arbitrary threshold of 0.5 km^2 (Leigh et al., 2019). There is a wide range of definitions and terms, with some focusing on the ice movement, others on the size, or the ice origin. Small ice masses include very small glaciers, such as ice apron, glacier niche, small cirque glacier and small ice caps (Cogley et al., 2011; Guillet and Ravanel, 2020; Haeberli et al., 2004), and ice patches that encompass all perennial ice bodies that are not an active glacier according to the broad definition proposed by Ødegård et al. (2017) and Serrano et al. (2011) to which we adhere here. Ice patches consist of thin accumulations of ice generally overlaid by firn, i.e. a metamorphized snow that survived at least one ablation season and in which the pore space is at least partially interconnected (Cogley et al., 2011). Perennial ice patches exist continuously for centuries or millennia while semi-permanent ice patches persist for several consecutive years but disappear completely occasionally during warm summers (Meulendyk et al., 2012; Ødegård et al., 2017; Woo and Young, 2014). They are thus distinguished from snow patches (also referred to as late-lying snow patches or snowbank) which melt every summer. Ice patches are in fact interpreted as an intermediate state in the seasonal snow patch-to-glacier continuum, making the

semantic boundary between ice patches and very small glaciers unclear. The major criterion to differentiate an ice patch from a very small glacier is the absence of dynamic deformations and creep of the ice mass due to the low basal shear stress (Ballantyne and Benn, 1994; Ødegård et al., 2017). Within ice patches, Serrano et al. (2011) distinguished two kinds of ice patches according to their origins and the resulting internal structure (i.e. ice physics and ice stratigraphy). First, “nival ice patches” refer to ice patches created by local high accumulations of snow in favourable topographic sites (e.g. concavities, break-of-slopes), either by drifting snow or avalanching. These local persistent snow accumulations gradually turn into firn and ice through thermo-physical processes, including the formation of superimposed ice in early summer and the refreezing of meltwater in the fall (Kawashima et al., 1993). The second ice mass type, called “glacial ice patches”, refers to ice patches formed by relict glacial ice in a paraglacial landscape during a period of deglaciation. The ice physics and structure thus retain signs of past glacial dynamics (e.g. features such as the deformation of glacier banding, foliations, closed or filled crevasses; Serrano et al., 2011). In a favourable topographical context (e.g. bottom of glacial cirque, under rock wall), glacial ice masses can be well preserved by an active snow input that leads to the development of a hybrid system in which a nival ice patch forms on a basement made of glacier ice (Gachev et al., 2016; Yamamoto and Yoshida, 1987).

Despite their limited individual size, ice patches are ubiquitous, making them an important contributor to the regional and local hydrological cycle, landscape evolution and ecosystem functioning. Across the Canadian Arctic Archipelago, where ~ 44% of the ice-free land is occupied by a polar desert ecozone (Bliss and Gold, 1999), ice patches are numerous (Lauriol et al., 1986), represent an important reservoir for freshwater and are a primary contributor to the hydrological cycle of small watersheds by sustaining meltwater flow on slopes throughout the summer (Lewkowicz and Young, 1990; Paquette et al., 2018; Young et al., 2017). Their presence is associated with mass transfers on slopes, especially solifluction (Christiansen, 1998; Verpaelst et al., 2017; Washburn, 1999; Wilkinson and Bunting, 1975) and affects the surface energy budget, the ground thermal regime (Lewkowicz and Young, 1991) and biological activities involving microbes, vegetation and animals (Gooseff et al., 2003). This wide range of implications on the physical and biological environment highlights that ice patches deserve particular attention, especially in the polar desert where water supplies are strongly limited, in order to understand their response to climate change and to assess how such responses will impact water discharge,

geochemistry, sediment fluxes on slopes and vegetation dynamics. To achieve this, knowledge on the internal structure and basic properties of the ice (i.e. crystallography, air bubble concentration and shape, sediment inclusions) is an important prerequisite. To date, only few glaciological investigations have been made on ice patches and ice physics has never been investigated in detail. Most studies were undertaken in mid-latitude mountains, since the 1970s in Japan (e.g. Kawashima et al., 1993; Sakai et al., 2006; Wakahama and Narita, 1975; Yamamoto and Yoshida, 1987) and more recently in Scandinavia (Hirvas et al., 2000; Ødegård et al., 2017) and in Western Canada (Meulendyk et al., 2012). Specifically, in Polar Regions, empirical knowledge on ice patches is so far limited to only two studies: Østrem (1963) who undertook an analysis of the ice physics of subpolar and polar ice patches in Scandinavia and on Baffin Island; and Lewkowicz and Harry (1991) who studied a polar ice patch on Melville Island in Nunavut (Canada). Both studies proposed an analysis of the internal structure through ice core description (e.g. porosity, sediment inclusions) and isotopic composition. Despite those pioneering studies, large knowledge gaps persist regarding the properties and the formation of polar ice patches. Little is known about the different processes that lead to the formation of new ice and about the variability of the ice facies across an ice patch. Moreover, the stratigraphy and properties of preferential snow accumulation have not yet been investigated in the polar desert. Since the seasonal snow represents the major input of mass to ice patch systems, snow physical properties are expected to modulate the heat and liquid water fluxes, which in turn control the ice growth processes.

To fill these gaps and gain a deeper understanding of the processes behind ice patch formation and its annual and pluriannual dynamic, we performed a detailed analysis of two ice patches located on Ward Hunt Island, a polar desert site situated at the northern edge of the terrestrial Canadian Arctic. This study addressed the question of how the seasonal snow properties modulate the ice formation and which thermodynamic processes are involved in the transformation of the snow to ice under polar desert conditions. The objectives were (i) to characterize in detail the physical properties and metamorphic processes of the snowpack that feed the ice patches: and (ii) to analyze the internal ice features (ice crystallography, bubble sizes and shapes, sediment inclusion) and structure of the ice patches. A secondary aim was to consider these ice features in the context of long-term and current climate variations, including the extreme warming that has been recorded at this site over the last decade. This research is a contribution to the project “Terrestrial Multidisciplinary distributed Observatories for the Study of Arctic Connections” (T-

MOSAiC), which places emphasis on system-level properties, including responses of the cryosphere to rapid warming (Vincent et al., 2019).

2.5. Study site

Ward Hunt Island ($83^{\circ}05'09''$ N, $74^{\circ}06'19''$ W; hereinafter: WHI) is located at the northern tip of the Canadian Arctic Archipelago (**Figure 15a,b**) and is characterized by a polar desert landscape. A general description of the physiography, geomorphology and vegetation is given in Vincent et al. (2011b). The mean annual air temperature recorded at the SILA weather station (**Figure 15c**) was -17.1°C for the period 2005-2019 with a monthly mean ranging between -31.6°C in February and 1.7°C in July (CEN, 2021). The melting season extends generally from mid-June to the end of August, with days below freezing where melt pauses. No long-term precipitation data is available for WHI, but it is likely similar to the average of $185\text{ mm w.e. year}^{-1}$ measured at Alert, located 170 km to the southeast. About 90% of the total precipitation amount falls as snow (Environment Canada, 2021). The prevailing winds blow from the south-southwest according to measurements recorded at the SILA station from 2005 to 2019. The strongest maximum hourly-average wind speeds have been recorded for the alongshore westerly winds with wind speeds exceeding 20 m s^{-1} during major storms (CEN, 2021). The persistence of high winds in winter leads to an important redistribution of snow across the landscape that produces large heterogeneities in snow depths which rarely exceed 40 cm on exposed terrain but can reach over 150 cm in areas of preferential accumulation ([Davesne et al., 2021](#); Domine et al. 2018a). Unlike Ellesmere Island, WHI has no glaciers but the cryosphere is omnipresent on the island and its surroundings (**Figure 15c**). The sea channel between the south coast of the island and Ellesmere is occupied by pack ice and the remnants of the Ward Hunt Ice Shelf (WHIS) that disintegrated in summer 2011 (Copland and Mueller, 2017). The north and west coast are bordered by the Ward Hunt Ice Rise (WHIR) (Braun et al., 2004). On the island, the largest and most conspicuous perennial ice masses are the ice patches. Most of them are found between 20 and 50 m above sea level (a.s.l.) along the main break-of-slope at the junction of steep faces with scree slopes below and on the leeward concave hillslopes at higher elevations (**Figure 15c**). These ice patches play a key role as the main provider of water to the hydrological system throughout the summer, feeding the surface and subsurface drainage network, the WH Lake and lowland wetlands. The rapid circulation of this water via water tracks favours sediment transfers and slope denudation processes

(Paquette et al., 2020a). On Ward Hunt Lake (WHL) a semi-perennial ice cover is present. Beneath the ground surface, WHI is characterized by cold continuous permafrost several hundred meters thick with a mean annual temperature of -13.5°C at 3 m depth according to the measurements provided by a thermistor cable for the period July 2015-July 2019 (CEN, 2021).

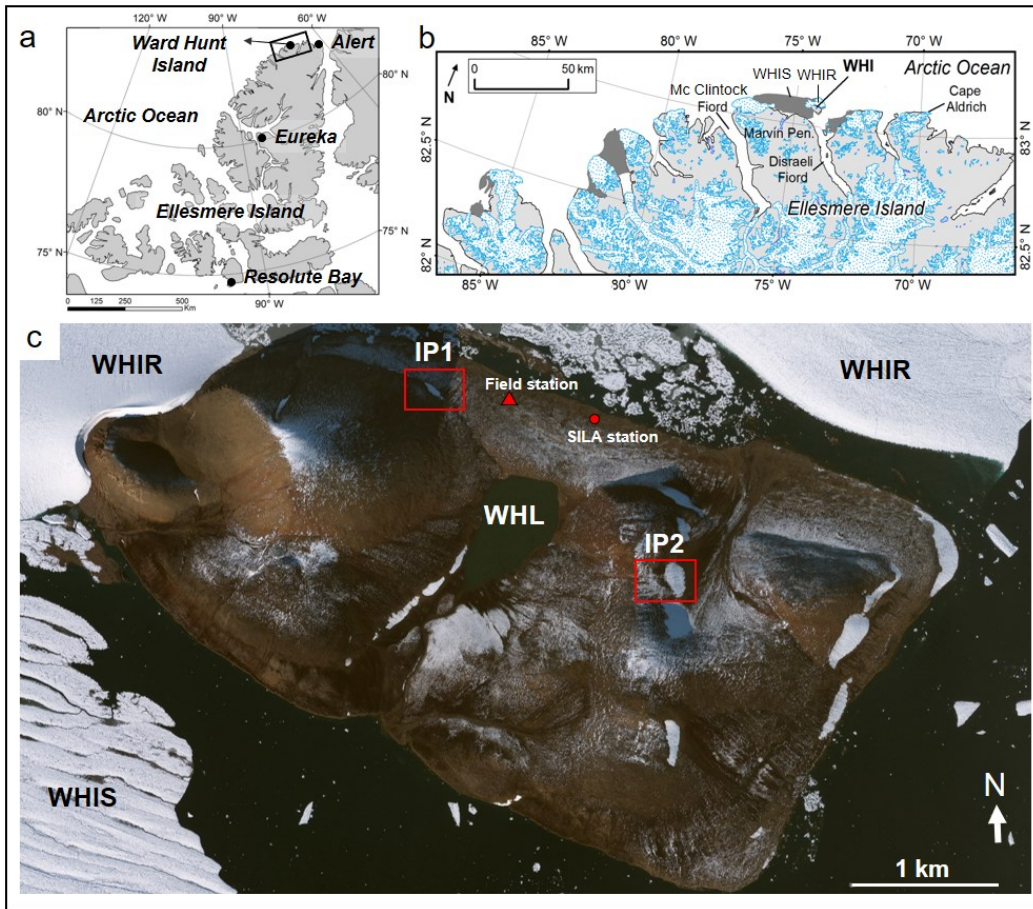


Figure 15. Location of Ward Hunt Island (WHI) at the northern tip of Ellesmere Island (a, b); WHIS: Ward Hunt Ice Shelf; WHIR: Ward Hunt Ice Rise (delimitation of the end of summer 2012). GeoEye satellite image (c) taken on 26 August 2011. The red squares indicate the investigated ice patch 1 (IP1) and ice patch 2 (IP2). The GeoEYE image shows the ice patches at their minimal extent at the end of the warm summer 2011 which was marked by the complete disappearance of the perennial ice cover on Ward Hunt Lake (WHL) for the first time since observations began in the 1950s (Paquette et al., 2015).

2.6. Materials and methods

This study of ice patches on WHI comprised a detailed description of (i) the seasonal snow accumulation that feeds the ice patches and (ii) ice cores based on a combination of thin sections and tomodensitometric (CT-scan) image analysis. This study focuses on two ice patches, named

IP1 (Ice patch 1) and IP2 (Ice patch 2) (**Figure 15c**; **Figure 16**). These ice patches were selected after initial field surveys and examination of a GEOEYE image taken on 26 August 2011 during a period of substantial warming. They were chosen for their different topographic settings (i.e. elevation, orientation, position on the slope), their different morphology, their large size and their accessibility from the research station.

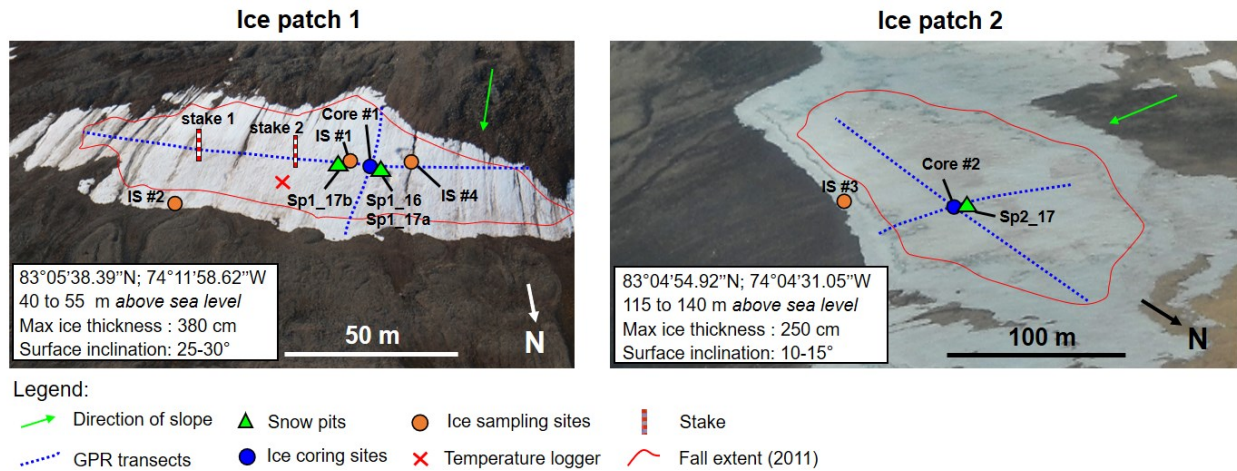


Figure 16. Oblique photograph taken from helicopter showing the ice patches selected for this study: IP1 (transverse ice patch) and 2 (circular ice patch). The snow analysis and ice coring were undertaken in summers 2016 and 2017. The extent of the ice patches at the end of the particularly warm summer 2011 was inferred from the GEOEYE image shown in **Figure 15**. Details of snowpits, ice cores and ice samples are presented in Table S1 in the supplementary material.

2.6.1. Seasonal snowpack characterization

Snowpits were dug on both ice patches in early June 2017 (*Sp1_17a* and *Sp2_17*) before any melting event had occurred (**Figure 16**). On IP1, the snowpit *Sp1_17a* was compared with another one made in early June 2016 (*Sp1_16*) at the same location to study the interannual variability of the snow properties. At IP1, an additional snowpit was dug in early July 2017 (*Sp1_17b*), three weeks after the beginning of the melt season. This pit, made four meters away from *Sp1_17a*, was used to document the structure of the snowpack in an advanced melting stage and to understand the evolution of the snow properties and the formation of basal ice throughout the melt season. To estimate ice growth at the base of the snowpack, two graduated stakes were inserted vertically into the snowpack down to the ice surface on IP1 in early June 2017 (**Figure 16**). The level reached by the newly formed superimposed ice was then read on 8 July. Data on the snowpits and the snow analysis procedure are detailed in [Appendix A1-1](#) (section 2.13) and supplementary material (section 2.14; [Table S1-1](#)).

To interpret the snow metamorphic processes that occurred throughout the cold season, the bulk temperature gradient in the snowpack and wind speed were measured for IP1. We relied on measurements of the air and ice surface temperature throughout the cold season 2016/17 to estimate the temperature gradient through the snowpack. The air temperature was recorded at hourly intervals by a sheltered sensor U22-001 (Hobo®; resolution of 0.02 °C, uncertainty of ± 0.21 °C) set at 1 m above the soil surface and installed 30 m off the front of the ice patch. The ice surface temperature was recorded at hourly intervals by a data logger Trix-8 (LogTag®; resolution 0.1°C, uncertainty of ± 0.5 °C) installed 15 cm above the ice surface on a wooden pole frozen in the ice, 4 meters above the frontal edge of IP1. The height of snow measured above the sensors was 205 cm in early June 2017. The average temperature gradient (ΔT in K m⁻¹) was calculated using equation 2.1:

$$\Delta T = \frac{T_{is} - T_{ss}}{h} \quad (2.1)$$

where h is the snowpack height, T_{is} is the temperature at the snow/ice interface, T_{ss} is the temperature at the snow surface and is assumed to be equal to the air temperature, except when the latter is above 0 °C in which case T_{ss} is assumed to be equal to 0°C. Since T_{ss} in the dark or under low insolation was equal or less than the air temperature and given that the U22-001 sensor was on a north-facing slope that received little insolation, the gradient calculated here is, therefore, a lower limit of the actual gradient. The height of snow through the cold season 2016/17 was inferred from the data provided by a Sonic SR50 (Campbell Scientific; resolution 0.25 mm; uncertainty ± 1 cm) installed at the SILA weather station located 1 km west of IP1 (**Figure 15c**). The snow gauge is installed on a seasonal snow patch and provides reliable data to understand the snow dynamics in a preferential accumulation site. The raw data was adjusted using a correction coefficient (x1.5) to make the end-of-winter snow height recorded at SILA consistent with the snow height measured in the central part of IP1 in June 2017.

2.6.2. Ice sampling procedure

The microstructural study of the ice was based on the analysis of ice cored in both patches (see [Table S1-1](#) for detailed information). A complete sequence of the ice body, from the top layers to the bottom, was retrieved from IP1 (core #1) and IP2 (core #2) (**Figure 16**) during the 2017 field season. The coring procedure is detailed in [Appendix A1-2](#). For both sites, the coring location was

selected according to Ground Penetrating Radar (GPR) surveys which allowed identifying where the ice was deepest. Additional ice samples were collected on IP1 and IP2 for comparison (**Figure 16**; [Table S1-1](#)). Seasonal basal ice samples were collected at the bottom of the snowpit *Sp1_17b* (IS #1) and at the frontal margin (seasonal fringe) of IP1 (IS #2) and IP2 (IS #3) where the basal ice was newly exposed. Ice samples were also extracted from the sides of a supra-ice channel that drained the meltwater on IP1 (IS #4) (**Figure 16**). The aim was to understand the properties of the newly formed ice to infer the transformation processes of snow to ice and to document the consequence of water inputs to the ice transformation and recrystallization processes. All ice cores and samples were described, measured and photographed in the field. They were then sealed in plastic bags and kept frozen in a cold room at – 12 °C.

2.6.3. The crystalline structure of the ice

A total of 120 thin sections were made for this study. The thin section preparation, detailed in [Appendix A1-3](#), followed the procedure reported in Langway (1958) and Østrem (1963). The post-processing step consisted of automatically detecting the crystal boundaries using the open-source imaging software ImageJ® (**Figure 17a**). The high resolution of the photography allows the detection of crystals as small as 0.2 mm. A computation of the two-dimensional morphometrics properties of each ice crystal detected in a thin section was performed using ImageJ (Analyze particle function) to measure the crystal size, defined by the surface area (A , mm²) and the major axis length (L , mm) and the crystal shape obtained by computing the roundness parameter (R) ([Appendix A1-3](#)). We used the following crystal-size classes derived from Ragle et al. (1964): very fine, < 5 mm²; fine, 5–10 mm²; medium, 10–50 mm²; coarse, 50–100 mm²; very coarse, > 100 mm². Finally, the 2D shape and organization of the crystals were studied using shape anisotropy (Gay and Weiss 1999), which describes the elongation of the crystals in a preferential direction. It was calculated by the ratio between the length of the crystal measured in the horizontal (L_x , mm) and vertical (L_z , mm) planes ([Figure S1-1](#)). C-axis orientations were not determined. The major limitation with the thin section is the impossibility to measure accurately a 3D structure with a 2D perspective. The planar thin section randomly cuts ice crystals and their apparent shape and size do not necessarily reflect the true values. Some methods have been proposed to correct this bias (e.g. Alley and Woods, 1996; Gow 1969), but the most common and accepted practice in the literature is to present uncorrected results (Coulombe et al., 2019; Thorsteinsson et al., 1995).

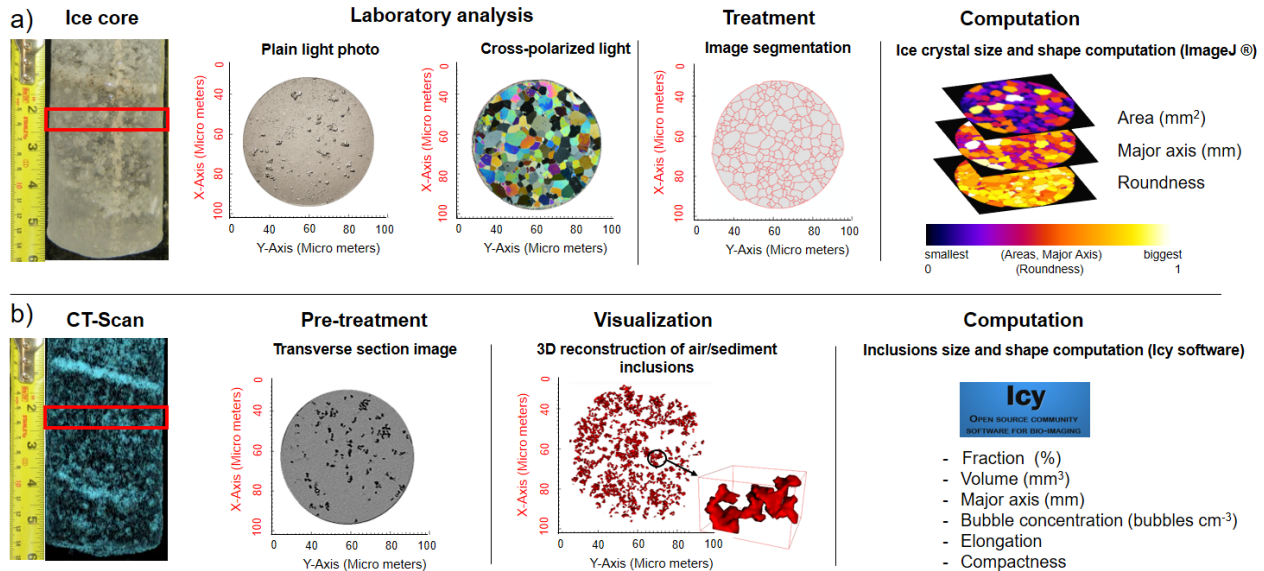


Figure 17. Investigation of the ice properties through a) ice crystal analysis using thin sections and b) gas and sediment inclusion analysis using microtomodensitometry (CT-scan).

2.6.4. Gas and sediments inclusions in the ice

To complement ice crystallography, a description of the inclusions of air and sediment (shapes, sizes, concentrations and distributions) trapped in the ice gives insights into ice forming conditions (**Figure 17b**). The characterization of the air and sediment inclusions in both ice cores was done with high-resolution ($0.195 \times 0.195 \times 0.4$ mm voxel volume) 3D X-ray computed tomography scans (CT-scans) provided by a Siemens Somatom 64 scanner at the Institut National de la Recherche Scientifique (INRS-ETE) in Québec City (Canada) ([Appendix A1-4](#), CT-scan images are available in open-access files; Fortier and Davesne, 2021a). Processing of the DICOM images was performed using the ImageJ software® following the procedure of Crabeck et al. (2016). From the stack of images, a high-resolution sub-millimeter profile of the porosity (i.e. air fraction) was extracted. Air fraction was expressed by the porosity (ϕ in %) for a given volume of ice (V) and was then converted into bulk density (ρ_i in $\text{kg} \cdot \text{m}^{-3}$) of the ice ([Appendix A1-4](#); [Figure S1-2](#)). For the ice samples IS#1 to 4 for which no CT-scan images were obtained, the bulk density was obtained in the laboratory by cutting a disk 5 cm thick from the core for which mass was measured with an electronic balance (resolution: 0.001g). When a sample had an irregular shape, its gross volume was determined by submerging samples sealed in plastic bags into 2 liters of cold water in a 20 cm diameter graduated cylinder and by measuring the water displacement (Kawamura, 1990).

The bubble number-density (bubbles cm⁻³), the size and morphology of air bubbles were computed from the three-dimensional CT images using the Icy imagery software package (De Chaumont et al., 2012, Legland et al., 2016). The software allowed detecting each bubble larger than the voxel resolution (0.0152 mm³) and to reconstruct their surface by triangular meshing. The 3D visualization of air bubbles into the ice, coupled with naked-eye observation of the thin sections, was used to detect and count the fracture density in the ice cores ([Figure S1-3](#)). In addition, a 3D morphological analysis of the air bubbles was performed using the plugin *3D-analysis* that allowed to compute the long-axis (L, mm), the volume (V, mm³), the compactness (C) and the elongation index (El) of each mesh ([Figure 17](#)). According to their volume, the air bubbles derived from the CT were classified into 3 categories: micro-bubbles (V<1 mm³), large bubbles (1<V< 10 mm³) and macro bubbles (V>10 mm³) (Crabeck et al., 2016). The compactness is the normalized ratio between the surface areas and the volume of a bubble and is related to the shape and the roundness of bubbles (Zhao and Wang, 2016). Values tend to 1 for a sphere while it tends to 0 for a highly irregular shape. The elongation index was calculated from the ratio between the largest radius and middle radius of the bubbles. The elongation value is close to 1 for rounded bubbles and increases for elongated ones. From those shape descriptors, air bubbles were divided into 4 classes: Elongated cylindrical bubbles (ECb) (C> 0.15; El> 2), Sub-spherical bubbles (SSb) (0.15< C <0.4; El< 2), Spherical bubbles (Sb) (C> 0.4; El< 2) and Irregular bubbles (Irb) (C< 0.15; El< 2).

The concentration of sediments (kg m⁻³) was measured in the laboratory by cutting slices of ice cores, calculating their volume and melting them in individual pre-weighed aluminum containers. The samples were then dried in an oven and weighted with a high accuracy scale (resolution: 0.001g). The measurements of sediment concentration were only made in the core sections where sediments were visible to the naked eye. Finally, we collected a sample of material which was a mixture of two distinct bands of sediments between 212 and 218 cm deep in core #2 (IP2) for radiocarbon dating. The sample contained organic debris, including well-preserved fragments of moss, branches, flowers, and leaves ([Figure S1-4](#)). The sample was pretreated (HCl, NaOH, HCl) at the Radiocarbon Dating Laboratory (Université Laval, Québec, QC, Canada) and ¹⁴C dated by accelerator mass spectrometry (AMS) at Keck Carbon Cycle AMS Facility (University of California, Irvine, CA, USA). The radiocarbon date was calibrated with the CALIB 8.2 online program (Stuiver et al., 2021) using the IntCal13 calibration data set (Reimer et al., 2013).

2.6.5. Environmental monitoring

To infer the formation processes of the ice, we also relied on a set of environmental data monitored at IP1 including time-lapse photographs, ice temperature and meltwater outflow discharge. The time-lapse photographs were taken by an automatic camera (Spypoint® Force-11D) installed in front of IP1 since July 2016 (Fortier and Davesne, 2021b). The ice temperature data were measured between July 2017 and July 2019 by a chain of thermistors (resolution $\pm 0.001^\circ\text{C}$; uncertainty $\pm 0.1^\circ\text{C}$) at depths of 0, 50, 100, 150, 200, 250, 300 and 320 cm installed in the drill hole of Core #1 on IP1 (Fortier and Davesne, 2021b). A white perforated PVC pipe was placed into the borehole in which the cable was inserted. Water was then poured in and around the pipe to set it and guarantee optimal thermal contact with the ice body. The deepest thermistor, at 320 cm, was in contact with the bedrock. Thermistors were connected to a multichannel data logger (Systems Smart Reader Plus 8™, ACR Systems Inc.) which recorded temperatures at an hourly interval.

2.7. Results

2.7.1. Seasonal snow accumulation over the ice patches

The snowpack properties and vertical structure of the pits *Sp1_17a*, *Sp2_17*, *Sp1_16* and *Sp1_17b* are shown in **Figure 18**. In early June 2017, the snowpack stratigraphy shows the same structure on IP1 (*Sp1_17a*) and IP2 (*Sp2_17*). The upper section consisted of hard wind slabs with density values exceeding 400 kg m^{-3} (**Figure 18a, b**). These slabs were topped by a surface layer of fresh snow made of fragmented snow crystals. In both snowpits, the proportion of faceted grains gradually increased with depth. Below a certain height (160 cm in *Sp1_17a* and 80 cm in *Sp2_17*), the wind slabs exhibited an early stage of recrystallization. The grain size was slightly larger than in the upper sections. The bottom-most layer was a thin layer of depth hoar (DH) (less than 10 cm thick) with crystal size not exceeding 2–4 mm near the contact with the ice substratum. In both cases, the first few centimetres of the ice surface consisted of weathered ice with loose coarse crystals of ~5 mm in size. Specifically for the snowpit *Sp2_17*, a layer (~15–20 cm) of sediment and very hard-packed snow ($\rho_s = 580 \text{ kg m}^{-3}$) was found just above the DH (**Figure 18b** and [Figure S1-5](#)). The sediment content of this snow layer reached $10.9 \pm 0.97 \text{ kg m}^{-3}$. The snowpit *Sp1_16* dug in early June 2016 (**Figure 18c**) showed properties similar to *Sp1_17a* made one year later at

the same location, with the difference that in 2016 the basal DH layer was lying on a surface of granular and compact old snow identified as firn.

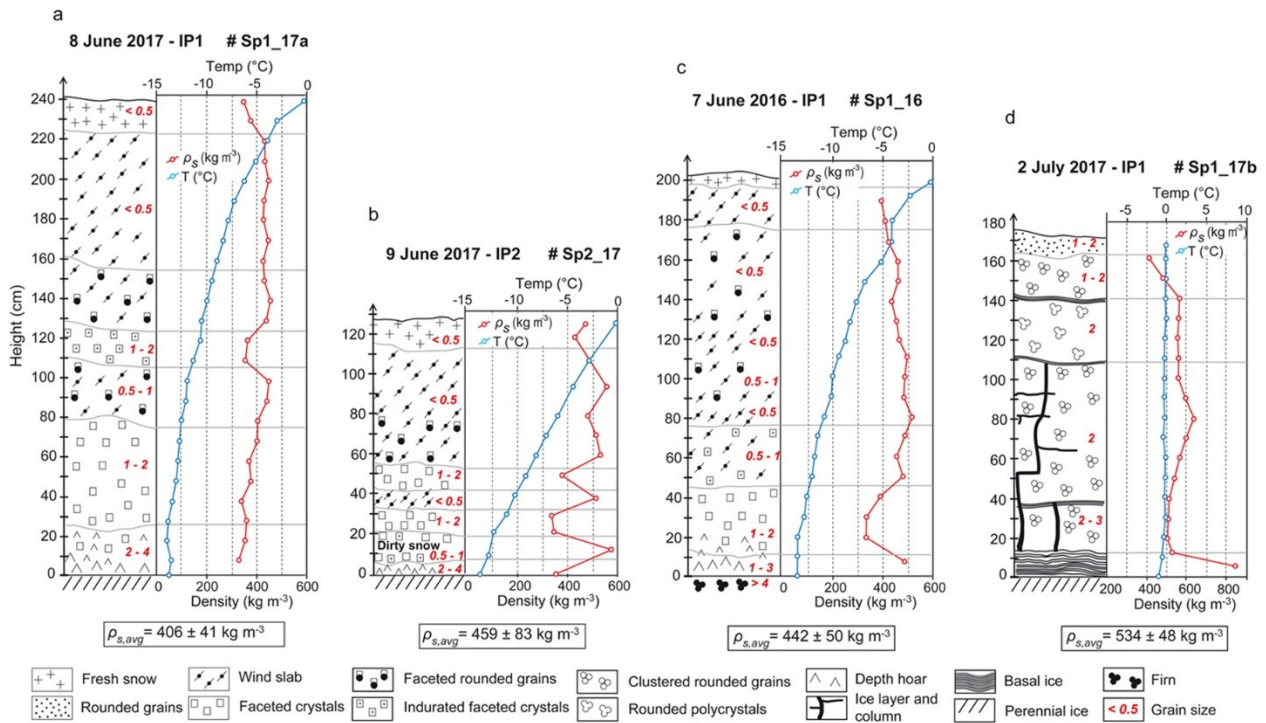


Figure 18. Graphical representation of the stratigraphy and physical properties of the seasonal snowpack measured over perennial ice patches. Snowpits Sp1_17a and Sp2_17 (a and b) were dug on IP1 and IP2, respectively, in early June 2017, the snowpit Sp1_16 (c) was dug one year earlier (7 June 2016) at the same site than Sp1_17a and the snowpit Sp1_17b (d) was dug on 2 July 2017 close to the site of Sp1_17a. Snow-type symbols are those used by Fierz et al. (2009) and Domine et al. (2018a). The horizontal grey lines represent the stratigraphic discontinuities that delimit the different layers observed in the snowpack.

On 2 July 2017, the snowpack at the snowpit Sp1_17b was 175 cm deep including a ~15 cm deep surface layer of fresh snow added by a storm on 29–30 June 2017 (Figure 18d). At that time, the entire profile was isothermal and consisted of unsaturated wet snow comprised of clustered rounded grains, and snow density reached values up to 640 kg m^{-3} . Within the snowpack, discontinuous horizontal ice layers, up to 3 cm thick, and large vertical percolation channels made of solid ice up to 6 cm in width were present (Figure S1-6). The lowest part of the snowpit consisted of a basal ice layer overlaid by a water-saturated layer of coarse granular snow. All the percolation channels reached the basal ice layer. On 8 July 2017, the reading of the stakes installed in IP1 gave a new ice layer of 27 cm and 34 cm upon the former ice surface for stakes 1 and 2, respectively. The density of the samples of basal ice collected at the base of Sp1_17b was $876 \pm 19 \text{ kg m}^{-3}$ ($n=5$)

on average (**Table 1**, sample IS#1) and the overall density of the snowpack, excluding the basal ice and internal ice structures, was $534 \pm 48 \text{ kg m}^{-3}$.

Table 1. Mean ($\pm SD$) of major axis, crystal surface area, roundness (inverse of the aspect ratio) and density of the upper and lower section of IP1 and IP2. In addition, the same data were obtained for the ice samples collected at the bottom of the seasonal snowpack on IP1 (IS#1), on the freshly exposed ice near the frontal margin on IP1 (IS#2) and IP2 (IS#3), and on the side of a supra-ice channel on IP1 (IS#4). Values in parentheses are the number of samples for which the hydrostatic density was measured. See Figure S8 for examples of photographs of thin sections of ice samples. X means the horizontal plan while Z means the vertical plan of ice cores.

			Major Axis (mm)	Surface Area (mm ²)	Roundness (Index)	Density (kg m ⁻³)
Ice cores	Upper section	IP1	X Z	1.55 \pm 1.05 1.51 \pm 0.92	2.35 \pm 1.78 1.88 \pm 0.79	0.70 \pm 0.01 0.69 \pm 0.01
		IP2	X Z	1.80 \pm 0.54 1.51 \pm 0.26	2.23 \pm 3.94 2.04 \pm 2.99	0.70 \pm 0.02 0.69 \pm 0.02
	Lower section	IP1	X Z	7.69 \pm 2.29 6.22 \pm 1.92	43.42 \pm 25.69 36.13 \pm 20.67	0.63 \pm 0.03 0.64 \pm 0.02
		IP2	X Z	6.03 \pm 1.86 7.11 \pm 1.44	28.83 \pm 11.40 30.39 \pm 9.95	0.67 \pm 0.01 0.65 \pm 0.02
Ice samples	Basal ice	IS#1		2.67 \pm 0.29	4.91 \pm 1.21	0.73 \pm 0.02
		IS#2		2.17 \pm 0.13	3.15 \pm 0.50	0.73 \pm 0.01
		IS#3		1.58 \pm 0.34	1.66 \pm 0.66	0.75 \pm 0.01
	Channel ice	IS#4		10.48 \pm 3.51	68.80 \pm 55.44	0.47 \pm 0.05
						876 \pm 19 (n=5) 862 \pm 12 (n=3) 865 \pm 14 (n=3) 909 \pm 03 (n=4)

The bulk temperature gradient values in the snowpack on IP1 through the cold season 2016/17 is shown in **Figure 19**. Three main periods can be identified. Period 1 is short and consists of the early cold season when a large temperature gradient ($>100 \text{ K m}^{-1}$) developed into the shallow snowpack (5 to 15 cm deep). Period 2 started when the snowpack became deep enough to drastically reduce the bulk temperature gradient ($<20 \text{ K m}^{-1}$). These low gradient conditions extended during most of the cold season and the gradients then approached 0 K m^{-1} when the snowpack started to warm up in April. At the end of the cold season, almost all of the snowpack was at 0°C except the very basal layer. The temperature gradient was therefore zero.

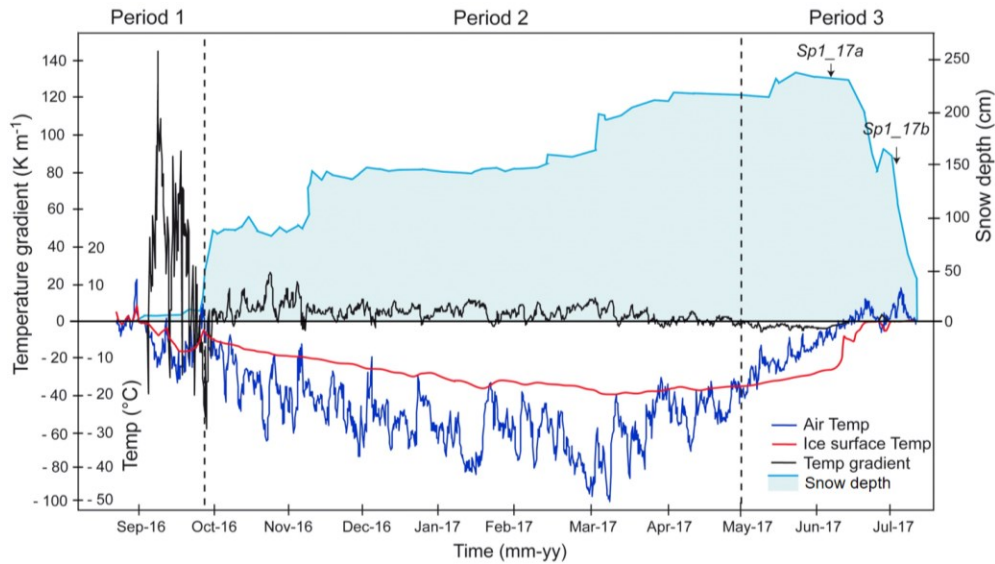
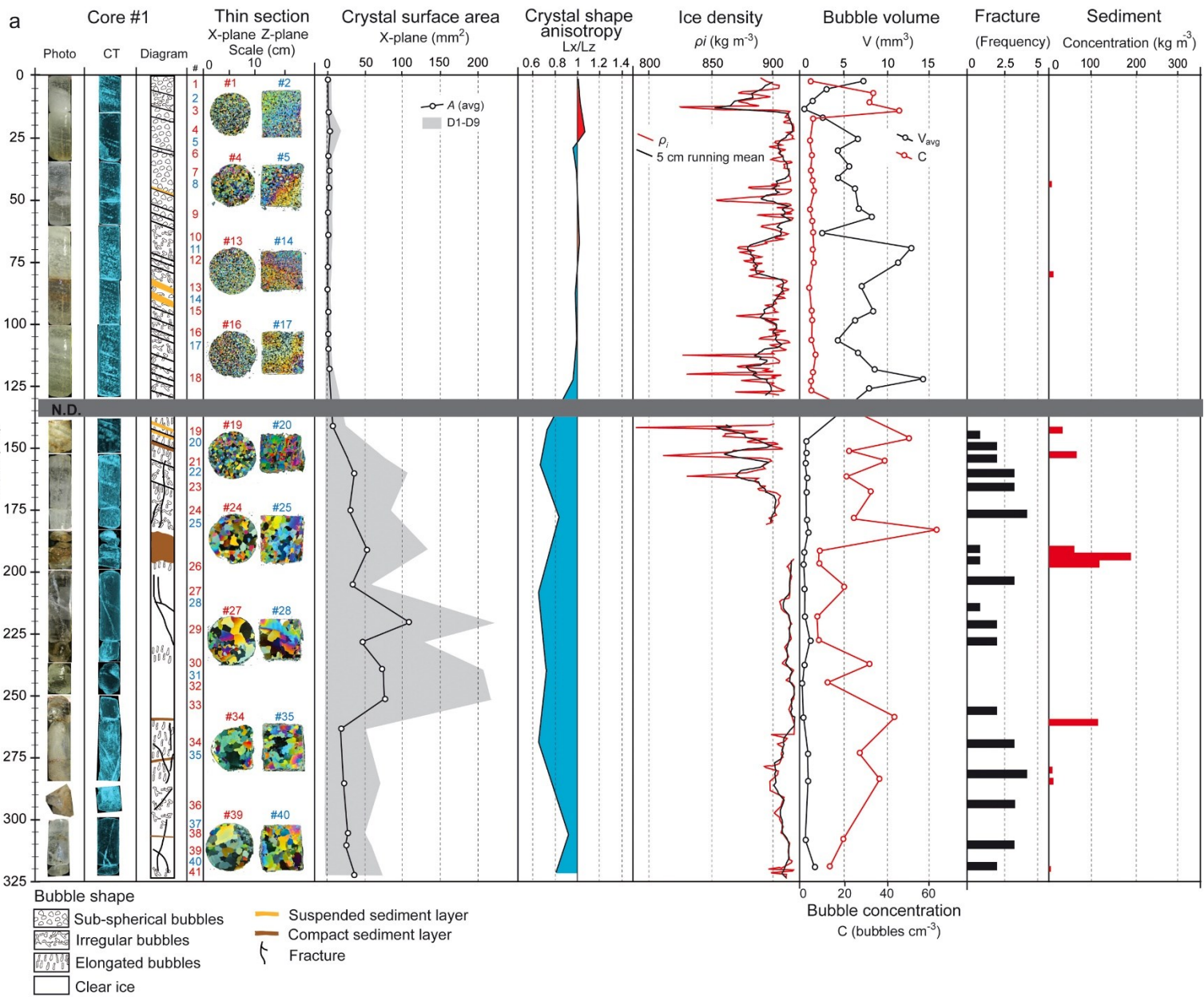


Figure 19. Evolution of the daily air and ice surface temperature, of the daily snow depth (inferred from the SILA station) and of the temperature gradient in the snowpack on IP1 through the cold season 2016/17 calculated from Equation 2.1. Vertical dash lines delimit the three periods in the temperature gradient evolution. “Sp” during period 3 shows when snow pits were dug.

2.7.2. Perennial ice properties

2.7.2.1. General ice structure of ice cores

The visual examination of the overall ice cores IP1 and IP2 (**Figure 20**) shows an abrupt change in the physical parameters of the ice at a depth of 130 cm. In the upper section, the vertical variation in ice porosity creates an interplay of milky ice and clear translucent ice facies. Some brownish-red shaded, more or less opaque layers are also present at various intervals due to dust and coarser sediment inclusions. Various ice facies and the sediment layers formed a series of bands with the same inclination and orientation. They dip downward with an angle of 20 to 25° for IP1 and 13–18° for IP2 which follows the ground surface slope angle (**Figure 16**). The lower sections present a higher proportion of clear ice and are marked by larger sediment inclusions than in the upper sections. The oblique banded pattern is less evident and absent in some parts. The lower sections are marked by a high frequency of micro-fractures that randomly cut across the cores (**Figure 20**).



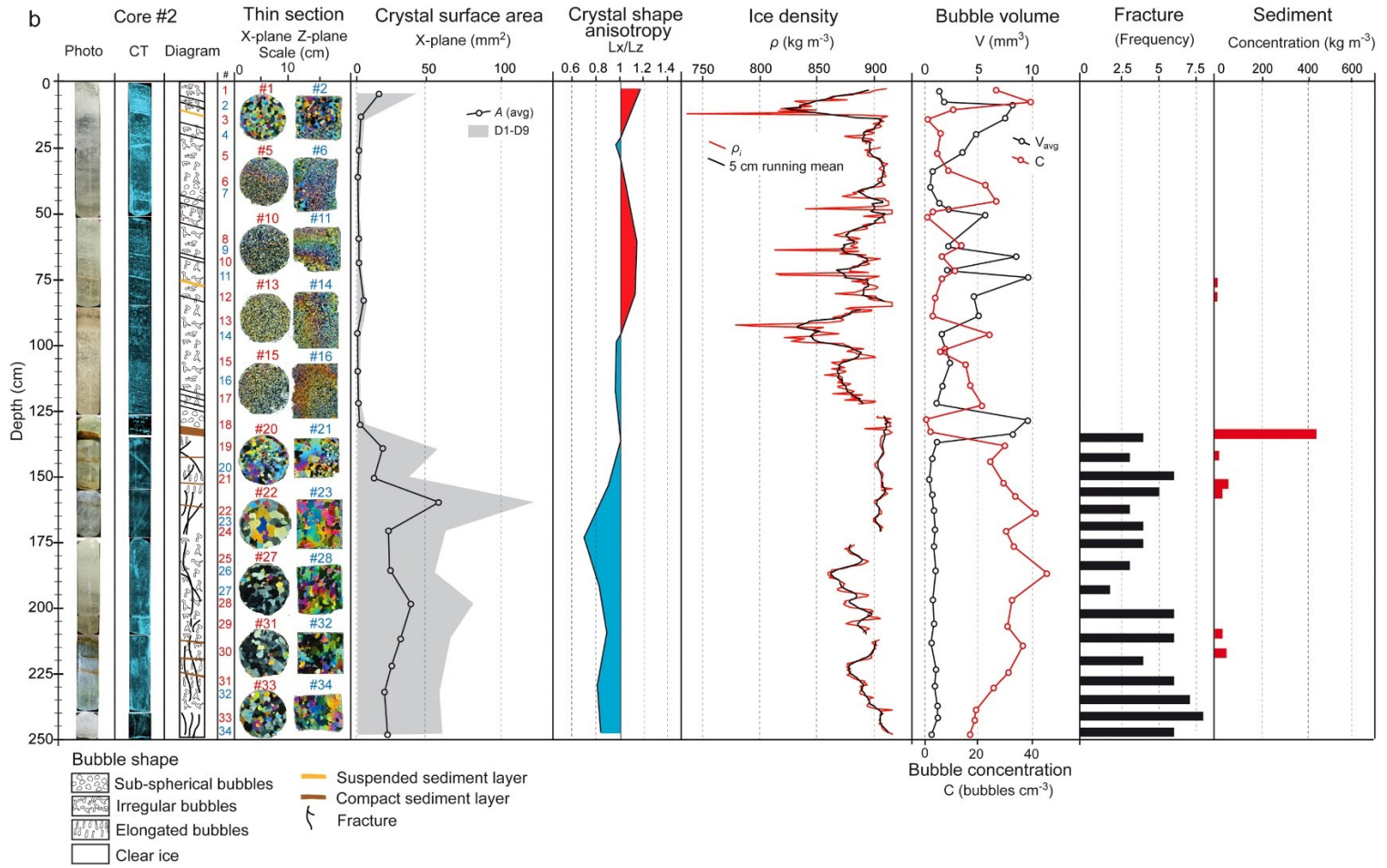


Figure 20. Physical description of the ice cores retrieved at the IP1 (a) and IP2 (b) sites. A is the crystal surface area, D1 and D9 are 10th percentile and the 90th percentile, respectively; Lx and Lz are the maximum length of the ice crystals for the horizontal plane (X-plane) and vertical plane (Z-plane), respectively; ρ_i is the ice density, V and C are the bubble volume and bubble concentration, respectively.

2.7.2.2. Crystal size and shape

The upper section of both ice cores #1 and #2 exhibited similar ice petrography. The thin section analysis revealed a pattern consisting of randomly-arranged very fine polygonal crystals (**Figure 20**; **Table 1** and [Figure S1-7](#)). The crystal size distribution is narrow (low variance) and is nearly constant along the vertical profile. The comparison between the measurements obtained from horizontal (X plane) and vertical (Z plane) thin sections shows an anisotropy ratio close to 1 along the upper sections, indicating no preferential elongation of the crystals. This equiaxial character of ice crystals is also revealed by the similar high roundness values (R) for both X and Z planes. Under cross-polarized light, the thin sections revealed a wide range of crystals interference

colours (**Figure 20**), indicating that they have a randomly oriented c-axis. In the lower sections of the ice cores #1 and #2, the crystal size is significantly higher ranging from medium to coarse size (**Figure 20; Table 1** and [Figure S1-7](#)). The variance in the crystal size is higher and the vertical variability is much more pronounced than in the upper sections. Very coarse crystals exceeding 100 mm^2 are found in the sections where the ice is the most translucent. Coarser crystals are up to 500 mm^2 in core #1 and 230 mm^2 in core #2. The ice crystals have a more irregular shape and a slight vertical elongation as suggested by the lower R values and the shape anisotropy ratio values below 1.

The crystallography of additional ice samples is presented in **Table 1** and [Figure S1-8](#). The basal ice collected at the bottom of the snowpit *Sp1_17b* (IS#1) and in the frontal edge of IP1 (IS#2) and IP2 (IS#3) consists of very fine rounded grains. The ice samples collected on the sides of a supra-ice channel (IS#4) are characterized by very coarse ice crystals. Larger crystals had a major axis up to 50 mm and were mostly elongated ($R = 0.47 \pm 0.05$).

2.7.2.3. Gas inclusion and density of the ice

In the upper sections of both ice cores #1 and #2, air inclusions are characterized by high variability of sizes, concentrations and shapes (**Figure 20** and [Figure S1-9](#)). Large ($1 < V < 10 \text{ mm}^3$) and macro-bubbles ($V > 10 \text{ mm}^3$) account together for 49% and 47% of the bubble population, respectively (**Figure 21**). The larger bubbles are well dispersed into the ice and they are occasionally concentrated into thin oblique layers, which form high porosity bands (Fig. S9). The general bubble concentration is low, especially in core #1. Examination of the morphology of the air inclusions showed a high occurrence of irregular shapes in the large and macro-bubble population while sub-spherical shapes dominate the micro-bubbles ($V < 1 \text{ mm}^3$) (**Figure 20, Figure 21** and [Figure S1-9](#)). In the lower section of cores, the micro-bubbles predominate with 85% and 75% of the bubble population for IP1 and IP2 while macro-bubbles are mostly absent (<0.5% in both cases). On the other hand, the average bubble number-density is higher (**Figure 21**). The micro-bubbles are heterogeneously dispersed through the ice, so that no well-developed banded structure exists. The larger bubbles are mainly concentrated in fractures, forming trains of sub-spherical to elongated bubbles ([Figures S1-3](#) and [S1-9](#)). The small and large bubbles are generally elongated along the Z plane while the micro-bubbles are roughly spherical ([Figure S1-9](#)). Translucent ice was typically associated with coarser ice crystals (**Figure 20**).

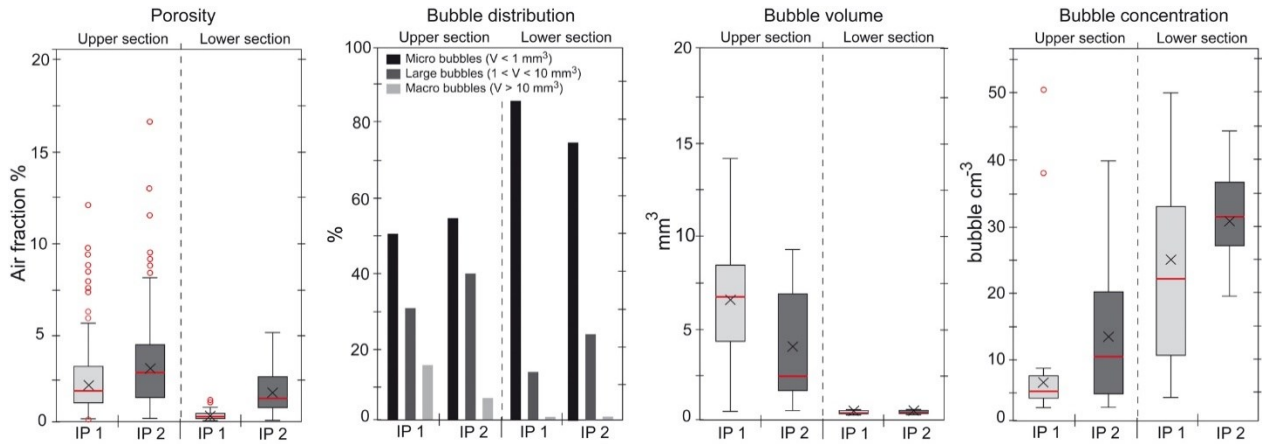


Figure 21. Summary of the ice porosity, and the bubble size distribution, bubble volume and bubble concentration in the upper and lower sections of IP1 and IP2. V is the bubble volume. The red line in the box plot is the median, the black cross is the mean and the circles represent the outliers.

The high proportion of large and macro-bubbles in the upper sections of cores #1 and #2 led to a higher ice porosity (**Figure 21**), explaining density values around 890 kg m^{-3} . The density profiles revealed pronounced micro-scale variations. The ice with lower density ($< 850 \text{ kg m}^{-3}$, **Figure 20**) was generally in the layer with a high proportion of macro-bubbles. In contrast, the lower section of core #1 is marked by a very low porosity, given a high density of $914 \pm 3 \text{ kg m}^{-3}$ on average. Sections of translucent ice are very close to pure ice value. For core #2, the density is lower with an average value of $901 \pm 4 \text{ kg m}^{-3}$, due to a higher porosity (**Figure 20** and **Figure 21**). The density of the ice samples IS#1 to IS#4 is presented in **Table 1**.

2.7.2.4. Sediment content

Both ice cores #1 and #2 contained sediment inclusions. In the upper sections, the presence of sediment occurred as oblique bands of suspended silty sediment into the ice (**Figure 20** and **Figure 22a**). Their concentrations were very low ($> 10 \text{ kg m}^{-3}$) and their composition mainly consisted of mineral particles, derived from local limestone and volcanic rock (Trettin 1991), in which sparse organic fragments were observed. In contrast, the lower sections of ice cores are marked by several compact bands of material. The sediment deposits most often consisted of thin sheets of silty to sandy particles, sometimes mixed with organic fragments (**Figure 22b**) and occasionally formed layers up to several centimetres thick (**Figure 22c**). The larger sediment inclusion was found in core #1 at 190 cm depth. This consisted of a 15 cm thick layer of poorly-sorted angular rock fragments and sand mixture bonded by ice (**Figure 22d**).

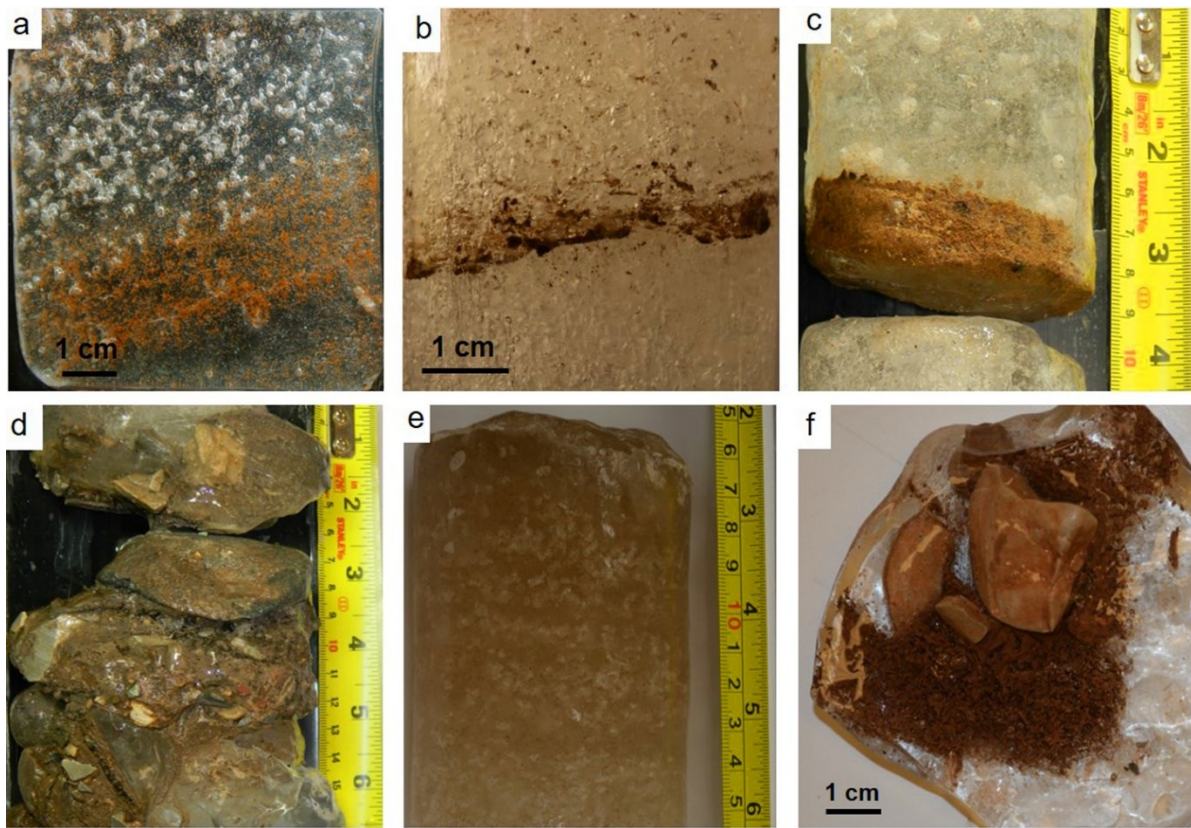


Figure 22. Examples of the various forms of sediment inclusions found in the ice; a) A band of suspended sediments at 45 cm depth in the upper section of IP1; b) A thin layer of fine-grained sediments at 145 cm (lower section) depth in IP2; c) A 2 cm thick band of compact fine-grained sediments at 135 cm depth (lower section) in IP2; d) A 15 cm thick band of ice-bonded gravel and sand at 190 cm depth in IP1; e) Brown coloration of ice sample IS #2 collected in the seasonal fringe of IP1 due to suspended very fine sediments; f) Mix of gravels and fine-grained sediments frozen in the side of a supra-ice channel on IP1.

The hiatus in the sequence of core #1 between 130 and 140 cm corresponded to a layer of fine-grained sediment that was lost during the coring operation. As shown in **Figure 22e**, samples of newly-formed ice collected in the seasonal fringe of IP1 (IS #2, 0–20 cm) contained fine-grained sediments suspended in the ice as suggested by the brown-red coloration of the ice. In the samples collected in the supra-ice channel on IP1, a mixture of coarse gravel and sand is embedded into the ice (**Figure 22f**). AMS radiocarbon dating of organic fragments found in a sediment layer embedded in the ice at 212–218 cm depth in IP2 gave an age range of 3453–3561 cal BP (2-sigma) with a median value of 3487 ± 20 cal BP.

2.7.2.5. Thermal regime of the ice patch and snow conditions

The mean annual ice temperature averaged over the two years of records (July 2017 to June 2019) gives a value from -13.2°C at the ice surface to -11.1°C at the ice-bedrock contact (**Figure 23a**). The ice surface and subsurface (-50 cm) showed a contrasting thermal regime between the two years, reflecting interannual variabilities in the snowpack regime and the severity of summer ablation.

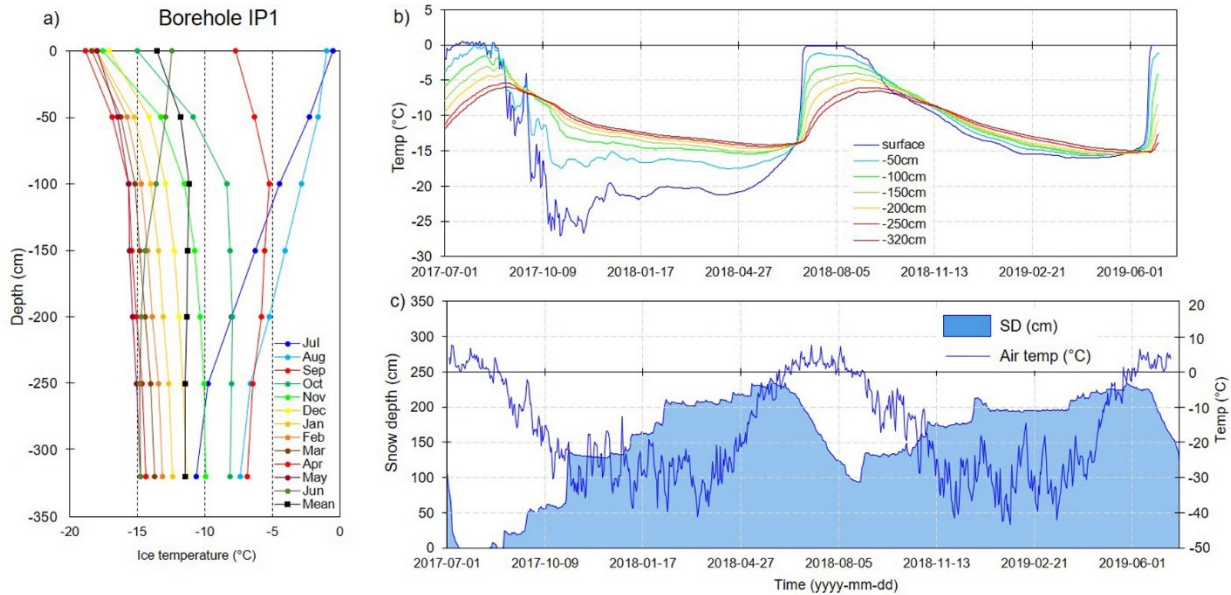


Figure 23. Thermal regime of the perennial ice patch IP1; a) Mean monthly and annual ice temperature profile averaged over the two years of record (July 2017-June 2019) from the 320 cm deep borehole drilled in IP1 (Fortier and Davesne, 2021b); b) Daily evolution of ice temperature at various thermistor depths and b) Daily evolution of the air temperature and snow depth provided by SILA station between July 2017 and June 2019 (CEN, 2021). The snow depth dataset was corrected by a multiplication coefficient ($\times 1.5$) to be representative of the maximal snow depth measured on IP1.

The time-lapse photograph presented in **Figure 24a** shows that the surface of the ice patch experienced an advanced stage of melting in late summer 2017 as most of its surface was exposed ice. The following fall, the onset of a deep snowpack was late as the snow depth did not exceed 100 cm until October 29 (**Figure 23c**). Consequently, the ice surface cooled rapidly with the temperature dropping to -27°C on October 19 (**Figure 23b**). In contrast, in summer 2018, the ice surface from the previous summer remained buried under the seasonal snowpack throughout the summer (**Figure 24b**). In addition, significant precipitation on 24 August brought a high amount of fresh snow early in the season (**Figure 23c**). This thick snowpack reduced the cooling of the ice

body at the beginning of the cold season. These contrasted surface conditions, however, did not have a significant effect at depth. At the contact between the ice body and the bedrock, the temperature fluctuated from about -6°C during the first half of September to about -15°C in mid-June for the two years (**Figure 23a,b**). All depths experienced an abrupt rise in temperature in June. The highest temperature change occurred at the surface and subsurface (-50 cm) where the daily temperature increased by nearly 15°C within a few days to reach the melting point (**Figure 23b**).

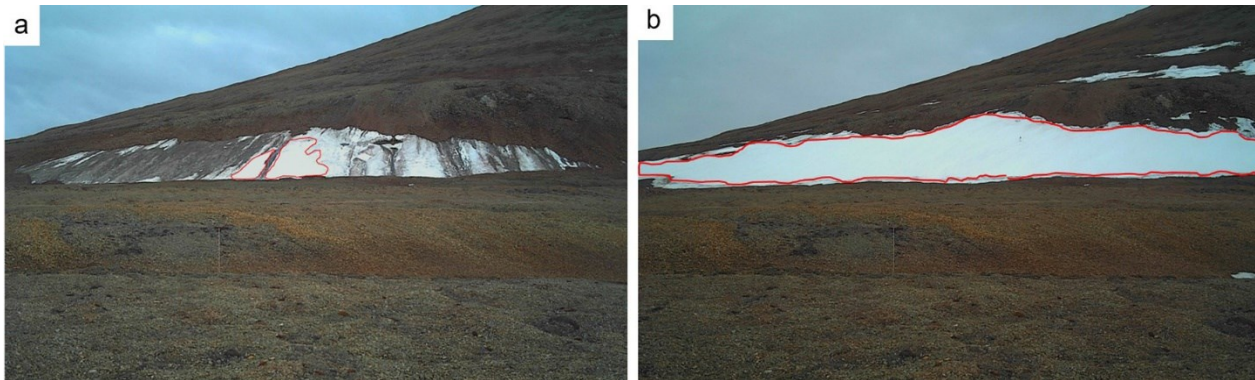


Figure 24. Automatic time-lapse photographs of the ice patch IP1. Photo (a) was taken in the late summer 2017 (2017-08-06), during which most of the ice patch surface consisted of exposed ice after particularly warm conditions. Photo (b) was taken at the end of the cool summer 2018 (2018-08-08) during which a thick seasonal snowpack remained over the ice surface to form a firn layer. The red line delineates the seasonal snow extent from the exposed ice surface.

2.8. Discussion

2.8.1. Snow stratigraphy and metamorphism over the ice patches

The typical polar desert snowpack is shallow and generally $<30\text{ cm}$ deep (Domine et al., 2018a; Royer et al., 2021). The physical properties of this snow, such as density and microstructure, evolve throughout the cold season according to metamorphic processes driven by meteorological conditions – mostly wind, air temperature, and cloudiness – as well as water vapour gradient within the snow (Colbeck, 1982). In polar deserts, the period of strong vertical temperature gradient ($>20\text{ K m}^{-1}$) is typically short as the soil temperature drops quickly in the early winter because of the lack of soil moisture (Domine et al., 2018a). As a result, the depth hoar (DH) layer that formed at the bottom of the seasonal snowpack is shallow, ranging from 25–30% of the snow column, although significant local variations may occur depending on the spatial variability of soil moisture

and microtopography (Davesne et al., 2021; Domine et al., 2018a; Royer et al., 2021). Later in the season, the temperature gradient decreases as the snowpack thickens and the temperature of the frozen soil drops (Domine et al., 2018a). Under those conditions, the wind slabs that form in polar deserts cannot be transformed into indurated DH, so that the top layers of the snowpack are comprised of small rounded grains showing little if any sign of recrystallization and growth (Royer et al., 2021).

In the case of ice patches, seasonal snow evolved under markedly different conditions (**Figure 18**). Our observations suggest that the end-of-winter physical properties of snow observed on the ice patches were mainly due to wind-driven processes that determined the initial snow structure and by the deep snow accumulation that led to snow compaction. As indicated by **Figure 19**, the strong temperature gradient ($>20\text{ }^{\circ}\text{C m}^{-1}$) was short-lived, just 3 weeks in fall 2016 (Period 1). This only allowed the transformation of the very basal layer into DH (**Figure 18**), the fraction of which was typically less than 5% of the snow column. Given the high recurrence drifting snow episodes in polar desert environments and the resulting rapid accumulation of snow on the ice patch in fall, we consider that unfavourable conditions for the development of DH to be the rule at WHI (Domine et al., 2018a). In the lower section of the snowpack, the weight of snow accumulation led to further compaction by overburden pressure. This densification increased the thermal conductivity and decreased the permeability of the snow. Both these factors combined to reduce the temperature gradient and water vapor transport, limiting metamorphism to low-grade (Period 2; **Figure 19**). In the uppermost layers, snow also underwent low-temperature gradient metamorphism ($<10\text{ K m}^{-1}$) during most of the cold season leading to slow sintering of the fragmented crystals (**Figure 18**; Colbeck, 1982; Domine et al., 2008). The resulting snowpack, therefore, had properties distinct from those of a typical Arctic snowpack since DH was confined to a thin layer and the compaction increases snow density to values in excess of most values reported in polar deserts (Domine et al., 2002; Royer et al., 2021) and also in Arctic tundra (Benson and Sturm, 1993; Derksen et al., 2009).

In early summer, the onset of the snowmelt period brought rapid changes to the physical and thermal properties of the snowpack. The first stage of snowmelt, known as the warming phase, started with the onset of sustained positive air temperatures, typically during the first half of June (**Figure 19** and **Figure 23b**). At that time, the greater energy input to the snow surface resulted in

increased temperature and liquid water content in the topmost layers of the snowpack. Once the snow temperature had reached 0°C, the melting front then gradually propagated towards the base of the snowpack, initializing rapid wet-snow metamorphism which consisted of growth, rounding, and sintering of the snow grains (Colbeck, 1982; Pomeroy and Brun, 2001). Compaction and high liquid water content of the melting snow raised the snow density to 550 kg m⁻³ (e.g. *Sp1_17b*; **Figure 18**).

As the melting front progressed, the snow became wet and liquid water derived from the melt of the upper snow layers percolated down into the snowpack (Flow fingers; Marsh, 2006). Over nearly a month (early June to early July) the initial height of snowpack decreased by about 27% (i.e. 70 cm of snow at 500 kg m⁻³ given 35 cm w.e.) (**Figure 18**). Much of the percolating meltwater refroze deeper in the snowpack to form ice columns and ice layers (**Figure 18** and [Figure S1-6](#)) (Marsh 2006). When the percolating meltwater reached the cold and impermeable ice substratum, the base of the snowpack became water-saturated and froze, leading to the upward growth of basal ice as superimposed ice, similar to what occurs on Arctic glaciers (**Figure 18**) (Marsh, 2006; Obleitner and Lehning, 2004; Woo et al., 1982;).

The refreezing of meltwater into the snow led to the release of latent heat that enhanced snowpack warming as suggested by the rapid temperature increase at the snow-ice interface (**Figure 19**; **Figure 23b**). Once the snowpack was ripe, the snow depth decreased rapidly as almost all the energy input produced snowmelt. At depth, the percolation of the water enhanced the progressive compaction of the snowpack that led to a density increase as summer progressed.

2.8.2. Structural characteristics and origin of the ice patches

In this section, the structure and the ice properties found in the ice patches IP1 and IP2 are discussed and compared with similar research carried on ice patches in polar (Lewkowicz and Harry, 1991; Østrem, 1963), subpolar (Hirvas et al., 2000; Lacelle et al., 2009; Meulendyk et al., 2012) and mid-latitude mountain environments (Wakahama and Narita, 1975; Yamamoto and Yoshida, 1987) (**Table 2**). We also explore the potential similarities with the ice properties reported for nearby cryospheric features, such as the Ward Hunt Ice Shelf (Jeffries et al., 1991; Ragle et al., 1964) and the northern High-Arctic ice caps and glaciers (e.g. Meighen and Devon ice caps) (Koerner, 1968; 1970a, b; Koerner and Paterson, 1974).

Table 2. Summary of physical properties of the ice found in perennial and semi-permanent ice patches (modern and buried) in various environments. For the crystal shape: Eq =Equidimensionnal; Poly = polygonal; Ir=irregular and El = elongated. For the bubble shape: Sb= Spherical bubble; SSb= Sub-spherical bubble; Ecb= Elongated cylindrical bubble; Irb = Irregular bubble. For sediment: Si= Silt; Sa= sand and Gr= gravel. References: [1] Østrem (1963); [2] Wakahama and Narita (1975); [3] Lewkowicz and Harry (1991); [4] Meulendyk et al. (2012); [5] Lacelle et al. (2009); [6] Hirvas et al. (2000); [7] Yamamoto and Yoshida (1987); [8] This study. “n.d.” means “no data”.

Environment	System	Crystal size (mm ²)	Crystal shape	Ice facies	Bubble shape	Sediment inclusion	Structure	Fracture	Ref.
Sub-arctic mountains	Nival	Fine (~9)	Eq/Poly	Bubble-rich	n.d.	Si	Oblique bands	no	[1]
Mid-latitude mountains	Nival	Fine (<10)	n.d.	Bubble-rich	n.d.	Si	Oblique bands	no	[2]
Arctic polar desert	Nival	Fine	n.d.	Bubble-rich	Sp/Ecb/Irb	Si to Gr	Oblique bands	no	[3]
Sub-arctic mountains	Nival	Fine (~8)	Eq/Poly	Bubble-rich	Sp/Ecb	Si to Sa	Oblique bands	no	[4]
High-Arctic	Nival (buried)	Very fine (~4)	Eq/Poly	Bubble-rich	n.d.	Si	Oblique bands	no	[1]
Sub-Arctic mountains	Nival (buried)	Medium (~14)	Eq/Poly	Bubble-rich	Sp/SSb/Ecb	Si to Sa	Oblique bands	no	[5]
Sub-Arctic mountains	Nival	n.d.	n.d.	Bubble-rich	Sp/Irb	Si	Oblique bands	no	[6]
Hybrid									
Mid-latitude mountains	Upper part	Very fine (<5)	n.d.	n.d.	n.d.	Gr	Sub-horizontal bands	no	[7]
	Lower part	Coarse (> 100)	n.d.	n.d.	n.d.	Gr	Oblique bands	yes	
Nival									
High Arctic polar desert	Upper part	Very fine (~2 ^a)	Eq/Poly	Bubble-rich	Sp/SSb/Irb	Si	Oblique bands	no	[8]
	Lower part	Med. to coarse (~34 ^a)	n.d.	Bubble-rich/clear ice	SSb/Ecb	Si to Gr	No clear pattern	yes	

2.8.2.1. Ice patch stratigraphy

Both ice patches IP1 and IP2 are stratigraphically composed of two ice units, referred to as Unit 1 (upper section) and Unit 2 (lower section). Comparison between both units revealed contrasted bubbliness, sediment inclusion and degree of fracturing (**Figure 20**). In both ice patches, the transition between Unit 1 and Unit 2 is sharp and is interpreted as a melt unconformity corresponding to a relict ablation surface that developed during a period of net ablation. The melting of the upper section of the ice patches caused a concentration of sediments on the surface of the remnant ice, *i.e.* Unit 2 (cryoconite surface), at 135 cm depth. The resulting sediment layer

was then buried by the aggradation of new ice, *i.e.* Unit 1. For IP1, the sediment layer cannot be observed because it corresponds to the missing core section between 130 and 140 cm depth. For IP2, the sediment layer that demarcates the unconformity is easily discernable as it represents the thickest sediment layer in the core sequence. Comparable unconformities were reported by Yamamoto and Yoshida (1987) within the Kuranosuke ice patch in the Japanese Alps.

2.8.2.2. Unit 1

The ice texture in Unit 1 typically consisted of randomly oriented, very fine ($< 5 \text{ mm}^2$) and equidimensional crystals with no evidence of interlocking patterns. It gives the ice a polygonal granular texture, typical of the ice formed from the refreezing of water-saturated snow (Koerner, 1968). The ice of Unit 1 is similar to the newly formed ice sampled on IP1 and IP2 (samples IS#1, IS#2, IS#3). These observations are consistent with those reported for most of the ice patches originating from a nival system listed in Table 2. In terms of air and sediment inclusions, the ice had a bubbly-ice facies and contained sporadic thin layers of suspended silt (eolian dust) as well as some compact bands of sediments including coarse particles. Such inclusions and the resulting well-developed oblique banded structure are also common to most nival ice patches (**Table 2**) (Lewkowicz and Harry, 1991; Meulendyk et al., 2012; Østrem, 1963). Based on our results and comparison with previous studies, we therefore propose that the bulk of Unit 1 originated from the aggradation of superimposed ice which is the dominant process in nival ice patch systems of Polar Regions due to the large cold content of the ice bodies. Regionally, superimposed ice is also known to be widespread in the upper strata of Ellesmere Island ice caps (Meighen and Devon ice caps) and of the Ward Hunt Ice Shelf (Jeffries et al., 1991; Koerner, 1968; 1970a; Ragle et al., 1964).

2.8.2.3. Unit 2

Unit 2 exhibits contrasting properties in terms of crystallography and ice structure compared to Unit 1 and stands out by some specificity compared to typical ice that composed nival ice patches (**Table 2**). Firstly, the entirety of Unit 2 is made of medium to coarse ice crystals (15 to 20 times larger than in Unit 1, with no layer of very fine crystals. Secondly, it has a low proportion of large and macro bubbles which have an elongated shape. Clear-ice layers are also present. This contrasts with the bubbly ice and its whitish appearance observed in Unit 1. Finally, the presence of micro-fractures was not observed in Unit 1 and they are normally absent in ice patches originating from a nival system (**Table 2**).

In order to clarify the ambiguous origins of the ice that forms Unit 2 of both IP1 and IP2, we explore two main hypotheses: glacial origin and nival origin. In the hybrid system of ice patches, relict englacial ice serves as a basement for meteoric ice aggradation (Sakai et al., 2006; Yamamoto and Yoshida, 1987). Even if the ice of Unit 2 shares some characteristics with englacial ice (large crystals), there are two major objections to this interpretation. First, there is no evidence to support the presence of a glacier at WHI during the last maximum glacial extent, attained around 11 000 BP on Marvin Peninsula just south of WHI, because the severe aridity considerably limited the ice extent during the Wisconsinian (Lemmen and England, 1992). Second, even if the presence of very local ice caps on WHI cannot be excluded during cold periods, as is still the case with the ice rise (Braun et al., 2004), we suggest that the ice patches most likely remained stable in size. Both investigated ice patches indeed could not grow into glacial systems because they are topographically constrained (Glazirin et al., 2004). This hypothesis is supported by the absence of field evidence of a former greater extent of the ice patches in their frontal zones, such as protalus ramparts, pronival ridges or moraines (Ballantyne and Benn, 1994; Hedding, 2016). For these reasons, the nival origin of Unit 2 is supported.

If Units 1 and 2 originate from the same processes, how to explain the difference in ice properties between them, especially regarding crystal size? Our interpretation is that two crystal growth processes, one rapid and one slow, may be involved in the formation of Unit 2.

The rapid process is related to water freezing on or within ice patches. On IP1, ice samples #4 collected from a supra-ice channel ([Figure S1-8](#)) illustrates this process well. The refreezing of the water in the melt channels leads to the local formation of clear ice depleted in bubbles and with large and elongated crystals, similar to columnar ice (e.g. lake and pond ice; Jeffries et al., 1991; Koerner and Paterson, 1974). Melt/freeze recrystallization is also involved in ice crystal growth on ice surfaces exposed to melting as demonstrated by the coarse crystals found in the weathered ice at the surface of the ice in the frontal edge of IP1 in July 2017 ([Figures S1-10](#) and [S1-11](#)). Under current conditions, these rapid ice growth processes are localized, but they may have been more intense during past warmer periods, thus forming sequences of coarse ice layers. This hypothesis is supported by the presence of compact layers of sediment in the ice interpreted as ablation surfaces ([Figure 20](#)). These were often present above bands of ice with elongated bubbles that indicate the continuous expulsion of air from the supersaturated meltwater during freezing between

the larger crystals. Slow freezing of water and slush accumulation in fall could also explain the layers of clear ice with coarse crystals (e.g. between 200 to 250 cm in Unit 2 of IP1; **Figure 20a** and [Figures S1-9](#) and [S1-13](#)). Water freezing and melt-freeze recrystallization, however, did not affect all ice layers in Unit 2 because large sections show no evidence of this rapid ice growth, especially in Unit 2 of IP2 (**Figure 20b**). Therefore, another process must be involved to explain the coarser ice crystals.

In the absence of compressive stress, a slow steady growth of ice crystals occurs as a function of time and temperature following the normal grain growth law (Cuffey and Paterson 2010; Gow, 1969). This coarsening process is driven by the reduction of the total grain boundary energy and is recognized as an important process of recrystallization of firn and ice on glaciers and polar ice caps (Duval, 1985; Gay and Weiss, 1999; Gow, 1969; Montagnat et al., 2009). The grain size of Unit 2 of the ice patches is most likely the result of a much longer period of kinetic crystal growth. Based on this interpretation, the approximate age of Unit 2 could therefore be estimated from the crystal size of the sections showing no evidence of water freezing and melt-freeze recrystallization (e.g. [Figure S1-14](#)). The mean annual growth rate k ($\text{mm}^2 \text{ a}^{-1}$) was calculated using the mean monthly ice temperature measured on IP1 (**Figure 23a**) (see [Appendix A1-5](#) for the calculation). In Unit 2 of IP1, k was on average $\sim 4.8 \times 10^{-2} \text{ mm}^2 \text{ a}^{-1}$ for July 2017 to July 2019 ([Figure S1-12](#)). Since the ice temperature was not measured in IP2, the same k values as for IP1 were used. Assuming that the initial ice was similar to the "young" superimposed ice of Unit 1, the estimated age of the ice is shown in **Figure 25**. In the core sections of Unit 2 not affected by rapid ice growth, it would have taken $\sim 500\text{--}1\,000$ years to reach the observed average crystal sizes in the sections. This estimated age represents a lower limit of the actual age because particles and air bubbles "pin" grain boundaries and stop or at least considerably retard their motion and hence grain growth ([Figure S1-14](#); Cuffey and Paterson, 2010; Durand et al., 2006). The vertical variability in crystal size along Unit 2 may be explained by different concentrations of impurities and bubbles that would lead to variations in the extent of grain boundary pinning. This explains that layers with the highest concentration in bubbles and sediments in Unit 2 generally are those with the finest crystals and hence the youngest apparent age. A further age underestimation can also be caused by the fact that present-day ice temperatures are likely much warmer than during the late Holocene. To evaluate the impact of colder temperature, we ran our age calculation assuming temperatures 2°C colder and the ages were increased by ~ 250 years for the bubbly ice layers (**Figure 25**).

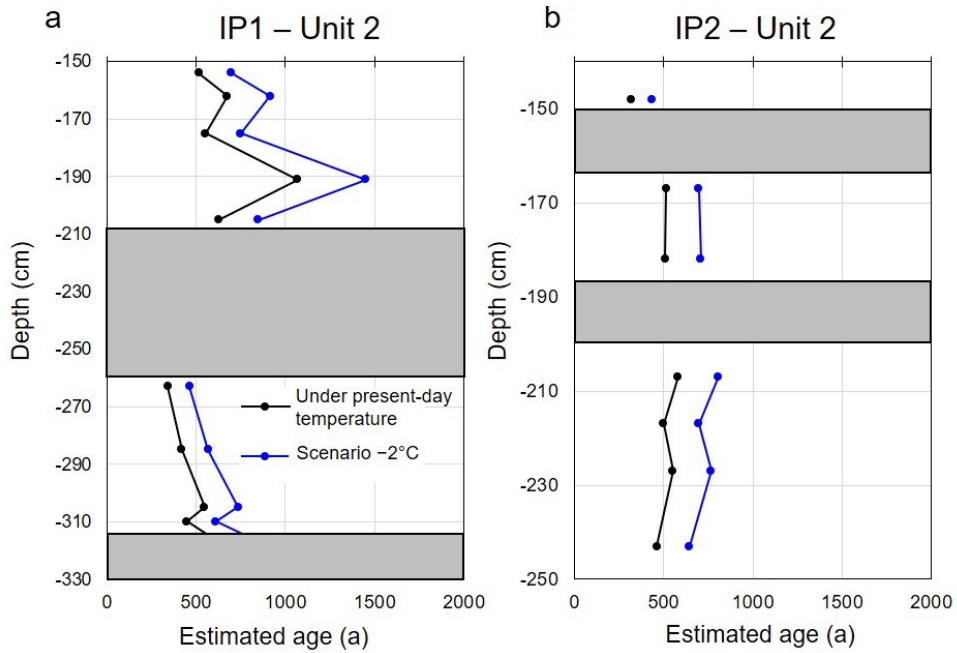


Figure 25. Vertical variation of the estimated age of the ice derived from the normal grain growth law in solid-phase for Unit 2 of the ice patch IP1 (a) and IP2 (b). The black curve represents the age profile at current ice temperature (see **Figure 23**) and the blue curve represents the age profile with ice temperature 2°C colder than today. The grey bands indicate core sections with clear-ice facies where ice crystal size is partly the result of water freezing processes.

As the hypothesis of a glacial origin has been rejected, we consider that the fractures in Unit 2 are most likely the result of the thermal contraction and cracking of the ice when it undergoes rapid temperature change which is concordant with their random orientation (Fortier and Allard, 2005; Shumskii, 1964, p. 305;). This process is expected to occur in the early cold season when the exposed ice surface cools rapidly before being covered by a deep snowpack (e.g. fall 2017; **Figure 23**). These micro-fractures are later filled in spring by percolating meltwater which freezes rapidly to form ice veins with a high concentration in very fine bubbles ([Figure S1-3](#)). These fractures are present exclusively in Unit 2 which implies that such conditions have not occurred since Unit 1 ice formed. This supports the assumption that Unit 2 would have experienced a period of strong ablation during which the ice surface was frequently exposed in late summer. Furthermore, the high frequency of fractures in Unit 2 indicates that this ice has undergone several episodes of cracking, providing further evidence that Unit 2 is much older than Unit 1.

2.8.3. Mechanisms of the ice formation

In this section, we propose a conceptual model for the ice growth processes and sediment incorporation in the polar ice patches (**Figure 26**) based on our observations made at WHI and the existing literature. Ice patches and their seasonal snowpacks together form a complex system in which snow and ice interact and coevolve. From this point of view, the processes involved in the aggradation of ice in ice patches are similar to what has been observed on Arctic glaciers in the so-called “superimposed ice zone” located above the equilibrium line (Koerner, 1970b; Obleitner and Lehning, 2004). Ice formation by refreezing is triggered by two distinct mechanisms that develop under different thermodynamic processes, and hence produce different kinds of ice. The first one is the refreezing of meltwater at the base of the snowpack over an ice mass in spring/summer to form superimposed ice and the second is the refreezing of soaked firn or weathered ice surface early in the cold season.

2.8.3.1. Superimposed ice aggradation

On WHI, as in polar regions in general, the formation of superimposed ice occurred exclusively in summer since the air temperature remains continuously below 0 °C between mid-September to mid-June (**Figure 19**; **Figure 26a**). The ice growth starts early in the melt season during the warming phase of the snowpack (**Figure 26b**). At this stage, the cold content of the snowpack and the underlying ice was sufficiently high that all meltwater refreezes throughout the snowpack (ice structures) and at the snow/ice interface (superimposed ice). The process thus consists of a mass transfer without mass loss at the scale of an ice patch system (assuming sublimation is negligible). In an advanced stage of the warming phase (**Figure 26c**), the melting of the seasonal snowpack and snowbanks over upslope terrains can provide substantial input of meltwater into the ice patch system. As the ice patches overlie continuous permafrost (i.e. cold-based ice patch; **Figure 23**) no infiltration under the ice body is possible. This meltwater is thus forced to flow on the ice surface (Ballantyne, 1978). Much of this additional water is converted into superimposed ice and thus constitutes a net mass gain.

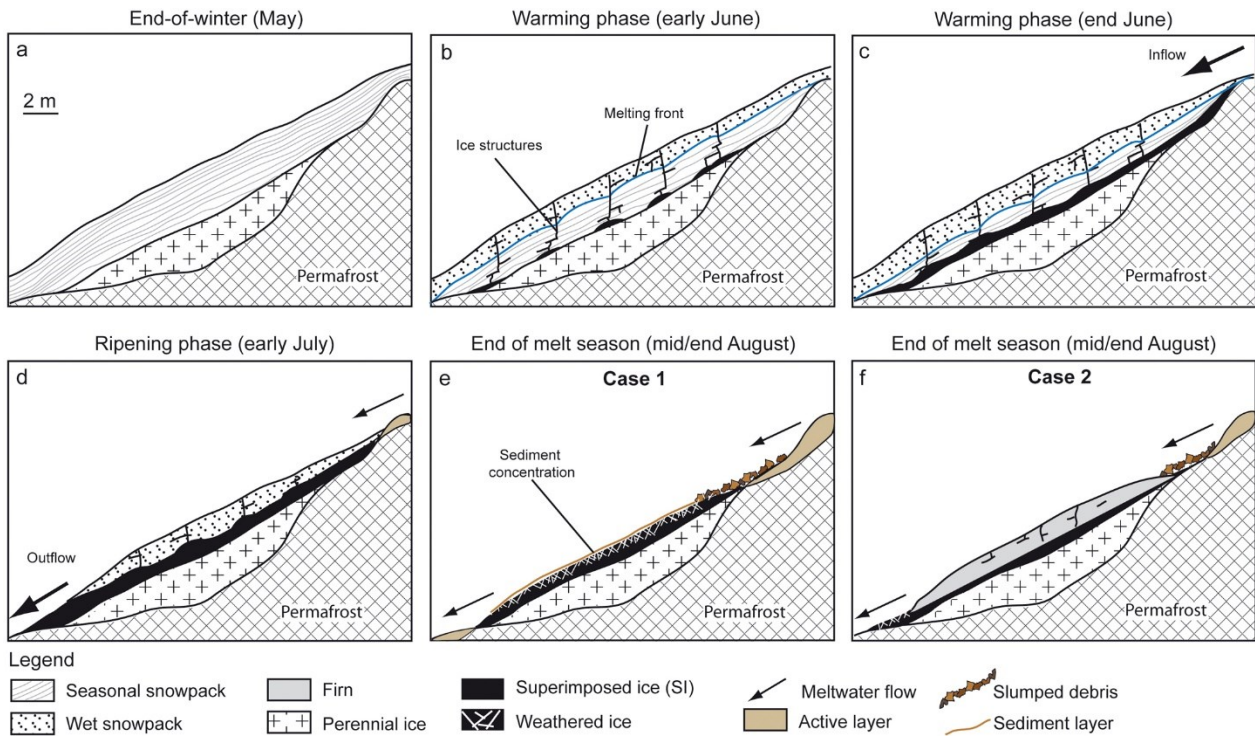


Figure 26. Conceptual model of ice aggradation on a polar ice patch system: a) Seasonal snow accumulation at the end of the cold season; b) Early stage of warming phase; c) Advanced stage of warming phase; d) Ripening phase; e) End of the melt season after a strong ablation resulting in the complete disappearance of the seasonal snow (case 1); f) End of the season after weak ablation resulting in the persistence of part of the seasonal snow layer that forms firn layer with the fall freeze-back (case 2).

Assuming a high degree of wetness in the basal snow layers in the early summer, we suggest that the properties of the superimposed ice are mainly related to the size and the number density of snow grains of the original snow (Koerner, 1970a; Shumskii, 1964, p. 295). Snow grains indeed act as nuclei from which the new crystals form. This secondary ice growth is constricted to the available pore space between pre-existing snow grains. At the bottom of the seasonal snow, the shallow depth hoar layer is made of rather large and spaced crystals so that it is expected to form a discrete (few centimeters) superimposed ice layer with fine to medium ice crystals and with large air bubbles. Above the depth hoar, the fine-grained nature of the seasonal snowpack predisposes to form superimposed ice with very fine equiaxed, randomly oriented ice crystals and with fine air bubbles. Due to the rapid freezing of meltwater within the cold snow, snow grain coarsening by wet metamorphism is limited in early summer. The vertical variation of the air bubbles concentration and size that forms the banded structure likely reflect short-term fluctuations in the freezing rate and the degree of soaking of the snow throughout the melt-freeze period (Lewkowicz

and Harry, 1991) as well as the discontinuities in the snow stratigraphy, especially the transition between the basal depth hoar layer and upper finer snow (**Figure 18**).

The phase of superimposed ice aggradation is associated with the incorporation of sediments that appear suspended in the ice. This process is syngenetic when the sediments have a niveo-aeolian origin (**Figure 18** and **Figure 27a**, [Figure S1-5](#)) (Lewkowicz and Young, 1991). Sediment incorporation can also be epigenetic in the case of ice patches that collect upslope runoff, percolating through the snow porosity (**Figure 27b**). Due to its fine porosity, the snowpack acts as a filter that only allows finer sediments to be transported by intranival flows (**Figure 27c**) while coarser material remains temporarily trapped in the inlet at the upslope margin of the ice patches (**Figure 27d,e** and [Figure S1-15](#)). Because the snow-ice interface is still cold, part of this meltwater with high suspended sediment loads re-froze into superimposed ice. The filtering effect of the snowpack only occurred for a brief interval of time, because rapidly, channelled flow took place at the snow-ice interface forming slush flows and subnival pipes (**Figure 27e**). During the ripening phase, the supra-ice streams may incise superimposed ice by thermal erosion and can carry a substantial amount of coarse and angular slope material (bedload transport) that accumulates and freezes in the ice channels (**Figure 27f** and [Figure S1-15](#)).

Conditions at WHI can sustain a long period of superimposed ice growth. First, the ice patches are covered by deep snowpacks that persist over much of the melt season and whose high density gives it a high thermal inertia (Colombo et al., 2019). In summer 2017, it resulted in a lag of 15 days between the time when the air temperature turned positive and the time when the snow-ice interface reached 0 °C (**Figure 19**). This lag was 21 and 20 days in June 2018 and 2019, respectively, according to borehole data (**Figure 23b**). Second, the combination of meltwater input derived from *in situ* snowpack and from upslope runoff brings a high rate of water supply to the ice patch system. Third, the extreme polar winter and the cold permafrost produce low temperatures of the ice body, even under the deep seasonal snowpack (**Figure 23b,c**).

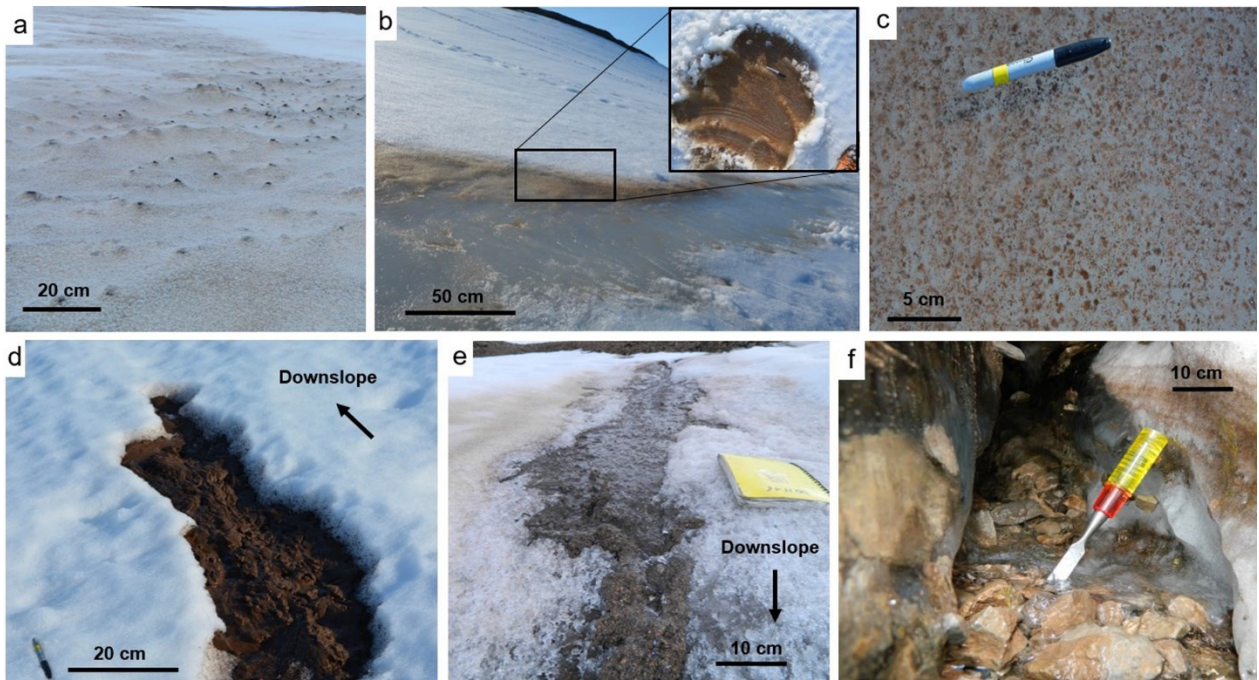


Figure 27. Observations of sediment deposits on ice patches IP1 and IP2. a) Niveo-aeolian deposits emerging on the seasonal snow surface over IP2 in mid-June 2017; b) Fine-grained sediment retained in the snow porosity (filtering effect) and incorporated in the superimposed ice in the downslope edge of IP1 at the end of June 2019; c) Zoom in on the newly formed superimposed ice (black square in b) where entrapped fine-grained sediment are visible; d) Silty-sand deposits (up to 5 cm thick) in the inlet of a rill flow in the upper edge of IP1 due to snow filtering (early July 2019); e) Slush flow transporting silty to coarse sandy material over the ice surface of IP1 (mid-July 2019); f) Streamflow carved in perennial ice revealing large pebbles incorporated in blue ice (site where the sample IS#4 was collected).

During the ripening phase (**Figure 26d**), the aggradation of superimposed ice gradually slows down as the cold content of the underlying ice surface was depleted due to latent heat absorption (Obleitner and Lehning, 2004). We can estimate from the borehole data that when subsurface ice temperatures at 50 cm depth reached values close to 0 °C, the cold content of the upper layers of the ice body may have become too small to sustain the superimposed ice growth (Bøggild, 2007). In summer 2017, it occurred around 25 July, namely 31 days after the snow-ice interface reached 0 °C (**Figure 23b**). Our measurements indicated the growth of superimposed ice was rapid since ~ 30 cm of new ice was formed on 8 July. During the summer of 2018 (**Figure 23b**), the temperature at 50 cm depth reached a brief thermal peak of – 1 °C around July 20 before decreasing again so that the ice formation process likely occurred throughout the summer.

2.8.3.2. Late-season processes

Late summer conditions on ice patches are highly variable depending on the severity of ablation that will lead to the complete disappearance or not of the seasonal snow. This is critical in the ice formation processes that occur during freeze-up in the fall. The two possible scenarios have been observed (**Figure 24**). In summers with significant ablation (Case 1; **Figure 26e**), newly formed superimposed ice or old ice from previous summers is exposed at the surface as most of the snowpack has melted (e.g. summer 2017, **Figure 24a**). Due to high levels of solar radiation and above-freezing air temperature, the exposed ice surface gets weathered and forms a crust a few centimetres thick composed of porous ice with loosely interlocking crystals, whose size is generally coarse due to melt-freeze metamorphism (**Figure S1-10**). Melting of the snowpack and superimposed ice resulted in a concentration of the sediments they contained upon the melting ice surface in the form of a thin sheet of fine material (**Figure 24a**). Locally, coarser deposits have also formed associated with sediment inputs from the upslope section of the ice patches by small mass movements.

Conversely, when the ablation is low (Case 2; **Figure 26f**), the end-of-summer ice patch is still covered by a significant layer of snow and the ice is only exposed at the edges (e.g. summer 2018; **Figure 24b**). The remaining snowpack is typically composed of coarse granular snow due to prolonged wet metamorphism and multiple freeze/thaw cycles it had undergone (**Figure 18c**). When the soaked firn freezes at the beginning of the cold season, this results in the formation of a layer of consolidated firn (Cogley et al., 2011; Fierz et al., 2009) on top of which the new seasonal snow layer will settle (e.g. *Sp1_16*).

2.8.4. A long-term preservation of ice patches at WHI?

Although more research is needed to establish an accurate history of ice patches at WHI, some assumptions are proposed here based on our results and local paleoclimatic indicators.

2.8.4.1. Unit 2: an old basement

The ^{14}C age of $\sim 3\ 500$ years BP from a sample collected at 212–218 cm in Unit 2 of IP2 gives an interesting insight into the potential existence of old ice patches. This result must be considered carefully, however, because it cannot be excluded that the dated carbon was remobilized from a source of old carbon by wind or surface runoff before being deposited on the ice patch

(Lewkowicz and Harry, 1991). As IP2 is at the top of the slope, no runoff comes from the upslope, so all sediment layers are aeolian deposits. The dated sample included fragments of organic material of various sizes and nature (e.g., branch, flower, moss) and from two distinct successive layers ([Figure S1-4](#)), yet the ^{14}C age standard deviation is low which suggests that the dated fragments are nearly contemporaneous. Based on the ^{14}C age and the age estimated from normal ice crystal growth law, the latter being a minimal age, we feel the most likely age is that provided by the ^{14}C dating. Regardless of the uncertainties, the ages obtained by both methods indicate the existence of old ice patches at WHI and demonstrate that ice in Unit 2 is much older than that in Unit 1. This confirms that the distinct physical properties of the ice between Units 1 and 2, and the relict ablation surface between them reflect a hiatus in the chronostratigraphy of the ice patches.

The estimated old age of the ice patches implies their continuous existence since the Late Holocene (Meghalayan 4 200 BP to the present) and that they survived subsequent warm periods (e.g. the Medieval Warm Period between 1 100 to 7 00 BP; Werner et al., 2018). This is consistent with other regional cryospheric and paleoclimatic records. Bradley (1990) demonstrated a decrease in summer temperature in northern Ellesmere over the last 3 500 years which correlates with a decline in driftwood after 4 500–3 000 BP along the northern coast of Ellesmere Island as reported by Koerner and Paterson (1974) and Lyons and Mielke (1973). This period was marked by the onset of more severe ice conditions leading to the development of ice shelves, including the Ward Hunt Ice Shelf (England et al. 2017; Lyons and Mielke, 1973). The long-standing presence of the ice patches is also indicated by their resistance to the recent regional warming which has brought temperatures to a level not seen in the Arctic for at least 4 000 years (Fisher et al, 2012; Lecavalier et al., 2017). The potential old age of ice patches at WHI is consistent with radiocarbon age reported for subarctic ice patches existing under a warmer climate from similar nival system in Northwest Territories (e.g. 4 400 years BP; Meulendyk et al., 2012) and Yukon (e.g. 4 700 years BP; Farnell et al., 2004).

2.8.4.2. A recent formation of Unit 1

With the modern climate warming that accelerated after the 1990s (Post et al., 2019), strong ablation years truncated the ancient Unit 2 of ice patches. At WHI, a major melt event could be tied with a series of warm summers from 2008 to 2012 ([Figure S1-16](#)) which considerably accelerated the shrinkage of the local cryosphere. It led to the complete disappearance of the

permanent ice cover on the Ward Hunt Lake for the first time in at least 60 years (**Figure 15c**; Paquette et al., 2015), the disintegration of the WHIS (Mueller et al., 2017; Vincent and Mueller, 2020), and recorded low minimum sea ice coverage (Fetterer et al., 2017). Despite a pronounced ablation, most perennial ice patches at WHI surprisingly survived these exceptional summers as shown by the GEOEYE image taken on 26 August 2011 presented in **Figure 1c**. After 2012, the remaining ice from Unit 2 of IP1 was then buried by Unit 1 that aggraded as a result of cooler summers, especially in 2013 and 2014 ([Figure S1-16](#)). Part of this newly formed ice likely melted in summer 2016, the warmest since the temperature measurements began at WHI, the warmest year in the climate record at Alert (**Figure 15a**). Considering that Unit 1 was still 135 cm deep when coring work was done in July 2017, we can infer that the depth of new ice formed between 2013 and 2015 probably exceeded 150–200 cm. This rapid regeneration of ice patches after a major ablation event highlights their current resilience to warm summers. The deep snowpack and upper ice layer of ice patches act as a buffer layer that is truncated during warm summers but new superimposed ice rapidly aggrades again during years with cooler summers, so that the older and deeper ice remains preserved. This cycle of strong ablation/regeneration is primarily controlled by the topography which in turn controls the annual snow recharge of the system. Glazirin et al. (2004) described a regulating mechanism in which strong ablation events free up space in the topographic niche where the ice patch had formed allowing for greater accumulation of drifting snow during the following winter, and conversely. This control of the topography and associated feedback is the key explanation of the long-term existence of the ice patches and the partial decoupling of their mass balance from climate trend (Fujita et al., 2010; Lewkowicz and Harry, 1991).

Despite their current resilience to climate change, the expected continuation of temperature warming and the multiplication of exceptionally warm summers could soon become critical for the preservation of the ice patches at WHI that could quickly lose their perennial status to become semi-permanent ice patches or even seasonal snow patches. This shift has already occurred further south, at Resolute Bay (**Figure 15a**) where the summer temperature (JJA) was 2.9 °C warmer than at WHI over the period 2006–2019 ([Figure S1-13](#)) and where most of the perennial ice patches and snowbanks have completely melted after the summers of 2011 and 2012 as reported by Woo and Young (2014). At this time, it is not known what summer temperature threshold would be critical for the preservation of ice patches and how winter snow supply and summer ablation will evolve. Since their disappearance will lead to major hydrological and ecological changes in polar deserts,

monitoring of the ice patches and a more detailed understanding of their current and projected functioning appears as an objective of high importance for the understanding of Arctic change.

2.9. Conclusions

This study yielded a unique dataset of the physical properties of perennial ice patches in the polar desert landscape of Ward Hunt Island (WHI), providing new insight into the formation processes and behaviour of these small poorly-studied ice masses.

Our results showed that the seasonal snowpack that accumulated on the ice patch exceeded 2 m at the end of the winter and had a high density due to the combined effect of compaction and the absence of high-temperature gradient metamorphism. Below, the ice body was composed of two unconformable ice units with different properties in terms of ice texture and structure. The upper unit exhibited ice with fine, equidimensional ice crystals, as well as bubbly-ice facies and sporadic thin layers of fine-grained sediments creating a vertical banded structure. This ice resembled in all aspects the superimposed ice observed in other polar and mountain ice patches as well as glaciers. The ice of the lower unit differed substantially from that of the upper ones and from the ice of typical ice patches from nival origins by the coarseness of the crystals, the lower porosity, the absence of well-defined oblique layers, inclusions of coarser sediments and the presence of many fractures. We proposed that most of this ice was also superimposed ice with a few layers interspersed showing evidence of water or slush freezing and melt-freeze recrystallization inherited from periods of strong ablation. The coarse crystals observed in layers identified as superimposed ice suggest that the lower unit would have evolved over a long period by temperature-dependent crystal growth.

We have developed a conceptual model of the functioning of a snow-derived ice patch system in a cold permafrost environment. The model explains the multiple steps of ice aggradation throughout the summer and represents the interactions between snowpack, upslope input in water and sediment, and the perennial ice body. We emphasized that the properties of the seasonal snow where the superimposed ice formed, such as temperature, microstructure, density and permeability, have a great influence on sediment retention, meltwater percolation and the refreezing rate which ultimately determine the texture and structure of the ice. Our results showed that the phase of the superimposed ice aggradation can last more than a month due to the high cold content of the ice and snow body which results in the formation of several decimeters of new ice every summer. In

warm summers, much of the seasonal snow melts and newly superimposed ice gets exposed to melting and weathering processes. In cooler summers, a snow layer persists over most of the ice patch surface and forms a consolidated firn layer with the subsequent fall freeze-back. As such, the seasonal and interannual evolution of surface conditions of the ice patches and the ice aggradation processes involved are similar to what occurs near the equilibrium line of a polar glacier.

From the ^{14}C dating and the estimated age based on the normal crystal growth law, we inferred that the ice of the lower unit has existed continuously during most of the last Holocene period (Meghalayan 4 200 to the present). The establishment of favourable conditions for the ice patch development at that time is consistent with the evolution of the climate and cryosphere on northern Ellesmere Island. With the recent climate warming that accelerated since the 1990s, strong summer melt events became recurrent. Old ice unit were thus probably truncated recently by a major ablation event associated with a series of warm summers between 2008 and 2012. New ice then aggraded on the old ice during a subsequent brief cooler period. This rapid regeneration of ice patches after a major ablation event highlights their current resilience to warming due to regulating mechanisms related to topography and the ice patch shape. However, even though ice patch systems seem partially decoupled from medium- and long-term climate fluctuations, we expect that the predicted further warming will bring critical conditions for their survival, thus ending several centuries to millennia of continuous presence at WHI.

The long-term preservation of the polar ice patches identified in this study is a particularly important issue for the polar desert hydrology and the stability of the morpho-hydrological system that depends on it. This question therefore needs to be further explored through new dating work and research on the mass and energy balance of ice patch systems to better understand their response to climate and environmental changes in the past, present and future.

2.10. Acknowledgments

This research was conducted with the financial support of the Natural Sciences and Engineering Research Council of Canada (NSERC), including the Discovery Frontiers project Arctic Development and Adaptation to Permafrost in Transition (ADAPT); the Networks of Centres of Excellence program ArcticNet; the Canada Research Chair program; the Northern Scientific Training Program; the Canadian Foundation for Innovation: Canadian Northern Studies Trust; Centre d'études Nordiques (CEN); and Fond de Recherche du Québec- Nature et

Technologie (FRQNT). FD was supported in part by the French Polar Institute (IPEV). Logistical support was provided by the Polar Continental Shelf Program (PCSP) and Parks Canada graciously granted us the use of their facility. The authors would like to thank Karine Rioux, Audrey Veillette and Michel Paquette for their field assistance. We also thank Maurine Montagnat for discussions on ice crystal growth. Finally, we are also grateful to the two anonymous reviewers and the editor for their insightful comments and advice on the manuscript and to Warwick Vincent for providing helpful comments on the draft manuscript.

2.11. Appendices A1

Appendix A1-1: Snow pits

All snowpits were dug down to the perennial ice surface. For each of them, a snow face was opened on about 1.5 m wide where the measurements were made. The snow stratigraphy and the physical properties (density, grain size and shape, and temperature) were analyzed *in-situ* following the procedure of Domine et al. (2018a) and Fierz et al. (2009). The snow density (ρ_s , kg m⁻³) was measured by collecting snow samples with a 10 cm vertical resolution using a metal cylinder of 224.1 cm³ for horizontal sampling. The samples were weighed in the field with an electronic high-precision scale (resolution: 0.1 g). The mass was then converted into density. Snow temperature was measured at the same vertical resolution as density using a handheld thermistor thermometer HH41 (uncertainty ± 0.015 °C; resolution 0.01 °C; Omega®). The average grain size (E, mm) and shape were determined in the field by placing a sample of snow on a black millimeter-gridded crystal card and examining it with an 8x magnifying glass.

Appendix A1-2: Drilling procedure

The ice cores were retrieved using a 75 mm inner diameter SIPRE-corer driven by a Stihl® powerhead. The coring was made vertically. The SIPRE-corer was able to drill through bands of ice with a high content of fine-grained sediments. When a drilling refusal occurred because of a coarser sediment layer (*i.e.* gravel, blocky material), the SIPRE-corer was changed to an 82.5 mm diamond carbide core barrel. The bottom of the ice patches was considered to be met when the corer extracted large pieces of rock or frozen soil interpreted as the bed of the ice patch.

Appendix A1-3: Thin section procedure

Thin sections were prepared from 10 mm thick slices of ice cut horizontally, every 10 cm, and vertically, every 20 cm, in the ice cores using a band-saw. For the ice samples, IS#1 to IS#4, 4 thin sections per sample were made. Ice slices were then frozen on glass plates of 10 cm² by injecting droplets of near-freezing water on the edges of the samples to create a thin ice bond. The last step consisted of thinning the ice slices to 0.2-0.5 mm using a manually driven microtome (Leica™). The thin sections were then placed between two cross linear polarizing filters illuminated from below by a light table. Due to the birefringence (*i.e.* double refractivity) of the

ice crystals and their variable c-axis orientation along which the light is transmitted, individual ice crystals appear in different colors and brightness.

The thin sections were first photographed with transmitted light to detect the gas/sediment inclusions and fractures. Then, they were photographed under cross-polarized light to reveal crystals. A single image is often not sufficient to clearly distinguish all individual crystals because an individual crystal could remain dark for a certain angle and being illumined from another (Gay and Weiss 1999). For this reason, a total of 5 cross-polarized pictures were taken at 0, 45, 90, 135 and 180° while the thin section stays fixed with respect to the camera. The post-processing step consisted of automatically detecting the crystal boundaries using the open-source imaging software ImageJ (**Figure 17**). A semi-automatic segmentation, based on watershed flooding algorithms, was performed using the ImageJ plugin MorphoLib (Legland et al., 2016). The high resolution of the photography allows the detection of crystals as small as 0.2 mm. The output raster files of grain boundary networks were converted to shapefile (polygons) in ArcGIS (EsriTM) and then manually cleaned when necessary. The main error inherent to the automatic detection of crystal boundaries is the clustering of contiguous crystals in the same polygon when they appear in the same color tone (similar c-axis orientation). In this case, a careful analysis of the thin section with the naked eye allows applying a correction. When contiguous crystals have their c-axis perpendicular to the thin section, they remain dark whatever the viewing angle. In this case, the best way to reduce the error is to remove them as suggested by Gay and Weiss (1999). The corrected images are then re-imported to ImageJ and the two-dimensional morphometrics properties of the ice crystals that compose a thin section were computed. The size of each crystal was measured by the surface area (A , mm²) and the major axis length (L , mm). The shape (elongated, rounded, subrounded) of the crystals is analyzed by computing the roundness parameter (R) which takes into consideration the major axis of the best fit ellipse (Zhao and Wang, 2016). The lower the value, the more elongated the shape is.

Appendix A1-4: CT-scan technology and image analysis

CT-scans were obtained by a Siemens Somatom 64 scanner at the Institut National de la Recherche Scientifique (INRS-ETE) in Québec City (Canada). This is a non-destructive tool that preserves the integrity of the sample. This technique has already been used to analyze lake ice, sea ice (Crabeck et al. 2016) and permafrost (Coulombe et al., 2019). The cores were scanned from top

to bottom, providing transverse and longitudinal slices images that create a three-dimensional “stack” of images after compilation. The pixel resolution of each horizontal (X) and vertical (Y) image was 0.195×0.195 mm giving a two-dimensional pixel resolution of 0.038 mm 2 . Each slice integrated a thickness (Z) of 0.4 mm, making the voxel resolution of 0.0152 mm 3 . The output of the scanning is a set of DICOM 16-bit greyscale images representing a 3D reconstruction of the cores with a high degree of accuracy. The pixel value, expressed in Hounsfield units (HU), represents the linear attenuation of the X-ray which depends on the density of the material. Lower density materials (i.e. gas) appear in darker tones while lighter tones indicate higher density material (i.e. ice, sediments).

The processing of the images first consisted of converting them into binary images. The manual adjustment of the segmentation threshold made it possible to detect air bubbles larger than 0.2 mm in diameter (Crabeck et al., 2016). It provided a high-resolution sub-millimeter profile of the air fraction, expressed by the porosity (ϕ in %) for a given volume of ice (V). Then, the bulk density (ρ_i , kg·m $^{-3}$) of the ice was calculated using the equation A1-1 (Kawamura, 1990):

$$\rho_i = (1 - \phi) \cdot \rho_{pi} \quad (\text{A1-1})$$

where ρ_i is the density of the pure ice (free of air and sediment) at 0 °C (916.8 kg m $^{-3}$). The values of bulk density derived from CT images were then validated with laboratory measurements based on weighing samples of known volume. We found good agreement between both methods (Figure S1-2).

Appendix A1-5: Calculation of ice crystal kinetic growth

A mixture of grains with a given size distribution evolves naturally, the driving force being the reduction of interface energy. This process has been documented for grains in a solvent or air where it is known as Ostwald ripening (or coarsening) (Ostwald, 1901). Interface energy minimization also applies to a solid formed of grains such as ice in ice sheets (Durand et al., 2006). In the absence of non-hydrostatic stress, ice crystals grow by recrystallization following a temperature-dependent rate (Gow, 1969). This normal grain growth law to describe this process is expressed by (Cuffey and Paterson, 2010):

$$A = A_0 + kt \quad (\text{A1-2})$$

where A is the mean surface area of crystals (mm^2) at time t ; A_0 is the initial surface area; k is the growth factor ($\text{mm}^2 \text{ a}^{-1}$) which has an Arrhenius temperature dependence. Considering that the initial ice is superimposed ice, we assumed A_0 is equal to the average value of crystal size found in Unit 1. k was calculated as follow (Cuffey and Paterson, 2010):

$$k = k_0 e^{-Q/RT} \quad (\text{A1-3})$$

where Q is the activation energy, k_0 is the pre-exponential factor, R is the gas constant ($8.314 \text{ J K}^{-1} \text{ mol}^{-1}$) and T is the absolute temperature (Kelvin). The activation energy is generally inferred by plotting $\ln(k)$ as a linear function of $1/T$. Compilation of published values of k reported by Cuffey and Paterson (2010), Duval (1985) and Jacka and Li (1994) gives a constant value for the activation energy of $\sim 51 \text{ kJ mol}^{-1}$ for the range of temperature -4 to -50°C (**Figure A1-1**). At $\sim -4^\circ\text{C}$, a break occurs in the linear relation of $\ln(k)$ with $1/T$ due to a drastic increase of Q when the temperature approaches the melting point (Jacka and Li, 1994). In this study, we postulate that the temperature of the lower unit of the ice patches remained below -4°C as indicated by the thermal regime of the ice body below 150 cm depth (**Figure 23a**).

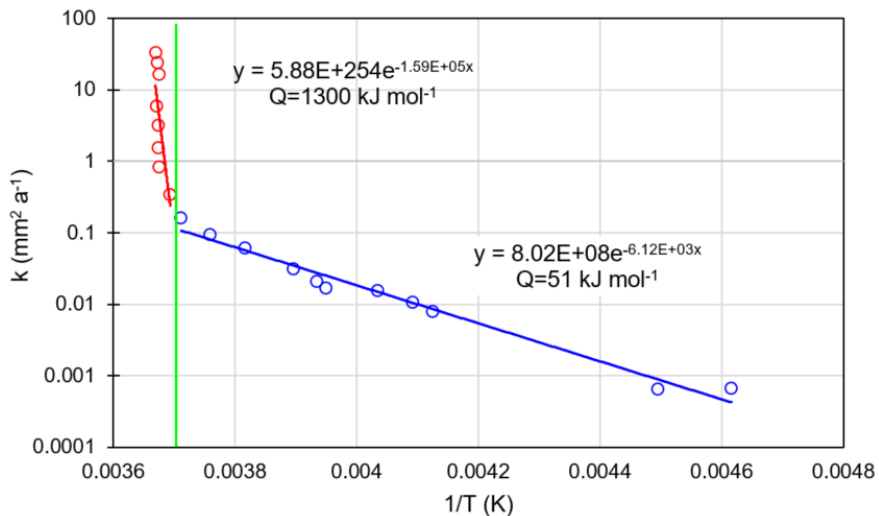


Figure A1-1. Plot of the ice crystal growth factor (k , $\text{mm}^2 \text{ a}^{-1}$) in a logarithmic scale as a function of $1/T$. Data were obtained by field and laboratory experiments by Jacka and Li (1994); Duval (1985) and Cuffey and Paterson (2010). Below -4°C (green vertical line), the blue linear regression line was used to obtain the activation energy (Q).

2.12. Supplementary material S1

Table S1-1. Detailed information about the seasonal snow and ice studies. See **Figure 16** in the manuscript for the localization of sampling sites.

Snow pits	Location	Date	Comments
Sp1_16	Ice patch 1	7 June 2016	Core #1 site
Sp1_17a	Ice patch 1	8 June 2017	Core #2 site
Sp1_17b	Ice patch 1	2 July 2017	3 m away from Sp1_17a
Sp2_17	Ice patch 2	9 June 2017	Core #2 site
Ice drilling			
Core #1	Ice patch 1	8 June 2017	Core 0 to 320 cm depth; missing part between 130 to 140 cm
Core #2	Ice patch 2	12 June 2017	Core 0 to 249 cm depth; complete sequence
Ice sampling			
IS #1	Ice patch 1	2 July 2017	Basal ice, bottom of snowpit Sp1_17b, 4 pieces of ice
IS #2	Ice patch 1	5 July 2017	Basal ice, exposed ice in the frontal margin, 2 cores of 15 cm
IS #3	Ice patch 2	7 July 2017	Basal ice, exposed ice in the frontal margin, 2 cores of 15 cm
IS #4	Ice patch 1	11 July 2017	Supra ice-channel, 4 pieces of ice

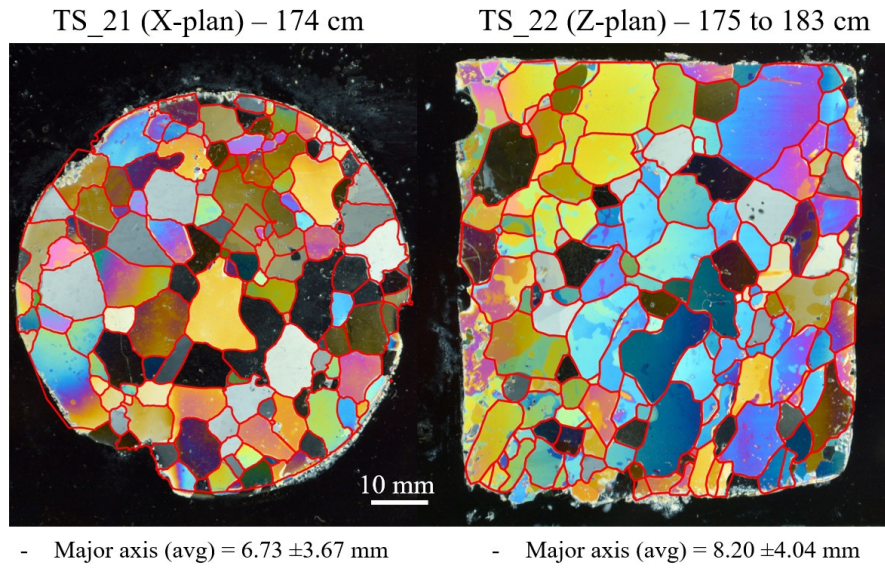


Figure S1-1. Two-dimensional morphology of ice crystals: example of the calculation of the shape anisotropy obtained by computing the ratio between the average long axis in the X-plan (Thin section 21 of the core #1) and the average long axis of the Z-plan (Thin section 22 of the core #1). As suggested by the ratio below 1, the crystals are slightly flattened along the vertical plane.

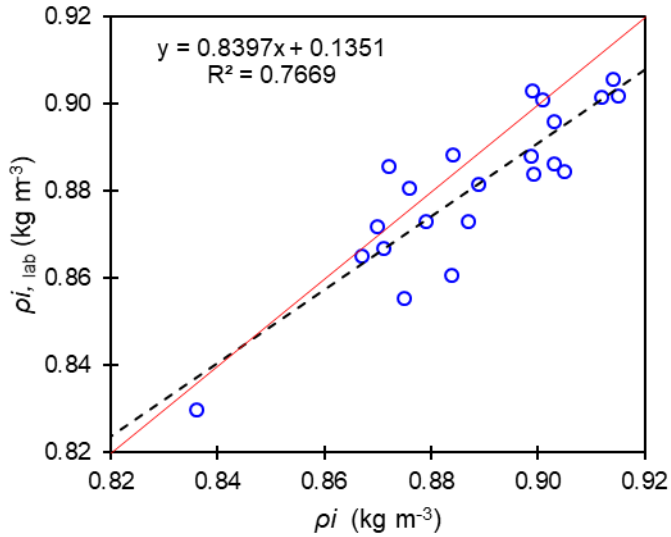


Figure S1-2. Comparison between the ice densities calculated from CT-derived air volume fraction (ρ_i) and measured in lab ($\rho_{i, lab}$). Red line represents the 1:1 relationship line.

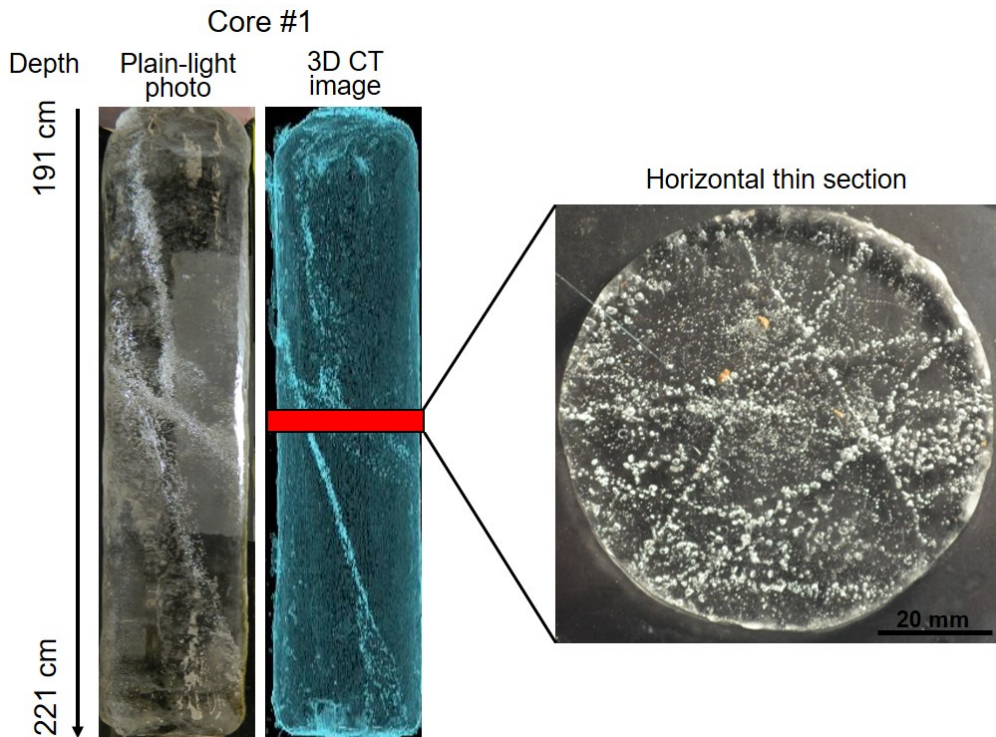


Figure S1-3. Example of a core section extracted from the lower section of core #1 characterized by a high fracture frequency. The fractures are detected by the presence of sheets of air bubbles. The combination of a plain-light photo, 3D reconstruction of CT-images and transverse thin sections allows to easily observe and count the fractures.

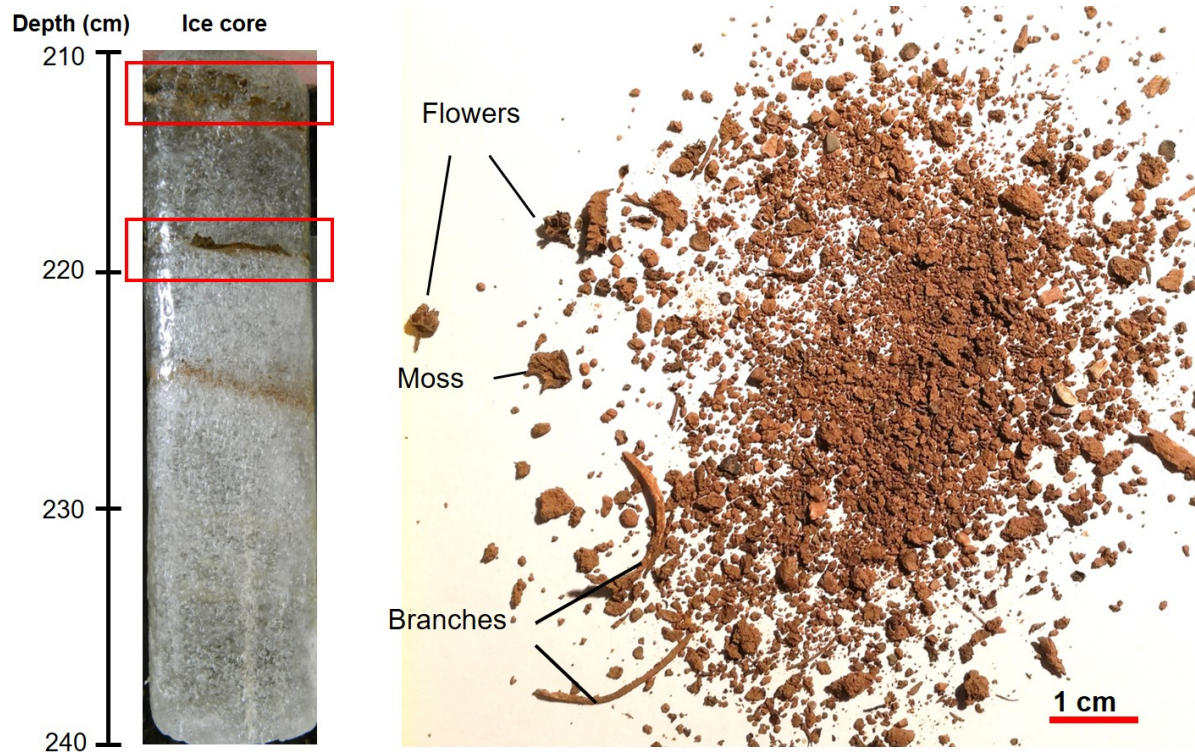


Figure S1-4. Left, photograph of the section of core#2 (Ice patch 2) where the two sediment layers were sampled (212 cm and 218 cm depth); right, photograph of the sediment sample with the well-preserved organic fragments that ^{14}C dated to 3487 ± 20 cal BP to estimate the age of the deepest section of the ice patch.

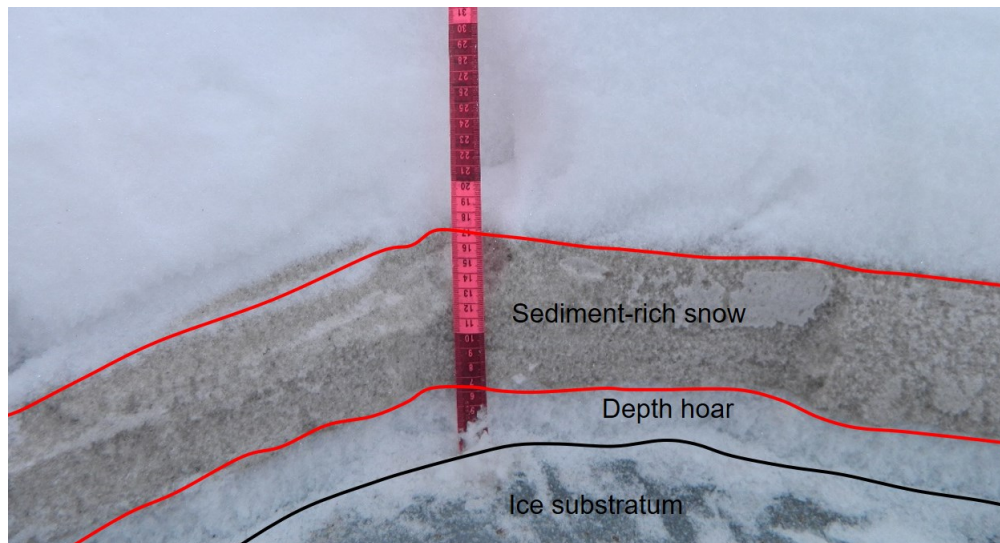


Figure S1-5. The bottom section of the snowpit Sp2_17 dug on IP2, where a layer of sediment-rich snow was found. Between this layer and the ice substratum, a thin layer of depth hoar was present.

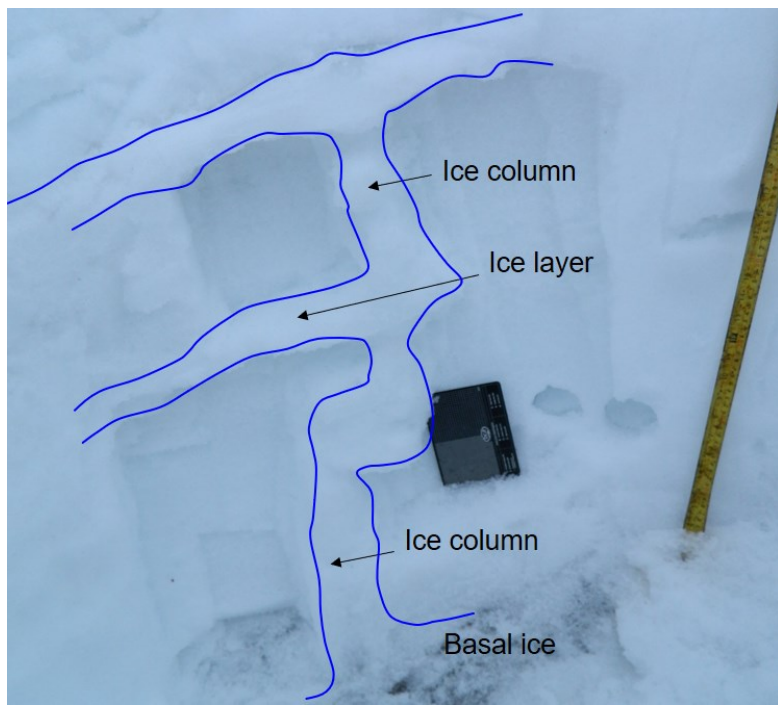


Figure S1-6. Illustration of the ice structures (ice layers, ice columns) formed into the snowpack in Sp1_17b by the refreezing of percolating meltwater in the early melt season. These intra-snow ice structures are connected to the basal ice layer at the snow/ice interface.

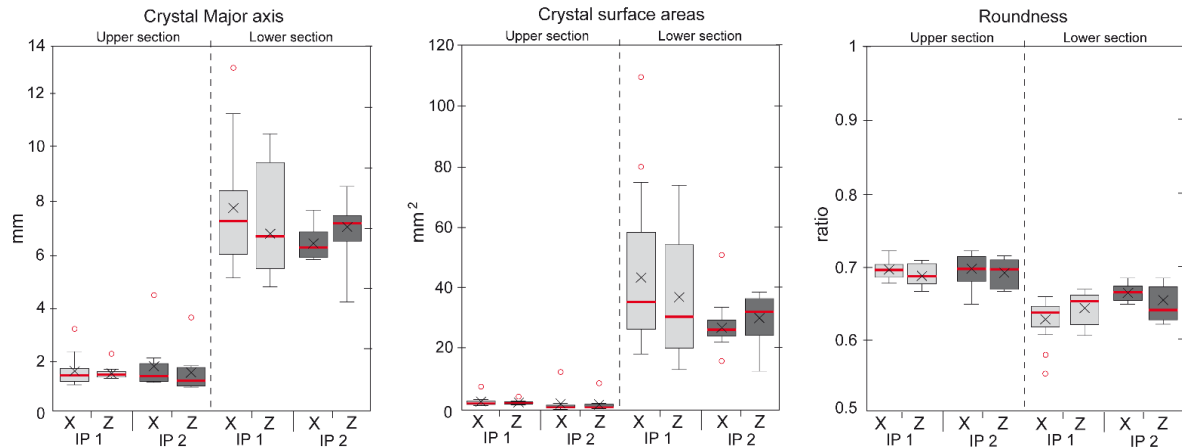


Figure S1-7. Box plots summarizing the ice crystal characteristics, namely the ice crystals major axis, surface areas and roundness, along the X plane (horizontal thin section) and the Z plane (vertical thin section) of the upper and lower sections of IP1 and IP2. Red lines and black crosses represent the median and the average, respectively, and red circles are the outliers.

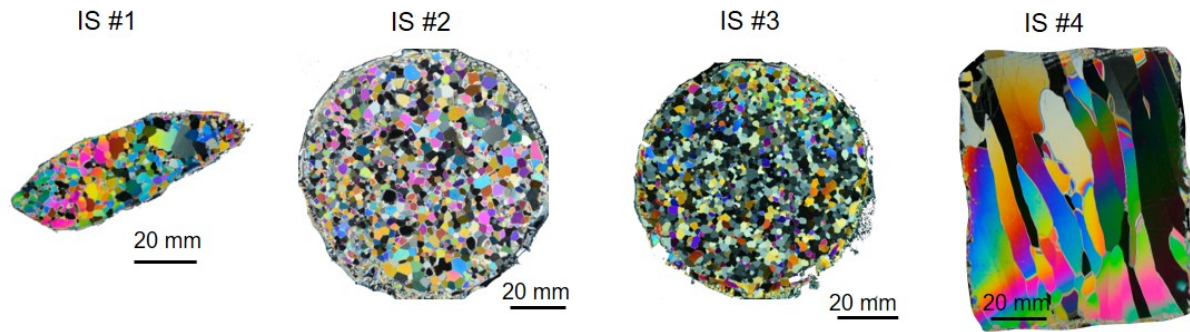


Figure S1-8. Thin sections of ice samples collected at the bottom of the snow snowpit Sp1_17b (IS#1), in the frontal edge of IP1 (IS#2) and IP2 (IS#3) and on the sides of the supra-ice channel (IS#4) viewed under direct cross-polarized light.

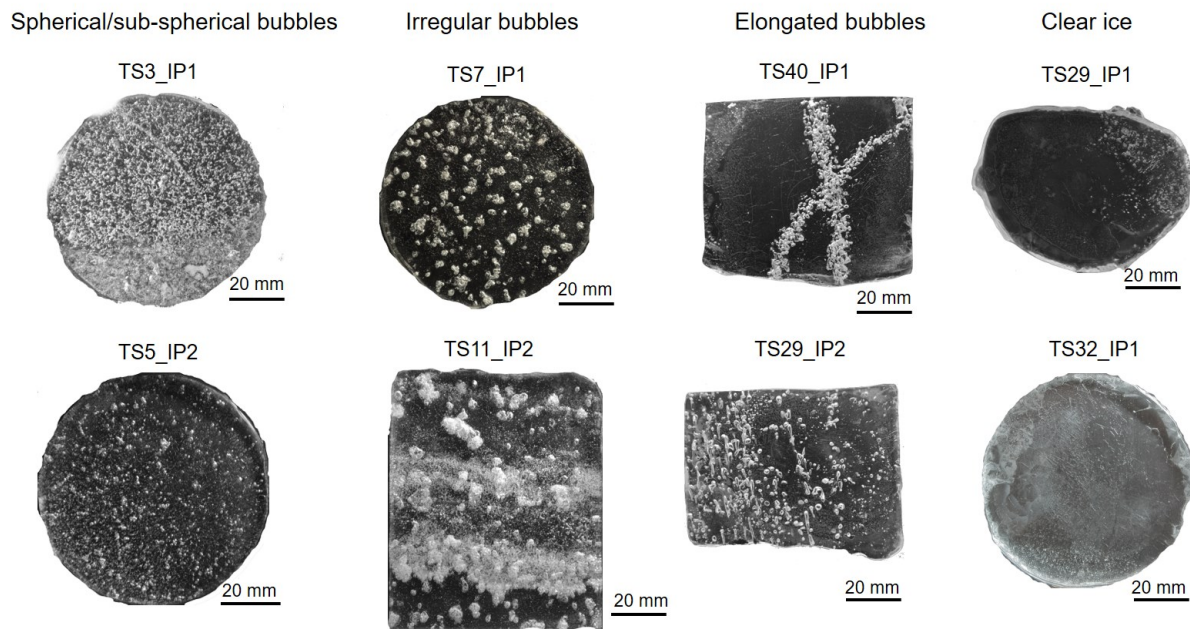


Figure S1-9. Plain-light photographs of thin sections showing examples of various air inclusions embedded in the ice of the investigated ice patches.



Figure S1-10. Weathered superimposed ice exposed in the frontal margin of IP1 in early July 2017 with ice crystals up to 2-3 cm in size. The disintegration of the ice structure is the result of differential melting along grain boundaries caused by the absorption of solar radiation. Multiple melt-freeze cycles lead to the growth of ice crystals.

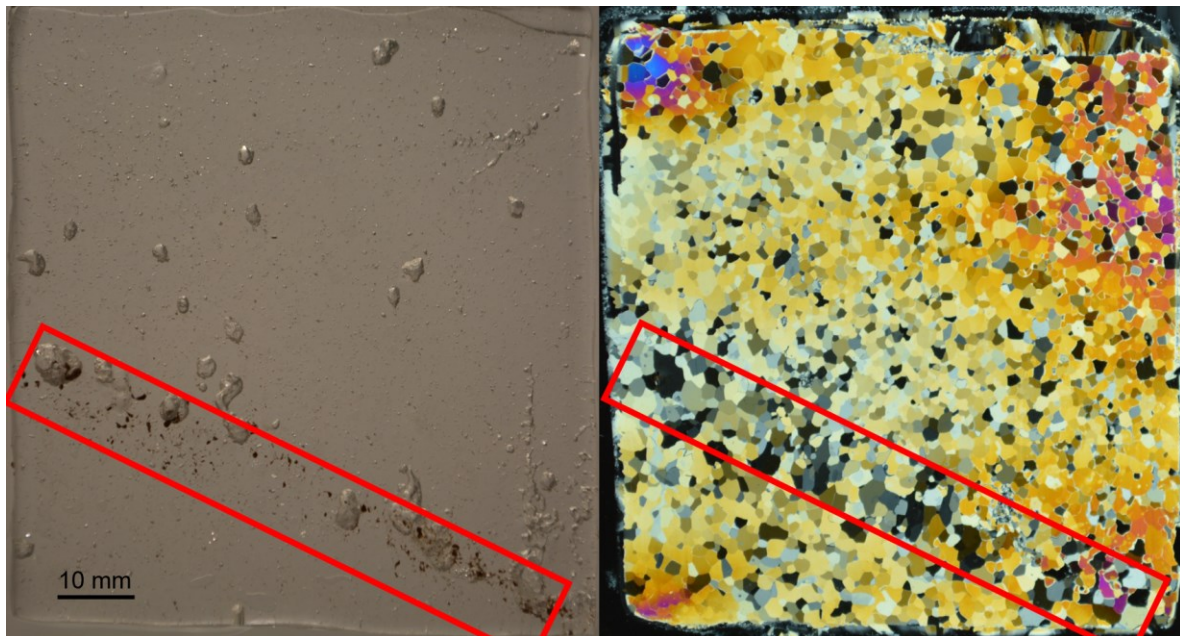


Figure S1-11. Plain-light (right) and cross-polarized light (left) image of TS8 collected at 50 cm depth in core#1 (Ice patch 1) which shows an example of a thin (~1cm) layer of coarse ice linked to the refreezing of a weathered crust. The melt-concentration of sediment indicating the ablation surface is clearly observable on the plain-light image.

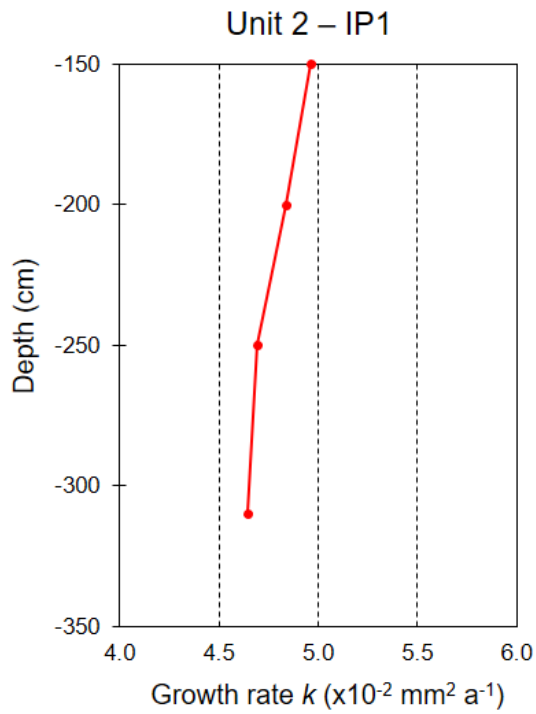


Figure S1-12. Calculated ice crystal annual growth rate (k) from Unit 2 of the ice patch 1 (IP1) based on the ice temperature collected in the 320 cm deep borehole (see Appendix E for the calculation).

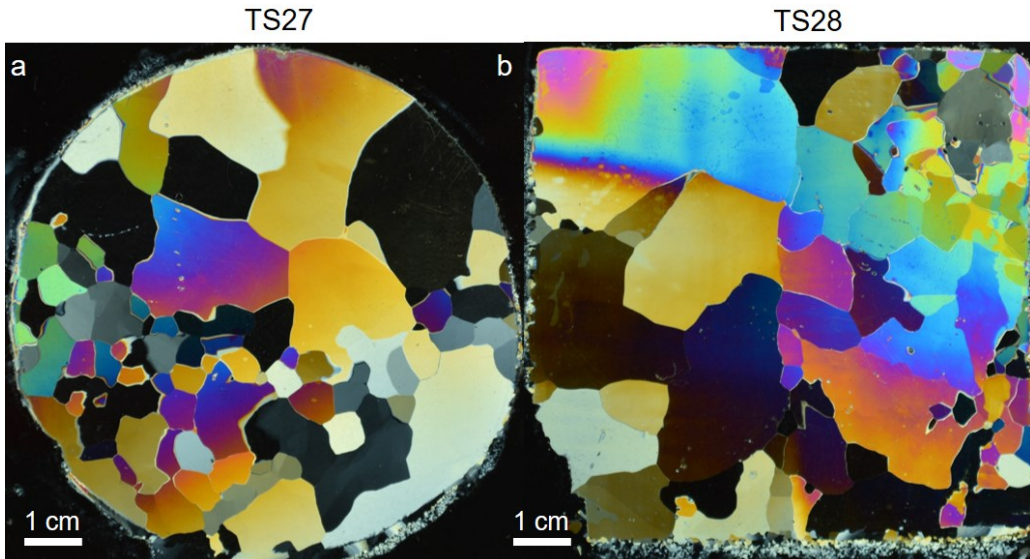


Figure S1-13. Paired thin sections TS27 (a) (X-plane) and TS28 (b) (Z-plane) sampled at 205-215 cm in core#1 (IP1) showing clear ice composed of coarse ice crystals of irregular shape. The crystals in TS28 are slightly coarser and more elongated than in TS27 but the elongation axis is variable. This ice is most likely the result of slow water freezing or melt-freeze recrystallization.

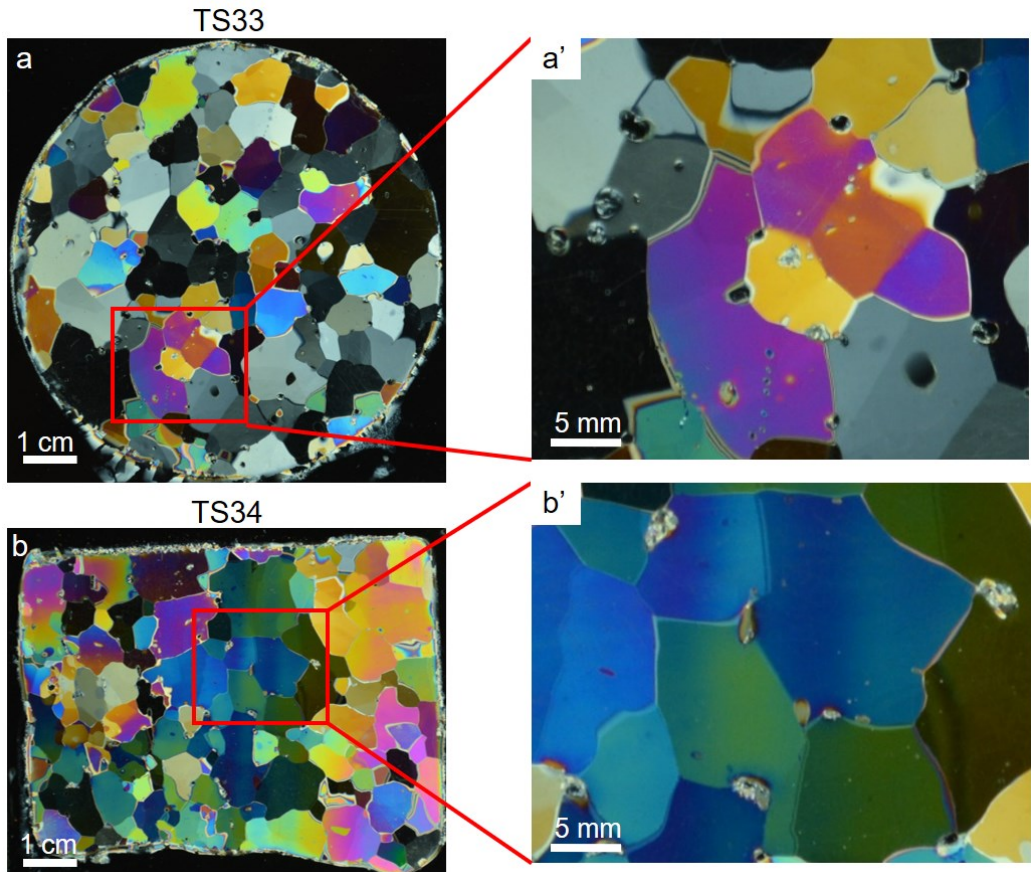


Figure S1-14. Paired thin sections TS33 (a) (X-plane) and (b) TS34 (Z-plane) sampled between 240-249 cm in core#2 (IP2) and close-up (a' and b'). This ice does not exhibit the characteristics of growth from water, so it probably results primarily from solid phase recrystallization. Such ice is therefore suitable to estimate its age from the normal grain growth law. However, as illustrated by the close-ups a' and b', the presence of air inclusions has “pinned” crystals in several places. Such grain boundary pinning slows the motion of crystal boundary and thus its growth. The position of bubbles sometimes only favors the growth of ice crystals in one direction only, which leads to the development of an elongated shape (e.g. pink crystal in a').

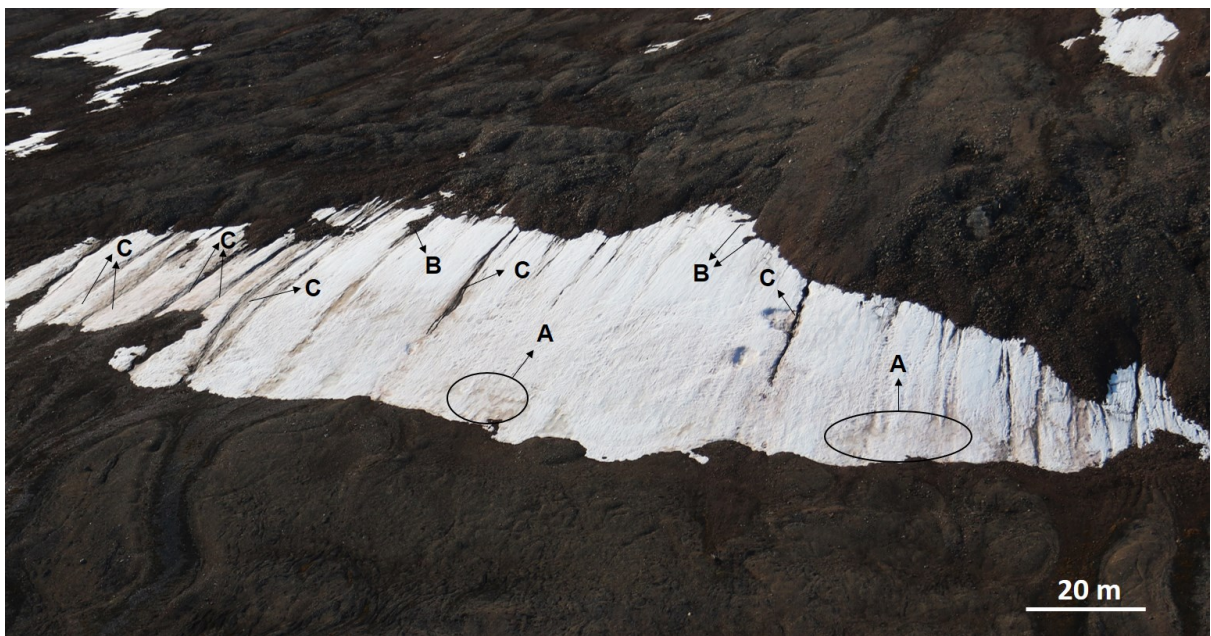


Figure S1-15. Oblique view of the ice patch IP1 photographed on 16 July 2016 where various forms of sediment depositions are visible: A) Niveo-aeolian deposits, B) Colluvial sediment deposits from upslope, C) Channels incised in the snow and ice surface with high sediment concentration.

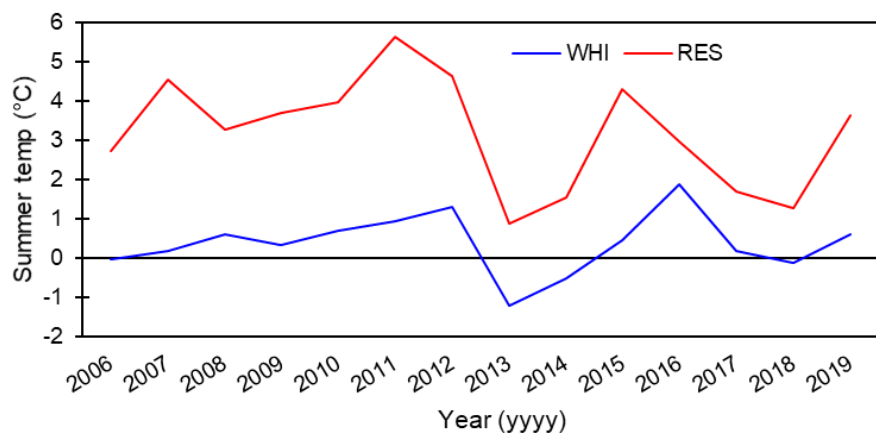


Figure S1-16. Evolution of the summer temperature (June/July/August) recorded at Ward Hunt Island by the SILA station and at Resolute Bay on Cornwallis Island, nearly 1000 km south from Ward Hunt (Environment Canada, 2021).

Chapitre 3 – Mass balance and ablation processes of a perennial ice patch on the northern coast of Ellesmere

Auteurs : Gautier Davesne, Daniel Fortier, Florent Domine

3.1. Avant-propos

Le manuscrit qui constitue le **chapitre 3** répond à l'[objectif 2](#) de la thèse en s'intéressant aux processus d'accumulation et d'ablation d'une plaque de glace permanente à Ward Hunt. Afin de comprendre les facteurs de contrôle du bilan de masse et d'énergie de la plaque de glace, cette recherche s'est basée sur des mesures d'épaisseur de neige et du taux d'ablation de surface par scanner laser terrestre haute résolution. Les mesures d'ablation ont été couplées avec la mesure des paramètres micrométéorologiques sur la plaque de glace afin de déterminer la contribution des différentes variables du bilan d'énergie de surface dans l'ablation estivale. De plus, la distribution spatiale et la variabilité interannuelle de la plaque de glace à l'échelle de l'île Ward Hunt ont été étudiées par télédétection sur la base d'images satellites. Cette recherche a permis d'identifier les facteurs clés dans le développement et le maintien des plaques de glace et de tirer des conclusions importantes quant à la variabilité temporelle des plaques de glace et leur sensibilité aux changements climatiques. Le manuscrit est en préparation en vue d'une soumission après le dépôt initial de la thèse.

3.2. Résumé

Dans le désert polaire, les systèmes de plaques de glace exercent un grand contrôle sur la dynamique des paysages et des écosystèmes. Cependant, leur variabilité spatio-temporelle et les facteurs qui les contrôlent sont encore mal compris. Nous avons effectué des mesures de terrain du bilan de masse et du bilan énergétique de surface d'une plaque de glace à l'île Ward Hunt (WHI ; 83°N, Haut Arctique canadien), combinées à l'analyse de la distribution spatiale et la variabilité interannuelle des plaques de glace à l'échelle de WHI par télédétection. Les résultats ont démontré que la distribution des plaques de glace à l'échelle du paysage reflète les patrons spatiaux des accumulations préférentielles de neige et de l'ablation minimale qui dépendent principalement de

la topographie et du régime des vents. À l'échelle d'un système de plaques de glace, les gains de masse principaux se produisent par des épisodes de transport éolien de la neige, rendant ainsi l'approvisionnement saisonnier en neige fortement dépendant de la fréquence et de l'ampleur des événements de vent. Les vents modérés (vents de $4\text{--}10 \text{ m s}^{-1}$) favorisent le chargement en neige tandis que les vents forts (vents de $>15 \text{ m s}^{-1}$) le limitent considérablement. En été, l'ablation est due au rayonnement net, mais les flux de chaleur sensible expliquent en grande partie la variance de l'énergie de fonte. Les taux d'ablation les plus élevés se sont produits pendant les périodes de temps perturbé, lorsque des vents forts sont combinés à l'arrivée d'une masse d'air chaud. Les jours de brouillard, en revanche, ont été marqués par la réduction importante de la fonte, en raison d'une diminution des apports en énergie à la surface par rayonnement solaire et par flux de chaleur sensible. La préservation à long terme des plaques de glace et leur résistance actuelle au réchauffement récent suggèrent que ce système est partiellement déconnecté de la tendance climatique en raison d'un mécanisme de rétroaction sur l'accumulation de neige apporté par les contraintes topographiques. Cependant, bien que la sensibilité climatique des plaques de glace soit moindre que celle des autres éléments cryosphériques sur le long terme, le taux d'ablation à l'échelle d'un été est néanmoins fortement influencé par les facteurs micrométéorologiques (c.-à-d. température de l'air, le vent et le brouillard). L'évolution prévue par les modèles de ces facteurs au cours de la prochaine décennie laisse penser que les conditions deviendront rapidement très critiques pour assurer le maintien futur des plaques de glace à WHI.

3.3. Abstract

In the polar desert, ice patch systems have great control over the landscape and ecosystem dynamics. However, their spatio-temporal variability and the driving factors that control them are poorly understood. We performed field measurements of the surface mass and energy balance of an ice patch at Ward Hunt Island (WHI; 83°N , Canadian High Arctic), combined with remote sensing to assess the spatial distribution and interannual variability of ice patches at the scale of WHI. Results demonstrated that the distribution of ice patches at the landscape scale reflects spatial patterns in preferential snow accumulations and minimum ablation which are mainly dependent on topography and wind field. At the scale of an ice patch system, primary mass gains occur through drifting snow events, thereby making the seasonal snow supply highly dependent on the frequency

and magnitude of wind events. Moderate winds (winds of $4\text{--}10 \text{ m s}^{-1}$) promote snow loading while strong winds (winds of $>15 \text{ m s}^{-1}$) significantly limit it. In summer, ablation is driven by net radiation but sensible heat fluxes largely explained the variance in the melt energy. The highest ablation rates occurred during periods of disturbed weather when strong winds are combined with warm air. Foggy days in contrast were marked by melt suppression since it reduced the solar radiation heating and sensible heat fluxes to the snow/ice surface. The long-term preservation of the ice patches and their current resilience to recent warming suggested that this system is partly disconnected from the climate trend due to a feedback mechanism on snow accumulation brought by topographical constraints. However, although the climatic sensitivity of ice patches is less than that of other cryospheric elements over the long term, the ablation rate at a summer scale is nevertheless strongly influenced by micrometeorological factors (i.e. air temperature, wind and fog). Model projections of these factors over the next decade suggest that conditions will quickly become very critical to sustain the future survival of the ice patches at WHI, as most of them may lose their permanent status in the next few years.

3.4. Introduction

Perennial land ice masses consist of a broad spectrum of sizes, ranging from perennial ice patches (10^{-2} km 2) to ice sheets (10 7 km 2), and these various ice features do not have the same response and sensitivity to climate fluctuations (White and Copland, 2018). Given the ongoing acceleration of climate changes, the understanding of the spatio-temporal dynamics of the cryosphere has become a research priority. However, research efforts have focused on the study of larger systems such as glaciers and ice caps, while smaller ice masses have attracted little attention. As a result, ice patches are among the least understood elements of the polar cryosphere despite their widespread distribution across the landscape (Eveland et al., 2013a,b; Lewkowicz and Harry, 1991; Woo and Young, 2014). They have been recognized as a primary contributor to the hydrological cycle in sustaining meltwater flow throughout the summer (Lewkowicz and Young, 1990) and as a driver in the development of landscape and ecosystems (Christiansen, 1996; Woo and Young, 2003). As such, their recent disappearance in response to climate changes has been identified as a critical issue for the stability of the whole polar geosystem (Abnizova and Young, 2008; Woo and Young, 2014).

The ice patch system is intermediate between seasonal snow patches and glaciers. The system includes the perennial ice body overlain by multi-year accumulation layers of firn and a deep seasonal snow layer. These dynamics are controlled by the net surface mass balance (SMB), i.e. the difference between inputs and losses of mass over a hydrological year. Unlike glaciers, they are static and have no distinct accumulation and ablation (Glazirin et al., 2004; Meulendyk et al., 2012). Inputs of mass to the systems primarily consist of seasonal snow accumulation which depends on the precipitation at the regional scale and redistribution processes driven by topography and local winds. Ice patches are typically found in sites with abundant snow supply during winter, up to several meters and more, either by avalanching at the bottom of steep slopes (Mott et al., 2019) or by wind-driven snowdrift in sheltered gullies, concavities and leeward slopes (Brown and Ward, 1996; Watson, 1994). In polar regions, the combination of treeless terrain, strong winds and the dry nature of the snow makes wind transport the dominant process of snow redistribution (Eveland et al., 2013a,b; Parr et al., 2020). In spring and summer, ice accumulation mainly occurs through the formation of superimposed ice, when in situ snowmelt and upslope runoff percolate and refreeze within the snow and underlying firn layer when presents (Ballantyne, 1978; Lewkowicz and Harry, 1991; [Chap. 2](#)). Mass losses, on the other hand, occur through the melting

and sublimation of snow/ice which are both a function of the surface energy balance (SEB). The SEB is primarily controlled by the regional climate which depends on the latitudinal position, altitude, synoptic circulation patterns and land-sea contrasts (Alt, 1987; Gardner and Sharp, 2007). These regional patterns are modulated at finer scales by topography which affects micrometeorological parameters (Mott et al., 2011; Mott et al., 2018; Schirmer and Pomeroy, 2020), and by snow/ice properties (Domine et al. 2012; Jennings et al., 2018). In mid-latitude mountains, extensive field and modelling work on the ablation of snow/ice patches (e.g. Canadian Rockies: Pohl and Marsh, 2006; DeBeer and Pomeroy, 2017; Swiss Alps: Grünwald et al., 2010; Mott et al., 2019) allowed identifying a set of local effects brought by the topography and the size of the snow/ice patches themselves on microclimate conditions and heat exchange processes. It includes topographic shading (DeBeer and Sharp, 2009; Fujita et al., 2010; Mott et al., 2019), development of katabatic flow and turbulent heat fluxes (Mott et al., 2015; Schlögl et al., 2018), cold-air pooling (Mott et al., 2013), and advective heat fluxes from the adjacent bare ground (Essery et al., 2006; Harder et al., 2017; Mott et al., 2011; Neumann and Marsh, 1998).

In Polar Regions, the scarcity of field studies limits our understanding of both regional and local effects and drivers in the ablation processes of ice patch systems. In a pioneer investigation on an ice patch on Melville Island in the southern Canadian High Arctic, Young and Lewkowicz (1990) demonstrated the large dominance of net solar radiation in the summer SEB due to the presence of an aeolian sediment cover that significantly decreased the snow albedo. The contribution of sensible heat fluxes, on the contrary was low due to the prevalence of calm and cold weather yielding latent heat fluxes that were almost negligible. More recently, a second study carried out by Leppäranta et al., (2013) on a snow patch at Basen Nunatak in western Dronning Maud Land in Antarctica highlighted the great importance of sublimation processes which represent a major loss of mass and heat sink because of the aridity and the coldness of the climate. These earlier studies demonstrated the importance of considering the region-specific drivers and effects to understand the ablation processes at the scale of an ice patch system. Given that the climate of polar deserts encompasses a broad spectrum of summer temperature, humidity conditions and topography, it is likely that the dominant drivers of ablation processes vary greatly between polar sub-regions.

To improve the understanding of ice patch dynamics in the polar desert, we propose the first study addressing the mass and surface energy balance of a perennial ice patch on the northern coast of Ellesmere Island where semi-permanent and perennial ice patches are ubiquitous. This region exhibits a specific climate due to the influence of the Arctic Ocean which maintains cooler and moister conditions in summer than in the interior Arctic (Maxwell, 1981). We hypothesize that both fog and wind have an important control on energy-exchange processes at the snow/ice surfaces, the former by limiting the amount of incoming solar radiation and the latter by increasing sensible heat fluxes (Essery et al., 2006; Grünwald et al., 2010; Mott et al., 2013; 2015). Besides, wind conditions may also be crucial in winter by controlling snow redistribution processes and snow physical properties, with important implications for the mass balance of ice patch systems (Eveland et al., 2013a,b; Parr et al., 2020). Our study relied on experimental work consisting of measuring the mass and energy balance of an ice patch at Ward Hunt Island, at the northern tip of Ellesmere Island, combined with remote sensing work for analyzing the spatial and temporal patterns of ice patches at the scale of the island. More specifically, we address the following aims: (1) understand the spatial distribution of the ice patches and infer the main terrain factors controlling them at the landscape scale; (2) quantify the winter snow accumulation regime and summer ablation rate; (3) identify the regional and local drivers involved in the ice patch energy and mass balance, and (4) assess the sensitivity of the ice patch system to climate change.

3.5. Study site

The northern coast of Ellesmere Island experiences (**Figure 28a,b**) a polar desert climate characterized by winter temperature that drops well below -30°C in winter and rarely rise above 5°C in summer, low annual precipitation ($<250 \text{ mm yr}^{-1}$), snowpack on the ground 8–10 months of the year, annual net solar radiation $<100 \text{ MJ m}^{-2} \text{ yr}^{-1}$, and an extreme seasonality with complete darkness in winter and 24h-daylight during the summer (Maxwell, 1981). At the synoptic scale, the north coast of Ellesmere Island is influenced by maritime air masses from the Arctic Ocean and the Arctic Cordillera which act as barriers in the regional airflow and moisture circulation from the west/northwest. In summer, cold and moist air moving from the nearby Arctic Ocean is blocked along the coast which favours the formation of persistent fog and low stratus clouds, especially in July and August when the sea ice starts to open.

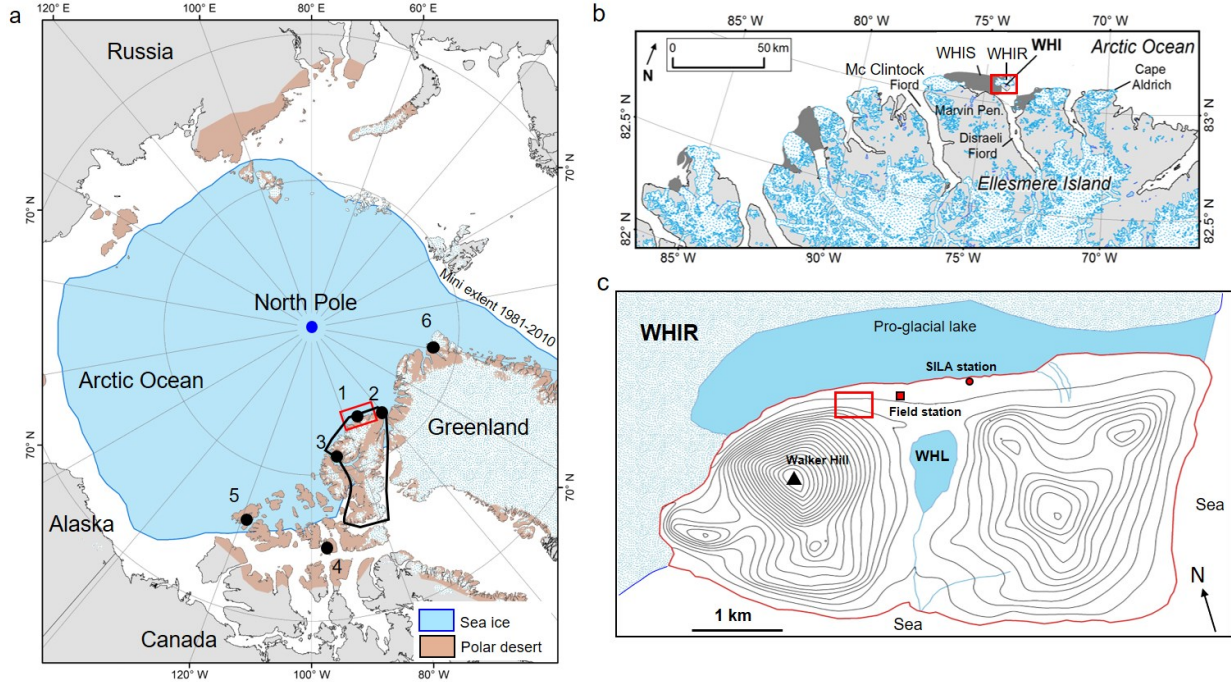


Figure 28. a) Map showing the ~2.7 million km² of the ice-free land surface characterized as polar desert in the circumpolar Arctic (annual precipitation <250 mm and July temperature <5 °C). The black line delineates Ellesmere Island, which is the northernmost large island of the Canadian Arctic Archipelago, and the black circles locate weather stations of the arctic desert detailed in **Table 3**. 1: Ward Hunt Island (Ca); 2: Alert (Ca); 3: Eureka (Ca); 4: Resolute Bay (Ca); 5: Mould Bay (Ca); 6: Station Nord (Dk); b) Localization of Ward Hunt Island (WHI) 6 km north of the nearest shore of Ellesmere Island and about 760 km from the North Pole; c) Topographic map of WHI (10 meter contours) showing the Ward Hunt Lake (WHL), the Ward Hunt Ice Rise (WHIR), the field station and the SILA weather station managed by the CEN. The red square indicates the location of the studied ice patch at the foot of the north face of Walker Hill.

This climate of the coastal fringe contrasts with the interior of Ellesmere such as at Eureka where warmer and drier summer conditions prevail (**Table 3**) (Barry and Hall-Mckim, 2018; Edlund and Alt, 1989; Maxwell, 1981). This “Arctic Ocean effect” significantly reduces the summer melt along the coast of Ellesmere Island and causes a local lowering of the glacier equilibrium line altitudes (ELAs) (Miller et al., 1975; Wolken et al., 2008) which favour the existence of low-elevation, coastal glacier and ice caps, ice rises and ice shelves, and the persistence of numerous snowbanks and ice patches (Braun et al. 2004; Jeffries, 1982; Vincent et al., 2011b).

At Ward Hunt Island (hereinafter WHI) (83°05'09"N, 74°06'19"W) (**Figure 28b,c**), climate data provided by the SILA weather station represent the climate of the northern coast of Ellesmere

(CEN, 2021). The mean annual air temperature (MAAT) and the average winter and summer temperature were -17.1°C and 0.4°C respectively for the period 2006-2019.

Table 3. Climate of the Ellesmere Island's northern coast (Ward Hunt Island and Alert) relative to other polar desert localities of the Canadian High Arctic, Greenland and Antarctica for the period 1980-2019, unless for Ward Hunt (2006-2019). Mean annual air temperature (MAAT), Mean summer and winter air temperature (MAT_s and MAT_w), mean annual precipitation and mean annual and summer relative humidity (RH_{annual} and RH_s). Summer averages are calculated for Jun-Jul-Aug for Northern Hemisphere sites and Dec-Jan-Feb for Southern Hemisphere sites, and conversely for winter averages (Source: CEN, 2021; Environment Canada, 2021; www.ncdc.noaa.gov/cdo-web/; Doran and Fountain, 2019).

Station	Position	MAAT	MAT _s	MAT _w	P _{annual}	RH _{annual}	RH _s
Ward Hunt Island (NU)	83.08°N; 74.10°W	-17.1	0.4	-30.3	-	77.6	85.5
Alert (NU)	82.50°N; 62.30°W	-17.5	1.2	-31.5	158	75.8	86.1
Eureka (NU)	79.98°N; 85.94°W	-18.8	3.9	-35.7	81	70.1	72.2
Resolute (NU)	74.67°N; 94.83°W	-15.6	2.2	-30.7	164	75.5	83.4
Mould Bay (NU)	76.75°N; 119.50°W	-17.2	2.3	-32.3	117	76.1	81.9
Station Nord (Gl)	81.72°N; 17.79°W	-16.8	1.7	-29.7	188	73.7	81.0
McMurdo Station (Antar.)	77.85°S; 166.66°E	-17.3	-5.0	-25.4	112	63.7	66.4
Wright Valley (Antar.)	77.52°S; 161.69°E	-19.3	-0.5	-33.3	<100	62.0	65.3

Summer temperatures were therefore colder than at other stations in the High-Arctic but not as cold as in the dry valleys of McMurdo in Antarctica (**Table 3**). The melt season is short, generally spanning from mid-June to the end of August and is characterized by high relative humidity (85.5% on average). Precipitation data are not available for WHI, but it is likely similar to the average of 158 mm year^{-1} (w.e.) measured at Alert, 170 km to the southeast (Environment Canada, 2021). Although WHI does not currently have glaciers, the cryosphere is omnipresent on and around the island (**Figure 28b,c**). The sea channel between the south coast of the island and Ellesmere is occupied by pack ice and the remnants pieces of the Ward Hunt Ice Shelf (WHIS) (Mueller et al, 2003) while the north and west coast of WHI is bordered by the Ward Hunt Ice Rise (WHIR) (Braun et al., 2004). On the island, large perennial ice patches constitute the most prominent cryospheric elements at the surface. Our study focuses on one of these located at the base of the

north face of Walker Hill (**Figure 28c**). This ice patch (hereinafter IP1) lies between 40 to 60 m a.s.l. and is about 150 m long, 25 wide and 3.2 m thick of ice in the central section. In a previous study ([Chap. 2](#)), we gave a complete description of physical characteristics and stratigraphy of this ice body. They found that IP1 is made of superimposed ice, characterized by very fine granular and bubbly ice in the upper 130 cm and by coarser crystals and lower porosity in the lower section.

3.6. Instrumentation and data acquisition

3.6.1. Snow regime

At the SILA weather station (**Figure 28c**; [Table S2-1](#)), the hourly snow height (SH , cm) was recorded by a Sonic SR50 sensor (Campbell Sci.) from August 2006 to July 2019. The sensor was installed on a topographic break produced by a raised-beach ridge where a semi-permanent snowdrift occurs. These data from a preferential accumulation site were used to infer the snow regime on IP1, since both sites have the same orientation north/north-east. To explore in detail the relationships between snowpack development and the wind conditions, we used the hourly wind data, i.e. maximum wind speed (V_{max} , $m\ s^{-1}$) and direction (DIR , $^{\circ}$), recorded by an RM Young 05103-10 anemometer ([Table S2-1](#)). The maximum hourly wind speed was analyzed to capture wind gusts that have the potential to transport snow. These data were used to calculate the wind index (WI) which describes the sum of hourly wind speeds above the threshold for snow transport. We used the threshold of $6\ m\ s^{-1}$ commonly used for unconsolidated snow (Li and Pomeroy, 1997; Royer et al., 2021; Sturm et al., 2001). Deposition/erosion events (i.e. a rapid change in SH of ± 5 cm) for each cold season from 2005 to 2019 were identified and their relation with wind conditions was examined.

3.6.2. Mass balance variables

3.6.2.1. Ice patch thickness and volume

The total volume of IP1 was calculated by measuring the volume of seasonal snow and the ice body. A snow volume map was obtained by kriging interpolation in ArcGIS (Esri, version 10.5.1) of snow height (SH , cm) that were manually probed every two meters along ten GPS-tagged transects (**Figure 29**) using a 350 cm-graduated rod.

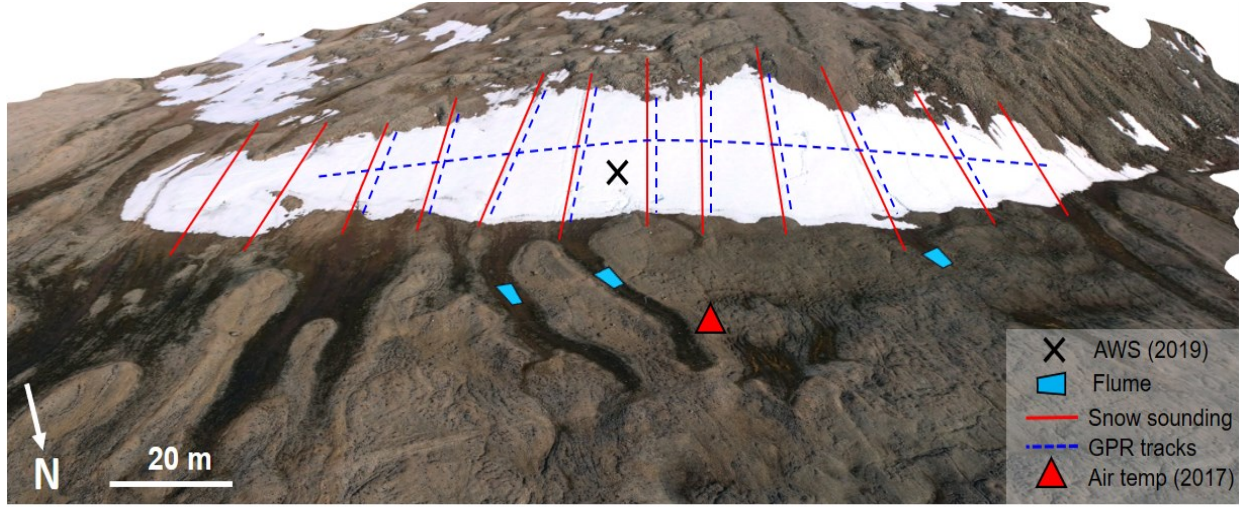


Figure 29. 3D view of the studied ice patch (IP1). Red lines indicate the snow-depth measurement transects and blue dotted lines indicate the GPR profile. The black cross locates the AWS installed during field season 2019, the red triangle shows the site where the air temperature was recorded in 2017 and the blue polygons indicate the location of the cut-throat flumes in the downslope margin of IP1. The background image is an orthomosaic captured with an unmanned aerial vehicle (UAV) on 17 July 2019.

The survey was carried out on 5 June 2016, 8 June 2017 and 12 June 2019 when the snowpack was at its maximum thickness according to the SR50 measurement at SILA station. In 2019, an additional survey was conducted during the melt season on July 5. The total volume of ice was estimated by ground-penetrating radar (GPR) surveys conducted on 7 July 7 2019 with 100 MHz antennas (Pulse EKKOpro System, Sensors and software®) (detailed in [Appendix A2-1](#)). We collected 8 GPR tracks as shown in **Figure 29**. The resulting dataset was imported and interpolated by kriging in ArcGIS, providing a raster of the ice thickness from which a digital terrain model (DTM) of the ice patch bed was produced (Ødegård et al., 2017). The total volume of snow and ice (V_{total} , m^3) was then converted into water equivalent (w.e.) using Equation 3.1.:

$$V_{total} = V_i \times \frac{\rho_i}{\rho_w} + V_s \times \frac{\rho_s}{\rho_w} \quad (3.1.)$$

where V_i and V_s are the volume of ice and snow (m^3), ρ_i , ρ_s and ρ_w are the ice, snow and water densities (kg m^{-3}). We assumed average densities of $\sim 905 \text{ kg m}^{-3}$ for the ice body as reported in [Chap. 2](#). For the dry snow in early June, we also relied on average values reported in [Chap. 2](#) for the snowpack on IP1 in 2016 ($\rho_s = 442 \text{ kg m}^{-3}$) and 2017 ($\rho_s = 406 \text{ kg m}^{-3}$) and we made an additional snowpit excavation on 6 June 2019 following the method detailed in Domine et al.,

(2012). For melting snow, we used the density ($\rho_s = 534 \text{ kg m}^{-3}$) measured in the snowpack on IP1 on 2 July 2017 ([Chap. 2](#)).

3.6.2.2. Daily ablation of the snow/ice over the ice patch

The summer ablation in IP1 was monitored by combining high-resolution measurements of snow/ice surface changes using Terrestrial Laser Scanning (TLS) (VX spatial station Trimble®) with measurements of the ice patch extent based on a continuous record of pictures taken by an automatic time-lapse camera. We performed daily repeated TLS surveys of the ice patch surface from June 10 to July 12 in 2017 (32 days) and from June 10 to July 20 in 2019 (40 days) (details in [Appendix A2-2](#) and [Figure S2-1a,b](#)). The daily height changes of the snow surface (ΔH_{TLS} , in cm d^{-1}) on the ice patch system was calculated by subtracting two consecutive scans. The results were then statistically validated by comparison with daily snow height data provided by the SILA station (ΔH_{SILA} , cm) where the melt rate is expected to be similar to that of IP1 since the two sites are close and share the same orientation. ΔH_{TLS} was then converted into volume of water equivalent in ArcGIS using the Surface Volume tool (3D Analyst) and the aforementioned density value for melting snow, yielding the daily volume change (ΔV_{TLS} in $\text{m}^3 \text{ d}^{-1}$ w.e.). When ΔV negative, it represents the daily melt rate (M in $\text{m}^3 \text{ d}^{-1}$ w.e.). The DTM of the ice patch bed measured on 7 July 2019 by GPR served as the reference to assess the daily evolution of the total volume of the ice patch.

Melting of the seasonal snow and ice patch was monitored daily by an automatic time-lapse camera (Spypoint® Force-11D) operating since July 2017 150 m downslope of the frontal edge of IP1 ([Figure S2-1a](#); Fortier and Davesne, 2021b). The set of daily images was then analyzed using the open-source imaging software ImageJ®. An automatic segmentation threshold, verified by visual inspection, was performed to discriminate the snow/ice surfaces from the bare ground. The output results provided the snow/ice extent in the area fraction of the images. Then, a first analysis was made to monitor the seasonal snow cover fraction (SCF in %) outside the ice patch system (Zone A in [Figure S2-1c](#)). Then, a second analysis was performed at the scale of ice patch system IP1 within Zone B ($\sim 17\,000 \text{ m}^2$; [Figure S2-1c](#)) which delineates the maximum extension of preferential snow accumulation. Due to the high obliquity of the time-lapse images with respect to the land surface, no orthorectification could be performed on the raw images. However, for Zone B, the SCF was converted to a horizontal projected areal extent (A , m^2) using the relationship

between the SCF derived from time-lapse photos and A obtained from a set of georeferenced orthomosaics derived from unmanned aerial vehicle (UAV) surveys on 9 different dates during the 2019 field season ([Appendix A2-3](#)).

3.6.3. Environmental monitoring during the melt season

3.6.3.1. Meteorological data

The analysis of the ablation processes relied on detailed knowledge of the micrometeorological conditions on the ice patch. In 2017, only the air temperature (T_a , °C) was recorded at hourly intervals near the frontal edge of IP1 by a sensor (U22, Hobo®) installed in a radiation shield 1.5 m above the ground surface ([Figure 29](#); [Table S2-1](#)). The wind conditions were extrapolated from the wind data recorded at the SILA station ([Appendix A2-4](#)). In 2019, an automatic weather station (AWS) was installed on IP1 from 10 June to 19 July 2019 ([Figure 29](#)). The AWS monitored T_a , relative humidity (RH , %), wind speed (WS , ms^{-1}), wind direction (DIR , °), incoming shortwave radiation ($SW\downarrow$, $W\ m^{-2}$) and net radiation (Qr , $W\ m^{-2}$), and atmospheric pressure (AP). The station consisted of a 5 m-high steel mast inserted into a hole drilled into 2 m of snow and 50 cm of underlying ice ([Table S2-1](#)). T_a and RH sensors were installed in a radiation shield and data were sampled every 15 minutes and recorded by a data logger (Micro station, Hobo®). $SW\downarrow$, Qr and WS/DIR were sampled every 30 seconds, and 15 minute averages were recorded by a Campbell Scientific CR1000 datalogger. The pyranometer and net radiometer were installed parallel to the surface of the ice patch (~20°). The height of all sensors was adjusted as the melting progressed to keep the sensors orientations and heights as constant as possible. In addition to the AWS, snow temperature (T_{snow}) was monitored by a thermistor cable inserted into the snowpack (230 cm) from 7 June to 19 July ([Table S2-1](#)). It consisted of a series of 7 thermistors at 190, 150, 120, 90, 60, 30 and 5 cm above the ice surface connected to a data logger (Systems Smart Reader Plus 8, ACR system) that recorded temperatures at hourly intervals. Liquid precipitation was measured using a metric rain gauge (resolution 0.2 mm) installed near the base camp and read each day at 20:00hr. Snowfall was negligible. For both study seasons 2017 and 2019, the dominant daily sky conditions (fog, overcast, clear sky) were inferred from the visual inspection of time-lapse photographs.

3.6.3.2. The hydrological regime of the ice patch

The outflow discharge of meltwater was monitored by three cut-throat flumes (1 m long and 40 cm high) installed in major streams that drained IP1 (**Figure 29**). The flumes were equipped with a pressure sensor (Hobo U20; [Table S2-1](#)) that continuously recorded the water level (h_u , cm) into the flume (Paquette et al., 2017). h_u was then converted to free-flow discharge (Q_f , $\text{cm}^3 \text{ s}^{-1}$) (Siddiqui et al., 1996). The sums of the flows measured at the three flumes were calculated $Q_{f\ total}$. This dataset was used as a proxy to infer the fluctuation in the outflow hydrograph during the study period and correlating it with the melt rate.

3.6.4. Surface Energy balance

As the ice patch IP1 was covered by a thick seasonal snowpack throughout the study period, we used the standard approach for the computation of the surface energy balance (SEB) of a melting snow surface (Boike et al., 2003a; Gray and Male, 1981; Harder et al., 2018). The SEB is given by:

$$Q^* = Q_r + Q_h + Q_e + Q_c + Q_p \quad (3.2)$$

where Q^* is the net energy flux at the snow surface, Q_r is the net radiation, Q_h and Q_e are the sensible and latent heat exchange respectively, Q_c is conductive heat flux to the underlying snow and ice (W m^{-2}), Q_p is heat flux due to precipitation. All energy terms are expressed in W m^{-2} and are positive when they contribute energy to the snow surface and were calculated on an hourly basis and then averaged to obtain the daily energy fluxes. Since the slope of the snow surface was about 20° during the study period and that Q_r was measured parallel to the surface and not vertically (see [section 3.6.3](#)), the SEB was calculated parallel to the snow surface. Turbulent energy exchange Q_h and Q_e were estimated by the bulk aerodynamic approach based on the gradient of temperature, vapor pressure and wind speed between the snow surface and the lower atmosphere (Boike et al., 2003a). The SEB was calculated by hourly mean AWS measurements of Q_r , T_a , RH , WS . Equations for Q_h , Q_e and Q_c are detailed in [Appendix A2-5](#).

For deep and cold snowpack, modelling the melt rate in the early warm season is challenging because the surface starts to melt during the ripening phase before the cold content (CC) of the whole snow column is exhausted. In order to avoid an underestimation of the surface melt, we considered a top layer of 25 cm (Garen and Marks, 2005). We assumed that part of Q^* is first used

to change the energy stored within the top snow layer by raising the snow temperature (T_{snow}). The snowmelt (Q_m) then starts when the top snow layer becomes isothermal at the melting point (T_m) (cold content =0), as suggested by Equation. 3.3:

$$\begin{aligned} Q^* &= \Delta CC, \text{ if } T_{snow} < T_m \\ Q^* &= Q_m, \text{ if } T_{snow} = T_m \end{aligned} \quad (3.3)$$

The cold content (CC) of the snow layer is calculated by (Dingman, 2002):

$$CC = -c_i \cdot \rho_s \cdot h \cdot (T_{snow} - T_m) \quad (3.4)$$

where c_i is the heat capacity of the ice, ρ_s the density of snow derived from the snowpit dug on 6 June 2019 and h is the height of the snow layer, T_{snow} is the average temperature of the snow layer derived from thermistors.

The melt energy Q_m was then used to estimate the melt of the snow surface (ΔSWE_{SEB} , mm d⁻¹ w.e.) given in water equivalent by (Liston and Hall, 1995; Oke, 1987):

$$\Delta SWE_{SEB} = \frac{Q_m}{\rho_w \cdot L_f} \cdot 10^3 \quad (3.5)$$

where ρ_w is the density of liquid water and L_f is the latent heat of fusion (334 kJ kg⁻¹). ΔSWE_{SEB} was then corrected [$\div \cos(20^\circ)$] to give the surface melt along the vertical plane to be consistent with TLS measurements.

3.6.5. Spatio-temporal distribution of late summer ice-snow surfaces

At the scale of WHI, the spatial distribution of the late summer ice/snow surfaces, including the semi-permanent and the perennial ice patches, has been mapped using a set of optical satellite imagery (Landsat 8; Worldview; GeoEye) and aerial photographs available for 7 different years from 1959 to 2019 (**Table 4**). Images and photographs provided total coverage of the island and were obtained at the end of the melt season from late July to late August. The identification of ice/snow surfaces was done by a supervised classification using the Image Classification tool. The quality of the classification was evaluated by visual check for each image and manually adjusted if necessary.

Table 4. Summary of remote sensing data used. Sources: National Air Photo Library, of the U.S. Geological Survey, Pax Arctica and Planet Action Initiative © NSPO 2008 - National Space Organization, TaiwanDistribution Spot Image S.A., France All rights reserved.

Date	Image type	Resolution	Source
1959-08-10	Aerial	2.2 m	National Air Photo Library
1984-07-22	Aerial	0.8 m	National Air Photo Library
1988-08-18	SPOT-1	1.5 m	Water and Ice Research Lab
2008-08-18	Formosat	2 m	Planet Action Initiative
2011-08-26	Geo-EYE	0.44 m	Geocryolab
2016-07-17	Landsat-8	15 m	U.S. Geological Survey
2019-08-14	WorldView-3	0.37 m	Geocryolab

The resulting multi-year maps of the late summer ice-snow surface were merged into a raster and pixels were then classified according to the proportion of time they were occupied by a snow or ice surface at the end of the summer. Pixels where ice/snow was detected for all years (i.e. 100% of the time) were classified as “perennial ice patches”. Pixels where the presence of snow/ice is not permanent, but occurs more than half the time, fall into the category of “semi-permanent ice patches” and those where snow or ice occurs less than half the time were classified as “snow patches”. The distribution of the ice patches was then examined through its dependency on topoclimatic variables such as the elevation, slope aspect, topographic position (Topographic Position Index, TPI), summer potential incoming solar radiation (PISR) and wind field (Wind velocity index) ([Figure S2-2](#)). All these variables were derived from a 5-meter resolution DEM provided by the Polar Geospatial Center of the University of Minnesota (ArcticDEM v3.0) (Porter et al., 2018) ([Appendix A2-6](#)).

The temporal evolution of the late summer ice/snow patches was analyzed at two different spatial scales. First, we examined it over the whole island based on the satellite images detailed in **Table 4**. Second, we studied the evolution in the late-summer extent of the ice patch IP1 by analyzing a set of photographs from various sources (terrestrial, helicopter, aircraft) collected during previous field expeditions. Photographs with an oblique angle as small as possible and acquired as late as possible in the summer were preferred. The whole set of photographs were orthorectified based on georeferenced high-resolution UAV orthomosaics. The snow-ice extent

was then manually digitized in ArcGIS. These historical data were studied along with the air temperature trend. At WHI, the hourly air temperatures were recorded by a station managed by Parks Canada (2002-2005) which was then replaced by the SILA station (2005-2019) ([Table S2-1](#)). From these data, the mean monthly air temperatures (MMAT) and the cumulative positive degree-day (PDD_{air}, i.e. the sum of daily air temperature above 0°C) were calculated. Before 2002, the MMAT and PDD_{air} were reconstructed from the NCEP-NCAR reanalysis, bias-corrected with AWS observations (Kalnay et al., 1996) ([Appendix A2-7](#)). Finally, we also estimated the long-term variability of fog occurrence in summer at WHI based on the relative humidity (RH) time-series recorded at the SILA station ([Table S2-1](#)) which is a good proxy to infer the presence of fog. From the hourly RH, we calculated a fog index, i.e. the total number of hours with relative humidity above 95%, for the summer period (June to August) between 2006 and 2016, after which the sensor stopped working.

3.7. Results

3.7.1. Snow and wind regimes

At the SILA snow gauge, the mean end-of-winter snowpack thickness (SH_{max}) was 152 cm over the period 2006-2019 and was characterized by a low interannual variability (Std Dev. =25 cm) ([Figure 30a](#)). Only 2018 and 2019 stand out with a thicker snowpack, up to 200 cm. In 2014 and 2018, the snow patch persisted throughout the melt season. Detailed analysis of the hourly snow regime revealed that on average 7.5 ± 2.3 accumulation events ($\Delta SH > 5$ cm) that brought 27 ± 18 cm of snow were recorded during the cold season during the study period. 100% of the deposition events were associated with maximum hourly winds (V_{max}) above 6 m s^{-1} , indicating that snowdrift was a key process in the snowpack build-up.

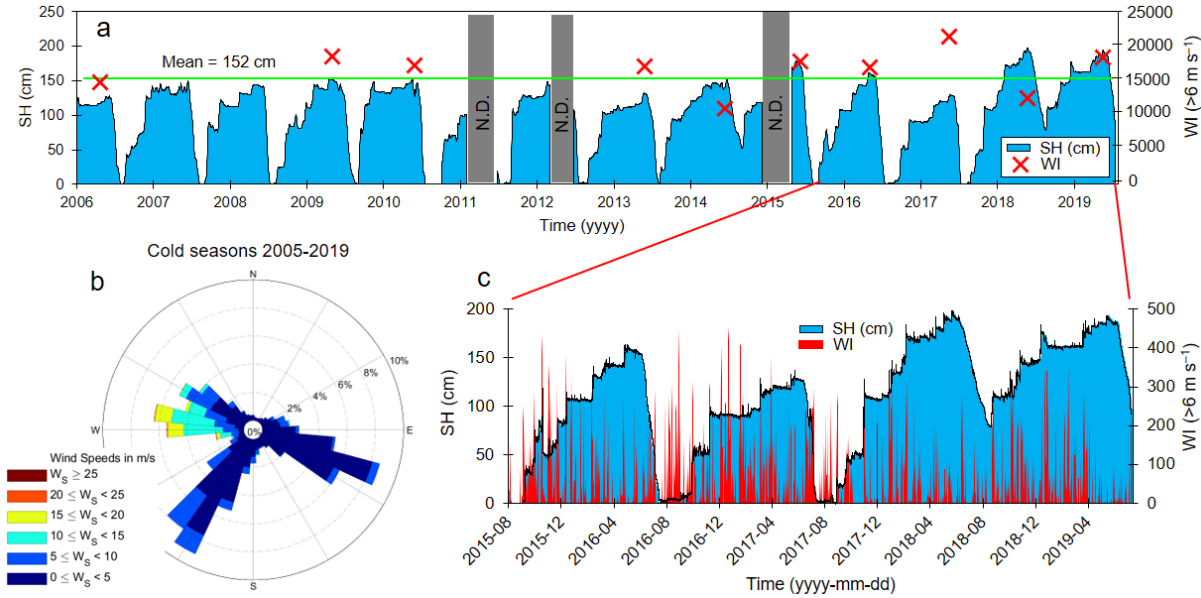


Figure 30. Snow and wind regimes recorded at SILA station from 2006 to 2019; a) Time-series of the daily snow height (incomplete data in 2010/11, 2011/12, 2014/15) and wind index (WI) of the cold season (Sept-May) (red crosses; incomplete wind data in 2006/07, 2007/08, 2010/11 and 2011/12). The wind index represents the cumulative maximum hourly wind speed $> 6 \text{ m s}^{-1}$, for the cold season (Sep-May). The green line represents the mean maximum snow height from 2006 to 2019; b) Wind rose of the cold season (Sept-May) constructed from hourly wind data for the 2006-2019 period; c) Close up on cold seasons 2015/16, 2016/17, 2017/18 and 2018/19 showing the hourly snow height and daily WI.

Deposition events were also usually associated with erosion events that removed partially, and sometimes completely, fresh deposits within hours (e.g. 17 October 2015; **Figure 30c**, [Figure S2-3](#)). The net mass balance between deposition and erosion of each snowdrift event was largely positive in the early cold season (**Figure 31a**). On average, maximum gains occurred in September (+40 cm on average) and they progressively tended to zero as the season progresses and the topographic hollow was filled. On average, ~78% of SH_{max} was already accumulated by the end of December (**Figure 31b**). Nearly 75 % of the wind events $> 6 \text{ m s}^{-1}$ were associated with snowdrift events ($\Delta SH > 5\text{cm}$) in October while this fraction dropped to 40% later in the season (**Figure 31b**). The most extreme snowdrift events, generally observed in September, can bring a considerable amount of snow over a very short time (e.g. 7 September 2011: +116 cm; 19 September 2007: +90 cm; 11 September 2009: +75 cm).

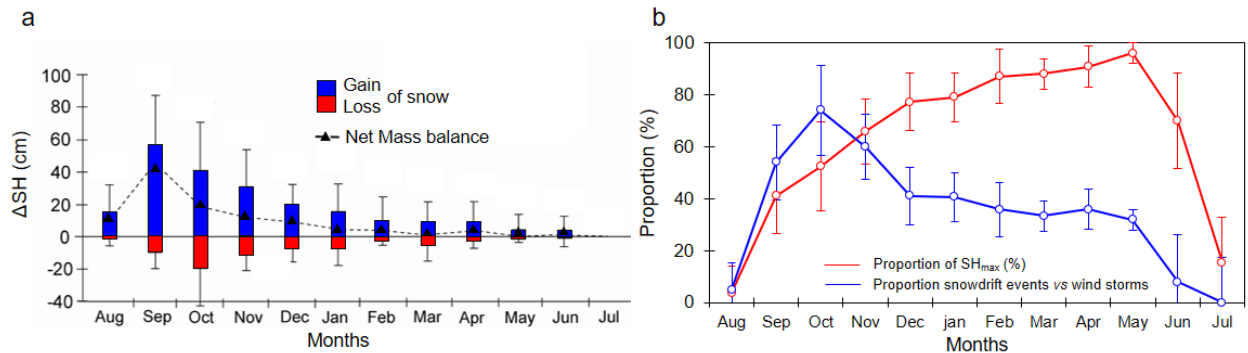


Figure 31. Average evolution of the snow regime throughout the cold season in the snow patch at the SILA station for the period 2006-2019. a) Mean monthly snow gains and losses (including erosion and compaction) and the resulting net mass balance and b) mean monthly snow height expressed as a proportion of the total end-of-winter snow height (SH_{max}) and the number of snowdrift events ($\Delta SH > 5\text{ cm}$) as a proportion of the total number of potential blowing snow events ($V_{max} > 6 \text{ m s}^{-1}$). Vertical bars indicate the standard deviation.

The prevailing direction for the winter wind for the speed range $5\text{--}10 \text{ m s}^{-1}$ was from SSW and WNW while strong winds ($>10 \text{ m s}^{-1}$) were mainly from the W. This same pattern repeated year after year (Figure S2-4) but the intensity of wind events was subject to substantial interannual variation as revealed by the cumulative hourly wind index (WI) calculated for each cold season (Figure 31a,b). The windiest cold season was recorded in 2016/17 ($WI=21410$) while the calmest was in 2013/14 ($WI=10600$).

3.7.2. Mass balance variables at the ice patch IP1

3.7.2.1. Seasonal snow accumulation

Figure 32 shows the snow conditions on IP1 and its surrounding area at the beginning of melt seasons 2016, 2017 and 2019. Photographs coupled with the snow depth measurements show great year-to-year variability in snow distribution. Maximum snow depth exceeded 200 cm on IP1 for the three years studied, however, very contrasting conditions existed regarding the spatial extent of the deep snow ($>150 \text{ cm}$). The greatest difference was between summer 2017, when deep snow was restricted to a narrow band along the upper ridge of IP1, and summer 2019, when it evenly covered the entire ice patch. Notable differences were also observed in snow density since the average density of the snow column was significantly higher in early summer 2016 (442 kg m^{-3}) than in 2017 (406 kg m^{-3}) and 2019 (395 kg m^{-3} , Figure S2-5). Together, these differences in snow

depth and density have produced significant interannual variability in the total volume of accumulated snow (V_{snow} m³ w.e., **Figure 32**).

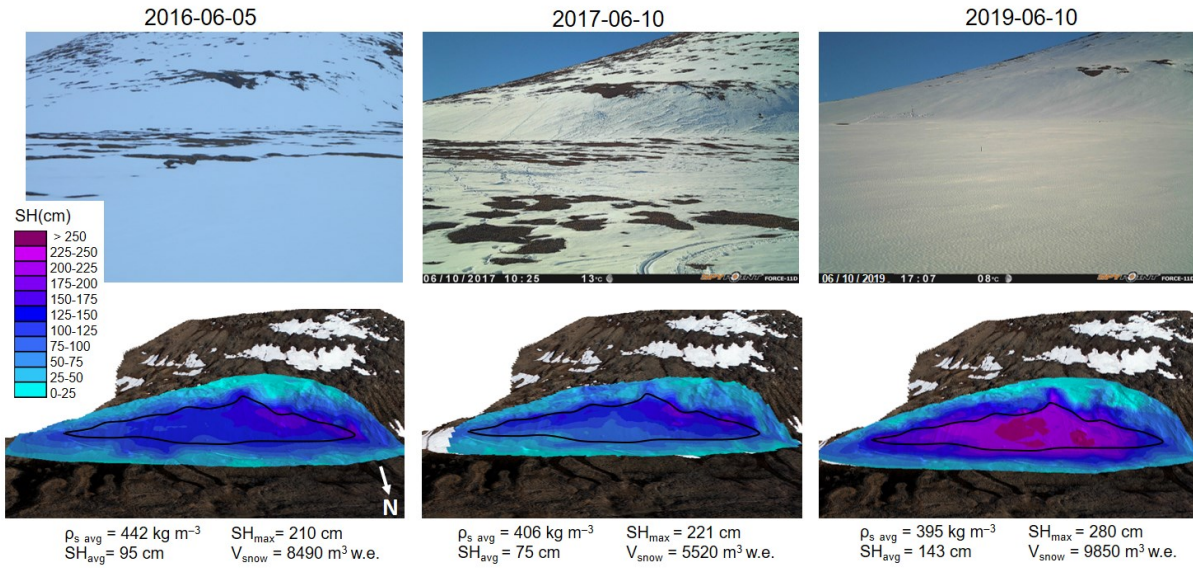


Figure 32. Time-lapse photographs of the ice patch system and its surrounding terrain and maps of the end-of-winter snow height (SH_{max}) on 5 June 2016, 6 June 2017 and 10 June 2019. The black line delimits the contour of the ice body as it was at the end of summer 2016. The average density of the snow column obtained by excavating the snow pit (ρ_s , kg m⁻³), the average and maximum snow height (SH, cm) and the total volume of snow (V_{snow} , m³ w.e.) for each of the three dates are shown at the bottom of the figure.

3.7.2.2. Ice thickness

The strongest GPR reflections (red dotted line in **Figure 33a**) reveal a discontinuity below the ice patch that was identified as the contact between the ice body and the bedrock substratum. The uppermost reflection (blue dotted line) corresponds to the contact between the seasonal snowpack and the ice surface. The topography of the bed of IP1 had a concave shape with a steep slope in the upper section with a break around 45 m from the start of the line and at 47 m a.s.l. The map of ice thickness presented in **Figure 33b** shows that in July 2019 the ice body thickness reached ~380 cm and the total volume of ice (V_{ice}) was estimated at ~14 100 m³, giving a w.e. of ~12 500 m³. Including the remaining snowpack above as measured on 5 July 2019 ($V_{snow} = 10 500$ m³, giving 5 500 m³ w.e; **Figure S2-6**), the total volume of the ice patch system (V_{total}) was 24 600 m³ for a w.e. of 19 600 m³.

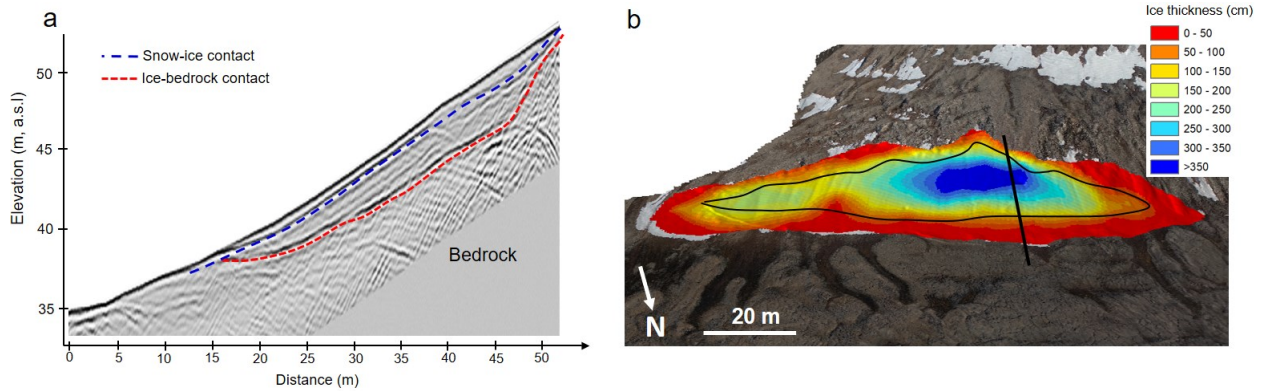


Figure 33. a) 2D visualization of a profile made in the central part of the ice patch in 2019 using 200 MHz antennas (the track is represented by the black line in b); b) Interpolated map of the ice thickness based on the series of GPR tracks made in July 2019 (see **Figure 29** for all GPR tracks location). The black line in b delimits the contour of the ice body as it was at the end of summer 2016.

3.7.2.3. Snowmelt monitoring in summers 2017 and 2019

At the scale of the ice patch IP1, the spatial pattern in ablation (ΔSH_{TLS} , cm) for both study periods 2017 and 2019 is shown in **Figure 34**. The snow height decreased by 85 cm between 10 June and 12 July 2017 and by 133 cm between 10 June and 20 July 2019. The maps revealed strong spatial variability in the surface ablation over the ice patch with a repeated pattern in both years.

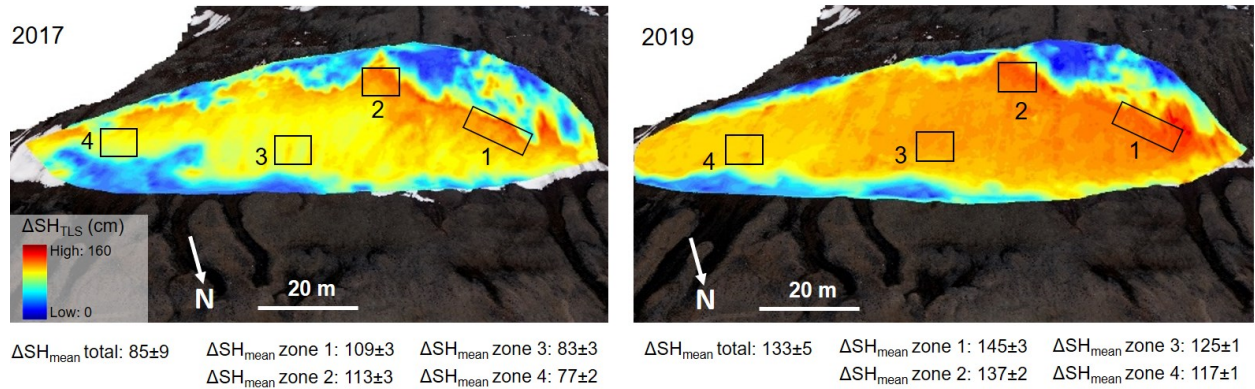


Figure 34. Maps of the total surface ablation (ΔSH_{TLS} , in cm) during the study periods 2017 and 2019 based on daily terrestrial laser scan (TLS) surveys of snow/ice surface position. The black boxes represent the averaging area used to highlight the spatial variability of the ablation. Mean (\pm Std Dev) values for the whole ice patch and each zone are presented below each panel. See **Figure S7** for the daily evolution of ΔSH_{TLS} of each zone.

The highest values were measured immediately below the upper edge and on the west side of the ice patch (Zones 1 and 2) while the central and east parts (Zones 3 and 4) exhibited values slightly

below the average for the whole ice patch. The spatial variability of the ablation tended to increase over time ([Figure S2-7](#)).

The daily evolution of snowmelt on IP1 and its surroundings during the study period 2017 and 2019 is shown in [Figure 35](#). In 2017, the seasonal snowpack was already discontinuous on 10 June and declined rapidly to disappear almost completely on 25 June ([Figure 35a](#)). The total volume of the ice patch system, which combines the volume of ice and seasonal snow, was $\sim 25\ 500\ m^3$ at the beginning of the melt season ([Figure 35b](#)).

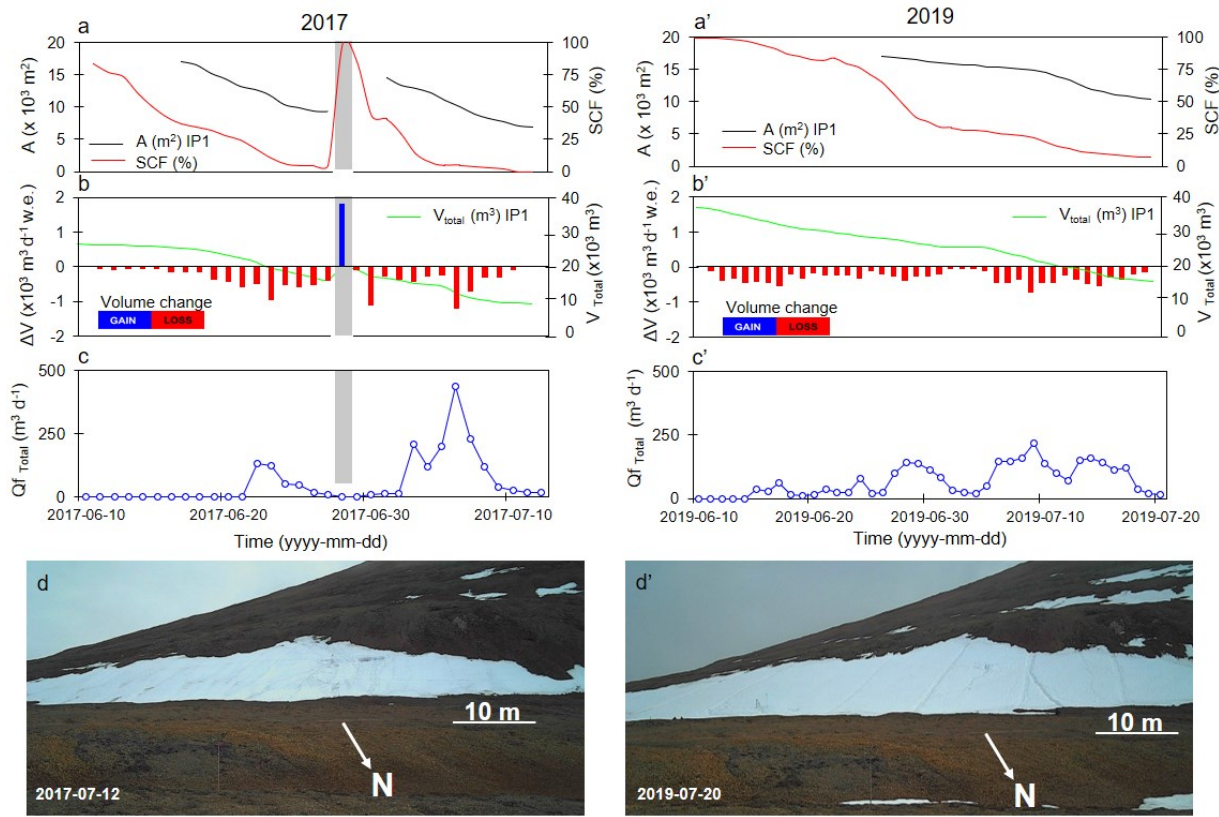


Figure 35. Monitoring of the snowmelt from 10 June 2017 to 12 July 2017 (left side) and from 10 June to 20 July 2019 (right side): a and a') The daily evolution of the areal extent of the ice patch system IP1 (A , m^2) within Zone B ([Fig. S2-1](#)) and of the seasonal snow cover fraction (SCF, %) within Zone A ([Fig. S2-1](#)) derived from a time-lapse camera; b and b') daily evolution of the total ice patch system volume (snow and ice together) (V_{total} , m^3) along with the daily volume change in water equivalent (ΔV , $m^3\ d^{-1}$ w.e.) measured by terrestrial laser scan (TLS). The red bars (negative ΔV) give an estimation of the melt rate (M , $m^3\ d^{-1}$ w.e.); c and c') Daily meltwater outflow discharge ($Q_{f, total}$) measured at flumes; d and d') Picture of IP1 illustrating the condition the system at the end of each study period.

The melt rate (M) was low between 10 to 16 June 2017 ([Figure 35b](#)) and then increased rapidly to reach a first peak on 23 June ($-950\ m^3\ d^{-1}$ w.e.). Meltwater started to flow out at this time at the

flumes (**Figure 35c**). On 28 June, a major snowstorm re-filled the ice patch system with $\sim 1\ 850\ \text{m}^3$ w.e. of new snow and temporally interrupted the water outflow. The rapid melt of this snow in the following days led to a peak in ablation on 30 June ($1\ 100\ \text{m}^3\ \text{d}^{-1}$ w.e. on). The highest ablation occurred on 6 July ($1\ 200\ \text{m}^3\ \text{d}^{-1}$ w.e.), leading to a high peak in the meltwater discharge (Q_{total}). At the end of the study period on 10 July 2017, the total volume of the ice patch was $9\ 500\ \text{m}^3$ and its areal extent was $6\ 500\ \text{m}^2$ (**Figure 35b,d**). Analysis of the time-lapse photograph dataset revealed that the minimum extent was reached on 11 August with $3\ 850\ \text{m}^2$ ([Figure S2-8](#)).

In 2019, the decline of the seasonal snowpack was slower than in 2017 in the first half of June, but it accelerated considerably in the second half of the month. Some seasonal snow patches around IP1 persisted until the end of the period (**Figure 35a'**). The total volume of the IP1 system was $\sim 38\ 000\ \text{m}^3$ in early June, 50% higher than in 2017 (**Figure 35b'**). The melt rate exhibited less pronounced daily variations and peak flows were weaker than in 2017 (**Figure 35c**). The highest daily ablation peak over the study period was reached on 9 July with a loss of $720\ \text{m}^3\ \text{d}^{-1}$ w.e., resulting in a peak flow of $217\ \text{m}^3\ \text{d}^{-1}$ at the flumes. At the end of the study period on 20 July 2019, the total ice patch volume reached $16\ 200\ \text{m}^3$ (**Figure 35d'**). It represents a loss of 58% of its initial volume in 40 days. At the end of field season 2019 (20 July), the ice patch extent was $10\ 300\ \text{m}^2$ (**Figure 35**, Photo d').

For both study periods 2017 and 2019, the daily changes in snow height (ΔSH_{TLS}) measured for IP1 were similar to those measured by the snow gauge at SILA station (ΔSH_{SILA}) (Pearson's correlation test, $r = 0.91$, $p < 0.0001$ in 2017 and $r = 0.83$, $p < 0.0001$; [Figure S2-9](#)). The daily fluctuations of Q_{total} show a strong correlation with M measured on IP1 (Pearson's correlation test, $r = 0.67$, $p < 0.01$ in 2017 and $r = 0.87$, $p < 0.0001$ in 2019 ([Figure S2-10b](#)) except at the beginning of the melt season and during the snowstorm event in 2017 ([Figure S2-10a](#)) due to the lag in the response of the hydrograph to the surface melt rate.

3.7.3. Surface energy balance

3.7.3.1. Meteorological conditions

An overview of the meteorological and environmental variables for the study periods 2017 and 2019 is given in **Figure 36**.

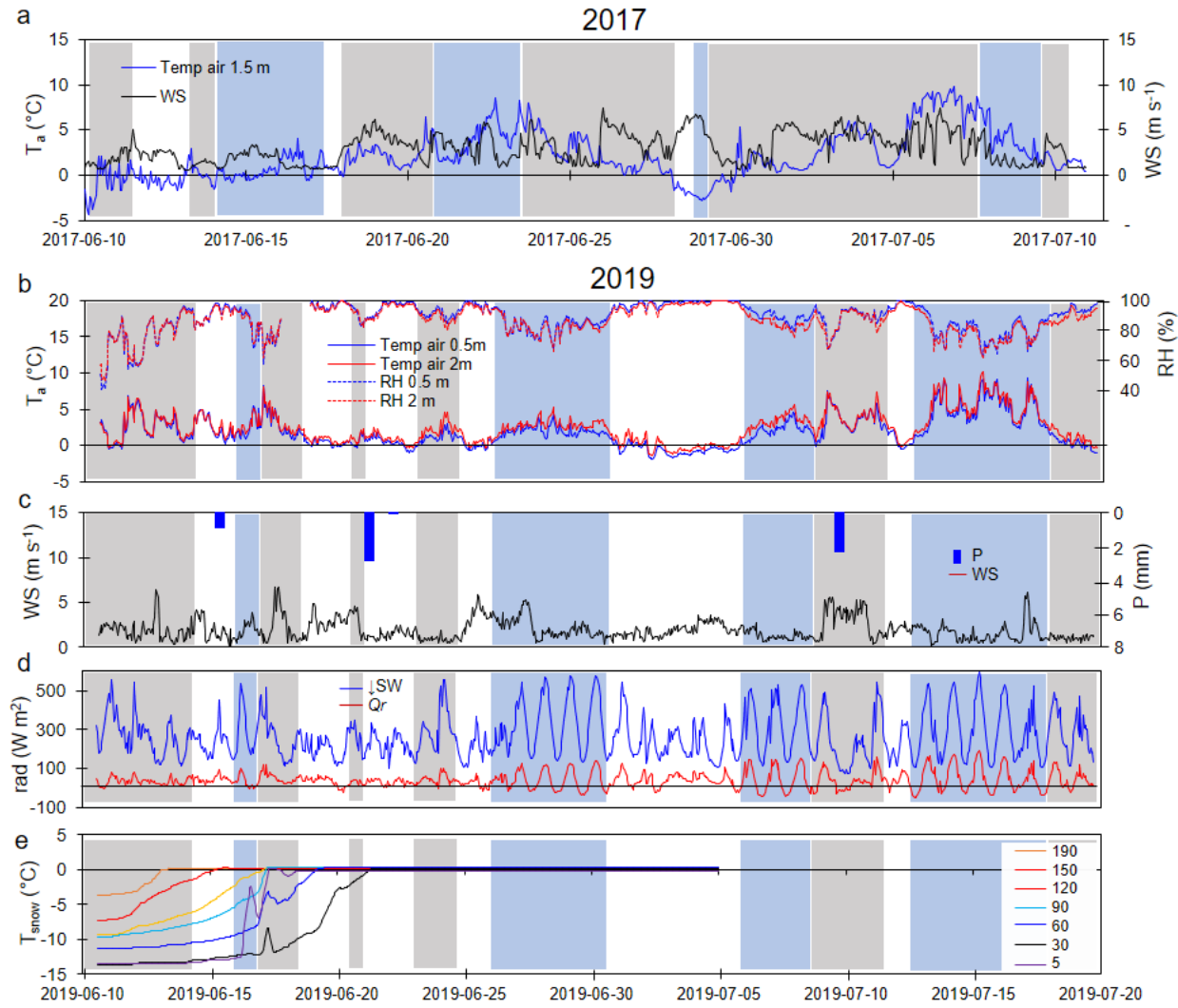


Figure 36. Summary of hourly measured meteorological variables during the study periods. (a) 2017 air temperature (T_a) and mean wind speed (WS). (b) 2019 T_a and relative humidity (RH); (c) 2019 WS and daily precipitation; d) 2019 Incoming solar radiation ($SW\downarrow$) and net radiation (Qr); and e) 2019 snow temperature (T_{snow}). The upper two thermistors (190 and 150 cm above the ice surface) emerged from the snow due to melting on June 21 and June 29, respectively. Subsequent temperatures are not shown in the graph. The cable was removed on July 5. The background colors indicate the sky conditions; white for fog, grey for overcast and blue for clear sky.

In summer 2017 (Figure 36a), the mean daily air temperature (T_a), recorded in the downslope margin of the ice patch fluctuated from -4°C to 9°C , with an average of 1.7°C for the whole period. The wind records (data based on SILA measurements, modified with correlations; Appendix A2-4) gave mean hourly wind speed of 3 m s^{-1} on average over the study period and a maximum mean hourly value of 8 m s^{-1} , and a prevailing direction from the west. Over the study period, there was fog, cloud cover and clear sky, 10%, 65% and 25% of the time, respectively. In

summer 2019 (**Figure 36b**), T_a at 0.5 and 2 m above the snow surface had an average of 1.7°C and 2.4°C respectively over the study period. The minimum T_a (-2°C) was recorded at 0.5 m during foggy and calm conditions on 2 July while the highest value (10.1 °C) was recorded during warm and dry spells associated with high winds on July 13. The relative humidity (RH) was generally high, reflecting the common foggy conditions, and fluctuated in opposite phase to the air temperature.

In 2019, the mean hourly wind speed of 1.9 m s⁻¹ on average over the study period with a maximum mean hourly value of 7 m s⁻¹, and a prevailing direction from the west similar to 2017 (**Figure 36c**; [Figure S1-11](#)). There was fog 30% of the time, a cloud cover 30% of the time and clear-sky 34% of the time. The precipitation fell essentially as rain and drizzle during the study period 2019 and reached a cumulative value of only 7 mm. During clear-sky conditions, the incoming solar radiation ($SW\downarrow$) and the net radiations (Qr) followed a diurnal cycle with maxima > 500 W m⁻² and minima between < 150 W m⁻² for the former, and negative minima, as low as -50 W m⁻², and maxima from 110 W m⁻² to 175 W m⁻² as the summer progressed for the latter (**Figure 36d**). Finally, the thermistors chain in the snowpack showed that the snow temperature (T_{snow}) at a height of 190 cm above the ice surface (i.e. ~40 cm below snow surface) reached the melting point on 11 June while the temperature was ~ -13°C near the snow/ice interface (height of 5 cm). The temperature of the snow gradually increased at first. Then two thermal peaks occurred, thus perturbing the thermal gradient within the snowpack (**Figure 36e** and [Figure S2-12](#)). The deepest thermistor (5 cm) was the first to be affected by a drastic rise in snow temperature, rising T_{snow} from -12.5 to -2.6°C in a few hours, thus indicating a sudden pulse of liquid water on the impermeable surface of the ice (horizontal flow). The second thermal peak was more moderate but occurred simultaneously at heights of 60 cm, 30 cm and 5 cm above the ice surface, reflecting the vertical percolation of meltwater into the snowpack. These thermal peaks brought the temperature of the snow/ice interface close to 0 °C from 17 June while it was still around -10 °C at 30 cm height. The whole snow column became isothermal at 0 °C after June 21.

3.7.3.2. Daily mean evolution of the SEB terms in 2019

The daily variability of the SEB is presented in **Figure 37a**. Both net surface radiation Qr and the sensible heat flux Qh were sources of heat to the snow surface throughout the period. Qr varied from 16 to 70 W m⁻², with the highest values generally reached under clear sky conditions

and the lowest under overcast conditions. Sensible heat flux Qh varied from 0 to 75 W m^{-2} . The highest values of Qh were observed during windy and warm days (e.g. 9–10 and 17 July). The latent heat flux Qe was also a source of heat through condensation, except in the early period (June 10–11) when a net loss of latent heat occurred at the surface through evapo-sublimation. Qe varied between -15 to 27 W m^{-2} . Maximum gains of heat by Qe were observed on 9–10 July, similar to Qh , due to condensation. Heat loss by conduction (Qc) at the snow surface was small (-1.7 W m^{-2}) and was limited to the first two days of the period as the cold content (CC) of the surface layer (0–25 cm below snow surface) was rapidly eliminated (Figure 37a). The sum of all SEB terms gives a net gain of heat (Qm) throughout the period, peaking on July 9 with 138 W m^{-2} .

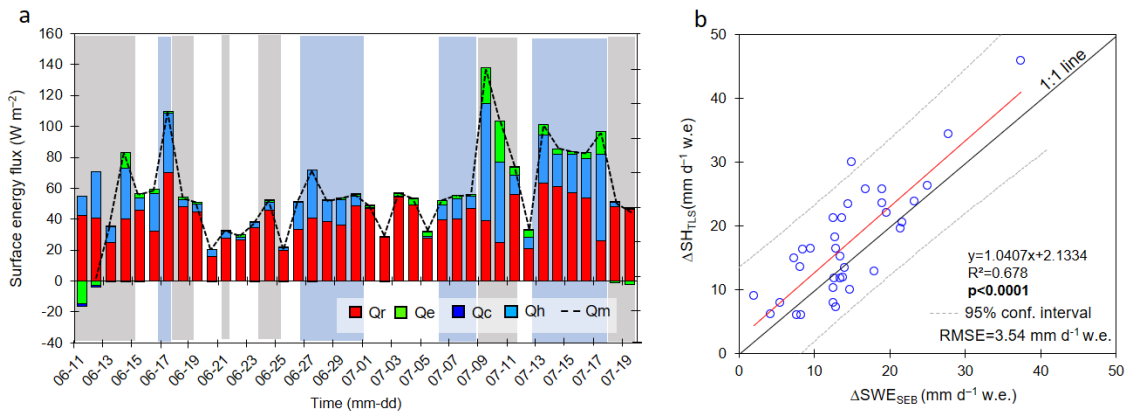


Figure 37. a) Daily mean values of energy balance terms with net radiation (Qr), sensible heat flux (Qh), latent heat flux (Qe), heat flux by conduction to the underlying ice (Qc) and the melt flux (Qm). The background colors indicate the sky condition; white for fog, grey for overcast and blue for clear-sky; b) Comparison between daily melt rate calculated from the surface energy balance (ΔSWE_{SEB} , $\text{mm d}^{-1} \text{ w.e.}$) and measured by TLS (ΔSH_{TLS} , $\text{mm d}^{-1} \text{ w.e.}$). The red line is the linear regression line and the grey lines are the 95% confidence intervals. RMSE means Root Mean Square Error.

The relative contribution of each term to the SEB is given in Figure S2-13. On average, Qr provided 74% of total energy gains to the ice patch system while the remaining 26% came from Qh (21.5%) and Qe (4.5%). However, an ANOVA analysis indicated that 77% of the variance in the Qm is explained by Qh . The comparison between the daily melt rate derived from TLS (ΔSH_{TLS}) and the one obtained from SEB (ΔSWE_{SEB}) shows good agreement ($R^2=0.68$; RMSE= 3.54 mm d^{-1}) even though calculated values are slightly underestimated by $\sim 3 \text{ mm d}^{-1} \text{ w.e.}$ on average (Figure 37b).

Specific days representative of three different synoptic conditions (Figure 38) common in

summer along the northern coast of Ellesmere were selected: clear sky (28 June), fog (5 July) and overcast (9 July) days. A summary of measured meteorological and calculated SEB terms for each case is given in [Table S2-2](#) and an overview of the synoptic conditions (i.e. 500-hPa geopotential heights and 850-hPa air temperature) obtained from the NCEP–NCAR reanalysis are present in [Figure S2-14](#):

- a) Case 1 (June 28; [Figure 38a](#)): That day was under the influence of a high-pressure system over the Arctic Ocean ([Figure S2-14](#)). At our site, there was a pressure of 1029 hPa, cloudless conditions, cool air temperatures (T_a daily = 3.1 °C and 2.2 °C at 2 m and 0.5 m) and low winds ([Table S2-2](#)). $SW\downarrow$ reached 550 W m⁻² around 7:00 hr (local time), corresponding to a peak in Qr of ~120 W m⁻². The combination of low westerly winds and cold temperatures limited Qh . Qe remained negligible. On average, the ice patch gained 48.4 W m⁻² over this day, leading to melting of 14.5 mm d⁻¹ w.e. Qr was the dominant heat source (79%) followed by Qh (20%).
- b) Case 2 (5 July; [Figure 38b](#)): Synoptic conditions were characterized by a shallow trough between two low pressure systems ([Figure S2-14](#)). The conditions were calm with low winds and fog that was present all day. T_a remained near the freezing point (T_a daily = 0.3 and -0.4°C at 1.5 and 0.5 m respectively) ([Table S2-2](#)). Maximum $SW\downarrow$ reached ~450 W m⁻² and Qr peaked at only 110 W m⁻² around 8:00 hr. Because of the calm and near-freezing conditions, both Qh and Qe remained low. The supply of heat to the ice patch was only 32 W m⁻² on average for the day, producing melting of 8.8 mm d⁻¹ w.e. Qr contributed for 90% while Qh and Qe contributed for 2% and 8% respectively.
- c) Case 3 (9 July; [Figure 38c](#)): That day was under the influence of a low-pressure system that circulated further south over central Ellesmere Island and that advected warm air (>5 °C at 850 hPa) from the southwest ([Figure S2-14](#)). At WHI, it was cloudy and windy with light rain and drizzle. The 15-min average wind (WS) reached 7.9 m s⁻¹ with gusts exceeding 10 m s⁻¹ ([Table S2-2](#)). T_a reached slightly above 8°C around 5:00 hr. T_a daily were 4.6 and 4.3°C at 2 and 0.5 m respectively. Qh peaked at 180 W m⁻² and remained higher than Qr during most of the day. Qe remained weak with a maximum value of 40 W m⁻². The gain of energy to the ice patch was 144.5 W m², resulting in substantial melting of 38.2 mm d⁻¹ w.e. Qh was the main term of the SEB by providing 57% of the total energy. Qr and Qe contributed about 27% and 16% respectively.

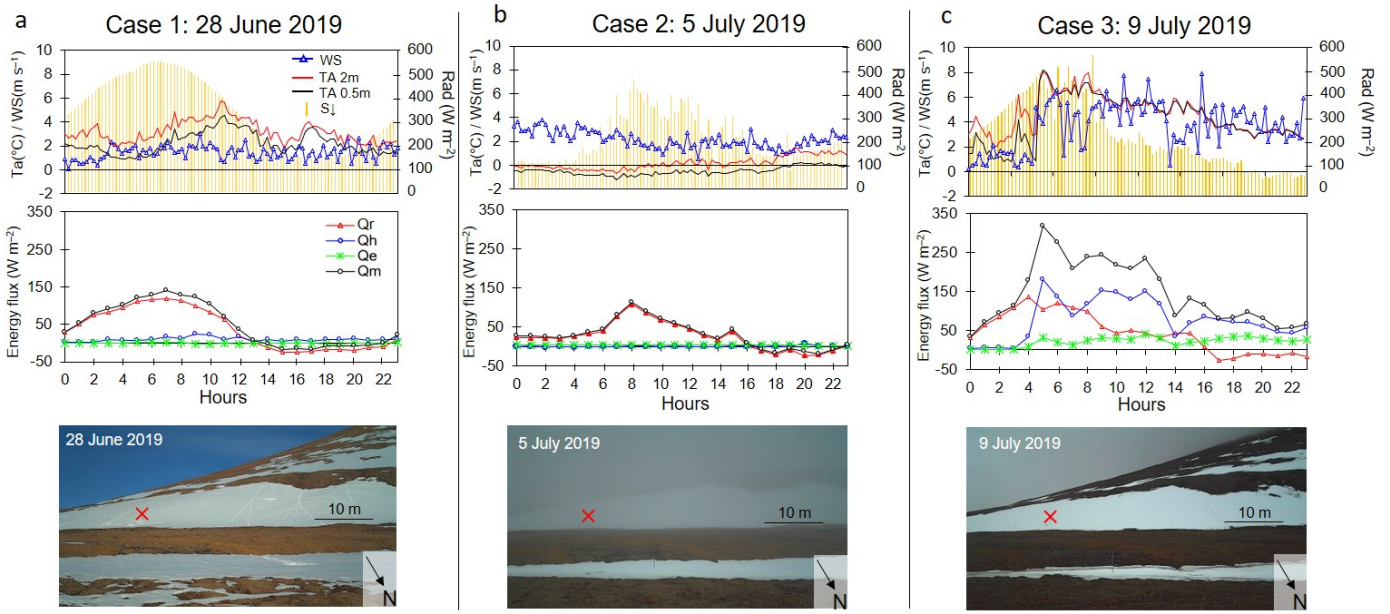


Figure 38. Diurnal cycle of the meteorological variables, including the 15-min average air temperature (T_a , $^{\circ}\text{C}$) at 2 m and 0.5 m above the snow surface, wind speed (WS , m s^{-1}) and incoming solar radiation (SW_{\downarrow} , W m^{-2}), and the hourly evolution of surface energy balance terms, i.e. net radiations (Q_r , W m^{-2}), sensible heat fluxes (Q_h , W m^{-2}), latent heat fluxes (Q_e , W m^{-2}), the melt fluxes (Q_m) and time-lapse photos for the three different cases that reflected the dominant conditions encountered along the north coast of Ellesmere Island: (a) Case 1 (28 June 2019) was characterized by sunny and calm conditions; (b) Case 2 (5 July 2019) was a foggy day and (c) Case 3 (9 July 2019) was marked by the influence of a low-pressure system with high winds and warm air advection. Red cross on the picture locates the automatic weather station on the ice patch. Note that the daily solar radiation peak early in the morning due to the northeast orientation of the ice patch.

3.7.4. Spatio-temporal evolution of the ice patch and late summer snow patches at the scale of Ward Hunt Island

3.7.4.1. Distribution patterns

Perennial ice patches covered $\sim 350\,000 \text{ m}^2$ (2.5% of WHI's total surface area) while the semi-permanent ones covered a total of $\sim 1\,070\,400 \text{ m}^2$ (8% of WHI's total surface area) (Figure 39). WHI features ~ 20 main individual perennial ice patches. They mostly have an elongated shape (Mean aspect ratio of 4.1 ± 2.3) and have a minimum extent of $\sim 20\,000 \text{ m}^2$ on average (Figure S2-15). Their distributions with respect to elevation, landforms, slope aspect, and wind and solar radiation exposure are summarized in Figure 39.

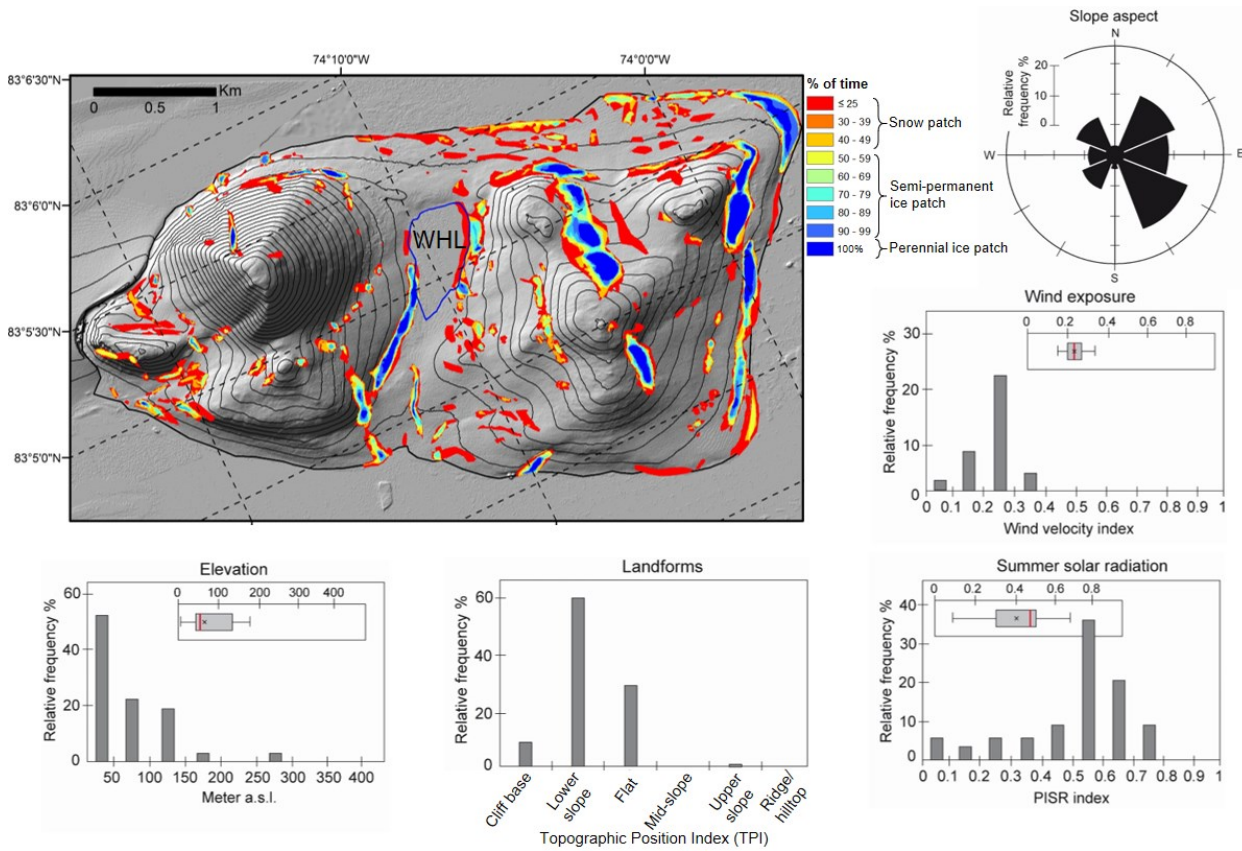


Figure 39. Map of the seasonal, semi-permanent and perennial ice patches on Ward Hunt (WHL=Ward Hunt Lake). Graphs show the distribution of the perennial ice patches with respect to topo-climatic parameters. Maps of topographic position index (TPI), slope aspect, wind exposure index and potential incoming solar radiation (PISR) index are presented in [Figure S2-2](#).

Most of the ice patches are found at lower elevations (mean=67±6 m a.s.l) and are preferentially present on lower concave slopes, cliff base and flat terrain. Easterly-facing slopes and wind-sheltered slopes (wind velocity index <0.4) are most favourable to the presence of ice patches. In contrast, the effect of exposure to insolation is more difficult to detect because most ice patches are present in moderately exposed areas (Potential incoming solar radiation index ~0.5). There are no ice patches over the areas that received the largest amount of solar radiation (PISR index >0.8).

3.7.4.2. Temporal evolution

At WHI, the evolution of the mean annual air temperature (MAAT) shows a period of relative stability from the 1950s to the end of the 1980s, being -20.1 ± 0.7 °C on average ([Figure 40a](#)). Since the early 1990s, in contrast, it increased rapidly by 3.5 °C to present (+1.16 °C

decade^{-1}). The warmest year was in 2016 (-15.4°C), closely followed by 2010 (-15.8°C). This recent warming translated into an increase in the cumulative melting degree-day (PDD_{air}) (**Figure 40a**). After three decades of cool summers (avg PDD_{air} <60), a trend of increasing PDD_{air} emerged in the 1990s. Since 2000, abnormally warm summers ($>2\sigma$ of 1980–2010 avg PDD_{air}) have been recurrent as in 2003; 2008; 2011 and 2012, and particularly 2016 (PDD_{air} =196). The shift in the air temperature trend was also marked by larger interannual variability since warm summers regularly alternate with cool ones exhibiting PDD_{air} below 70 (e.g. 2004, 2005, 2013, 2014, 2018). Closely related to the temperature conditions near the surface, the fog frequency, studied through the summer (JJA) fog index, derived from the relative air humidity data from the SILA station, also exhibited a high interannual variability from 2006 to 2017 ([Figure S2-16a](#)). Fog was more frequent in August, but it mainly influenced the air temperature of July, since PDDs show a clear inverse correlation with the fog index (Pearson's correlation test, $r=-0.65$, $p<0.04$; [Figure S2-16b](#)).

Extents of the late-summer snow and ice patches at the scale of WHI (A_{WHI} , m^2) and the ice patch IP1 (A_{IP1} , m^2) are given in **Figure 40b**. Over the island, A_{WHI} was highly variable between the 8 years of analysis, ranging from $17 \times 10^5 \text{ m}^2$ at the end of the cool summer 2018 (67 PDD_{air}) to $3 \times 10^5 \text{ m}^2$ in 2011 (133 PDD_{air}). IP1 never disappeared over the study period, even in abnormally warm summers 2008, 2011 and 2016 ($>2\sigma$ of 1980–2010 avg of PDD_{air}; **Figure 40a**). From 2001 to 2019, A_{IP1} was 7 700 m^2 on average and similarly to A_{WHI} the interannual variability was high (Std Dev.= 2 526 m^2). The highest extent was measured in 2014 with 11 502 m^2 and the lowest one in 2017 with 3 821 m^2 . Summer 2017 was particularly critical since the ice body was exposed to ablation from the end of July ([Figure S2-8](#)). Behind the high interannual variability, there is no statistically significant trend in the ice patch extent from 2001 to 2019 and the earlier sporadic observations in 1959, 1984 and 1988 were of a comparable order of magnitude to the recent period.

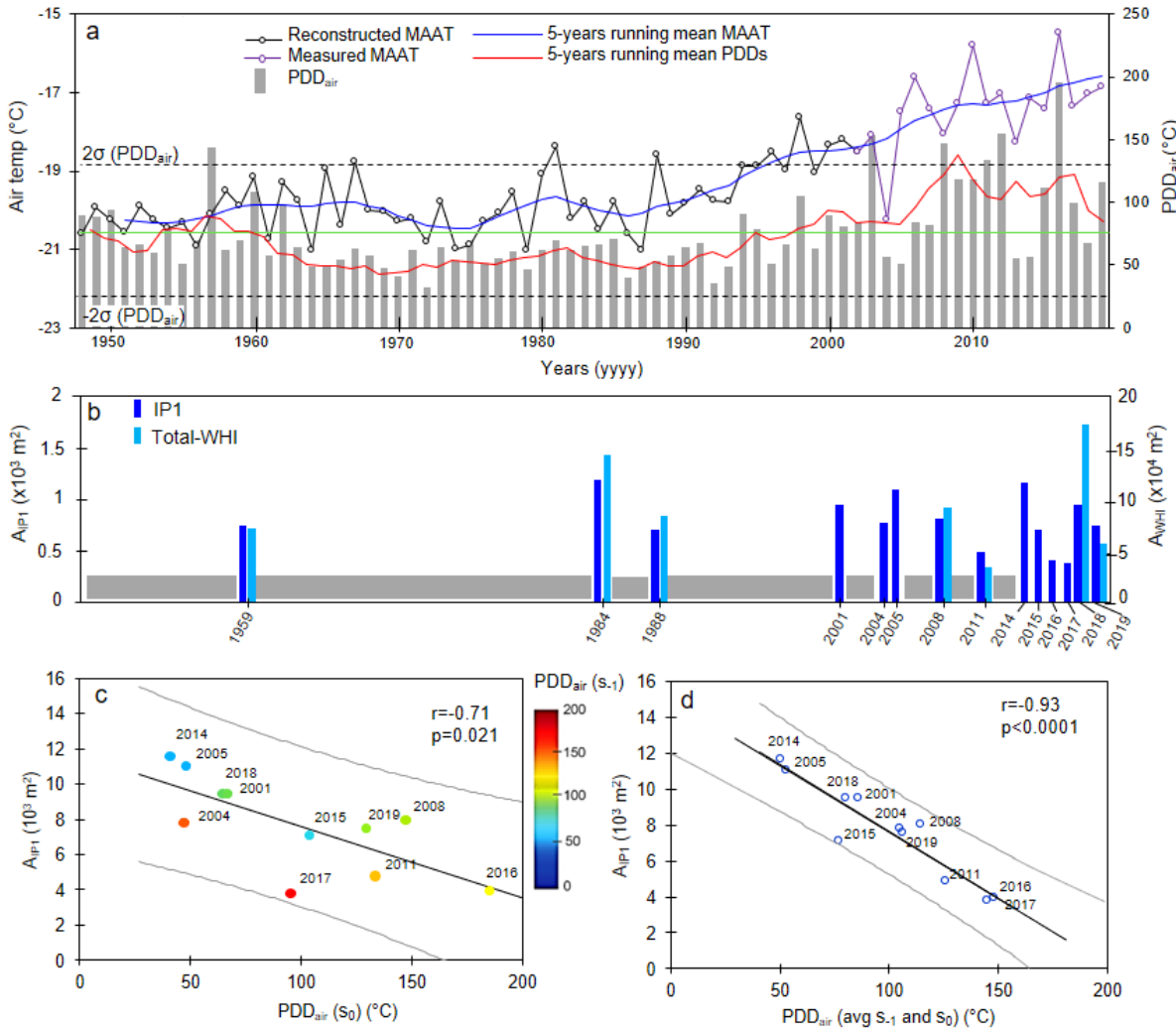


Figure 40. a) Reconstructed (NCEP/NCAR re-analysis, 1948-2002) and measured mean annual air temperatures (2003-2019) (MAAT) and corresponding positive degree-days (PDD_{air}) for the warm season from 1948 to 2019 at WHI. The colour solid lines represent the 5-year running mean for MAAT (blue) and PDD_{air} (red) and the green line marked the 1980-2010 average of PDD_{air} with black dashed lines representing the two-standard deviation line (-2σ and $+2\sigma$). Summers with PDD_{air} above the $+2\sigma$ line are considered abnormally warm; b) Long-term evolution of extents of the late summer snow/ice surfaces at the scale of WHI (A_{WHi}) and the ice patch IP1 (A_{IP1}); c) Relationship between A_{IP1} and PDD_{air} for the period from 2001-2019 with the colour scale of points according to the previous summer PDD_{air} (s_{-1}), and d) Relationship between A_{IP1} and the average between PDD_{air} of a given summer (s_0) and PDD_{air} of the previous summer (s_{-1}). For c and d, the black line is the linear regression line and grey lines are the 95% confidence interval.

As suggested by Figure 40c, the minimum ice patch extent A_{IP1} was inversely correlated with PDD_{air} of warm seasons for the period 2001–2019 (Pearson's correlation test, $r = -0.71$, $p < 0.05$). The dispersion of individual years was mainly related to the PDD_{air} of the previous summer (s_{-1}). Thus, averaging PDD_{air} value of a given summer (s_0) with that of the previous summer (s_{-1}) yields

a much stronger correlation (Pearson's correlation test, $r=-0.93$, $p<0.0001$) (**Figure 40b**), meaning that this averaged value is suitable for predicting the ice patch extent.

3.8. Discussion

3.8.1. Main mass gain to the ice patch system

Ice mass gain in IP1 occurred primarily through the aggradation of superimposed ice by the refreezing of meltwater upon the old ice surface at the beginning of the warm season ([Chap. 2](#)). Although inflows of water from upslope occur and contribute to feeding ice growth (Ballantyne, 1978; Lewkowicz and Harry, 1991), we consider that seasonal snow accumulation represents the primary mass gain to the system.

Along the north coast of Ellesmere Island, precipitation is limited during the cold season, being most likely lower than 100 mm from September to May as at Alert (Environment Canada, 2021). In addition, a significant part of this precipitation is lost by sublimation due to the dry and windy conditions that prevail in winter. Estimating the sublimation rate is difficult but, at WHI, we assume it is likely comparable to what Liston and Sturm (2002) reported for the north coast of Alaska where more than 30% of the winter precipitation sublimates. These low precipitation amounts are unevenly redistributed across the landscape by winds so that the overall snowpack in polar deserts is thin and discontinuous (< 30 cm; [Davesne et al., 2021](#); Domine et al., 2018a; Royer et al. 2021), but locally significant amounts of snow can accumulate (**Figure 30** and **Figure 32**) by wind action. The proxy data from the SILA station emphasized that wind-driven processes – i.e. the snow erosion, transport and deposition – are the main contributors to deep snow accumulation in specific places (**Figure 30**). As shown in **Figure 31**, the topographic snow traps filled up quickly at the beginning of the cold season (80% of SH_{max} was reached before January on average at SILA) due to frequent winds above 6 m s^{-1} beyond which snow drifting starts to occur. Although September-October is the snowiest period of the cold season ([Figure S2-17a](#)), the total amount of precipitation is still too low to explain the rapid accumulation of deep snow. We consider that the apparent high availability of snow at WHI is likely due to a virtually unlimited fetch created by the smooth surface of the surrounding cryosphere (i.e. ice rise, sea ice) (Benson and Sturm, 1993; Pomeroy et al., 1997). Later in the winter, the retention capacity of the snow trapping sites rapidly decreases as it reaches its equilibrium profile (Tabler, 1975) and the mass balance of snowdrift

events then tended towards zero, regardless of the increase in precipitation at the end of the winter ([Figure S2-17a](#)) and the magnitude of drifting snow fluxes ([Figure 31](#)) (Benson and Sturm, 1993; Mases et al., 1998; Sturm et al., 2001).

The equilibrium profile of the seasonal snow accumulation is primarily controlled by topography (e.g. a break of slope caused by a cliff base in the case of IP1; [Figure 33](#) and [Figure 39](#)). The interannual variability of maximum snow accumulation in topographic niches does not appear to be affected by the amount of precipitation during the cold season ([Figure S2-17b](#)), but it is strongly modulated by wind conditions (speed and direction; storm frequency). Wind data show that the prevalent westerly orientation of the strongest winds is repeated year after year, as it is mainly driven by the synoptic-scale air mass circulation along the Ellesmere coast ([Figure 30b](#); [Figure S2-3](#)). The frequency and magnitude of wind events, however, are subject to important interannual variability as highlighted by the calculation of the wind index ([Figure 30a, c](#)). The contrasted snow conditions observed over the 2016–2019 period at the SILA site ([Figure 30a, c](#)) and IP1 ([Figure 32](#)) are clear evidence of the effects of varying winter wind intensities on the maximum volume of snow that accumulates in snow traps. [Figure 41](#) shows that SH_{max} is positively correlated with the number of wind events in the range of $4\text{--}10 \text{ m s}^{-1}$, the range for snow saltation transport (Li and Pomeroy, 1997). These conditions are favourable to substantial erosion in exposed terrain and re-deposition in sheltered sites where wind velocity is lower (e.g. winters 2017/18; 2018/19; [Figure 30](#) and [Figure 32](#)). Conversely, SH_{max} is inversely correlated with wind events above 15 m s^{-1} , the thresholds for snow transport by suspension (Pomeroy, 1989). Such winds are associated with high erosion and sublimation rates and are unfavourable to accumulation, even in sheltered areas, due to high turbulences (Pomeroy, 1989). It results in a lowering of the equilibrium profile which leads to a decrease of SH_{max} (e.g. winter 2016/17).

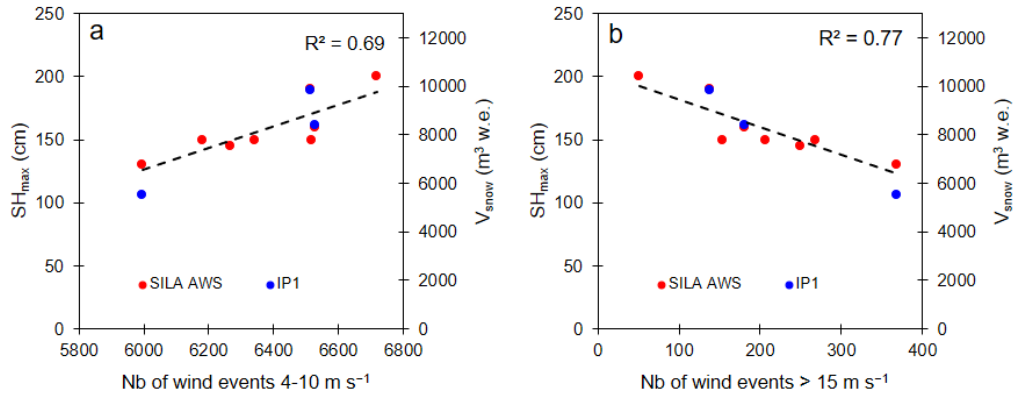


Figure 41. Scatter plots showing the relationship between the frequency of wind events and the maximum snow height (SH_{max}) observed at the SILA site (left Y-axis) and the maximum snow volume (V_{snow}) measured on IP1 (right Y-axis). a) for wind events in the range of $4-10\text{ m s}^{-1}$; b) for wind events with speed $> 15\text{ m s}^{-1}$. The dashed black lines are linear regressions for the SILA station only.

An additional explanation for **Figure 41** is the indirect effect of wind on snow redistribution through its influence on snow properties and its ability to be eroded. Under strong winds, snow grains are rapidly fragmented by mechanical metamorphism forming a hard dense wind slabs made of small and mostly rounded grains (Domine et al., 2002). The hardness and density of this snow are generally proportional to the wind speed during the snow accumulation. Thus, stronger winds produce a snowpack with a higher threshold for erosion (Jaedicke and Sandvik, 2002) so that the snow will be less likely to be eroded during moderate wind events ($4-10\text{ m s}^{-1}$) which limits snow supply. Although denser snow increases SWE, this does not balance out the reduced snow supply to the ice patch system (**Figure 32**).

From our interpretations, we thus suggest that the high frequency of moderate wind events ($4-10\text{ m s}^{-1}$) represents the best conditions for snow trap filling (e.g. 2018; 2019, **Figure 30** and **Figure 32**) while a high frequency of strong wind events ($>15\text{ m s}^{-1}$) considerably limits accumulations even in the most sheltered sites (e.g. 2017; **Figure 30** and **Figure 32**).

3.8.2. Factors controlling the summer ablation

At the beginning of the warm season, snowmelt becomes important as soon as the upper snow layers reach the melting point (**Figure 36** and **Figure S2-12**) so that all energy inputs to the snow surface are almost exclusively consumed as latent heat by melting or sublimation of the snow, which represents the main energy sink in the surface energy balance (SEB) of the snow surface

(**Figure 37**). During the study period 2019, the SEB was dominated by net radiation (74%) which is consistent with what has been reported by other studies addressing the melting of seasonal snow cover and snow patches in the Arctic (e.g. Boike et al., 2003a,b; Heron, 1979; Westermann et al., 2009; Young and Lewkowicz, 1990) and in Antarctica (Leppäranta et al., 2013). The daily variability in the energy gains, however, was primarily driven by the evolution of turbulent fluxes and in particular by the sensible heat flux (Q_h). Turbulent fluxes are closely related to weather conditions (air temperature, relative humidity, wind speed) and are therefore expected to be highly variable in time and space and to be strongly impacted by climate fluctuation.

3.8.2.1. Synoptic control on surface energy balance and melt rate

The severity of the ablation depends on weather patterns which themselves are controlled by the synoptic situation that develops over the Arctic Basin. The analysis of the 3 cases detailed in **Figure 38** has allowed us to identify fog and wind speed as key meteorological variables for ice patch ablation, the first by reducing it and the second by increasing it. Their occurrence was examined in the regional context to determine under what synoptic-type situations they typically occur along the northern coast of the Canadian High Arctic (Alt, 1987; [Table S2-3](#)).

Fog represents the most favourable condition for ice patch preservation since it reduces incoming solar radiation and causes a drop in the air temperature of the boundary layer around the freezing point (Case 2, **Figure 36**, **Figure 38** and [Figure S2-14](#)). Heat gains by Q_h then become negligible which considerably limits ablation. Fog forms under high-pressure systems over the Arctic Ocean or shallow low patterns characterized by low wind, which favours persistent temperature inversions and high humidity (synoptic Type I of Alt, 1987) ([Figure S2-14](#); Pope et al., 2017). Along the north coast of Ellesmere Island, fog forms when near-surface air is cooled and becomes laden with moisture as it circulates over the fractured melting sea ice (early July in 2019). The frequent fog cools the summer climate of the North coastal fringe considerably ([Figure S2-16b](#); **Table 3**; Maxwell, 1981). This “Arctic Ocean effect” (Edlund and Alt, 1989) is the main explanation of the large number of late summer snow patches and perennial ice patches along the Northern Ellesmere Island coast as well as of the sharp lowering of the glacier equilibrium line altitudes (ELAs) which favours the preservation of glacial systems down to low elevations, such as the Meighen Ice Cap (Koerner, 2005) and the Ward Hunt Ice Rise (Braun, 2017). Mueller and

Vincent (2006) suggested that the distribution of fog at the local scale can explain the contrasting surface ablation pattern observed on the Ward Hunt Ice Shelf.

Wind, on the other hand, represents the unfavorable condition for the preservation of ice patches for several reasons. First, wind is a limiting factor in fog formation. Windy summers are therefore generally less foggy ([Figure S2-16c](#)). Wind also prevents the formation of the stable cold air layer above the snow/ice surface that allows thermal inversions to develop (e.g. colder temperature at 0.5 m than at 2 m above the snow surface observed in Case 1; [Figure 36](#), [Figure 38](#)) (Mott et al., 2011). Finally, wind significantly enhances turbulent heat transfers to the snow/ice surfaces. Even more ablation occurs when strong winds are combined with warm temperatures (e.g. 6 July 2017, [Figure 36](#); Case 3 in [Figure 38](#); [Figure S2-14](#)). Such conditions were brought by low 500-hPa geopotential heights centred on southern Ellesmere and high pressures over Greenland, dragging warm (TA at 850 hPa $> 5^{\circ}\text{C}$) and moist air to the northern Ellesmere by southeasterly airflow ([Figure S2-14](#); Type II to Type III classes, Alt, 1987). This configuration is also known to sustain high melt rates of glaciers and sea ice in the northern Canadian Archipelago (Pope et al., 2017).

3.8.2.2. Dirty ice exposure

Ice exposure and its timing are also factors that greatly influence summer ablation since it drastically alters the albedo. As illustrated by [Figure 42](#), the optical properties of the ice patch surface can vary greatly throughout the summer and from one year to the next. When seasonal snow persists for a long time on the ice patch (e.g. 2018 and 2019; [Figure 42](#) and [Figure S2-6](#)), the albedo remains high which favours the preservation of the underlying ice body. In contrast, summers with severe ablation or limited snow thickness (e.g., 2017) are marked by the rapid exposure of superimposed ice, resulting in a drop in surface albedo from ~ 0.6 for the old snow to 0.4 for clean white ice (Gardner and Sharp, 2010), hence increases the absorption of solar radiation and ice patch melting. This shift in surface albedo is even more drastic when the exposed ice is sediment-rich or gets covered with a thin layer of sediment through melt concentration and from upslope runoff ([Chap. 2](#)). This can lower the surface albedo to 0.2 (Young and Lewkowicz, 1990; Fujita et al., 2010). Summer snowstorms, such as in 2017 ([Figure 35](#)), can significantly increase the surface albedo of the ice patch. However, the melting of this summer snow is generally fast (within a few days) and this kind of event is rather unusual so that the effect on the energy balance is very limited during the warm season.

The relationship between ice exposure and ablation intensity yields significant positive feedback in which the stronger the ablation, the earlier the ice is exposed which enhances ablation.



Figure 42. Time-lapse photographs of the ice patch during the melt season 2017 and 2018 showing a contrasting situation in terms of surface albedo. In 2017, the pronounced ablation led to progressive exposure of the dirty ice surface giving a dark colouration to the ice patch while in 2018 the seasonal snowpack persisted throughout the summer.

3.8.2.3. Small-scale processes

Repeated TLS surveys highlighted the small-scale variability in melt rate (**Figure 34**) that reflects the development of local processes related to heat advection (i.e. lateral heat transport), either by wind (turbulent heat) and by running water.

In the case of IP1, the westerly prevailing wind produced local advection of sensible heat from the upwind blocky ground surfaces towards the western edge of the ice patch (**Figure 34**). As the season progresses, the advection process becomes more pronounced due to the reduction of snow-covered areas around the ice patch (**Figure 35**), which enhances the turbulent exchange between the solar-heated ground and the air. As a result, the melt rate increased faster on the upwind edge than on the downwind edge ([Figure S2-7](#)). Such local-scale heat transfers towards patchy snowpacks have also widely been documented in the alpine context (e.g. Essery et al., 2006; Mott et al., 2011, 2017).

Advection of heat by running water can also have a significant impact on local-scale ablation as explained by the higher melt rates measured along the upper edge of the ice patch (**Figure 34**). Inflow of water to the ice patch system leads to strong ablation by thermal-erosion processes (Fortier et al., 2007) as indicated by a series of linear channels, sometimes up to 100 cm

deep and 50 cm, carved into the ice patch ([Chap. 2](#)). At WHI, Paquette et al (2015) reported an analogous process involved in the development of the inshore moat in the ice cover of the Ward Hunt Lake due to water inflow from the slope that increases Qh and the melting rate.

These local processes are strongly conditioned by the ground surface thermal regime in the surrounding areas. Any change in the ground surface conditions (e.g. albedo, vegetation, and hydrology) could therefore greatly modify the intensity of heat advection to the ice patch systems.

3.8.3. Spatial distribution of the ice patches at the landscape scale

Topographical settings and wind conditions are the most important factors explaining the distribution of the ice patches at WHI ([Figure 39](#)) by affecting the spatial patterns in snow accumulation and melt rates. Most of the ice patches lie along the break-of-slope between steep hillsides and lower gentle slopes ([Figure 33](#), see “cliff base” in [Figure S2-2](#)) where the snow retention capacity is highest. Since the strongest winds are predominantly from the west, east-facing slopes are the most snow-laden. The variability in melt rate at the landscape scale depends primarily on the spatial variations in the potential incoming solar radiation (PISR) received at the surface, the main component of the SEB. At the latitude of WHI, the sun elevation angle reaches a maximum of 30° during the summer solstice so only the steepest south-facing slopes receive a substantial heat gain by solar radiation ([Figure 43a](#)). Exposure to the prevailing winds is also a critical factor for ice patch preservation since the second main component of the SEB is Qh (Mott et al., 2011). A simple simulation implemented in ArcGIS ([Figure 43b](#)) allows visualizing the spatial distribution of Qh during a disturbed weather event similar to Case 3 detailed in [Figure 38](#) (see [Appendix A2-8](#) for details).

We assume a homogeneous temperature of 6°C and an average wind of 5 m s⁻¹ at the IP1 site from the west ([Figure S2-11](#)). The model demonstrates that predicted turbulent heat fluxes are 3 times higher in the wind-exposed sites such as the hill ridges than in sheltered sites as in IP1. The combination of enhanced snow accumulation and less turbulent sensible heat fluxes therefore explains the preferential location of the ice patches on the east-facing slopes on WHI while the important radiative heating explains their absence in south-facing slopes ([Figure 39](#)).

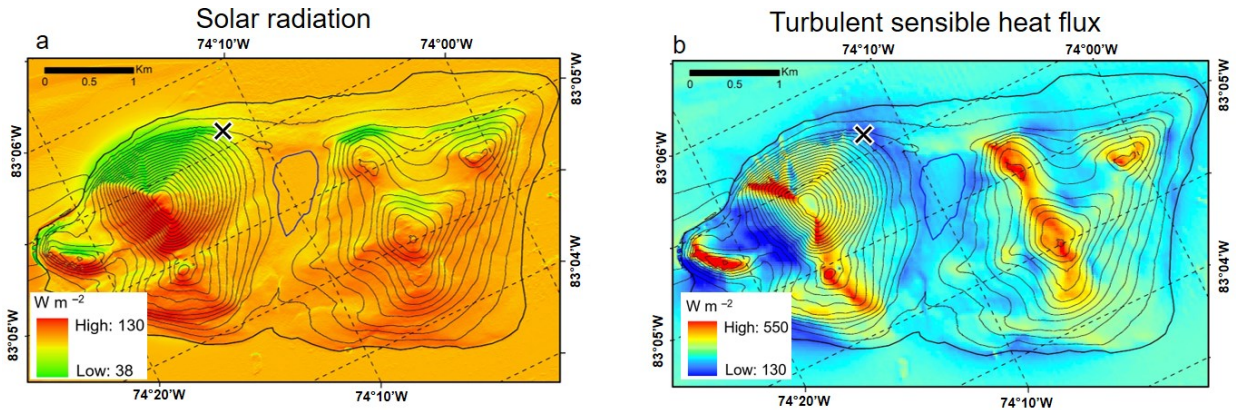


Figure 43. Spatial variation of (a) the total potential incoming solar radiation (PISR, $W\ m^{-2}$) from June to September and (b) of the mean hourly turbulent sensible heat flux during a hypothetical high wind event ($5\ m\ s^{-1}$ from the west at IP1) with an air temperature of $6\ ^\circ C$. The black cross shows the location of the ice patch IP1.

3.8.4. Sensitivity of the ice patches to climate change

3.8.4.1. Long term evolution

The significance of the ice patch to the polar landscape and ecosystem development (Christiansen, 1998; Woo and Young, 2003) makes their long-term preservation a key issue for the stability of the polar eco-geosystem. Based on historical data on the ice extent at WHI, we assume that the ice patch IP1 has never completely melted over the last few decades insofar as it withstood the recent series of abnormally warm summers since the late 2000s (Figure 40a and b). This confirms the previous findings of [Chap. 2](#) when suggested, based on the analysis of ice cores retrieved from the ice patch IP1, that the ice is likely at least several centuries old, potentially even dating back to the end of the Mid-Holocene Warm Period. As such, despite its limited size, the ice patch IP1, and more broadly the whole ice patch systems of WHI, seem less sensitive to climate change than the nearby cryosphere which has experienced an unprecedented decline over the last two decades (Braun et al., 2004; Mueller et al., 2003; 2017; Paquette et al., 2015). The current preservation of ice patches until today, despite the recent warmer summers, is indicative of a partial decoupling of their dynamics from the climatic trend due to the primary control by the topographical constraints. This confirms the early findings reported for ice patches (Fujita et al., 2010; Lewkowicz and Harry, 1991; Ødegård et al., 2017) and glacierets (e.g. DeBeer and Sharp, 2009; Kuhn, 1995; Hoffman et al., 2007).

We suggest that the key factor in maintaining a long-term mass balance close to zero at WHI is the development of a negative feedback between summer ablation and winter accumulation. Indeed, for ice patch systems fed by drifting snow, winter accumulations are generally negatively correlated with the end-of-summer ice patch size and volume because the amount of new snow that can accumulate in the system in winter will depend on the space available in the topographic niche (Glazirin et al., 2004). However, the three years of data in IP1 show that this relationship is not straightforward since snow availability is modulated by wind conditions which can favour ($4\text{--}10 \text{ m s}^{-1}$ winds) snow loading after a summer of low ablation (e.g. 2017/18, **Figure 32**) or limit it ($>15 \text{ m s}^{-1}$ winds) after a summer of strong ablation (e.g. 2017/17, **Figure 40**).

This negative feedback mechanism dampens the effects of climate variations on ice patch mass balance but does not suppress them since the summer ablation remains greatly influenced by the air temperature. Despite the rapid warming over the last two last decades (**Figure 40a**), we believe that the key element in the current preservation of the ice patches at WHI is related to the regular alternation between abnormally warm summers and cool summers with PDD_{air} close to or below 1980-2010 climate normal. Cool summers allow the ice patch to regenerate by promoting aggradation of superimposed ice which increases ice patch resilience to a warm summer (e.g. 2016) ([Chap. 2](#)). For the investigated ice patch IP1, correlations between PDD_{air} and the minimum ice patch extent (**Figure 40c** and d) suggest that average PDD_{air} of two consecutive warm summers exceeding 200 would be detrimental to its preservation.

3.8.4.2. Potential future evolution

According to the Coupled Model Intercomparison Project 5 (CMIP5) ensemble simulations under the intermediate RCP 4.5 greenhouse gas concentration scenario (Taylor et al., 2012), the mean annual temperature is modelled to increase by $3 \text{ }^{\circ}\text{C}$ by 2050 on the northern coast of Ellesmere Island. Sea ice extent in the Arctic Basin would consequently continue to decline rapidly which has the potential for a large increase in sensible and latent heat fluxes from the open ocean to the atmosphere. This would exacerbate the rise in air temperature in fall ($+4.5 \text{ }^{\circ}\text{C}$) ([Figure S2-18a](#)) and lead to a modification of Arctic cyclone characteristics with more frequent and more severe storms, especially in fall (Akperov et al. 2019; Oh et al., 2020), as revealed by projected negative sea-level pressure anomaly on the northern coast of Ellesmere Island by the CMIP5 model ([Figure S2-18b](#)). This phenomenon would be associated with a substantial increase in precipitation,

especially in fall (+28%) and winter (+29%) by 2050 (Fig. S18c). Regional increase in cyclonic activity is also expected to result in more extreme surface winds for the coming decades (Mioduszewski et al., 2018; Oh et al., 2020).

These expected climate changes will produce contrasting effects on the snow regime at WHI. On the one hand, increased precipitation ([Figure S2-18c](#)) could bring increased snow availability during the cold season with the potential of higher snow drifting. On the other hand, the increase in cyclonic activity would potentially be accompanied by more frequent extreme wind events ($>15 \text{ m s}^{-1}$), providing less favourable conditions for a complete snow filling of the topographic niches with a situation like that observed in 2017 becoming more frequent. Projected increases in air temperature could alter snowpack conditions, particularly in the fall, with potentially wetter snow. In addition, an increase in rain-on-snow events in winter is also projected across the High Arctic due to more frequent warm spells (Bintanja and Andry, 2017). Although rain-on-snow events are unlikely at the latitude of WHI by 2050 during winter, they could occur in fall (Sept-Oct). A wetter snowpack with ice layers would then be less likely to be eroded and transported. Warmer conditions in winter and spring would also increase the temperature of the end-of-winter snow and the underlying ice body, reducing the duration of superimposed ice growth (lower cold content) in early summer ([Chap. 2](#)). Water from in situ snowpack melt would leave the system quickly in spring rather than contributing to ice patch mass gain by being stored as superimposed ice. Therefore, despite increased precipitation, we anticipate that climate change will result in a decline in mass inputs to the ice patch system.

Although summer warming is expected to be moderate by 2050 ($+1^\circ\text{C}$) under the scenario RCP4.5 ([Figure S2-18](#)), it would suffice to bring mean PDD_{air} above 150, which is twice the mean value for the period 1980-2010 ([Figure 44](#)), resulting in a more intense and longer melt season. The threshold of 200 PDD_{air} (average of two consecutive summers) that would lead to the complete melting of IP1 could thus be crossed episodically by 2050. Several positive feedback loops could be triggered in response to rising air temperatures, leading to an exponential increase in ablation and that could cause the loss of permanent ice patches to occur even faster than expected. At the scale of ice patch systems, the complete disappearance of the seasonal snowpack is likely to become more frequent and to occur earlier, exposing dirty ice as in 2017, and thus further enhancing ice ablation. Also, early melt of the seasonal snowpack in spring around ice patches

would lead to more intense warming of the soil surface, enhancing heat advection processes and thus melting of the ice patch margins.

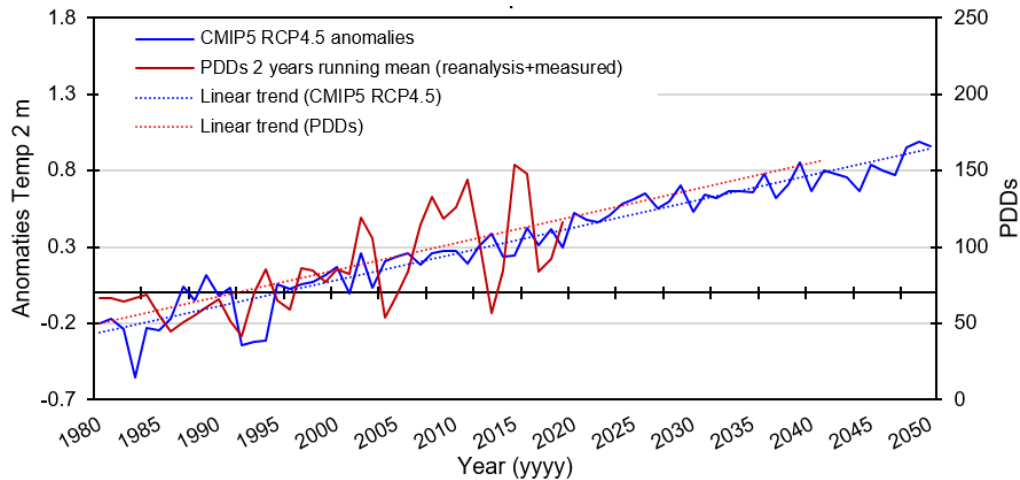


Figure 44. Projection of summer temperature at Ward Hunt Island to 2050 based on the Coupled Model Intercomparison Project phase 5 (CMIP5) for the scenario RCP4.5 ensemble average (Data from Climate Change Institute, 2021). Modelled summer (JJA) air temperature anomalies at 2 m over the period 1980-2050 are presented along with the 2 years running mean of the PDD_{air} at Ward Hunt Island reconstructed from NCEP-NCAR reanalysis for the period 1980-2005 and measured at SILA for the period 2005-2019.

How fog and wind conditions will evolve under a warmer Arctic climate is also a key element in assessing the fate of ice patches. These two variables are closely related to each other because they both depend strongly on sea ice conditions in the Arctic Basin. First, an increase in open water surface will likely produce more frequent fog and thus preserve the coastal cryosphere, giving rise to a negative feedback that could counteract, or at least dampen, the effect of temperature warming. However, the expected enhanced cyclonic activity and stronger surface winds in summer would result in unfavourable conditions for fog formation ([Figure S2-16c](#)). In addition to limiting fog, the more frequent wind in summer would increase turbulent heat transfer to ice patch systems with a potentially higher frequency of strong melting events (e.g. Case 3; [Figure 38](#)). Finally, the higher humidity in the Arctic Basin could also result in increased cloud cover which, unlike fog, would enhance surface warming by emitting more long-wave radiation (Huang et al., 2021).

Because of their limited size ([Figure S2-15](#)), ice patches have a short response to the annual climatic signal compared to larger ice masses. Even after a long period of continuous existence, they can disappear extremely rapidly (within 1 or 2 years) when summer temperatures become too

warm for local topo-climatic factors to support the preservation of ice masses. Based on the recent evolution of the ice patch IP1 and regional climate projections, we speculate that most of the ice patches at WHI will lose their perennial status in the next decade, turning into semi-permanent ice patches or even snow patches, as has already happened further south in the Arctic (Woo and Young, 2014). A cycle of ice patches destruction-restoration following short-term fluctuations in summer conditions (e.g. Arctic and North Atlantic Oscillations; Holland, 2003) will create a higher interannual variability in the water supply to the ecosystem, with likely important consequences for the evolution of vegetation and geomorphic processes.

3.9. Conclusion

This study provided the first investigation of the surface mass and energy balance of a perennial ice patch along the northern Ellesmere coast where these small ice masses are ubiquitous in this polar desert environment. The primary objective was to identify the key regional and local factors controlling winter snow accumulation and summer ablation on an ice patch system to understand its long-term evolution and speculate on its future fate in the context of climate change.

At the scale of the landscape, the distribution of the ice patches reflected spatial patterns of sites of anomalous snow accumulation and minimum ablation which predictably always occur at the same locations since they are mainly dependent on topography and wind field configuration. Despite the aridity of the region, topographic depressions and breaks of slope accumulate a large amount of snow due to the large fetch around WHI that provides a large influx of snow through wind-driven processes. Snow trapping sites fill up quickly at the beginning of the cold season. However, the equilibrium profile of deep snow accumulation that determines the total volume of snow trapped displays pronounced interannual variability. We showed that this was primarily related to the frequency and magnitude of winter wind events, since frequent but not excessive winds ($4\text{--}10 \text{ m s}^{-1}$) are conducive to significant deposition, whereas a high recurrence of strong winds ($>15 \text{ m s}^{-1}$) results in intense snow erosion.

Although net radiation was the main source of heat (74% of the net energy gained), the short-term variability in the melt rate was mainly explained by changes in sensible heat fluxes. In addition to air temperature, we highlighted that fog frequency and wind intensity are two key factors controlling the ablation of the investigated ice patch. Fog episodes typically suppress melt by limiting solar radiation and sensible heat flux due to thermal inversion. The high frequency of fog

in summer along the northern Ellesmere Island coast is the primary reason for the preservation of a large number of ice patches in the region. Wind, on the other hand, increases turbulent heat transfer to the snow/ice surfaces. The highest melt rates were recorded during a disturbed weather episode when strong winds were combined with warm air masses. The future frequency of fog episodes and cyclonic activity will therefore be critical to the preservation of ice patches.

We established that the long-term evolution of IP1 was partially disconnected from the climate trend of the last decades since it never melted completely despite a pronounced increase in summer temperature and the rapid declining trend of the nearby cryosphere (i.e. Ward Hunt Lake, ice rise and ice shelf). This apparent stability and resilience to the recent warming emphasized that the ice patch system is modulated by a feedback mechanism that operates on winter accumulation (i.e. greater accumulation after strong ablation, and conversely) and which dampens, but does not eliminate, the effects of climate variations on ice patch dynamics. Despite this negative feedback process that favours ice patch preservation, we speculate that continued rising temperatures will lead to very critical conditions for the maintenance of the IP1 and other WHI ice patches over the next decade. In addition, warming will cause a positive feedback as declining sea ice in the Arctic Basin could lead to more intense cyclonic activity and thus increase the intensity and frequency of strong wind events. Other critical changes in conditions such as the occurrence of rain-on-snow events may further limit accumulation on ice patches. Reduced winter accumulation and enhanced summer ablation make it highly probable that most ice patches at WHI and along the northern coast of Ellesmere will turn into semi-permanent ice patches and snow patches in coming decades with direct consequences on the supply of water and ecological evolution of polar desert ecosystems.

3.10. Acknowledgements

This research has been supported by the Natural Sciences and Engineering Research Council of Canada (NSERC), including the Discovery Frontiers project Arctic Development and Adaptation to Permafrost in Transition (ADAPT); the Networks of Centres of Excellence program ArcticNet; the Canada Research Chair program; the Northern Scientific Training Program; the Canadian Foundation for Innovation: Canadian Northern Studies Trust; Centre d'études Nordiques (CEN); and Fond de Recherche du Québec- Nature et Technologie (FRQNT). FD was supported in part by the French Polar Institute (IPEV). Logistical support was provided by the Polar Continental Shelf Program (PCSP) and Parks Canada graciously granted us the use of their facility.

We are also grateful to Derek Mueller (Water and Ice Research Laboratory, Carleton University) for providing SPOT and Formosat images and Denis Sarrazin (CEN) for digging through 20 years of his field photo archives to find photos of the IP1 ice patch.

3.11. Appendices A2

Appendix A2-1: Ground Penetrating radar (GPR)

GPR is a powerful tool for non-destructively imaging the subsurface and has already been used to survey the stratigraphy and thickness of ice patches, (Meulendyk et al., 2012; Sakai et al., 2006; Yamamoto et Yoshida, 1987). For this study, GPR data were sampled in standard reflection mode with a step size of 1 m using a hand-held antenna. Because of the great difference between the dielectric properties of the firn/ice and the underlying soil/bedrock, the detection of ice thickness is reliable and requires minimal signal processing. This work was implemented with the software EKKO project V2R3. The low-frequency noise of the signal was removed using the filter “dewow” (Meulendyk et al., 2012). The conversion of the electromagnetic signal propagation time to depth was made using a mean velocity (m ns^{-1}) deduced from common midpoint (CMP) surveys. A topographic correction was applied to the GPR data based on terrestrial laser scan (VX spatial station (Trimble ®) surveys and the ice thickness was extracted at 1 m interval along each track. The ice thickness estimation was then validated with the ice coring made in 2017 ([Chap. 2](#)).

Appendix A2-2: Terrestrial Laser Scanning (TLS)

Measurement of the ice patch surface change was performed by repeated Terrestrial Laser Scanning (TLS) surveys. The TLS consists of a highly accurate method to obtain dense point clouds of a target surface. This method has already been used to monitor the melting of seasonal snow cover, ice patches or glaciers (Fischer et al., 2016; Grunewald et al., 2010; Mott et al., 2019). We used a VX spatial station (Trimble®, single 3D point accuracy 10 mm at ≤ 250 m). The deviation in the z-direction between various scans, estimated using unchanged reference surfaces such as boulders or rock outcrops, was lower than ± 15 mm on average. The station remained at the same location through the monitoring periods to reduce the potential error linked to the instrumentation resettlement. The station position was linked to a geodesic landmark recorded using a Global Navigation Satellite System (R8 GNSS; Trimble®, precision x–y ± 8 mm and z ± 15 mm). Elevations obtained were corrected by the Canadian Centre for Remote Sensing and orthometric heights were used. The postprocessing consisted of cleaning the point clouds using the commercial software Trimble RealWork 7.1. They were subsequently used to create high-resolution 3D digital surface models using a triangulated irregular network method in ArcGIS (Esri, version 10.5.1).

Appendix A2-3: Time-lapse photograph

From the raw set of time-lapse photographs, only one image per day was selected for analysis. Images captured in the afternoon were preferred because the ice patch is in the shadow of Walker Hill, avoiding light saturation issues. For Zone B which focuses on the ice patch system IP1, we relied on a set of 10 georeferenced images, including orthomosaics derived from unmanned aerial vehicle (UAV) surveys undertaken during the 2019 melt season and aerial photograph taken in summer 2017, to convert the snow/ice cover fraction derived from the time-lapse camera into a horizontal projected areal extent (A , m^2). The georeferenced images were analyzed in ArcGIS to manually delineate the perimeter of IP1 and extract the horizontal projected areal extent. The relation between the fraction area and the corresponding value of areal extent is shown in **Figure A2-1**:

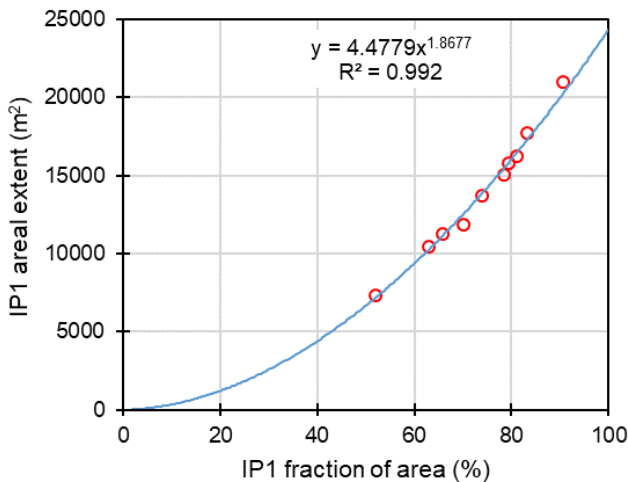


Figure A2-1. Relation between the fraction of area of the IP1 system derived from the time-lapse camera and the corresponding value of areal extent derived from detection on ArcGIS.

Appendix A2-4: Wind speed estimation

The wind data at IP1 were extrapolated from the time series of the SILA station recorded the 10 m-high anemometer of the SILA station. The first step was to extrapolate the wind speed for a height of 2 m, corresponding to the height of the anemometer installed in 2019 at IP1. This extrapolation was based on the logarithmic wind law that is generally been used to model the vertical profile of wind speed over flat terrain (Oke, 1987) as:

$$WS = WS_{ref} \times \frac{\ln\left(\frac{z}{z_0}\right)}{\ln\left(\frac{z_{ref}}{z_0}\right)} \quad (\text{A2-1})$$

with WS is the wind speed at a height of 2 m above ground level (z), v_{ref} is the wind speed measured at z_{ref} of 10 m, z_0 is the roughness length. Since the terrain around SILA consists of a gravelly surface, we assumed a z_0 of 0.01 m. We then used the relationship between the average hourly wind speed (m s^{-1}) recorded by the automatic weather station (AWS) installed on IP1 during the study period 2019 with the data extrapolated for a 2 m-height at SILA station. **Figure A2-2** shows the good relationship between both data sets ($R^2=0.71$). The equation associated with the linear regression line ($WS_{IP1}=0.6087 \times WS_{SILA}+0.4832$) was used to estimate the wind speed at 2 m on IP1 in 2017.

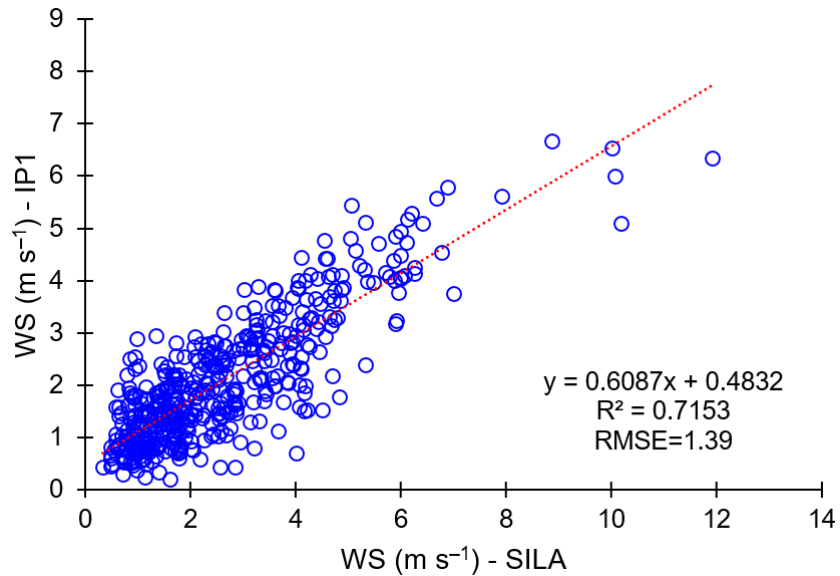


Figure A2-2. Correlation between the hourly average wind speeds derived from SILA measurements adjusted using equation A2-1 for a 2m-height level at the SILA station from time-series provided by the anemometer at 10 m and by the AWS on IP1 during the study period 2019. The red dashed line represents the linear regression line.

Appendix A2-5: Surface Energy Balance

The turbulent heat fluxes Qh and Qe (W m^{-2}) were calculated based on the bulk aerodynamic approach, including stability correction, as formulated by Price and Dunne (1976). This method is based on differences in wind speed, potential temperature and specific humidity between the

measurement level and the surface. It has been successfully applied to estimate the SEB of melting snow surfaces (Boike et al., 2003a; Young and Lewkowicz, 1990). Equations (A2-2) and (A2-3) describe the calculation method of Qh and Qe , respectively using measurements of wind speed, temperature, and humidity at the 0.5 m level:

$$Qh = \rho_a \times C_a \times D(T_a - T_{ss}) \quad (\text{A2-2})$$

$$Qe = \rho_a \times L_v \times D\left(\frac{0.622}{AP}\right)(e_a - e_{ss}) \quad (\text{A2-3})$$

where ρ_a and C_a are the air density (1.27 kg m^{-3}) and specific heat of air ($1.005 \times 10^3 \text{ J kg}^{-1} \text{ K}^{-1}$), D is bulk exchange coefficients, T_a and T_{ss} air the air and snow surface temperature respectively, L_v is the latent heat of vaporization or sublimation (being $2.48 \times 10^6 \text{ J kg}^{-1}$ and $2.83 \times 10^6 \text{ J kg}^{-1}$, respectively), AP is atmospheric pressure (mbar), e_a is the air vapor pressure and e_{ss} the saturated water vapor pressure over the surface of a melting snowpack. The snow surface temperature T_{ss} has not been measured but it is assumed to be 0°C when the T_a is positive and to be equal to T_a when T_a is negative.

For neutral conditions, D is equal to the momentum D_m :

$$D_m = \frac{WS_z \kappa^2}{\left(\ln\left(\frac{z}{z_0}\right)\right)^2} \quad (\text{A2-4})$$

where WS_z is the wind speed (m s^{-1}) at height z , κ is von Karman's constant (0.4) and z_0 is the roughness length. For the snow, z_0 values of 0.001 to 0.005 m are commonly assumed (Bash et al., 2020; Liston and Hall, 1995). Here, we calculated the turbulent fluxes with an intermediate value of $z_0 = 0.0025$. Given the relative importance of the surface roughness, a sensitivity analysis was performed using values of 0.001 and 0.005. It resulted in <10% change to melt energy (Qm) on average at the scale of the study period, considered here as a small error.

Under conditions other than neutral, D is adjusted with the bulk Richardson number (R_i) expressed as:

$$R_i = \frac{gz(T_a - T_{ss})}{WS_z^2 T_a} \quad (\text{A2-5})$$

where g is the gravitational constant.

Under stable conditions $R_i < 0$:

$$D = \frac{D_m}{(1+10R_i)} \quad (\text{A2-6})$$

Under unstable conditions $R_i > 0$:

$$D = \frac{D_m}{(1-10R_i)} \quad (\text{A2-7})$$

The heat flux by conduction through the snowpack (Q_c , W m^{-2}) was calculated from the temperature gradient between the temperature of the snow surface (T_{ss}) and the snow temperature at -25 cm (T_{snow}) and using the average snow thermal conductivity measured during snowpit excavation on 6 June 2019 ([Figure S2-5](#)). Since the upper thermistor was at 40 cm below the snow surface, we linearly interpolate the snow temperature at 25 cm below the surface from the temperature profile.

Q_c was expressed as:

$$Q_c = \frac{-\Delta T}{R_T} \quad (\text{A2-8})$$

where ΔT is the temperature gradient between the snow surface and the snowpack bottom and R is the thermal insulance of the snow. R_T ($\text{m}^2 \text{K W}^{-1}$) can be calculated from the thickness h (m) and thermal conductivity $k_{eff}(i)$ ($\text{W m}^{-1} \text{K}^{-1}$) of the various snow layers (i) that comprise the snowpack as (Domine et al., 2016a):

$$R_T = \sum \frac{h_i}{k_{effi}} \quad (\text{A2-9})$$

Appendix A2-6: Topographical variables derived from a DEM

Elevation (in m a.s.l.) and slope aspect (expressed as eight cardinal directions) were obtained using ArcGIS spatial analyst tool. The slope position classification (cliff base/depression, lower slope, flat surface, middle slope, upper slope, ridge) were extracted from the DEM using the ArcGeomorphometry extension (Rigol-Sanchez et al., 2015) through the calculation of the Topographic Position Index (TPI) based on the algorithm developed by Weiss (2001). The potential incoming solar radiation (in Wh m^{-2}) was calculated using the Solar Radiation analysis tools in

ArcGIS for the melt season period (June to August). Finally, the wind exposure index was obtained from a model of wind flow field over WHI implemented using WindNinja which is a wind model suitable to capture topography-induced flow features (Forthofer et al., 2014). The wind input is parameterized based on the prevalent direction and average wind speed recorded at the SILA-CEN weather station from 2005 to 2019.

Appendix A2-7: Longterm air temperature reconstruction

NCEP/NCAR re-analysis was used to reconstruct long-term near-surface air temperature at Ward Hunt Island. This re-analysis provides mean monthly air temperature (MMAT) data from 1948 to 2019 in a $2.5^\circ \times 2.5^\circ$ grid at 1000 hPa (i.e. ~at sea level). Data reconstruction was achieved by combining various data sources such as upper air radiosonde, aircraft and satellite observations, and land surface (e.g. regional meteorological stations) and oceanic reports (Kalnay et al., 1996). The raw MMAT re-analysis data were debiased by calculating the mean monthly bias with respect to MMAT measured by the SILA weather station over the period 2002-2019. The good correspondence between the debiased re-analysis data and the MMAT measured by the SILA weather station (**Figure A2-3**) shows that the NCEP/NCAR reanalysis is suitable to reconstruct long-term air temperature evolution on WHI.

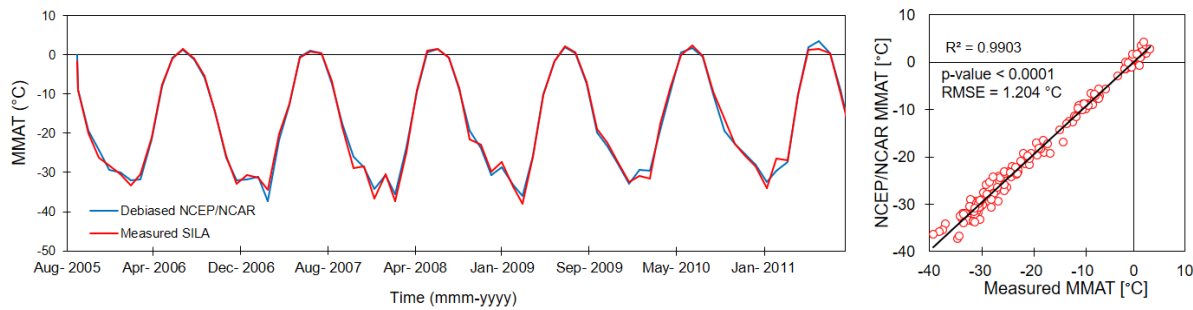


Figure A2-3. Left: Time series of the debiased NCEP/NCAR re-analysis MMAT and measured MMAT from August 2005 to December 2019. Right: Scatter plot of reconstructed versus measured MMAT. RMSE = Root mean square error.

Appendix A2-8: Map of turbulent sensible heat flux

The map the spatial evolution of hourly turbulent heat fluxes Q_h ([Figure S2-16b](#)), we relied on a GIS-based model (Pohl et al., 2006). The model was built in a simplistic way to represent the spatial heterogeneity in Q_h during a disturbed weather episode as the Case 3 (9 July 2019). We

assumed a homogeneous air temperature of 6°C at all levels, a melting snowpack, and an average westerly wind of 5 m s⁻¹ at the site of IP1 ([Figure S2-11](#)). We first computed a map of the topography-induced flow features at the WHI scale using WindNinja. Then, we calculated in ArcGIS the turbulent heat flux for each pixel of the raster based on equation A2-2 using the Math Algebra tool (Spatial Analyst Tools).

3.12. Supplementary material S2

Table S2-1. Details of monitoring instruments

Variable	Site	Symbol (unit)	Instrument	height (m)	Instrument source	Accuracy	Range	Record period
Snow height	SILA-AWS	SH (cm)	Sonic distance sensor	1.5	SR50, Campbell Sci.	±1 cm	0.5 to 10 m	2005-2019
Wind speed	SILA-AWS	WS (m s ⁻¹)	Anemometer	10	05103-10 R.M Young	±0.3 m s ⁻¹	0 to 100 m s ⁻¹	2005-2019
Wind direction	SILA-AWS	DIR (°)	Anemometer	10	05103-10 R.M Young	±3°	0 to 360°	2005-2019
Air temperature	SILA-AWS	TA (°C)	Thermohydrometer	1.5	HMP35CF Vaisala	±0.2°C	-53 to 48°C	2005-2019
Relative humidity	SILA-AWS	RH (%)	Thermohydrometer	1.5	HMP35CF Vaisala	±2% (0-90%)	0-100%	2005-2019
Air temperature	IP1-AWS	TA (°C)	Temperature logger	1.5	Hobo U22-001 Onset	±0.21°C	-40 to 70°C	10 Jun -10 Jul 2017
Air temperature	IP1-AWS	TA (°C)	Thermohydrometer	0.5 / 2	S-THB-M002 Onset®	±0.21°C	-40 to 75°C	10 Jun -19 Jul 2019
Relative humidity	IP1-AWS	RH (%)	Thermohydrometer	0.5 / 2	S-THB-M003 Onset®	±2.5%	0-100%	10 Jun -19 Jul 2019
Wind speed	IP1-AWS	WS (m s ⁻¹)	Ultrasonic anemometer	2.5	WindSonic 4 Gill instr.	±2% at 12 m s ⁻¹	0-60 m s ⁻¹	10 Jun -19 Jul 2019
Wind direction	IP1-AWS	DIR (°)	Ultrasonic anemometer	2.5	WindSonic 4 Gill instr.	±2° at 12 m s ⁻²	0-360°	10 Jun -19 Jul 2019
Shortwave rad. (incoming)	IP1-AWS	SW↓ (W m ⁻²)	Pyranometer	1	Kipp & Zonen SP-Lite	<10%	0.4 to 1.1 μm	10 Jun -19 Jul 2019
Net radiation	IP1-AWS	Qr (W m ⁻²)	Net radiometer	1	Kipp & Zonen NR-Lite	±5-10 W m ⁻²	0.2 to 100 μm	10 Jun -19 Jul 2019
Atmos. pressure	IP1-AWS	AP (kPa)	Pressure sensor	2	Hobo U20L-04 Onset®	±6.2 mbar	0 to 1450 mbar	10 Jun -19 Jul 2019
Snow temperature	IP1-AWS	T _{snow} (°C)	Thermistors	0.05; 0.3; 0.6, 0.9; 1.2; 1.5; 1.9	Geocryolab	±0.1°C	-40 to 70°C	10 Jun -19 Jul 2019
Discharge	Flume	Qf (cm ³ s ⁻¹)	Water level sensor		Hobo U20L-04 Onset®	±6.2 mbar	0 to 1450 mbar	10 Jun -19 Jul 2019

Table S2-2. Summary of the micrometeorological variables; i.e. mean daily atmospheric pressure (AP in hPa), mean daily, maximum and minimum air temperature (TA_{daily} ; TA_{max} ; TA_{min} , in $^{\circ}C$), mean daily relative humidity (RH_{daily} , in %), maximum 15-min average wind speed (WS_{max} , in $m s^{-1}$), mean daily maximum wind speed (WS_{daily} in $m s^{-1}$) and mean daily incoming solar radiation (SW_{\downarrow} , $W m^{-2}$) recorded by the AWS and the resulting terms of the surface energy balance; i.e. net radiations (Qr , $W m^{-2}$), sensible heat fluxes (Qh , $W m^{-2}$), latent heat fluxes (QE , $W m^{-2}$), the melt fluxes (Qm) and the melt rate ($mm d^{-1}$ w.e.) on the ice patch IP1 for the three different cases that reflected the dominant conditions encountered in summer along the north coast of Ellesmere. Case 1 (28 June 2019) was characterized by sunny and calm conditions; Case 2 (5 July 2019) was a foggy day; Case 3 (9 July 2019) was marked by the influence of a low-pressure system and overcast conditions.

	Case 1 (28 June)	Case 2 (5 July)	Case 3 (9 July)
AP (hPa)	1029	1016	1010
TA_{daily} 0.5 m ($^{\circ}C$)	2.2	-0.4	4.3
TA_{max} 0.5 m ($^{\circ}C$)	4.6	2.1	8.2
TA_{min} 0.5 m ($^{\circ}C$)	0.9	-1.2	0.8
RH 0.5 m (%)	81.9	99.1	82.9
TA_{daily} 2 m ($^{\circ}C$)	3.1	0.3	4.6
TA_{max} 2 m ($^{\circ}C$)	5.8	2.3	8.1
TA_{min} 2 m ($^{\circ}C$)	1.9	-0.7	2.1
RH 2 m (%)	80.2	97.9	82.4
WS_{daily} ($m s^{-1}$)	1.5	2.1	3.9
WS_{max} ($m s^{-1}$)	3.1	3.8	7.86
$SW_{\downarrow mean}$ ($W m^{-2}$)	347.5	228.8	239.8
Qr ($W m^{-2}$)	38.4	28.0	39.3
QH ($W m^{-2}$)	13.9	0.7	75.3
QE ($W m^{-2}$)	0.2	3.2	23.1
Qm ($W m^{-2}$)	52.5	32.0	144.5
M (mm we)	14.5	8.8	38.2

Table S2-3. Synoptic-type classification for the Canadian High Arctic and the resulting dominant weather along the northern coast of Ellesmere (after Alt, 1987 and Pope et al., 2017).

Type	Name	Synoptic	Weather along the coast of Ellesmere
I	Polar Ocean circulation	Anticyclone in the Arctic Ocean /low-pressure over Baffin Bay	High pressure, clear-sky or low-stratus, fog
II _s	Cyclonic system with rain	Low 500-hPa geopotential heights in Beaufort sea	Rainfall with high wind, cold temperature
II _r	Cyclonic system with snow	Low 500-hPa geopotential heights moving across islands from central Polar Ocean	Snowfall with high wind, cool temperature
III	Island circulation	Ridge development in eastern North America due to low 500-hPa geopotential heights in the Asian side of the Arctic Ocean	Wind, warm air advection, overcast, slight rain

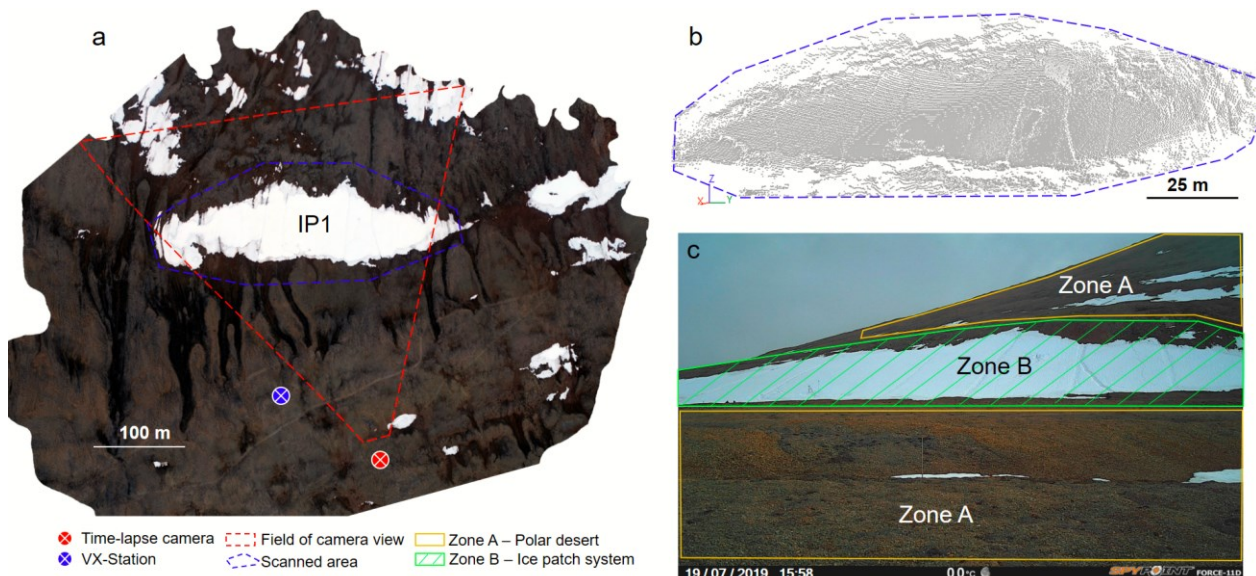


Figure S2-1. a) Overview of the study area overflowed by an unmanned aerial vehicle (UAV) on 19 July 2019 showing the location of the time-lapse camera and its field of view, and of the VX-station and the polygon used to delineate the scans; b) example of a scan of the ice patch (frontal view) taken on 19 July 2019 and c) the corresponding oblique photograph showing zone A considered as a “polar desert” zone where the seasonal snow cover fraction (SCF, in %) outside the ice patch system was calculated and Zone B where the ice patch extent was calculated.

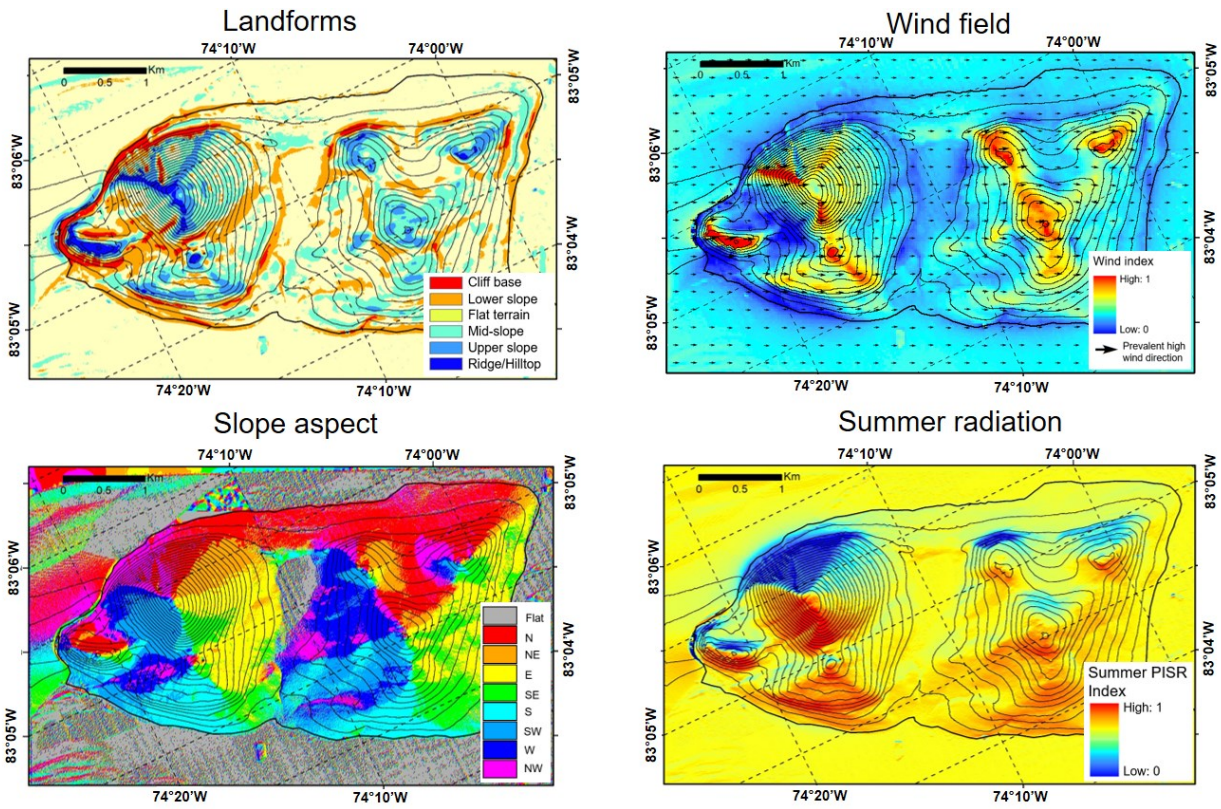


Figure S2-2. Maps of landform features calculated from the Topographic Position Index (TPI) algorithm, of wind field modelled with WindNinja given the Wind velocity index; of slope aspect and of the summer potential incoming solar radiation (PISR) (May to September).

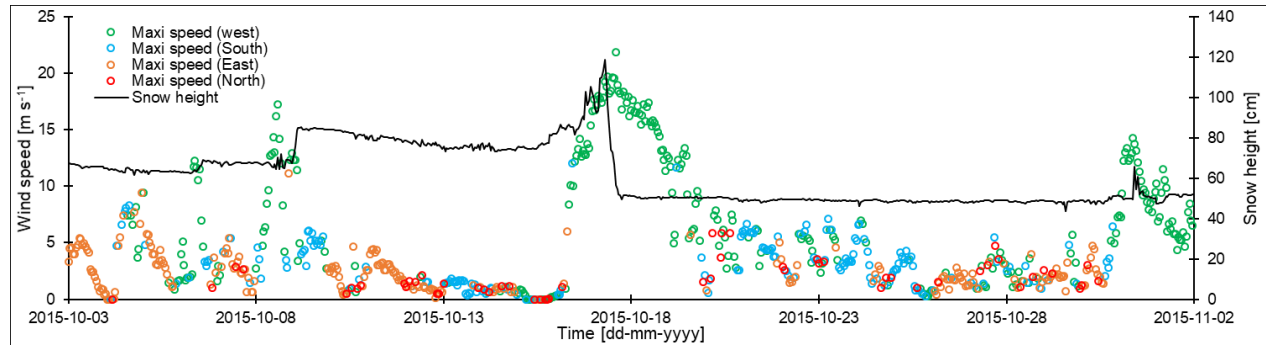


Figure S2-3. Hourly evolution of the wind speeds (filtered by orientations) and snow height (SH, cm) throughout October 2015 showing an extreme erosion event on October 17 during which ~70 cm of snow was removed in a few hours from the snow patch of the SILA site at Ward Hunt Island.

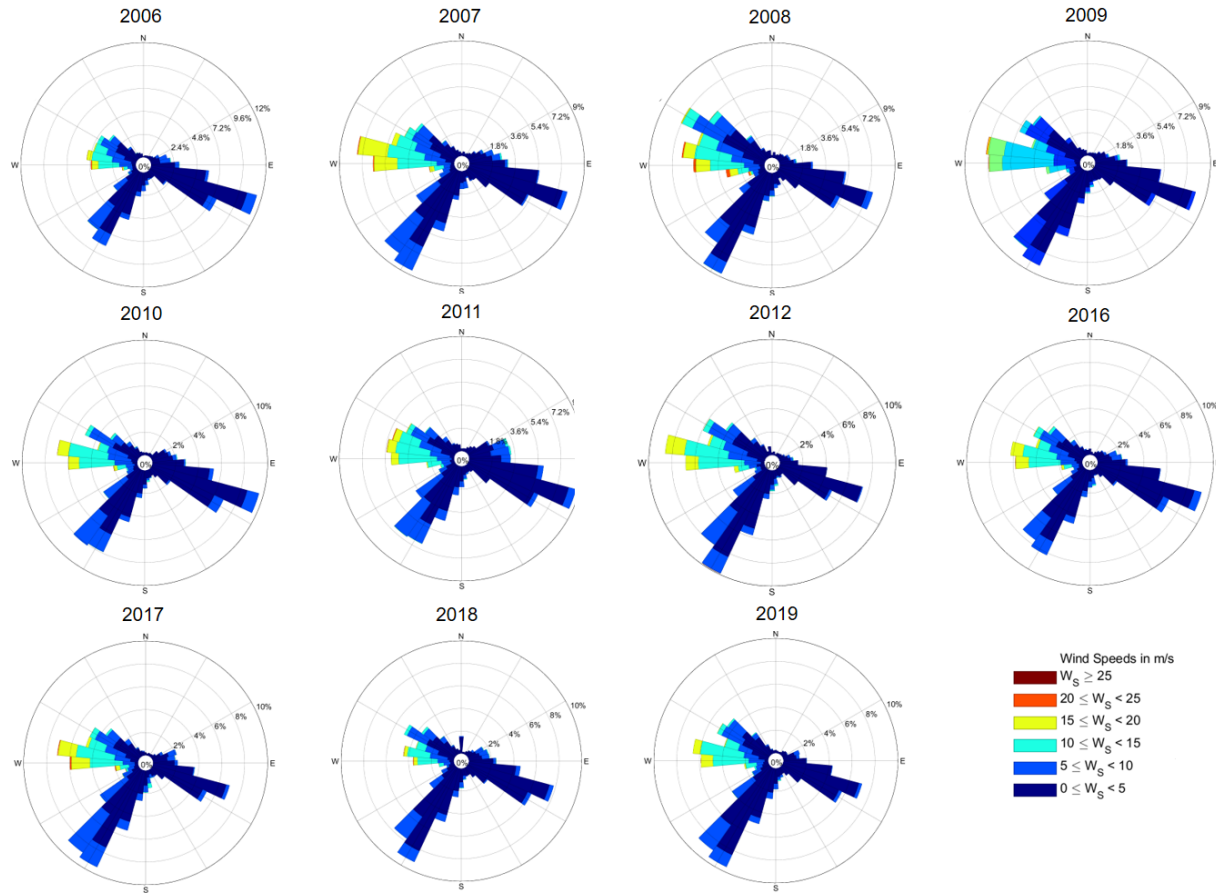


Figure S2-4. Wind-rose diagrams for the hourly wind speed and direction data monitored during cold seasons 2006 to 2019 (Sep-May). Note that the years 2013, 2014 and 2015 are missing due to large data gaps.

6 June 2019 - IP1

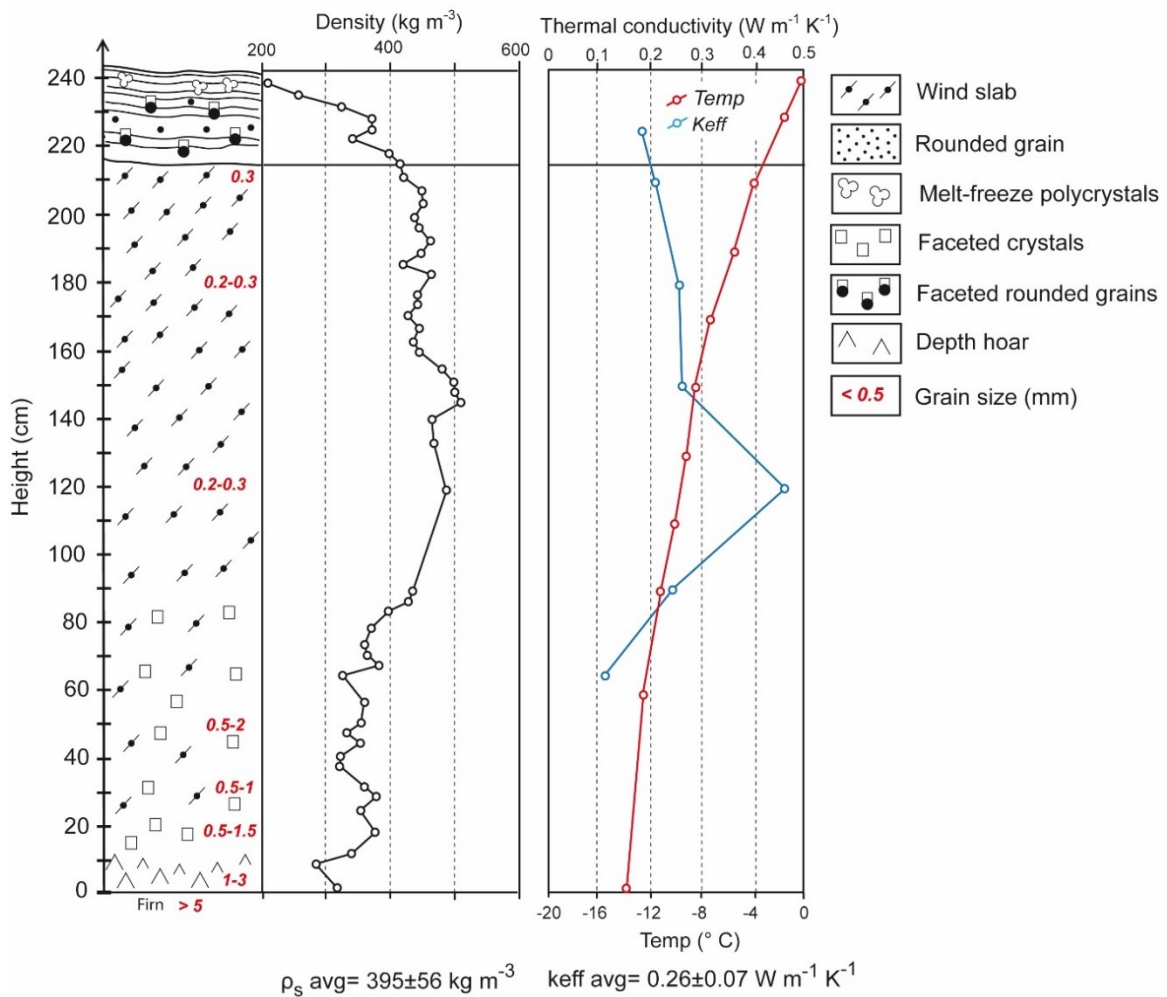


Figure S2-5. Snow stratigraphy of a snowpit dug in the seasonal snow accumulation of the ice patch IP1 showing the snow grain type and size, the snow density (ρ_s , kg m^{-3}), the snow temperature and thermal conductivity (k_{eff} , $\text{W m}^{-1} \text{ K}^{-1}$).

2019-07-05

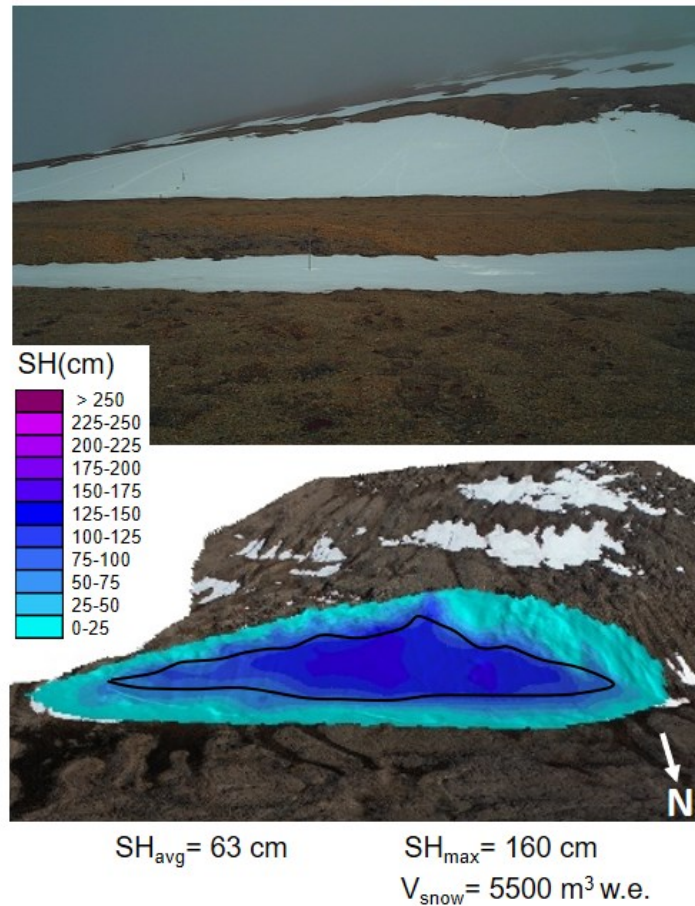


Figure S2-6. Time-lapse photographs of the ice patch system and its surrounding terrain and map of the end-of-summer snow height (SH_{max}) on 5 July 2019. The black line delimits the contour of the ice body as it was at the end of summer 2016. The average and maximum snow height (SH, cm) and the total volume of snow (V_{snow} , m^3 w.e.) are shown at the bottom of the figure.

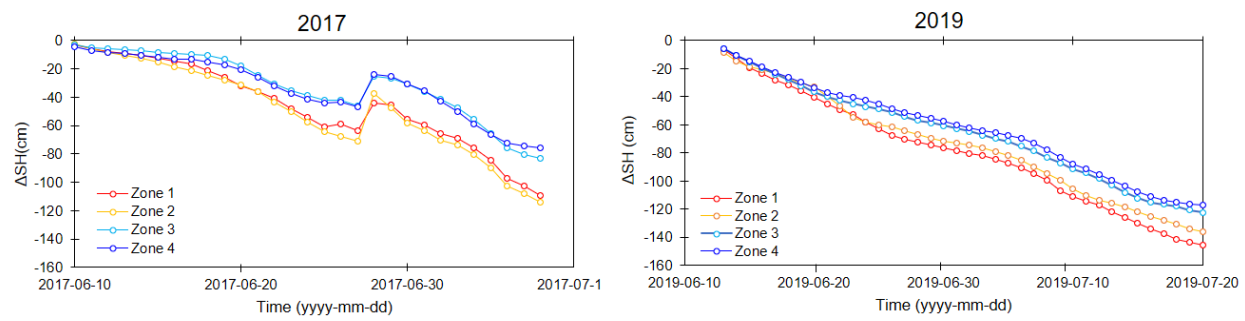


Figure S2-7. Daily evolution of the snow height change (ΔSH_{TLS} , cm) for the 4 zones described in Figure 35.



Figure S2-8. Photograph of the ice patch IP1 at its minimum extent on 11 August 2017.

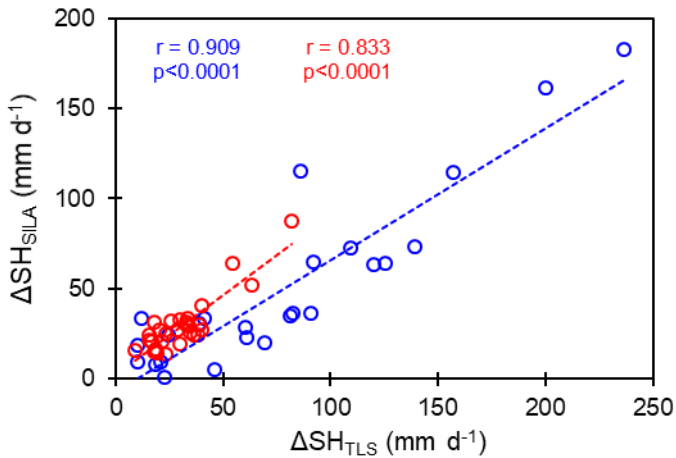


Figure S2-9. Comparison (Pearson's correlation test) between the daily snow height changes recorded at SILA station (ΔSH_{SILA} in $mm\ d^{-1}$) and measured by TLS (ΔSH_{TLS} in $mm\ d^{-1}$) on the ice patch IPI. The red color is for 2017 and the blue for 2019.

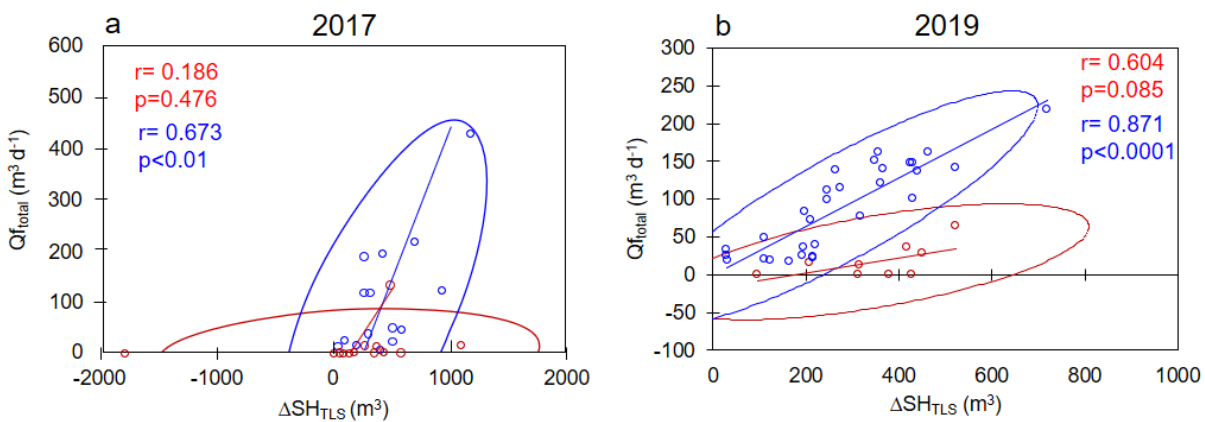


Figure S2-10. Comparison (Pearson's correlation test) between the daily meltwater discharge (Qf_{total} , $m^3\ d^{-1}$) measured at flumes and the daily ablation rate (ΔSH_{TLS} , $m^3\ d^{-1}$) measured by TLS for 2017 (a) and 2019 (b). The red color represents the data collected at the beginnings of the melt seasons and includes the snow storm of 28 June for the 2017 data while the blue color represents data collected outside these periods.

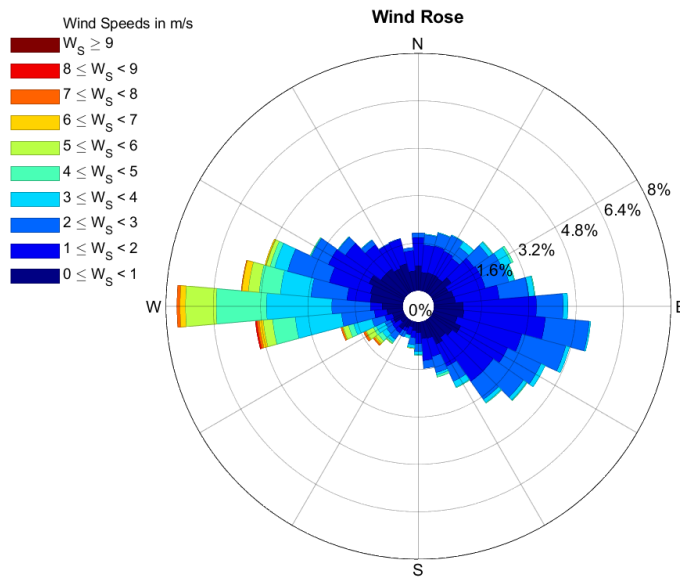


Figure S2-11. Wind-rose of the hourly average wind recorded by the AWS on IP1 during the study period 2019

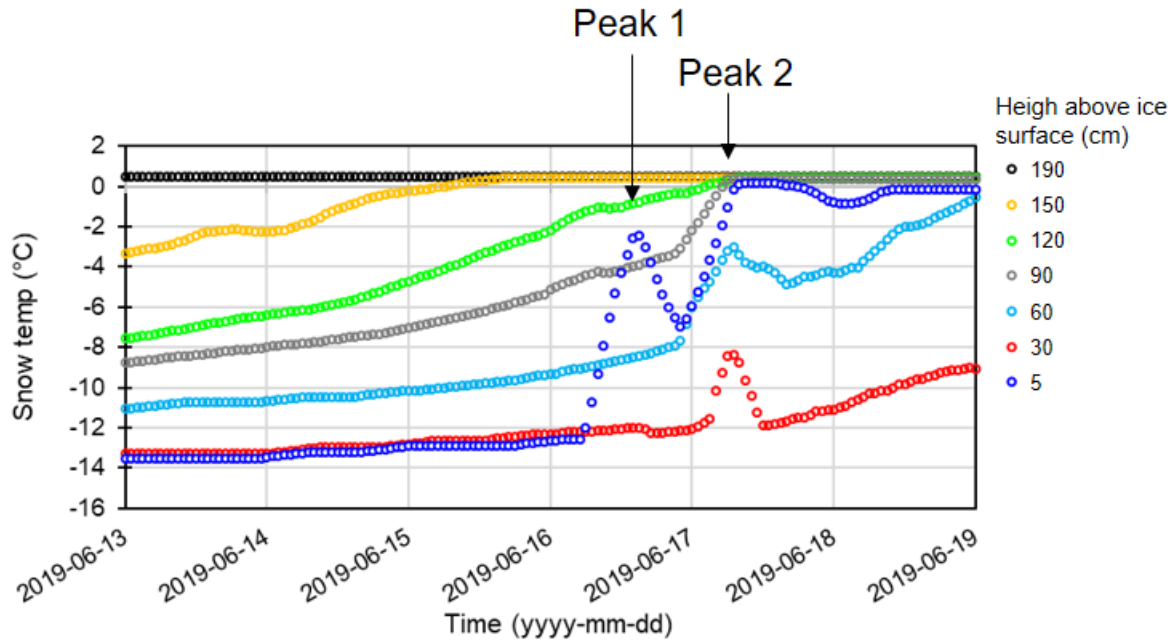


Figure S2-12. Close-up on the thermal peaks in the hourly evolution of the snow temperature measured by the thermistor chain in the snowpack. Thermistors are identified by height above the ice surface. The complete time series is shown in **Figure 36**.

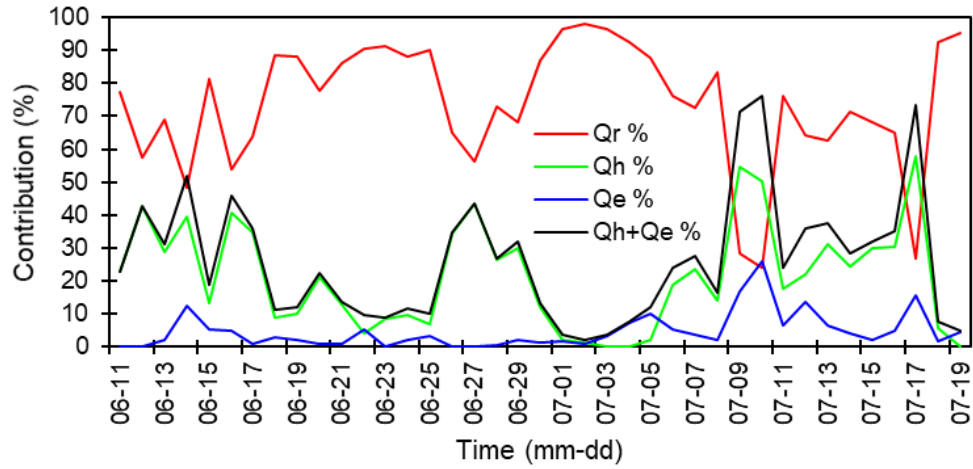


Figure S2-13. Relative contribution of Q_r , Q_h and Q_e to the total surface energy balance during the study period 2019. The sum of the positive fluxes is scaled to 100%.

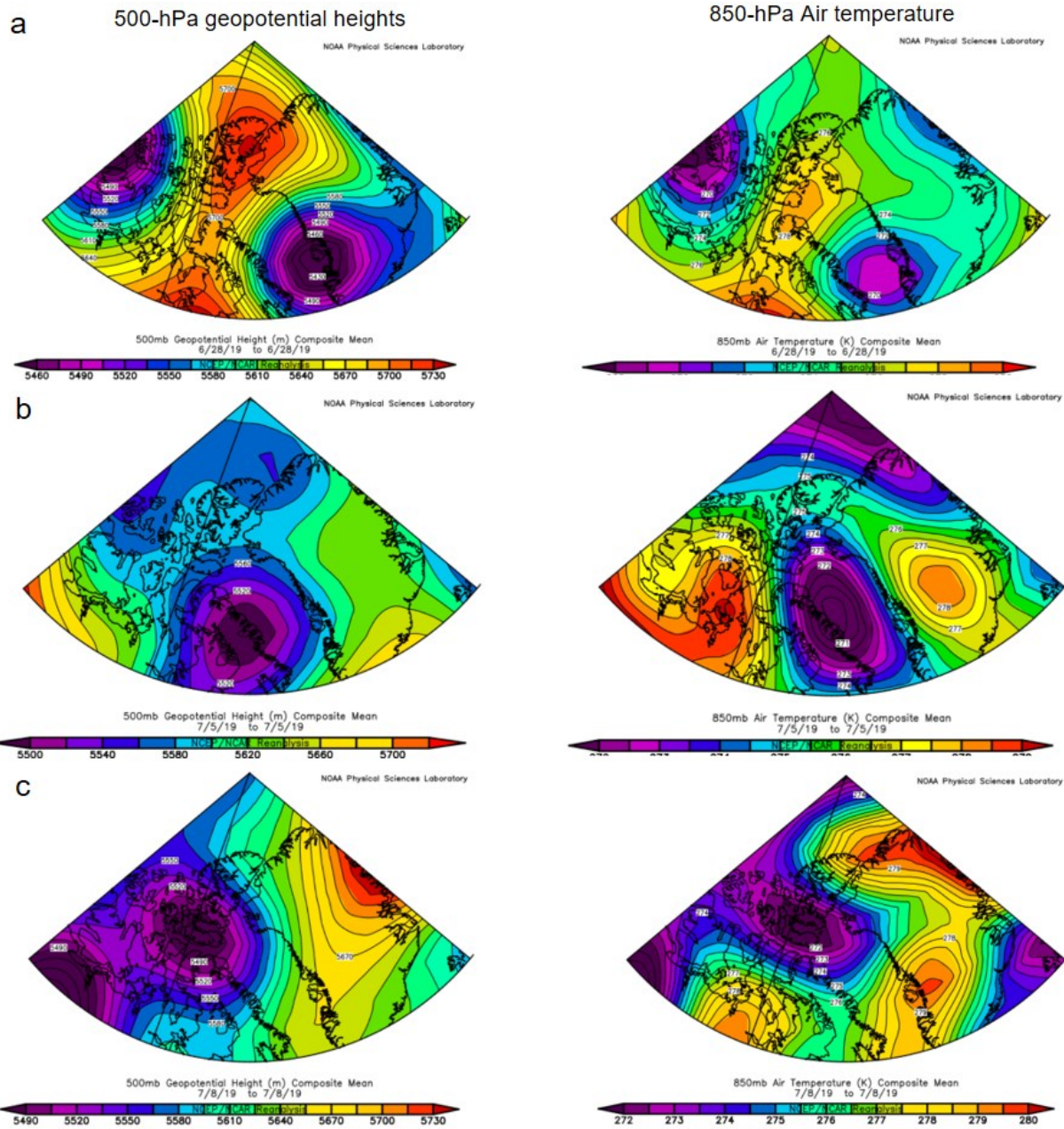


Figure S2-14. Contour map of the 500-hPa geopotential heights (left) and 850-hPa air temperature (right) during the three days considered to be representative of dominant summer weather conditions on the north coast of Ellesmere: a) Case 1 (28 June 2019); b) Case 2 (5 July 2019) and c) Case 3 (9 July 2019). The geopotential at 500 hPa is the altitude at which 500 hPa is reached. What appears in orange/red here corresponds to high geopotentials, i.e. anticyclones, and what appears in pink/purple corresponds to low geopotential, i.e. depressions. Data were obtained from NCEP/NCAR reanalysis available at : www.psl.noaa.gov/data/composites/day/.

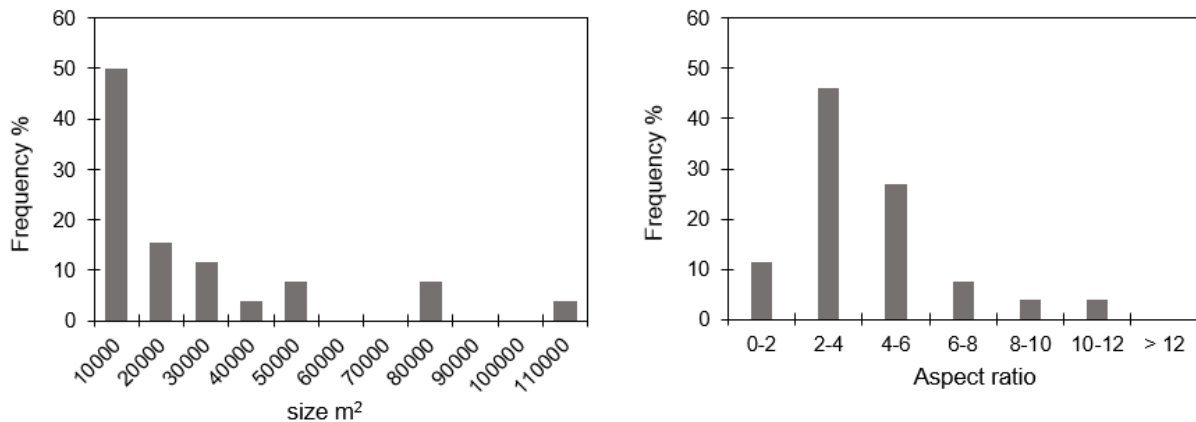


Figure S2-15. Morphometric characteristics of the perennial ice patches on Ward Hunt Island.

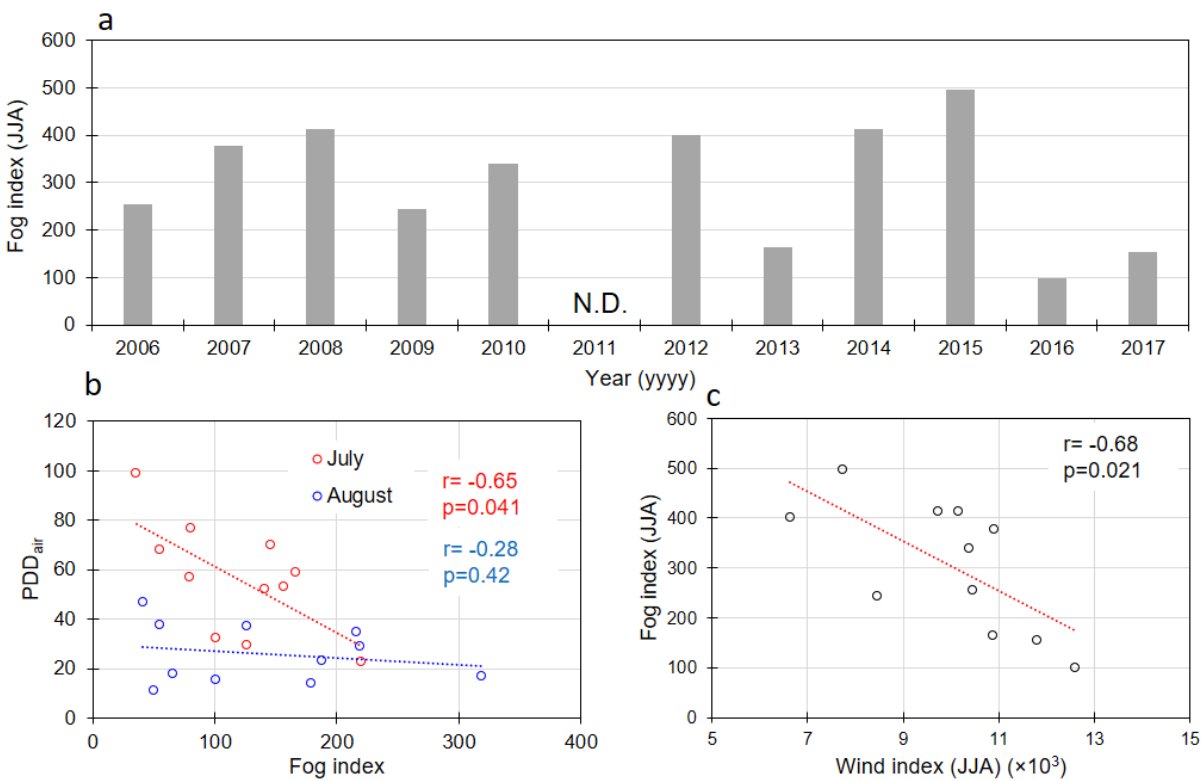
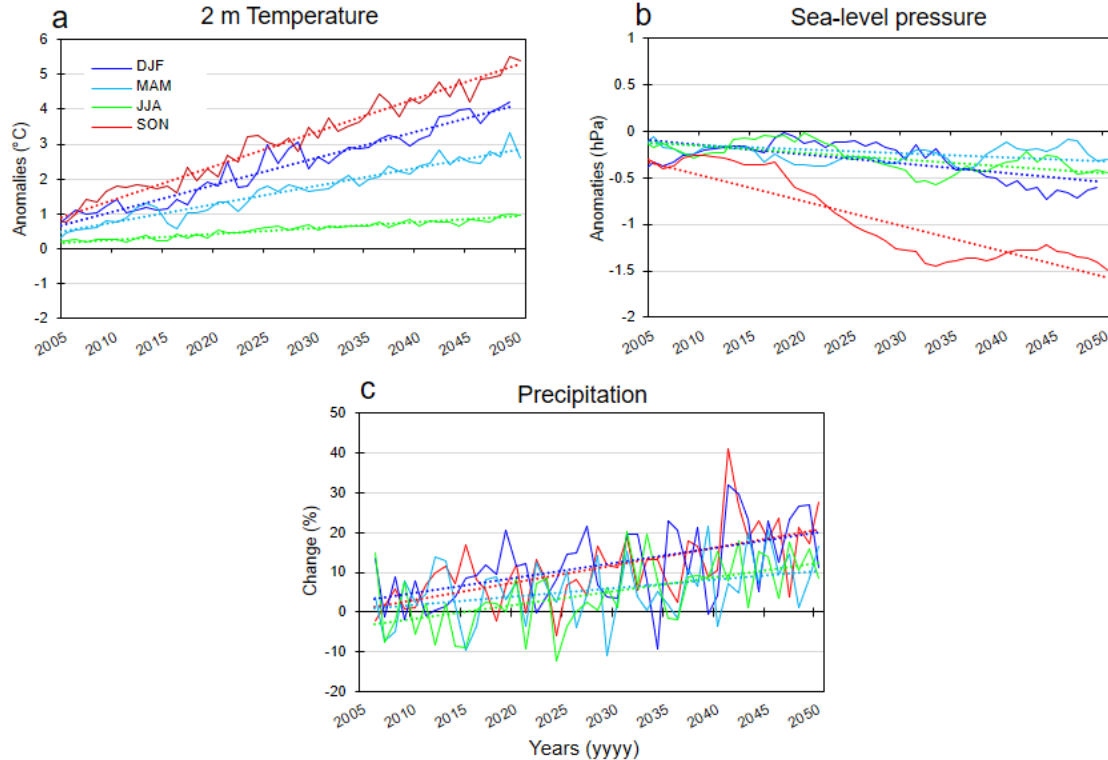
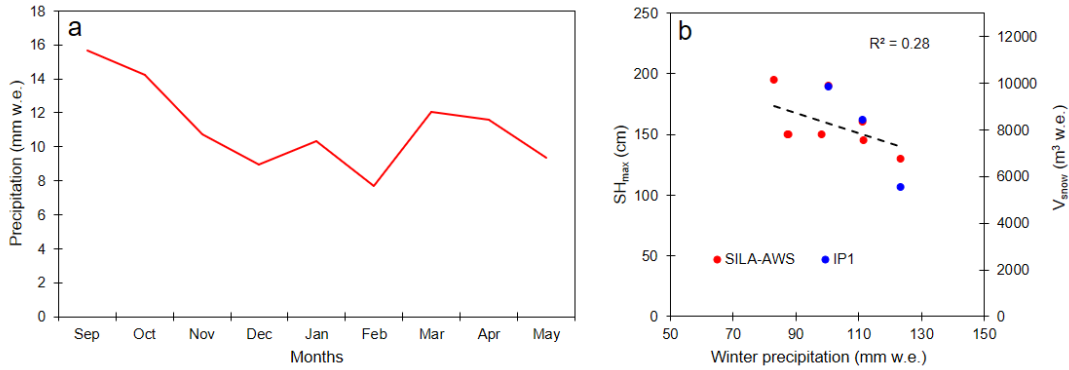


Figure S2-16. a) Evolution of the summer (JJA) fog index, consisting of the sum of hours with relative air humidity above 95% at SILA station for the period 2006-2017; b) Relationship between fog index of July and August and the positive degree-day (PDD_{air}) for the period 2006-2017; c) Relationship between summer wind index and fog index for the period 2006-2017.



Chapitre 4 – Ice patches and their biogeomorphic system in the High Arctic polar desert

Auteurs : Gautier Davesne, Daniel Fortier

4.1. Avant-propos

Le chapitre 4 s'intéresse au système biogéomorphologique qui se développe sur la section d'un versant en aval des plaques de glace dans le désert polaire. Ces environnements pronivaux forment des unités de paysage particulières qui se démarquent des terrains stériles et arides dominants dans le désert polaire par des écoulements de surface durable, des formes de terrain dominées par le triage du sol et la solifluxion et un couvert végétal plus dense et diversifié. En particulier, cette étude vise à comprendre le développement et le fonctionnement de ces environnements liés aux plaques de glace et répond ainsi à l'objectif 3 de la thèse. Cette recherche repose sur un protocole expérimental inédit, alliant un suivi pluriannuel (température du sol, solifluxion), des observations de terrain (échantillonnage de sol, relevé de végétation, mesure de couche active) et une cartographie géomorphologique à partir de photographie aérienne par drone. Ce jeu de données a permis d'examiner les interactions et les rétroactions à fine échelle entre la plaque de glace, les flux d'eau de fonte et de sédiments, les régimes thermiques et d'humidité du sol, ainsi que la végétation et les processus géomorphologiques. À partir des interprétations tirées des résultats et de la littérature existante, un modèle conceptuel de développement des systèmes biogéomorphologiques de plaque de glace a été proposé. Le manuscrit est en préparation pour être soumis suite aux commentaires du jury.

4.2. Résumé

Dans le désert polaire, les systèmes abiotiques et biotiques de nombreux versants dépendent de manière critique de la présence des plaques de glace permanentes qui sont très répandues à l'échelle paysage. Pourtant, très peu d'études ont porté sur la structure et le fonctionnement des environnements qui se développent en aval de ces plaques de glace. En particulier, on connaît peu la nature des interactions et les rétroactions à petite échelle entre les plaques de glace, les flux (eau

et sédiment), le régime thermiques et d'humidité du sol, la végétation et les processus géomorphologiques qui forment ensemble un système biogéomorphologique complexe sur les versants. Pour combler ces lacunes, nous proposons une étude holistique combinant des études géomorphologiques, hydrologiques et biologiques d'une section de versant en aval d'une plaque de glace permanente à l'île Ward Hunt (83°N, Haut-Arctique canadien) afin de fournir une compréhension qualitative et quantitative du rôle des plaques de glace sur le fonctionnement et l'organisation d'un géosystème de désert polaire. Nos résultats ont démontré que la plaque de glace étudiée joue un rôle clé dans le contrôle des flux d'eau et de masse le long du versant en stockant l'eau et les sédiments en hiver et au début de l'été et en les libérant pendant la période de fonte. Ces apports d'eau et de sédiments concentrés par la plaque de glace le long de sa marge aval activent une suite de processus hydrologiques, géomorphologiques et biologiques qui aboutissent au développement d'un système biogéomorphologique que nous avons décrit par un modèle conceptuel en 3 étapes. Le stade 1 représente un stage embryonnaire durant lequel le système est dominé par l'activité fluviale. Une importante rétroaction positive se développe alors entre les processus de sédimentation et les écoulements de surface. Au stade 2, l'expansion des dépôts de sédiments fin et leur humidification durable permet la colonisation de croutes organiques et d'espèces pionnières qui initient d'importantes rétroactions sur les processus géomorphologiques (ex. sédimentation, stabilisation des sols) et le régime thermique du sol (ex. effet réchauffant des croutes organiques noires). Ces processus apportent des conditions favorables à l'activation de processus de solifluxion et de triage du sol. Le stade 3 représente l'état actuel du système qui peut être qualifié de « mature ». La section du versant en aval de la plaque de glace est dominée par des lobes de solifluxion qui délimitent des zones humides. Notre modèle conceptuel est une première étape vers le développement d'un modèle numérique quantitatif de la dynamique des versants du désert polaire.

4.3. Abstract

In polar deserts, abiotic and biotic systems on many slopes are critically dependent on the presence of permanent ice patches that are widespread at the landscape scale. Yet, the structure and functioning of the microenvironments that develop downslope of these ice patches are poorly documented. In particular, little is known about the nature of the small-scale interactions and feedbacks between ice patches, meltwater and sediment fluxes, soil thermal and moisture regimes,

vegetation and geomorphic processes that together form a complex biogeomorphic system on the slopes. To address these gaps, we propose a holistic study combining physical and biological surveys of a slope section below a permanent ice patch at Ward Hunt Island (83°N , Canadian High Arctic). The aim was to provide a qualitative and quantitative understanding of the role of ice patches on the functioning and organization of a polar desert slope geosystem. Our results showed that the studied ice patch plays a key role in controlling water and mass fluxes along the slope by storing water and sediment in winter and early summer and releasing it during the melt period. These supplies of water and sediment, concentrated by the ice patch along its downstream margin, activate a suite of hydrological, geomorphological and biological processes that results in the development of a biogeomorphic system that we have described through a 3-stage conceptual model. Stage 1 represents an embryonic stage during which the system is dominated by fluvial activity. An important positive feedback develops between sedimentation processes and surface flows. In stage 2, the expansion of fine sediment deposits and their sustained wetting allows the colonization of organic crusts and pioneer species which initiate important feedbacks on geomorphological processes (e.g. sedimentation, soil stabilization) and the soil thermal regime (e.g. warming effect of black organic crusts). These processes provide favourable conditions for the activation of solifluction and soil sorting processes. Stage 3 represents the current state of the system which can be described as "mature". The section of the slope downslope of the ice patch is dominated by solifluction lobes that delimit humid zones. Our conceptual model is a first step towards the development of a quantitative numerical model of polar desert slope dynamics.

4.4. Introduction

In the non-glaciated polar desert, perennial ice patches are widespread and represent a prominent cryospheric feature in the landscape ([Chap. 3](#)). They consist of a small cryospheric system composed of a static mass of superimposed ice overlaid by thick wind-drifted snow accumulations (Lewkowicz and Harry, 1991; [Chap. 3](#)). Ice patches form typically in deep topographic niches (e.g. break-of-slope, concave slope) and since their mass balance is mainly governed by self-regulating mechanisms linked to topoclimatic conditions, they are relatively stable over time (Fujita et al., 2010; [Chap. 3](#)). Ice patches can exist continuously for centuries, even millennia, making them a fundamental agent in the long-term dynamics of polar desert slopes ([Chap. 2](#)). The primary role of the ice patches is to provide liquid water to the slope in summer, making them of great hydrological significance for the freshwater cycle of the polar desert where rainfalls are scarce (Ballantyne, 1978; Carey and Woo, 2001; Langford et al, 2015; Lewkowicz and Young, 1990). On the downslope margin of the ice patches (referred to as pronival margin), the prolonged soil moisture, coupled with sediments and energy influxes associated with meltwater runoff, create localized conditions that support enhanced geomorphic and biological activities.

The slope-shaping processes triggered by meltwater include chemical and mechanical weathering (Berrisford, 1991), erosion and mass movement, mainly through sheet wash and solifluction (St-Onge and Gullentops, 2005; Washburn, 1999). The whole suite of processes was generally discussed under the concept of nivation (Ballantyne, 1985; Thorn, 1978). Recent studies on nivation are scarce and focus mainly on alpine regions so that little is known about nivation in the polar desert. The most extensive work has been done by Christiansen (1998) who described a landform assemblage related to snowbanks in unconsolidated sediment slope in eastern Greenland. It included pronival solifluction, retrogressive erosion by backwall recession, pronival stone pavements and alluvial processes. More recently, Paquette et al., (2020a) described the toposequence of a nival slope in the polar desert of Ward Hunt Island (Canadian High-Arctic) which is characterized by nivation hollows, where seasonal snowdrifts and perennial ice patches are present, from which solifluction lobes developed (Verpaelst et al, 2017), while further downslope, patterned ground emerges. In the semi-arid Antarctica Peninsula, an interesting description of nivation processes was also proposed by Kňažková et al. (2021) who reported that ice patches promote downslope transport of fine sediments and at the same time act as a barrier to solifluction movements from the upper slope. These preliminary studies therefore show that the

geomorphological effects of ice patches on a slope are variable and depend on the topographical context and the nature of the soils. The biological function of the ice patch is also particularly important in the polar desert. The prolonged hydration of the soil in the pronival margin is known to provide suitable conditions for vegetation growth and microbial activity (Bliss et al., 1984; Desjardins et al., 2021; Gold and Bliss, 1995; Lennihan et al., 1994). By supporting the development of microhabitats with abundant vegetation, snow/ice patches contribute to form patchy wetlands across the polar desert, as conceptualized by Woo and Young (2003).

Despite these few existing studies, knowledge on geomorphic and biological activities linked to ice patches on the polar desert slopes remains superficial, particularly because it is mainly based on reconnaissance-level field observations. Surprisingly, no holistic investigation combining the study of biotic and abiotic components of the pronival margins has been carried out so far, although these two elements seem to be intimately linked. In particular, it is unclear how an ice patch initiates the development of pronival geomorphic and biological processes and how the resulting pronival slope system functions and evolves in time and space. Such integrated studies are challenging, but the use of a biogeomorphic approach applied to the ice patch system can help fill this knowledge gap. This approach has become increasingly popular in recent years in the geosciences as it has proven to be useful for studying and understanding the feedbacks between geomorphic and vegetation dynamics in various natural systems (e.g. fluvial, Corenblit et al., 2016; periglacial and paraglacial slopes, Eichel et al., 2016; 2017; and glacier forelands, Eichel et al., 2013; Moreau et al. 2006).

In this study, we propose to apply, for the first time, a biogeomorphic approach to the study of an ice patch geosystem present on a polar desert slope. The main goal is to identify and quantify the small-scale processes, linkage and feedback between the ice patch, slope processes, landforms and vegetation that govern the functioning of an ice patch-related slope geosystem. To address it, we collected a large dataset by combining geomorphological, hydrological, and biological studies during fieldwork conducted on the pronival margins of a perennial ice patch located at Ward Hunt Island located at the northern limit of the Canadian Arctic Archipelago. Our objectives were to (1) characterize and map the assemblage of landforms that composed the biogeomorphic system of ice patch; (2) quantify fluxes of water and sediment, and establish the physical properties and thermal regime of the soil around the pronival margin of the ice patch; (3) document the ecological

significance of the humid zones connected to the ice patch; (4) identify and discuss the key functional interactions, linkages and feedbacks controlling the development and evolution of the pronival biogeomorphic system.

4.5. Study site

Ward Hunt Island (hereafter WHI; $83^{\circ}05'09''\text{N}$, $74^{\circ}06'19''\text{W}$) (**Figure 45a**) is an ideal site to study the impact of ice patches on slopes development because it is completely ice-free and it has escaped glaciations for as much as $> 400\,000$ years (Lemmen and England, 1992; Vincent et al., 2011b). WHI has a cold desert climate with a mean annual air temperature of $-17.07\,^{\circ}\text{C}$ for the period 2005-2019, and a monthly mean ranging between $-31.6\,^{\circ}\text{C}$ in February and $1.7\,^{\circ}\text{C}$ in July (CEN, 2021).

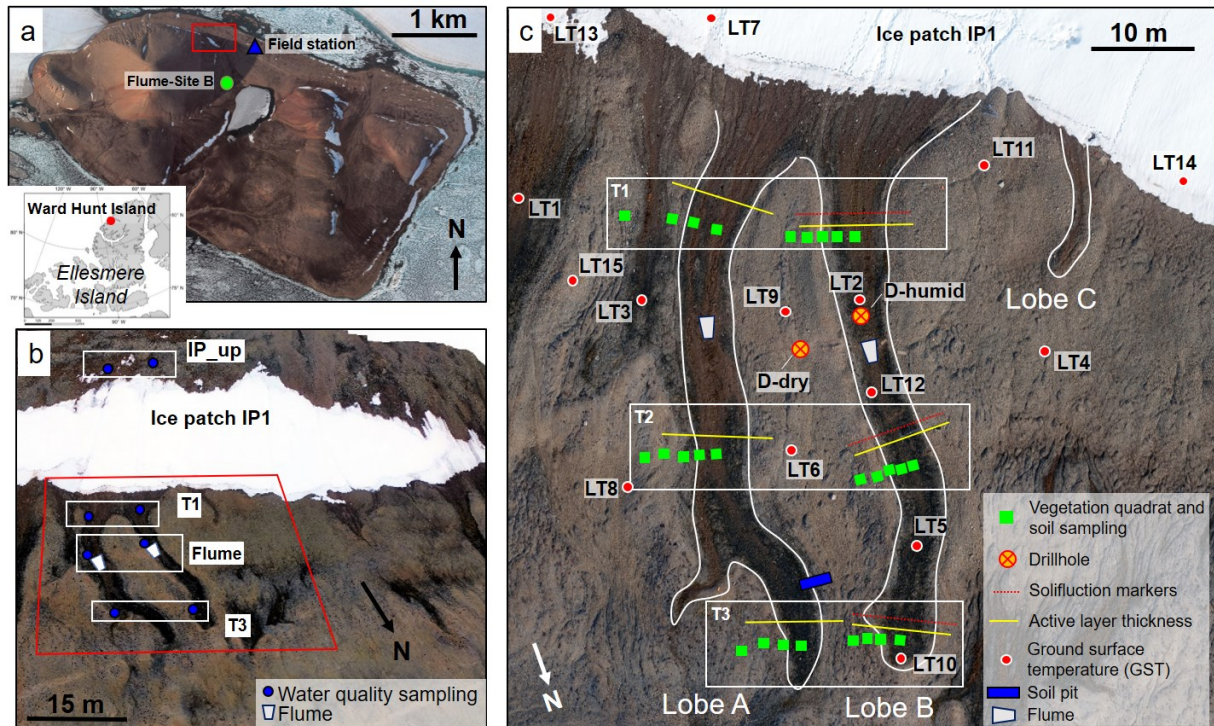


Figure 45. Study site: a) Location of Ward Hunt Island (WHI) at the northern tip of Ellesmere Island (Canadian High-Arctic Archipelago) and World-View 3 image of the whole island taken on 19 August 2019 showing the study site in the red box. North is up in (a) map unlike in (b) and (c). b) 3D visualization of the studied ice patch (IP1) and its biogeomorphic system (red box) based on UAV orthomosaic (flight carried out on 22 July 2019) and ESRI ArcScene 10.6 software. The location of the water quality sampling sites and the flumes are shown in this image; c) close-up of the studied biogeomorphic system (red box in b) showing the solifluction lobes A and B, where most of the fieldworks was undertaken, and small lobe C.

No precipitation record is available but it is likely similar to the annual average of 185 mm year⁻¹ (water equivalent) measured at Alert, located 170 km to the southeast (Environment Canada, 2021). In winter, the seasonal snow is scoured from the exposed surface by prevailing westerly winds (Davesne et al., 2021) and wind-drifted snow accumulates in sheltered slopes and topographic discontinuities to form deep seasonal snow patches and nourishes perennial ice patches ([Chap. 3](#)). In the present-day, these ice patches represent the largest and most conspicuous perennial ice masses on the island (**Figure 45a**). Most of them are found between 20 and 50 m a.s.l. along the main break-of-slope at the junction of the steep faces with the scree slope ([Chap. 3](#)). Beneath the surface, WHI presents continuous permafrost with a mean annual temperature of –13.5 °C at 3 m depth (CEN, 2021). The physiography of WHI is marked by Walker Hill (412 m a.s.l.) which occupies the western part of the island. The central depression is occupied by the ultra-oligotrophic Ward Hunt Lake (WHL). Most of the limestone slopes of Walker Hill exhibit a rectilinear profile (Richter slope) with angles around 30–35°. Below the Holocene marine limit (~62 m a.s.l.; Lemmen, 1989), the gentle slopes present successive levels of raised-beach ridges built in the sand and gravel deposits. The hillslopes are notched by hollows and terraces interpreted as nivation forms and by glacial grooves and are covered by a mix of weathering – mostly frost shattered – mantle, colluvial debris and glacial drift veneer (Vincent et al., 2011b). Early vegetation studies reported only 36 taxa. The sparse patches of vascular plants and mosses covering <5% of the land surface (Vincent et al., 2011b). Soil development is minimal with the bulk of the matrix being composed of mineral materials.

The studied ice patch (hereafter IP1) is lying in a slope break at ~50 m a.s.l. between the steep calcareous (25–30°) north face of Walker hill and the lower, gentler section of the slope (5 to 10°) (**Figure 45b**). The study focused on the biogeomorphic system of a section of the pronival margin of IP1 delineate by the red box in **Figure 45b**. The biogeomorphic system presents two principal solifluction lobes (lobe A and lobe B) (**Figure 45b**), with well-defined central tread, lateral risers and a frontal riser, and a small lobe (Lobe C) at an early stage of development. Soils that are wet during most of the summer are called "humid soils" and the well-drained gravelly soils that made up the parent slope (i.e. outside lobes) are called "dry soils". In contact with the frontal edge of the ice patch, the "seasonal margin" represents a band where the soil is uncovered during the summer as the snow and ice front retreats.

4.6. Methods

4.6.1. UAV-based mapping of the pronival margin of the ice patch

In this study, we use a quadcopter drone (DJI Phantom 4 pro) equipped with a standard Red-Green-Blue (RGB) camera to collect aerial photos (see methodological details in [Appendix A3](#)). We relied on a single flight on 8 July 2019 that covered most of the lower part of the hillslope of Walker Hill including IP1 and its pronival margin (flight elevation of 90 m). The set of images were then processed in Pix4Dmapper (Pix4D SA 2016) based on the Structure from Motion (SfM) algorithm to produce digital surface models (DSMs) and orthomosaics with a high spatial resolution (~ 2 cm; [Appendix A3](#)).

The geomorphic features and soil surface composition and characteristics over the pronival margin of IP1 were mapped based on the analysis of UAV products coupled with the rich collection of field photographs and observations. The map was generated on-screen in ArcGIS by vectorizing the terrain features based on a careful analysis of the orthomosaics ([Figure S3-1a](#)) and DSMs-derived surface models (i.e. shaded relief, slope angle, topographic position index (TPI); [Figure S3-1b,c,d](#); [Appendix A3](#)). The geomorphic map focused (i) on surficial deposits and the soil surface composition, including inorganic and organic soil, (ii) on the recognized landforms that resulted from contemporary processes and inherited from the Holocene sea-level changes, (iii) on the surface hydrological and cryospheric elements and (iv) on the soil moisture distribution which was inferred by supervised classification in ArcGISPro based on the darker colouration of humid soils compared to dry soils (Langford et al., 2015).

4.6.2. Instrumentation and field measurements

4.6.2.1. Ground surface thermal regime

The ground surface temperature (GST) over the pronival margin of IP1 was recorded at hourly intervals from 16 June 2016 to 19 July 2019 by 15 dataloggers Trix-8 (LogTag®; resolution 0.1 °C, uncertainty of ± 0.5 °C), installed about 5 cm below the ground surface and named LT1 to LT15 ([Table S3-1](#)). Six were installed in dry soils, six in humid soils and three in the seasonal margin of IP1 ([Figure 45c](#)). The raw data were used to calculate the mean July GST (GST_{JULY}), the warmest month of the summer. The degree-day of thawing at the ground surface (PDD_{surf}; sum

of daily mean GST above 0 °C), and the degree-day of growing at the ground surface (GDD_{surf} ; sum of daily mean GST above of 5 °C; Weijers et al., 2013) were also calculated. The duration of the growing season (GSD, days) was calculated by summing the number of days with $\text{GDD}_{\text{surf}} > 0$ throughout the summer. The air temperature (T_a) was recorded from 14 June 2016 to 19 July 2019 by a U22, Hobo® (resolution of 0.2 °C, uncertainty of ± 0.21 °C) installed in a radiation shield 1.5 m above the ground surface. To diagnose reasons for spatial variability in GST_{JULY} , Pearson correlation coefficients were calculated using several potential explanatory variables measured on the field or obtained by GIS for each sensor site. It included: (1) the end-of-winter snow height measured by hand-probing on 10 June 2019, (2) the soil volumetric water content (VWC) measured using an EC-5 sensor (resolution: 0.001 m³/m³; uncertainty ± 0.03 m³/m³) on 14 July 2019, (3) the Topographic position index (TPI) derived from DSMs, (4) the distance from the ice patch frontal edge and (5) the soil surface composition.

Finally, the thaw depth was measured at the end of the field period on 19 July 2019 along 3 transects (T1; T2 and T3) that bisected the solifluction lobes A and B and extended ~ 5 m on both sides of the parent slope (**Figure 45c**). Measurements were made every meter along transects by pushing a frost probe into the soil until it hit the frost table. Triplicate measurements were performed to minimize errors.

4.6.2.2. Hydrological regime and meltwater quality

Streams flowing out of IP1 and supplying the lobes A and B were monitored by two cut-throat flumes (Flumes A and B, respectively) installed in the main channels (**Figure 45b**). An additional flume was installed in a water track on the east slope of Walker Hill, corresponding to Site B in the study of Paquette et al., (2017 and 2018) (**Figure 45a**). The calculation used to obtain the hourly free flow rate (Q_f , cm³ s⁻¹) from the flumes is detailed in [Appendix A3-2](#). The discharge measured at the flumes gives a glimpse of the surface flow regime but does not allow quantifying the total flow as minor surface runoff occurs at other locations along the solifluction lobes and because subsurface flow wasn't measured.

Runoff water quality, including water temperature (T_w), specific electrical conductivity (SpC), pH and turbidity, had been measured manually twice a day during the field period 2019 around 9:00 hr and 18:00 hr (local time), which are close to the diurnal high and low flow stage respectively. Measurements were made at 3 sites (sampling sites T1; Flume and T3) along each

monitored lobes A and B and at one site (sampling site IP_up) upslope of IP1, in line with lobes A and B (**Figure 45b**). At Flumes A and B, T_w and SpC were measured continuously from 17 June to 20 July 2019. Details of the instrumentation and techniques used are presented in [Appendix A3-2](#). Furthermore, on 1 July 2019, turbidity at flumes A and B was sampled every hour from 5:00 hr to 22:00 hr to catch its evolution during the daily rising curve, the peak flow and the recession of the hydrograph. Based on this dataset, the strong linear relationship between the observed hourly discharge and the turbidity values was established ($R^2=0.90$; $p < 0.0001$; [Figure S3-2a](#)) and allowed to interpolate hourly turbidity for the whole study period (Braun et al., 2000).

The sediment concentration in water was also determined. The total suspended solid concentration (TSS, mg L⁻¹) was measured from water samples collected twice a day (around 9:00 hr and 18:00 hr) at the different sampling sites ([Appendix A3-2](#)). Comparison between TSS and turbidity showed a strong linear relationship ($R^2=0.82$; $p < 0.0001$; Fig. S1b) which was used to reconstruct the hourly evolution of TSS based on interpolated hourly turbidity. For the solute load, the total dissolved solid concentration (TDS, mg L⁻¹) was calculated from the SpC values based on a coefficient (0.65) used by Paquette et al., (2020a).

4.6.2.3. Soil and vegetation studies

- Soil movements

Soil surface movements at Lobe B were measured using the traditional method of repeatedly surveying the position of surface markers relative to a stable benchmark (Kinnard and Lewkowicz, 2005; Washburn, 1999). The markers were installed in July 2016 along 3 transects (T1, T2, T3) that intersected Lobe B (**Figure 45c**), therefore covering various environments (lobe central tread and lateral riser, parent slope). Transects were made 1.5 m upslope of those for frost table measurements to avoid any perturbation of the soil surface. The markers consisted of 15 cm-long nails with plastic tags inserted vertically into the soil every meter and small pebbles painted orange deposited on the soil surface every 20 cm between the nails. Markers were installed using a tensioned rope to ensure perfect alignment. The position of markers was surveyed after their installation on 10 July 2016 and three years later on 17 July 2019 using a VX spatial station (TrimbleTM; uncertainty 2 ± 1 mm with the prism). The difference between the surveys gave the total displacement (mm). The potential error was evaluated by comparing the position of 15

markers between 2016 and 2019 considered as stable on the parent slope, including erratic rocks and steel stakes inserted in the gravel. The error was calculated to be ± 0.9 cm.

- *Vegetation surveys*

Vegetation community composition was surveyed between 12-15 July 2019 over the pronival margin of IP1 to evaluate which disturbance tolerant species can colonize active zones of the lobes and compare the species diversity and abundance with dryer stable communities in the parent slopes (**Figure 45c**). The plant cover was assessed visually in a 50×50 cm quadrat with a 5×5 cm grid using the modified Braun-Blanquet method (Braun-Blanquet, 1932) for vascular plants (by species), lichens, mosses, organic crust (black and white) as well as gravel, freshly deposited sediments and surficial water. For lobes A and B, quadrats were deployed along the transects T1, T2 and T3 so that they covered the different habitats observed in the studied zone, i.e. the central tread of lobes and their mesic lateral margins, the lateral risers of lobes and the parent slope (**Figure 45c**). A total of 37 quadrats were described and their position was surveyed with the VX station. This dataset was used to implement a canonical correspondence analysis (CCA) to identify the primary relationships between the cover data and the explanatory environmental variables ([Appendix A3-3](#)).

- *Soil physical properties*

Soil samples were collected from drilling in lobe B (site D-humid) and the adjacent parent slope (site D-dry) (**Figure 45c**) using an earth auger (BT360; Stihl®) equipped with a 10.8 cm diamond carbide core barrel. Drilling was conducted on 16 June 2017 when the active layer was still frozen. Due to a freezer failure, all of the ice cores thawed before ice content analyses were performed. However, some samples were recovered for soil analyses. For D-dry, samples S1 and S2 were collected at 20-35 cm and 50-65 cm depth, respectively, and for D-humid, samples S3 and S4 were collected at 20-40 cm and 45-60 cm depth. Also, a 2 m-wide soil pit was excavated to the frost table at the transition between the humid soils of the central tread of Lobe A and the dry soil of the parent slope on 3 July 2017 (**Figure 45c**). Two soil samples were collected above the frost table on the humid side of the pit (samples P1 and P2) and two others on the dry side (samples P3 and P4). A description of the main soil units was performed in the field. Finally, two samples of freshly deposited sediment on the ground surface were collected on 17 July 2019, one upstream of the flume A (sample F1) and the second on a pronival alluvial fan (sample F2). All of these samples

were analyzed to obtain grain size distribution as well as mineralogical characterization and chemical compositions ([Appendix A3-4](#)). Finally, soil moisture at each quadrat site in Lobes A and B was obtained by collecting samples from the soil surface (~10 cm deep, 15 cm long and 5 cm wide) on July 15, 2019. Moisture content was obtained by oven drying at 105°C to a stable mass.

4.7. Results

4.7.1. Geomorphic assemblage of the pronival margin

A geomorphological map of the pronival margin of the ice patch IP1 is presented in [Figure 46](#). The area consisted of a low-gradient slope marked by successive steps and terraces formed by a sequence of raised beaches inherited from the last Holocene marine phase. The most identifiable ridges were at an elevation of ~32 m, ~29 m and ~25 m a.s.l. The surficial deposits over the studied zone were composed of marine material consisting of washed gravels of various lithology with rounded to sub-angular shapes. This material was occasionally mixed with coarse angular calcareous frost-shattered colluvium coming from Walker Hill ([Figure 47a](#)). Glacial erratic boulders, up to 90 cm in diameter and of allochthonous lithologies (i.e. igneous and metamorphic rocks), were also widespread across the studied zone ([Figure 47b](#)). Downslope of IP1, a complex biogeomorphic system was present, resulting from the extensive reworking of the pre-existing surface material and slope topography ([Figure 46](#)). The most prominent landforms on the studied slope section were solifluction lobes. Lobes A and B were the largest and most developed with a length of ~90 m and 80 m, respectively ([Figure 46](#)). The lobe morphology was characterized by a lateral riser of gravel ~15 to 30 cm tall and a frontal riser up to ~30-40 cm hight for both lobe A and lobe B ([Figure S3-3](#)). Within the lobes, the central tread consisted of a platform supporting saturated soil and vegetation including vascular plants, lichens, and mosses. A vegetation survey is given [in Section 4.7.4](#). Towards the front of the lobes, the treads tend to be higher than the level of the surrounding of the parent slope ([Figure S3-3](#)). Because the solifluction lobes overrode the beach deposits, the lobes had erased the beach ridges and the tread surface exhibited a gentle and regular inclination of 6-10°. At a smaller scale, however, some tread sections presented a series of terracettes, less than 5-15 cm high, formed by moss patches ([Figure 47c](#)).

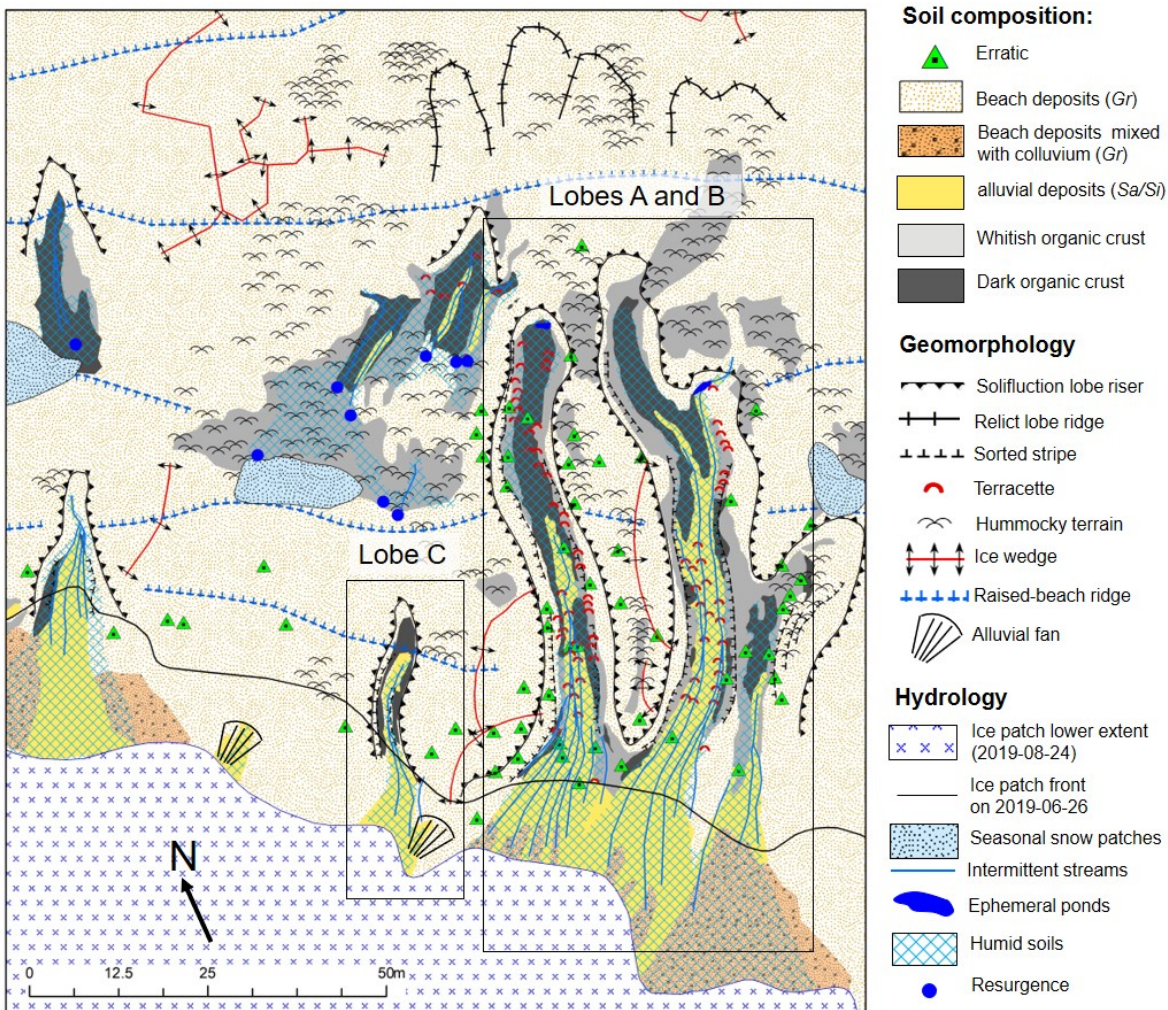


Figure 46. Geomorphological map of the pronival margin of the perennial ice patch IPI illustrating the complex biogeomorphic system. The map details the soil composition, geomorphology and hydrology of the studied slope section. For the soil composition: Gr=gravel, Sa=sand; Si=silt. Black boxes show the paired lobes A and B and the lobe C in an early stage of development.

In the upper section of lobes, the soil surface of the tread was composed of fresh deposits of fine-grained alluvium while lower down, in the middle and lower part of the lobes, the dark organic crust cover became dominant (**Figure 46** and [Figure S3-3](#)). The fine-grained matrix in the upper sections was reworked by sorting processes into small sorted stripes (**Figure 46**). These features channeled the surface flows leading to the development of multiple rectilinear rills (up to 2-5 cm deep; **Figure 47d**). These rills merged downslope into one or two little incised channels that concentrated the surface flow. During low flows, water circulation remained mostly underground over the lower section of lobes, while during meltwater pulses, sheet flows occurred over the entire tread surface and shallow ponds usually formed upstream of the frontal riser (**Figure 47e**). Between

the central tread and the lateral gravelly risers, the coarse materials were usually well-sorted, forming lateral stripes (**Figure 46** and **Figure 47f**). The soil surface of the lateral risers had typically a thin, discontinuous cover of whitish organic matter (**Figure 46** and [Figure S3-3](#)).

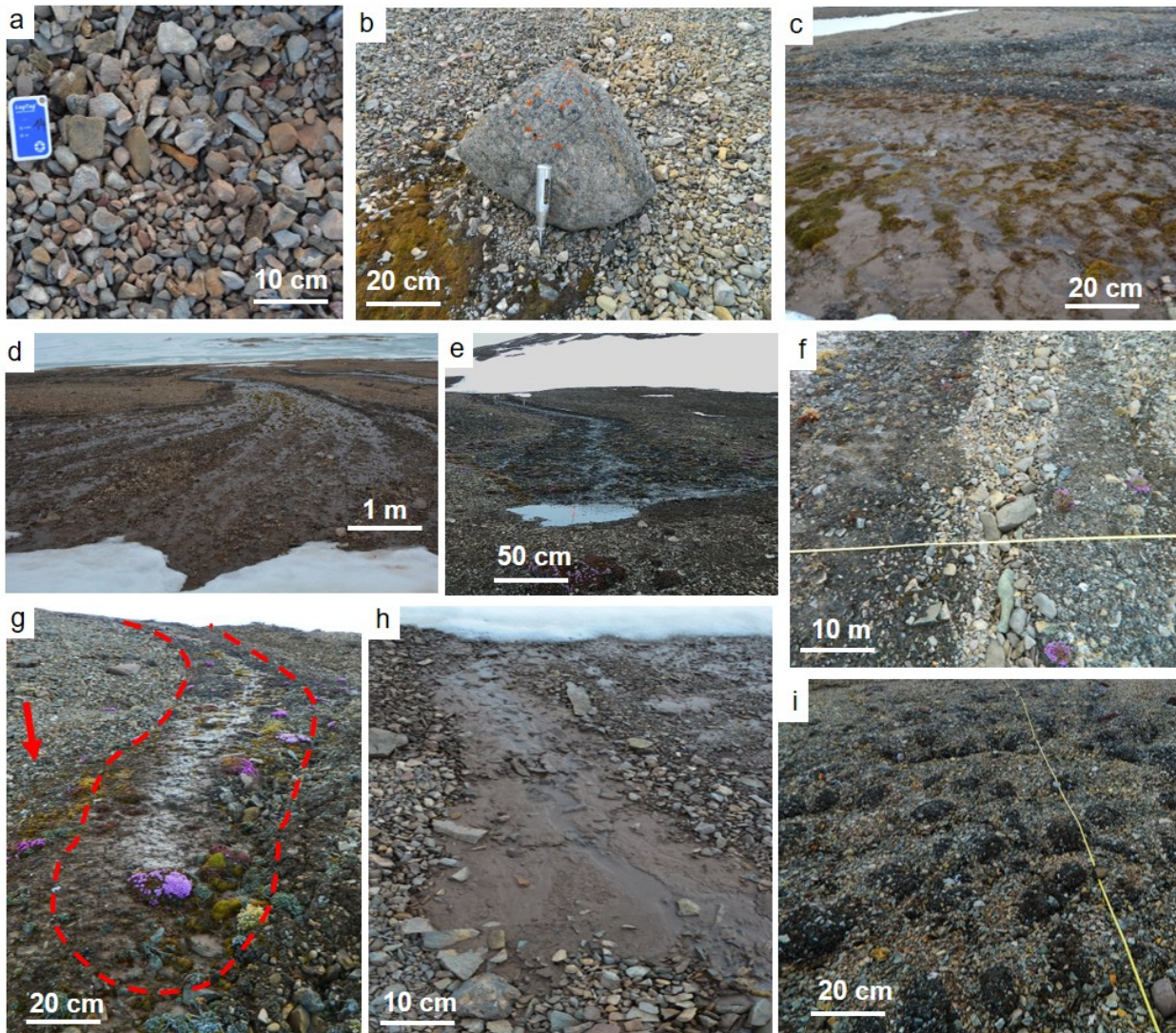


Figure 47. Geomorphic features encountered in the pronival margin of the ice patch IP1: a) Beach deposits characterized by coarse rounded and sub-angular gravel of diverse lithology; b) Erratic rock observed in the parent slope between lobe A and B; c) Series of terracettes with turf front that trap a significant amount of fine-grained sediments on the lobe treads; d) Parallel rills in the upper section of lobe B that drained the meltwater on the tread of lobes; e) Ephemeral small pond in the front of lobe B during peak flows; f) Sorted stripe between the lateral riser and the central tread of lobe A; g) Lobe C is delineated by the red dotted line. The arrow points downslope; h) Small alluvial fan that overrode the beach gravels in front of IP1; i) Field of hummocks downslope of lobe B.

Multiple lobes at a less advanced stage of development than lobes A and B were also present downslope of IP1, among which was lobe C (**Figure 47g**). Lobe C consisted of a longitudinal ridge of 17 m in length and was bordered on each side by sorted stripes. The central ridge was topped by sparse vascular plants and mosses as well as lateral bands of dark organic crust. Fresh sediment deposits were present all along the central tread and supported a slightly incised stream that drained meltwater from the ice patch edge to the front of the lobe where it infiltrated into the gravelly soil. Some lobes were not directly connected by surface flow to IP1 but developed downstream of meltwater resurgence along slope breaks caused by the raised-beached levels (**Figure 46**).

In addition to solifluction and sorting forms, the studied zone also exhibited small pronival alluvial fans (**Figure 46**) which overlaid beach deposits and that supported surface runoff (**Figure 47h**). The beach deposits had also numerous surface cracks indicating the presence of ice wedges (**Figure 46**). Finally, bumpy terrain formed by hummock was a prominent feature along and downslope of the solifluction lobes. Hummocks were composed of gravels usually mixed with a matrix of old organic matter and fine-grained sediments (**Figure 46** and **Figure 47i**).

4.7.2. Hydrology and meltwater quality of the pronival zone of IP1

4.7.2.1. The hydrograph analysis

At both flumes, the meltwater delivered by IP1 started to flow on 16 June 2019 but it remained weak during the first 10 days of measurements (until 27 June) despite a pronounced calculated melt rate (ΔSWE_{SEB} , mm d⁻¹ w.e.) ([Chap. 3](#)). Throughout the study period, the discharge was greater at Flume A than in B (**Figure 48a**). Three main peak flows occurred throughout the study period, the first one between 27 to 30 June, the second one between 6 to 11 July and the last one between 13 to 16 July. They were mainly associated with melt events following great energy input to the surface since there were no significant precipitation events ([Figure S3-4](#)). For flumes A and B, the general linear trend over the study period is towards an increase in discharge intensity as the season progresses ([Figure S3-5](#)). By comparison, at site B located in a water track on the east slope of Walker Hill (**Figure 45a**), the seasonal peak flow was reached earlier (28 June) and the discharge tended to diminish as the melt season progressed ([Figure S3-5](#)).

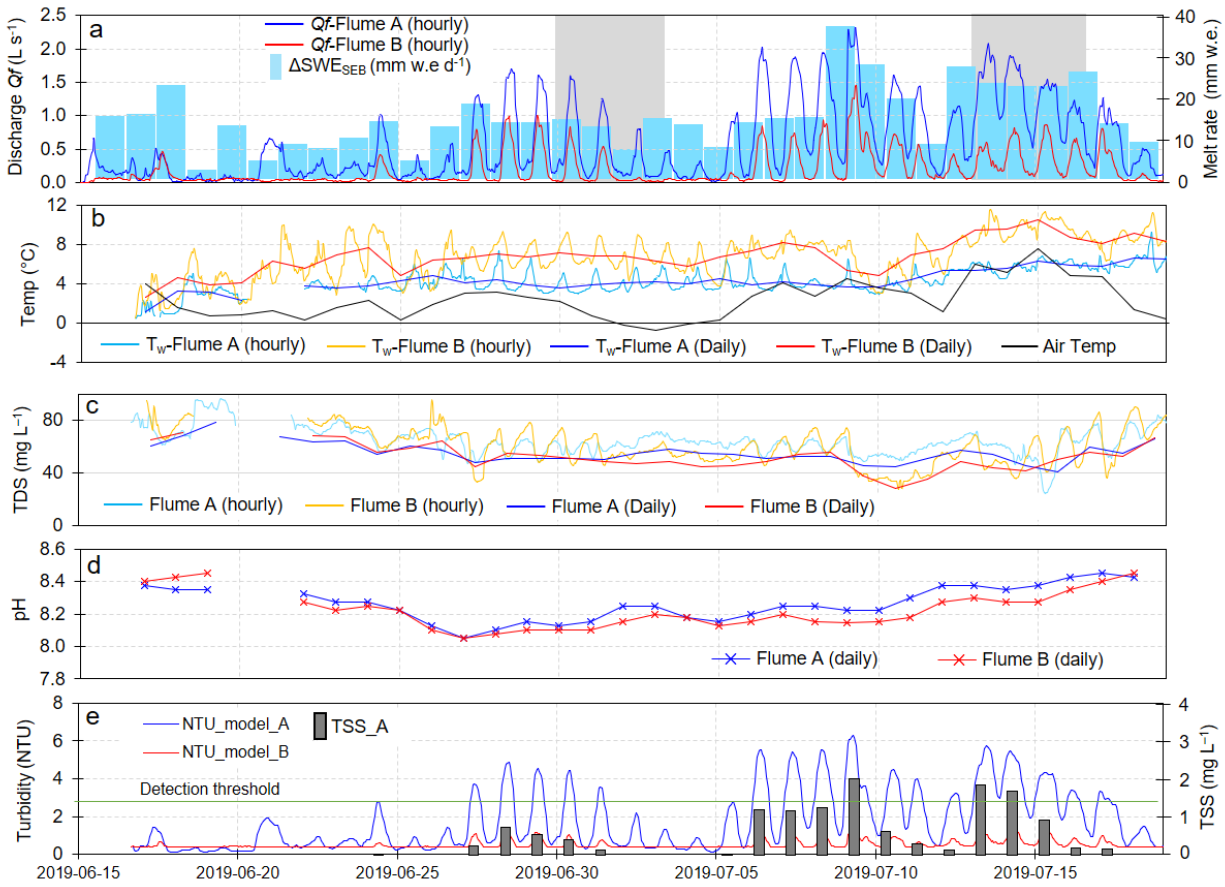


Figure 48. The hydrological regime and water quality at flumes A and B in the pronival margin of the ice patch IP1. a) Daily evolution of the discharge of the surface runoff along with the daily melt rate of the ice patch system (ΔSWE_{SEB} , mm w.e. d^{-1}) calculated from the surface energy balance (SEB) in Chap. 2 for the period from 11 June to 20 July 2019; b) Hourly and mean daily water temperature at flumes A and B along with the mean daily air temperature; c) Hourly and mean daily total dissolved sediment (TDS, mg L^{-1}) calculated from continuous specific conductivity measurements; d) Mean daily value of pH obtained from bi-daily measurements; e) Reconstructed hourly evolution of the turbidity (NTU) based on the close relationship between bi-daily turbidity measurements and discharge (see Fig. S3-2a). The green line indicates the detection threshold (2.5 NTU) below which the TSS is considered negligible. The grey bars show the daily fluxes of TSS at flume A calculated from the linear correlation between NTU and TSS obtained by filtration (see Fig. S3-2b).

4.7.2.2. Temporal evolution of water quality and sediment transfers at flumes

- Temperature

For both flumes, the water temperature (T_w) increased rapidly in the days following the flow onset (Figure 48b). T_w at Flume B was 2.4 °C warmer on average than that measured at Flume A over the study period (Table S3-1). At flume A, daily maxima reached values of 6–7°C until 10

July and up to ~ 9 °C at the end of the period (18 July). At Flume B, daily maxima were up to 10 °C by 21 June and reached the highest value of 11.6 °C on 13 July. For both sites, the daily average T_w was typically much higher than the air temperature and the daily maximum T_w occurred during the rising curve (**Figure 48b**).

- *Solutes and pH*

Flumes A and B both exhibited comparable total dissolved solids concentration (TDS) with an average of 65.7 ± 12.9 mg L⁻¹ and 60.9 ± 15.0 mg L⁻¹ respectively and an average pH of 8.27 ± 0.15 and 8.19 ± 0.12 respectively over the study period (**Figure 48c,d; Table S3-2**). In the early period, high values of TDS and pH were measured (**Figure 48c,d** around 80 mg L⁻¹ and 8.4 respectively), then, they decreased as the discharge increased. TDS values stabilized around 60–70 mg L⁻¹ from 27 June and decreased again slightly between 8 July and 12 July before increasing at the end of the study period to reach similar values to those of mid-June. The pH reached a minimum on 27 June with a daily average of 8.05 to reach values around 8.4 at the end of the period. The TDS fluxes (kg d⁻¹) at flumes A and B were 2.80 ± 2.0 kg d⁻¹ and 0.82 ± 0.65 kg d⁻¹ respectively, giving total fluxes of ~ 94 kg and ~ 27 kg of sediment for the entire study period.

- *Suspended solid sediments*

At flume A, the highest daily average was recorded on 9 July with ~ 2 mg L⁻¹. TSS fluxes (kg d⁻¹) that passed through flume A were 0.4 ± 0.6 kg d⁻¹, giving total fluxes of ~ 13.6 kg over the entire study period ([Table S3-2](#)). At Flume B, NTU values remained below the detection threshold and the TSS was thus considered negligible for the whole study period.

4.7.2.3. Spatial variation in water quality and sediment concentration

Upslope of IP1, subsurface water flows remained at, or near, 0°C throughout the study period (**Figure 49a; Table S3-2**). Field observations showed that this water came directly from the seasonal snow patches on the north slope of Walker Hill and flowed through coarse materials with a significant amount of interstitial ice. Downslope of IP1, T_w varied with the distance from the frontal edge of the ice patch. Close to the snowline, Site T1 experienced the coldest T_w with 1.4 ± 0.9 °C and 2.2 ± 1.3 °C on average for the study period for lobe A and B, respectively (**Figure 49a** and [Table S3-2](#)). Conversely, near the ends of lobes, Site T3 experienced the warmest T_w with 5.3 ± 2.1 °C and 8.1 ± 2.4 °C on average, respectively (**Figure 49a** and [Table S3-2](#)). The warmest daily

T_w was recorded at Site T3 of lobe B with 13.7 °C on 15 July. On average, T_w largely exceeded the air temperature at Site T3 and the Flumes, while it was slightly cooler at Site T1 (**Figure 49a**).

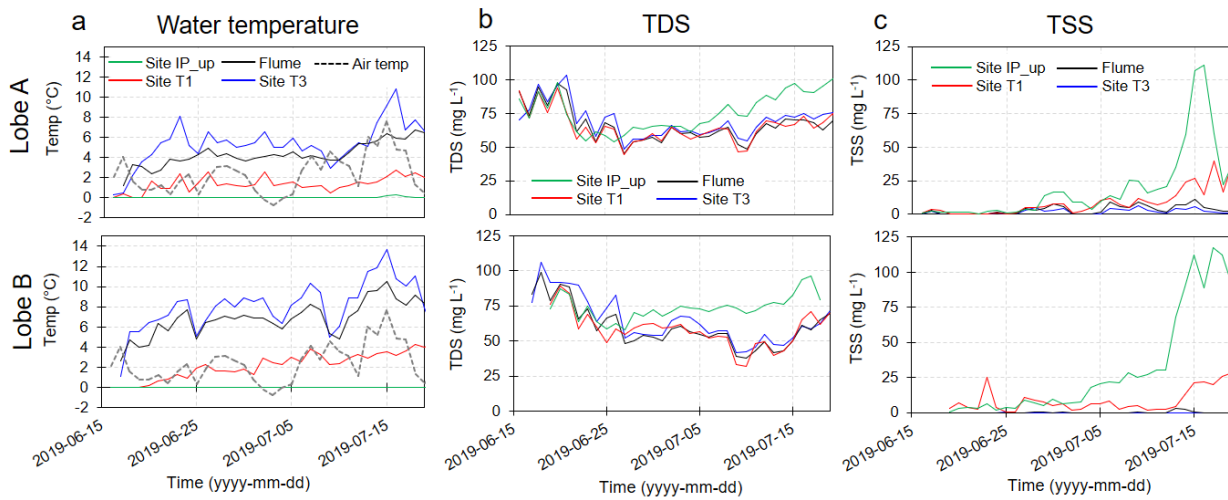


Figure 49. Daily evolution of the water temperature (T_w), total dissolved sediment concentration (TDS) and total suspended sediment concentration (TSS) at the three sample sites along lobes A and B in the margin of the ice patch IP1 (i.e. T1; Flume and T3) and at the sites above the ice patch (sites IP_up).

With regards to the solute content in water, all sampling sites show similar values at the beginning of the study period. Then, from 25 June, sites IP_up stood out with higher values than sites downslope of IP1 (**Figure 49b**). This difference tended to increase with time. TDS concentrations reached values of $76.2 \pm 14.2 \text{ mg L}^{-1}$ and $73.8 \pm 8.8 \text{ mg L}^{-1}$ on average throughout the study period for sites IP_up above lobe A and lobe B, respectively ([Table S3-2](#)). Downslope of IP1, the lower values of TDS were measured at site T1 with averages of $64.5 \pm 11.8 \text{ mg L}^{-1}$ and $57.9 \pm 12.7 \text{ mg L}^{-1}$ for lobes A and B, respectively. The solute content tended to slightly increase with distance downslope of IP1 since averages at Site T3 were $69.2 \pm 12.2 \text{ mg L}^{-1}$ and $64.7 \pm 16.2 \text{ mg L}^{-1}$ for A and B, respectively ([Table S3-2](#)).

Finally, the daily evolution of the turbidity was also contrasted between the upslope and the downslope sections of IP1 (**Figure 49c**). At the end of the study period, TSS concentration rapidly increased at Sites IP_up reaching values $> 100 \text{ mg L}^{-1}$. Downslope of IP1, the highest TSS concentrations were measured at Site T1 near the ice patch front. The daily average concentrations reached values of $4.4 \pm 4.2 \text{ mg L}^{-1}$ and $4.0 \pm 3.3 \text{ mg L}^{-1}$ on A and B, respectively. Concentrations then decreased rapidly downstream to become low at the flume and site T3 of lobe A and insignificant for the same sites in lobe B ([Table S3-2](#)).

4.7.3. The ground thermal regime of pronival margin

4.7.3.1. Ground surface temperature

On average over the summers of 2016, 2017 and 2018, the warmest GST_{JULY} were recorded in the lower section of the central tread of Lobe B (sensors LT10 and LT5 with a mean GST_{JULY} of 7.8 °C and 6.8 °C, respectively; **Figure 50a**) while the coldest GST_{JULY} were recorded in the seasonal margin of IP1 ([Table S3-3a](#)) as the sensors remained covered with snow and ice for most of the summers.

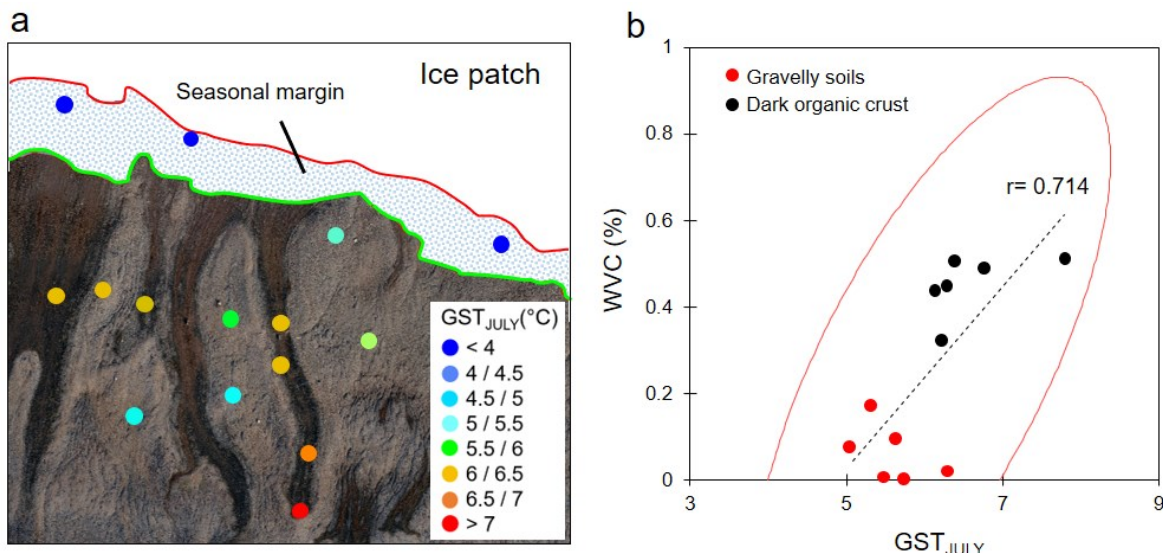


Figure 50. a) Map of the mean summer ground surface temperature (GST_{JULY}) for summer 2016, 2017, 2018 measured over the pronival margin of the ice patch IP1. The seasonal margin on the map is bounded by the snow line on 26 June 2019 (green line) and on 19 August 2019 (red line). b) Scatterplots representing the regression between GST_{JULY} and the volumetric water content of soil (VWC) which is the variable that explained most of the GST spatial variability over the pronival margin IP1 (excluding the seasonal margin) as identified in the correlation matrix in [Table S3-4](#). The colour of the dots indicates the dominant surface composition of each site ([Table S3-1](#)). The background image in (a) is a high-resolution orthomosaic acquired by UAV on 8 July 2019.

Apart from the seasonal margin of IP1, the spatial pattern in the GST_{JULY} mainly reflected the composition of the soil surface, especially the distribution of dark organic crust which strongly depends on soil moisture (**Figure 46**). This explains that the mean GST_{JULY} was positively related to the volumetric water content (VWC) of the soil surface ($r=0.71$; $p\text{-value}=0.0009$) (**Figure 50b**). On average, the mean GST_{JULY} was 6.6. °C in humid sites which was 1.1°C warmer than in dry

sites (mean= 5.6 °C) ([Table S3-3a](#)) and 4.2 °C warmer than the average summer air temperature of July (TA_{JULY}) for the same period ([Table S3-3b](#)). This difference was statistically significant (Student t-test p-value <0.0001). The distance of the ice patch front appeared as the secondary explanatory variable ($r=0.62$; p-value=0.032) but it mostly affected the mean GST_{JULY} in humid sites (**Figure 50a**; [Table S3-4](#)).

At the scale of summer, the thawing degree-days of the ground surface (PDD_{surf}) were always higher than those of the air (PDD_{air}) ([Table S3-3a,b](#)). Humid sites exhibited the higher PDD_{surf} with a mean value of 343 while it was only 279 and 159 for dry sites and the seasonal margin of IP1, respectively. From a biological perspective, humid soils were more favourable to vegetation growth due to a higher degree-day of growing (GDD_{surf}) (233 in humid soils vs 160 in dry soils) and a growing season ~10 days longer than in dry sites on average ([Table S3-3a](#)).

4.7.3.2. Active layer thickness

Similar to the GST, thaw depth soundings conducted on 18 July 2019 over the pronival margin of IP1 revealed a great spatial variability (**Figure 51a**). In well-drained gravels that dominated the soil in the parent slope, the thaw depth was on average 49 ± 13 cm (**Figure 51b**). It was much deeper under the dark, saturated organic matter (73 ± 12 cm on average) present in the central tread of the lobes A and B and in soils composed of mixtures of gravel and organic matter (70 ± 14 cm on average) that characterized the lateral risers of lobes (**Figure 51b**). Sites with a partial cover of vegetation and moss in the central tread – essentially found in the central tread along T1 – exhibited average thaw depths of 47 ± 10 cm (**Figure 51b**). The comparison between the three transects T1, T2 and T3 shows that the thaw depths in the central tread of lobes increased significantly with the distance from the ice patch, varying from 55 ± 9 cm on average for transects T1 to 82 ± 14 cm for transects T3 (**Figure 51a,c**). The deepest thaw depths were measured in the central section of T3 in lobe B with values up to 100 cm (**Figure 51a**). Thaw depths on the parent slope and the lateral risers of lobes were less dependent on the slope position (**Figure 51a,c**).

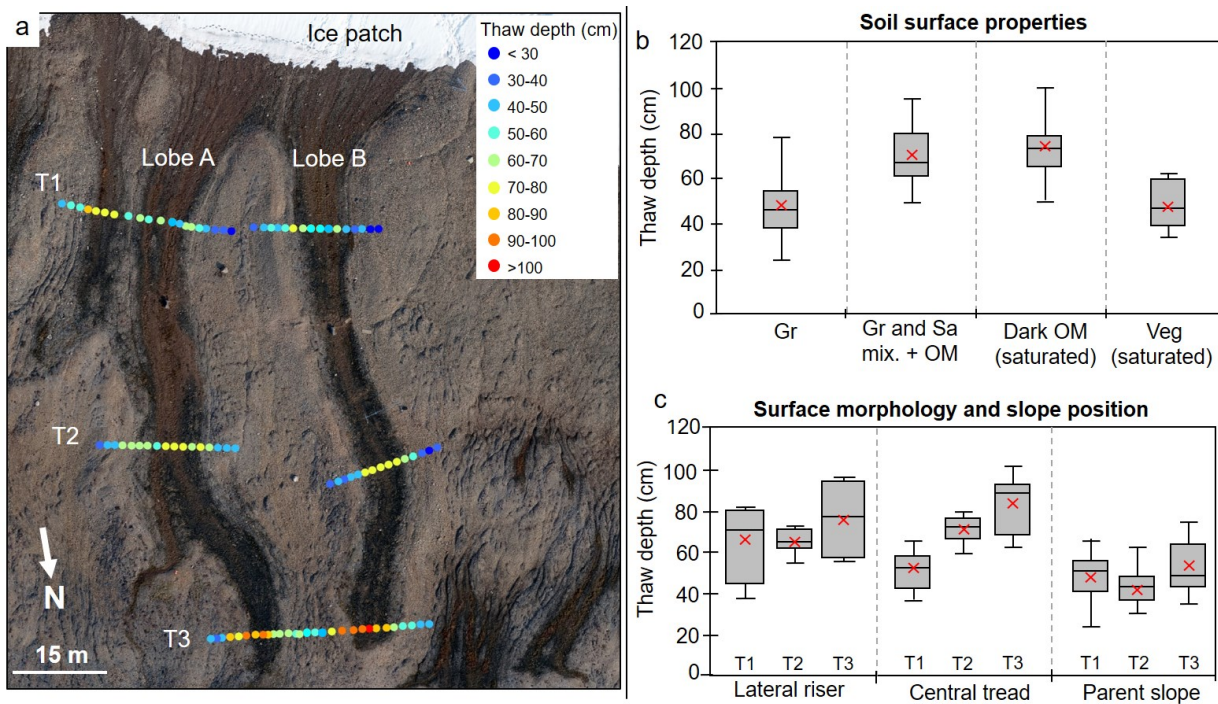


Figure 51. Thaw depth measurements carried out on 18 July 2019. a) Map showing thaw depth at each probing point along transect T1, T2 and T3 that cut lobes A and B; b) Box plots comparing the thaw depth between the dominant soil surface found along the transects (Gr=gravel, Sa=sand, OM=organic matter, Veg=vegetation cover); c) Evolution of thaw depths as a function of surface morphology and position on the slope: T1=upper section of lobes; T2=middle section; T3 =frontal section. The background image in (a) is the same as in **Figure 50**.

4.7.4. Soil and ecological studies

4.7.4.1. Solifluction

Downward creep of the soil surface was detected in Lobe B between 2016 and 2019. As shown in **Figure 52**, the largest horizontal displacements were measured in the central tread of transects T2 and especially T3. For the latter, average displacement values were 3.4 ± 0.9 cm (1.1 cm a^{-1}) with a maximum value of 5.5 ± 0.9 (1.8 cm a^{-1}) cm. The measurements showed that the displacement rates were higher along the central axis of the lobe. On the parent slope, the detected displacement was negligible as the values were generally close to or below the calculated accuracy of the method used (~ 0.9 cm). The parent slope is therefore considered stable. As indicated by the arrows in **Figure 52**, the largest displacement detected for transects T2 and T3 pointed downslope. For the upper transect T1, the displacement was much more limited, even in the central section as the largest value detected was 1.84 cm for the 3 years. However, several markers were lost in the

central section due to their burial under new deposits of fresh fine-grained sediment, explaining the large gaps in the transect T1.

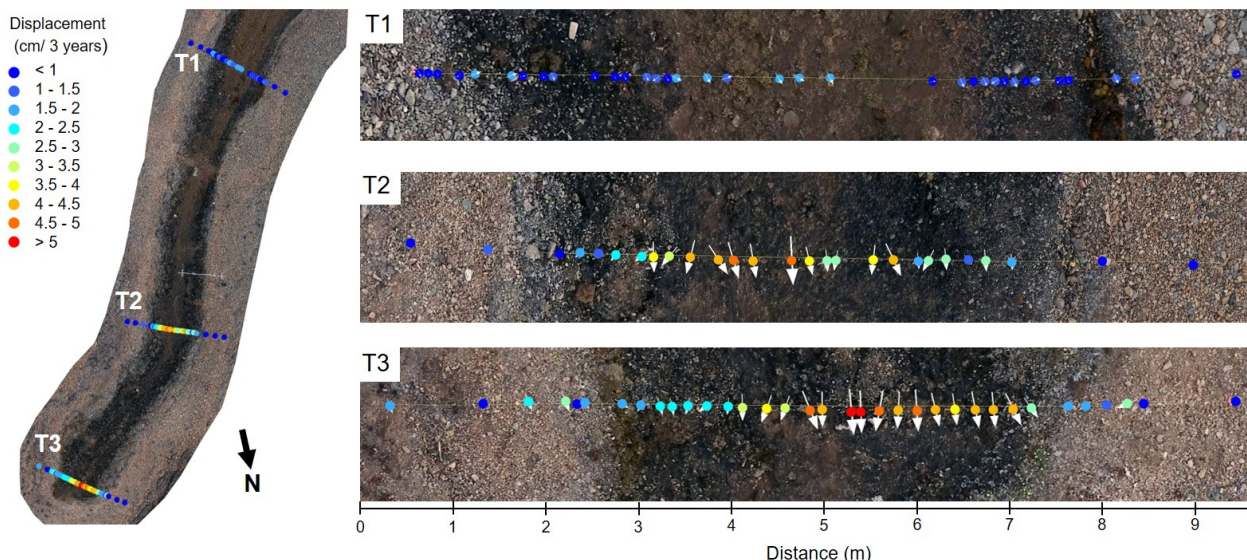


Figure 52. Displacement rates derived from VX station measurements in 2016 and 2019 along transects T1, T2 and T3 on lobe B. On the left, general view of the lobe B; on the right, close-up on each transect. Points represent surface marker and arrows represent the direction of the movement. The size of the arrows is proportional to the magnitude of the displacement rate. The background image is the same as in **Figure 50**.

4.7.4.2. Soil properties and structure

The soil pit in lobe A (**Figure 53**, [Figure S6-3a](#)) shows the sharp transition between the central tread and the lateral riser of the lobe in terms of material properties and moisture. The tread had a thin (1-2 cm) dark organic crust and the soil was made of poorly sorted muddy sandy gravel according to grain size analysis (samples P1 and P2, averaged $D_{50}=5.2$ mm). This material was saturated and some inclusions of buried organic matter were observed in the sediment matrix, particularly near the transition with the riser. Samples P3 and P4 were composed of gravel (averaged $D_{50}=24.5$ mm). The sorting processes concentrated the coarser gravels and cobbles along a stripe under which a water track was present (**Figure 52**). The samples collected by drilling revealed the same clear distinction between the central tread of lobe B and the dry soils in the parent slope (**Figure 45**). In D-dry, material consisted of gravel in the upper section (sample S1, 20-35 cm; $D_{50}=26.2$ mm) and tended to muddy sandy gravel at greater depth (sample S2, 50-65 cm; $D_{50}=15.9$ mm) ([Figure S6-3a](#)). In D-humid, the upper sections were muddy sandy gravel (sample S3, 20-40 cm; $D_{50}=4.4$ mm) while greater depths were muddy gravel (sample S4, 45-60 cm;

$D_{50}=6.2$ mm) ([Figure S6-3a](#)). Finally, fresh sediments collected at the soil surface on the central tread of lobe A (sample F1) and a pronival alluvial fan (sample F2) were classified as very poorly sorted silty sand ($D_{50}= 0.069$ mm) and sandy silt ($D_{50}= 0.064$ mm), respectively ([Figure S6-3b](#)).

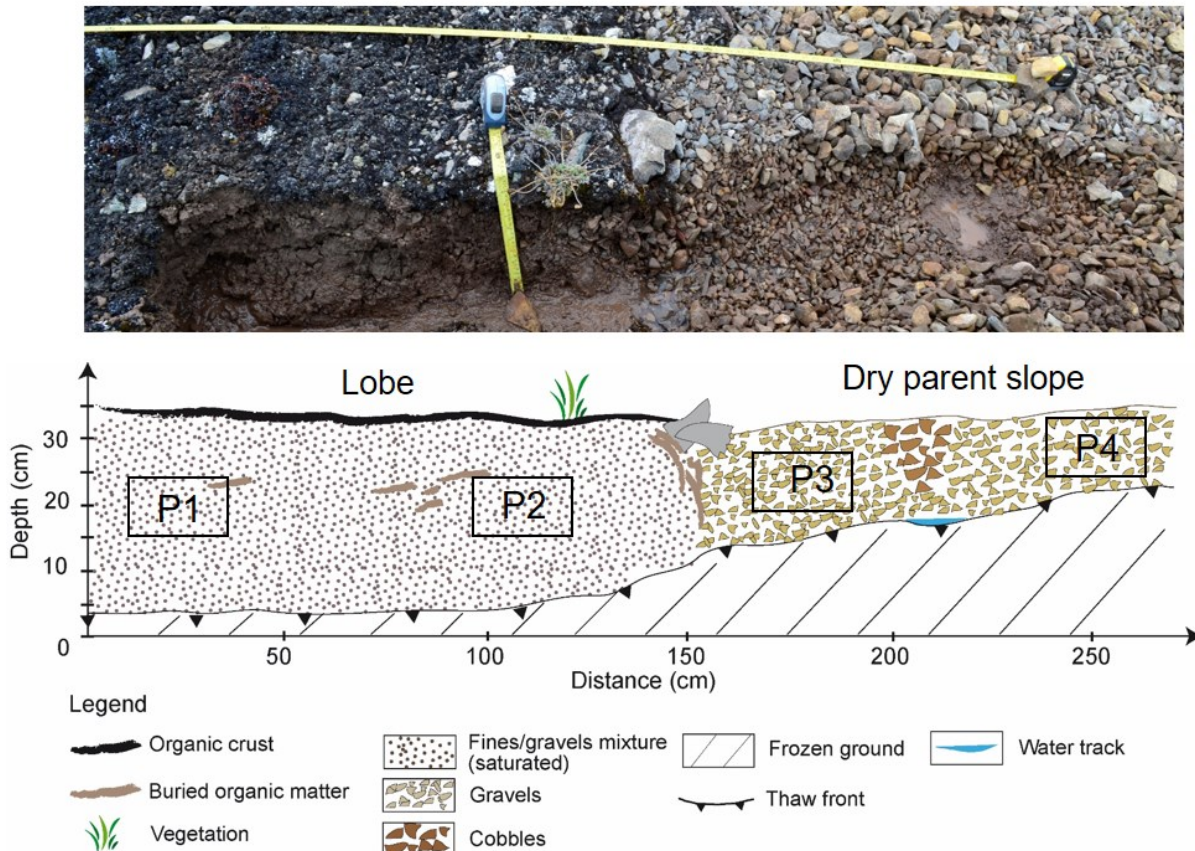


Figure 53. Mosaic of photographs and sketch illustrating the soil pit excavated in Lobe A (see [Figure 45](#)) that showed the transition between the central tread of the lobe and the adjacent dry soil that composes the lateral riser and parent slope. The black boxes in the sketch indicate where samples P1, P2, P3 and P4 were collected.

4.7.4.3. Vegetation and soil cover surveys

- Plant community analysis

Vegetation surveys carried on lobes A and B identified 13 vascular plant species from six vascular families (**Table 5**). The total vascular plant cover and dominant species were spatially heterogeneous among habitats. Total vascular plant cover ranged from ~10% over the tread (both central and external) of lobes to only 3.5% in the parent slope. The lateral risers act as a transitional mesic environment where the total vascular plants cover was on average 8.9%. In the central tread,

the most frequent species was by far the Poaceae *Phippsia algida* which accounted for 79.2% of the total vascular plant cover in this habitat (**Table 5**; [Figure S3-7a](#)).

Table 5. Cover of vascular plants (by species), non-vascular taxa, organic crust (black and white) and inorganic soil surface (gravel/barren soil and freshly deposited sediments) in each of the four habitat types that characterized the downslope margin of the ice patch IP1, namely the central tread and external treads of the lobes which are humid zones, and lateral risers as well as the parent slope. Sign “<” means a cover <0.1 %. Values in brackets indicate the proportion of the total vascular plant cover for each habitat. Species names were retrieved from the Integrated Taxonomic Information System (ITIS) (<http://www.itis.gov>).

	Parent slope	Riser	External tread	Central tread
Vascular taxa				
Caryophyllaceae				
<i>Cerastium alpinum</i>	0.2 (7.0)	0.5 (5.9)	0.6 (5.3)	0.2 (2.2)
<i>Minuartia rubella</i>	0.3 (9.4)	<	0.1 (1.3)	<
<i>Stellaria longipes</i>	--	0.3 (3.3)	1.3 (11.9)	0.4 (4.5)
Brassicaceae				
<i>Draba corymbosa</i>	0.1 (3.6)	<	<	0.2 (1.9)
<i>Draba spectabilis</i>	--	--	--	<
<i>Draba subcapitata</i>	0.4 (11.0)	0.7 (7.4)	0.4 (3.4)	0.1 (1.2)
<i>Cochlearia groenlandica</i>	--	--	--	<
Papaveraceae				
<i>Papaver labradoricum</i>	0.2 (5.01)	0.7 (8.1)	0.7 (6.5)	<
Poaceae				
<i>Phippsia algida</i>	--	--	1.6 (14.3)	7.4 (79.2)
<i>Poa abbreviata</i>	0.2 (5.9)	0.9 (9.8)	<	<
Rosaceae				
<i>Dryas integrifolia</i>	--	--	0.8 (7.8)	--
Saxifragaceae				
<i>Saxifraga cernua</i>	0.1 (3.6)	1.4 (16.0)	1.2 (11.5)	0.5 (5.9)
<i>Saxifraga oppositifolia</i>	1.9 (54.6)	4.2 (47.4)	4.1 (37.5)	0.3 (2.9)
Total Vascular taxa	3.5	8.9	10.9	9.33
Non-Vascular taxa				
Mosses	0.4	1.4	9.5	10.1
Lichens	0.5	0.3	0.3	<
Cyanobacteria	--	--	2.3	0.3
Total Non-vascular taxa	0.9	1.6	12.0	10.4
Black Organic crust				
White Organic crust	0.1	-	39.4	33.8
Total biological soils	14.2	32.4	55.9	34.8
Gravel/Bare soil	77.6	55.4	16.9	3.4
Fresh sediments	1.4	0.7	1.8	46.6
Total inorganic soils	79.0	56.1	18.7	50.0

In the external treads, *Saxifraga oppositifolia* was the most abundant (37.5%) but other species such as *Phippsia algida* (14.3%), *Stellaria longipes* (11.9%) and *Saxifraga cernua* (11.5%) were also commonly found (**Table 5**; [Figure S3-7c](#)). On the lateral risers of lobes, *Saxifraga oppositifolia* and *Saxifraga cernua* were also the most frequent species since they accounted together for 63.4% of the total vascular plant cover in this habitat (**Table 5**; [Figure S3-7d](#)). Among the other vascular plant species frequently found, there are also *Poa abbreviate* (9.8%), *Papaver labradoricum* (8.1%) and *Draba subcapitata* (7.4%). Finally, on the parent slope, the sparse plant cover was dominated by *Saxifraga oppositifolia* that accounted for 55% of the total vascular plant cover in this habitat. For non-vascular taxa, similar contrasts were observed among habitats (**Table 5**), especially with regard to mosses which were mostly observed in the external and central tread of lobes (**Table 5**; [Figure S3-7a](#)). Lichen cover was scarce and was mainly found on the parent slope. The cover of the mat forming cyanobacteria *Nostoc* sp. was also limited and mainly observed on the external treads while it was absent in the parent slope and risers (**Table 5**; [Figure S3-7b](#)). Biological soil crust was very widespread over pronival margin and exhibited a distinct distribution of the two crust types: whitish and dark-coloured ([Figure 46](#)). The dark crust was abundant in the external and central tread of lobes (**Table 5**; [Figure S3-7b; c](#)) while it was absent elsewhere. The whitish organic crust was most abundant in the lateral risers ([Figure S3-7d](#)) but was also commonly found in the parent slope and on the external tread. Finally, with regards to the inorganic soil, the gravelly surface dominated the parent slope and the risers ([Figure S3-7e;f](#)) while it became sporadic in the central treads. Conversely, the proportion of the soil surface consisting of fresh sediment was greatest in the central tread ([Figure S3-7a](#)) while it was almost nil elsewhere.

- *Control of environmental variables on vegetation and soil surface distribution*

According to the canonical correspondence analysis (CCA) ([Figure 54](#)), the first and second axis retained together 93.4% of the total variation in vegetation cover. The soil moisture and surficial water were the only tested variables that were significant within the canonical model ($p<0.05$, 1000 permutations). They were strongly related to the canonical axis 1 (F1) and explained respectively 40.3% and 15.4% of the species and soil surface composition variability ([Table S3-4](#)). In contrast, the thaw depth, distance to ice patch and snow height appeared as secondary variables.

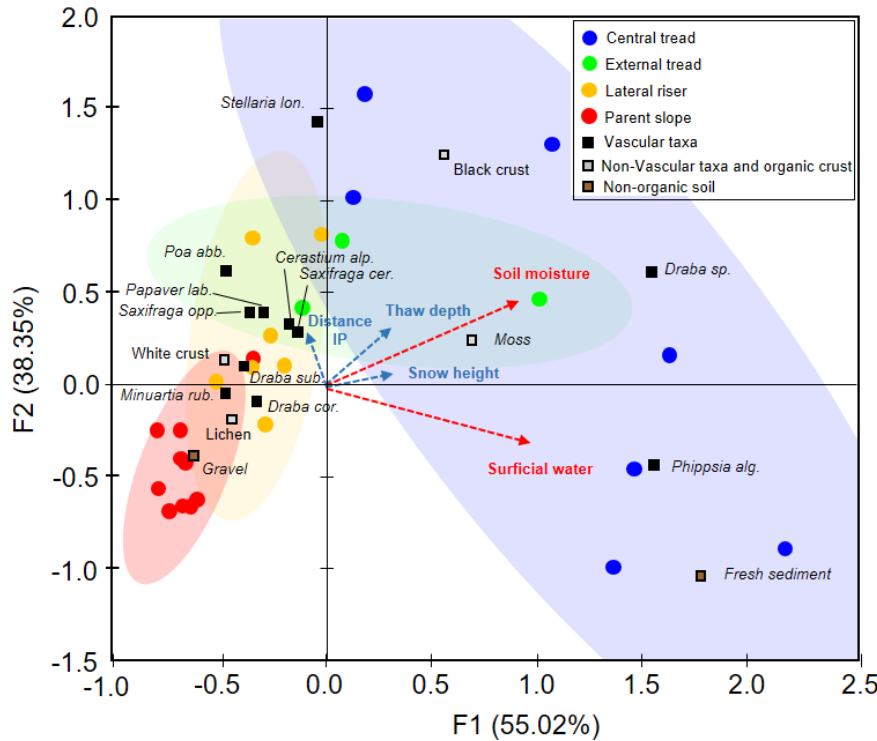


Figure 54. Canonical correspondence analysis (CCA) ordination plots for species and soil surface composition of various habitats and four environmental variables on the 27 sites sampled over the downslope margin of the ice patch IP1 at WHI. Filled coloured circles indicate the sampling sites (blue = central section of lobes; green = internal side of lateral risers; orange = external side of lateral risers and red = parent slope) and coloured squares represent vegetation and soil surface compositions (black = Vascular taxa; grey = Non-vascular taxa and organic crust; brown = Non-organic soils). Arrows represent environmental explanatory variables (red = statistically significant; blue = non statistically significant) with arrowheads indicating their direction of increase. The 95% confidence ellipses highlight the clustering of sampling sites according to the CCA analysis and the overlap between the different ellipses illustrates the contact and transitions between habitats.

In the ordination plot, the relationship between vegetation and soil surface composition with the environmental variables was well established and various habitats were successfully discriminated. Species and soil composition were clearly distributed according to a moisture gradient. Covers of *Draba spectabilis*, *Phippsia algida*, *Stellaria longipes*, mosses and black organic crust were all positively associated with the soil moisture indicating that they are essentially found in the humid soils in the central treads of lobes and the internal lateral risers. *Phippsia algida*, the most abundant species in the central tread (**Table 5**), was associated with areas that supported surface flow and fresh deposits of fines, typically in the upper section of lobes (**Figure 55a**). In contrast, dark organic crust and *Stellaria longipes* developed in sites farther from the ice patch, and thus the least disturbed (**Figure 55b**). Species preferring moderate to high soil moisture were

concentrated along the external tread (e.g. *Cerastium alpinum*; *Saxifraga cernua*; *Papaver labradoricum*) while species more adapted to mesic environments were found along the risers (eg. *Draba subcapitata*; *Minuartia rubella*). Finally, the sites in the parent slope were logically inversely related to the soil moisture and thereby dominated by gravelly substrates and lichens (**Figure 54**).

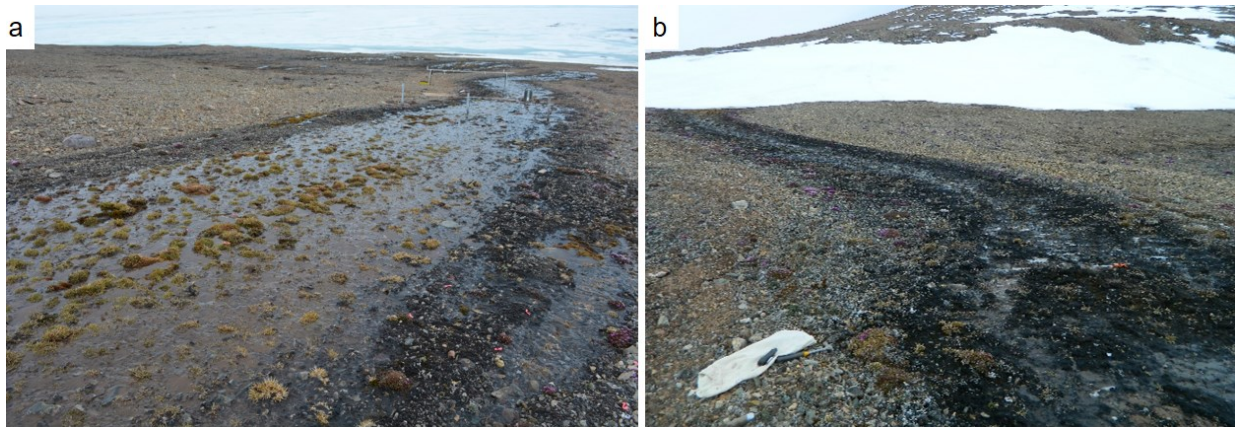


Figure 55. a) Photograph of the upper section of Lobe B (near T1) showing the dense distribution of *Phippsia algida* associated with moss patches in the central tread of the lobe. On each side, the external tread is covered by black organic matter b) Terminal section of the lobe B dominated by a cover of black organic matter and scattered patches of *Saxifraga*.

4.8. Discussion

4.8.1. Water and mass transfers related to the ice patch system

4.8.1.1. Hydrological regime

The ice patch IP1 acts as a water reservoir on slopes which is mainly fed by seasonal accumulations of wind-drifted snow in winter ([Chap. 2](#) and [Chap. 3](#)). Due to its longitudinal shape and position on the slope (**Figure 45**), IP1 also collects snowmelt water from the upper section of the north face of Walker Hill (Paquette et al., 2018). As flows cannot infiltrate under the cold base ice mass ([Chap. 2](#)), they are forced to enter into the ice patch system and flow at the snow-ice interface (Ballantyne, 1978; Lewkowicz and Young, 1990). At the beginning of the warm season, the ice patch therefore cuts off the hydrologic connectivity of the slope because part of the meltwater from the upslope is trapped in the system during the ripening phase by filling the snow

porosity and promoting superimposed ice growth ([Chap. 2](#)). Once most of the snowpack above the ice patch gets fully ripe (i.e. melting throughout; Marsh, 2006), meltwater started to flow out of the system to supply the pronival margin of the ice patch ([Figure 48](#)), thus re-establishing the hydrologic connectivity between the upslope and downslope sections of the ice patch. During the outflow phase, water fluxes from upslope and in-situ snow/ice melt are concentrated in supra-ice rectilinear channels incised in the superimposed ice that promote rapid drainage from the patch ([Chap. 2](#)).

The contribution of meltwater inflow from the slope of Walker Hill versus the ice patch ablation in the outflow is difficult to quantify but our data suggest that it increased as the melt season progressed in 2019. The discharge events recorded by flumes A and B remained high and even tended to increase in intensity over the studied period ([Figure 48](#) and [Figure S3-6](#)) while the discharge recorded in the water track WT-B, fed solely by seasonal snowmelt, gradually decreased ([Figure S3-6](#)). Although the measurements stopped on July 19, we can assume that the melting of IP1 sustained meltwater flows until refreezing, making the hydrological regime of the ice patch resemble the proglacial regime (Woo, 2012).

The discharge exhibited significant daily variability that reflects the ablation rates of the ice patch and thus the surface energy balance (SEB) ([Figure 48](#)) (Lewkowicz and Young, 1990; [Chap. 3](#)). The highest discharges were recorded during periods of windy and warm days while periods of calm and foggy weather produced low discharges with even occasional interruptions ([Figure 48](#)). The recurrence of weather patterns during the summer have thus a significant impact on the hydrological regime of the ice patch, so that it is subject to significant interannual variability in response to short-term climate fluctuations ([Chap. 3](#)).

4.8.1.2. Sediment dynamics related to the ice patch system

Given its cold base ([Chap. 2](#)), the ice patch IP1 probably does not erode the wall and floor of its topographic niche and therefore does not produce sediment itself. Nevertheless, it exerts a major control on the solute and solid sediment delivery over the pronival margin by modulating the sediment connectivity along the hillslope.

Measurements of sediment concentration at sampling sites in the pronival margin demonstrated that the total sediment fluxes were largely dominated by solutes ([Figure 48](#); [Table](#)

S3-2). The TDS fluxes measured at flumes were of the same order of magnitude as those reported by Paquette et al., (2020a) in water tracks. As snowmelt water is generally solute-poor, the TDS fluxes observed in surface runoff over pronival margin actually reflect the contribution of upslope subsurface flows enriched in solutes by the leaching of mobile ions of calcium (Ca^{2+}) from the Walker Hill calcareous slope (Paquette et al., 2020a). At sampling sites located upslope of IP1 (IP_up), seasonal changes in TDS concentration likely reflected the shift in the dominant water source contributing to slope and in the drainage organization (Paquette et al., 2018; 2020a). Three phases can be identified in the TDS evolution presented in **Figure 49b**. Phase 1 consists of the early period when the high TDS were measured at IP_up sites ($\sim 90\text{-}100 \text{ mg L}^{-1}$) due to the slow drainage of early meltwater flows on the slope that resulted in high solute enrichment of the water. Similar values were measured at pronival sites indicating that the solutes from upslope were poorly diluted by the meltwater from the ice patch. Phase 2 consists of a rapid decrease in TDS concentration from ~ 100 to 50 mg L^{-1} (20-26 June). This likely reflected the development of more efficient and rapid drainage along the upper slope of Walker Hill since the deepening of the active layer resulted in the development of a subsurface drainage network across the patterned ground (Levy et al., 2011; Paquette et al., 2020a). Finally, phase 3 (26 June to the end of the study period) consists of the gradual increase in solute concentration at IP_up sites up to $90\text{-}100 \text{ mg L}^{-1}$ that was supported by the increasing contribution of solute-rich ground ice melt as the active layer further deepened (Lewkowicz and French, 1982b; Paquette et al., 2020a). During this phase, TDS concentration between IP_up and pronival sites were increasingly differentiated due to the increasing contribution of the meltwater derived from the melting of IP1 which diluted the upslope solute inputs.

In terms of suspended sediments, very low TSS fluxes were measured through the study period near the front of IP1 (Site T1; **Figure 48** and **Figure 49c**). At Flume A, TSS was 7 times lower than TDS (Table S3-2). This reflects that the ice patch remained in an early stage of melting as almost its entire surface was still covered by a thick layer of snow at the end of fieldwork. However, field evidence such as fresh deposition of fines observed in the zone of rillwash of lobes and small pronival alluvial fans (**Figure 46** and **Figure 47c**; h) suggest that significant sediment supply and deposition occurred in previous summers on the pronival margin of IP1. These alluvial processes are part of nivation (Christiansen, 1998; Lewkowicz and French, 1982a; Lewkowicz and Kokelj, 2002). Although on carbonate rock slopes, suspended sediment transport is generally low

(Paquette et al., 2020a), the ice patch has the effect of concentrating solid sediment. Previous work on IP1 ([Chap. 2](#)) has highlighted the mechanisms of solid sediment trapping within the ice patch system through the incorporation of fine-grained sediments into seasonal snow accumulation by aeolian transport in winter and through the retention of washed fine sediments from upslope in the snow porosity (i.e filtering effect of the snow) in early summer. Some of these sediments are then incorporated into the superimposed ice (Lewkowicz and Harry, 1991; Østrem, 1963; Wilkinson and Bunting, 1975; Woo et al., 1982; [Chap. 2](#)). With the gradual melting of snow and ice, sediments are released and transported by meltwater, which means that sediment pulses usually occur in late summer. Considering the expected close link between the melting rate of ice patch and the release of the sediments it contains, a strong variability in seasonal and interannual sediment dynamics is expected. In years of high ablation (e.g. 2017, [Chap. 3](#)), the melting of the seasonal snowpack and a portion of the multi-year ice body results in a concentration of sediments on the exposed ice that are subsequently flushed from the system ([Chap. 2](#)). Therefore, large amounts of sediment, sometimes stored for long periods in the ice patch, are released in a short time. On the contrary, in years with low ablation, a thick snowpack is preserved on the ice patch and most of the sediment trapped in the snow and ice remains in the system.

4.8.2. Functioning of the biogeomorphic system of ice patch

The dynamics of the pronival slope of IP1 critically depends on the ice patch presence and regime. The supplies of meltwater and sediment by the ice patch to its pronival margin give rise to azonal soil conditions which initiated a suite of biological and geomorphic processes that collectively form a complex biogeomorphic system ([Figure 46](#)). As with all open natural systems, the functioning of an ice patch-related biogeomorphic system is controlled by interactions and feedbacks between fluxes (water, mass, heat), processes and forms that operate at small-scale but are modulated by larger-scale "external" elements such as the climate, geology and post-glacial history (Woo and Young, 2003). We propose here, based on our results, a description of the key interactions and feedbacks between hydrological, sedimentary and biological processes involved in the functioning of an ice patch-related biogeomorphic system on a polar desert slope.

4.8.2.1. Pronival runoff and alluvial processes

Surface flow and alluvial processes on the pronival margin closely interact, giving rise to negative feedback to soil hydraulic conductivity with the transfer and deposition of fines. On the

slope of Walker Hill, the washed beach gravel deposits have high hydraulic conductivity (**Figure 47a**) so that most meltwater is transported downslope by subsurface pathways through the active layer (Paquette et al., 2017). In the central tread of the lobes, however, a large supply of fine-grained sediments by melt flows (**Figure 46** and **Figure 47d,h**) has clogged the porosity of the pre-existing beach deposits, thus significantly reducing soil permeability. Verpaelst et al. (2017) demonstrated that the hydraulic conductivity of muddy sandy gravels present in the central tread of a solifluction lobe at a site close to ours at WHI was 4-6 orders of magnitude lower than that of the gravels. The low-permeability of these soils therefore favours moisture concentration and surface runoff along the central axis of lobes which in turn promotes fine sediment deposition at the soil surface. In addition, sustained moisture supports the growth of organic soil crust, especially nitrogen-fixing cyanobacteria, which contribute to reduce water infiltration and thus enhance runoff (Breen and Levesque, 2008; Woo and Xia, 1995; Woo and Young, 2003).

4.8.2.2. Interaction between plants and sediment dynamics

The vegetation that colonizes the pronival margin plays a key role in the functioning of the biogeomorphic system by providing important feedback on the sedimentary dynamics. Vascular and non-vascular plants observed over the lobe treads and their lateral risers over the pronival margin of ice patches (**Table 5**) form a so-called snowflush community where vegetation cover and diversity are higher than elsewhere in the polar desert where barren gravel soils dominate. These plants communities are widespread in the polar desert and represent hot spots of polar biodiversity (Bliss et al., 1984; Desjardins et al. 2021). The spatial distribution of the vegetation was mainly controlled by the moisture and the disturbance gradients (**Figure 54**; [Figure S3-7](#)). The external tread of lobes had the densest vegetation cover and organic crust (Table 1) due to the high availability of moisture and a relatively stable soil surface. In contrast, in the central tread of the upper lobe section, alluvial processes limited vegetation establishment. The only vascular plant that colonized these localities was *Phippsia algida* which affectionates silty soil and tolerates adverse conditions produced by soil disturbance and cold water temperature (**Figure 54**; Bliss et al., 1984; Woo and Young, 2003; Desjardin et al., 2021). *Phippsia algida* was frequently associated with moss patches. Together, *Phippsia algida* and mosses (**Table 5**; **Figure 54**; [Figure S3-7a](#)) act as ecosystem engineers that play a central role in the sedimentary dynamics on the lobe treads by reducing transport energy and thereby trapping efficiently the suspended silt-sized sediments and stabilizing soil surface (**Figure 47c** and **Figure 55**). In turn, the accretion of fine and moist soil

contributes to providing favourable conditions for plant and organic crust growth (Pushkareva et al., 2016).

4.8.2.3. Interaction between biotic conditions and ground surface thermal regime

The ground surface thermal regime of the pronival margin in July was marked by significant spatial variability (**Figure 50**; [Table S3-2](#)) which is related to the interaction between water runoff and soil surface properties. Our results revealed warmer ground surface temperature on the humid soils of the central tread of lobes than on the dry soils of the parent slope. We consider that this warming effect was provided by a decrease in surface albedo linked to the fine and saturated sediment deposition at soil surface as well as to the presence of a thin dark organic crust that covers a large part of the tread surface (**Figure 46**; **Figure 55b**; **Table 5**). It thus modifies the soil surface energy balance by increasing the absorption of radiative heat by the surface (Gold, 1998; Pushkareva et al., 2016). The circulation of water over the heated soil surface affects the thermal regime of pronival lobes by redistributing the heat across the system (heat advection). During the daily flow peaks, the water level rose and sheet flow generally occurred over the central tread where dark organic crust had been previously heated by solar radiation. As a result, the water was heated up rapidly as it flowed downslope. This process explains why the daily thermal peak in water temperature usually occurred during the rising curve of the hydrograph (**Figure 48a,b**). As meltwater flowed from the IP1 at 0°C, the warming effect provided by the soil crust resulted in large water temperature gradients in summer, sometimes exceeding 10°C in a few tens of metres on sunny days, between the edge of the ice patch and the end of the lobes (**Figure 49**). This gradient is clearly reflected in the soil surface temperatures and in the thaw depths (**Figure 50** and **Figure 51**).

4.8.2.4. Soil creep and topography modification

On the pronival margin of IP1, the development of solifluction lobes has profoundly modified the slope morphology (**Figure 46** and [Figure S3-3](#)) with consequences for the surface hydrology. The lobe acts as a funnel that concentrates soil moisture, surface runoff and alluvial deposition along its central axis, which in turn provides favourable conditions for solifluction. This results in a feedback mechanism between the morphology of the lobes and the variable that favours their development. Solifluction is the result of several soil movement processes including frost creep caused by repeated cycles of frost heave in fine-grained soil, gelifluction by the creep of the

saturated active layer and plug-like flow by active-layer sliding on ice-rich permafrost (French, 2017; Kinnard and Lewkowicz, 2005, 2006; Mackay, 1981; Matsuoka, 2001). On the pronival margin of IP1, the soil with a high fraction of fines (**Figure 53** and **Figure S3-6**) is highly frost-susceptible and has a higher water-holding capacity, resulting in higher water content during thawing. As a result, these finer soils exhibit more frost heave by segregated ice growth and hence have a higher excess ice content. In addition, the liquid and plastic limits are lower in finer soils, making the active layer more susceptible to creep by gelifluction. The latter is also favoured by segregated ice growth (e.g. ice lenses) which locally increases shear stress and leads to translational movements (Matsuoka, 2001) and a thick active layer. Monitoring of solifluction rates in lobe B demonstrated that the maximum displacements occurred along the central axis of the lobe and in its lower part with measured values up to $\sim 2 \text{ cm a}^{-1}$ on average from 2016 to 2019 (**Figure 52**). These preliminary results are consistent with those reported in the few existing studies in polar desert environments; e.g. Bennett and French (1991) at Melville Island (NU) ($0.9\text{-}2.4 \text{ cm a}^{-1}$), Lewkowicz and Clarke (1998) north of Ellesmere (NU) ($1.7\text{-}3.1 \text{ cm a}^{-1}$) and Washburn (1999) at Resolute Bay (NU) ($\sim 3.1 \text{ cm a}^{-1}$).

At the scale of WHI, solifluction lobes connected to snow and ice patches, such as lobes A and B, are the most prominent landforms across the landscape (Paquette et al., 2020a; Verpaelst et al., 2017; Vincent et al., 2011b) and represent the most tangible evidence of the role played by snow and ice patches in the slope evolution.

4.8.3. Various stages of development of slope below an ice patch

Based on the description of key processes and interactions between the biotic and abiotic elements involved in the functioning of the biogeomorphic system connected to IP1, we developed a three-stage conceptual model of pronival slope development in a polar desert (**Figure 56**). Stages represent the activation of processes and feedback mechanisms in response to local changes in soil surface properties and slope morphology.

4.8.3.1. Stage 1: Alluvial processes and sediment transfers

The development of an embryonic system starts with the activation of alluvial processes immediately downslope of the ice front, linked to the concentration of water and suspended sediments at the outlet of supra-ice channels (**Figure 56a**). Along the edge of the cold-based ice

patch, the permafrost table is close to the surface so that infiltration of meltwater is limited and runoff initiates. As water decelerates as it flows over the pronival slope, sediment is deposited which results in the development of fan-like alluvial deposits composed of fine-grained sediments that have filled the porosity of gravelly slope material ([section 4.8.2.1](#).; [Figure 46](#); [Figure 47h](#)).

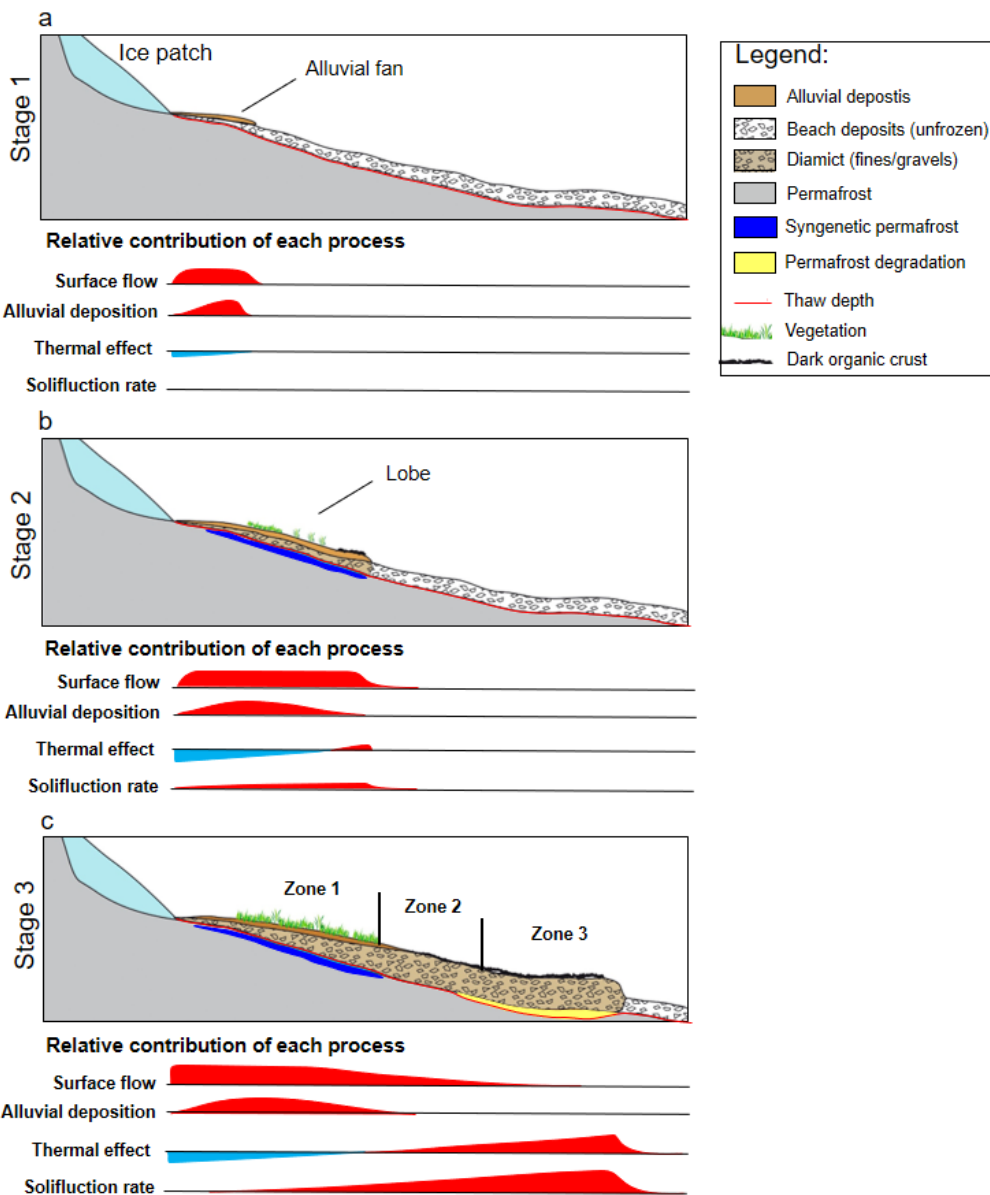


Figure 56. A three-stage conceptual model of the development of an ice patch biogeomorphic system on a low-gradient polar desert slope. a) Stage 1: Initiation stage characterized by the formation of an alluvial fan-like deposit in front of the ice patch; b) Stage 2: Growth stage marked by the colonization of pioneer species and by the activation of sorting and solifluction processes; c) Mature stage during which the solifluction lobe gets fully developed and exhibits zonation of processes and feedback mechanisms as a function of distance from the ice patch front.

These depositions of fines tend to expand downslope by self-constructing an impermeable bed through the transfer of sediment from the ice patch front to the seepage zone at the distal edge of deposits. These alluvial microforms appear as embryonic solifluction lobes.

4.8.3.2. Stage 2: Solifluction processes initiation

The widening, thickening, and downslope extension of alluvial deposits lead to the activation of a suite of abiotic and biotic processes (**Figure 56b**; e.g. Lobe C, **Figure 46** and **Figure 47g**). The sustained saturation of fine-grained soils provides reliable conditions for colonization of cyanobacteria which creates edaphic environments (e.g. nitrogen fixation) favourable to the growth of pioneer and ecosystem engineer plant species (e.g. *Phippia algida*) (Breen and Lévesque, 2008). Due to the trapping effect of the vegetation ([section 4.8.2.2](#)), more sediment accumulates along the channel that supports surface runoff but less sediments reaches the distal edge of the alluvial deposit. As the fraction of frost-susceptible fines increases, frost heave, sorting and solifluction processes activate and begin to modify the slope morphology ([section 4.8.2.3](#)). The combination of these processes explains the development of a longitudinal ridge with the migration of the coarse materials to the periphery (**Figure 47g**). Along this ridge, the downslope sediment transfers occur through a combination of slow soil creep by solifluction and rapid alluvial processes associated with high flow episodes during which meltwater cuts into alluvial deposits. Collectively, the cold water flow (near 0 °C immediately below the ice patch edge), the sediment accretion and the vegetation colonization probably results in upward migration of the permafrost table below the ridge, leading to the development of an intermediate layer with ice-rich cryofacies (Shur et al. 2004; Verpaelst et al., 2017).

4.8.3.3. Stage 3: Mature biogeomorphic system

At their mature stage, ice patch-related biogeomorphic systems are dominated by solifluction processes that create tongue-shaped lobes (**Figure 46**). As the lobes extend downslope, a spatial heterogeneity emerges in terms of vegetation, thermal regime, sediment dynamics and hydrology (**Figure 56c**). The upper section of the lobe (Zone 1) is dominated by alluvial processes. Surface runoff occurs generally in several parallel rills formed by small sorted stripes (**Figure 46**; Wilkinson and Bunting, 1975) or as sheet flow across the width of the central tread of lobes during major melt events. Due to the low gradient of the slope and the presence of ecosystem engineer species along the rills, this section is the most important sediment sink of the system ([Figure S3](#)).

[2e](#)). Vegetation, sediment accretion and the cold water temperature due to the proximity to the ice front (**Figure 49a**) limits thaw penetration (**Figure 51**) and likely favour the development of a syngenetic permafrost layer in Zone 1 (**Figure 56c**). In the middle section (Zone 2), the rills merge into one or two channels that concentrate the flow. Outside the channels, the soil surface of the central tread is more stable. As most of the solid sediments remain trapped in Zone 1, the sediment input by runoff is limited (**Figure 49c**). Consequently, most of the downslope sediment transit occurs by solifluction sheet flow, which allows the sediment accumulated in Zone 1 to be slowly conveyed to the front of the lobes. As the proportion of dark organic crust cover increases downslope (**Table 5**), Zone 2 is marked by a rapid rise in water temperature (**Figure 49a**) which results in deeper thaw depths than in Zone 1 (**Figure 51**). Finally, the lower part (Zone 3) consists of the frontal section of the lobes which tends to progress downslope and progressively bury the pre-existing beach deposits. The soil is continuously saturated in this section, but the water circulates mainly in the subsurface, except during the highest melt peaks, when sheet flow may occur to the front of the lobes. Alluvial deposition is limited and the primary sediment delivery occurs by solifluction (**Figure 52**). The soil surface is dominated by dark soil crust (**Table 5**; **Figure 53**) which provides an important warming effect over the central tread of lobes. The large heat input to the soil surface combined with the high percentage of fines, that allowed more heat to be conducted to depth, resulted in localized permafrost degradation and a permafrost table deeper than it was prior to lobe formation (**Figure 56c**).

The organic crust that is omnipresent in lobes A and B under current conditions can be regarded as an initial stage in plant succession by providing favourable conditions for the colonization of vascular plants (e.g. N₂ fixation, nutrients, increased degree-day of growth at the soil surface; longer growth season; [Table S3-2](#)) (Bliss and Gold, 1999; Breen and Lévesque, 2008). Thus, we assume that lobes A and B could evolve into more vegetated lobes with a denser cover of moss and vascular plants in the central tread ([Figure S3-8](#)). Such a plant succession would lead to colder ground surface temperatures due to the insulation effect provided by vegetation. Consequently, upward migration of the permafrost table would occur all along the central tread of lobes, contributing to the growth of an ice-rich layer of syngenetic permafrost (Verpaelst et al., 2017; Young et al., 1997).

4.8.4. Long-term evolution of the studied pronival slope

The continuous presence of ice patches at WHI over the long term explains the development of mature biogeomorphic systems with well-developed and large solifluction lobes. Based on current displacement rates (**Figure 52**) and lobe lengths downslope of IP1, we can roughly estimate that lobe development began around 3000-4000 years ago. This age is consistent with the estimated age of the perennial ice patches at WHI, dating back to the early Neoglacial ([Chap. 2](#)). Between the emergence of the IP1 site from the glacio-isostatic uplift (7000-6000 years ago; Lyon and Mielke, 1973) and the establishment of a permanent ice patch, there was a period of relatively warm climate (the Holocene Optimum; Bradley, 1990; Fisher et al., 2012; Gajewski, 2015) during which the topographic niche of IP1 was likely occupied by a seasonal snow patch. Consequently, biotic and abiotic activity remained likely limited.

During the Neoglacial Period, the growth of the biogeomorphic system was likely not linear. Phases of greater or lesser biogeomorphic activity presumably occurred depending on the evolution of water and sediment supplies provided by the ice patch. These key variables themselves depend directly on the intensity of the summer ablation ([Chap. 3](#)). Biogeomorphic systems therefore most likely follow a cyclical pattern alternating between phases of reduced activity, or even degradation, during periods of low ablation (e.g. the Little Ice Age) and phases of growth during periods of intense summer ablation (e.g. the Medieval Warm Period). We believe, however, that there is a threshold above which excessive water supply would be critical for solifluction as it would promote erosion of the central tread and frontal lobe (Washburn, 1980). Field evidence of lobe degradation was found in a secondary branch of Lobe A ([Figure S3-9](#)) where surface flow had breached the front of the lobe.

The evolution of a biogeomorphic system is also controlled by the individual evolution of its components which has repercussions on the overall functioning of the system. As mentioned in [section 4.8.3.3](#), ecological succession can lead to important modifications of the sediment fluxes and thermal regime over the pronival margins which directly affect solifluction processes and structure of the permafrost. Solifluction lobes are also governed by internal mechanisms related to their stage of development. The growth of a lobe also generally leads to its collapse when shear stress exerted by the thick lobe tread overcomes riser shear strength (Kinnard and Lewkowicz, 2006). In addition, the microtopography produced by the lobes may favour the formation of

seasonal snow patches downslope of the lobe front ([Chap. 5](#)) that can lead to lobe failure (Price, 1974).

This combination of external and internal variables and mechanisms that control the functioning of the biogeomorphic system makes its past long-term evolution very complex. Additional data on lobe stratigraphy and dating of buried organic material fragments will be needed in future work to establish an accurate chronology of lobe development phases and to link them to palaeoclimatic data and ice patch evolution.

4.9. Conclusion

Understanding the role of perennial ice patches in slope development is crucial in the polar desert where these small elements of the cryosphere are ubiquitous. By applying for the first time the biogeomorphic approach to the study of an ice patch-related system, new insights have been gained into the complex interaction between the ice patch regime, fluxes (water, sediment, and heat), geomorphology and vegetation.

Based on a geomorphological map and field observations, the direct link between meltwater flow from an ice patch and the presence of a specific geomorphic and biological assemblage in the pronival margin was demonstrated. We have emphasized that the primary role of the ice patch system is to control and modulate water and sediment fluxes along the slope. On one hand, it acts as a water reservoir and sediment trap through the accumulation of drifted snow in winter and superimposed ice growth in early summer. On the other hand, part of the stored water and sediment is released, to which is added the meltwater and sediment fluxes from the upslope that are collected and concentrated by the ice patch. The key effect of the ice patch is therefore to supply sustained water and sediment to the pronival margin throughout the summer. Since fluxes in water and sediment are dependent on the magnitude of the ablation, they are expected to be greater during summer marked by severe ablations. Our results showed that this surface meltwater runoff over pronival sections initiates azonal geomorphic and biological processes that operate together through a series of interactions and feedbacks leading to the development of a complex biogeomorphic system. The identification of various feedbacks and the quantification of small-scale fluxes of water, sediment and heat allowed us to develop a conceptual model of ice patch-related biogeomorphic system development in 3 stages. At Stage 1, important positive feedback occurs between sedimentation processes and the surface runoff in the pronival margin. It results in

the formation of alluvial fan-type deposits of silty sediment below the ice patch that represent the embryo of a biogeomorphic system. In Stage 2, the expansion of fine-grained saturated soils allows the colonization of organic crust and engineer plant species. This initiates important feedback between vegetation and sedimentation. In parallel, the fine-grained frost-susceptible sediments favour frost heave, soil sorting and solifluction. Stage 3 represents the mature biogeomorphic system dominated by solifluction that modifies the local topography and strongly controls the distribution of soil moisture. The colonization of the organic crust over most of the lobe treads plays a key role in the soil surface thermal regime by decreasing the surface albedo resulting in increased soil heating and deeper thaw depths. The functioning and evolution of this “mature” system are based on a dynamic equilibrium between the fluxes of water, matter and heat as well as the evolution of individual components of the system (e.g. vegetation succession and cyclic development in solifluction lobes).

This study thus highlighted that ice patches are an important factor in the long-term shaping of the polar desert landscape. The large number of ice patches across the landscape makes it an important biogeomorphic agent not only at the local scale but also regionally. Azonal geomorphic and biological processes triggered by ice patches result in a partitioning of the landscape, giving it a mosaic-like appearance with rich and dynamic micro-environments scattered throughout the barren polar desert. This study paves the way for further research on a larger scale that should, for example, establish a spatial correlation between ice patches and humid zones distribution. Special attention should also be paid to studying the effects of ice patch-related biogeomorphic systems on the spatial variability of permafrost structure and seasonal snowpack, both of which are key elements of the polar desert ecosystem.

4.10. Acknowledgments

This research has been supported by the Natural Sciences and Engineering Research Council of Canada (NSERC), including the Discovery Frontiers project Arctic Development and Adaptation to Permafrost in Transition (ADAPT); the Networks of Centres of Excellence program ArcticNet; the Canada Research Chair program; the Northern Scientific Training Program; the Canadian Foundation for Innovation: Canadian Northern Studies Trust; Centre d'études Nordiques (CEN); and Fond de Recherche du Québec- Nature et Technologie (FRQNT). Logistical support was provided by the Polar Continental Shelf Program (PCSP) and Parks Canada graciously granted

us the use of their facility. We would like to thanks Audrey Veillette and Karine Rioux for the field assistance in summer 2016 and 2019. We are also grateful to Esther Lévesque (Université du Québec à Trois-Rivières) for her help and guidance with the vegetation survey.

4.11. Appendices A3

Appendix A3-1: UAV surveys and image processing

Combined with the digital photogrammetry based on the Structure from Motion (SfM) algorithm, the Unmanned aerial vehicles (UAV) surveys represent a low-cost tool to produce digital surface models (DSMs), and orthomosaics with a high spatial resolution, down to the centimetre level. This technique is particularly suitable for the treeless terrain of Polar Regions and is now widely used in geomorphology (Dąbski et al., 2017; Tomczyk et al., 2019), glaciology (Bashand and Moorman, 2020) and ecology (Fraser et al, 2016).

RGB data was collected with a DJI Phantom 4 Pro using its original 20-megapixels resolution, 25.4 mm CMOS camera. Due to the high latitude of the study site, magnetic interference disturbs the internal compass and GPS of the DJI Phantom 4 pro which prevents performing pre-programmed and automatic flights. A single flight was made in manual piloting on 8 July 2019. We tried to keep the flight altitude as constant as possible (around 90 m above ground level giving a ground sampling distance of ~0.5 cm) and to collect a high-density image coverage of the study area to ensure a high overlap between images. Around 600 images (20-megapixel) were captured for each flight covering the lower section of the hillslope of Walker hill. Raw images were processed using the Pix4D software (Pix4D, SA 2019) which produces orthomosaics and extremely dense point clouds that were then interpolated to digital surface models (DSMs). Orthomosaics and DSMs were then imported in ArcGIS and accurately georeferenced using 10 targets (plastic panels of 30 cm diameter) distributed across the study areas to serve as photo-identifiable ground control points (GCPs). The coordinates of all GCPs were measured using a total station (Trimble VX spatial station) survey linked to a geodesic landmark recorded using a Global Navigation Satellite System (R8 GNSS; Trimble®, precision x–y ± 8 mm and z ± 15 mm).

DSMs-derived Shaded relief and slope angle surface models were created in ArcGIS using Spatial analyst tool. Topographic position index model was extracted from DSMs using the ArcGeomorphometry extension (Rigol-Sanchez et al., 2015) through the calculation of the Topographic Position Index (TPI) based on the algorithm developed by Weiss (2001).

Appendix A3-2: Water discharge and quality

Within the cut-throat flumes (1 m long and 40 cm high), the water level was recorded from the absolute pressures exerted by the water column on a Hobo U20 pressure sensor (uncertainty of $\pm 0.62 \text{ kPa}$; $\pm 0.5 \text{ cm}$) obtained after subtracting the atmospheric pressure recorded by a second Hobo U20 installed above the water.

The water level recorded was then used to calculate the free flow discharge ($Q_f, \text{cm}^3 \text{ s}^{-1}$) based on the equation:

$$Q_f = K_f \times C_f \times h_u^{n_f} \quad (\text{A3-1})$$

where K_f is a free flow correction factor calculated from the specific dimensions of the flume, C_f is the free flow coefficient, and n_f is the free flow exponent, both of which can be extracted from tables according to flume standard dimensions (Siddiqui et al. 1996).

As regards the water quality, the Specific electrical Conductivity (SpC in micro Siemens cm^{-1}), water temperature (T_w , in $^\circ\text{C}$) and pH were measured using a portable multi-parameter PCStestr 35 (Oakton ®). At flumes A and B, SpC and T_w were measured continuously by a decagon ES-2 (resolution SpC/Temp: $0.001 \text{ dS m}^{-1} / 0.1 \text{ }^\circ\text{C}$; uncertainty SpC/Temp: $+ 0.01 \text{ dS m}^{-1} / +1 \text{ }^\circ\text{C}$) connected to an EM50 data logger (Decagon Devices, Pullman, WA). The turbidity of the water, given in nephelometric turbidity units (NTU), was measured in the field using a Lamotte 2020we turbidity meter (Lamotte®). Triplicate samples were analyzed each time. The PCstestr and the Lamotte 2020we were calibrated before use with standard buffer solution and several checks were carried out during the field period.

Appendix A3-3: Canonical Correspondence Analysis

The vegetation data were analyzed by implementing a Canonical correspondence analysis (CCA) to test for unimodal relationships between the cover of vegetation as well as the soil surface composition over the pronival section of the ice patch IP1 and explanatory environmental variables. CCA was made using the “vegan” package (Oksanen et al., 2015) in R 4.1.0 (R development core team, 2019). Data were compiled into two matrices, one with mean cover per habitat of vascular and non-vascular taxa and the second one with 5 environmental variables that were measured in the field, *i.e.* soil moisture, end-of-winter snow height, thaw front depth, the presence of surficial water and the distance from the ice patch front of quadrats at the time of sampling. A total of 1000

permutations were performed and the results of the analysis were presented in the form of an ordination diagram

Appendix A3-4: Sediment analysis in the laboratory

All the sediment samples were analyzed for grain size distribution after being dried and crushed. Sediments coarser than 1 mm were sieved in the laboratory at the University of Montreal, following a modified ASTM D6913 standard and fines portion below 1 mm was analyzed by laser diffraction analysis. Sediments were classified according to the Udden - Wentworth scale (Gravel and cobbles \geq 2 mm; Sand from 2 mm to 0.063 mm; Silt and clay \leq 0.063 mm). Descriptive statistics (mean grain size, sorting, and skewness) and Folk and Ward sediment classes were determined using the Gradistat software (Blott and Pye 2001).

4.12. Supplementary material S3

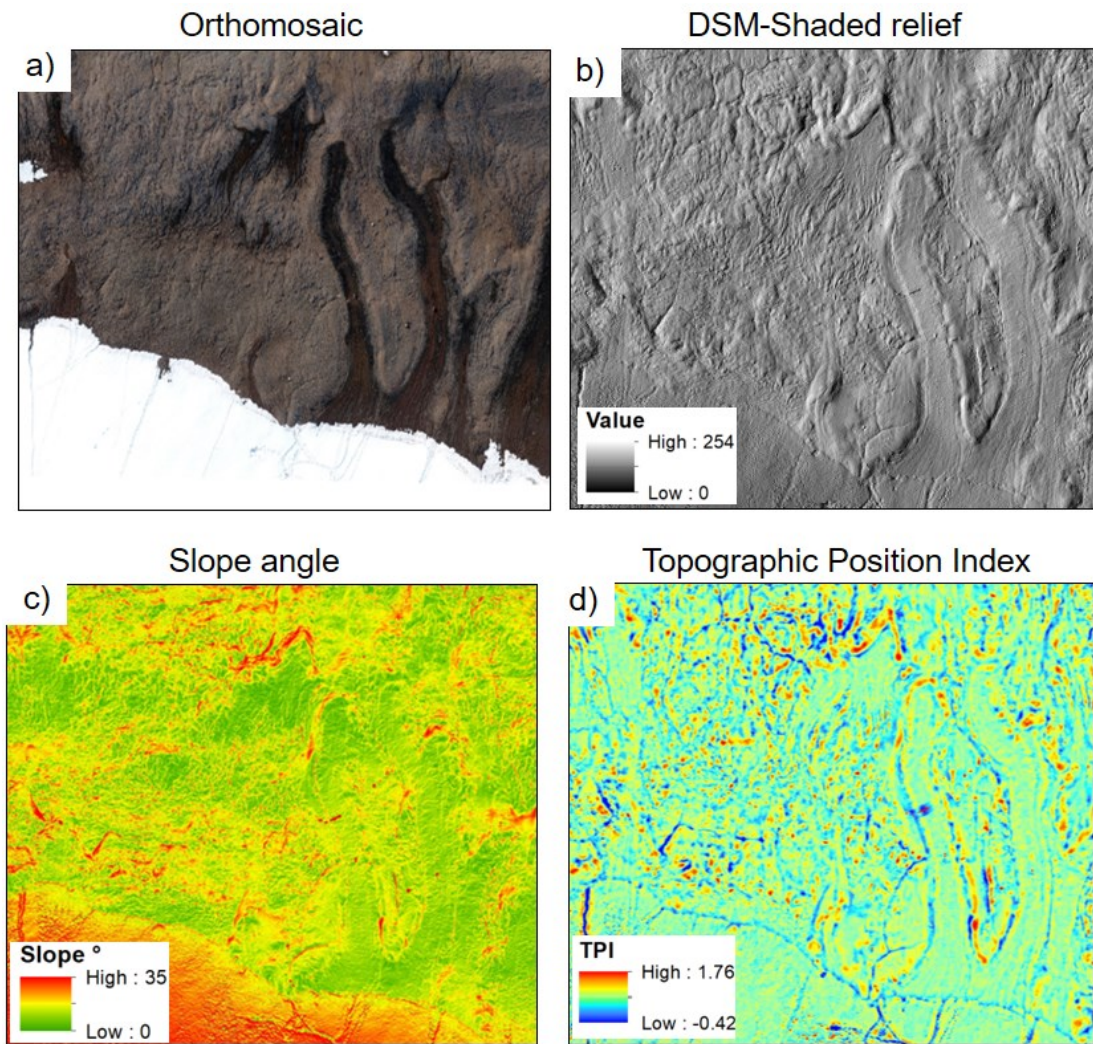


Figure S3-1. Unmanned aerial vehicles (UAV)-derived products used to create the geomorphic map of the studied zone downslope of the ice patch IP1. a) Orthomosaic generated from a set of images taken during flights carried out on 8 July 2019; b) Hillshade model based on the DSM obtained by photogrammetry based on 8 July from images c and d) Slope and TPI of the calculated from DSM.

Table S3-1. Detailed information of sensors location. For the soil surface, DOC=Dark organic crust, WOC=white organic crust; VP=vascular plants, Gr=gravel.

ID	Position	Elev. (m)	Aspect	Slope(°)	Environm.	Soil surface	Comment
LT1	83°5'37.69"N 74°11'27.39"W	32.1	N	8.4	Solif. lobe	DOC	-
LT2	83°5'38.49"N 74°11'38.00"W	33.1	N	7.6	Solif. lobe	DOC+VP	Surface runoff
LT3	83°5'38"N 74°11'31.41"W	32.4	NE	6.5	Solif. lobe	DOC	-
LT4	83°5'38.88"N 74°11'41.91"W	31.8	N	12	Parent slope	Gr	-
LT5	83°5'39.37"N 74°11'36.14"W	28.3	NW	3.3	Solif. lobe	DOC+VP	-
LT6	83°5'38.80"N 74°11'33.88"W	29.8	N	12.7	Parent slope	Gr	-
LT7	83°5'37.16"N 74°11'37.78"W	37.6	N	14.6	Seasonal margin IP	Gr	-
LT8	83°5'38.63"N 74°11'28.41"W	29.1	NE	8.8	Parent slope	Gr	-
LT9	83°5'38.34"N 74°11'35.57"W	32.2	NE	15	Parent slope	Gr+WOC	Hummocky terrain
LT10	83°5'39.70"N 74°11'34.14"W	27.2	E	2.8	Solif. lobe	DOC+VP	Near front of lobe B
LT11	83°5'38.15"N 74°11'42.66"W	35.5	N	8.2	Parent slope	Gr	-
LT12	83°5'38.74"N 74°11'36.76"W	30.9	NE	6.5	Solif. lobe	DOC+VP	-
LT13	83°5'36.57"N 74°11'32.38"W	37.7	N	12.7	Seasonal margin IP	Gr	-
LT14	83°5'38.66"N 74°11'50.61"W	36.1	NE	16.4	Seasonal margin IP	Gr	-
LT15	83°5'37.79"N 74°11'29.95"W	33.0	NW	10.9	Parent slope	Gr	top of a ridge

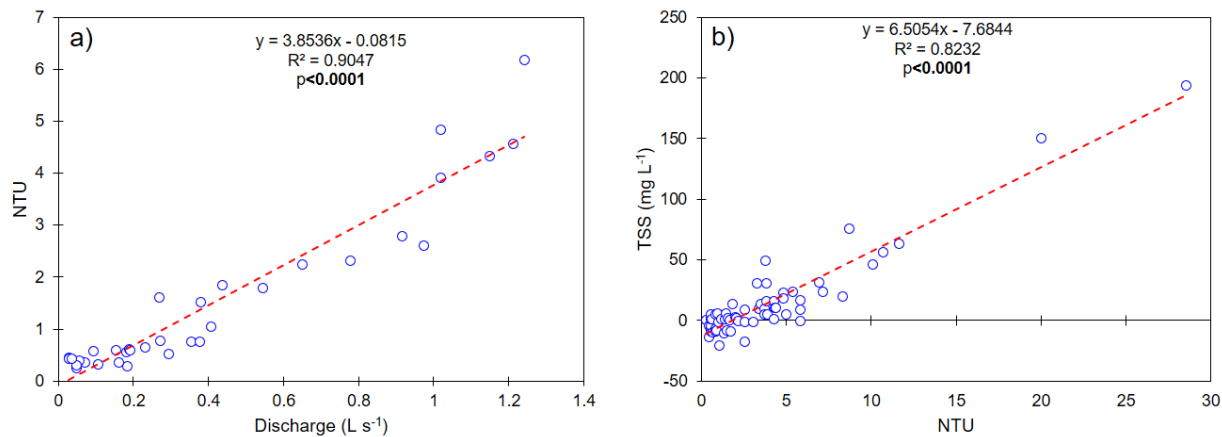


Figure S3-2. a) Relationship between hourly discharge and turbidity (NTU) of the water at flumes A and B during hourly water sampling carried on 1 July 2019 from 5:00hr to 22:00h; b) Relationship between NTU values measured at different sampling sites and the total suspended sediment concentration obtained by filtration in the laboratory of water samples collected on the field.

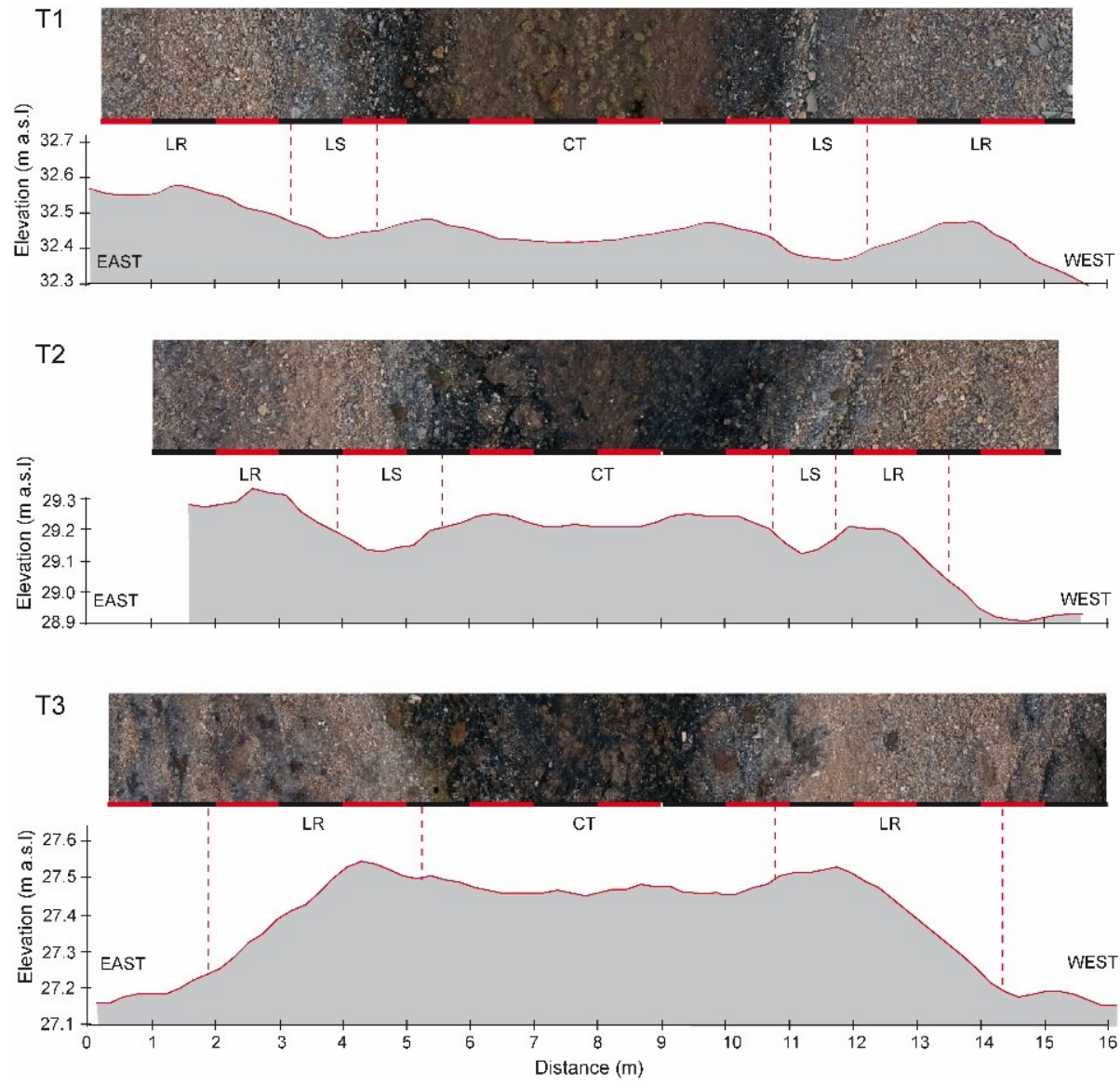


Figure S3-3. Transversal topographic profiles of the solifluction lobe B along the transect T1, T2 and T3. The profiles were extracted from UAV-DSM and the images were extracted from the orthomosaic of 16 July 2019. LR=Lateral riser, LS=lateral sorted-stripe; CT=central tread.

- 5.
- 6.
- 7.

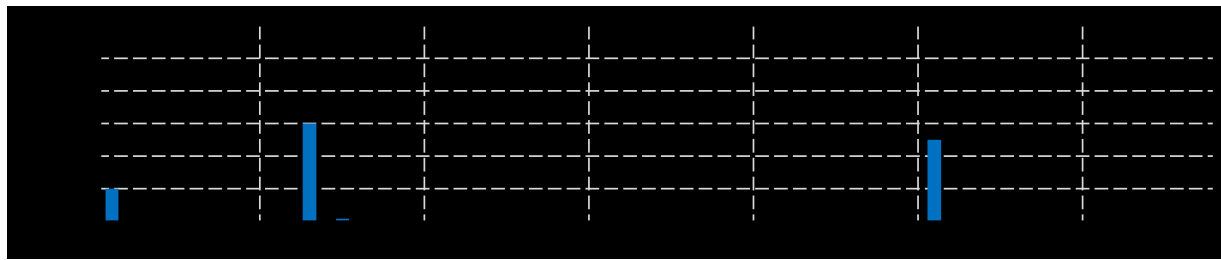


Figure S3-4. Precipitation measured during the field season 2019 from 15 June to 18 July near the base camp at Ward Hunt.

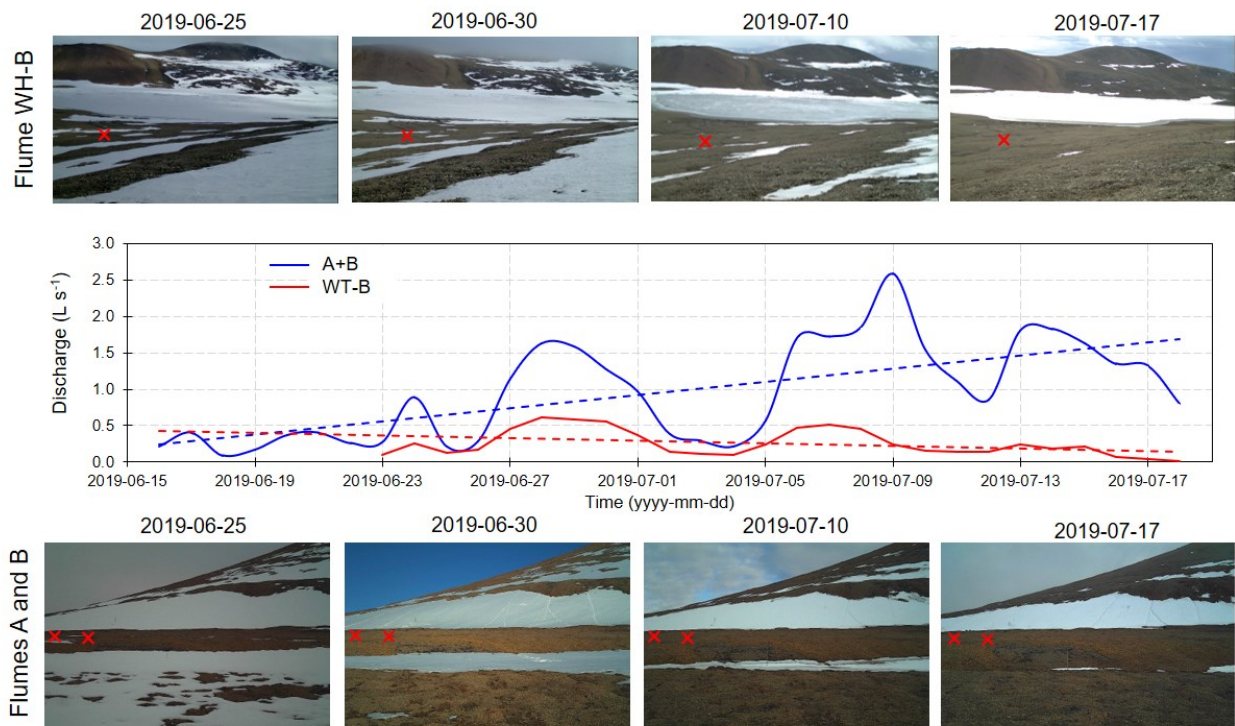


Figure S3-5. Comparison between the sum of the mean daily discharge measured at flumes A and B and the mean daily discharge measured at the flume WT-B. The photographs above the graph show the snow conditions over the east slope of Walker Hill where the flume WH-B is located (red cross) on 25 June, 30 June, 10 July and 17 July 2019. The photographs below the graph show the snow conditions and the ice patch IPI on the Nord face of Walker Hill for the same date.

Table S3-2. Water temperature, pH, sediment concentrations and fluxes for the sampling sites along lobes A and B (T1, Flume and T3 and above the ice patch (sites IP_up).

	Water temperature		pH	Total dissolved sediment			Total suspended sediment		
Site	Mean (°C)	Maxi (°C)	Mean	Spc ($\mu\text{s cm}^{-1}$)	C (mg L $^{-1}$)	Flux (kg d $^{-1}$)	Turb. (NTU)	C (mg L $^{-1}$)	Flux (kg d $^{-1}$)
Lobe A	IP_up	0.0±0.1	0.3	8.45±0.13	117.2±21.8	76.2±14.2	-	8.59±10.8	19.8±27.0
	T1	1.4±0.7	2.5	8.34±0.22	99.3±18.2	64.5±11.8	-	4.4±4.2	9.3±10.6
	Flume	4.4±1.4	9.25	8.27±0.15	101.1±19.8	65.7±12.9	2.8±2.0	1.94±1.32	3.2±3.2
Lobe B	T3	5.3±2.1	10.8	8.32±0.15	106.4±18.7	69.2±12.2	-	1.4±0.8	1.9±1.9
	IP_up	0.0±0.1	1	8.47±0.11	113.5±13.5	73.8±8.8	-	13.3±15.2	31.5±37.9
	T1	2.2±1.3	4.4	8.22±0.14	89.2±19.4	57.9±12.7	-	4.0±3.3	8.4±8.24
	Flume	6.8±1.7	11.62	8.19±0.12	92.3±23.1	60.9±15.0	0.82±0.65	0.6±0.6	0.2±0.7
	T3	8.1±2.4	13.7	8.20±0.11	99.5±24.9	64.7±16.2	-	0.4±0.2	0.0±0.0

Table S3-3. Summary of the mean (a) air temperature (TA) and (b) ground surface temperatures of July (GST_{JULY}) over pronival margin of the ice patch IP1 calculated from data of summers 2016, 2017 and 2018. PDD_{air} and PDD_{suf} are degree-days of thawing of the air and ground surface, respectively; GDD_{air} and GDD_{suf} are degree-days of growing of the air and ground surface, respectively; GSD is the growing season duration. In b) Data are presented separately by environment: humid soils, dry soils and the seasonal margin are present separately.

a)	Year	GST _{JULY} (°C)	PDD _{suf} (°C)	GDD _{suf} (°C)	GSD (days)
Humid soils	2016	7.4	352	241	31
	2017	5.8	325	186	28
	2018	6.5	352	272	40
	Mean± SD	6.6±0.6	343±15	233±44	32.9±6.5
Dry soils	2016	6.6	302	199	26
	2017	4.7	246	114	18
	2018	5.4	290	165	25
	Mean± SD	5.6±0.4	279±29	160±43	23.1±4.4
Seasonal margin	2016	3.9	272	183	25
	2017	3.3	144	29	5
	2018	-0.1	61	3	1
	Mean± SD	2.4±1.6	159±106	72±97	10.2±13.0

b)	Year	TA _{JULY} (°C)	PDD _{air} (°C)	GDD _{air} (°C)
	2016	3.2	196	50.2
	2017	1.7	99	32.5
	2018	0.9	69	36.8
	Mean± SD	1.9 ±1.1	121 ±54	39.8 ±6.9

8.

Table S3-4. Pearson correlation matrices between the mean ground surface temperatures of July (GST_{JULY}) of 2016-2017-2018 measured over the pronival margin of the ice patch IP1 and environmental variables: Distance from the ice patch; volumetric water content (WVC); Topographic position index (TPI) and end-of-winter snow height (SH). For this statistical analysis, the sensors located in the seasonal fringe in front of IP1 have been excluded because the strong effect of thick snowpack in this zone masks the implications of other factors.

Variables	GST_{JULY}	Distance IP	WVC	TPI	SH
Distance IP	0.617*	1			
WVC	0.714*	0.315	1		
TPI	0.036	-0.069	-0.220	1	
SH	-0.282	0.138	-0.112	-0.764*	1

*Correlation coefficient significantly different from 0 (p-value ≤ 0.05)

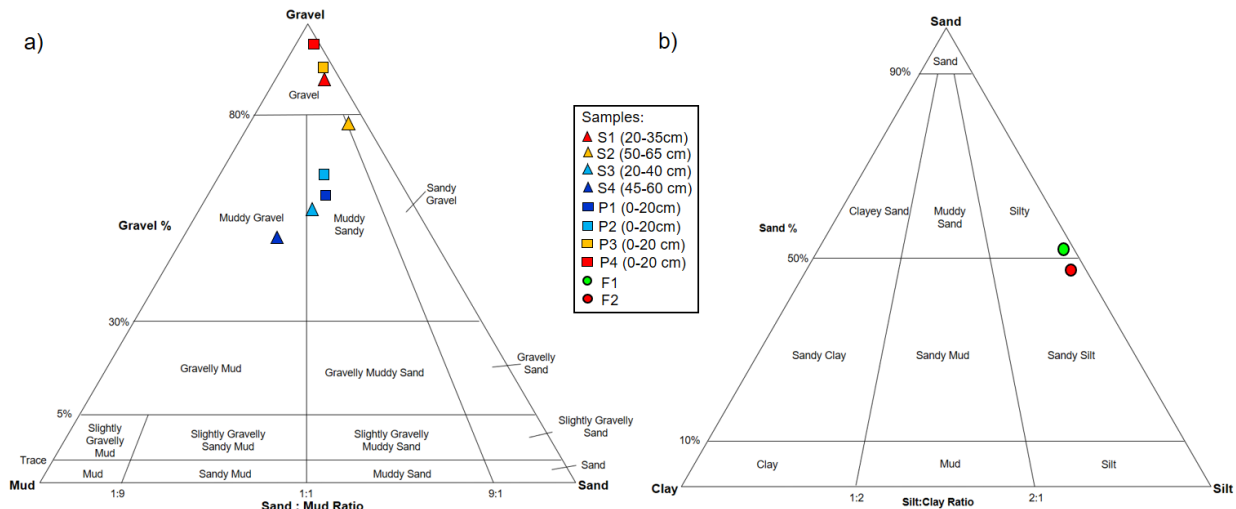


Figure S3-6. a) Textural ternary diagram (gravel-sand-mud) for sediment samples collected by drilling in parent slope (D-dry, samples S1 and S2) and in Lobe B (D-Humid, samples S3 and S4) and along the soil pit made in Lobe A (P1, P2 in humid section and P3 and P4 in dry zone) and b) ternary diagram (Sand-silt-Clay) for the sample of fresh sediment collected on the central section of lobe A.

Table S4. Canonical Correspondence Analysis (CCA) permutation results examining the association between vegetation and soil composition sampled in various habitats over the downslope margin of the ice patch IP1 with environmental variables.

Environmental variables	df	χ^2	F	P	Explains (%)
Soil moisture	1	2.71	20.58	0.004*	40.32
Surficial water	1	1.03	7.87	0.005*	15.41
Snow height	1	0.13	0.96	0.38	1.88
Thaw depth	1	0.06	0.44	0.82	0.86
Distance IP	1	0.03	0.20	1.00	0.38
<i>Residuals</i>	21	2.76			
<i>Total</i>	26	6.71			

* Statistically significant value after 1000 permutations ($P < 0.05$)

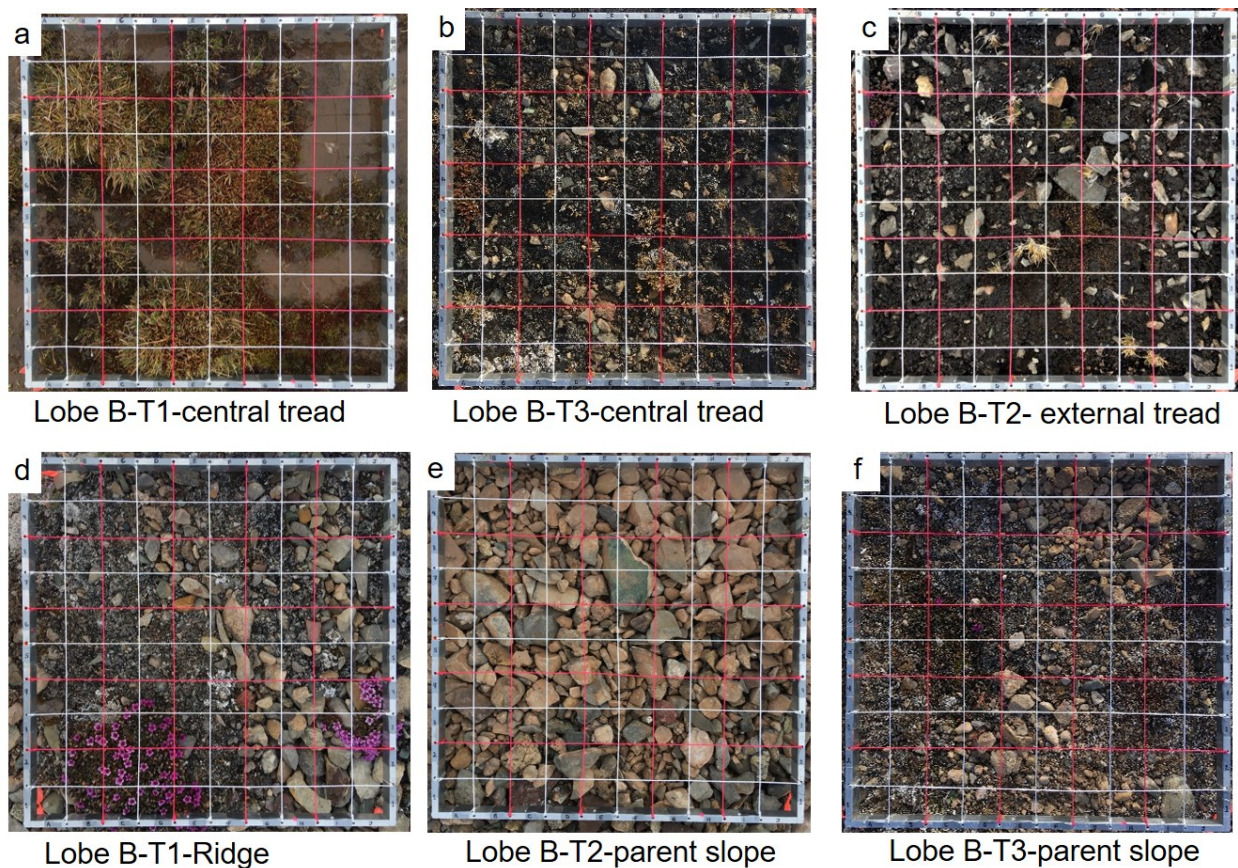


Figure S3-7. Photographs of the quadrats (50 cm x 50 cm) sampled along T1, T2 and T3 in Lobe B representing differences in vegetation cover and soil composition between various habitats that characterized the downslope margin of the ice patch IP1. a) high density of *Phippsia algida* in the upper central tread of the lobe (T1) associated with mosses and abundant surficial water and fresh deposits of fine-grained sediments; b) Continuous black organic crust with sparse *Stellaria longipes* ($n=58$), *Draba subcapitata* ($n=19$) and *Phippsia algida* ($n=14$) in the central tread near the front of the lobe (T3); c) External tread of lobe B (T2) characterized by a continuous cover of black organic crust, including *Nostoc* spp. and mosses species, and with *Phippsia algida* ($n=20$), *Saxifraga cernua* ($n=5$), *Saxifraga oppositifolia* ($n=4$), *Cerastium alpinum* ($n=4$); d) Lateral ridge of the lobe with whitish organic crust, including lichens, mixed with gravel and with *Cerastium alpinum* ($n=8$), *Draba subcapitata* ($n=5$), *Saxifraga cernua* ($n=4$), *Saxifraga oppositifolia* ($n=2$) and *Papaver labradoricum* ($n=2$); e) Soil surface in parent slope of the transect T2 which was exclusively composed of gravel material; f) Soil surface in the parent slope of transect T3 characterized by a hummocky terrain with a mixture of gravel and fine-grained sediments covered by whitish organic cover and lichens that supported some vascular plants such as *Minuartia rubella* ($n=20$), *Draba subcapitata* ($n=6$) and *Saxifraga oppositifolia* ($n=3$).



Figure S3-8. Example of a proinal solifluction lobe with a dense cover of moss and plants over the central tread.

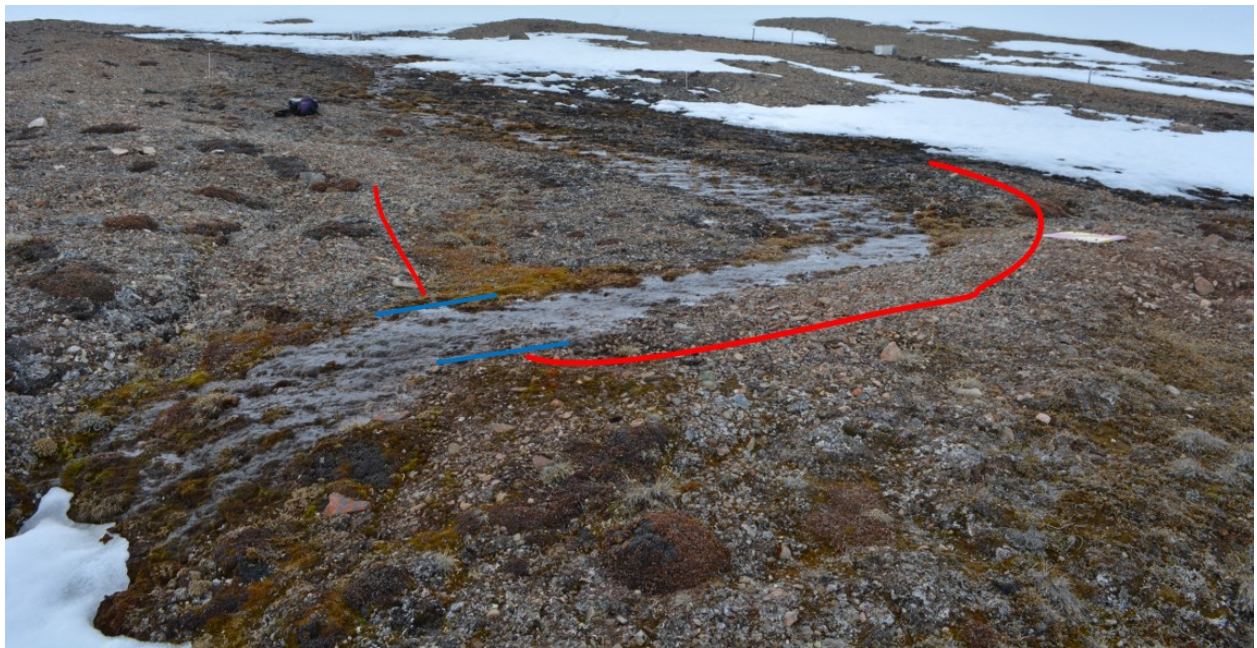


Figure S3-9. Photograph of a branch of lobe A whose front ridge has been breached by a surface flow.

Chapitre 5 – Effects of meteorology and soil moisture on the spatio-temporal evolution of the depth hoar layer in the polar desert snowpack

Auteurs : Gautier Davesne, Florent Domine, Daniel Fortier

5.1. Avant-propos

Le **chapitre 5** consiste en un article publié dans la revue *Journal of Glaciology* (Davesne, Domine, et Fortier, 2021). Cette étude propose pour la première fois de déterminer les facteurs météorologiques et environnementaux qui contrôlent la variabilité spatio-temporelle du couvert de neige saisonnier de désert polaire. Cette recherche fait suite aux travaux préliminaires de Domine et al. (2018a) qui ont montré la grande hétérogénéité des propriétés physiques de la neige des déserts polaires et répond au besoin crucial de combler les lacunes dans la compréhension actuelle du manteau neigeux de ses régions (Royer et al., 2021). Cette étude explore notamment si et comment l'humidité du sol – qui est fortement influencée par la distribution des plaques de neige et de glace – a une incidence sur les processus de métamorphisme. Plus spécifiquement, nous nous sommes intéressés à la croissance du givre de profondeur qui forme typiquement la strate basale du couvert nival arctique et dont la présence influence fortement les propriétés thermiques et optiques de la neige. Ce chapitre s'inscrit donc dans l'[objectif 4](#) de la thèse et permet de mettre en évidence une autre facette des effets de la présence des plaques de glace sur le milieu physique. Cette étude s'est basée sur des données de coupes stratigraphiques de neige couplées à des mesures de données environnementales (humidité du sol, température de l'air et du sol, mesure de vent) obtenues à l'île Ward Hunt.

Citation complète: Davesne, G.; Fortier, D. & Domine, F. (2021) Effects of meteorology and soil moisture on the spatio-temporal evolution of the depth hoar layer in the polar desert snowpack, *Journal of Glaciology*, 1-16. doi:10.1017/jog.2021.105

5.2. Résumé

Dans les déserts polaires, la croissance de givre de profondeur (*Depth hoar*, abrégé en DH) n'est pas systématique contrairement à la toundra, ce qui est critique pour les propriétés du manteau

neigeux. Nous abordons ici la variabilité spatio-temporelle de la couche de DH dans le désert polaire sur deux sites du Haut Arctique canadien : l'île Ward Hunt (83°N) et Resolute Bay (75°N). Nos données montrent que, au-dessus des zones humides, le DH représentait une plus grande fraction du manteau neigeux et était caractérisé par une densité plus faible et des cristaux plus grossiers qu'au-dessus des zones sèches constituées principalement de graviers. L'augmentation de l'humidité du sol prolonge la période du *zero curtain effect* pendant la période de gel, ce qui entraîne des gradients de température plus forts dans le manteau neigeux et un métamorphisme cinétique plus important. Nos résultats démontrent également que la grande variabilité interannuelle du DH est principalement déterminée par les conditions de vent à l'automne, puisque cette variable clé contrôle la densité initiale de la neige et la date d'apparition de la neige. Ces forts contrôles exercés par l'humidité du sol et les conditions météorologiques sur la croissance du DH dans les déserts polaires soulignent la possibilité de changements majeurs dans les propriétés physiques des manteaux neigeux polaires en réponse aux changements climatiques et environnementaux rapides qui affectent actuellement ces régions.

5.3. Abstract

In polar deserts, depth hoar (hereinafter: DH) growth is not systematic unlike on tundra and this is critical for snowpack properties. Here we address the spatio-temporal variability of the DH layer in the polar desert at two sites in the Canadian High Arctic; Ward Hunt Island (83°N) and Resolute Bay (75°N). Our data show that, over humid zones, DH represented a larger fraction of the snowpack and was characterized by lower density and coarser crystals than over dry gravelly areas. Increased soil moisture extends the zero-curtain period during freeze-up, leading to stronger temperature gradients in the snowpack and greater kinetic metamorphism. Our results also demonstrate that the large inter-annual variability in DH is primarily driven by wind conditions in the fall since this key variable controls the initial snow density and snow onset date. These strong controls exerted by soil moisture and meteorological conditions on DH growth in polar deserts highlight the possibility of major changes in polar snowpacks physical properties in response to the rapid climate and environmental changes currently affecting these regions.

5.4. Introduction

As a mix of air and ice, snow exhibits unique thermophysical and optical properties, which include: (1) its high short-wave albedo and high thermal emissivity; (2) its high thermal insulation capacity; (3) its capacity to store and release water and energy as latent heat (Pomeroy and Brun, 2001; Warren, 1982). The seasonal snowpack therefore has critical effects on the whole polar geosystem through many complex feedback mechanisms on aspects such as climate, permafrost, hydrology and plant ecology (Callaghan et al., 2011a,b; Park et al., 2015) and these effects are potentially strongest at the highest latitudes and in particular in polar deserts (Young et al., 2018), where snow covers the ground surface for up to ten months of the year.

Polar deserts are characterized by low winter precipitation, unevenly redistributed across the landscape during and after snowfalls by strong winds, and the predominance of non-vegetated mineral soils. These conditions make polar deserts fundamentally different from Arctic tundra regions in terms of climatic and environmental conditions (soil composition, vegetation, surface hydrology) with direct consequences on the snowpack. This recently motivated Royer et al. (2021) to rethink the well-accepted classification of seasonal polar snowpack of Sturm et al. (1995) by creating a specific category for the polar desert snow. In particular, the polar desert snowpack stands out from that of the Arctic tundra snow by its lower height (~20 cm vs. 40 cm respectively) and higher density (~409 kg m⁻³ vs. 315 kg m⁻³, respectively) (Royer et al., 2021). As a thermodynamically unstable medium, snow on the ground undergoes a constant evolution through the winter following metamorphic processes (Sommerfeld and Lachapelle, 1970; Colbeck, 1982). In polar deserts, the snowpack is generally comprised of two main layer types: a thin basal depth hoar layer, typically < 10 cm, topped by a wind slab (Domine et al., 2018a; Royer et al., 2021). Depth hoar (hereinafter DH) crystals are large poorly connected hollow faceted crystals forming layers of low density and low thermal conductivity, while wind slabs have opposite properties. DH formation is related to a strong vertical temperature gradient (>20 °C m⁻¹) within the early season snowpack which induces a water vapour pressure gradient. It results in an intense upward water vapour flux by diffusion from the warmer to the cooler layers of the snowpack leading to kinetic grain growth by recrystallization (Sturm and Benson, 1997). These upward heat and mass transfers

can be enhanced by convection (Sturm and Benson, 1997; Trabant and Benson, 1972) and wind-induced air advection (wind-pumping; Albert et al., 2002; Cunningham and Waddington, 1993).

The formation of DH has attracted renewed scientific interest over the last decade since it causes drastic changes in the snowpack properties and has strong interactions and feedbacks with the ground surface. Indeed, the DH layer contributes most to snowpack thermal insulation. Its thickness and thermal conductivity are critical since they deeply affect the winter ground surface temperature and hence the permafrost thermal regime (Domine et al., 2016a; Gouttevin et al., 2018; Sturm and Johnson, 1992; Sturm et al., 2002; Zhang et al., 1996). DH also affects the polar ecosystem, especially the vegetation (Domine et al., 2016b) and the subnivean life (Domine et al., 2018b; Poirier et al., 2019) as well as soil microbial processes (Schimel et al., 2004) by providing protection from cold temperature. Given the present and future exacerbation of climate warming in the highest latitudes, any changes in conditions required to form DH would alter the snowpack properties and would have cascading effects on permafrost and ecosystems and would change its feedback on climate. Knowledge of the processes governing DH formation in the polar snowpack and its spatio-temporal evolution is therefore essential to improve our understanding of the polar snow and its far-reaching implications on the whole polar desert ecosystem. Up to now, field observations regarding DH are scarce in polar desert regions and current snow physics models are not capable of simulating Arctic snowpack properties and in particular DH formation (Barrere et al., 2017; Domine et al., 2016b; Domine et al., 2019;).

While the DH layer is considered ubiquitous on the Arctic tundra, it is generally thinner and highly heterogeneous in the polar desert regions (Royer et al., 2021). However, the paucity of snow studies in polar desert environments considerably limits our understanding of the spatio-temporal evolution of DH. Recently, Domine et al. (2018a) have observed that in the polar desert of Ward Hunt Island (Canadian High Arctic), it was totally absent at the end of winter 2015/16 in most places. In contrast, data analysis in 2017 concluded that DH was present at that site. That study thus highlighted that the formation of DH is not systematic in polar deserts and Domine et al. (2018a) argued that it mainly depends on soil moisture and wind conditions. The authors hypothesized that low soil moisture allowed rapid soil freezing with little or no zero-curtain period, during which the freezing of the soil releases latent heat that maintains the temperature at 0°C (Cook, 1955; van Everdingen, 1998). A fast soil cooling prevented the establishment of the strong temperature gradient required for DH formation. High wind speeds, combined with the low Arctic

precipitation, delayed the establishment of a continuous snow cover, further hastening soil cooling. High wind speeds in the near-surface boundary layer also favour the formation of dense hard wind slabs, whose transformation into DH requires prolonged intense temperature gradients (Domine et al., 2016b; Marbouy, 1980). The hypothesis of a critical effect of soil moisture and wind conditions on the development of DH in polar desert context deserves further detailed and quantitative investigation which motivated this study.

Those previous findings demonstrated the importance of considering meteorology and soil moisture to better understand DH formation in polar deserts. Here, we explore how soil moisture, microtopography and meteorology control the spatio-temporal variability of DH formation in two polar desert sites in the Canadian High-Arctic: a main site which was Ward Hunt Island (83°N) and where extensive atmospheric and soil monitoring data are available and a secondary one, Resolute Bay (75°N), where atmospheric data are available. More specifically, this study explores whether DH is better developed over humid zones than over well-drained dry mineral soils due to the moist conditions which are expected to enhance kinetic grain growth. We also investigate whether the year-to-year variability in the thickness and properties of DH can be explained by the variability in snow and meteorological conditions, particularly regarding the snow onset date, snowpack erodability and wind conditions. To address these questions, we (1) evaluated the interannual variability in DH formation by comparing the results of Domine et al. (2018a) in 2016 and 2017 with our observations in 2019 and analyzed their differences as a function of meteorological and soil (temperature and moisture, monitored at specific sites and inferred from vegetation and topography at others); and (2) investigated the small-scale variability of the DH layer and its link to soil moisture.

5.5. Study site

Most field investigations were conducted at Ward Hunt Island (hereinafter: WHI) ($83^{\circ}05'\text{N}$, $74^{\circ}06'\text{W}$) which is located at the northern tip of the Canadian Arctic Archipelago (**Figure 57a**) (Vincent et al., 2011b). WHI is characterized by an extremely cold and dry climate. Meteorological variables have been measured at the SILA weather station (operated by the Center for Northern Studies, CEN) located at 5 m a.s.l. on the north shore of the island (**Figure 57a**). The mean annual air temperature (MAAT) has been -17.1°C for the period 2005–2019 with a monthly mean ranging between -31.6°C in February and 1.7°C in July. No long-term precipitation data are available for

WHI, but it is likely similar to the average of 185 mm year⁻¹ (water equivalent) measured at Alert, located 170 km to the southeast (**Figure 57a**), where ~90% of the total precipitation falls as snow (Environment Canada, 2021). The prevailing and strongest winds are from the southwest to west with maximum wind speeds up to 20 m s⁻¹.

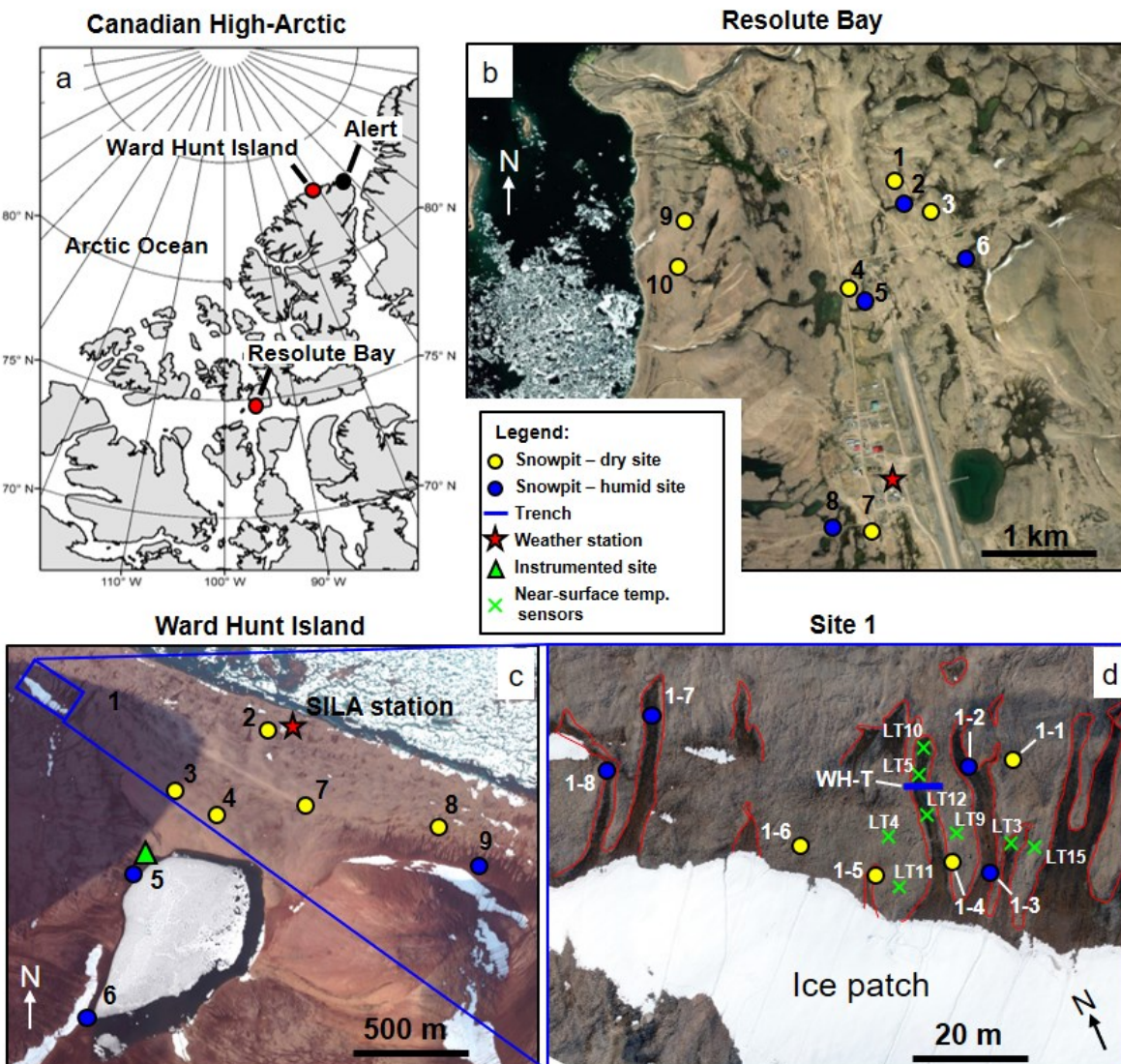


Figure 57. a) Location of the study sites within the Canadian Arctic Archipelago; b and c) Map showing the location of snowpits and the trench as well as the instrumented sites at Resolute Bay and Ward Hunt Island; d) Close-up of Site 1 of WHI located in the downslope margin of a perennial ice patch. The red lines delimit the humid soils which are mostly associated with solifluction lobes. Background image for (b): Worldview-2 taken on 26 July 2019 (source: Esri, DigitalGlobe, GeoEye, i-cubed, USDA FSA, USGS, AEX, Getmapping, Aerogrid, IGN, IGP, swisstopo, and the GIS User Community); for (c) Worldview-3 taken on 14 August 2019 and for (d): High-resolution orthomosaic derived from unmanned aerial vehicle (UAV) images taken on 18 July 2019.

The island is a polar desert (vascular plant cover <5% and low lichen and bryophyte cover) but many humid zones are scattered across the landscape. Outside the hyporheic zones of Ward Hunt Lake (WHL), notable sources of water include the summer melting of the seasonal and perennial snow/ice patches, and the melting of ground ice formed in the active layer of permafrost (Paquette et al., 2017). These humid soils shelter diversity of cyanobacteria, bryophytes, lichens and plants in comparison to the adjacent dry zones dominated by well-drained coarse-grained sediments (Vincent et al., 2011b). Underneath the surface, the continuous permafrost has a mean annual temperature of -13.5°C at 3 m depth (2005–2019 period) and its active layer thickness varies from 20 to 80 cm depending on the soil composition and moisture (Paquette et al., 2017; Vincent et al., 2011b).

The other study site is located near Resolute Bay (a.k.a. Qausuittuq; hereinafter: RB) ($74^{\circ}45'\text{N}$, $94^{\circ}50'\text{W}$) on Cornwallis Island, 1060 km to the south of WHI (**Figure 57a**). Despite the distance, the region presents strong similarities with the polar desert of WHI. The permafrost is continuous and most of the land surface is largely vegetation-free (gravelly material), except in lowland patchy wetlands that support tundra vegetation (Braun et al., 2000; Woo and Young, 2006). The climate is warmer than at WHI. The MAAT was -14.19°C for the period 2005–2019 with a monthly mean ranging between -31.3°C in February and 5.1°C in July. The mean annual precipitation was 145 mm, 70% of which fell as snow, for the same period. The prevailing winds are from north to east (Environment Canada, 2021). No data of soil temperature and moisture are available for this site. The total annual precipitations measured at Alert and Resolute Bay were probably underestimated due to systematic errors of gauge-measured solid precipitation under snowdrift conditions (Woo et al. 1983).

5.6. Methods

We observed snow stratigraphy in numerous snowpits, made snow physical measurements, and analyzed these data in light of soil properties (moisture, temperature, substrate and vegetation cover) and meteorological variables.

5.6.1. Snow studies

5.6.1.1. Snow physics

A total of 34 snowpits were dug during field campaigns in spring (late May and early June) 2019 at WHI and RB (**Figure 57b** and c, **Figure 58**). The most comprehensive work was undertaken at WHI because numerous environmental variables are monitored (see [section 5.6.2](#)). The choice of snowpit location was previously guided by the analysis of late-summer high-resolution satellite images to target both humid and dry zones (**Figure 57b**). Sites selection was validated in the field during snowpit excavations: dry sites had a bare gravelly surface and humid sites had a vegetation cover, a high fraction of fine-grained sediments and an organic crust (**Figure 58**) that ensures greater soil moisture-holding capacity. We have considered here that humid soils define all soils that are characterized by a high liquid water content throughout the summer. Metadata information on the snowpits is provided in [Table S4-1](#) in the supplementary material.

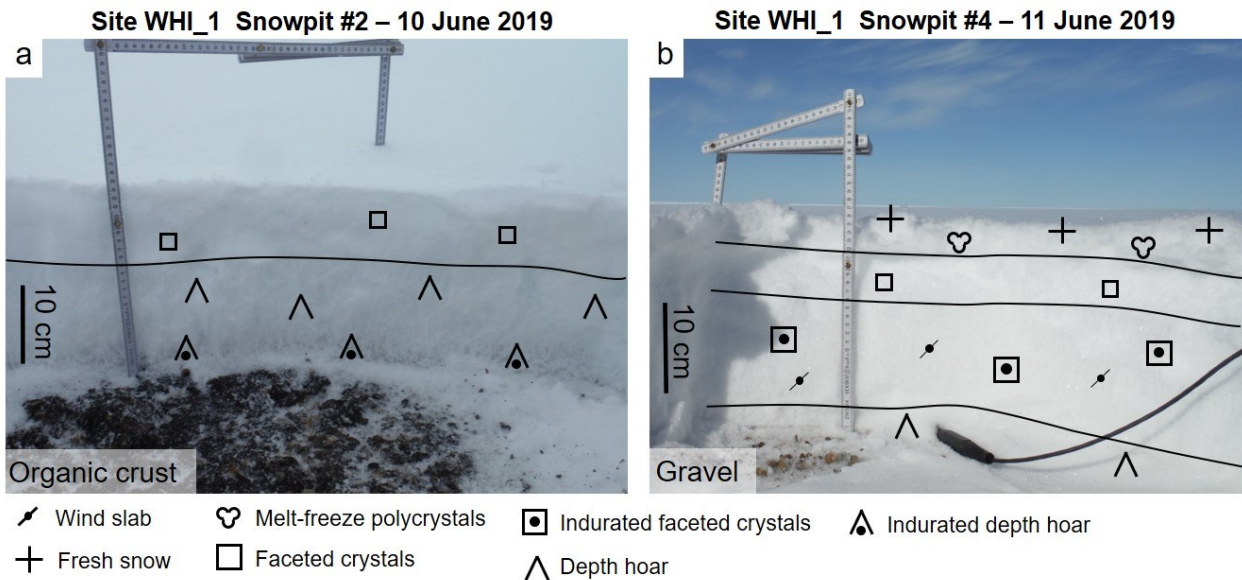


Figure 58. Example of snowpit excavations made at WHI in early June 2019 on a humid site (a: snowpit #2) and a dry site (b: snowpit #4).

Snowpit work consisted in detailed observation of stratigraphy and measurements of vertical profiles of physical properties: density, visual grain size and shape, specific surface area, thermal conductivity and temperature. Snow density ρ_s (kg m^{-3}) was obtained by weighing snow samples extracted with a vertical resolution of ~ 3 cm from the snowpack using a 100 cm^3 metal box cutter (3 cm high). The visual grain size E (mm) and shape were determined using a millimetre-gridded plate and an 8x magnifying glass. The grain type identification and the graphical

representation of snowpits used the classification of Fierz et al. (2009). The specific surface area (SSA) of the snow, which is an interesting indicator of metamorphism and snow microstructure (Calonne et al., 2012), was determined from the snow reflectance at 1310 nm using an integrating sphere (DUFISSS instrument; Gallet et al., 2009), from which SSA was derived. Finally, the snow thermal conductivity was measured with a heated needle probe (TP02 model from Hukseflux; uncertainty $\pm 3\% + 0.02 \text{ W m}^{-1} \text{ K}^{-1}$ at 20°C) connected to a CR1000 datalogger (Campbell Scientific) (Domine et al., 2011). Finally, at WHI, a 13 m long snow trench (WH-T) covering humid soil in a solifluction lobe and the adjacent dry zones was excavated to investigate the transition between both zones. The DH thickness and density were measured at 50 cm intervals along the trench.

5.6.1.2. Snow mapping

The spatial distribution of the snowpack over Site 1 at WHI (**Figure 57d**) was measured based on Unmanned Aerial Vehicle (UAV) photogrammetry survey conducted in late spring 2019. We use a quadcopter drone (DJI Phantom 4 pro) equipped with a consumer-grade Red-Green-Blue (RGB) camera. We made two surveys, one on 12 June at peak accumulation and before any melt event and the second one on 18 July under snow-free conditions. The set of images collected were then processed in Pix4D mapper software (Pix4DTM) which relies on SfM (Structure from Motion) technology to generate dense 3D point clouds of the study area. We performed low elevation flights ($\sim 30\text{--}40$ m above the ground surface) with front and side overlaps of $\sim 75\%$ so that ground sampling distance is lower than 0.5 cm. Each point cloud was accurately georeferenced using 10 targets 30 cm in diameter distributed across the study areas to serve as photo-identifiable ground control points (GCPs). The targets were installed on topographic highs (e.g. ridge of solifluction lobes) that were snow-free. The coordinates of all GCPs were measured using a VX spatial station survey linked to a geodesic landmark recorded using a Global Navigation Satellite System receiver (R8 GNSS; Trimble®, precision $x\text{--}y \pm 8$ mm and $z \pm 15$ mm).. The method for measuring snow height consists of calculating the distance (in mm) between the snow surface cover cloud from the snow-free cloud (Nolan et al., 2015; Lendzioch et al., 2019) using the Multiscale Model to Model Cloud Comparison (M3C2) plug-in included in the CloudCompare V2.11 open-source software (CloudCompare, 2020). The accuracy of the final map of snow height (in cm) was then evaluated (Root Mean Square Error, RMSE) using 21 hand-probe snow height measurements made across

the study area. The DSM of the snow-free surface was used to calculate microtopography parameters using the Topographic Position Index (TPI) based on the algorithm developed by Weiss (2001) which allows detecting the topographic lows and highs. The TPI was calculated in ArcGIS 10.5.1. using the ArcGeomorphometry extension (Rigol-Sanchez et al., 2015).

5.6.2. Environmental Monitoring

The snowpits were interpreted based on the environmental observations, including meteorological variables and soil surface conditions (temperature and moisture) available at WHI and RB. All data were considered for the period from 15 August 2018 to 31 May 2019, hereafter called snow season 2018/19.

5.6.2.1. Meteorological Variables

At WHI, the meteorological data were provided by the SILA automatic weather station (**Figure 57c**; CEN, 2021) which recorded air temperature (150 cm above the ground level; a.g.l.) and soil surface temperature (0 cm) (44033, YSI; uncertainty $\pm 0.1^\circ\text{C}$ from 0 to 70°C), wind speed and direction at 10 m a.g.l. (05103-10, RM Young; uncertainty $\pm 0.3 \text{ m s}^{-1} \pm 3^\circ$) as well as snow height (Sonic ranger SR50A, Campbell Scientific; uncertainty $\pm 1 \text{ cm}$; installed 2 m a.g.l.) (**Figure 59**). All data were sampled every minute and then hourly-averaged by a CR10X datalogger (Campbell Scientific). The snow gauge is located in a slight topographic break-of-slope produced by a raised-beach ridge which leads to a local snow height greater than the surrounding areas. For this reason, the raw snow height data was corrected based on the reading of a snow stake installed outside the snowdrift from daily time-lapse photographs taken by a camera installed on the SILA tower (**Figure 59**; [Figure S4-1](#)). The snow height, air and soil surface temperature were used to estimate the temperature gradient (ΔT in K m^{-1}) through the snowpack over the snow season 2018/19 based on Equation (5.1):

$$\Delta T = \frac{T_{\text{soil}} - T_{\text{snow}}}{h} \quad (5.1)$$

where T_{soil} and T_{snow} are the temperatures at the soil and snow surfaces, respectively. The latter has not been measured directly but is considered to be equal to the air temperature measured at the SILA station during the freezing period. Since the snow surface temperature is almost always lower than the air temperature due to radiative cooling, the gradient calculated here is in fact a

lower limit of the actual gradient. For RB, only hourly air temperature, wind conditions (speed and direction) and snow height were available, provided by the weather station operated by Environment and Climate Change Canada (Environment Canada, 2021).

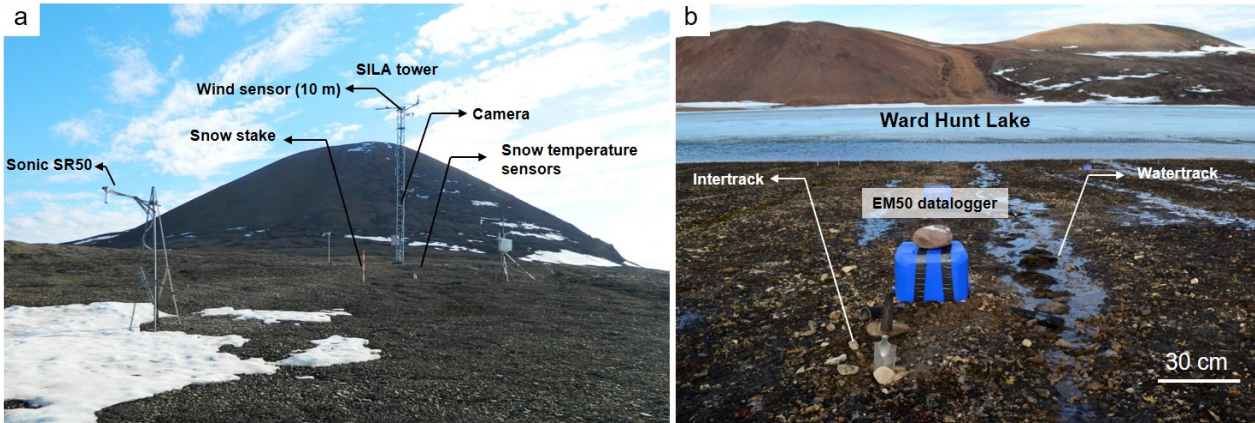


Figure 59. a) view of the SILA weather station on 11 July 2016 at WHI. Note the remaining snowdrift at the forefront where the Sonic ranger SR50A is installed; b) view of the site 5 on 6 July 2017, looking towards Ward Hunt Lake. The surface runoff in water tracks is clearly visible.

5.6.2.2. Soil Surface moisture and temperature

At WHI, near-surface soil temperature and volumetric liquid water content (VWC) were recorded at the SILA weather station by a thermistor (44033, YSI) and a water content reflectometer (CS-616, Campbell Scientific; uncertainty $\pm 2.5\%$ VWC), respectively, installed 5 cm depth below the soil surface. The soil surface near the station mainly consists of well-drained sand and gravel with sparse patches of vegetation (**Figure 59**). We also used soil VWC and temperature data measured at a second instrumented site located in a humid zone near the shore of Ward Hunt Lake (Site 5; **Figure 57c**). The site is characterized by a low gradient slope with a series of sub-parallel water tracks mainly fed by meltwater from upslope snow patches. The soil is composed of gravel mixed with a sandy/muddy matrix with organic matter and black organic crust on the surface. It is water-saturated during most of the summer (Paquette et al., 2017; **Figure 59**). The soil VWC and temperature are measured at 5 cm depth in a water track and an adjacent drier intertrack. Data were recorded by Decagon 5TM probes (uncertainty $\pm 3\%$ WVC and $\pm 1^\circ\text{C}$) connected to an EM50 data logger (Meter Devices). We also used the near-surface temperature for the period from August 2015 to July 2019 provided by the upper thermistor (2 cm below the soil surface) of a cable installed in a borehole of 3 m depth located 20 m north of Site 5 in the same humid zone. Finally, we relied on a dataset of near-surface temperature recorded by a series of 8

data loggers Trix-8 (LogTag; resolution 0.1°C, uncertainty of 0.5 °C) installed in the downslope margin of a perennial ice patch (Site 1; **Figure 57d**). Three sensors (LT3, 5, 10, 12) were installed in various humid zones formed by solifluction lobes fed by meltwater while the other four (LT4, 9, 11 and 15) were installed in adjacent dry sandy-gravelly zones. The sensors were protected from humidity and ice by airtight plastic boxes and were placed about 5 cm below the soil surface to avoid any effect of direct solar radiation. To estimate the magnitude of metamorphic processes between humid and dry zones in Site 1, the average temperature gradient through the snowpack was calculated using equation (5.1). The soil surface temperature was estimated from the temperature recorded by the Trix-8 sensors and the air temperature as well as the snow height recorded at SILA station were used.

5.6.2.3. Snow Conditions

Information on the snowpack formation at WHI, especially its onset date and the erosion events, was derived from time-lapse photographs provided by two automatic cameras (photographs every 4h). The first one, installed on the SILA tower since 2015, takes pictures of the instrumented sites and the second one, installed since 2017, of the downslope margin of the ice patch at Site 1 (**Figure 57d**; Fortier and Davesne, 2021b).

5.7. Results

5.7.1. Small-scale variability of the snow height

Figure 60 presents the UAV-based map of snow height distribution over Site 1 on 12 June 2019 (**Figure 60a**) along with the TPI map showing the microtopography of this site (**Figure 60b**). On average, the snow height over the study area was 34.5 ± 14.8 cm. The topographic highs, which most often correspond to the frontal lobes and lateral ridges of solifluction lobes (Verpaelst et al., 2017) were almost free of snow, while depressions accumulated up to 95 cm of snow for the deepest ones. The close relationship between the snow height observed at Site 1 and the microtopography is also highlighted by **Figure 60c, d and e**. The comparison between the UAV-derived snow heights and the 21 manual measurement points over Site 1 shows a strong statistical agreement ($R^2=0.91$, std dev. of 3.26 cm and RMSE of 4.1cm; **Figure S4-2**). Part of the offset between UAV and manual measurements can also be attributed to the bias associated with the snow probing which can

overestimate by a few centimeters when the probe penetrates the ground, especially on gravel surfaces or organic soils (Stuefer et al., 2020).

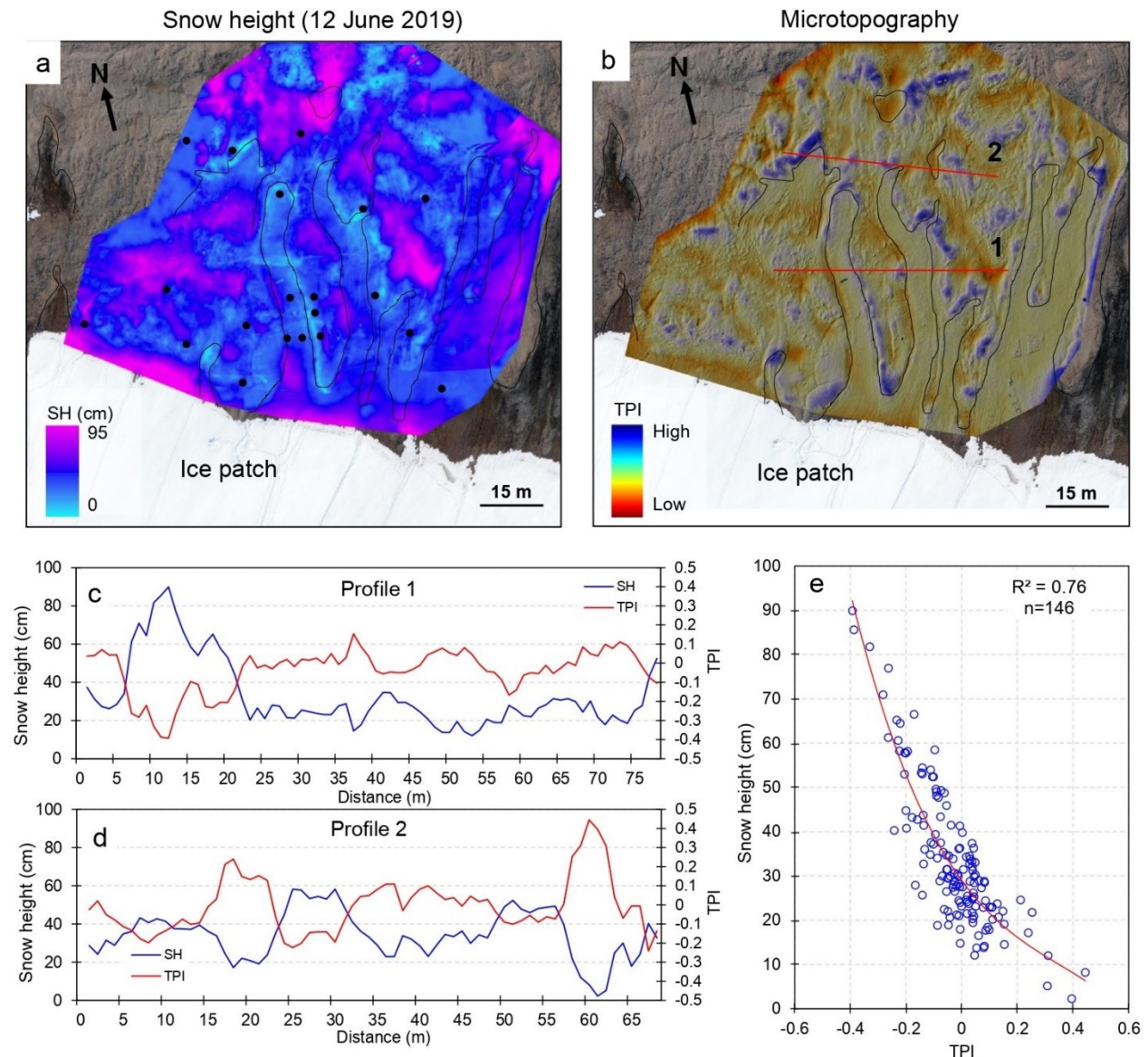


Figure 60. a) Map of small-scale distribution of the snowpack on 12 June 2019 over Site 1 at Ward Hunt Island obtained by UAV surveys, b) Map of the microtopographic features based on the Topographic Position Index (TPI) computation. The black dots represent the 21 manual snow height measurement points. The black line delimits the humid soils. Snow height (cm) and TPI along the profile 1 (c) and 2 (d) identified by red lines in b, and e) shows the relationship between the snow height and the TPI for both profiles 1 and 2 with the best-fitting regression curve.

5.7.2. Snow physics

5.7.2.1. Depth hoar fraction

Based on the 18 snowpits excavated at WHI (WH-SP) we found a DH layer at the base of the snowpack of at least 5 cm thick at all sites except at sites #2 and #4 where it was only 1 cm and 4 cm thick, respectively.

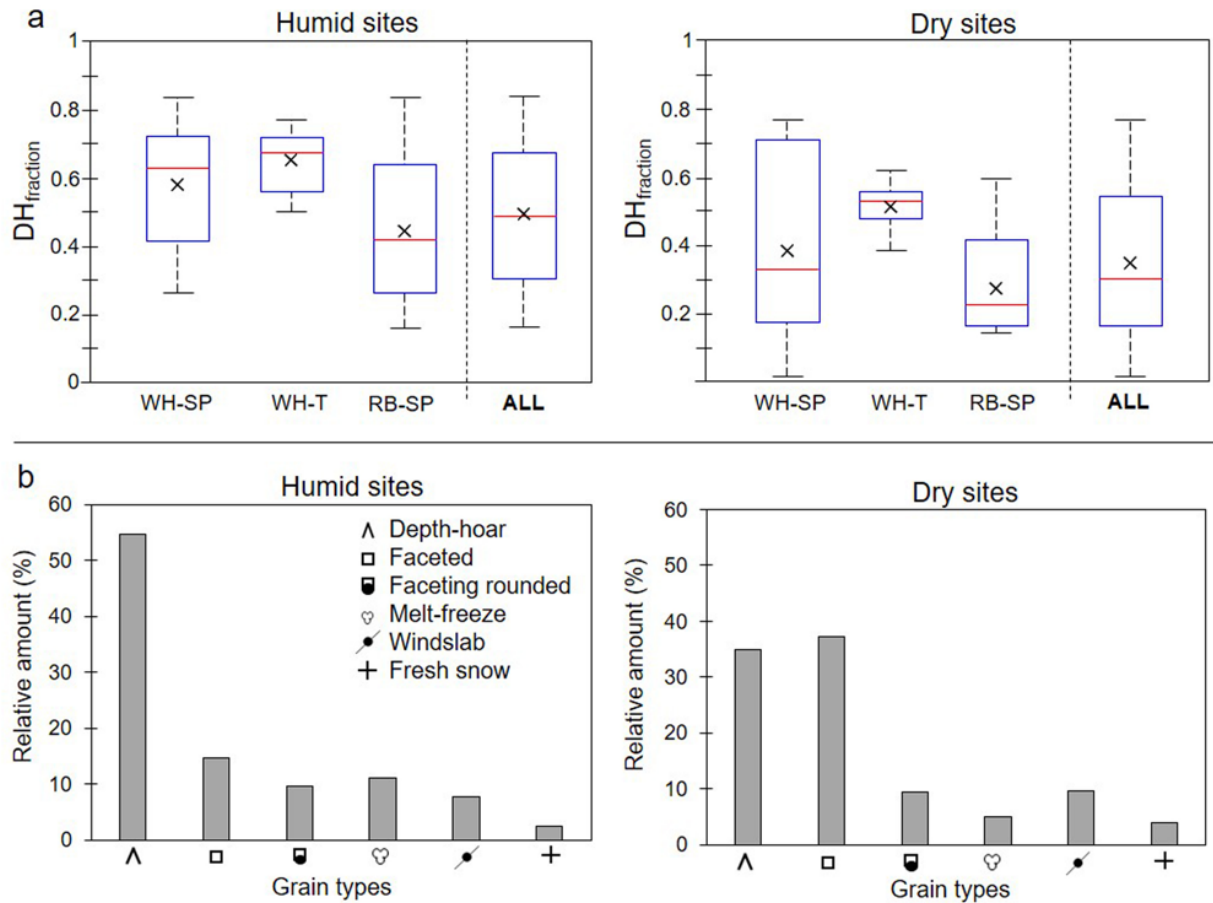


Figure 61. a) Boxplots of the depth hoar fraction ($DH_{fraction}$) measured in snowpits made in Ward Hunt Island snowpits (WH-SP) and Resolute Bay snowpits (RB-SP) in humid and dry sites, and measured along the trench dug at Ward Hunt Island in Site 1 (WH-T). The red line is the median, the black cross is the mean, the blue box delineates the interquartile range, and whiskers extend to the highest and lowest values; b) Histograms showing the relative contribution (%) of the snow grain types in both humid and dry sites.

On average, basal DH thickness was higher in humid sites (19.1 ± 3.9 cm) than in dry sites (13.4 ± 8.1 cm), giving a DH thickness-to-total snow height fraction ($DH_{fraction}$) of 0.57 ± 0.19 and 0.38 ± 0.25 respectively (Figure 61a). This difference is, however, not statistically significant at the 95%

level according to an unpaired t-test ($p=0.129$) which is likely due to the large standard deviation in dry sites. The variability of the DH thickness along the trench WH-T that crossed the central tread of a solifluction lobe supporting a humid zone is illustrated in **Figure 62**. We observed that the DH layer was laterally continuous but was the thinnest (~5 cm) on the lateral ridge of the solifluction lobe that delimits the humid zone from the adjacent dry zone. Humid zones had a higher $DH_{fraction}$ (0.66 ± 0.07) than dry surfaces composed of coarse gravels (0.52 ± 0.06) (**Figure 61a**; difference significant at 95% level, $p<0.0001$). Measurements conducted on the 16 snowpits at RB showed results similar to those of WHI (**Figure 61a**). The $DH_{fraction}$ was 0.45 ± 0.22 in humid zones and 0.28 ± 0.16 in dry zones (difference significant at 95% level, $p=0.04$).

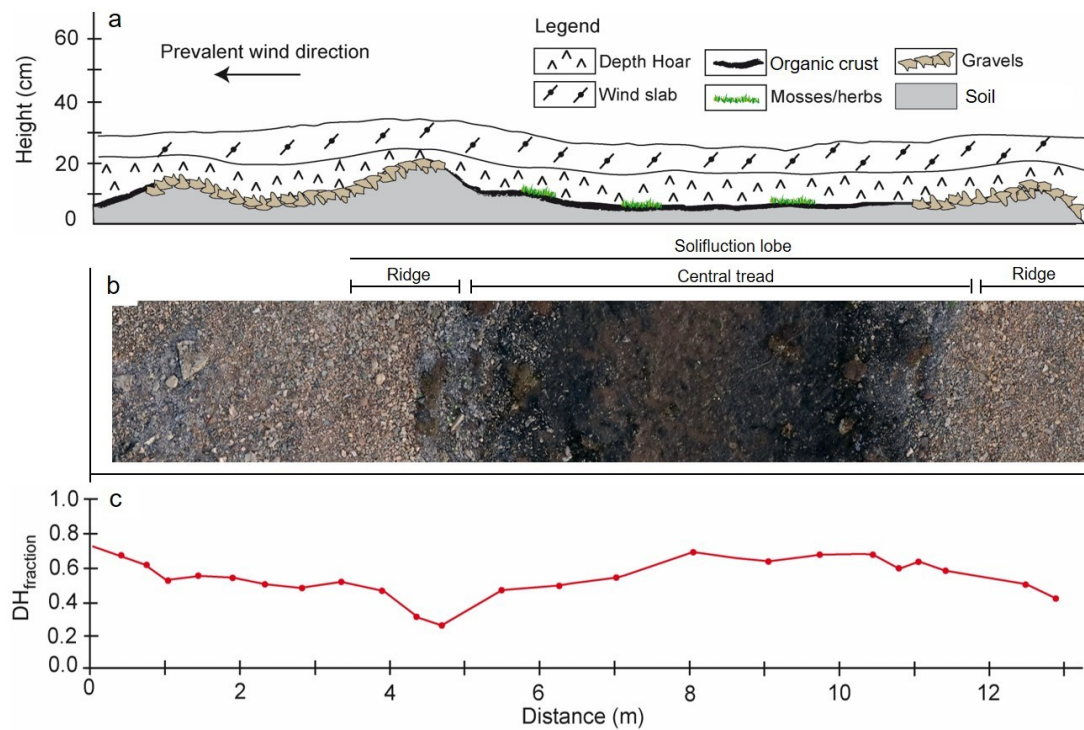


Figure 62. a) Schematic representation of the depth hoar layer and soil surface observed along the trench WH-T that crossed a solifluction lobe in Site 1 at Ward Hund Island in early June 2019; b) High-resolution UAV orthomosaic showing the soil surface at the trench location on 16 July 2019; c) Spatial evolution of the $DH_{fraction}$ along the trench.

Regarding the proportion of snow grain types observed in snowpits made at WHI, a clear difference between humid and dry sites was found (**Figure 61b**). In humid sites, DH crystals were dominant since they represent ~55% of the observed snow type. Conversely, faceted crystals dominated (38%) in dry sites, followed by DH (35%). Measurements of snow grain size demonstrated that DH crystals tended to be coarser (~4 mm) on humid sites than on dry sites (~2.4

mm).

5.7.2.2. Snow physical properties

The vertical profiles of density, SSA and thermal conductivity measured in snowpits made at WHI and RB in 2019 are presented in **Figure 63** and the average values of DH properties for each site are presented in **Figure 64**. At WHI, the density of the lowest 15 cm in snowpits, where the proportion of DH is variable, ranged from 200 to 400 kg m⁻³ in dry sites.

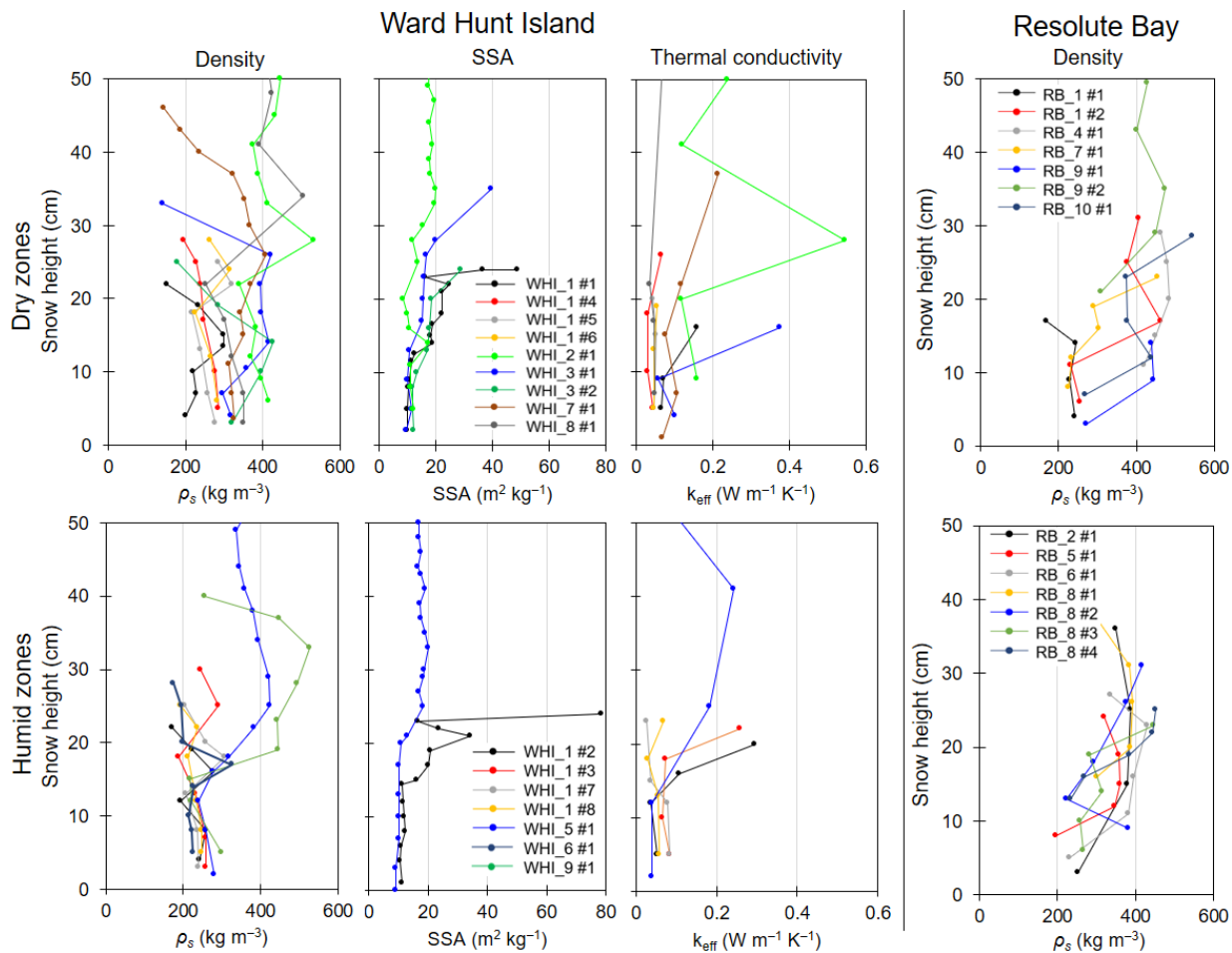


Figure 63. Vertical profiles of density (ρ_s), SSA and thermal conductivity (k_{eff}) for snowpits dug in dry and humid zones at Ward Hunt Island and Resolute Bay (only density) in early June 2019. The high Thermal conductivity values of WH_2#1 ($0.55 \text{ W m}^{-1} \text{ K}^{-1}$) and WH_3#1 ($0.38 \text{ W m}^{-1} \text{ K}^{-1}$) are due to the presence of a dense melt-freeze layer. The site RB_3 at Resolute Bay, does not appear because only one density measurement was done.

The variability was smaller in humid sites with values varying between 250 to 300 kg m⁻³. On average, the density of DH layers found at the bottom of the snowpack was significantly lower in

humid sites ($237 \pm 10 \text{ kg m}^{-3}$) than in dry sites ($310 \pm 69 \text{ kg m}^{-3}$) (Difference significant at 95% level, $p=0.007$; **Figure 64a**). At RB, the average density of the DH layers also showed a clear difference between both environments, being $231 \pm 16 \text{ kg m}^{-3}$ for humid zones and $255 \pm 16 \text{ kg m}^{-3}$ for dry zones and (Difference significant at 95% level, $p=0.0021$).

The thermal conductivity of basal layers in snowpits at WHI also showed lower variability in humid sites, where it varied between 0.04 to $0.07 \text{ W m}^{-1} \text{ K}^{-1}$, than in dry sites, where it varied between 0.03 to $0.17 \text{ W m}^{-1} \text{ K}^{-1}$. The average conductivity of DH in humid areas was $0.05 \pm 0.02 \text{ W m}^{-1} \text{ K}^{-1}$ in dry areas was $0.07 \pm 0.03 \text{ W m}^{-1} \text{ K}^{-1}$ (difference not significant at the 95% level, $p=0.08$; **Figure 64b**). Finally, SSA values were similar between the two environments with values close to $11 \text{ m}^2 \text{ kg}^{-1}$. The one high SSA value, close to $80 \text{ m}^2 \text{ kg}^{-1}$ for surface snow on 4 June 2019 on a humid zone, reflects a measurement done shortly after a snowfall.

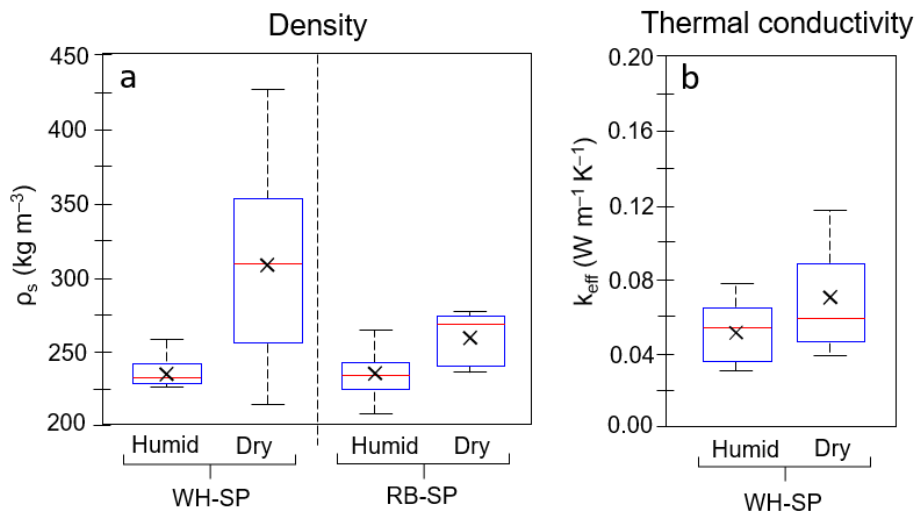


Figure 64. a) Boxplot of basal DH density (ρ_s) values in humid and dry zones at Ward Hunt Island (WHI) and Resolute Bay (RB) and b) the same as (a) but for the thermal conductivity (k_{eff}) and only for WHI.

5.7.3. Monitoring data

5.7.3.1. Snow season 2018/19 at WHI

Figure 65 presents the time series of snow height and wind data as well as the thermal gradient in the snow cover for the snow season 2018/19. The snowpack was established permanently on the ground at the SILA site on 24 August following a major storm (**Figure 65a** and **Figure S4-3**). This early snowfall deposited 30 cm of snow at temperatures very close to the melting

point. The surface conditions before and after this event are shown in photos (e) and (f) in **Figure 65** at SILA and in photos a and b in [Figure S4-4](#) at Site 1. The snowpack was continuous at both sites and no signs of snowdrift were visible although the snowfall was associated with strong wind episodes in excess of 10 m s^{-1} .

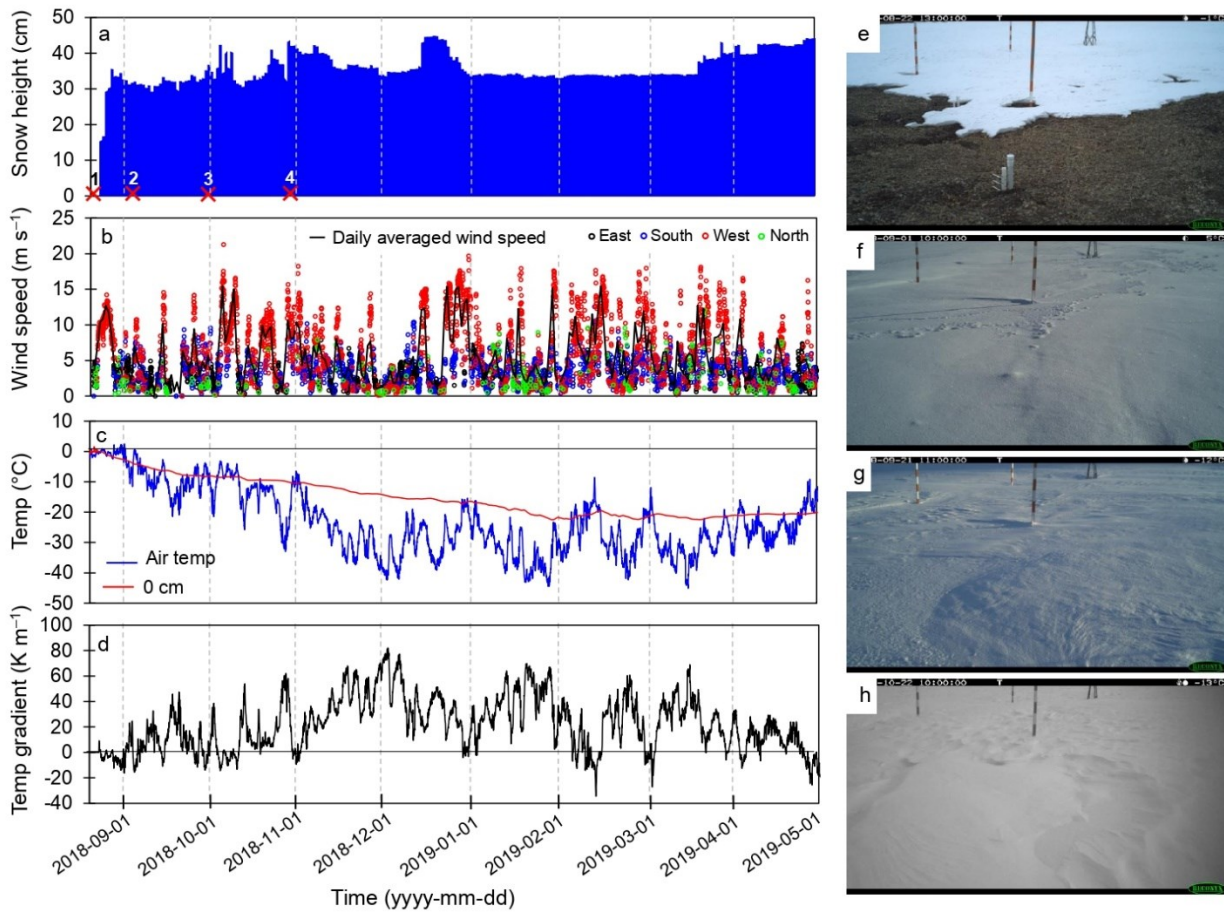


Figure 65. Environmental monitoring at the SILA station at Ward Hunt Island during the snow season 2018/19. a) Snow height measurements by the snow gauge and normalized with the readings of the snow stakes visible on the time-lapse photos; b) Hourly maximum wind speed according to their direction (North/East/South/West) and averaged daily maximum wind speed; c) Hourly temperature records at the soil surface (0 cm) and of the air; d) Hourly temperature gradient in the snowpack calculated from equation 5-1. Photographs on the right side were taken by the automatic time-lapse camera of the SILA tower, showing the snow surface evolution in the early cold season. Their dates are represented by red crosses in graph a; e) 22 August; f) 1 September; g) 21 September; h) 22 October. A close-up of the 5 weeks after snow onset is presented in [Fig. S4-3](#).

The four weeks following the snow onset were relatively calm with little wind which kept the snow height very stable. Windier conditions then occurred and strongly reworked and sculpted the snow

surface as shown in **Figure 65g** and **h** taken on 21 September and 22 October respectively where ripple marks, barchans and sastrugi are clearly visible ([Figure S4-4c and d](#)). The strongest winds of the winter were recorded at the end of September with a peak at 22 m s^{-1} . Five strong wind episodes ($> 15 \text{ m s}^{-1}$) were recorded from the snow onset to 1 December and a total of 22 throughout the entire snow season 2018/19 (**Figure 65b**). Episodes of snowdrifts raised the snow temporarily height up to 45 cm but the high winds generally eroded this new snow within hours or days after its deposition, always reducing the thickness to about 35 cm at the SILA station. This value is well representative of the average snow height measured by UAV over Site 1 ($34.5 \pm 14.8 \text{ cm}$) and those measured at the snowpits ($33.7 \pm 10.9 \text{ cm}$) at the end of snow season 2018/19. After the snow onset, the air temperature remained close to 0°C until 1 September, fluctuating between $+2^\circ\text{C}$ and -3°C . After this date, the first cold spells arrived (**Figure 65c**; [Figure S4-3b](#)). After 11 October, the air temperature dropped consistently below -10°C and reached -30°C on 27 October. The temperature dropped to -40°C for the first time on 2 December.

The soil surface temperature dropped below 0°C after the snow onset on 24 August and gradually decreased without being affected by short-term fluctuations in air temperatures due to the low thermal conductivity of the snowpack (**Figure 65c**; [Figure S4-3b](#)). The cooling was quite rapid in September as the soil surface reached -8°C on the 24th. During that period, the temperature gradient in the snowpack thus remained low, generally less than 20 K m^{-1} except between 15 and 20 September when a cold spell produced gradients up to 40 K m^{-1} (**Figure 65d**; [Figure S4-3c](#)). Subsequently, the soil cooling slowed down from early October while the air temperature continued to drop (**Figure 65c** and [Figure S4-3b](#)). It resulted in the establishment of a moderate to strong temperature gradient during much of the snow season. The strongest gradient occurred on 2 December with values up to 82 K m^{-1} (**Figure 65d**).

The spatial variability of the soil moisture between dry and humid sites at WHI during the snow season 2018/19 is presented in **Figure 66**. **Figure 66a** shows the difference in near-surface soil moisture (-5 cm) between the SILA weather station and Site 5. At SILA, as expected, the soil moisture was very low, varying from 0.05 to $0.15 \text{ m}^3/\text{m}^3$ at the beginning of the winter period. Conversely, at humid site 5, the moisture varied from $0.6 \text{ m}^3/\text{m}^3$ in the water track to $0.4 \text{ m}^3/\text{m}^3$ in the intertrack before freeze-up. This difference in soil moisture had direct consequences on the near-surface thermal regime during the early snow season, as demonstrated by near-surface temperature evolution recorded at SILA and Site 5 (**Figure 66a** and **b**) and at the sensors installed

in Site 1 (**Figure 66c**). A summary of thermal conditions between dry and humid monitoring sites (Site 1; Site 5 and SILA site) is given in [Table S4-2](#). On average, the zero curtain period lasted 27 ± 5 days in humid sites, starting on 23 August with the onset of the snow on the ground which coincided with the beginning of freeze-up, while it was only 8 ± 3 days in the dry areas. As a result, the thermal difference between the near-surface and the air temperatures as well as the temperature gradient through the snowpack during the first month after the snow onset were much greater in humid sites ($6.6 \pm 0.1^\circ\text{C}$, $21.4 \pm 0.7 \text{ K m}^{-1}$ on average) than in dry sites ($2.2 \pm 0.8^\circ\text{C}$, $6.6 \pm 3.4 \text{ K m}^{-1}$ on average). At the scale of the snow season (**Figure 66d**), the difference in the temperature gradient remained significant until April, when the temperature gradient became negative because of atmospheric spring warming.

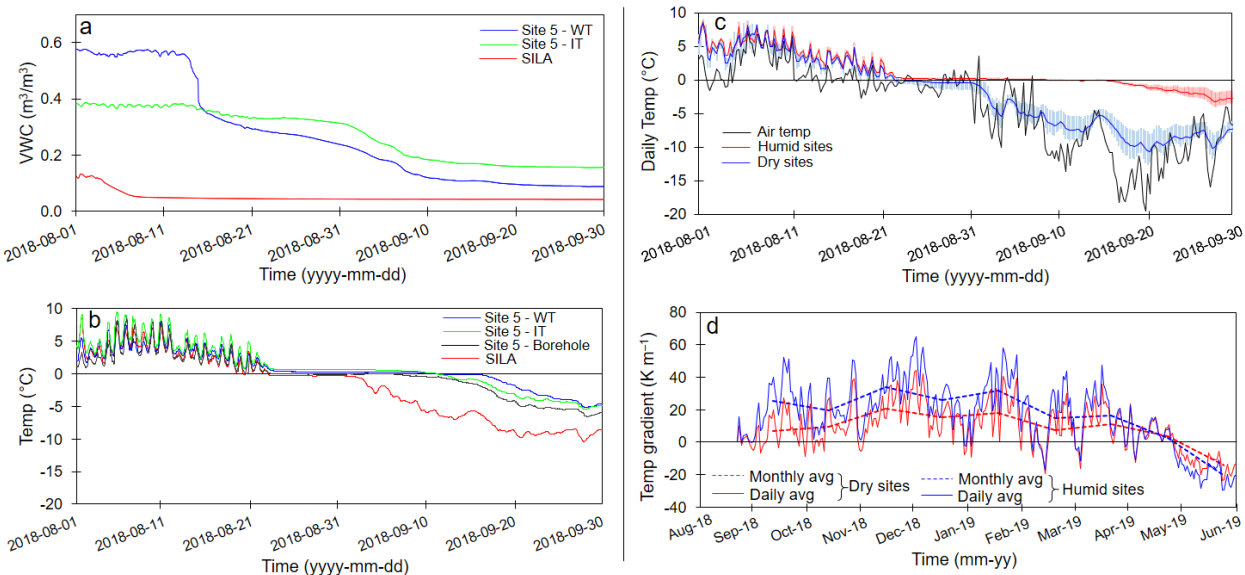


Figure 66. Spatial variability of the moisture and temperature conditions at Ward Hunt Island during the 2018/19 snow season. a and b) Time-series of near-surface (-5 cm) volumetric water content (VWC, m^3/m^3) and temperature at the SILA site and Site 5 in intertrack (IT), water track (WT) and upper thermistor of the borehole; c) Time-series of average near-surface temperature (-5 cm) recorded by Trix-8 sensors in humid zones and dry zones in Site 1. The shaded bands delimit the maximum and minimum values. d) Average calculated temperature gradient (daily and monthly averages) based on equation 5-1 between sensors in humid and dry monitoring sites (Site 1; Site 5 and SILA site) during the snow season 2018/19.

5.7.3.2. Winter 2018–2019 at RB

The time series of snow height, wind data and the air temperature for winter 2018–2019 are shown in [Figure S4-5](#). Unfortunately, the temperature gradient could not be calculated because no

soil surface temperature data were available. Continuous snow cover started on 7 September and reached 20 cm at the beginning of October after several events of accumulation and erosion. The snow height remained stable until the beginning of December when a new wind event occurred and quickly eroded most of the new snow accumulations. During the rest of the winter, the snow height remained close to 20 cm at the snow gauge. The average snow height measured at snowpits at RB was 31.3 ± 7.9 cm. The air temperature decreased gradually at the beginning of winter to reach -20°C on 25 October 25. As at WH, high winds were recurrent with 6 episodes of wind above 15 m s^{-1} recorded from the snow onset to 1 December.

5.8. Discussion

5.8.1. Mechanism of DH formation

A pioneering study by Yosida (1955) established that DH is formed by water vapour diffusion induced by a temperature gradient in the snowpack. He hypothesized that water vapour transfers from one snow crystal to another, in a "hand-to-hand" delivery mechanism. This and subsequent studies (e.g. Marbouy, 1980) proposed that diffusive vapour fluxes (F) at the macroscale could be calculated from equation (5.2):

$$F = -D_{\text{eff}} \times \Delta P \quad (5.2)$$

where D_{eff} is the effective diffusion coefficient for water vapour in the snow. The minimum temperature gradient required to induce depth hoar formation was proposed from experiments to be 20 K m^{-1} (Marbouy, 1980) and also required low to moderate-density snow ($<350 \text{ kg m}^{-3}$). However, field investigations as early as 1972 (Benson and Trabant, 1973; Trabant and Benson, 1972) pointed out that the high rates of metamorphism observed in the subarctic snowpack cannot be explained solely by diffusion. They proposed that strong temperature gradients also initiate convective processes, leading to efficient transfers of heat and vapour through the snow porosity. The convection in the subarctic snowpack was later confirmed in dedicated studies by Sturm and Benson (1997) and Sturm and Johnson (1991) who estimated that layer-to-layer vapour fluxes by air movements in the pore spaces were 10 times higher than by water vapour diffusion. The ability of the snow to allow the air to circulate through it, defined as permeability (noted K_p), is therefore a critical parameter in the activation of convection. The snow permeability depends on the snow density and the SSA as expressed by equation (5.3) (Calonne et al., 2012):

$$K_p = 3r_{es}^2 \times e^{-0.013 \times \rho_s} \quad (5.3)$$

where r_{es} is the equivalent sphere radius given by equation (5.4) and ρ_s is the snow density.

$$r_{es} = 3 / (SSA \times \rho_i) \quad (5.4)$$

where SSA is the specific surface area of snow (Legagneux et al., 2002) and ρ_i is ice density. The studies of Sturm and Benson (1997) and Sturm and Johnson (1991) were performed in the subarctic snowpack in the boreal forest where the wind is weak, leading to the accumulation of uncompacted snow with a density typically around 200 kg m^{-3} (Domine et al., 2008; Sturm et al., 1995). Such snow has a high permeability ranging from 50 to $100 \times 10^{-10} \text{ m}^2$ (Domine et al., 2013) which facilitates the development of convection through the pore spaces. This enhances DH growth that further decreases the density and increases permeability. DH growth thus results in important positive feedback between the permeability and the magnitude of vapour transfers. In an advanced stage of metamorphism, a well-developed DH layer can feature permeability as high as $650 \times 10^{-10} \text{ m}^2$ (Domine et al., 2013).

A key question is whether convection processes can be active in the polar desert snowpack, where frequent strong wind episodes often remobilize the snow and compact it into hard wind slabs of very high density, typically ranging from 350 to 500 kg m^{-3} (Domine et al., 2002; 2012 and 2018b). Investigations in the Arctic tundra snowpack observed that hard depth hoar (“indurated”) can form in some basal wind slabs (Derksen et al., 2009; Domine et al., 2012) subjected to elevated temperature gradients in the fall. This suggests that layers of moderate permeability may be subject to convection. Other layers in Arctic snow never transform into DH and alternations between DH and wind slabs have been observed in Arctic snowpacks (Domine et al., 2002; Sturm and Benson, 2004), suggesting that there may be a permeability threshold below which convection cannot be initiated (Domine et al., 2018a). At present, the value of this threshold, which probably depends on the value of the temperature gradient, has not been established.

In light of these previous studies, we will interpret our observations for the polar desert snow within the simplified framework that DH formation requires a temperature gradient in the snowpack higher than 20 K m^{-1} and a sufficiently high snow permeability to allow convection.

5.8.2. Characteristics of the snow season 2018/19

At WHI, fall 2018 was characterized by a snowpack that formed very early in the season and remained stable throughout winter 2018/19. The early massive snowfall on 24 August brought ~80% of the late-winter snow height recorded at the SILA site ([Figure 65](#)). This snowfall occurred under mild conditions producing wet and sticky snow, perhaps even with some melting, which was less affected by the strong winds. Thus, the redistribution processes were reduced, as demonstrated by the homogenous snowpack and its little-reworked surface ([Figure 65f](#); [Figure S4-4b](#)), and the snow likely accumulated with a density lower than $300\text{--}350 \text{ kg m}^{-3}$ since wind-induced sintering and compaction were limited. If we assume a snow SSA of at least $30 \text{ m}^2 \text{ kg}^{-1}$ for recent wet snow (Legagneux et al., 2002), the permeability of this snow was then likely higher than $40\text{--}70 \times 10^{-10} \text{ m}^2$ according to equation (5.3). The three weeks following snow onset were characterized by calm weather with few cold spells which allowed the snowpack to sinter and thus stabilize. For all these reasons, the first snow of the season 2018/19 resembled more alpine snow than polar snow (Domine et al., 2008). The snow dynamics in fall 2018 was therefore completely different from that observed in fall 2015 during which the snowpack remained discontinuous until November due to extreme wind conditions (Domine et al., 2018a). In RB, the snow onset in fall 2018 occurred two weeks later than in WHI, but the snowpack also quickly became stable at the snow gauge site, reaching 90% of its late winter height at the end of September ([Figure S4-5a](#)).

The onset of a stable snowpack is known to be a critical factor for the soil surface thermal regime (Ling and Zhang, 2003), and hence for the temperature gradient in the snowpack. An early snow onset, as it occurred at WHI and RB in the fall of 2018, prevents rapid cooling of the soil because it is partially disconnected from atmospheric conditions (Davesne et al., 2017; Ishikawa, 2003). However, data from WHI show that the soil surface temperature cooled quite rapidly despite the presence of the snowpack ([Figure 65a,c](#); [Figure S4-3a,b](#)). We explain this by rapid upward freezing and cooling of the shallow active layer by the low temperature of the permafrost ($\sim -13^\circ\text{C}$) (Woo et al., 2004). Paquette et al. (2020a) suggested such a process to explain the ground ice aggradation in the active layer during freeze-back at RB. This phenomenon, combined with the fact that the air temperature remained around 0°C until early September, resulted in a small temperature gradient in the snowpack for over a week. Subsequently, cold spells produced temperature gradients quite variable in magnitude, but which exceeded 20 K m^{-1} for 9 days in September, 8 days in October and 25 days in November, and even reached 82 K m^{-1} on 2 December

(**Figure 65d**; [Figure S4-3c](#)). These periods with elevated gradients combined with the high permeability of the snow were conducive to the development of strong upward vapour fluxes by diffusion and convection mechanisms. It thus resulted in the transformation of at least part of the snowpack established on August 24 into a continuous DH layer. Elevated temperature gradients persisted until 23 April which was the last occurrence of gradient $>20 \text{ K m}^{-1}$, so that DH could keep developing in the basal layer during most of the snow season. Furthermore, the temperature gradient shown in **Figure 66d** and [Figure S4-3c](#) is the average gradient in the whole snowpack. Given that the thermal conductivity of the lower layer, made of DH, is in general lower than in layers above, the gradient was in fact greater in this lower layer, further favouring DH development there.

The presence of a DH layer in all snowpits dug in spring 2019, both at WHI and RB, indicate that favourable conditions for DH development as observed at the SILA station were widespread and allowed DH formation everywhere. However, some spatial variabilities in the height and physical properties of DH were observed (**Figure 61** and **Figure 63**).

5.8.3. Small-scale variability of DH

A comparison of the stratigraphy and snow properties between humid and dry areas in the polar desert of WHI and RB revealed noteworthy differences in the thermo-physical properties and thickness of DH layers. The greatest difference is in DH density and visual grain size (**Figure 63** and **Figure 64**). Both these variables are of particular interest because they are indicative of the history of snow metamorphism throughout the winter. Our measurements demonstrated that humid sites exhibited significantly lower DH density values than dry sites both at WHI and RB. At WHI, the thermal conductivity measurements also tended to be lower in humid sites than in dry sites. This result was expected considering the strong dependency of thermal conductivity on snow density (Domine et al., 2011; Sturm et al., 1997). The SSA, in contrast, exhibited similar values between both environments, showing that it was not affected by variables such as soil moisture. This is consistent with the finding of Domine et al. (2016b) and Taillandier et al. (2007) who observed that the SSA of DH typically stops decreasing when it reaches about $10 \text{ m}^2 \text{ kg}^{-1}$, and is uncorrelated to visual grain size, as SSA does not decrease when DH crystals keep growing.

The lower density and larger visual grain size found in humid zones is a consequence of the thermodynamic effects of the soil moisture (details in the following [section 5.8.4.](#)) and

subsequent positive feedback mechanisms in which kinetic metamorphism is enhanced over humid zones. Indeed, the formation of DH leads to a decrease in density and thermal conductivity, thereby increasing the insulation effect of the snow and the temperature gradient through it (Zhang et al., 1996). This triggers greater water vapour fluxes by diffusion and hence greater mass transfer from the basal to the top layers. Furthermore, the DH layer has a greater permeability that further enhances the vapour flux by convection and amplifies the feedback, greatly favouring DH development in humid zones. The snowpack in humid zones and the one in dry areas therefore have a different history of metamorphism, initially determined in part by soil moisture. At the scale of the snow season, this leads to significant small-scale variability in the snow properties, which reflects the mosaic of microenvironments that partitions the polar desert landscape (Woo and Young, 2003).

5.8.4. Factors controlling DH spatial variability in 2018/19

The spatial variability in DH height and its physical properties in a polar desert context can be attributed to two main variables: microtopography and soil moisture.

5.8.4.1. Effect of the microtopography

In polar deserts, the microtopography is induced by the complex assemblage of landforms, such as solifluction lobes, patterned ground, raised beach ridges, and nivation hollows (**Figure 60**; Paquette et al., 2020a; Verpaelst et al., 2017; Vincent et al., 2011b; Woo and Young, 2003; [Chap. 4](#)). The snow redistribution by the wind is in part a function of the surface roughness created by the periglacial microtopography. The spatial pattern of the first snow accumulation at the beginning of the season is particularly important since it will later constitute the basal layers of the snowpack that may transform into DH. In typical years, in the polar desert where snowdrift and wind erosion events are frequent, the areas sheltered from the wind (e.g. depression, leeward side of obstacles) are logically those where the snowpack builds up more quickly in the early season and where the snow is deepest and has the lowest density and highest permeability. Consequently, these areas are most likely to form a thick layer of well-developed DH. Inversely, on topographic highs, the snowpack remained thin and discontinuous, and the snow has a shorter residence time (**Figure 60**) (Sturm and Benson, 2004). DH is therefore less likely to develop there (**Figure 62**). The fall of 2018 was however atypical because the homogenous and stable snowpack that formed on 24 August 2018 (**Figure 66f** and [Figure S4-4b](#)) allowed the development of a continuous layer of DH

which was less influence by the microtopography. Although the observations from the trench WH-T show a certain tendency for the DH layer to be thinner over ridges, the effect of microtopography was not detectable in the relationship between the end-of-season snow height and the DH thickness in the snowpits ([Figure S4-6](#)). This strengthens our suggestion that microtopography had a minimal effect on DH development in fall 2018 because conditions were more alpine-like (i.e. thick snow at a temperature close to the melting point) than polar desert-like. Later in the snow season, however, multiple episodes of snowdrift and erosion redistributed subsequent snowfalls, explaining the high spatial heterogeneity of the late-winter snowpack (**Figure 60**). **Figure 60a** therefore may be a representative example of the interaction between wind, microtopography and snow height under “normal” polar desert conditions with a strong wind effect, despite the atypical fall conditions. This clear relationship between the microtopography and snow height is well illustrated by **Figure 60e**. During most years, this correlation between topography and snow height is visible in fall, and an example of normal snow conditions for the polar desert is shown in [Figure S4-4e](#) taken on 2 October 2017, where eroded highs and lows with accumulation are clearly visible.

5.8.4.2. Effects of soil moisture and temperature

In the polar desert, soil moisture mainly depends on the geomorphological context which controls the spatial distribution of water sources on slopes, as well as how this water is transferred and where it accumulates in the system of catchments (Langford et al., 2015; Paquette et al., 2020a; Woo and Young, 2003). Dry, well-drained soils largely dominate in the polar desert, but locally, humid zones can develop, giving rise to great heterogeneity in moisture conditions at the landscape scale (e.g. Site 1, [Figure 57](#)). At WHI as at RB, most humid zones lie downslope from semi-permanent and perennial ice patches, whose melting ensures a steady supply of meltwater to the hydrological system throughout most of the summer (Woo and Young, 2003; [Chap. 3](#) and [Chap. 4](#)). Multiple years of hydrological studies at WHI have revealed a high degree of consistency in the spatial and temporal dynamics of surface and subsurface water transfers and annual humid zone development, although minor variations may occur from year to year due to micrometeorological conditions (Paquette et al., 2018). In the context of climate change, however, the decline of perennial ice patches threatens the sustainability of humid soils in the polar desert. At RB, many perennial ice patches have already became semi-permanent over the past decade producing greater interannual variability in soil moisture (Woo and Young, 2014; [Chap. 3](#)). With the projected

continuation atmospheric warming, we can expect a rapid transition from ice patches to seasonal snow patches across the polar desert, resulting in a decrease in soil drying before the end of summer.

The soil moisture can influence DH formation in different ways. First, the water content of a soil modulates the rapidity at which it will freeze and cool down in the fall. Given the latent heat of freezing of water, humid areas require more time to freeze-back than drier areas. As shown in **Figure 66**, the longer zero curtain period in the humid sites implied that soil cooling below 0°C was delayed, which ensured that the temperature gradient between the soil at 0°C and the cold atmosphere was greater than at dry sites where the soil rapidly dropped below 0°C. Also, the zero curtain effect maintains the basal layers of the snowpack at temperatures close to 0°C in humid zones, which means a higher vapour concentration in the pore spaces and hence higher vapour fluxes. This confirms the hypothesis proposed by Domine et al. (2018a) concerning the effect of soil moisture on vapour gradients and DH growth in the polar desert snowpack. Secondly, the temperature gradient between the soil and the basal layers of the snowpack can also lead to mass transfer of water vapour from the soil to the snow. This process is difficult to quantify but some studies, such as Domine et al. (2016b); Smith and Burn (1987), Sturm and Benson (1997) and Woo (1982) have demonstrated that the upward vapour fluxes by both diffusion and convection from humid soil enhance the development of DH at the bottom of the Arctic snowpack. However, Woo (1982) suggests that this process is likely less effective in polar desert environments than in tundra areas because of the low soil temperature.

In summary, the unusually windless conditions at the beginning of the 2018/19 snow season produced a snow layer of fairly constant thickness over the whole landscape, making that year an ideal one to capture the role of soil moisture without being distorted by the effect of microtopography. We were thus able to clearly identify the soil moisture effects on DH height, density and grain size. Under normal conditions, wind erodes topographic highs (usually drier soil) and accumulates snow in topographic lows (usually more humid soil), so that microtopography has an additional effect on the DH development and height. This would make observations dependent on two factors, moisture and snow height, making the role of moisture more difficult to discern.

5.8.5. The inter-annual variability in the DH development

Comparison of the 2018/19 snow season at WH with the 2015/16 and 2016/17 seasons presented in Domine et al. (2018a) highlights the strong inter-annual variability in the development of DH in polar desert. The snow conditions in 2015/16 were drastically different than in 2018/19 because DH was near-absent at most sites, including humid sites. Less information is available for 2016/17 but Domine et al. (2018a) deduced from the monitoring of snow thermal conductivity, temperature and meteorological variables that a well-developed DH layer was present at the SILA site, meaning that snow conditions were closer to those of 2018/19.

The detailed analysis of the meteorological dataset recorded by the SILA station allows identifying the wind conditions as the main variable that strongly varied from one year to another. The wind frequency with speed above 6 m s^{-1} – a reasonable threshold for snowdrift (Sturm et al., 2001; Royer et al., 2021) – during the 60 days after snow onset (**Figure 67a**) demonstrated the largest differences between the three years concern the strongest winds ($>10 \text{ m s}^{-1}$).

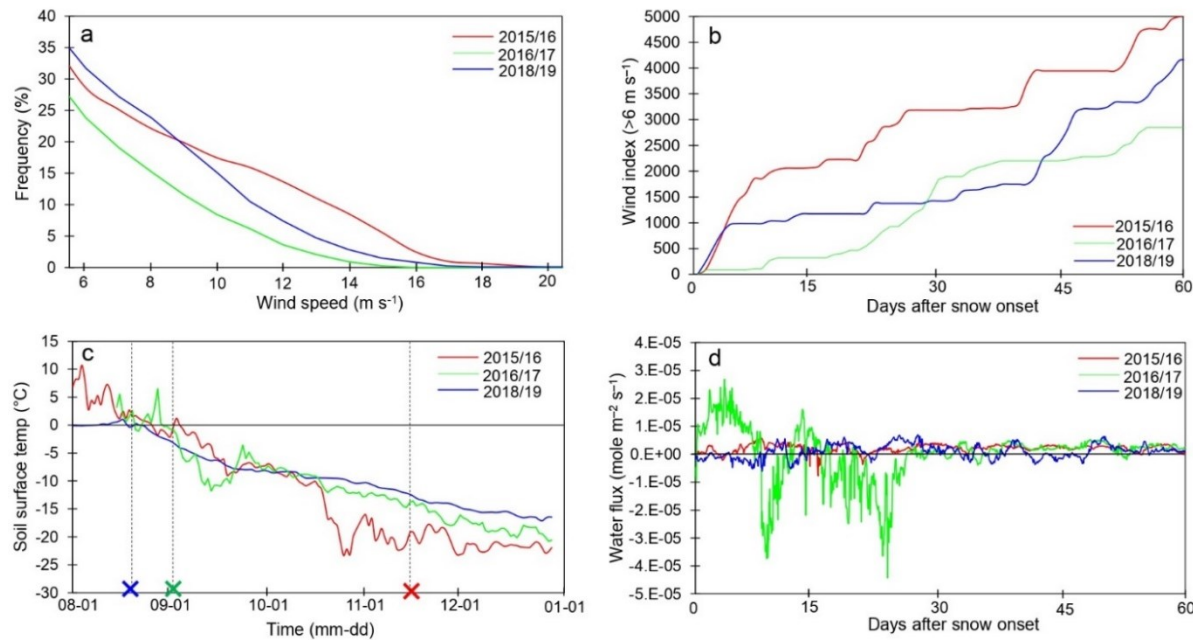


Figure 67. Comparison between thermal and wind conditions at the SILA station between falls 2015, 2016- and 2018, a) Wind speed distribution of hourly maximum above 6 m s^{-1} for 60 days after the snow onset; b) Wind index for wind speed over 6 m s^{-1} for the 60 days following the snow onset; c) Soil surface temperature for the August to December period, the crosses marked the snow onset date for each date; d) Diffusive water vapour fluxes through the snowpack calculated from equation (5.2) for the 60 days following the snow onset.

The calculation of the wind index (*WI*) for the winds above 6 m s^{-1} (the sum of speed values of hourly winds $>6 \text{ m s}^{-1}$; Sturm et al., 2001) clearly shows that the windier conditions occurred in 2015/16, especially within the 30 days after the snow onset since the *WI* (3100) was twice as high as in 2016/17 and 2018/19 (1500) (**Figure 67b**). The frequent strong wind events associated with few calm periods ($<6 \text{ m s}^{-1}$), such as in 2015/16, generated two combined effects.

First, it resulted in the development of very hard dense wind slabs with high thermal conductivity and low permeability. Dense wind slabs formed under conditions as windy as in 2015 produces snow with a density typically exceeding 400 kg m^{-3} and have SSAs of at least $30 \text{ m}^2 \text{ kg}^{-1}$ (Domine et al., 2012 and 2018b). This gives a permeability of $\sim 20 \times 10^{-10} \text{ m}^2$ according to equation (5.3), suggesting that the snow permeability in fall 2015 likely was too low to allow convection (Domine et al., 2013). On the other hand, periods of calm weather in falls of 2016 and 2018 resulted in snow with lower density and hence higher permeability.

Secondly, the multiple episodes of erosion/accumulation under wind action led to a regular renewal of the shallow snowpack, including basal layers. During severe windstorms, the snow was swept away from most of the surface ([Figure S4-4e](#)). Due to this short residence time, the snow had no time to undergo advanced metamorphism. Furthermore, when the first half of the snow seasons were marked by recurrent erosion events, the date of onset of a continuous snowpack occurred very late. In fall 2015, the snow onset occurred more than 70 days later than in fall 2016 and 80 days later than in fall 2018 (Domine et al., 2018a). Consequently, the zero curtain effect that marked the freeze-back period in Site 5 did not affect the snowpack and the soil surface was already around -20°C in mid- November 2015 in both dry (SILA site) and humid zones (Site 5) when the snow started to accumulate ([Figure 67c](#) and [Figure S4-7a](#)). Such low soil temperature limited the temperature gradient in the snowpack. Furthermore, the snow accumulated under an air temperature between -20 and -30°C ([Figure S4-7a](#)). Considering the exponential increase of water vapour pressure with temperature, the vapour pressure at -30°C was only $\sim 50 \text{ Pa}$ in the pore space, which was 8 times lower than at -5°C ($\sim 400 \text{ Pa}$). Consequently, the diffusive and convective vapour fluxes in the snowpack were low (**Figure 67d**) giving rise to additional unfavourable conditions for efficient kinetic metamorphism. In fall 2016, in contrast, the earlier snow onset (5 September) allowed the soil surface and the snow to be warmer, being close to 0°C at Site 5 and -5°C at SILA. It resulted in stronger vapour fluxes within 10 days after snow onset (**Figure 67d** and [Figure S4-7b](#)) that brought particularly favourable conditions for rapid DH growth. In fall 2018,

surprisingly, diffusive vapour fluxes remained weak at the SILA site, being of the same order of magnitude as in 2015 (**Figure 67d**), despite an earlier snow onset and much warmer soil and snow temperatures in the weeks following it. We attribute this to a thicker snowpack and to the fact that snow onset occurred early in fall 2018, limited the temperature difference between the soil surface and the air. In Site 5, however, the long zero curtain period after the snow onset probably favoured a stronger temperature gradient during the first half of September ([Figure S4-7c](#)). The fact that DH was nevertheless found in dry areas such as at SILA in 2019 suggests that convection played a key role in the mechanism of water vapour transport due to the low-density and coarse-grained nature of the snow that accumulated in early snow season 2018/19 which ensured a high permeability of the snowpack.

Due to the close link between wind conditions and the degree of metamorphism in a polar desert environment, we would expect a strong interannual variability in the presence of DH that would be correlated to the yearly variations in wind climatology. The wind statistics for the first half of the winters (Sept/Oct/Nov) over the period 2007–2019 at WHI demonstrate that wind conditions have been highly variable from one year to the next with a regular alternation between windy and calmer falls giving a sawtooth pattern to the curve. As shown by [Figure S4-8](#), WI for speeds above 6 m s^{-1} for Sep/Oct/Nov period varied from 4500 to 8500 in 2012 and 2015 respectively. This variability is similar for extreme winds above 10 m s^{-1} . These data also suggest a biannual pattern in wind conditions in which windy years alternated with calmer years. We preliminarily propose, based on these 11 years of meteorological data, that the snowpack in the polar desert is discontinuous, thin and with little or no DH every two years and that, conversely, it is more characteristic of the Arctic tundra snowpack (Royer et al., 2021) in the other years. These results suggest that potential changes in wind regimes resulting from climate change could thus have a major impact on future snow conditions in the polar desert.

5.9. Conclusion

Our study provides new insights into DH development and its spatio-temporal variability at Ward Hunt Island, the main site, and Resolute Bay, the secondary site, which are both representative of polar desert environments in terms of landscape and climate conditions. From our results, we conclude that wind is the most critical factor in the development of DH in the polar desert. When fall periods were windy and cold (e.g. 2015), the conditions prevented DH

development whereas it was favored when winds were calmer and air temperature milder (e.g. 2018). Strong winds lead to alternating episodes of erosion and accumulation that form dense slabs of high density and low permeability. This snow prevents vapour transfers by convection and vapour diffusion is limited by the low temperature gradients in the snowpack, therefore reducing the possibility of transforming windslabs into DH. Calm weather during early snowfalls and in the weeks that follow or/and snow that falls under mild temperature allowed snow to accumulate and remain on the ground with a moderate density and high permeability, which favored convection processes, intense snow metamorphism and growth of well-developed DH.

Soil moisture is a second-order environmental factor that modulates snow metamorphism and DH dynamics. We demonstrated that DH development is stronger in zones with humid soil than in dryer, better drained, zones and that DH thickness and properties change according to the periglacial landscape microtopography. The difference between humid and dry zones in the degree of metamorphism is initially induced by soil moisture which delays freeze-back of the active layer in humid zones. It therefore promotes strong thermal gradients for longer periods, leading to greater water vapour fluxes, and hence greater mass transfer from the basal to the top layers. Metamorphism in humid areas is subsequently enhanced by the structure of the snow itself (lower density, lower thermal conductivity, higher permeability) which brings an additional warming effect to the soil which positively feeds back on DH formation. This close link between soil moisture and DH formation leads to significant small-scale variability in snow properties, which reflects the mosaic of environments that structure the landscape of the polar desert. In polar desert conditions, frequent snowdrift and erosion episodes redistribute the early snowpack according to microtopography and hence bring an additional factor of small-scale variation in DH thickness.

This study also highlighted that the conclusion drawn from our main site appears to apply as well to our secondary site, located over 1000 km away and over 8° of latitude to the south. We can therefore anticipate that our findings are transferable to other regions of the high Arctic polar desert that exhibit similar patchy humid zones whose distribution is tightly linked to the presence of long-lying and perennial snow/ice patches and where the wind is a key element of the climate. In light of this study, we propose that the high interannual variability and the high spatial variability in DH formation is one of the most distinctive features of the polar desert snowpack from that on Arctic tundra where DH is usually ubiquitous. Given the great importance of the presence and amounts of DH for snowpack properties, its formation in the polar desert deserves further research

in additional locations to confirm the transferability of our findings to other polar desert sites and to better understand and model the interactions between the seasonal snowpack on the ground thermal regime and ecosystem functioning, as well as the future evolution of polar desert snow in response to climate change.

5.10. Acknowledgments

This research was conducted with the financial support of the Natural Sciences and Engineering Research Council of Canada (NSERC), including the Discovery Frontiers project Arctic Development and Adaptation to Permafrost in Transition (ADAPT); the Networks of Centres of Excellence program ArcticNet; the Canada Research Chair program; the Northern Scientific Training Program; the Canadian Foundation for Innovation: Canadian Northern Studies Trust; Centre d'études Nordiques (CEN); and Fond de Recherche du Québec- Nature et Technologie (FRQNT). FD was supported in part by the French Polar Institute (IPEV). Logistical support was provided by the Polar Continental Shelf Program (PCSP) which also granted us the use of their facility at RB. The authors thank Parks Canada and the communities of Resolute Bay (Qausuittuq) for permission to work in the different study sites. The authors would like to thank Karine Rioux for her field assistance and Denis Sarrazin (CEN) for the installation and maintenance of the SILA weather station. Finally, we are also grateful to the two anonymous reviewers and the editor for their insightful comments and advice on the manuscript.

5.11. Supplementary material S4

Table S4-1. Detailed information on snowpits dug in 2019 at Ward Hunt Island and Resolute Bay

Site	Snowpit	Date	Substrate
WHI_1	#1	2019-06-04	dry; gravels; no vegetation
WHI_1	#2	2019-06-10	humid; organic crust; vegetation
WHI_1	#3	2019-06-11	humid; organic crust; vegetation
WHI_1	#4	2019-06-11	dry; gravels; no vegetation
WHI_1	#5	2019-06-04	dry; gravels; no vegetation
WHI_1	#6	2019-06-10	dry; gravels; no vegetation
WHI_1	#7	2019-06-10	humid; organic crust; vegetation
WHI_1	#8	2019-06-11	humid; organic crust; vegetation
WHI_2	#1	2019-06-05	dry; gravels; sparse vegetation
WHI_3	#1	2019-06-05	dry; gravels; sparse vegetation
WHI_3	#2	2019-06-05	dry; gravels; sparse vegetation
WHI_4	#1	2019-06-08	dry; gravels; sparse vegetation
WHI_4	#2	2019-06-08	dry; gravels; sparse vegetation
WHI_5	#1	2019-06-07	humid; organic crust; vegetation
WHI_6	#1	2019-06-08	humid; organic crust; vegetation
WHI_7	#1	2019-06-09	dry; gravels; no vegetation
WHI_8	#1	2019-06-12	dry; gravels; no vegetation
WHI_9	#1	2019-06-12	humid; organic crust; vegetation
RB_1	#1	2019-05-28	dry; gravel; no vegetation
RB_1	#2	2019-05-28	dry; gravel; no vegetation
RB_2	#1	2019-05-28	humid; thin moss layer
RB_3	#1	2019-05-31	dry; gravel and fine mix; no vegetation
RB_4	#1	2019-05-28	dry; gravel; sparse vegetation
RB_5	#1	2019-05-28	humid; thin moss layer
RB_6	#1	2019-05-31	humid; grass and moss
RB_6	#2	2019-05-31	humid; grass and moss
RB_7	#1	2019-05-29	dry; gravel; no vegetation
RB_8	#1	2019-05-29	humid; grass and moss
RB_8	#2	2019-05-29	humid; grass and moss
RB_8	#3	2019-05-29	humid; grass and moss
RB_8	#4	2019-05-29	humid; grass and moss
RB_9	#1	2019-05-30	dry; gravel; sparse vegetation
RB_9	#2	2019-05-30	dry; gravel; sparse vegetation
RB_10	#1	2019-05-30	dry; gravel; sparse vegetation

Table S4-2. Summary table of the end-of-winter snow heights (SH, cm) measured in early June 2019 and of thermal conditions in the early snow season (30 days after the snow onset) between dry and humid monitoring sites at Ward Hunt Island. The thermal conditions include the duration of zero-curtain period (ZC period), the thermal offset between the air and the soil near-surface temperatures, and the calculated temperature gradient into the snowpack.

	Sensor ID	SH (cm)	ZC period (d)	Offset (°C)	Grad T (K m ⁻¹)
Humid sites	LT3	25	27	6.5	21.1
	LT5	22	29	6.4	20.6
	LT10	31	32	6.6	21.4
	LT12	30	27	6.4	21.2
	Site 5 ¹	46	20	6.7	22.4
	AVG	31	27	6.5	21.3
Dry sites	STD	10	5	0.1	0.7
	LT15	35	9	3.2	7.7
	LT9	20	3	2.5	6.8
	LT4	17	11	2.1	1.1
	LT11	18	8	1.1	10.4
	SILA	35	8	2.1	6.8
AVG	25	8	2.2	6.6	
	STD	9	3	0.8	3.4

¹ for the WT site, the average between the water track and inter-track was used.

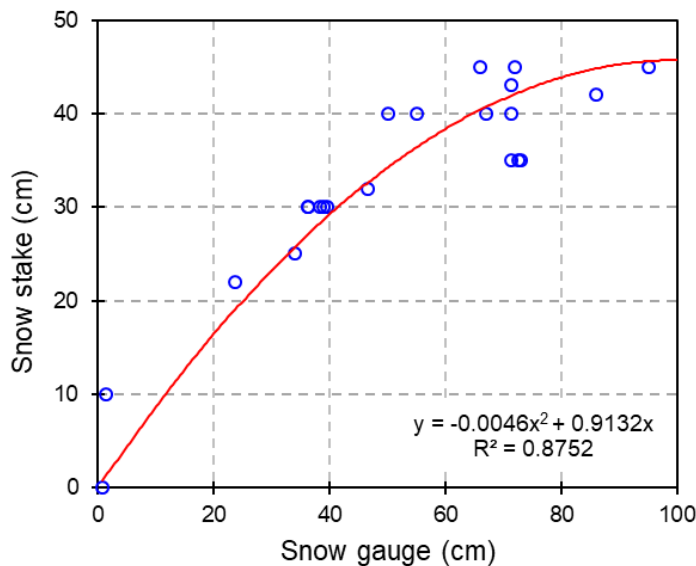


Figure. S4-1. Comparison between the snow height measurements recorded by the snow gauge SR50 at the SILA station and the daily snow height read on the snow stake installed in the field of view of the automatic camera (see Fig. 3). The equation was used to correct the snow gauge measurements which overestimated the snow height due to its position in a slight depression making it unrepresentative of typical snow height in the polar desert.

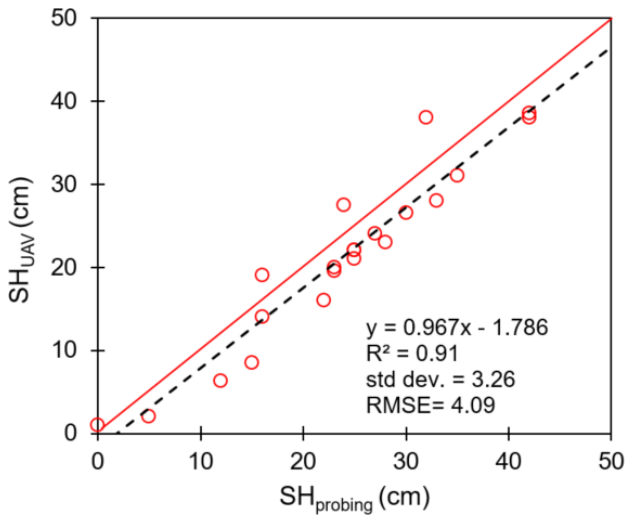


Figure S4-2. Scatter plot of the snow heights derived by UAV surveys (SH_{UAV}) versus the manual measurements ($SH_{probing}$) made over Site 1. The dashed black line is the linear regression line and the red line is the 1:1 line. Std dev. = Standard deviation; RMSE=Root mean square error.

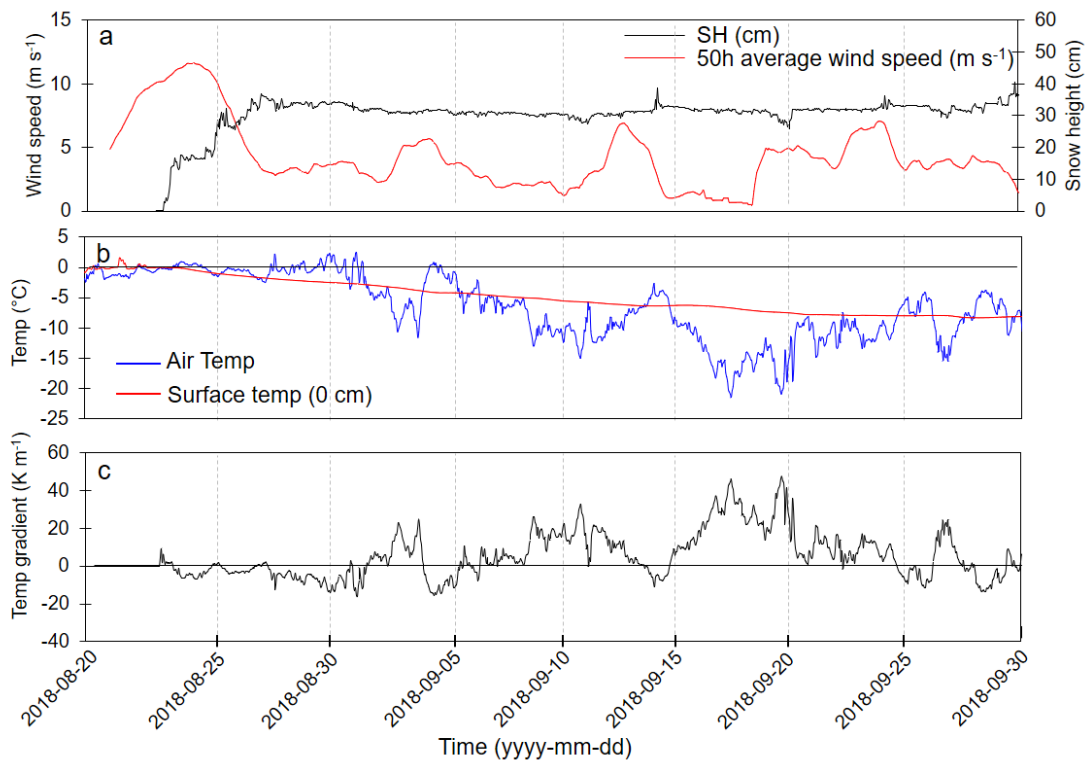


Figure S3-3. Environmental variables monitored at the SILA station at Ward Hunt Island during the cold season 2018/19 between August 20 and September 30. a) Snow height measurements by the snow gauge and normalized with the readings of the snow stakes visible on the time-lapse photos and hourly maximum wind speed averaged over 50 h; b) Hourly temperature records at the soil surface (0 cm) and of the air; c) Hourly temperature gradient calculated from equation (5.1).

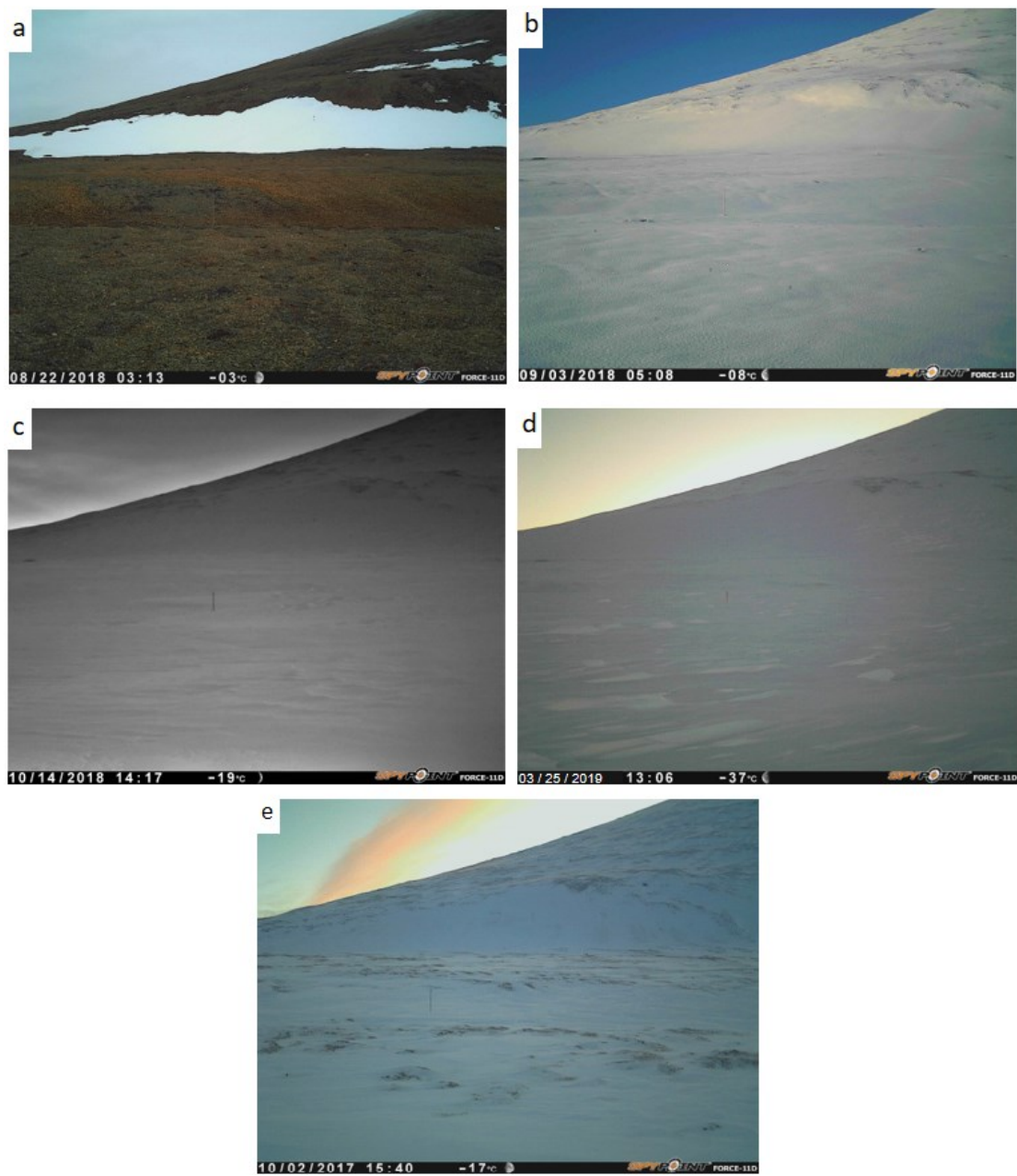


Figure S4-4. Photograph of the ice patch IP1 and its downslope margin (Site 1) taken on 22 August (a), the day before the first snowstorms, on 3 September (b) showing the continuous snow cover, on 14 October (c), on 25 March 2019 (d) and on 2 October 2017 (e).

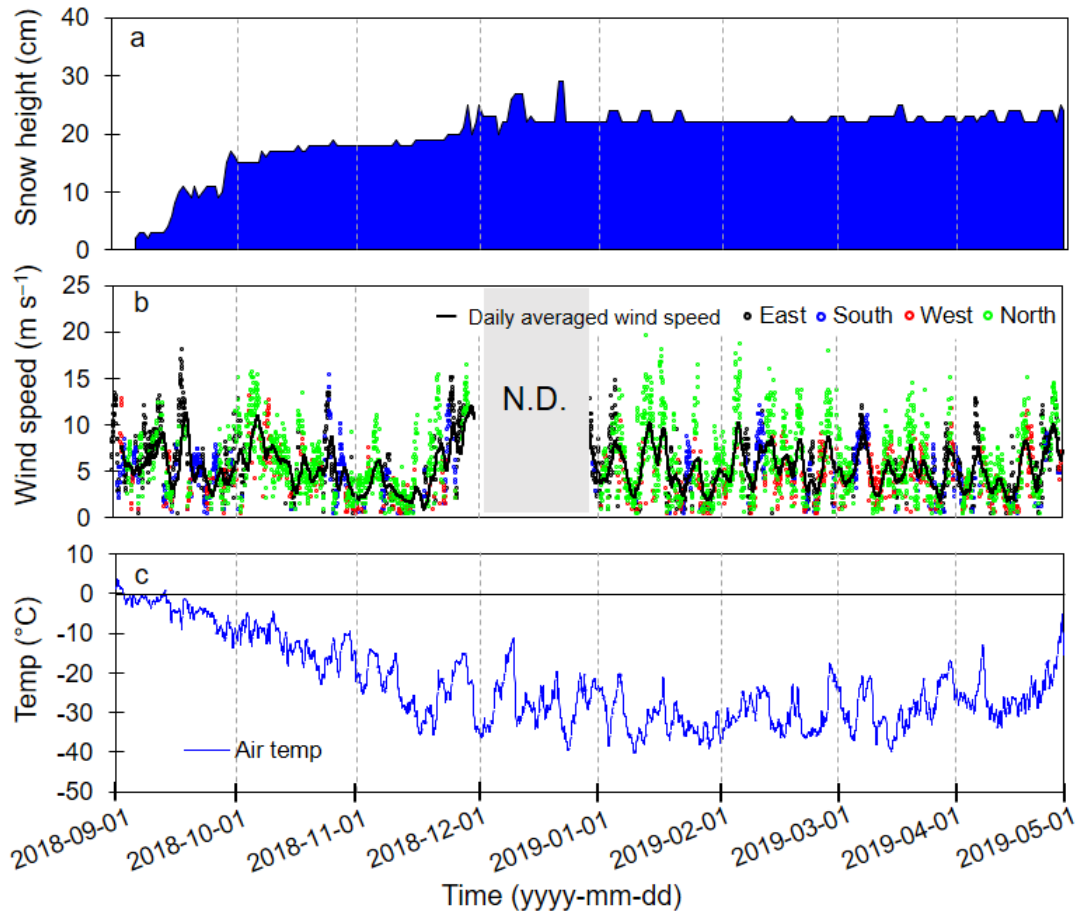


Figure S4-5. Environmental monitoring at RB during the cold season 2018/19. a) Snow height measured at the snow gauge; b) Hourly maximum wind speed according to their direction (North/East/South/West); c) Hourly air temperature (Environment Canada, 2021).

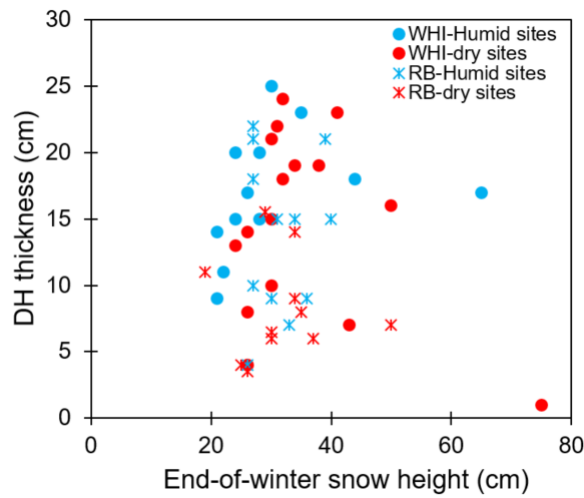


Figure S4-6. Relationship between the end-of-winter snow height and the DH thickness measured at snowpits dug at WHI and RB.

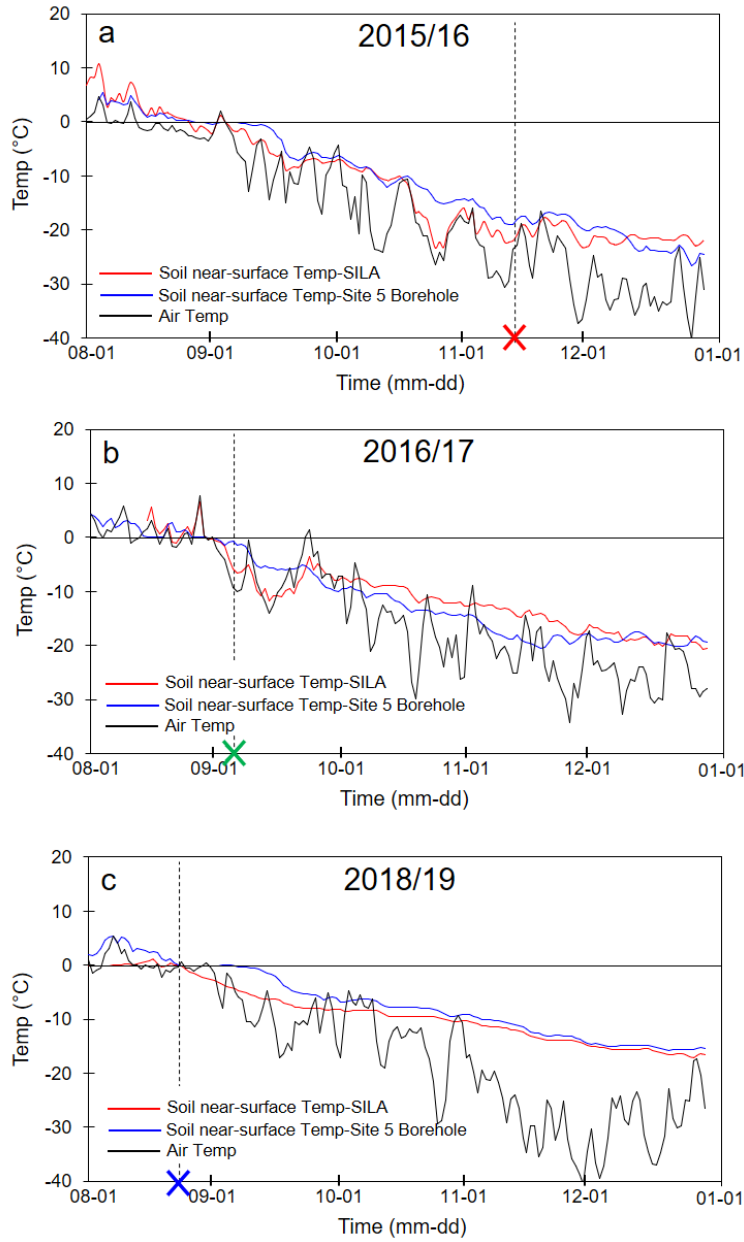


Figure S4-7. Hourly evolution of the near-surface soil temperature at SILA and at the borehole of Site 5 along with the air temperature also recorded at SILA for the first half of the snow season 2015/16 (a), 2016/17 (b) and 2018/19 (c). The crosses marked the snow onset date for each year.

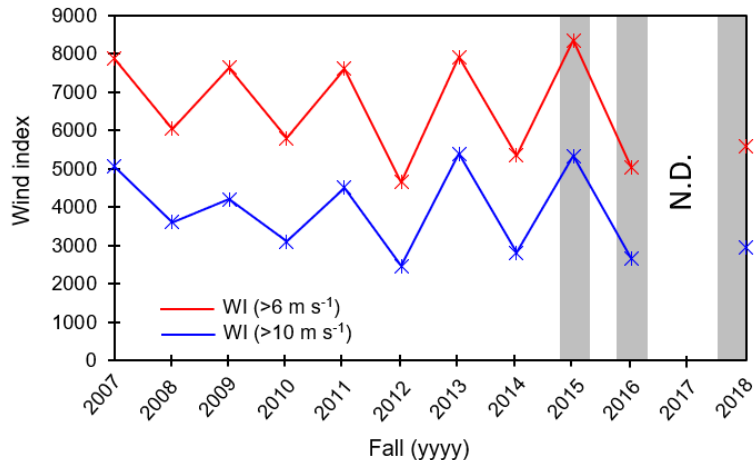


Figure S4-8. Early snow season (Sept/Oct/Nov) wind indices for wind speed over 6 and 10 m s⁻¹ (i.e. sum of hourly wind speed values $>6\text{ m s}^{-1}$ and $>10\text{ m s}^{-1}$) calculated from fall 2007 to fall 2018. The shaded bars indicate falls 2015, 2016 and 2018 detailed in our study. No data in 2017.

Chapitre 6 – Conclusion générale et perspectives

Cette thèse s'est intéressée aux plaques de glace permanentes qui ont été abordées comme un élément à part entière de la cryosphère terrestre. Du fait de leur caractéristique et de leur régime, les plaques de glace sont à mi-chemin entre le domaine périglaciaire et le domaine glaciaire, ce qui leur a valu de tomber dans une « zone floue » en marge des centres d'intérêt traditionnels de ces disciplines. Par conséquent, les études de terrain sur les plaques de glace sont rares, limitant la compréhension non seulement de leurs caractéristiques intrinsèques et de leur évolution temporelle, mais aussi de leurs interactions et effets sur leur environnement physique proximal. Ce manque de données et de connaissances a maintenu des lacunes importantes dans la compréhension de la dynamique du biogéosystème de désert polaire qui dépendent de manière critique des plaques de glace.

Cette recherche, réalisée sur l'île Ward Hunt (Nunavut), avait pour objectif principal de documenter et comprendre de la nature, l'origine et le fonctionnement des plaques de glace polaires ainsi que leurs effets sur le géosystème de désert polaire dans un contexte de changement climatique. Dans cette perspective, cette thèse a proposé une recherche multidisciplinaire sur les plaques de glace amenant à la réalisation d'études glaciologiques, nivologiques, hydrologiques et biogéomorphologiques. Cette recherche a intégré une dimension explicative et quantitative importante en mettant l'accent sur les liens et les interactions entre les plaques de glace et leur environnement. Elle a ainsi apporté à une compréhension holistique des plaques de glace polaires et a permis de poser un cadre empirique et conceptuel important pour développer de futures recherches sur le sujet, que ce soit en Arctique ou en Antarctique. Les nouvelles connaissances établies dans cette thèse contribuent à faire avancer la recherche scientifique sur les déserts polaires à un moment charnière où ces environnements sont en transition rapide en réponse au changement climatique.

6.1. Synthèse des résultats et avancées scientifiques

Ensemble, les quatre articles complémentaires présentés dans cette thèse contribuent à montrer que les plaques de glace sont des systèmes cryosphériques uniques du fait de leur composition et de leur fonctionnement et qu'elles jouent un rôle central dans le développement et

la dynamique des versants de désert polaire. Plus spécifiquement, les principaux résultats et avancées scientifiques sont synthétisés dans les quatre points suivants qui répondent aux objectifs de recherche ([Chap. 1](#)).

6.1.1. L'origine et les mécanismes de formation des plaques de glace ([Obj. 1](#))

L'analyse des propriétés physiques du manteau neigeux saisonnier et l'étude glaciologique du corps de glace permanent ([Chap. 2](#)) a fourni des informations importantes concernant la l'origine et le fonctionnement des plaques de glace polaires. Nos résultats ont permis d'identifier que les plaques de glace à l'île Ward Hunt appartiennent au système morphodynamique nival (Serrano et al., 2011; [Chap. 2](#)) et qu'elles sont fortement contrôlées par le contexte topoclimatique local. Sur la base de nos observations et interprétations, un modèle conceptuel de la formation des plaques de glace a été proposé pour la première fois. Ce modèle est valide pour les systèmes des plaques de glace dont la recharge est principalement assurée par des apports éoliens de neige, lesquels sont dominants dans les régions polaires. Nous avons identifié que le corps de glace permanent est principalement formé par l'aggradation saisonnière de glace surimposée qui est formée par le regel de l'eau de fonte percolant à travers la neige jusqu'à l'interface neige-glace ([Chap. 2](#)). Ce résultat confirme les observations préliminaires faites dans les régions polaires (Lewkowicz et Harry, 1991; Østrem, 1963). Le processus d'aggradation des plaques de glace est de ce point de vue similaire aux processus observés sur la plateforme de glace (*Ice shelf*) et le dôme de glace (*Ice Rise*) présents autour de l'île Ward Hunt (Jeffries et al. 1991). Nous avons montré que les propriétés et la croissance de cette glace surimposée sont étroitement liées aux conditions thermiques du manteau neigeux et du corps de glace ainsi qu'aux propriétés de la neige à partir de laquelle la glace se forme. Les plaques de glace représentent de ce fait un système au sein duquel le corps de glace et l'épaisse accumulation de neige saisonnière s'influencent mutuellement par des flux de chaleur et de matière. Dans les régions polaires, les températures très froides de la masse de glace en fin d'hiver assurent une croissance rapide de la glace surimposée. Le processus s'étend sur plusieurs semaines, souvent jusqu'à la mi-juillet et peut même éventuellement se prolonger jusqu'à la fin de l'été lors des années froides. Chaque année, ce sont donc plusieurs dizaines de centimètres de « nouvelle » glace qui se forment sur la surface de glace de l'été précédent. Par ailleurs, le vent fort produit une neige généralement fine en raison du frittage des cristaux pendant et après les précipitations. Les propriétés de cette neige ventée (*windslab*) prédisposent à la formation de glace surimposée à cristaux fins.

Nos observations ont en effet souligné qu'au sein d'un même système de plaque de glace, différents faciès de glace peuvent être présents, dont certains partagent certaines similitudes avec la glace de glacier (c.-à-d. gros cristaux, fractures, densité élevée). Même en l'absence de contrainte interne, la glace des plaques peut subir des processus de recristallisation dynamiques qui se traduisent par une croissance des cristaux de glace. Ces processus peuvent être localisés et rapides (c.-à-d. les cycles de gel et de dégel) ou lents et généralisés (c.-à-d. la croissance cinétique). Dans le second cas, la taille des cristaux est proportionnelle à l'âge de la glace (Montagnat et al., 2009). La teneur en sédiments de la glace est également très variable et dépend étroitement des processus thermodynamiques qui contrôlent la formation et le fonctionnement d'une plaque de glace. Les couches de glace ayant la plus forte teneur en sédiments sont généralement associées à des apports alluviaux et intégrés à la glace surimposée. Elles peuvent également résulter de la concentration de sédiments nivéo-éoliens sur une surface d'ablation qui est ensuite enfouie par de la nouvelle glace.

6.1.2. Les facteurs de contrôle spatio-temporels du bilan de masse des plaques de glace ([Obj. 2](#))

À l'île Ward Hunt, la plupart des plaques de glace est présente en dessous de la limite d'équilibre des glaciers (ELA) qui se situe entre 300-400 m d'altitude le long de la côte nord d'Ellesmere (White et Copland, 2018). De ce fait, ces masses de glace ne sont pas en équilibre avec les conditions climatiques régionales et ne doivent leur existence qu'aux conditions topoclimatiques locales qui contrôlent leur évolution spatio-temporelle.

L'existence des plaques de glace est liée à des accumulations préférentielles de neige qui sont formées par d'importants apports nivéo-éoliens ([Chap. 2](#) et [3](#)). Le remplissage des systèmes de plaque de glace est régi par un mécanisme de rétroaction entre le vent, la topographie et la taille de plaque de glace, selon lequel l'accumulation de neige en hiver est inversement proportionnelle au volume de la plaque de glace à la fin de la saison d'ablation précédente ([Chap. 3](#)) (Glazirin et al, 2014). Le contexte topographique et le vent conditionnent le profil d'équilibre qui détermine le volume maximal de neige que peut accueillir une niche topographique. La direction du vent étant similaire d'une année à l'autre, seule l'intensité des vents d'hiver est un facteur de variation interannuelle du profil. Les hivers dominés par des épisodes de vents forts connaissent généralement une accumulation de neige maximale moindre que les hivers marqués par des vents plus modérés ([Chap. 3](#)).

Durant la saison chaude, l'ablation des plaques de glace est contrôlée par le bilan d'énergie de surface. Nos résultats ont montré que l'ablation estivale est fortement modulée par la fréquence des vents, qui exacerbent l'apport de chaleur par les flux turbulents, et par la fréquence du brouillard, qui réduit l'apport de chaleur par le rayonnement solaire et la chaleur sensible ([Chap. 3](#)). À l'île Ward Hunt, la fréquence élevée des conditions de brouillard est l'élément clé dans la préservation de petites plaques de glace à basse altitude en été. La variabilité interannuelle de l'ablation dépend donc principalement du contexte synoptique (température, vent, brouillard) et, par conséquent, de la position des systèmes de basse pression sur l'Arctique. Puisque les conditions synoptiques sont contrôlées par les patrons de circulation atmosphérique, l'intensité de l'ablation des plaques de glace suit une cyclicité à court terme entre des phases de forte ablation et des phases de faible ablation ([Chap. 3](#)) en réponse notamment aux oscillations nord-atlantique (NAO) et arctique (AO) (Prowse et al., 2011). En raison de leur petite taille, les plaques de glace sont également influencées des phénomènes très localisés liés à l'advection de chaleur depuis les terrains environnants (ex. par les écoulements amont, par l'influence du sol déneigé).

À l'échelle du paysage, la distribution des plaques de glace reflète avant tout le contexte structural, qui détermine la répartition des niches topographiques, ainsi que le régime des vents dominants, conditionné par le climat régional et le relief local ([Chap. 3](#)).

6.1.3. Évolution sur le long terme des plaques de glace : entre résilience et vulnérabilité aux changements climatiques ([Obj. 2](#))

L'évolution des systèmes de plaques de glace est complexe car leur bilan de masse est dominé à la fois par le contrôle topographique en hiver et le contrôle synoptique, et donc climatique, en été. À long terme, le contexte topographique joue un rôle prépondérant dans l'évolution du bilan de masse des plaques de glace par le biais du mécanisme d'autorégulation entre ablation et accumulation. Ainsi, les plaques de glace sont partiellement déconnectées du climat régional, ce qui explique leur préservation sur le long terme en dessous de la ELA ([Chap. 2](#) et [3](#)). Cette évolution non-linéaire du bilan de masse des plaques par rapport au climat, leur confère ainsi une certaine résilience face aux fluctuations climatiques malgré leur petite taille, ce qui les rend uniques au sein de la cryosphère, dont la plupart des composantes sont étroitement liées aux tendances climatiques, et donc actuellement en déclin (Box et al., 2019). Nos résultats d'analyse de la glace (datation et

texture), combinés au fait que les plaques de glace sont toujours présentes aujourd'hui à l'île Ward Hunt alors que la température de l'air a atteint un niveau jamais vu depuis près de 4000 ans dans le Haut-Arctique (Lecavalier et al., 2017), suggèrent qu'elles sont présentes de manière continue depuis au moins plusieurs siècles à Ward Hunt. Cela implique que les plaques de glace auraient pu être préservées pendant certaines périodes chaudes de l'Holocène tardif (ex. l'Optimum climatique médiéval) grâce à leur capacité de résilience ([Chap. 3](#)).

Cette résilience des systèmes de plaques de glace aux fluctuations climatiques a néanmoins ses limites. L'évolution des plaques de glace sur le long terme obéit en fait à un effet de seuil qui implique qu'elles peuvent rester stables sur de longues périodes (plusieurs siècles à millénaires) mais qu'elles peuvent disparaître brutalement (quelques années) dès lors que l'ablation estivale devient trop importante pour que les facteurs topoclimatiques assurent leur préservation. Le comportement des plaques de glace est donc complexe, car malgré leur stabilité, leur petite taille les rend très sensibles et vulnérables à une hausse de l'ablation estivale. L'évolution future des plaques de glace est donc difficile à anticiper car elle dépendra de la forme des futurs changements climatiques (ex. la température, le régime des vents, la fréquence des brouillards, les cycles NAO et AO). Nos résultats ont montré qu'au cours de la période de réchauffement récente, le maintien de la plupart des plaques de glace à l'île Ward Hunt a été favorisé par la forte variabilité interannuelle des températures estivales. Bien que la tendance au réchauffement de la planète entraîne des séquences d'été de plus en plus chauds, ceux-ci sont toujours entrecoupés d'été froids qui permettent aux systèmes de plaques de glace de reconstituer leur stock de glace ([Chap. 2](#) et [3](#)). Il est fort probable qu'une série de deux ou trois étés consécutifs comme 2011, 2012 et 2016 suffirait à faire perdre leur statut « permanent » à la plupart des plaques de glace à Ward Hunt.

6.1.4. Le rôle central des plaques de glace dans le géosystème de désert polaire ([Obj. 3 et 4](#))

L'approche géosystémique adoptée dans cette thèse a permis d'établir et de quantifier les liens et interactions entre une plaque de glace et son environnement physique ([Chap. 4](#) et [5](#)). Ces travaux fournissent des informations importantes sur les effets des plaques de glace sur le milieu physique et représentent un premier pas vers le développement d'un modèle numérique quantitatif de la dynamique des versants de désert polaire.

Le principal effet des plaques de glace est de fournir un apport d'eau et de sédiment à la marge pronivale. Les régimes hydrologiques et sédimentaires des systèmes de plaques de glace sont à la fois contrôlés par la dynamique saisonnière et interannuelle des plaques (i.e. accumulation de neige, aggradation de glace surimposée, ablation ; [Chap. 2](#) et [3](#)) et par l'interaction entre les plaques et les flux d'eau et de sédiment en provenance des sections amont du versant ([Chap. 4](#)). En hiver et au début de l'été, les plaques de glace agissent comme un réservoir d'eau et un piège à sédiments ([Chap. 2](#)). Avec la fonte estivale, l'eau et les sédiments sont graduellement remis en circulation et alimentent la marge pronivale jusqu'à la fin de l'été. Le régime hydrologique des plaques de glace s'apparente donc au régime glaciaire ([Chap. 4](#)).

Dans la marge pronivale, les écoulements de fonte et leur charge sédimentaire initient des processus alluviaux localisés ([Chap. 4](#)). Les dépôts silteux qui s'y accumulent modifient les propriétés du sol ce qui enclenche une série de processus biologiques et géomorphologiques qui interagissent fortement entre eux. Les processus clés comprennent les interactions sédiments-végétation, l'effet de la végétation et des croûtes biologiques sur le régime thermique du sol et l'activation des processus de solifluxion et de triage du sol. Il en résulte le développement d'un système biogéomorphologique connecté à la plaque de glace que nous avons décrit par un modèle conceptuel basé sur des mesures empiriques et observations de terrain. Ce système est dominé par des lobes de solifluxion qui modifient profondément le profil topographique et le réseau hydrologique des pentes. Grâce à l'humidification durable du sol, la plateforme centrale des lobes forme un milieu humide qui abrite une végétation plus riche et diversifiée que sur les sols secs et stériles avoisinants.

Les écoulements de surface et le couvert végétal amènent des conditions thermiques de surface du sol très contrastées sur la marge pronivale. En raison de l'humidification de la surface du sol et de la présence d'une croûte biologique, les plateformes centrales des lobes étudiés connaissent des températures de surface du sol plus chaudes, en particulier vers la section terminale des lobes. Il en résulte des profondeurs de dégel plus importantes qu'à l'extérieur des lobes. Le développement des lobes dans la marge pronivale de la plaque de glace IP1 a donc entraîné un approfondissement localisé du toit du pergélisol. Ce résultat vient nuancer les conclusions de Verpaelst et al. (2017) et Paquette et al. (2020b) qui ont montré que le développement des lobes de solifluxion dans le désert polaire est associé à une remontée locale du toit du pergélisol conduisant

à la croissance d'une couche syngénétique de pergélisol riche en glace. Ces résultats divergents soulignent en fait le rôle critique du stade de succession écologique des lobes sur les conditions thermiques du sol et la dynamique du pergélisol. Dans le cas des lobes étudiés dans le chapitre 4, la présence de la croûte organique peut être considérée comme le stade initial d'une succession écologique amenant à la colonisation de mousse et plantes modifiant le régime thermique de surface (Breen et Lévesque, 2008). Cette transition conduirait donc éventuellement à la formation d'un pergélisol syngénétique.

L'hétérogénéité des conditions de surface produite par les plaques de glace et leur système biogéomorphologique influence également la variabilité spatiale des conditions de neige saisonnière ([Chap. 5](#)). Premièrement, le remodelage de la morphologie des pentes par la solifluxion modifie les patrons de redistribution de la neige par le vent pendant la saison froide et produit un manteau neigeux plus hétérogène. Les lobes bien développés peuvent même produire des discontinuités topographiques suffisantes pour former des plaques de neige saisonnières qui activeront à leur tour des processus biologiques et géomorphologiques ([Chap. 4](#)). Deuxièmement, le développement des zones humides en aval des plaques de glace est un facteur d'hétérogénéité spatiale des propriétés physiques de la neige saisonnière. L'humidification durable du sol et les températures de surface plus chaudes dans les zones humides accentuent le métamorphisme cinétique de la neige en début d'hiver. Il en résulte une couche de givre de profondeur plus épaisse à la base du couvert nival dans les zones humides ce qui renforce la capacité d'isolation du manteau neigeux. Cela entraîne un effet de réchauffement des températures de surface qui contribue à produire des conditions plus chaudes dans les zones humides que dans les zones sèches. Cette interaction entre la température du sol et le givre de profondeur entraîne une rétroaction positive, car un sol moins froid et des profondeurs de dégel plus importantes en été impliquent un gel plus long de la couche active en automne, ce qui accroît l'intensité et la durée du métamorphisme cinétique. L'effet isolant de la couche de givre de profondeur à la base du manteau neigeux est également bénéfique pour la croissance de la végétation et la prolifération de la vie subnivale (Poirier et al., 2019; Domine et al., 2018b ; Schimel et al., 2004).

En raison de leur présence sur le long terme ([Chap. 2](#) et [3](#)), les plaques de glace jouent donc un rôle fondamental dans le développement et l'organisation du géosystème et du paysage du désert polaire de l'île Ward Hunt. L'activation des processus azonaux dans un environnement

normalement dominé par l'action du gel et l'aridité a permis le développement d'un assemblage complexe de micro-environnements qui confèrent une grande hétérogénéité au désert polaire en termes d'hydrologie, de géomorphologie, de dynamique du pergélisol, de végétation et de propriétés du couvert de neige. Le fait que les environnements pronival dépendent directement des apports en eau et en sédiments fournis par les plaques de glace les rend très sensibles à l'évolution temporelle de leur bilan de masse.

6.2. Plaques de glace et géosystème polaire en transition

Dans cette section, nous nous appuyons sur les connaissances acquises dans cette thèse pour élaborer des hypothèses sur l'évolution potentielle des environnements de désert polaire sous l'influence des plaques de glace en réponse aux changements climatiques anticipés dans les prochaines décennies.

6.2.1. Vers une disparition des plaques de glace permanentes?

La poursuite de la hausse des températures de l'air, combinée à une augmentation de l'activité dépressionnaire dans le Haut-Arctique liée au déclin de la banquise, devrait apporter des conditions de plus en plus critiques pour le maintien des plaques de glace permanentes à l'île Ward Hunt ([Chap. 3](#)). Le scénario le plus probable serait donc que le seuil pour la préservation des plaques de glace soit franchi au cours des prochaines décennies entraînant leur disparition rapide à Ward Hunt, et plus largement le long de la côte nord et l'Ile d'Ellesmere. Cela mettrait donc fin à plusieurs siècles, voire millénaires, de présence continue des plaques de glace dans le paysage. Un nouveau régime se mettra alors en place avec dans un premier temps un cycle régulier de disparition et de restauration des plaques de glace, qui deviendraient alors semi-permanentes. Ce cycle sera largement influencé par les oscillations climatiques à court et moyen terme. Une telle transition s'est déjà opérée plus au sud, à Resolute Bay, comme reporté par Woo et Young (2014). À plus long terme, les plaques de glace semi-permanentes laisseraient leur place à des plaques de neige saisonnières si le réchauffement se poursuit.

6.2.2. Changement de régime et réactions en chaîne

La transition abrupte d'un régime stable de plaques de glace permanentes à un régime discontinu de plaques de glace semi-permanentes, voire saisonnières, devrait avoir de profondes répercussions sur la dynamique du géosystème polaire. Par un effet de réactions en chaîne (Rocha

et al., 2018), la disparition des plaques de glace permanentes entraînerait une modification du régime hydrologique et sédimentaire des versants, qui à son tour conduirait à des perturbations dans le fonctionnement de la plupart des composantes des systèmes biogéomorphologiques. Cela aboutirait à une réorganisation du géosystème de désert polaire qui évoluerait vers un nouvel équilibre.

Dans un scénario où les plaques de glace permanentes seraient remplacées par des plaques de neige saisonnières, le régime hydrologique évoluerait vers un régime de type nival arctique (Woo, 2012) avec des conséquences sur la durée et l'intensité du ruissellement de la fonte printanière. Les apports en eau aux versants seraient en effet plus intenses car la fonte des accumulations de neige dans la niche topographique serait concentrée sur une période plus courte. Il en résulterait des écoulements de surface plus forts au début de la saison chaude qui pourraient conduire à une érosion de la bande centrale et du front des lobes de solifluxion ([Chap. 4](#); Washburn, 1980). Leur contenu en sédiments fins se déverserait alors en aval entraîné par les écoulements. L'activité fluviale accrue au début de l'été, couplée à une interruption précoce des écoulements due à la disparition complète des plaques de neige, pourrait amener à un ralentissement des processus de solifluxion dans la marge pronivale. En outre, après la fonte des plaques de neige saisonnière, une couche active se développerait dans la niche topographique de sorte que l'eau en provenance de la section du versant amont ne serait plus forcée à faire surface (Woo et Young, 2014). Ainsi, le nouvel assemblage géomorphologique qui pourrait résulter de la disparition des plaques de glace permanentes amènerait à une transition vers une marge pronivale dominée par des écoulements souterrains à travers la macro porosité du sol. Dans le bassin versant du lac Ward Hunt, une telle transition pourrait accroître considérablement les flux de sédiments solides vers le lac au début de l'été (Paquette et al., 2020a) car ceux-ci ne seraient plus stockées dans les marge pronivales. Cela pourrait avoir des conséquences importantes sur la bathymétrie et les conditions limnologiques (ex. turbidité de l'eau) (Vincent et al., 2011b ; Bégin et al., 2020).

La transition vers un régime hydrologique de type nival et dominé par un drainage souterrain conduirait à un assèchement de la surface du sol des marges pronivales durant l'été qui aboutirait à un déclin de la diversité et la richesse des espèces végétales (Woo et Young, 2014) et une altération des communautés microbiennes (Comte et al., 2018). L'ensemble des modifications des propriétés de la surface du sol des sections pronivales, à savoir le déclin du couvert végétal, la

diminution de l'humidité du sol et de la fraction de sédiments fins, pourraient profondément modifier le bilan d'énergie de surface et le régime thermique de surface du sol. Paradoxalement, pour les lobes étudiés, une diminution de la croûte organique noire ([Chap. 4](#)) pourrait induire une rétroaction négative en conduisant à un refroidissement localisé de la surface du sol. De plus, la transition vers un système dominé par les écoulements souterrains pourrait également favoriser un refroidissement au niveau du sol le long des chemins d'écoulement préférentiels (*water tracks*) comme observé par Paquette et al. (2020a). En somme, la disparition de plaque de glace IP1 pourrait conduire à une remontée locale, mais certainement temporaire, du toit du pergélisol dans la marge pronivale. À l'inverse, dans les marges pronivales dominées par des lobes de solifluxion bien végétalisés (Verpaelst et al., 2017), le déclin du couvert végétal réduirait son effet isolant sur le sol. Pour ces sites, la dynamique future du pergélisol dépendra de la balance entre d'une part les effets du déclin de la végétation et, d'autre part, la réduction de l'humidité du sol qui réduirait la conductivité thermique de la couche active.

La modification du régime thermique et d'humidité du sol pourrait également avoir des répercussions majeures sur les propriétés physiques du couvert de neige saisonnier. L'assèchement des zones pronivales avant la fin de l'été réduira fortement la durée de la période de *zero curtain effect* qui permet le développement d'un gradient thermique et de vapeur d'eau suffisamment important pour la mise en place d'un métamorphisme cinétique. Ainsi, les conditions de surface du sol seraient moins favorables à la croissance du givre de profondeur à la base du couvert de neige ([Chap. 5](#)) qui serait remplacé par des cristaux facettés plus fins (métamorphisme de faible gradient). Avec l'assèchement du sol, la couverture neigeuse deviendrait donc plus dense et moins isolante, ce qui pourrait fournir une rétroaction négative supplémentaire sur la température du sol (effet refroidissant du sol) (Domine et al., 2016a). D'un point de vue biologique, cette modification des propriétés de la neige serait critique pour la végétation et la faune sous nivales (Domine et al., 2018b ; Poirier et al., 2019).

Globalement, la transition entre un paysage dominé par des plaques de glace permanentes et un paysage dominé par des plaques de neige saisonnières pourrait conduire à une uniformisation des environnements physiques de désert polaire en raison du déclin des processus azonaux. Les réactions en chaîne et les perturbations associées à la disparition des plaques de glace s'ajouteraient à d'autres phénomènes déjà observés dans le désert polaire liés à un déclin de la cryosphère, tels

que l'approfondissement de la couche de pergélisol actif (Paquette et al., 2020a) et la disparition de la couverture de glace permanente des lacs polaires (Bégin et al., 2020 ; Mueller et al., 2009). Ensemble, ces phénomènes contribueront à une transition généralisée du géosystème de désert polaire vers un nouvel équilibre.

6.3. Recommandations pour de futurs travaux :

Les avancées conceptuelles et empiriques qui émanent de cette recherche doctorale soulignent le potentiel et la nécessité de poursuivre des études sur les plaques de glace polaires et ont pour vocation de servir de socle pour la formulation des nouvelles questions de recherche qui guideront de futurs travaux. La section ci-dessous détaille certains aspects qui nous semblent particulièrement importants à développer ou à approfondir.

- *Modélisation physique d'un système de plaque de glace :*

À partir du cadre conceptuel établi dans cette thèse ([Chap. 2](#) et [3](#)), nous suggérons de développer un modèle physique intégré du bilan d'énergie d'un système de plaque de glace qui couplerait le bilan d'énergie de surface avec le bilan d'énergie de l'accumulation de neige et de la masse de glace sous-jacente. Les données de terrain collectées (ex. propriétés physiques de la neige et la glace) ainsi que l'instrumentation mise en place dans le cadre de cette thèse (ex. câble à thermistances dans la glace) permettront de paramétriser le modèle avec précision. Ce modèle pourrait être une adaptation des modèles physiques du couvert de neige existant qui intègrent les processus de fonte/regel internes (ex. SNOWPACK; Obleitner et Lehning, 2004; Crocus, Vionnet et al., 2012). Un tel modèle intégré permettrait d'évaluer le couplage entre le bilan de masse d'un système de plaque de glace et les conditions climatiques, et ainsi de mieux en prévoir l'évolution en réponse aux changements climatiques. Plus spécifiquement, le modèle pourrait simuler la croissance saisonnière de la glace surimposée et permettrait d'évaluer sa sensibilité aux facteurs de contrôle tels que les propriétés physiques de la neige, les flux d'eau et la température interne.

- *Datation des plaques de glace :*

Les résultats préliminaires obtenus sur l'âge des plaques de glace à l'île Ward Hunt ([Chap. 2](#)) offrent des perspectives très intéressantes sur le régime à long terme de ces petits éléments de la cryosphère et devront être confirmés et affinés par de nouvelles datations. Pour pallier le faible teneur en matière organique dans la glace, il serait pertinent d'avoir recours à la datation du carbone

organique particulaire (COP) et du CO₂ contenus dans la glace. Cette méthode a fait ses preuves pour la datation de la glace de glacier (Hoffmann et al., 2018 ; Guillet et al., 2021). Ces datations radiocarbone pourraient être complétées par des profils verticaux haute résolution de tritium (³H) à partir des carottes de glace, permettant éventuellement de détecter le pic de tritium atmosphérique qui a suivi les essais nucléaires des années 1950 et 1960 (Lewkowicz et Harry, 1991).

- *Poursuite des études biogéomorphologiques :*

L'étude biogéomorphologique réalisée dans le [Chap. 4](#) a montré le potentiel important de cette approche systémique et holistique pour comprendre le fonctionnement des environnements pronivaux, et plus largement pour comprendre l'évolution du paysage. Cependant, le modèle conceptuel développé dans cette étude préliminaire ne s'appuie que sur les résultats obtenus pour un site spécifique et devra donc être étayer par des études additionnelles sur d'autres systèmes biogéomorphologiques de plaques de glace à l'île Ward Hunt et dans le désert polaire arctique. En outre, plusieurs aspects mériteraient d'être étudiés en détail pour améliorer notre compréhension des environnements pronivaux. Il serait par exemple important de mesurer le régime hydrologique et le transport sédimentaire dans la marge des plaques de glace pendant toute la saison de fonte. Ces mesures permettraient de confirmer que les apports en sédiment se produisent en fin de saison lorsque la glace surimposée est exposée à la fonte. Il serait également important de mener des études de végétation plus poussées afin de comprendre les facteurs environnementaux qui expliquent les différents stades de succession écologique entre les lobes. Compte tenu du régime thermique de surface du sol très différent entre une couverture de croûte biologique noire et une couverture de végétation et de mousse, cette question est fondamentale pour comprendre la dynamique du pergélisol associée à la solifluxion.

- *Poursuite des mesures sur le long terme à l'île Ward Hunt :*

L'objectif derrière les efforts de mesure et d'instrumentation mis en place dans cette thèse est de faire de la plaque de glace IP1 et sa marge pronivale un site "sentinelle" pour suivre les changements environnementaux dans le désert polaire arctique en transition. Nous suggérons donc de poursuivre l'acquisition des données sur ce site afin d'obtenir des séries de données sur le long terme. Ce suivi aidera à mieux comprendre la réponse du bilan de masse aux oscillations climatiques (ex. AO, NAO) et nous permettra éventuellement d'enregistrer la disparition de la plaque de glace et d'en observer les multiples réactions en chaîne sur l'environnement physique.

L'une des priorités est donc de pérenniser l'instrumentation mise en place dans le cadre de cette thèse (c-à-d. le cable à thermistance, la caméra automatique, les capteurs de température de surface du sol) et de poursuivre les mesures de terrain à intervalle régulier (c-à-d. la couche active, les marqueurs de solifluxion, les études de végétation et du couvert nival).

- *Études à l'échelle régionale*

Les observations effectuées lors de multiples survols entre Resolute Bay et l'île Ward Hunt suggèrent que les conclusions établies dans cette thèse sur le rôle central des plaques de glace dans le façonnement des versants et l'organisation du paysage de désert polaire sont applicables à une grande partie de l'Arctique canadien. Nous suggérons donc d'élargir l'étude des plaques de glace à l'échelle du paysage, voire régionale.

L'amélioration récente de la résolution des images satellites (ex. Worldview 2-3) permet désormais de détecter les plus petites masses de glace. En outre, l'analyse d'un grand volume d'images à haute résolution est maintenant possible grâce à des techniques innovantes qui associent des techniques de télédétection à l'intelligence artificielle, notamment en ayant recours à l'apprentissage automatique (*deep learning*) (Zhang et al., 2018). Grâce à ces avancées, une carte régionale de la densité spatiale des plaques de glace à la fin de l'été pourrait être établie, ce qui permettrait de comprendre les facteurs climatiques et topographiques responsables de leur distribution régionale (ex. fréquence du brouillard, continentalité, altitude). Une analyse multidiates permettrait également d'étudier l'évolution temporelle des plaques de glace arctique, similairement à ce que nous avons produit à l'échelle de l'île Ward Hunt dans le [chapitre 3](#).

La cartographie des plaques de glace pourrait également intégrer les milieux humides pronivaux qui sont facilement détectables par télédétection en raison de leur couleur foncée (Langford et al., 2015). Ainsi, des statistiques spatiales relatives aux superficies du territoire qui sont affectées par les plaques de glace pourraient être établies et permettraient d'évaluer plus réaliste la vulnérabilité de désert polaire aux changements climatiques. En outre, l'identification des milieux humides pronivaux pourrait avoir une application importante pour la modélisation spatiale du pergélisol (ex. teneur en glace du sol) et du couvert neigeux dans les régions de désert polaire.

Références bibliographiques

- Abnizova, A., et Young, K. L. (2008). Hillslope hydrological linkages: importance to ponds within a polar desert High Arctic wetland. *Hydrology Research*, 39(4), 309–321. doi:10.2166/Nh.2008.007
- Abnizova, A., et Young, K. L. (2010). Sustainability of high arctic ponds in a polar desert environment. *Arctic*, 63(1), 67–84. doi:10.14430/arctic648
- Akperov, M., Rinke, A., Mokhov, I. I., Semenov, V. A., Parfenova, M. R., Matthes, H., ... et Zhang, W. (2019). Future projections of cyclone activity in the Arctic for the 21st century from regional climate models (Arctic-CORDEX). *Global and Planetary Change*, 182, 103005. doi:10.1016/j.gloplacha.2019.103005
- Albert, M. R., Grannas, A. M., Bottenheim, J., Shepson, P. B., et Perron, F. E. (2002). Processes and properties of snow-air transfer in the high Arctic with application to interstitial ozone at Alert, Canada. *Atmospheric Environment*, 36(15-16), 2779-2787. doi:10.1016/S1352-2310(02)00118-8
- Alley, R. B., et Woods, G. A. (1996). Impurity influence on normal grain growth in the GISP2 ice core, Greenland. *Journal of Glaciology*, 42(141), 255–260. doi:10.3189/S0022143000004111
- Alt, B. (1987). Developing synoptic analogs for extreme mass balance conditions on Queen Elizabeth Island ice caps. *Journal of Applied Meteorology and Climatology*, 26(12), 1605-1623. doi:10.1175/1520-0450(1987)026<1605:DSAFEM>2.0.CO;2
- AMAP. (2019). AMAP climate change update 2019: an update to key findings of snow, water, ice and permafrost in the Arctic (SWIPA) 2017. *Arctic Monitoring and Assessment Programme (AMAP)*, Oslo (Norway), 12. Repéré sur : www.apam.no/documents/doc/amap-climate-change-update-2019/1761
- Antoniades, D., Francus, P., Pienitz, R., St-Onge, G., et Vincent, W. F. (2011). Holocene dynamics of the Arctic's largest ice shelf. *Proceedings of the National Academy of Sciences of the United States of America*, 108(47), 18899–18904. doi:10.1073/pnas.1106378108

Assini, J., et Young, K. L. (2012). Snow cover and snowmelt of an extensive High Arctic wetland: spatial and temporal seasonal patterns. *Hydrological Sciences Journal*, 57(4), 738–755. doi:10.1080/02626667.2012.666853

Bahr, D. B., et Radić, V. (2012). Significant contribution to total mass from very small glaciers. *The Cryosphere*, 6(4), 763–770. doi:10.5194/tc-6-763-2012

Ball, B. A., Barrett, J. E., Gooseff, M. N., Virginia, R. A., et Wall, D. H. (2011). Implications of meltwater pulse events for soil biology and biogeochemical cycling in a polar desert. *Polar Research*, 30(1), 14555. doi:10.3402/polar.v30i0.14555

Ballantyne, C. K. (1978). The hydrologic significance of nivation feature in permafrost areas. *Geografiska Annaler Series A-Physical Geography*, 60(1), 51–54. doi:10.1080/04353676.1978.11879963

Ballantyne, C. K. (2002). A general model of paraglacial landscape response. *The Holocene*, 12(3), 371–376. doi:10.1191/0959683602hl553fa

Ballantyne, C. K. (1985). Nivation landforms and snowpatch erosion on two massifs in the Northern Highlands of Scotland. *Scottish Geographical Magazine*, 101(1), 40–49. doi:10.1080/00369228518736611

Ballantyne, C. K., et Benn, D. I. (1994). Glaciological constraints on protalus rampart development. *Permafrost and periglacial processes*, 5(3), 145-153. doi: 10.1002/ppp.3430050304.

Ballantyne, C. K., Black, N. M., et Finlay, D. P. (1989). Enhanced boulder weathering under late-lying snowpatches. *Earth surface processes and landforms*, 14(8), 745-750. doi:10.1002/esp.3290140808

Barrere, M., Domine, F., Decharme, B., Morin, S., Vionnet, V., et Lafaysse, M. (2017). Evaluating the performance of coupled snow-soil models in SURFEXv8 to simulate the permafrost thermal regime at a high Arctic site. *Geoscientific Model Development*, 10(9), 3461-3479. March, doi:10.5194/gmd-2017-50

Barrette, P. D., et Sinha, N. K. (1996). Crystallographic characterization of a core from the Ward Hunt Ice Shelf, Canada. In *Proceedings of the international symposium on snow and related manifestations* (pp. 26-28).

Barry, R. G., et Hall-McKim, E. A. (2018). *Polar environments and global change*. Cambridge University Press.

Bash, E. A., et Moorman, B. J. (2020). Surface melt and the importance of water flow—an analysis based on high-resolution unmanned aerial vehicle (UAV) data for an Arctic glacier. *The Cryosphere*, 14(2), 549-563. doi:10.5194/tc-14-549-2020

Bégin, P. N., Tanabe, Y., Kumagai, M., Culley, A. I., Paquette, M., Sarrazin, D., Uchida, M., et Vincent, W. F. (2020). Extreme warming and regime shift toward amplified variability in a far northern lake. *Limnology and Oceanography*, 66, 1–13. doi:10.1002/lno.11546

Bengtsson, L., Hodges, K. I., Koumoutsaris, S., Zahn, M., et Berrisford, P. (2013). The changing energy balance of the polar regions in a warmer climate. *Journal of climate*, 26(10), 3112-3129. doi:10.1175/JCLI-D-12-00233.1

Benn D. I. and Evans D. J. A. (2010) *Glaciers and Glaciation*. Hodder Education. Second edition. 802 pp.

Bennett, L. P., et French, H. M. (1991). Solifluction and the role of permafrost creep, eastern Melville Island, NWT, Canada. *Permafrost and Periglacial Processes*, 2(2), 95-102. doi:10.1002/ppp.3430020204

Benson, C. S., et Sturm, M. (1993). Structure and wind transport of seasonal snow on the Arctic slope of Alaska. *Annals of Glaciology*, 18, 261-267. doi:10.3189/S0260305500011629

Benson C. S., et Trabant D. C. (1973). Field measurements on the flux of water vapour through dry snow. International Association of Hydrological Sciences Publication 107 In *Proceedings Symposium on the Role of Snow and Ice in Hydrology*, September 1972, Banff, Canada, 291–298. Repéré sur: hydrologie.org/redbooks/a107/107022.pdf

Berrisford, M. S. (1991). Evidence for enhanced mechanical weathering associated with seasonally late- lying and perennial snow patches, Jotunheimen, Norway. *Permafrost and Periglacial Processes*, 2(4), 331-340. doi:10.1002/ppp.3430020408

Billings, W. D., et Bliss, L. C. (1959). An alpine snowbank environment and its effects on vegetation, plant development, and productivity. *Ecology*, 40(3), 388-397. doi:www.jstor.org/stable/pdf/1929755.pdf

Bintanja, R., et Andry, O. (2017). Towards a rain-dominated Arctic. *Nature Climate Change*, 7(4), 263-267. doi:10.1038/nclimate3240

Biskaborn, B. K., Smith, S. L., Noetzli, J., Matthes, H., Vieira, G., Streletschi, D. A., ... et Lantuit, H. (2019). Permafrost is warming at a global scale. *Nature communications*, 10(1), 1-11. doi:10.1038/s41467-018-08240-4

Bliss, L. C., et Gold, W. G. (1999). Vascular plant reproduction, establishment, and growth and the effects of cryptogamic crusts within a polar desert ecosystem, Devon Island, NWT, Canada. *Canadian Journal of Botany*, 77(5), 623-636. doi:10.1139/b99-031

Bliss, L. C., Svoboda, J., et Bliss, D. I. (1984). Polar deserts, their plant cover and plant production in the Canadian High Arctic. *Ecography*, 7(3), 305-324. Repéré: www.jstor.org/stable/3682753

Blott, S. J., et Pye, K. (2001). GRADISTAT: a grain size distribution and statistics package for the analysis of unconsolidated sediments. *Earth surface processes and Landforms*, 26(11), 1237-1248. doi:10.1002/esp.261

Bøggild, C. E. (2007). Simulation and parameterization of superimposed ice formation. *Hydrological Processes: An International Journal*, 21(12), 1561-1566. doi: 10.1002/hyp.6718.

Boike, J., Hinzman, L., Overduin, P. P., Romanovsky, V., Ippisch, O., et Roth, K. (2003a). A comparison of snow melt at three circumpolar sites: Spitsbergen, Siberia, Alaska. In *Proceedings of the 8th International Conference on Permafrost, Zürich, Switzerland* (pp. 21-25).

Boike, J., Roth, K., et Ippisch, O. (2003b). Seasonal snow cover on frozen ground: Energy balance calculations of a permafrost site near Ny-Ålesund, Spitsbergen. *Journal of Geophysical Research*, 108(D2), 1-11. doi:10.1029/2001JD000939

Box, J. E., Colgan, W. T., Christensen, T. R., Schmidt, N. M., Lund, M., Parmentier, F. J. W., ... et Olsen, M. S. (2019). Key indicators of Arctic climate change: 1971–2017. *Environmental Research Letters*, 14(4), 045010. doi:10.1088/1748-9326/aafc1b

Bradley, R. S. (1990). Holocene paleoclimatology of the Queen Elizabeth islands, Canadian high arctic. *Quaternary Science Reviews*, 9(4), 365-384. doi: 10.1016/0277-3791(90)90028-9.

Braun, C. (2017). The surface mass balance of the Ward Hunt Ice Shelf and Ward Hunt Ice Rise, Ellesmere Island, Nunavut, Canada. In *Arctic ice shelves and ice islands* (pp. 149-183). Springer, Dordrecht. doi:10.1029/2004JD004560

Braun-Blanquet, J. (1932). Plant sociology. The study of plant communities. *Plant sociology. The study of plant communities. First ed. Repéré sur :* www.cabdirect.org/cabdirect/abstract/19331600801

Braun, C., Hardy, D. R., Bradley, R. S., et Retelle, M. J. (2000). Streamflow and suspended sediment transfer to Lake Sophia, Cornwallis Island, Nunavut, Canada. *Arctic, Antarctic, and Alpine Research*, 32(4), 456-465. doi:10.1080/15230430.2000.12003390

Braun, C., Hardy, D. R., Bradley, R. S., et Sahanatien, V. (2004). Surface mass balance of the Ward Hunt Ice Rise and Ward Hunt Ice Shelf, Ellesmere Island , Nunavut , Canada. *Journal of Geophysical Research*, 109, 1-9. doi:10.1029/2004JD004560

Breen, K., et Lévesque, E. (2008). The influence of biological soil crusts on soil characteristics along a High Arctic glacier foreland, Nunavut, Canada. *Arctic, Antarctic, and Alpine Research*, 40(2), 287-297. doi:10.1657/1523-0430(06-098)[BREEN]2.0.CO;2

Brown, I., and Ward, R. (1996). The Influence of Topography on Snowpatch Distribution in Southern Iceland : A New Hypothesis for Glacier Formation. *Geografiska Annaler Series A-Physical Geography*, 78(4), 197–207.

Callaghan, T. V., Johansson, M., Brown, R. D., Groisman, P. Y., Labba, N., Radionov, V., ... et Wood, E. F. (2011a). Multiple effects of changes in Arctic snow cover. *Ambio*, 40(1), 32–45. doi:10.1007/s13280-011-0213-x

Callaghan, T. V., Johansson, M., Key, J., Prowse, T., Ananicheva, M., et Klepikov, A. (2011b). Feedbacks and interactions: From the Arctic cryosphere to the climate system. *Ambio*, 40(1), 75-86. doi:10.1007/s13280-011-0215-8

Calonne, N., Geindreau, C., Flin, F., Morin, S., Lesaffre, B., Rolland du Roscoat, S., et Charrier, P. (2012). 3-D image-based numerical computations of snow permeability: links to specific

surface area, density, and microstructural anisotropy. *The Cryosphere*, 6(5), 939-951. doi:10.5194/tc-6-939-2012

Carey, S. K., et Woo, M. K. (2001). Slope runoff processes and flow generation in a subarctic, subalpine catchment. *Journal of Hydrology*, 253(1–4), 110–129. doi:10.1016/S0022-1694(01)00478-4

CEN. (2020). Climate station data from Northern Ellesmere Island in Nunavut, Canada, v. 1.7 (2002-2019). Nordicana D1. doi:10.5885/44985SL-8F203FD3ACCD4138.

CEN. (2021). Climate station data from Northern Ellesmere Island in Nunavut, Canada, Nordicana D. doi: 10.5885/44985SL-8F203FD3ACCD4138

Christiansen, H. H. (1998). Nivation forms and processes in unconsolidated sediments, NE Greenland. *Earth Surface Processes and Landforms*, 23(8), 751–760. doi:10.1002/(SICI)1096-9837(199808)23:8<751::AID-ESP886>3.0.CO;2-A

CloudCompare. (2020). CloudCompare version 2.10. Repéré sur: www.cloudcompare.org

Climate Change Institute. 2021. Climate Reanalyzer. Repéré sur: <https://climatereanalyzer.org/>

Cogley, J. G., Arendt, A. A., Bauder, A., Braithwaite, R. J., Hock, R., Jansson, P., ... et Zemp, M. (2010). Glossary of glacier mass balance and related terms. *IHP-VII technical documents in hydrology*, 86, 114. Repéré sur unesco.org/images/0019/001925/192525e.pdf.

Colbeck, S. C. (1982). An overview of seasonal snow metamorphism. *Reviews of Geophysics*, 20(1), 45-61. doi: 10.1002/2016GL070875

Colombo, R., Garzonio, R., Di Mauro, B., Dumont, M., Tuzet, F., Cogliati, S., ... et Cremonese, E. (2019). Introducing thermal inertia for monitoring snowmelt processes with remote sensing. *Geophysical Research Letters*, 46(8), 4308-4319. doi: 10.1029/2019GL082193

Colucci, R. R., Forte, E., Boccali, C., Dossi, M., Lanza, L., Pipan, M., et Guglielmin, M. (2015). Evaluation of Internal Structure, Volume and Mass of Glacial Bodies by Integrated LiDAR and Ground Penetrating Radar Surveys: The Case Study of Canin Eastern Glacier (Julian Alps, Italy). *Surveys in Geophysics*, 36(2), 231–252. doi:10.1007/s10712-014-9311-1

- Colucci, R. R., Žebre, M., Torma, C. Z., Glasser, N. F., Maset, E., Gobbo, C. Del, et Pillon, S. (2021). Recent increases in winter snowfall provide resilience to very small glaciers in the Julian Alps, Europe. *Atmosphere*, 12(2), 263. doi:10.3390/atmos12020263
- Comte, J., Culley, A. I., Lovejoy, C., et Vincent, W. F. (2018). Microbial connectivity and sorting in a High Arctic watershed. *The ISME Journal*, 12(12), 2988–3000. doi:10.1038/s41396-018-0236-4
- Cook, F. A. (1955) Near surface soil temperature measurements at Resolute Bay, Northwest Territories. *Arctic*, 8(4), 237–249. Repéré sur: www.jstor.org/stable/40506702
- Copland, L., Mortimer, C., White, A., McCallum, M. R., et Mueller, D. (2017). Factors contributing to recent Arctic ice shelf losses. In *Arctic ice shelves and ice islands* (pp. 263–285). Springer, Dordrecht. doi: 10.1007/978-94-024-1101-0_5.
- Copland, L., Mueller, D. R., et Weir, L. (2007). Rapid loss of the Ayles ice shelf, Ellesmere Island, Canada. *Geophysical Research Letters*, 34(21), 1–6. doi:10.1029/2007GL031809
- Corenblit, D., Steiger, J., Charrier, G., Darrozes, J., Garofano- Gómez, V., Garreau, A., ... et Voldoire, O. (2016). *Populus nigra* L. establishment and fluvial landform construction: biogeomorphic dynamics within a channelized river. *Earth Surface Processes and Landforms*, 41(9), 1276-1292. doi:10.1002/esp.3954
- Coulombe, S., Fortier, D., Lacelle, D., Kanevskiy, M., et Shur, Y. (2019). Origin, burial and preservation of late Pleistocene-age glacier ice in Arctic permafrost (Bylot Island, NU, Canada). *The Cryosphere*, 13(1), 97-111. doi: 10.5194/tc-13-97-2019, 2019
- Crabeck, O., Galley, R., Delille, B., Else, B., Geilfus, N. X., Lemes, M., ... et Rysgaard, S. (2016). Imaging air volume fraction in sea ice using non-destructive X-ray tomography. *The Cryosphere*, 10(3), 1125-1145. doi: 10.5194/tc-10-1125-2016.
- Crary, A. P. (1960). Arctic ice island and ice shelf studies: Part II. *Arctic*, 13(1), 32-50. Repéré sur: pubs.aina.ucalgary.ca/arctic/Arctic11-1-2.pdf
- Cuffey, K.M., et Paterson, W.S.B. 2010. *The physics of glaciers*, 4th ed. Oxford: Elsevier

Cunningham, J., et Waddington, E. D. (1993). Air flow and dry deposition of non-sea salt sulfate in polar firn: paleoclimatic implications. *Atmospheric Environment. Part A. General Topics*, 27(17-18), 2943-2956. doi:10.1016/0960-1686(93)90327-U

Dąbski, M., Zmarz, A., Pabjanek, P., Korczak-Abshire, M., Karsznia, I., et Chwedorzewska, K. J. (2017). UAV-based detection and spatial analyses of periglacial landforms on Demay Point (King George Island, South Shetland Islands, Antarctica). *Geomorphology*, 290, 29-38. doi:10.1016/j.geomorph.2017.03.033

Dadic, R., Mott, R., Lehning, M., et Burlando, P. (2010). Wind influence on snow depth distribution and accumulation over glaciers. *Journal of Geophysical Research: Earth Surface*, 115(1), 1–8. doi:10.1029/2009JF001261

Dadic, R., Mott, R., Lehning, M., Carenzo, M., et Anderson, B. (2013). Sensitivity of turbulent fluxes to wind speed over snow surfaces in different climatic settings. *Advances in Water Resources*, 55, 178–189. doi:10.1016/j.advwatres.2012.06.010

Dahl, O. S., Bakke, J., Lie, Ø., et Nesje, A. (2003). Reconstruction of former glacier equilibrium-line altitudes based on proglacial sites: an evaluation of approaches and selection of sites. *Quaternary Science Reviews*, 22(2-4), 275-287. doi:10.1016/S0277-3791(02)00135-X

Davesne, G; Fortier, D. (2018) Characterization of the northernmost Canadian ice patches, *14th ArcticNet Annual Scientific Meeting*.

Davesne, G., Fortier, D., Domine, F., (2021) Effects of meteorology and soil moisture on the spatio-temporal evolution of the depth hoar layer in the polar desert snowpack. *Journal of Glaciology*, Manuscrit accepté pour publication.

Davesne, G., Fortier, D., Domine, F., et Gray, J. T. (2017). Wind-driven snow conditions control the occurrence of contemporary marginal mountain permafrost in the Chic-Choc Mountains, south-eastern Canada: a case study from Mont Jacques-Cartier. *The Cryosphere*, 11(3), 1351-1370. doi:10.5194/tc-11-1351-2017

Davesne, G., Fortier, D., Lévesque, E., et Rioux K. (2019) The polar ice patch project - Fieldwork 2019. *Presentation to Park Canada and the Resolute Bay HTA*. doi:10.13140/RG.2.2.21076.55686

- De Chaumont, F., Dallongeville, S., Chenouard, N., Hervé, N., Pop, S., Provoost, T., ... et Olivo-Marin, J. C. (2012). Icy: an open bioimage informatics platform for extended reproducible research. *Nature methods*, 9(7), 690-696. doi: 10.1038/nmeth.2075.
- DeBeer, C. M., et Pomeroy, J. W. (2017). Influence of snowpack and melt energy heterogeneity on snow cover depletion and snowmelt runoff simulation in a cold mountain environment. *Journal of Hydrology*, 553, 199–213. doi:10.1016/j.jhydrol.2017.07.051
- DeBeer, C. M., et Sharp, M. J. (2009). Topographic influences on recent changes of very small glaciers in the monashee mountains, British Columbia, Canada. *Journal of Glaciology*, 55(192), 691–700. doi:10.3189/002214309789470851
- Derkson, C., Silis, A., Sturm, M., Holmgren, J., Liston, G. E., Huntington, H., et Solie, D. (2009). Northwest Territories and Nunavut snow characteristics from a subarctic traverse: Implications for passive microwave remote sensing. *Journal of Hydrometeorology*, 10(2), 448-463. doi: 10.1175/2008jhm1074.1.
- Desjardins, É., Lai, S., Payette, S., Vézina, F., Tam, A., et Berteaux, D. (2021). Vascular plant communities in the polar desert of Alert (Ellesmere Island, Canada): Establishment of a baseline reference for the 21st century. *Écoscience*, 1-25. doi:10.1080/11956860.2021.1907974 CrossMark LogoCrossMark
- Dewalle, D. R. and Rango, A. (2008). *Principles of snow hydrology*, Cambridge University Press, Cambridge, UK, 428 pp.
- Dingman SL. 2002. *Physical hydrology*. Waveland Press: Long Grove, templateDwinter.html. IL.
- Domine, F., Albert, M., Huthwelker, T., Jacobi, H. W., Kokhanovsky, A. A., Lehning, M., ... et Simpson, W. R. (2008). Snow physics as relevant to snow photochemistry. *Atmospheric chemistry and physics*, 8(2), 171-208. doi: 10.5194/acpd-7-5941-2007
- Domine, F., Barrere, M., and Morin, S. (2016a). The growth of shrubs on high Arctic tundra at Bylot Island: impact on snow physical properties and permafrost thermal regime. *Biogeosciences*, 13(23), 6471-6486. doi: 0.5194/bg-13-6471-2016, 2016.

- Domine, F., Barrere, M., et Sarrazin, D. (2016b). Seasonal evolution of the effective thermal conductivity of the snow and the soil in high Arctic herb tundra at Bylot Island, Canada. *The Cryosphere*, 10(6), 2573–2588. doi:10.5194/tc-10-2573-2016
- Domine, F., Belke-brea, M., Sarrazin, D., Arnaud, L., Barrere, M., et Poirier, M. (2018a). Soil moisture, wind speed and depth hoar formation in the Arctic snowpack. *Journal of Glaciology*, 64(248), 990-1002. doi :10.1017/jog.2018.89
- Domine, F., Bock, J., Morin, S., et Giraud, G. (2011). Linking the effective thermal conductivity of snow to its shear strength and density. *Journal of Geophysical Research: Earth Surface*, 116(F4). doi:10.1029/2011JF002000.
- Domine, F., Cabanes, A., et Legagneux, L. (2002). Structure, microphysics, and surface area of the Arctic snowpack near Alert during the ALERT 2000 campaign. *Atmospheric Environment*, 36(15–16), 2753–2765. doi:10.1016/S1352-2310(02)00108-5
- Domine, F., Gallet, J. C., Bock, J., and Morin, S. (2012). Structure, specific surface area and thermal conductivity of the snowpack around Barrow, Alaska. *Journal of Geophysical Research: Atmospheres*, 117(D14). doi:10.1029/2011JD016647
- Domine, F., Gauthier, G., Vionnet, V., Fauteux, D., Dumont, M., et Barrere, M. (2018b). Snow physical properties may be a significant determinant of lemming population dynamics in the high Arctic. *Arctic Science*, 4(4), 813-826. doi:10.1139/as-2018-0008
- Domine, F., Morin, S., Brun, E., Lafaysse, M., et Carmagnola, C. M. (2013). Seasonal evolution of snow permeability under equi-temperature and temperature-gradient conditions. *The Cryosphere*, 7(6), 1915-1929. doi:10.5194/tc-7-1915-2013
- Domine, F., Picard, G., Morin, S., Barrere, M., Madore, J. B., et Langlois, A. (2019). Major Issues in Simulating Some Arctic Snowpack Properties Using Current Detailed Snow Physics Models: Consequences for the Thermal Regime and Water Budget of Permafrost. *Journal of Advances in Modeling Earth Systems*, 11(1), 34-44. doi:10.1029/2018MS001445
- Domine, F., Taillandier, A. S., et Simpson, W. R. (2007). A parameterization of the specific surface area of seasonal snow for field use and for models of snowpack evolution. *Journal of Geophysical Research: Earth Surface*, 112(2), 1–13. doi:10.1029/2006JF000512

Doran, P.T., and Fountain, A.G. 2019. High frequency measurements from Lake Vanda Meteorological Station (VAAM) in Wright Valley, Antarctica from 1994 to present. *Environmental Data Initiative*. doi: 10.6073/pasta/1d61bf888090e697d1eebee35b6e6bae.

Durand, G., Weiss, J., Lipenkov, V., Barnola, J. M., Krinner, G., Parrenin, F., ... et Bigler, M. (2006). Effect of impurities on grain growth in cold ice sheets. *Journal of Geophysical Research: Earth Surface*, 111(F1). doi: 10.1029/2005JF000320.

Duval, P. (1985). Grain growth and mechanical behaviour of polar ice. *Annals of Glaciology*, 6, 79-82. doi: 10.3189/1985AoG6-1-79-82

Edlund, S. A., et Alt, B. T. (1989). Regional congruence of vegetation and summer climate patterns in the Queen Elizabeth Islands, Northwest Territories, Canada. *Arctic*, 3-23. doi:10.14430/arctic1635

Eichel, J., Corenblit, D., et Dikau, R. (2016). Conditions for feedbacks between geomorphic and vegetation dynamics on lateral moraine slopes: a biogeomorphic feedback window. *Earth Surface Processes and Landforms*, 41(3), 406-419. doi:10.1002/esp.3859

Eichel, J., Draebing, D., Klingbeil, L., Wieland, M., Eling, C., Schmidlein, S., ... et Dikau, R. (2017). Solifluction meets vegetation: the role of biogeomorphic feedbacks for turf- banked solifluction lobe development. *Earth Surface Processes and Landforms*, 42(11), 1623-1635. doi: 10.1002/esp.4102

Eichel, J., Krautblatter, M., Schmidlein, S., et Dikau, R. (2013). Biogeomorphic interactions in the Turtmann glacier forefield, Switzerland. *Geomorphology*, 201, 98-110. doi:10.1016/j.geomorph.2013.06.012

England, J. H., Evans, D. J., et Lakeman, T. R. (2017). Holocene history of Arctic ice shelves. In *Arctic ice shelves and ice islands* (pp. 185-205). Springer, Dordrecht. doi :10.1007/978-94-024-1101-0_7

Environment Canada. (2021). Historical climate data, National climate data and information archive. Repéré sur: <http://www.climate.weatheroffice.gc.ca>

Essery, R., Granger, R., and Pomeroy, J. (2006). Boundary-layer growth and advection of heat over snow and soil patches: Modelling and parameterization. *Hydrological Processes*, 20(4),

953–967. doi: 10.1002/hyp.6122

Essery, R., et Pomeroy, J. (2004). Vegetation and topographic control of wind-blown snow distributions in distributed and aggregated simulations for an Arctic tundra basin. *Journal of Hydrometeorology*, 5(5), 735-744. doi:10.1175/1525-7541(2004)005<0735:VATCOW>2.0.CO;2

Eveland, J., Gooseff, M. N., Lampkin, D. J., Barrett, J. E., et Takacs-Vesbach, C. (2013a). Spatial and temporal patterns of snow accumulation and aerial ablation across the McMurdo Dry Valleys, Antarctica. *Hydrological Processes*, 27(20), 2864–2875. doi:10.1002/hyp.9407

Eveland, J. W., Gooseff, M. N., Lampkin, D. J., Barrett, J. E., et Takacs-Vesbach, C. D. (2013b). Seasonal controls on snow distribution and aerial ablation at the snow-patch and landscape scales, McMurdo Dry Valleys, Antarctica. *The Cryosphere*, 7(3), 917–931. doi:10.5194/tc-7-917-2013

Farnell, R., Hare, G., Blake, E., et Bowyer, V. (2004). Multidisciplinary Investigations of Alpine Ice Patches in Southwest Yukon, Ca. *Arctic*, 57(3), 247–259.

Fauchald, P., Park, T., Tømmervik, H., Myneni, R., et Hausner, V. H. (2017). Arctic greening from warming promotes declines in caribou populations. *Science Advances*, 3(4), e1601365. doi:10.1126/sciadv.1601365

Fetterer, F., K. Knowles, W. N. Meier, M. Savoie, and A. K. Windnagel. 2017 (updated daily). Sea Ice Index, Version 3. *Regional Daily Data*. National Snow and Ice Data Center. doi:10.7265/N5K072F8.

Filhol, S., et Sturm, M. (2015). Snow bedforms: A review, new data, and a formation model. *Journal of Geophysical Research: Earth Surface*, 120(9), 1645-1669. doi:10.1002/2015JF003529.Received

Fierz, C. R. L. A., Armstrong, R. L., Durand, Y., Etchevers, P., Greene, E., McClung, D. M., ... et Sokratov, S. A. (2009). *The international classification for seasonal snow on the ground*. 25. UNESCO/IHP. Repéré sur: unesdoc.unesco.org/ark:/48223/pf0000186462.

Fischer, M., Huss, M., Barboux, C., et Hoelzle, M. (2014). The new Swiss Glacier Inventory SGI2010: Relevance of using high-resolution source data in areas dominated by very small

glaciers. *Arctic, Antarctic, and Alpine Research*, 46(4), 933–945. doi:10.1657/1938-4246-46.4.933

Fischer, M., Huss, M., Kummert, M., and Hoelzle, M. (2016). Application and validation of long-range terrestrial laser scanning to monitor the mass balance of very small glaciers in the Swiss Alps. *The Cryosphere*, 10(3), 1279-1295. doi:10.5194/tc-10-1279-2016

Fisher, D., Zheng, J., Burgess, D., Zdanowicz, C., Kinnard, C., Sharp, M., et Bourgeois, J. (2012). Recent melt rates of Canadian arctic ice caps are the highest in four millennia. *Global and Planetary Change*, 84, 3-7. doi:10.1016/j.gloplacha.2011.06.005

Forthofer, J. M., Butler, B. W., and Wagenbrenner, N. S. 2014. WindNinja. Repéré sur: www.firelab.org/project/windninja.

Fortier, D., et Allard, M. (2005). Frost- cracking conditions, Bylot Island, eastern Canadian Arctic Archipelago. *Permafrost and Periglacial Processes*, 16(2), 145-161. doi: 10.1002/ppp.504.

Fortier, D., Allard, M., et Shur, Y. (2007). Observation of Rapid Drainage System Development by Thermal Erosion of Ice Wedges on Bylot Island, Canadian Arctic Archipelago. *Permafrost and Periglacial Processes*, 18(3), 229–243. doi:10.1002/ppp

Fortier, D., et Davesne, G. (2021a). Computed tomography (CT) scans of ice cores collected in two perennial ice patches at Ward Hunt Island, Nunavut, Canada, v. 1.0 (2018-2018). Nordicana D85, doi: 10.5885/45696CE-6CC0B447C7F84E6A.

Fortier, D., et Davesne, G. (2021b). Snow and temperature regime of a perennial ice patch, Ward Hunt Island, Nunavut, Canada., v. 1.0 (2017-2019). Nordicana D91, doi: 10.5885/45720CE-0F556C84D96948F7.

Fraser, R. H., Olthof, I., Lantz, T. C., et Schmitt, C. (2016). UAV photogrammetry for mapping vegetation in the low-Arctic. *Arctic Science*, 2(3), 79-102. doi:10.1139/as-2016-0008

French, H. M. (2017). *The periglacial environment*. John Wiley & Sons.

French, H. M. H., et Pollard, W. H. (1986). Ground-ice investigations, Klondike District, Yukon Territory. *Canadian Journal of Earth Sciences*, 23(4), 550-560. doi:10.1139/e86-055

Fujita, K., Hiyama, K., Iida, H., et Ageta, Y. (2010). Self-regulated fluctuations in the ablation of a snow patch over four decades. *Water Resources Research*, 46(11), 1–9. doi:10.1029/2009WR008383

Gachev, E. (2017). The unknown southernmost glaciers of Europe. Glaciers's evolution in a changing world. *InTech Publishers*, Zagreb, 77-102. doi:10.5772/intechopen.68899

Gachev, E., Stoyanov, K., et Gikov, A. (2016). Small glaciers on the Balkan Peninsula: State and changes in the last several years. *Quaternary International*, 415, 33–54. doi:10.1016/j.quaint.2015.10.042

Gądek, B. (2008). The problem of firn-ice patches in the polish tatras as an indicator of climatic fluctuations. *Geographia Polonica*, 81(1), 41–52.

Gajewski, K. (2015). Quantitative reconstruction of Holocene temperatures across the Canadian Arctic and Greenland. *Global and Planetary Change*, 128, 14-23. doi:10.1016/j.gloplacha.2015.02.003

Gallet, J., Domine, F., Zender, C. S., et Picard, G. (2009). Measurement of the specific surface area of snow using infrared reflectance in an integrating sphere at 1310 and 1550 nm. *The Cryosphere*, 3(2), 167-182. doi:10.5194/tc-3-167-2009

Gardner, A., Moholdt, G., Arendt, A., et Wouters, B. (2012). Accelerated contributions of Canada's Baffin and Bylot Island glaciers to sea level rise over the past half century. *The Cryosphere*, 6(5), 1103–1125. doi:10.5194/tc-6-1103-2012

Gardner, A. S., et Sharp, M. (2007). Influence of the Arctic circumpolar vortex on the mass balance of Canadian High Arctic glaciers. *Journal of Climate*, 20(18), 4586-4598. doi:10.1175/JCLI4268.1

Gardner, A. S., et Sharp, M. J. (2010). A review of snow and ice albedo and the development of a new physically based broadband albedo parameterization. *Journal of Geophysical Research: Earth Surface*, 115(F1). doi:10.1029/2009JF001444

Garen, D. C., et Marks, D. (2005). Spatially distributed energy balance snowmelt modelling in a mountainous river basin: Estimation of meteorological inputs and verification of model results. *Journal of Hydrology*, 315(1–4), 126–153. doi:10.1016/j.jhydrol.2005.03.026

Gay, M., et Weiss, J. (1999). Automatic reconstruction of polycrystalline ice microstructure from image analysis: application to the EPICA ice core at Dome Concordia, Antarctica. *Journal of Glaciology*, 45(151), 547-554. doi: 10.3189/S0022143000001416.

Gilbert, G. L., Kanevskiy, M., et Murton, J. B. (2016). Recent advances (2008–2015) in the study of ground ice and cryostratigraphy. *Permafrost and Periglacial Processes*, 27(4), 377-389. doi:10.1002/ppp.1912

Glazirin, G. E., Kodama, Y., et Ohata, T. (2004). Stability of drifting snow-type perennial snow patches. *In Bulletin of glaciological research*, 21, 1–8.

Gold, W. G., et Bliss, L. C. (1995). Water limitations and plant community development in a polar desert. *Ecology*, 76(5), 1558-1568. doi:10.2307/1938157.

Gold, W. G. (1998). The influence of cryptogamic crusts on the thermal environment and temperature relations of plants in a high arctic polar desert, Devon Island, NWT, Canada. *Arctic and Alpine Research*, 30(2), 108-120. doi:10.1080/00040851.1998.12002882

Gooseff, M. N., Barrett, J. E., Adams, B. J., Doran, P. T., Fountain, A. G., Lyons, W. B., McKnight, D. M., Priscu, J. C., Sokol, E. R., Takacs-Vesbach, C., Vandegehuchte, M. L., Virginia, R. A., et Wall, D. H. (2017). Decadal ecosystem response to an anomalous melt season in a polar desert in Antarctica. *Nature Ecology and Evolution*, 1(9), 1334–1338. doi:10.1038/s41559-017-0253-0

Goosse, H., Kay, J. E., Armour, K. C., Bodas-Salcedo, A., Chepfer, H., Docquier, D., ... et Vancoppenolle, M. (2018). Quantifying climate feedbacks in polar regions. *Nature communications*, 9(1), 1-13. doi:10.1038/s41467-018-04173-0

Gouttevin, I., Langer, M., Löwe, H., Boike, J., Proksch, M., et Schneebeli, M. (2018). Observation and modelling of snow at a polygonal tundra permafrost site: spatial variability and thermal implications. *The Cryosphere*, 12(11), 3693-3717. doi:10.5194/tc-12-3693-2018

Gow, A. J. (1969). On the rates of growth of grains and crystals in South Polar firn. *Journal of Glaciology*, 8(53), 241-252. doi: 10.3189/S0022143000031233.

Gray, D. M., et Male, D. H. (1981). *Handbook of Snow: Principles, Processes, Management, and Use*. Toronto, Canada: Pergamon Press.

Grünewald, T., Schirmer, M., Mott, R., et Lehning, M. (2010). Spatial and temporal variability of snow depth and ablation rates in a small mountain catchment. *Cryosphere*, 4(2), 215–225. doi:10.5194/tc-4-215-2010

Guillet, G., et Ravanel, L. (2020). Variations in surface area of six ice aprons in the Mont-Blanc massif since the Little Ice Age. *Journal of Glaciology*, 66(259), 777-789. doi:10.1017/jog.2020.46

Guillet, G., Preunkert, S., Ravanel, L., Montagnat, M., et Friedrich, R. (2021). Investigation of a cold-based ice apron on a high-mountain permafrost rock wall using ice texture analysis and micro-¹⁴C dating: a case study of the Triangle du Tacul ice apron (Mont Blanc massif, France). *Journal of Glaciology*, 1-8. doi:10.1017/jog.2021.65

Haeberli, W., Frauenfelder, R., Kääb, A., et Wagner, S. (2004). Characteristics and potential climatic significance of “miniature ice caps” (crest- and cornice-type low-altitude ice archives). *Journal of Glaciology*, 50(168), 129–136. doi:10.3189/172756504781830330

Hall, K. (1980). Freeze-thaw activity at a nivation site in northern Norway. *Arctic and Alpine Research*, 12(2), 183–194. doi:10.1657/1523-0430(06-026)

Harder, P., Helgason, W. D., et Pomeroy, J. W. (2018). Modeling the Snowpack Energy Balance during Melt under Exposed Crop Stubble. *Journal of Hydrometeorology*, 19(7), 1191-1214. doi:10.1175/JHM-D-18-0039.1

Harder, Phillip, Pomeroy, J. W., et Helgason, W. (2017). Local-Scale Advection of Sensible and Latent Heat During Snowmelt. *Geophysical Research Letters*, 44(19), 9769–9777. doi:10.1002/2017GL074394

Hare, P. G., Thomas, C. D., Topper, T. N., et Gotthardt, R. M. (2012). The archaeology of Yukon ice patches: New artifacts, observations, and insights. *Arctic*, 118-135. doi:10.14430/arctic4188

Hedding, D. W. (2016). Pronival ramparts: A review. *Progress in Physical Geography*, 40(6), 835-855. doi: 10.1177/0309133316678148.

Héron, R. (1979) Computation of snowmelt at a high Arctic site, *Master thesis*, Department of Geography, McMaster University, Hamilton, Ontario.

- Higuchi, K., Iozawa, T., Fujii, Y., et Kodama, H. (1980). Inventory of perennial snow patches in Central Japan. *Geojournal*, 4(4), 303-311. doi:10.1007/BF00219577
- Hirvas, H., Lintinen, P., et Kosloff, P. (2000). An extensive permanent snowfield and the possible occurrence of permafrost in till in the RidnitSohkka area, Finnish Lapland. *Bulletin-Geological Society of Finland*, 47–56. doi: 10.17741/bgsf/72.1-2.003
- Hoffman, M. J., Fountain, A. G., et Achuff, J. M. (2007). 20th-century variations in area of cirque glaciers and glacierets, Rocky Mountain National Park, Rocky Mountains, Colorado, USA. *Annals of Glaciology*, 46, 349–354. doi:10.3189/172756407782871233
- Hoffmann, H., Preunkert, S., Legrand, M., Leinfelder, D., Bohleber, P., Friedrich, R., et Wagenbach, D. (2018). A new sample preparation system for Micro-¹⁴C dating of glacier ice with a first application to a high Alpine ice core from Colle Gnifetti (Switzerland). *Radiocarbon*, 60(2), 517-533. doi:10.1017/RDC.2017.99
- Holland, M. M. (2003). The North Atlantic Oscillation–Arctic Oscillation in the CCSM2 and its influence on Arctic climate variability. *Journal of Climate*, 16(16), 2767-2781. doi:10.1175/1520-0442(2003)016<2767:TNAOOI>2.0.CO;2
- Holmlund, P., et Holmlund, E. S. (2019). Recent climate-induced shape changes of the ice summit of Kebnekaise, Northern Sweden. *Geografiska Annaler, Series A: Physical Geography*, 101(1), 68–78. doi:10.1080/04353676.2018.1542130
- Hrbáček, F., Cannone, N., Kňažková, M., Malfasi, F., Convey, P., et Guglielmin, M. (2020). Effect of climate and moss vegetation on ground surface temperature and the active layer among different biogeographical regions in Antarctica. *Catena*, 190, 104562. doi:10.1016/j.catena.2020.104562
- Huang, Y., Ding, Q., Dong, X., Xi, B., et Baxter, I. (2021). Summertime low clouds mediate the impact of the large-scale circulation on Arctic sea ice. *Communications Earth & Environment*, 2(1), 1-10. doi: 10.1038/s43247-021-00114-w
- Huss, M., et Fischer, M. (2016). Sensitivity of very small glaciers in the Swiss Alps to future climate change. *Frontiers in Earth Science*, 4 (34), 1–17. doi:10.3389/feart.2016.00034

Ishikawa, M. (2003). Thermal regimes at the snow–ground interface and their implications for permafrost investigation. *Geomorphology*, 52(1-2), 105-120. doi:10.1016/S0169-555X(02)00251-9

Ishikawa, M., et Sawagaki, T. (2001). GIS-simulation of the spatial distribution of snow cover and observed ground temperatures in the Daisetsu Mountains, Japan. *Norsk Geografisk Tidsskrift - Norwegian Journal of Geography*, 55(4), 212–218. doi:10.1080/00291950152746540

Jaedicke, C., et Sandvik, A. D. (2002). High resolution snow distribution data from complex Arctic terrain: A tool for model validation. *Natural Hazards and Earth System Sciences*, 2(3–4), 147–155. doi:10.5194/nhess-2-147-2002

Jeffries, M. (1982). The Ward Hunt Ice Shelf, Spring 1982. *Arctic*, 35(4), 542–544. doi:10.14430/arctic2363

Jeffries, M. O., Serson, H. V., Krouse, H. R., et Sackinger, W. M. (1991). Ice physical properties, structural characteristics and stratigraphy in Hobson's Choice Ice Island and implications for the growth history of East Ward Hunt Ice Shelf, Canadian High Arctic. *Journal of Glaciology*, 37(126), 247-260. doi:10.3189/S0022143000007267

Jennings, K. S., Kittel, T. G., et Molotch, N. P. (2018). Observations and simulations of the seasonal evolution of snowpack cold content and its relation to snowmelt and the snowpack energy budget. *The Cryosphere*, 12(5), 1595–1614. doi:10.5194/tc-12-1595-2018

Jia, G. J., Epstein, H. E., et Walker, D. A. (2009). Vegetation greening in the Canadian Arctic related to decadal warming. *Journal of Environmental Monitoring*, 11(12), 2231-2238. doi:10.1039/B911677J

Kalnay, E., Kanamitsu, M., Kistler, R., Collins, W., Deaven, D., Gandin, L., ... et Joseph, D. (1996). The NCEP/NCAR 40-year reanalysis project. *Bulletin of the American meteorological Society*, 77(3), 437-472. doi: 10.1175/1520-0477(1996)077<0437:TNYRP>2.0.CO;2

Kawamura, T. (1990). Nondestructive, three- dimensional density measurements of ice core samples by X ray computed tomography. *Journal of Geophysical Research: Solid Earth*, 95(B8), 12407-12412. doi: 10.1029/JB095iB08p12407.

Kawamura, T., Jeffries, M. O., Tison, J. L., et Krouse, H. R. (2004). Superimposed-ice formation in summer on Ross Sea pack-ice floes. *Annals of Glaciology*, 39, 563-568. doi:10.3189/172756404781814168

Kawashima, K., Yamada, T., et Wakahama, G. (1993). Investigations of internal structure and transformational processes from firn to ice in a perennial snow patch. *Annals of Glaciology*, 18, 117-122. doi:10.3189/S0260305500011368

Kinnard, C., et Lewkowicz, A. G. (2005). Movement, moisture and thermal conditions at a turf-banked solifluction lobe, Kluane Range, Yukon Territory, Canada. *Permafrost and Periglacial Processes*, 16(3), 261-275. doi:10.1002/ppp.530

Kinnard, C., et Lewkowicz, A. G. (2006). Frontal advance of turf-banked solifluction lobes, Kluane Range, Yukon Territory, Canada. *Geomorphology*, 73(3-4), 261-276. doi:10.1016/j.geomorph.2005.06.010

Kňažková, M., Nývlt, D., et Hrbáček, F. (2021). Slope processes connected with snow patches in semi-arid ice-free areas of James Ross Island, Antarctic Peninsula. *Geomorphology*, 373, 107479. doi:10.1016/j.geomorph.2020.107479

Koerner, R. M. (1968). Fabric analysis of a core from the Meighen ice cap, Northwest Territories, Canada. *Journal of Glaciology*, 7(51), 421-430. doi:10.3189/S0022143000020621

Koerner, R. M. (1970a). Some Observations on Superimposition of Ice on the Devon Island Ice Cap, N.W.T. *Geografiska Annaler. Series A, Physical Geography*, 52(1), 57–67. doi:10.1080/04353676.1970.11879808

Koerner, R. M. (1970b). The mass balance of the Devon Island ice cap, Northwest Territories, Canada, 1961-66. *Journal of Glaciology*, 9(57), 325-336. doi:10.3189/S0022143000022863

Koerner, R. M. (2005). Mass balance of glaciers in the Queen Elizabeth Islands, Nunavut, Canada. *Annals of Glaciology*, 42, 417-423. doi:10.3189/172756405781813122

Koerner, R. M., Paterson, W. S. B., et Krouse, H. R. (1973). $\delta^{18}\text{O}$ Profile in Ice formed between the Equilibrium and Firn Lines. *Nature Physical Science*, 245(148), 137-140. doi:10.1038/246421a0

Koerner, R. M., et Paterson, W. S. B. (1974). Analysis of a core through the Meighen Ice Cap, Arctic Canada, and its paleoclimatic implications. *Quaternary Research*, 4(3), 253–263. doi:10.1016/0033-5894(74)90015-5

Kohshima, S., Yoshimura, Y., Seko, K., et Ohata, T. (1994). Albedo reduction by biotic impurities on a perennial snow patch in the Japan alps. *IAHS Publications-Series of Proceedings and Reports-Intern Assoc Hydrological Sciences*, 223(223), 323-330.

Kuhn, M. (1995). The mass balance of very small glaciers. *Zeitschrift Für Gletscherkunde Und Glazialgeologie*, 31, 171–179.

Kunitsky, V. V., Schirrmeyer, L., Grosse, G., et Kienast, F. (2000). Snow patches in nival landscapes and their role for the ice complex formation in the Laptev sea coastal lowlands. *Polarforschung*, 70(1–2), 53–67.

Lacelle, D., St-Jean, M., Lauriol, B., Clark, I. D., Lewkowicz, A., Froese, D. G., Kuehn, S. C., et Zazula, G. (2009). Burial and preservation of a 30,000 year old perennial snowbank in Red Creek valley, Ogilvie Mountains, central Yukon, Canada. *Quaternary Science Reviews*, 28(27–28), 3401–3413. doi:10.1016/j.quascirev.2009.09.013

Langford, Z. L., Gooseff, M. N., et Lampkin, D. J. (2015). Spatiotemporal dynamics of wetted soils across a polar desert landscape. *Antarctic Science*, 27(2), 197-209. doi:10.1017/S0954102014000601

Langway, C. C. (1958). Ice fabrics and the universal stage (Vol. 62). US Army Snow Ice and Permafrost Research Establishment. *Technical Report* 62, 16 pp

Lauriol, B., Carrier, Y., Beaudet, H., et Binda, G. (1986). The residual snow cover in the Canadian Arctic in July: a means to evaluate the regional maximum snow depth in winter. *Arctic*, 309-315. Repéré sur: <http://www.jstor.org/stable/40511027>.

Lecavalier, B. S., Fisher, D. A., Milne, G. A., Vinther, B. M., Tarasov, L., Huybrechts, P., ... et Dyke, A. S. (2017). High Arctic Holocene temperature record from the Agassiz ice cap and Greenland ice sheet evolution. *Proceedings of the National Academy of Sciences*, 114(23), 5952-5957. doi: 10.1073/pnas.1616287114.

Legagneux, L., Cabanes, A., et Dominé, F. (2002). Measurement of the specific surface area of 176 snow samples using methane adsorption at 77 K. *Journal of Geophysical Research: Atmospheres*, 107(D17), ACH-5. doi: 10.1029/2001JD001016

Legland, D., Arganda-Carreras, I., et Andrey, P. (2016). MorphoLibJ: integrated library and plugins for mathematical morphology with ImageJ. *Bioinformatics*, 32(22), 3532-3534. doi: 10.1093/bioinformatics/btw413.

Lehning, M., Bartelt, P., Brown, B., Fierz, C., et Satyawali, P. (2002). A physical SNOWPACK model for the Swiss avalanche warning Part II. Snow microstructure. *Cold Regions Science and Technology*, 35(3), 147–167. doi:10.1016/S0165-232X(02)00073-3

Leigh, J. R., Stokes, C. R., Carr, R. J., Evans, I. S., Andreassen, L. M., et Evans, D. J. A. (2019). Identifying and mapping very small ($<0.5 \text{ km}^2$) mountain glaciers on coarse to high-resolution imagery. *Journal of Glaciology*, 65(254), 873–888. doi:10.1017/jog.2019.50

Lemmen, D. S. (1989). The last glaciation of Marvin Peninsula, northern Ellesmere Island, High Arctic, Canada. *Canadian Journal of Earth Sciences*, 26(12), 2578-2590. doi:10.1139/e89-220

Lemmen, D. S., et England, J. (1992). Multiple glaciations and sea level changes, northern Ellesmere Island, high arctic Canada. *Boreas*, 21(2), 137-152. doi: 10.1111/j.1502-3885.1992.tb00021.x.

Lendzioch, T., Langhammer, J., et Jenicek, M. (2019). Estimating snow depth and leaf area index based on UAV digital photogrammetry. *Sensors*, 19(5), 1027. doi:10.3390/s19051027

Lennihan, R., Chapin, D. M., et Dickson, L. G. (1994). Nitrogen fixation and photosynthesis in high arctic forms of *Nostoc commune*. *Canadian Journal of Botany*, 72(7), 940-945. doi:10.1139/b94-119

Leppäranta, M., Järvinen, O., et Lindgren, E. (2013). Mass and heat balance of snow patches in basen nunatak, Dronning Maud Land, Antarctica, in summer. *Journal of Glaciology*, 59(218), 1093–1105. doi:10.3189/2013JoG12J236

Levy, J. S., Fountain, A. G., Gooseff, M. N., Welch, K. A., et Lyons, W. B. (2011). Water tracks and permafrost in Taylor Valley, Antarctica: Extensive and shallow groundwater

connectivity in a cold desert ecosystem. *Bulletin of the Geological Society of America*, 123(11–12), 2295–2311. doi:10.1130/B30436.1

Lewkowicz, A. G. (1998). Aeolian sediment transport during winter, Black Top Creek, Fosheim Peninsula, Ellesmere Island, Canadian Arctic. *Permafrost and Periglacial Processes*, 9(1), 35–46. doi:10.1002/(sici)1099-1530(199801/03)9:1<35::aid-ppp276>3.0.co;2-1

Lewkowicz, A. G., et Clarke, S. (1998). Late-summer solifluction and active layer depths, Fosheim Peninsula, Ellesmere Island, Canada. In *Proceedings of the 6th International Conference on Permafrost. Centre d'études nordiques, Université Laval* (pp. 641–666). Repéré sur : www.arlis.org/docs/vol1/ICOP/40770716/CD-ROM/Proceedings/PDF001189/099358.pdf

Lewkowicz, A. G., et French, H. M. (1982a). The hydrology of small runoff plots in an area of continuous permafrost, Banks Island, NWT. In *Proceedings, 4th Canadian Permafrost Conf., Calgary* (pp. 151–162). Ottawa: NRC. Repéré sur: pubs.aina.ucalgary.ca/cpc/CPC4-151.pdf

Lewkowicz, A. G., et French, H. M. (1982b). Downslope water movement and solute concentrations within the active layer, Banks Island, NWT. In *Proceedings fourth Canadian permafrost conference, National research council of Canada* (pp. 163–172).

Lewkowicz, A. G., et Harry, D. G. (1991). Internal structure and environmental significance of a perennial snowbank, Melville Island, NWT. *Arctic*, 44(1), 74–82. Repéré sur: <http://www.jstor.org/stable/40511056>.

Lewkowicz, A. G., et Kokelj, S. V. (2002). Slope sediment yield in arid lowland continuous permafrost environments, Canadian Arctic archipelago. *Catena*, 46(4), 261–283. doi:10.1016/S0341-8162(01)00156-4

Lewkowicz, A. G., et Young, K. L. (1990). Hydrology of a perennial snowbank in the continuous permafrost zone, Melville Island, Canada. *Geografiska Annaler*, 72(1), 13–21. doi:10.1080/04353676.1990.11880297

Lewkowicz, A. G., et Young, K. L. (1991). Observations of Aeolian Transport and Niveo-aeolian Deposition at Three Lowland Sites, Canadian Arctic Archipelago. *Permafrost and Periglacial Processes*, 2(3), 197–210. doi:10.1002/ppp.3430020304

- Li, L., et Pomeroy, J. W. (1997). Estimates of threshold wind speeds for snow transport using meteorological data. *Journal of Applied Meteorology*, 36(3), 205–213. doi:10.1175/1520-0450(1997)036<0205:EOTWSF>2.0.CO;2
- Liljedahl, A. K., Boike, J., Daanen, R. P., Fedorov, A. N., Frost, G. V., Grosse, G., Hinzman, L. D., Iijma, Y., Jorgenson, J. C., Matveyeva, N., Necsoiu, M., Raynolds, M. K., Romanovsky, V. E., Schulla, J., Tape, K. D., Walker, D. A., Wilson, C. J., Yabuki, H., et Zona, D. (2016). Pan-Arctic ice-wedge degradation in warming permafrost and its influence on tundra hydrology. *Nature Geoscience*, 9(4), 312–318. doi:10.1038/ngeo2674
- Ling, F., et Zhang, T. (2003). Impact of the timing and duration of seasonal snow cover on the active layer and permafrost in the Alaskan Arctic. *Permafrost and Periglacial Processes*, 14(2), 141-150. doi:10.1002/ppp.445
- Liston, G. E., et Hall, D. K. (1995). An energy-balance model of lake-ice evolution. *Journal of Glaciology*, 41(138), 373-382. doi:10.3189/S0022143000016245
- Liston, G. E., Mcfadden, J. P., Sturm, M., et Pielke, R. A. (2002). Modelled changes in arctic tundra snow, energy and moisture fluxes due to increased shrubs. *Global Change Biology*, 8(1), 17–32. doi:10.1046/j.1354-1013.2001.00416.x
- Liston, G. E., et Sturm, M. (1998). A snow-transport ID.odel for cotnplex terrain. *Journal of Glaciology*, 44(148).
- Liston, G. E., et Sturm, M. (2002). Winter Precipitation Patterns in Arctic Alaska Determined from a Blowing-Snow Model and Snow-Depth Observations. *Journal of Hydrometeorology*, 3(6), 646–659. doi:10.1175/1525-7541(2002)003<0646:WPPIAA>2.0.CO;2
- Li, L., et Pomeroy, J. W. (1997). Estimates of threshold wind speeds for snow transport using meteorological data. *Journal of Applied Meteorology*, 36(3), 205-213. doi:10.1175/1520-0450(1997)036<0205:EOTWSF>2.0.CO;2
- Lyons, J. B., et Mielke, J. E. (1973). Holocene history of a portion of northernmost Ellesmere Island. *Arctic*, 314-323. doi: 10.14430/arctic2930.

- Mackay, J. R. (1981). Active layer slope movement in a continuous permafrost environment, Garry Island, Northwest Territories, Canada. *Canadian Journal of Earth Sciences*, 18(11), 1666-1680. doi:10.1139/e81-154
- Marbouy, D. (1980). An experimental study of temperature-gradient metamorphism. *Journal of Glaciology*, 26(94), 303-312. doi:10.3189/S0022143000010844
- Marsh, P. (2005). Water flow through snow and firn. *Encyclopedia of Hydrological Sciences*, 4, Part 14, 97–123. doi:10.1002/0470848944.hsa167
- Mases, M., Font, D., et Vilaplana, J. M. (1998). Relationship between snowdrift development and drifted snow during a wind episode. *Annals of Glaciology*, 26, 144-148. doi:10.3189/1998AoG26-1-144-148
- Matsuoka, N. (2001). Solifluction rates, processes and landforms: a global review. *Earth-Science Reviews*, 55(1-2), 107-134. doi:10.1016/S0012-8252(01)00057-5
- Maxwell, J. B. (1981). Climatic regions of the Canadian Arctic islands. *Arctic*, 225-240.
- Metcalfe, D. B., Hermans, T. D., Ahlstrand, J., Becker, M., Berggren, M., Björk, R. G., ... et Abdi, A. M. (2018). Patchy field sampling biases understanding of climate change impacts across the Arctic. *Nature ecology & evolution*, 2(9), 1443-1448.doi:10.1038/s41559-018-0612-5
- Meredith, M., Sommerkorn, M., Cassotta, S., Derksen, C., Ekyakin, A., Hollowed, A., ... et Schuur, E. A. (2019). Polar Regions. Chapter 3, IPCC Special Report on the Ocean and Cryosphere in a Changing Climate. Repéré sur: www.ipcc.ch/srocc/
- Meulendyk, T., Moorman, B. J., Andrews, T. D., et MacKay, G. (2012). Morphology and development of ice patches in Northwest Territories, Canada. *Arctic*, 65 43-58. doi:10.14430/arctic4184
- Miller, G. H., Bradley, R. S., et Andrews, J. T. (1975). The glaciation level and lowest equilibrium line altitude in the high Canadian Arctic: maps and climatic interpretation. *Arctic and Alpine Research*, 7(2), 155–168. doi: 10.1080/00040851.1975.12003819
- Mioduszewski, J., Vavrus, S., et Wang, M. (2018). Diminishing Arctic sea ice promotes stronger surface winds. *Journal of Climate*, 31(19), 8101–8119. doi:10.1175/JCLI-D-18-0109.1

Mitchell, R. J., Nelson, F. E., et Nyland, K. E. (2021). Preliminary observations of nivation processes, Cathedral Massif, Northwestern British Columbia, Canada. *Physical Geography*, 1-16. doi:10.1080/02723646.2021.1893142

Montagnat, M., Durand, G., et Duval, P. (2009). Recrystallization processes in granular ice. *Low temperature science*, 68(Supplement), 81-90.

Moreno, A., Bartolomé, M., López-Moreno, J. I., Pey, J., Corella, J. P., García-Orellana, J., ... et García-Ruiz, J. M. (2021). The case of a southern European glacier which survived Roman and medieval warm periods but is disappearing under recent warming. *The Cryosphere*, 15(2), 1157-1172. doi:10.5194/tc-15-1157-2021

Moreau, M., Mercier, D., Laffly, D., et Roussel, E. (2008). Impacts of recent paraglacial dynamics on plant colonization: A case study on Midtre Lovénbreen foreland, Spitsbergen (79 N). *Geomorphology*, 95(1-2), 48-60. doi:10.1016/j.geomorph.2006.07.031

Mortimer, C. A., Sharp, M., et Van Wychen, W. (2018). Influence of recent warming and ice dynamics on glacier surface elevations in the Canadian High Arctic, 1995–2014. *Journal of Glaciology*, 64(245), 450-464. doi:10.1017/jog.2018.37

Mott, R., Egli, L., Grünwald, T., Dawes, N., Manes, C., Bavay, M., et Lehning, M. (2011). Micrometeorological processes driving snow ablation in an Alpine catchment. *The Cryosphere*, 5(4), 1083–1098. doi:10.5194/tc-5-1083-2011

Mott, R., Gromke, C., Grünwald, T., et Lehning, M. (2013). Relative importance of advective heat transport and boundary layer decoupling in the melt dynamics of a patchy snow cover. *Advances in Water Resources*, 55, 88–97. doi:10.1016/j.advwatres.2012.03.001

Mott, R., Daniels, M., et Lehning, M. (2015). Atmospheric flow development and associated changes in turbulent sensible heat flux over a patchy mountain snow cover. *Journal of Hydrometeorology*, 16(3), 1315–1340. doi:10.1175/JHM-D-14-0036.1

Mott, R., Schlögl, S., Dirks, L., et Lehning, M. (2017). Impact of Extreme Land Surface Heterogeneity on Micrometeorology over Spring Snow Cover. *Journal of Hydrometeorology*, 18(10), 2705–2722. doi:10.1175/jhm-d-17-0074.1

Mott, R., Vionnet, V., et Grunewald, T. (2018). The Seasonal Snow Cover Dynamics: Review on Wind-Driven Coupling Processes. *Frontiers in Earth Science*, 6, 197 doi:10.3389/feart.2018.00197

Mott, R., Wolf, A., Kehl, M., Kunstmann, H., Warscher, M., et Grunewald, T. (2019). Avalanches and micrometeorology driving mass and energy balance of the lowest perennial ice field of the Alps: a case study. *The Cryosphere*, 13(4), 1247-1265. doi:10.5194/tc-2018-255

Mueller, D. R., Copland, L., Hamilton, A., et Stern, D. (2008). Examining Arctic ice shelves prior to the 2008 breakup. *Eos, Transactions American Geophysical Union*, 89(49), 502-503. doi.org/10.1029/2008EO490002

Mueller, D. R., Copland, L., et Jeffries, M. O. (2017). Changes in Canadian Arctic ice shelf extent since 1906. In *Arctic ice shelves and ice islands* (pp. 109-148). Springer, Dordrecht. doi:10.1007/978-94-024-1101-0_5

Mueller, D. R., Van Hove, P., Antoniades, D., Jeffries, M. O., et Vincent, W. F. (2009). High Arctic lakes as sentinel ecosystems: Cascading regime shifts in climate, ice cover, and mixing. *Limnology and Oceanography*, 54(6part2), 2371-2385. doi:10.4319/lo.2009.54.6_part_2.2371

Mueller D. R. and Vincent W.F. (2006). Microbial habitat dynamics and ablation control on the Ward Hunt Ice Shelf. *Hydrological Processes*, 20, 857-876. doi: 10.1002/hyp.6113

Mueller, D. R., Vincent, W. F., and Jeffries, M. O. (2003). Break-up of the largest Arctic ice shelf and associated loss of an epishelf lake. *Geophysical Research Letters*, 30(20), 1-4. doi:10.1029/2003GL017931

Müller, F. (1962). Zonation in the accumulation area of the glaciers of Axel Heiberg Island, NWT, Canada. *Journal of Glaciology*, 4(33), 302-311. doi:10.3189/S0022143000027623

Nesje, A., Pilø, L. H., Finstad, E., Solli, B., Wangen, V., Ødegård, R. S., Isaksen, K., Støren, E. N., Bakke, D. I., et Andreassen, L. M. (2012). The climatic significance of artefacts related to prehistoric reindeer hunting exposed at melting ice patches in southern Norway. *Holocene*, 22(4), 485–496. doi:10.1177/0959683611425552

Neumann, N., et Marsh, P. (1998). Local advection of sensible heat in the snowmelt landscape of Arctic tundra. *Hydrological Processes*, 12(10- 11), 1547-1560. doi:10.1002/(SICI)1099-1085(199808/09)12:10/11<1547::AID-HYP680>3.0.CO;2-Z

Noël, B., Van De Berg, W. J., Lhermitte, S., Wouters, B., Schaffer, N., et van den Broeke, M. R. (2018). Six decades of glacial mass loss in the Canadian Arctic Archipelago. *Journal of Geophysical Research: Earth Surface*, 123(6), 1430-1449. doi:10.1029/2017JF004304

Nolan, M., Larsen, C., et Sturm, M. (2015). Mapping snow depth from manned aircraft on landscape scales at centimeter resolution using structure-from-motion photogrammetry. *The Cryosphere*, 9(4), 1445-1463. doi:10.5194/tc-9-1445-2015

Nyberg, R. (1986). Freeze-thaw activity at snowpatch sites. A progress report of studies in N. and S. Sweden. *Geografiska Annaler: Series A, Physical Geography*, 68(3), 207-211. doi:10.1080/04353676.1986.11880174

Nyland, K. E., et Nelson, F. E. (2020). Time- transgressive cryoplanation terrace development through nivation- driven scarp retreat. *Earth Surface Processes and Landforms*, 45(3), 526-534. doi :10.1002/esp.4751

Obleitner, F., et Lehning, M. (2004). Measurement and simulation of snow and superimposed ice at the Kongsvegen glacier, Svalbard (Spitzbergen). *Journal of Geophysical Research: Atmospheres*, 109(4). doi:10.1029/2003jd003945

Ødegård, R. S., Nesje, A., Isaksen, K., Andreassen, L. M., Eiken, T., Schwikowski, M., et Uglietti, C. (2017). Climate change threatens archaeologically significant ice patches: insights into their age, internal structure, mass balance and climate sensitivity. *The Cryosphere*, 11(1), 17-32. doi:10.5194/tc-11-17-2017

Oh, S. G., Sushama, L., et Teufel, B. (2020). Arctic precipitation and surface wind speed associated with cyclones in a changing climate. *Climate Dynamics*, 55(11), 3067-3085. doi: 10.1007/s00382-020-05425-w

Ohmura, A. (1984). Comparative energy balance study for arctic tundra, sea surface glaciers and boreal forests. *Geojournal*, 8(2), 221-228.

Oke, T.R. (1987). *Boundary layer climates* (second edition). London: Routledge, 435 pp.

Oksanen, J., Blanchet, F. G., Kindt, R., Legendre, P., Minchin, P. R., O'Hara, R. B., ... et Wagner, H. (2015). Vegan community ecology package: ordination methods, diversity analysis and other functions for community and vegetation ecologists. *R package ver*, 2-3. Repéré sur: cran.r-project.org/web/packages/vegan/index.html

Oliver, J. E. (Ed.). (2008). *Encyclopedia of world climatology*. Springer Science & Business Media.

Olsen, M. S., Callaghan, T. V., Reist, J. D., Reiersen, L. O., Dahl-Jensen, D., Granskog, M. A., ... et Walsh, J. (2011). The changing Arctic cryosphere and likely consequences: An overview. *Ambio*, 40(1), 111-118. doi:10.1007/s13280-011-0220-y

Østrem, G. (1963). Comparative Crystallographic Studies on Ice from Ice-Cored Moraines, Snow-Banks and Glaciers. *Geografiska Annaler*, 45(4), 210–240. doi:10.1080/20014422.1963.11881029

Ostwald, W. (1900). Über die vermeintliche Isomerie des roten und gelben Quecksilberoxyds und die Oberflächenspannung fester Körper. *Zeitschrift für physikalische Chemie*, 34(1), 495-503. doi: 10.1515/zpch-1900-3431

Paquette, M., Fortier, D., Lafrenière, M., et Vincent, W. F. (2020a). Periglacial slopewash dominated by solute transfers and subsurface erosion on a High Arctic slope. *Permafrost and Periglacial Processes*, 31(4), 472-486. doi:10.1002/ppp.2066

Paquette, M., Fortier, D., et Lamoureux, S. F. (2020b). Cryostratigraphical studies of ground ice formation and distribution in a High Arctic polar desert landscape, Resolute Bay, Nunavut. *Canadian Journal of Earth Sciences*, 1–48. doi:10.1139/cjes-2020-0134

Paquette, M., Fortier, D., Mueller, D. R., Sarrazin, D., et Vincent, W. F. (2015). Rapid disappearance of perennial ice on Canada's most northern lake. *Geophysical Research Letters*, 42(5), 1433-1440. doi:10.1002/2014GL062960.Received

Paquette, M., Fortier, D., et Vincent, W. F. (2017). Water tracks in the High Arctic: a hydrological network dominated by rapid subsurface flow through patterned ground. *Arctic Science*, 3(2), 334–353. doi:10.1139/as-2016-0014

- Paquette, M., Fortier, D., et Vincent, W. F. (2018). Hillslope water tracks in the High Arctic: Seasonal flow dynamics with changing water sources in preferential flow paths. *Hydrological Processes*, 32(8), 1077–1089. doi:10.1002/hyp.11483
- Park, H., Fedorov, A. N., Zheleznyak, M. N., Konstantinov, P. Y., et Walsh, J. E. (2015). Effect of snow cover on pan-Arctic permafrost thermal regimes. *Climate Dynamics*, 44(9), 2873-2895. doi:10.1007/s00382-014-2356-5
- Parr, C., Sturm, M., et Larsen, C. (2020). Snowdrift Landscape Patterns: An Arctic Investigation. *Water Resources Research*, 56(12). doi:10.1029/2020WR027823
- Paterson, W. S. B. (1969). The Meighen Ice Cap, Arctic Canada: Accumulation, Ablation and Flow. *Journal of Glaciology*, 8(54), 341–352. doi:10.3189/s0022143000026939
- Paterson, W. S. B. (1994). *The Physics of Glaciers*, 3rd ed., 480 pp., Pergamon, New York.
- Pilø, L. H., Barrett, J. H., Eiken, T., Finstad, E., Grønning, S., Post-Melbye, J. R., ... et Ødegård, R. S. (2021). Interpreting archaeological site-formation processes at a mountain ice patch: A case study from Langfonne, Norway. *The Holocene*, 31(3), 469-482. doi:10.1177/0959683620972775
- Pohl, S., Marsh, P., et Liston, G. E. (2006). Spatial-temporal variability in turbulent fluxes during spring snowmelt. *Arctic, Antarctic, and Alpine Research*, 38(1), 136–146. doi:10.1657/1523-0430(2006)038[0136:SVITFD]2.0.CO;2
- Pohl, S., Marsh, P., et Liston, G. E. (2006). Spatial-temporal variability in turbulent fluxes during spring snowmelt. *Arctic, Antarctic, and Alpine Research*, 38(1), 136–146. doi:10.1657/1523-0430(2006)038[0136:SVITFD]2.0.CO;2
- Poirier, M., Gauthier, G., et Domine, F. (2019). What guides lemmings movements through the snowpack?. *Journal of Mammalogy*, 100(5), 1416-1426. doi:10.1093/jmammal/gyz129
- Pomeroy, J. W. (1989). A process- based model of snow drifting. *Annals of Glaciology*, 13, 237–240. doi:10.3189/S0260305500007965
- Pomeroy, J. W., et Gray, D. M. (1990). Saltation of snow. *Water Resources Research*, 26(7), 1583–1594. doi:10.1029/WR026i007p01583

- Pomeroy, J. W., et Brun, E. (2001). Physical properties of snow. *Snow ecology: An interdisciplinary examination of snow-covered ecosystems*, 45, 118.
- Pomeroy, J. W., Marsh, P., et Gray, D. M. (1997). Application of a distributed blowing snow model to the Arctic. *Hydrological Processes*, 11(11), 1451–1464. doi:10.1002/(sici)1099-1085(199709)11:11<1451::aid-hyp449>3.3.co;2-h
- Pope, S., Copland, L., and Alt, B. (2017). Recent changes in sea ice plugs along the northern Canadian Arctic Archipelago. *Arctic ice shelves and ice islands*, 317-342.
- Post, E., Alley, R. B., Christensen, T. R., Macias-Fauria, M., Forbes, B. C., Gooseff, M. N., ... et Wang, M. (2019). The polar regions in a 2 C warmer world. *Science advances*, 5(12), eaaw9883. doi: 10.1126/sciadv.aaw9883. doi:10.1007/978-94-024-1101-0_12
- Prowse, T., Alfredsen, K., Beltaos, S., Bonsal, B., Duguay, C., Korhola, A., ... et Weyhenmeyer, G. A. (2011). Past and future changes in Arctic lake and river ice. *Ambio*, 40(1), 53-62. doi:10.1007/s13280-011-0216-7
- Pushkareva, E., Johansen, J. R., et Elster, J. (2016). A review of the ecology, ecophysiology and biodiversity of microalgae in Arctic soil crusts. *Polar Biology*, 39(12), 2227-2240. doi:10.1007/s00300-016-1902-5
- Ragle, R. H., Blair, R. G., et Persson, L. E. (1960). Ice core studies of ward hunt ice shelf. *Journal of Glaciology*, 19(604). doi:10.3189/S0022143000028562
- Rapp, A., et Nyberg, R. (1988). Mass movements, nivation processes and climatic fluctuations in northern Scandinavian mountains. *Norsk Geografisk Tidsskrift*, 42(4), 245–253. doi:10.1080/00291958808552207
- Reimer, P. J., Bard, E., Bayliss, A., Beck, J. W., Blackwell, P. G., Ramsey, C. B., ... et Van Der Plicht, J. (2013). IntCal13 and Marine13 radiocarbon age calibration curves 0–50,000 years cal BP. *radiocarbon*, 55(4), 1869-1887. doi: 10.2458/azu_js_rc.55.16947
- Rigol-Sanchez, J. P., Stuart, N., et Pulido-Bosch, A. (2015). ArcGeomorphometry: a toolbox for geomorphometric characterisation of DEMs in the ArcGIS environment. *Computers & Geosciences*, 85, 155-163. doi:10.1016/j.cageo.2015.09.020

Royer, A., Domine, F., Roy, A., Langlois, A., Davesne, G., Royer, A., Domine, F., Roy, A., et Langlois, A. (2021). New northern snowpack classification linked to vegetation cover on a latitudinal mega-transect across northeastern Canada. *Écoscience*, 00(00), 1–18. doi:10.1080/11956860.2021.1898775

Sakai, H., Ura, Y., Nakano, T., Iida, H., et Muroi, K. (2006). Study of the internal structure of the Kuranosuke snow patch in central Japan using ground penetrating radar survey. *Bulletin of Glaciological Research*, 77–84. Repéré sur: web.seppyo.org/bgr/pdf/23/BGR23P77.pdf

Sato, A., Takahashi, S., Naruse, R., et Wakahama, G. (1984). Ablation and heat balance of the Yukikabe snow patch in the Daisetsu mountains, Hokkaido, Japan. *Annals of Glaciology*, 5, 122-126. doi:10.3189/1984AoG5-1-122-126

Schiffer, C., et Stephenson, R. (2018). Regional crustal architecture of Ellesmere Island, Arctic Canada. *Geological Society Special Publication*, 460(1), 19–32. doi:10.1144/sp460.8

Schimel, J. P., Bilbrough, C., et Welker, J. M. (2004). Increased snow depth affects microbial activity and nitrogen mineralization in two Arctic tundra communities. *Soil Biology and Biochemistry*, 36(2), 217-227. doi:10.1016/j.soilbio.2003.09.008

Schirmer, M., et Pomeroy, J. W. (2020). Processes governing snow ablation in alpine terrain—detailed measurements from the Canadian Rockies. *Hydrology and Earth System Sciences*, 24(1), 143–157. doi: 10.5194/hess-24-143-2020

Schlögl, S., Lehning, M., et Mott, R. (2018). How are turbulent sensible heat fluxes and snow melt rates affected by a changing snow cover fraction? *Frontiers in Earth Science*, 6, 1–13. doi:10.3389/feart.2018.00154

Serrano, E., González-Trueba, J. J., Sanjosé, J. J., et Del Río, L. M. (2011). Ice patch origin, evolution and dynamics in a temperate high mountain environment: The Jou Negro, Picos de Europa (NW Spain). *Geografiska Annaler, Series A: Physical Geography*, 93(2), 57–70. doi:10.1111/j.1468-0459.2011.00006.x

Serreze, M. C., et Barry, R. G. (2014). *The Arctic climate system*. Cambridge University Press.

Serreze, M. C., Raup, B., Braun, C., Hardy, D. R., et Bradley, R. S. (2017). Rapid wastage of the Hazen Plateau ice caps, northeastern Ellesmere Island, Nunavut, Canada. *The Cryosphere*, 11(1), 169–177. doi:10.5194/tc-11-169-2017

Shi, F., Yang, B., Ljungqvist, F. C., et Yang, F. (2012). Multi-proxy reconstruction of Arctic summer temperatures over the past 1400 years. *Climate Research*, 54(2), 113-128. doi:10.3354/cr01112

Shumskii, P.A. 1964. *Ground (subsurface) ice*. National Research Council of Canada, Technical Translation 1130.

Shur, Y., French, H. M., Bray, M. T., et Anderson, D. A. (2004). Syngenetic permafrost growth: cryostratigraphic observations from the CRREL Tunnel near Fairbanks, Alaska. *Permafrost and Periglacial Processes*, 15(4), 339-347. doi:10.1002/ppp.486

Siddiqui, R., Lashari, B., and Skogerboe, G. V. (1996). Converting a fabricated cutthroat flume into a discharge measuring instrument (No. H019735). *International Water Management Institute*. Repéré sur : <http://publications.iwmi.org/pdf/H019735.pdf>

Smith, M. W., et Burn, C. R. (1987). Outward flux of vapour from frozen soils at Mayo, Yukon, Canada: results and interpretation. *Cold Regions Science and Technology*, 13(2), 143-152. doi:10.1016/0165-232X(87)90052-8

Smith, S. L., Throop, J., et Lewkowicz, A. G. (2012). Recent changes in climate and permafrost temperatures at forested and polar desert sites in northern Canada. *Canadian Journal of Earth Sciences*, 49(8), 979–986. doi:10.1139/e2012-015

Sommerfeld, R. A., et LaChapelle, E. (1970). The classification of snow metamorphism. *Journal of Glaciology*, 9(55), 3-18. doi:10.3189/S0022143000026757

Spektor, V. B., Spektor, V. V., et Bakulina, N. T. (2011). Buried snow in the Lena-Amga Plain. *Earth Cryosphere*, 15(4), 16-21. Repéré sur: www.izdatgeo.ru/pdf/krion/2011-4/16_eng.pdf

Stephani, E., Fortier, D., Shur, Y., Fortier, R., et Doré, G. (2014). A geosystems approach to permafrost investigations for engineering applications, an example from a road stabilization experiment, Beaver Creek, Yukon, Canada. *Cold Regions Science and Technology*, 100, 20-35. doi:10.1016/j.coldregions.2013.12.006

Strömquist, L. (1985). Geomorphic impact of snowmelt on slope erosion and sediment production. *Zeitschrift für Geomorphologie*, 29(2), 129-138. Repéré sur: www.researchgate.net/publication/285578055_Geomorphic_impact_of_snowmelt_on_slope_erosion_and_sediment_production

Stuefer, S. L., Kane, D. L., et Dean, K. M. (2020). Snow water equivalent measurements in remote Arctic Alaska watersheds. *Water Resources Research*, 56(4). doi:10.1029/2019WR025621

Stuiver, M., Reimer, P. J., et Reimer, R. W. 2021. CALIB 8.2, Repéré sur <http://calib.org>, accessed 2021-5-28

St-Onge, D. A., et Gullentops, F. (2005). Morphodynamics of Cold High Latitude Semiarid Regions: The Example of Ellef Ringnes Island, Nunavut. *Géographie Physique et Quaternaire*, 59(2-3), 103. doi:10.7202/014749ar

Sturm, M., et Benson, C. S. (1997). Vapor transport, grain growth and depth-hoar development in the subarctic snow. *Journal of Glaciology*, 43(143), 42-59. doi:10.3189/s0022143000002793

Sturm, M., Holmgren, J., König, M., et Morris, K. (1997). The thermal conductivity of seasonal snow. *Journal of Glaciology*, 43(143), 26-41. doi:10.3198/1997JoG43-143-26-41

Sturm, M., Holmgren, J., et Liston, G. E. (1995). A seasonal snow cover classification system for local to global applications. *Journal of Climate*, 8(5), 1261-1283. doi: 10.1175/1520-0442(1995)008<1261:ASSCCS>2.0.CO;2

Sturm, M., et Johnson, J. B. (1991). Natural convection in the subarctic snow cover. *Journal of Geophysical Research: Solid Earth*, 96(B7), 11657-11671. doi:10.1029/91JB00895

Sturm, M., et Johnson, J. B. (1992). Thermal conductivity measurements of depth hoar. *Journal of Geophysical Research: Solid Earth*, 97(B2), 2129-2139. doi:10.1029/91JB02685

Sturm, M., Liston, G. E., Benson, C. S., et Holmgren, J. (2001). Characteristics and Growth of a Snowdrift in Arctic Alaska, U.S.A. *Arctic, Antarctic, and Alpine Research*, 33(3), 319–329. doi:10.1080/15230430.2001.12003436

Sturm, M., Perovich, D. K., et Holmgren, J. (2002). Thermal conductivity and heat transfer through the snow on the ice of the Beaufort Sea. *Journal of Geophysical Research: Oceans*, 107(C10), SHE-19. doi:10.1029/2000JC000409

Tabler, R. D., 1975: Estimating the transport and evaporation of blowing snow. Proc. Symp. on Snow Management on the Great Plains, Bismarck, ND, *Great Plains Agricultural Council Publ.* 73, 85–104

Taillandier, A. S., Domine, F., Simpson, W. R., Sturm, M., et Douglas, T. A. (2007). Rate of decrease of the specific surface area of dry snow: Isothermal and temperature gradient conditions. *Journal of Geophysical Research: Earth Surface*, 112(F3). doi:10.1029/2006JF000514

Taylor, K. E., Stouffer, R. J., et Meehl, G. A. (2012). An overview of CMIP5 and the experiment design. *Bulletin of the American meteorological Society*, 93(4), 485-498. doi:10.1175/BAMS-D-11-00094.1

Thomas, D. S. (Ed.). (2011). *Arid zone geomorphology: process, form and change in drylands*. John Wiley & Sons.

Thorn, C. E. (1988). Nivation: a geomorphic Chimera. Dans M. J. Clark (dir.), *Advances in Periglacial Geomorphology* (p. 3-31). New York, É.-U.: Wiley

Thorn, C. E. (1978). the Geomorphic Role of Snow. *Annals of the Association of American Geographers*, 68(3), 414–425. doi:10.1111/j.1467-8306.1978.tb01205.x

Thorsteinsson, T., Kipfstuhl, J., Eicken, H., Johnsen, S. J., et Fuhrer, K. (1995). Crystal size variations in Eemian-age ice from the GRIP ice core, central Greenland. *Earth and Planetary Science Letters*, 131(3-4), 381-394. doi:10.1016/0012-821X(95)00031-7

Tomczyk, A. M., Ewertowski, M. W., Stawska, M., et Rachlewicz, G. (2019). Detailed alluvial fan geomorphology in a high-arctic periglacial environment, Svalbard: application of unmanned aerial vehicle (UAV) surveys. *Journal of Maps*, 15(2), 460-473. doi:10.1080/17445647.2019.1611498

Trabant, D., et Benson, C. (1972). Field experiments on the development of depth hoar. *Geological Society of America Memoir*, 135, 309-322. doi:10.1130/MEM135-p309

Trettin, H., (ed.), 1991. Geology of the Innuitian Orogen and Arctic Platform of Canada and Greenland. *Geological Survey of Canada*, Ottawa, Ontario.

van Everdingen, R. (1998). (revised May 2005) Multi-language glossary of permafrost and related ground-ice terms. National Snow and Ice Data Center/World Data Center for Glaciology, Boulder, CO. Repéré sur: nsidc.org/fgdc/glossary

Verpaelst, M., Fortier, D., Kanevskiy, M., Paquette, M., et Shur, Y. (2017). Syngenetic dynamic of permafrost of a polar desert solifluction lobe, Ward Hunt Island, Nunavut. *Arctic Science*, 3(2), 301–319. doi:10.1139/as-2016-0018

Vincent, W. F. (2020). Arctic climate change: Local impacts, global consequences, and policy implications. In *The Palgrave handbook of Arctic policy and politics* (pp. 507-526). Palgrave Macmillan, Cham. doi:10.1007/978-3-030-20557-7_31

Vincent, W. F., et Boike, J. (2019). Understanding the terrestrial effects of Arctic sea ice decline. In *Eos: Earth & Space News* (vol 100). doi: 10.1029/2019EO128471.

Vincent, W. F., Callaghan, T. V., Dahl-Jensen, D., Johansson, M., Kovacs, K. M., Michel, C., ... et Sharp, M. (2011a). Ecological implications of changes in the Arctic cryosphere. *Ambio*, 40(1), 87-99. doi:10.1007/s13280-011-0218-5

Vincent, W. F., Fortier, D., Lévesque, E., Boulanger-Lapointe, N., Tremblay, B., Sarrazin, D., ... et Mueller, D. R. (2011b). Extreme ecosystems and geosystems in the Canadian High Arctic: Ward Hunt Island and vicinity. *Ecoscience*, 18(3), 236-261. doi:10.2980/18-3-3448

Vincent, W. F., et Mueller, D. (2020). Witnessing ice habitat collapse in the Arctic. *Science*, 370(6520), 1031-1032. doi: 10.1126/science.abe4491.

Vionnet, V., Brun, E., Morin, S., Boone, A., Faroux, S., Le Moigne, P., Martin, E., et Willemet, J. M. (2012). The detailed snowpack scheme Crocus and its implementation in SURFEX v7.2. *Geoscientific Model Development*, 5(3), 773–791. doi:10.5194/gmd-5-773-2012

Vionnet, V., Guyomarc'h, G., Naaim Bouvet, F., Martin, E., Durand, Y., Bellot, H., Bel, C., et Puglièse, P. (2013). Occurrence of blowing snow events at an alpine site over a 10-year period: Observations and modelling. *Advances in Water Resources*, 55, 53–63. doi:10.1016/j.advwatres.2012.05.004

Wadham, J. L., et Nuttall, A. M. (2002). Multiphase formation of superimposed ice during a mass-balance year at a maritime high-Arctic glacier. *Journal of Glaciology*, 48(163), 545-551. doi:10.3189/172756502781831025

Wakahama, G. (1975). Metamorphism from snow to firn and ice in a small snow patch on Mt. Daisetsu, Hokkaido, Japan. *IAHS-AISH Publ.*, 104, 347-350. Repéré sur: http://hydrologie.org/redbooks/a104/iahs_104_0347.pdf

Walker, D. A., Billings, W. D., et De Molenaar, J. G. (2001). Snow-vegetation interactions in tundra environments. *Snow ecology*, 266, 324. Repéré sur: www.geobotany.org/library/pubs/WalkerDA2001_SnowEcol_ch6_266.pdf

Warren, S. G. (1982). Optical properties of snow. *Reviews of Geophysics*, 20(1), 67-89. doi:10.1029/RG020i001p0006

Washburn, A. L. (1980). *Geocryology: a survey of periglacial processes and environments*. Edward Arnold, London. 406 pp.

Washburn, A. L. (1999). A High Arctic frost- creep/gelifluction slope, 1981–89: Resolute Bay, Cornwallis Island, Northwest Territories, Canada. *Permafrost and Periglacial Processes*, 10(2), 163-186. doi: 10.1002/(SICI)1099-1530(199904/06)10:2<163::AID-PPP315>3.0.CO;2-B.

Watanabe, T. (1988). Studies of snow accumulation and ablation on perennial snow patches in the mountains of Japan. *Progress in Physical Geography*, 12(4), 560-581. doi:10.1177/030913338801200404

Watson, A., Davison, R. W., et French, D. D. (1994). Summer snow patches and climate in northeast Scotland, UK. *Arctic and Alpine Research*, 26(2), 141–151. doi:10.2307/1551777

Weijers, S., Wagner-Cremer, F., Sass-Klaassen, U., Broekman, R., et Rozema, J. (2013). Reconstructing High Arctic growing season intensity from shoot length growth of a dwarf shrub. *The Holocene*, 23(5), 721-731. doi:10.1177/0959683612470178

Weiss, A. 2001. Topographic position and landforms analysis. In Poster presentation, ESRI user conference, San Diego, CA (Vol. 200). Repéré sur : www.jennessent.com/downloads/tpi-poster-tnc_18x22.pdf

- Werner, J. P., Divine, D. V., Charpentier Ljungqvist, F., Nilsen, T., et Francus, P. (2018). Spatio-temporal variability of Arctic summer temperatures over the past 2 millennia. *Climate of the Past*, 14(4), 527-557. doi: 10.5194/cp-14-527-2018.
- Westermann, S., Lüers, J., Langer, M., Piel, K., et Boike, J. (2009). The annual surface energy budget of a high-arctic permafrost site on Svalbard, Norway. *The Cryosphere*, 3(2), 631–680. doi:10.5194/tcd-3-631-2009
- White, A., et Copland, L. (2018). Area change of glaciers across Northern Ellesmere Island, Nunavut, between ~1999 and ~2015. *Journal of Glaciology*, 64(246), 609–623. doi:10.1017/jog.2018.49
- Wilkinson, T. J., et Bunting, B. T. (1975). Overland transport of sediment by rill water in a periglacial environment in the Canadian High Arctic. *Geografiska Annaler: Series A, Physical Geography*, 57(1-2), 105-116. doi:10.1080/04353676.1975.11879908.
- Wolken, G. J., England, J. H., and Dyke, A. S. (2008). Changes in late-Neoglacial perennial snow/ice extent and equilibrium-line altitudes in the Queen Elizabeth Islands, *Arctic Canada. Holocene*, 18(4), 615–627. doi:10.1177/0959683608089215
- Woo, M. K. (2012). *Permafrost Hydrology*. New York, É.-U. : Springer Berlin Heidelberg.
- Woo, M. K., Arain, M. A., Mollinga, M., et Yi, S. (2004). A two- directional freeze and thaw algorithm for hydrologic and land surface modelling. *Geophysical Research Letters*, 31(12). doi:10.1029/2004GL019475
- Woo, M. K., Heron, R., et Marsh, P. (1982). Basal ice in high arctic snowpacks. *Arctic and Alpine Research*, 14(3), 251–260. doi:10.2307/1551157
- Woo, M. K., Heron, R., Marsh, P., et Steer, P. (1983). Comparison of weather station snowfall with winter snow accumulation in High Arctic basins. *Atmosphere-Ocean*, 21(3), 312-325. doi: 10.1080/07055900.1983.9649171)
- Woo, M. K., et Young, K. L. (2003). Hydrogeomorphology of Patchy Wetlands in the High Arctic, Polar Desert Environment. *Wetlands*, 23(2), 291–309. doi:10.1672/8-20

- Woo, M. K., et Young, K. L. (2006). High Arctic wetlands: their occurrence, hydrological characteristics and sustainability. *Journal of Hydrology*, 320(3-4), 432-450. doi:10.1016/j.jhydrol.2005.07.025
- Woo, M. K., et Young, K. L. (2014). Disappearing semi-permanent snow in the High Arctic and its consequences. *Journal of Glaciology*, 60(219), 192–200. doi:10.3189/2014JoG13J150
- Woo, M. K. (1982). Upward flux of vapor from frozen materials in the High Arctic. *Cold Regions Science and Technology*, 5, 269–274. doi:10.1016/0165-232X(82)90020-9
- Woo, M. K. (1983). Hydrology of a Drainage Basin in the Canadian High Arctic. *Annals of the Association of American Geographers*, 73(4), 577–596. doi:10.1111/j.1467-8306.1983.tb01860.x
- Woo, M. K., et Steer, P. (1982). Occurrence of surface flow on arctic slopes, southwestern Cornwallis Island. *Canadian Journal of Earth Science*, 19, 2368–2377. doi:10.1139/e82-206
- Woo, M. K., et Dubreuil, M. A. (1985). Empirical relationship between dust content and Arctic snow albedo. *Cold Regions Science and Technology*, 10(2), 125–132. doi:10.1016/0165-232X(85)90024-2
- Wrona, F., Johansson, M., M. Culp, J., Myers-smith, I. H., Prowse, T. D., Vincent, W. F., et Wookey, P. A. (2016). Transitions in Arctic ecosystems: Ecological implications of a changing hydrological regime. *Journal of Geophysical Research: Biogeosciences*, 121(3), 650–674. doi:10.1002/2015JG003133.Received
- Yamamoto, K., et Yoshida, M. (1987). Impulse radar sounding of fossil ice within the Kuranosuke perennial snow patch, Central Japan. *Annals of Glaciology*, 9, 218–220. doi:10.3189/S0260305500000653
- Yosida, Z. (1955). Physical Studies on Deposited Snow. I.; Thermal Properties. *Contributions from the Institute of Low Temperature Science*, 7, 19-74. Repéré sur: hdl.handle.net/2115/20216
- Young, K. L., Brown, L., et Labine, C. (2018). Snow cover variability at Polar Bear Pass, Nunavut. *Arctic Science*, 4(4), 669-690. doi:10.1139/as-2017-0016

Young, K. L., et Lewkowicz, A. G. (1990). Surface energy balance of a perennial snowbank, Melville Island, Northwest Territories, Canada. *Arctic and Alpine Research*, 22(3), 290-301. doi:10.2307/1551592.

Young, K. L., Scheffel, H. A., Abnizova, A., et Siferd, J. R. (2017). Spatial and temporal dynamics of groundwater flow across a wet meadow, Polar Bear Pass, Bathurst Island, Nunavut. *Permafrost and Periglacial Processes*, 28(2), 405-419. doi:10.1002/ppp.1931.

Young, K. L., Woo, M. K., et Edlund, S. A. (1997). Influence of local topography, soils, and vegetation on microclimate and hydrology at a high Arctic site, Ellesmere Island, Canada. *Arctic and Alpine Research*, 29(3), 270-284. doi:10.1080/00040851.1997.12003245

Zhang, T., Osterkamp, T. E., et Starnes, K. (1996). Influence of the depth hoar layer of the seasonal snow cover on the ground thermal regime. *Water Resources Research*, 32(7), 2075-2086. doi:10.1029/96WR00996

Zhang, W., Witharana, C., Liljedahl, A. K., et Kanevskiy, M. (2018). Deep convolutional neural networks for automated characterization of arctic ice-wedge polygons in very high spatial resolution aerial imagery. *Remote Sensing*, 10(9), 1487. doi:10.3390/rs10091487

Zhao, B., et Wang, J. (2016). 3D quantitative shape analysis on form, roundness, and compactness with μ CT. *Powder technology*, 291, 262-275. doi: 10.1016/j.powtec.2015.12.02

